The Discovery and Characterization of Methane-bearing Brown Dwarfs and the Definition of the T Spectral Class

Thesis by
Adam Jonathan Burgasser

In Partial Fulfillment of the Requirements
for the Degree of
Doctor of Philosophy

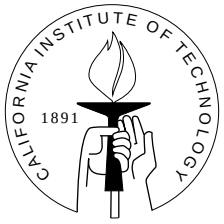

California Institute of Technology
Pasadena, California

2002
(Defended August 24, 2001)

Abstract

I present the discovery of 18 T dwarfs, brown dwarfs exhibiting CH_4 absorption analogous to Gliese 229B, identified in the Two Micron All Sky Survey. Follow-up spectroscopic observations reveal the presence of strong H_2O and CH_4 bands in these objects, as well as broadened Na I and K I absorption in the red optical; fine lines of K I, Cs I, and Rb I; and FeH absorption at 9896 Å. Three objects are analyzed in detail; the widely-separated companion brown dwarf Gliese 570D, the coolest known brown dwarf with $T_{eff} = 810\pm45$ K; the active T dwarf 2MASS 1237+6526, whose unique and steady Hα emission may be the result of Roche-lobe overflow accretion from a closely-separated companion; and 2MASS 0559-1404, the brightest T dwarf currently known, which appears to be overluminous but unresolved in HST images. The variation in spectral features amongst these objects and those identified by the Sloan Digital Sky Survey have been used to derive a near-infrared spectral classification scheme, tied to the observed strengths of H_2O and CH_4 bands, color ratios, and K-band spectral morphology. The grid of subclasses segregates the currently known population into seven distinct groups, ranging from T1 V to T8 V. I show that the possible presence of CH_4 in the L7 V DENIS 0205-1159AB argues for few subtypes between the latest known L dwarfs and the earliest T dwarfs. One peculiar object, 2MASS 0937+2931, has a highly suppressed K-band peak, likely due to increased H_2 opacity in a high-gravity or low-metallicity atmosphere. Examination of absolute brightness and effective temperature across the L/T transition indicates rapid evolution of spectral features, possibly linked to heterogenous cloud coverage as condensibles rain out of the photosphere. Finally, I have used the T dwarf search samples to constrain the substellar field mass function. Through rigorous analysis of selection biases and Monte Carlo simulations, I show that my results are consistent with a power-law mass function scaling as $0.5 < \alpha < 1.0$, consistent with young stellar cluster surveys but significantly less than current estimates in the field.

Acknowledgements

To have great poets, there must be great audiences too.
Walt Whitman, *Notes Left Over, Ventures on an Old Theme*

Despite what the particle physicists would tell you, good science does not derive from a vacuum, and I am indebted to many people for the work presented here, and some for maintaining my sanity while doing it.

First and foremost are my parents, Marcia and Albert, who passed on their collective intelligence both genetically and through excellent parenting; who raised me to ask that daunting question "Why?" and to seek out the answers in my own way. I cannot thank them enough for their love, for making me do my homework, for challenging me without pushing me, and for seeking out truth in life. It is with great pride that my father has followed in my footsteps and become an astronomer just like his son. I only hope someday I may do as well with my own children.

My advisors, Michael Brown and J. Davy Kirkpatrick, have been the yin and yang of my research education. The former took me on as a wandering graduate student with no direction or office to speak of, and kept me even when I decided not to be a Kuiper Belt astronomer. Perhaps the most important thing he has taught me is to look at the big picture — why do that observation, what do we learn, how is this interesting — questions that have helped me maintain focus in a rapidly developing field. Mike also taught me how to observe, which was no small feat for the mechanically un-inclined, and I will always follow his personal credo, "Publish early, publish often." Davy is above and beyond the expert in the field of cool stars and brown dwarfs, and I only hope that in the two years of this project I have gained half of his insight. Davy is an overly modest man, but those of us fortunate enough to have worked with him know his value. His attention to detail is par none, reflected in the fact that his publications are among the classical, most-referenced works in the field. I am the first student Davy has taken on, and I hope for the sake of the field I am not the last. I am truly fortunate to have both of these men as my advisors.

I would like to extend my sincere gratitude to the members of my thesis committee past and present — Mike Brown, Peter Goldreich, Lynne Hillenbrand, Davy Kirkpatrick, Shri Kulkarni, and Tom Soifer — who perhaps didn't realize the sheer magnitude of what they were about to read. Admittedly, it is with some trepidation that I submitted this work to some of the most esteemed astronomers in the world.

I have gained a great deal of insight, and have had many stimulating conversations (prompting a good portion of the work presented here), from various collaborators over the past few years. First and foremost are those members of the 2MASS Rare Objects Team, Charles Beichman, Adam Burrows, Roc Cutri, Conard Dahn, John Gizis, James Liebert, J. Davy Kirkpatrick (again), Dave Monet, and I. Neill Reid. Chaz is the consummate politician, which means I rarely saw him but his influence was pervasive. Adam and Jim have been extremely generous in leading me through the intricacies of brown dwarfs and passing on their excitement about this field, and I thank them for the very educational trips to UA they have supported. Roc has basically been the heart and soul of the IPAC 2MASS effort, and without his efforts some great NIR research (including mine!) would not have been possible. Conard and Dave have made a few of the more important measurements presented in this thesis, and their USNO Parallax Program is slowly revolutionizing our views on cool dwarfs. John's understanding of the global properties of cool dwarf stars — activity, space distribution, kinematics — is in my opinion highly underrated, and I greatly appreciate all of the

insight he has passed on to me. Finally, I think Neill is probably the most intelligent astronomer I know, and I am continually amazed at the various nooks and crannies of astronomy that he has investigated over the years. It has been an absolute pleasure to be part of this highly successful and supportive team.

I would also like to thank my other collaborators: John Wilson, for letting me take CorMASS for a spin, and for his contributions in the identification of 2MASS 0559-1404; Keith Matthews, for showing me what *real* observing is like on the 200"; Ian McLean, for allowing me to participate in the NIRSPEC Brown Dwarf Spectroscopic Sample, and who will be in charge of my money for the next few years (a very important man in my personal opinion); Mark Marley and Didier Saumon, for enlightening, in-depth discussions on brown dwarf theory, for their contributions of models, theoretical spectra, opacities, and ideas that have found their way into this thesis, and for the prospects of future collaboration; Chris Tinney, who I am eager to visit down under; Geoff Blake, for giving 2MASS 0559-1404 a shot with LWS; Cherie Miskey, for her assistance with HST data; Michelle Creech-Eakman, for pushing us into the mid-infrared; and Ben Weiss, Shabari Basu, and Christopher Boxe for their assistance at the Palomar 60".

During the course of my investigation, I have had many interesting discussions (in some cases hand-held guidance!) in developing some of the themes found in this work from various astronomers from all over the world. On the theoretical side, I am indebted to France Allard, Isabelle Baraffe, and Giles Chabrier — the "ABC" of the Lyon group — for a fresh point of view and for some of the models used here for interpretation; Caitlin Griffith for helping me see the planetary perspective; and Sterl Phinney, for assigning the interacting brown dwarf binary model used for 2MASS 1237+6526 as a homework assignment. On the observational side, I acknowledge useful discussions on substellar objects with Babar Ali, John Carpenter, Lynne Hillenbrand (again), Patrick Lowrance, Eduardo Martín, Maria Rosa Zapatero Osorio, and of course, the godfather of T dwarfs himself, Ben Oppenheimer. I would also like to thank Jean-Gabriel Cuby, Xavier Delfosse, Sandy Leggett, and Zlatan Tsvetanov for providing spectral data used in this thesis. Most importantly, I would like to acknowledge all of the wonderful insight I have gained through my discussions with Tom Geballe, David Golimowski, Gillian Knapp, Sandy Leggett (again), and Michael Strauss from the Sloan Team, a group of great observers who are probably the best people to be "in competition" with.

The objects discovered here would likely never have been observed without the development of the 2MASS database. Providing a tool by which to develop my thesis is only one of many miraculous accomplishments that can be attributed to this incredible project. It would be impossible to name every person whose contribution to this long-term ($>$ 15 years!) program was invaluable, but I would like to recognize PI Michael Skrutskie, Project Manager Rae Stiening, and Project Scientist Roc Cutri (again) for their leadership and commitment; and the Science Team: Chas Beichman (again), Richard Capps, John Carpenter (again), Tom Chester, Jay Elias, John Huchra, Jim Liebert (again), Carol Lonsdale, Dave Monet (again), Stephen Price, Steve Schneider, Pat Seitzer, and Martin Weinberg. I would also like to acknowledge the IRSA and IPAC staff: George Helou (Executive Director), Ron Beck, Bruce Berriman, Schuyler Van Dyk, Diane Engler, Tracey Evans, John Fowler, Robert Hurt, Helene Huynh, Tom Jarrett, Eugene Kopan, Howard McCallon, Brant Nelson, Jeonghee Rho, Bill Wheaton, Sherry Wheelock, and Angela Zhang. Many of these folks have contributed directly to the published work and/or have personally assisted me in parsing through 2MASS's ocean of data.

Without the assistance, guidance, and teachings of the various telescope operators and instrument specialists I have had the pleasure of working with, I would still be left with a few thousand candidates and no thesis. To that end, I would like to acknowledge Maria Theresa Acevedo, Alberto Alvarez, Robert Blum, Mauricio Fernandez, Angel Guerra, and Patricio Ugarte at CTIO; Teresa Chelminiak,

Bob Goodrich, Chuck Sorenson, and Meg Whittle at Keck; and Mike Doyle, Karl Dunscombe, Jean Mueller, Kevin Rykowski, Merle Sweet, and especially that mad man of the mountain Barrett "Skip" Staples at Palomar. I would also like to thank the various TACs that gave an inexperienced graduate student time on some very complex and expensive telescopes, and special thanks go out to Dipali and Rose at the Palomar Monastery for keeping me fed on long observing nights.

Additional thanks go out to Dave Koerner, who originally pointed me out to Davy as a potential student to work on this project; my early advisors for putting me on the right track: Sally Ride and Harding (Gene) Smith at UCSD, Tom Soifer and Gary Neugebauer at Caltech, and Rich Terrile at JPL; Michael Black, Ron Beck, Diane Engler, Helene Hyunh, and Steve Schurr, for keeping the computers running smoothly; Sarah Stewart-Mukhopadhyay, who I claim is the one-and-only Thesis Muse ("No one should ever have to write a thesis alone."); Daniel Durand, for explaining to me how not to crash the CADC webserver; Chris Baughman, for handling a substantial amount of travel as well as a flighty passenger; Donna Driscoll in the Physics Department, and Irma Black in the GPS Department, for all of their invaluable assistance over the past five years; Robert Hurt for his Gliese 570D artwork; Sarah Smiley for sending me the magic 8-ball; Ani Defranco, because I can; Shirley Marneus, Gavin Claypool, and the rest of the cast in TACIT for giving me a creative distraction from my real work; Clint Dodd and all of my divers — Garrett Blankenburg, Saskya Byerly, Liz Callaghan, Rachel Dexter, Mike Fisher, Justin Ho, Joanne Jang, Katharina Kohler, Dan Leibling, Auna Moser, Robert "Radoslaw" Osada, Matt Patterson, Phil Rodriquez, Barry Shapira, Rachel Steinberger, Heather Willey , and Kristy Young — who I consider my second family; and most importantly, to all of my family and friends for their support, for their love, and for a lot of laughs.

Finally, I would like to thank you for reading my thesis. I admit fully to having a biased opinion on the value of this research, and I welcome your comments, suggestions, and opinions on the results, ideas, and conjectures that follow this page. Whether it be tomorrow or 50 years down the road, please feel free to contact me through whatever medium of communication is in place at that time.

I acknowledge financial support over the course of this research from a NASA/JPL grant to 2MASS Core Project Science; HST proposal No. 8563, with funding provided by NASA through a grant from the Space Telescope Science Institute; the NCAA Post-Graduate Fellowship; and the NACDA Pre-Games Post-Graduate Fellowship. Additional funding support was provided through the CTIO graduate observing program and various conference grants provided by the Caltech Physics Department.

The Digitized Sky Survey was produced at the Space Telescope Science Institute under US Government grant NAG W-2166. SERC-EJ data were scanned by DSS from photographic data obtained using the UK Schmidt Telescope, operated by the Royal Observatory Edinburgh, with funding from the UK Science and Engineering Research Council. DSS images were obtained from the Canadian Astronomy Data Centre, which is operated by the Herzberg Institute of Astrophysics, National Research Council of Canada. IRAF is distributed by the National Optical Astronomy Observatories, which are operated by the Association of Universities for Research in Astronomy, Inc., under cooperative agreement with the National Science Foundation. This publication makes use of data from the Two Micron All Sky Survey, which is a joint project of the University of Massachusetts and the Infrared Processing and Analysis Center, funded by the National Aeronautics and Space Administration and the National Science Foundation. Portions of the data presented herein were obtained at the W. M. Keck Observatory which is operated as a scientific partnership among the California Institute of Technology, the University of California, and the National Aeronautics and Space Administration. The Observatory was made possible by the generous financial support of the W. M. Keck Foundation.

Contents

List of Figures

Introduction: So What's a T Dwarf?

I'll call for pen and ink, and write my mind.
William Shakespeare, *1 Henry V, act V, sc iii*

One of the great aspects of being an astronomer is the genuine fascination people have about my work. Any reply to the question, "So what do you do for a living," usually evolves into a lecture on the latest Hubble Space Telescope results, my last observing run in Hawaii, and of course whether or not I think aliens exist. But the conversation invariably winds its way to the prescient question,"So what's a T dwarf?"

The answer is straightforward — at least to a substellar astronomer. "T dwarf" denotes a particular class of brown dwarfs, ones that are distinguished by the presence of CH_4 in their atmospheres. The spectral features of CH_4 make T dwarfs appear quite similar to Jupiter, Saturn, and even the moon Titan. CH_4 forms only at very low temperatures (less than 1300–1500 K, depending on the *model d'jour*), so T dwarfs are the coolest and faintest varieties of brown dwarfs we have so far directly detected. Furthermore, since they lack an internal energy source and cool over time, all brown dwarfs are, have been, or will be T dwarfs at some point in their lifetime.

This explanation is often followed by an interested "Oh," a dazed, glassy-eyed pause, and (almost) without exception the follow-up question: "So what's a brown dwarf?"

Such is the popular ignorance of a field which has only recently become a growth industry. The observational study of brown dwarfs, let alone proof that they exist, is a fairly recent event, even if the theoretical background extends back to the works of Shiv Kumar and Chushiro Hayashi & Takenori Nakano in the early 1960s. Indeed, the first *bona fide* brown dwarf discoveries were made just before I started my graduate school career. I myself had very little knowledge or background in substellar astronomy when I came to Caltech; such objects were never mentioned in any of my prior astronomy classes. So I can sympathize with the lack of publicity brown dwarfs have gotten until quite recently, playing a distant third fiddle to the omnipresent stars and planets which permeate our collective literary works. Surely no one has ever seen a brown dwarf with his or her own eyes, so why do we care about them?

To understand the allure of brown dwarfs, and indeed what they are and what they mean to astronomy, it is helpful to examine the history of the subject. It turns out that I had been introduced to substellar dwarfs much earlier than I thought. In fact, I was eleven, eating my breakfast before school, watching the morning television program "Good Morning America." Two astronomers were talking about the discovery of "black dwarfs," mysterious, dark objects that pervade the Galaxy but are too faint to see with our own eyes. For some reason, that interview, the image of these dark stars, was retained in my perhaps overly imaginative young mind, and to this day I remember seeing the artist's renditions they showed to try to explain just what a black dwarf was.

The discovery was, of course, the fictitious, perhaps mythical, VB 8B, "found" by Don McCarthy and collaborators by speckle interferometry, but never seen again. It is a legendary non-detection, however, as it was part of, and helped spur on, an explosion in brown dwarf research in the mid-1980s, culminating in the rapid development of observing techniques, theoretical models, and nomenclature – it was at this time that Jill Tartar's "brown dwarf," meant to reflect the completely unknown spectral energy distributions of these objects, became widely accepted terminology. The nascent brown dwarf community undertook extensive searches, around nearby stars and in stellar clusters, from the ground and from space, in order to be the first to reveal these faint, cold objects. Rationales

varied. Many believed brown dwarfs could solve the dark matter problem; others sought to find the limits of the star formation process; still others proposed that a periodic encounter with a substellar companion to the Sun, a so-called "Nemesis," could explain periodic extinctions on Earth. But perhaps more importantly, brown dwarfs had never before been seen. Here was a new frontier in astronomy that pushed the limits of detector technology, gave new insight into the membership of the Solar Neighborhood, and extended our knowledge of stellar properties.

It took another ten years.

In the mid-1990s, brown dwarf searches finally saw fruition, with the first discoveries of substellar objects in young clusters and as companions to nearby stars. Of primary interest to this work was the identification of Gliese 229B in 1995, a brown dwarf companion to the nearby (5.77 pc), low-mass star Gliese 229A, by astronomers Tadashi Nakajima, Ben Oppenheimer, David Golimowski, and Shri Kulkarni. It wasn't long until a number of brown dwarfs were found, some identified as "free-floating" field objects. The observational era of brown dwarfs had finally begun.

Why were they so hard to find in the first place? Why are they so faint? The answer to this requires us to understand the nature of brown dwarfs. These objects start off as normal stars do, born in the stellar nurseries of giant molecular clouds, rapidly accumulating mass onto a central dense core, forming an accretion disk[1] which is eventually cleared, and finally settling into normal evolution. Only, for whatever reason (and many have been proposed), brown dwarfs do not accumulate enough mass to reach the critical core temperatures and pressures required to sustain hydrogen thermonuclear fusion reactions, the energy source of the stars. Without this, objects less massive than 0.075 solar masses, or roughly 72 Jupiter masses, radiate away their initial gravitational potential energy, and, in the words of Adam Burrows,

> "...cool off inexorably like dying embers plucked from a fire."

It is the lack of sustained Hydrogen burning that defines brown dwarfs and distinguishes them from normal stars.

After 1995, as more and more substellar objects were identified, it became increasingly clear that Gliese 229B stuck out like a sore thumb. Its spectrum, dominated by features of CH_4 and H_2O, was best described by Tom Geballe:

> "The spectrum of Titan provides the best overall spectral match to that of Gl 229B, and the spectra of the two exhibit several similar details."

A brown dwarf that looks like a moon? Incredibly, this object has an effective temperature over 700 K less than that of the coolest stars, but 500 K warmer than Jupiter. Was Gliese 229B a brown dwarf? Was it a planet? Was it something else entirely? Regardless of anyone's personal nomenclature, for four years Gliese 229B was quite simply unique.

The term "T dwarf" was first coined by J. Davy Kirkpatrick as recently as 1999, in a paper describing another new class of stars/brown dwarfs, the L dwarf class (Kirkpatrick et al., 1999b). The origins of the letters L and T for the new spectral classes is described in detail in this article. T dwarfs were defined by Kirkpatrick as objects that had the spectral appearance of Gliese 229B; i.e., the presence of CH_4 absorption bands in the near-infrared. In his own words:

> "We already know of one cooler object (Gl 229B) that does not fit into the new spectral sequence because it is so much colder than the others. Its spectrum is dominated by methane, much like the Jovian planets. Hence, once we have enough objects similar to Gl 229B, they too will require a new letter since they are fundamentally different from the dwarfs discussed here."

[1] Evidence for brown dwarf disks has only recently been identified by Fernando Comeron, August Muench, and collaborators.

Kirkpatrick predicted that many more objects like Gliese 229B would be found, having similar CH_4 absorption and similarly faint luminosities (Gliese 229B is over 15,000 times fainter than the Sun). This prediction was well-founded, as theoretical models had shown that Gliese 229B was simply an unusually cool brown dwarf[2], and that the appearance of CH_4 in the atmospheres of such objects was a natural consequence of their evolution. Moreover, the discovery of many warmer, L- and M-type brown dwarfs implied that T dwarfs must be present in the Solar Neighborhood. The problem was of course finding them.

Such was the state of affairs when I began my work with J. Davy Kirkpatrick, Michael Brown, and the 2MASS Rare Objects Team, looking for methane-bearing brown dwarfs like Gliese 229B. Certainly the typical motivations for brown dwarf searches had changed by this time. Brown dwarfs clearly did exist but did not appear to be numerous enough to contribute to dark matter; cluster surveys proved to be better suited for constraining the stellar/substellar initial mass function, due to the relative brightness of their brown dwarf members; and Nemesis was still – out there? But the opportunity to identify a new astronomical class, to find Solar neighbors never before seen, to explore a true astronomical frontier, was dangled like a scientific carrot before my thesis-hungry eyes.

The result, the following 333 pages before you, has been written in a historically-ordered manner whenever possible, to in some part preserve the learning process incurred as we discovered, examined, and ultimately interpreted the properties of T dwarfs. It is therefore my hope that somewhere in this thesis you may find an answer to your question, "So what's a T dwarf?"

[2]Even today, however, some of the spectral features seen in Gliese 229B remained unclear, including the red optical slope.

Chapter 1 Background Material

When I look down, I just miss all the good stuff.
When I look up, I just trip over things.
Ani Defranco, *As Is*

1.1 Introduction

In this chapter we review some of the background material related to the field of substellar astronomy. In §1.2, we summarize the basic physics of these objects, drawing from a vast collection of accumulated (and still accumulating) work by theoretical modelers. In §1.3, we review some of the early efforts to identify brown dwarfs in the field, in clusters, and as companions to nearby stars, leading to the identification of *bona-fide* brown dwarfs in the mid-1990s. Many of these objects are members of the L spectral class, reviewed in §1.4, the first major addition to the MK classification system (Morgan, Keenan, & Kellman, 1943) in over 65 years. We then review the properties of the prototype of the T spectral class (defined in Chapter 7), Gliese 229B, in §1.5. In §1.6 we summarize the properties of our primary astronomical search tool, the Two Micron All Sky Survey (Skrutskie et al., 1997, hereafter, 2MASS), and we use data from this rich database to examine the properties of various astronomical objects in the near-infrared in §1.7. A brief summary of this material is given in §1.8.

1.2 Brown Dwarf Theory

The theory of brown dwarfs has a rich history, drawing on fields as diverse as quantum and classical physics, high-pressure dynamics, atmospheric chemistry, high-volume computing, and more recently, meteorology. The extreme interior environments of these objects ($\rho_c \sim 10$–10^3 g cm^{-3}, $T_c \lesssim 10^6$ K, $P_c \sim 10^5$ Mbar; Burrows et al. 2001) test our understanding of degenerate plasmas and exotic molecular forms of hydrogen[1], while the molecular-rich atmospheres have led to new developments in the theories of line formation, atmospheric dynamics, and condensation. A great deal remains to be understood. In this section, we give a general overview of our current theoretical understanding of brown dwarfs. Excellent (and perhaps more complete) reviews can also be found in Stevenson (1991), Burrows & Liebert (1993), Allard et al. (1997), Oppenheimer, Kulkarni, & Stauffer (2000), Chabrier & Baraffe (2000), and Burrows et al. (2001).

1.2.1 A Historical Perspective

The theoretical study of brown dwarfs got its start in the early work of Kumar (1963) and Hayashi & Nakano (1963), who independently predicted that below a minimum mass, roughly 0.07–0.08 $M_\odot$, a collapsing star would be halted by electron degeneracy before the onset of hydrogen fusion. "Stars" less massive than this limiting mass never achieve core temperatures sufficient to ignite fusion reactions, and hence continually evolve to cooler temperatures. Such objects, as coined by Tarter (1975),

[1]Current shockwave experiments, e.g., Nellis, Ross, & Holmes (1995), fall short of the high pressures in the cores of brown dwarfs by orders of magnitude.

are called Brown Dwarfs. This evolution was clearly shown in the first detailed calculations of the interior physics and evolution of brown dwarfs by Hoxie (1970) and Grossman, Hays, & Graboske (1974), the latter taking into consideration the effects of both electron screening and light-element fusion, and first predicting a deuterium-burning phase for these objects down to 0.012 $M_\odot$. Additional early work by Vandenberg et al. (1983), D'Antona & Mazzitelli (1985), Nelson, Rappaport, & Joss (1986), Stringfellow (1986), Lunine, Hubbard, & Marley (1986), D'Antona (1987), Dorman, Nelson, & Chau (1989), Lunine et al. (1989), Burrows, Hubbard, & Lunine (1989), and Burrows et al. (1993) further expanded on the roles of metallicity, dust opacity, convection, conduction, and nuclear screening in the evolution of a substellar object. The basic picture of a brown dwarf as a high-pressure, fully-convective, mostly-degenerate body which steadily loses its incipient thermal and gravitational potential energy over time was firmly in place by the mid- to late-1980s.

The 1990s saw substantial advances in both interior theory and the development of accurate atmospheric models. Saumon, Chabrier, & Van Horn (1995), advancing the work of Marley & Hubbard (1988), rigorously determined the equation of state for hydrogen and Helium in the high-pressure, low-temperature environments of brown dwarf interiors, including the effects of internal pressure dissociation and ionization, which have a noticeable effect on the evolution of a substellar object. Significant advances were then made from the top down by Saumon et al. (1994) and Baraffe et al. (1995), who developed self-consistent evolutionary models using non-grey atmospheres, originally investigated by Allard (1990) and Kui (1991). Additional developments in the rich atmospheres of hot brown dwarfs (M dwarfs) came from Mould (1975, 1976), who produced the first set of M dwarf model atmospheres using a line-blanketing opacity grid; Brett & Plez (1993); Allard & Hauschildt (1995); Brett (1995a,b); and Tsuji, Ohnaka, & Aoki (1996a); while cooler models were also developed by Tsuji et al. (1996), Allard et al. (1996), and Marley et al. (1996), largely in response to the discovery of Gliese 229B (see §1.5). These early atmospheres could adequately reproduce many of the gross features observed in the first brown dwarf discoveries, including reddening by dust opacity and strong CH_4 in Gliese 229B, but failed to explain other important features, such as H_2O band depths, alkali line strengths, and the red optical slope of L and T dwarfs.

Recent work has developed rapidly, particularly in the realm of substellar atmospheres, where modelers are struggling to develop self-consistent models that include dust opacity (Tsuji, Ohnaka, & Aoki, 1999; Allard et al., 2001), cloud formation and sedimentation (Ackerman & Marley, 2001), pressure-broadening (Burrows, Marley, & Sharp, 2000), equilibrium chemistry (Fegley & Lodders, 1996; Burrows & Sharp, 1999; Lodders, 1999), and non-equilibrium mixing in the upper atmosphere (Griffith & Yelle, 1999; Saumon et al., 2000). We will touch on a number of these issues in the following sections.

1.2.2 Interior Physics

To understand the peculiarities of brown dwarf interiors, it is instructive to examine the evolution of stellar-like objects as a whole. Standard formation theories (e.g., Shu, Adams, & Lizano 1987) apply to the formation of both stars and brown dwarfs, via the fragmentation and collapse of dense pockets in cool molecular clouds, leading to the adiabatic contraction of a protostellar (or protosubstellar) object. As this protostar compresses with an essentially constant effective temperature (i.e., Hayashi track, Hayashi 1961), both its core temperature (Figure 1.1) and core density (Figure 1.2) increase, the former scaling roughly as $T_C \propto R^{-1}$ (Stahler, 1988). For objects with masses $M \gtrsim 0.35\ M_\odot$ (Chabrier & Baraffe, 1997), a radiative core forms and evolution follows the so-called "Henyey" tracks (Henyey, LeLevier, & Levee, 1955) of near-constant luminosity (i.e., increasing T_{eff}) toward the Hydrogen-Burning Main Sequence.

Eventually, contracting protostars with masses greater than the Hydrogen-Burning Minimum Mass (HBMM) will reach sufficiently high core temperatures and pressures to ignite the pp-I fusion

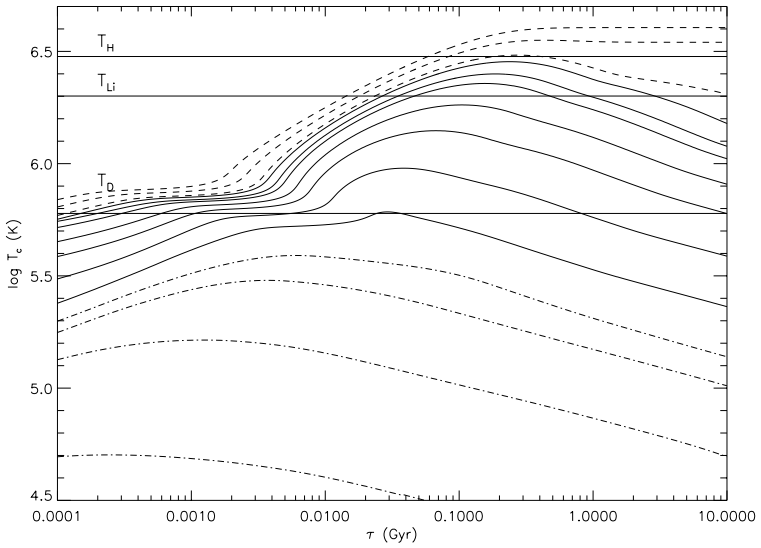

Figure 1.1: Evolution of the central temperature, T_C, in low-mass dwarfs as predicted by Burrows et al. (1997). Lines trace the evolution for masses of (from bottom to top) 1, 5, 10, 13 ("planets," dot-dashed lines), 20, 30, 42, 52, 63, 68, 75 (brown dwarfs, solid lines), 80, 90, and 100 M_{Jup} (stars, dashed lines). The critical temperatures for hydrogen (T_H), lithium (T_{Li}), and deuterium (T_D) fusion are indicated.

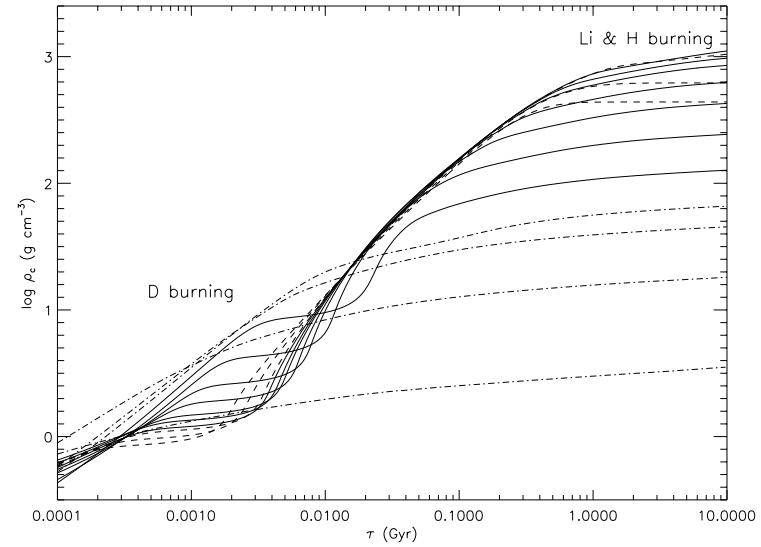

Figure 1.2: Evolution of the central density, ρ_C, in low-mass dwarfs as predicted by Burrows et al. (1997). Lines are those of Figure 1.1. Periods of hydrogen, lithium, and deuterium burning, where ρ_C remains constant, are indicated.

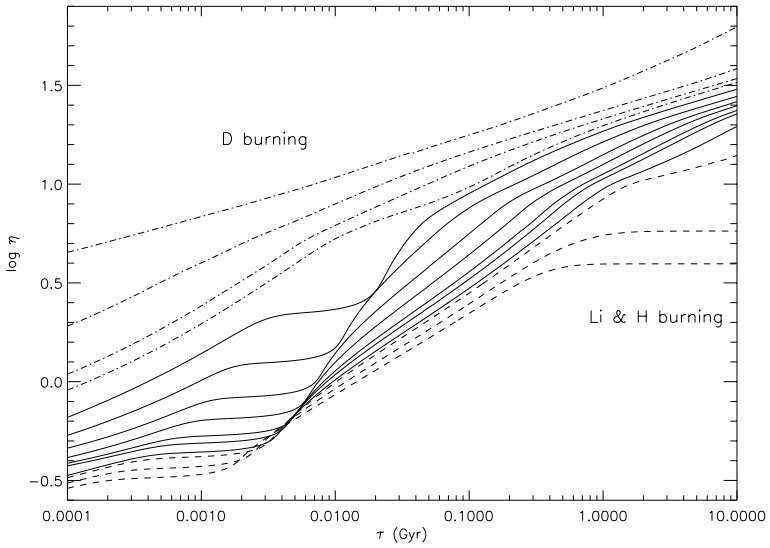

Figure 1.3: Evolution of the degeneracy parameter, η, in low-mass dwarfs as predicted by Burrows et al. (1997). Lines are those of Figure 1.1. Periods of hydrogen, lithium, and deuterium burning, where η remains constant, are indicated. μ_e is assumed to be 1.143 (Burrows & Liebert, 1993).

chain (Hansen & Kawaler, 1994; Ushomirsky et al., 1998; Chabrier et al., 2000a):

$$\begin{array}{rcll} p+p & \rightarrow & d+e^{+}+\nu_e & Q=1.442\ eV, \quad T_c=3{\times}10^6\ K \\ d+p & \rightarrow & {}^3He+\gamma & Q=5.493\ eV, \quad T_c=6{\times}10^5\ K \\ {}^3He+{}^3He & \rightarrow & {}^4He+p+p & Q=12.859\ eV, \quad T_c=6{\times}10^6\ K, \end{array} \tag{1.1}$$

which provides 99% of the nuclear energy for objects with $M < 0.7\ M_\odot$. Hydrogen fusion occurs over a fairly narrow temperature range due to the competing influences of the Maxwell-Boltzmann thermal distribution ($\sim e^{E/kT}$) and quantum tunneling through the Coulomb repulsion potential ($\sim e^{b/E^{1/2}}$), resulting in a strong Gamow energy peak centered at $E_o = 1.22(Z_1 Z_2 \mu T_6^2)^{1/3}$ keV (Hansen & Kawaler, 1994). The sensitivity of this peak to temperature implies that energy generation (ϵ) in the pp-I chain scales roughly as $\epsilon \propto \rho^{1.3} T^{6.3}$ in low-mass stars (Burrows & Liebert, 1993); i.e., fusion rapidly becomes efficient soon after the critical ignition temperature ($T_H \sim 3{\times}10^6$ K) is achieved. Note that the thermal and radiative pressure incurred by hydrogen fusion is sufficient to halt further protostellar contraction, which is reflected in plateaus in the evolution of ρ_c in Figure 1.2. The energy generated from hydrogen fusion accounts for radiative losses at the surface, and the resulting new-born star settles onto the Main Sequence.

At lower masses, the core temperature and pressure increase more slowly during contraction, requiring higher densities to achieve the critical ignition temperature. Below $M \sim 0.1\ M_\odot$ (Reid & Hawley, 2000), central densities become sufficiently high to cause the onset of electron degeneracy

in the core. The degeneracy parameter[2] (Burrows & Liebert, 1993)

$$\begin{aligned} \eta &\equiv \frac{kT_F}{kT} \\ &= \frac{(3\pi^2\hbar^3)^{2/3}}{2m_e kT}[\frac{\rho N_A}{\mu_e}]^{2/3} \\ &\approx 3.02{\times}10^5 \frac{1}{T}(\frac{\rho}{\mu_e})^{2/3} \end{aligned} \tag{1.2}$$

implies full degeneracy (i.e., Fermi-Dirac statistics) for $\eta \gg 1$, where $T_F = E_F/k$ is the electron Fermi temperature. As shown in Figure 1.3, young brown dwarfs and low-mass stars have $\eta \sim$ 0.3–3 and are only partially degenerate, while evolved substellar objects achieve $\eta \sim$ 10–100 at 10 Gyr. The core pressure in this non-relativistic regime is approximately (Stevenson, 1991; Burrows & Liebert, 1993)

$$P_c \sim 10^{13}(\frac{\rho}{\mu_e})^{5/3}(1 + \frac{5\mu_e}{2\mu\eta})\ dyne\ cm^{-2}, \tag{1.3}$$

which at large η becomes sufficient to halt further contraction of the evolving protostar. If this occurs before the core temperature reaches critical ignition, the resulting object is a brown dwarf. As shown in Figure 1.2, some compression continues in even the lowest mass objects at late times; this further contraction does not occur rapidly enough to make up for radiative losses, however, as nearly all of the gravitational potential energy goes into moving the degenerate electrons closer together.

The maximum core temperature, $T_c^{(max)}$, occurs when $\eta = \frac{5\mu_e}{2\mu}$ (Stevenson, 1991; Burrows & Liebert, 1993). Using polytropic relations it is possible to determine an approximate analytical form of this value as a function of mass. For example, Ushomirsky et al. (1998) derive an expression:

$$T_c^{(max)} = 3.43{\times}10^6(\frac{M}{0.075M_\odot})^{4/3}\ K, \tag{1.4}$$

which yields a HBMM of 0.068 $M_\odot$ for a critical hydrogen fusion temperature of $3{\times}10^6$ K. Refined theoretical models by Burrows et al. (1997) and Chabrier & Baraffe (2000) predict a HBMM of 0.070–0.075 $M_\odot$ for Solar metallicity, with a transition region of partial but insufficient hydrogen fusion extending to slightly lower masses.

1.2.3 Light Element Fusion

Both stars and brown dwarfs undergo early deuterium fusion, as shown in Figure 1.4. For M > 0.013 $M_\odot$ (Grossman, Hays, & Graboske, 1974), a Deuterium-Burning Main Sequence is achieved for $0.1 < \tau < 10$ Myr, during which roughly 95% of the total emitted luminosity is generated via the second reaction in Equation 1.1. Indeed, we can see the effects of this temporary radiative stability in the evolution of both T_c and ρ_c (Figures 1.1 and 1.2). However, the deuterium-burning phase is short-lived due to the small initial abundance of this element (D/H $\approx 1.6{\times}10^{-5}$ in the local ISM; Piskunov et al. 1997). All deuterium-burning dwarfs with M < 0.1 $M_\odot$ undergo a second contraction phase before stellar and transition-mass objects begin full or evanescent hydrogen fusion.

The lack of deuterium fusion in objects less massive than 0.013 $M_\odot$ has recently led Oppenheimer, Kulkarni, & Stauffer (2000) to define a new category of "planet" for these very low-mass brown dwarfs. Indeed, Shu, Adams, & Lizano (1987) propose that deuterium burning may halt stellar accretion in young protostars, implying a minimum mass to the star-forming process at 0.013 $M_\odot$. This terminology has found both favor (Lucas & Roche, 2000; Najita, Tiede, & Carr, 2000; Zapatero Osorio et al., 2000) and distaste (McCaughrean et al., 2001) in recent literature. While we

[2]Both Stevenson (1991) and Chabrier & Baraffe (2000) use the parameter $\psi = 1/\eta$.

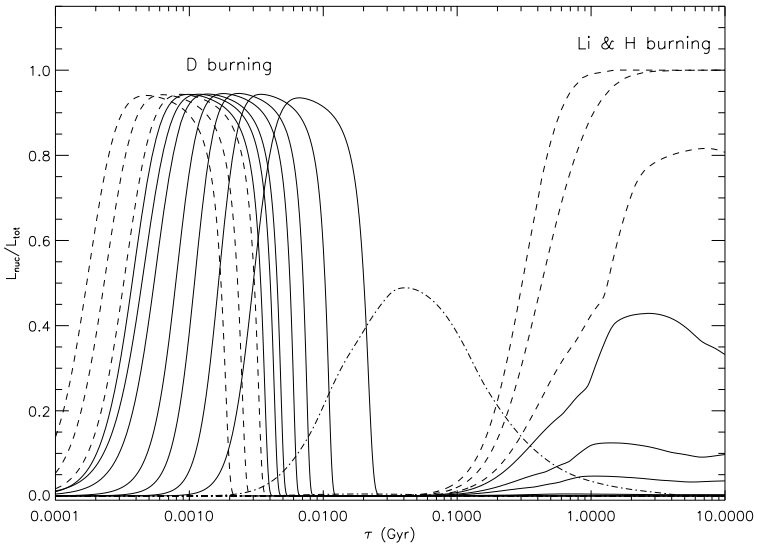

Figure 1.4: Evolution of the ratio of nuclear to total luminosity in low-mass dwarfs as predicted by Burrows et al. (1997). Lines are those of Figure 1.1. Periods of hydrogen, lithium, and deuterium burning are indicated.

differentiate non-deuterium-burning objects in the figures shown in this section in order to highlight their slightly different evolution, we dismiss the necessity of unique (and confusing) nomenclature and refer to these only as "low-mass brown dwarfs."

Another critical reaction occurring in stars and some brown dwarfs is that of lithium fusion, via the reaction (Hansen & Kawaler, 1994):

$$^7Li + p \quad \rightarrow \quad ^4He + ^4He \quad Q = 17.347\ eV, \quad T_c = 2{\times}10^6\ K, \tag{1.5}$$

which occurs in stars and brown dwarfs with M $\gtrsim$ 0.06 $M_\odot$ (Chabrier, Baraffe, & Plez, 1996). This mass is lower than the HBMM due to the lower critical temperature of lithium fusion. The depletion of lithium in lithium-burning objects occurs within roughly 100 Myr (Chabrier & Baraffe, 2000). For stars with M $<$ 0.3 $M_\odot$, the depletion is exhaustive, as convection cycles all of the interior material through the core; deuterium depletion is analogously exhaustive[3]. Because the critical mass for lithium burning lies close to the HBMM, Rebolo, Martín, & Magazzu (1992) have proposed a "lithium test" by which the substellar nature of a low-mass dwarf can be ascertained through the identification of the 6708 Å resonance line. This test has been applied to a number of brown dwarf searches in clusters (Marcy, Basri, & Graham, 1994; Martín et al., 1994, 1998a; Martín, Basri, & Zapatero Osorio, 1999; Basri, Marcy, & Graham, 1996; Rebolo et al., 1996; Oppenheimer et al., 1997; Stauffer, Schultz, & Kirkpatrick, 1998; Stauffer et al., 1998; Basri & Martín, 1999b), in the field (Ruiz, Leggett, & Allard, 1997; Thackrah, Jones, & Hawkins, 1997; Tinney & Reid, 1998; Martín et al., 1999; Martín, 1999; Goldman et al., 1999; Kirkpatrick et al., 1999b, 2000; Reid et al., 2000), and for stellar companions (Kirkpatrick et al., 2001a; Wilson et al., 2001c). Because the depletion of lithium occurs over longer time scales than that of deuterium, it is also possible to measure the age of

[3]The rate of reaction 1 in Equation 1.1 is much slower than that of reaction 2, so that deuterium remains depleted in low-mass stars as well.

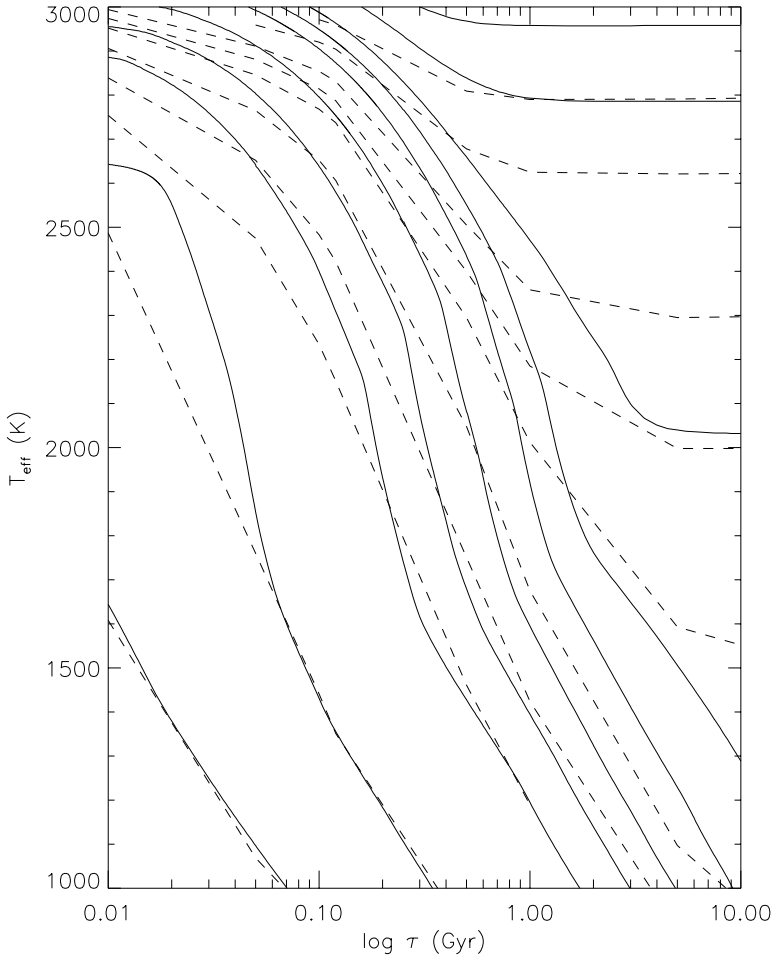

Figure 1.5: Evolution of T_{eff} in low-mass dwarfs as predicted by Burrows et al. (1997, solid lines) and Chabrier et al. (2000a, dashed lines), for masses of (from left to right and bottom to top) 10, 20, 40, 50, 60, 70, 75, 80, 90, and 100 M_{Jup}.

a young cluster by the self-consistent comparison between absolute brightness and lithium detection in low-mass cluster members; this has been done recently for the Pleiades (Stauffer, Schultz, & Kirkpatrick, 1998), αPer (Stauffer et al., 1999), and IC 2391 (Barrado y Navascués, Stauffer, & Patten, 1999).

1.2.4 Evolution and Observables

The evolution of a brown dwarf has been described most succinctly by Burrows et al. (2001), who compare cooling substellar objects to "dying embers plucked from a fire." This is due to the fact that radiative losses are never sufficiently balanced by the slow compression of these degenerate objects. As shown in Figure 1.1, this imbalance results in the steady decrease of the core temperature after

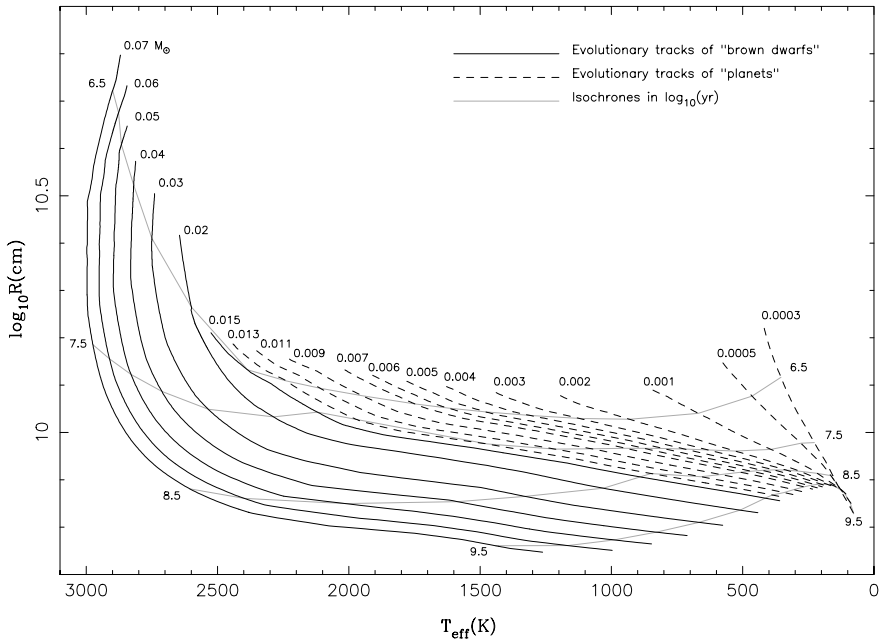

Figure 1.6: Radius versus effective temperature, T_{eff}, for dwarfs with masses 0.3 M_{Jup} to 0.237 $M_\odot$. Solid lines trace the evolution of brown dwarfs (0.015–0.07 $M_\odot$), while dashed lines trace the evolution of low-mass brown dwarfs ("planets"; 0.0003–0.015 $M_\odot$). Isochrones are indicated by faint dotted lines (from Burrows et al. 1997).

initial contraction. We can see these effects more dramatically by examining the evolution of the effective temperature (T_{eff}), as shown in Figure 1.5. Up until roughly 300 Myr, brown dwarfs with masses of 70 M_{Jup} can sustain temperatures similar to those of the coolest stars ($\sim$ 2000 K). Beyond 1 Gyr, however, a brown dwarf/stellar gap forms, as stars settle onto the Main Sequence while brown dwarfs fade into obscurity. Objects without deuterium burning generally dim earlier and more quickly, but as higher-mass objects deplete their deuterium stores, they too rapidly cool. A similar pattern is seen in the evolution of luminosity over time. The minimum temperature achieved by a star varies from model to model (compare solid and dashed lines in Figure 1.5) and is a function of metallicity, but is found to be in the neighborhood of 1700–1800 K, while the minimum stellar luminosity is roughly 6×10^{-5} $L_\odot$ (Burrows et al., 2001).

While the effective temperature of a brown dwarf evolves rapidly over time, its radius generally does not. This can be seen in Figure 1.6, which is taken from Burrows et al. (1997). This figure shows the variation of radius with T_{eff} for masses between 0.3 M_{Jup} (i.e., Saturn) and 0.07 $M_\odot$ and ages from 3 Myr to 3 Gyr. Except for a late stage of contraction in the more massive brown dwarfs through 30 Myr, the radii of these objects show little variation over time, other than a slow decrease caused by ongoing compression. This can be understood by the continual increase in the core degeneracy over time (Figure 1.3), which increases the internal pressure support and helps to slow further contraction. Furthermore, the radii of brown dwarfs appear to be fairly independent of mass. Degenerate interiors imply an equation of state $P \propto \rho^{5/3}$, so that brown dwarfs can be adequately described by a n=1.5 polytrope (Chandrasekhar, 1939), for which $R \propto M^{-1/3}$. In low-mass brown dwarfs, Coulomb potential corrections (for both ions and electrons) result in a polytrope that goes as n=1.0, so that R is independent of mass (Burrows & Liebert, 1993). Hence, brown

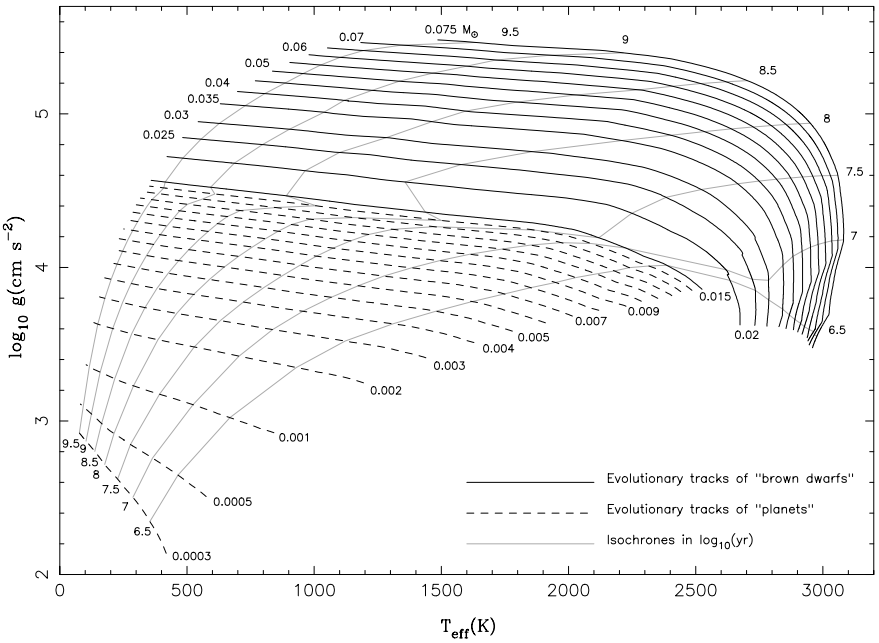

Figure 1.7: Gravity versus effective temperature, T_{eff}, for dwarfs with masses 0.3 M_{Jup} to 0.237 $M_\odot$. Lines are those of Figure 1.6 (from Burrows et al. 1997).

dwarfs are within 30–40% the size of Jupiter ($R_{Jup} = 7.15\times10^9$ cm; Tholen, Tejfel, & Cox 2000) over most of their evolution.

The constancy of brown dwarf radii implies that gravity is an excellent indicator of mass, as shown in Figure 1.7. Again, except for a brief period of contraction in the highest-mass brown dwarfs, lines of constant mass are nearly horizontal on this diagram, implying a roughly time-independent correlation with surface gravity. This is an important consideration, as gravity is a potential observable in brown dwarf spectra, as discussed in the case of 2MASS 0937+2931 in §7.7. This diagram is also a useful theoretical tool, as it relates the primary observables — gravity, effective temperature, and age — to mass in one compact diagram.

The roughly polytropic nature of brown dwarfs implies that simple analytical expressions can be formulated to relate the key quantities describing these objects. Burrows & Liebert (1993); Burrows et al. (2001) and Marley et al. (1996) have determined the following relations useful for a first-order estimate of the late or low-mass evolution of brown dwarfs:

$$L \sim 4\times10^{-5}\ L_\odot(\frac{t}{10^9 yr})^{-1.3}(\frac{M}{0.05M_\odot})^{2.64}(\frac{\kappa_R}{10^{-2}\ cm^2\ gm^{-1}})^{0.35} \quad (1.6)$$

$$T_{eff} \sim 1550\ K(\frac{t}{10^9 yr})^{-0.32}(\frac{M}{0.05M_\odot})^{0.83}(\frac{\kappa_R}{10^{-2}\ cm^2\ gm^{-1}})^{0.088} \quad (1.7)$$

$$M \sim 35\ M_{Jup}(\frac{g}{10^5\ cm\ s^{-2}})^{0.64}(\frac{T_{eff}}{1000\ K})^{0.23} \quad (1.8)$$

$$t \sim 1.0\ Gyr(\frac{g}{10^5\ cm\ s^{-2}})^{1.7}(\frac{T_{eff}}{1000\ K})^{-2.8} \quad (1.9)$$

$$R \sim 0.94\ R_{Jup}(\frac{g}{10^5\ cm\ s^{-2}})^{-0.18}(\frac{T_{eff}}{1000\ K})^{0.11}. \quad (1.10)$$

A caveat to these relations (and indeed for all of the figures shown in this section) is that they have been derived for Solar composition. Metallicity critically affects the evolution of brown dwarfs through its role in determining the atmospheric opacity. Low-metallicity brown dwarfs will generally have more transparent photospheres, resulting in increased radiative losses (i.e., larger luminosities). This implies that a higher core temperature is required to sustain hydrogen burning, and hence a higher HBMM, roughly 90 M_{Jup} for a zero-metallicity brown dwarf (Burrows & Liebert, 1993; Chabrier & Baraffe, 1997). The higher luminosities also cause low-metallicity brown dwarfs to evolve more rapidly. With our current technology, it is unlikely that we will directly detect any halo brown dwarfs, although they could be recovered indirectly through gravitational lensing experiments (Alcock et al., 1996).

1.2.5 Atmospheres

One of the more rapidly developing fields in astrophysics is that of low-mass star and brown dwarf atmospheres. With photospheric pressures of 0.1–10 bar and temperatures of 100–3000 K, these regions are rich with atmospheric chemistry. A self-consistent treatment of the photosphere of a brown dwarf must include as a minimum chemical equilibrium abundances for a sizable sample of atomic, molecular, and condensed species based on the latest thermochemical data; opacity tables for these species; adequate treatment of grain formation and condensation; and a self-consistent radiative code to derive the temperature-pressure profile. Cloud formation, atmospheric turbulence and convection, and rainout are increasingly seen as important considerations as well. Furthermore, the molecular species found in brown dwarf atmospheres may contribute thousands to billions of lines to the overlying opacity, all of which must be adequately treated for various line-broadening mechanisms. The management of these large opacity databases has become an industry of its own (Hauschildt, 2001). Characterizing the spectral energy distributions of brown dwarfs is important, as both a constraint for interior models (Saumon et al., 1994; Baraffe et al., 1995) and for the comparison to empirical data.

Chemical equilibrium calculations (e.g., Figure 2 from Fegley & Lodders, 1996) show that the most abundant molecular species in substellar atmospheres are H_2, H_2O, CO/CH_4, N_2/NH_3, and H_2S. Metal oxides (VO, TiO) are spectrally active in M dwarf atmospheres, but at cooler temperatures these are replaced by hydrides (FeH, CrH, CaH, MgH) and condensible species (Fe, VO, $CaTiO_3$). The subsequent "rainout" of the latter molecules plays an important role in the further chemical evolution of the atmosphere, as was first pointed out by Fegley & Lodders (1996), in analogy to what is seen in Jupiter. The observed overabundance of both H_2S and GeH_4 in the upper atmosphere of this planet is due to the depletion of Fe and Si (Lodders, 1999); similarly, the retention of Na and K in the atmospheres of cool brown dwarfs requires the depletion of Si and Al onto grains at warmer temperatures (Burrows et al., 2001). These less refractory alkali species — Na, K, Cs, and Rb — are indeed quite prominent in the spectra of L dwarfs and Gliese 229B as heavy metal opacity is lost (Kirkpatrick et al., 1999b; Burrows, Marley, & Sharp, 2000). At still cooler temperatures ($\sim$ 1400–1000 K), alkalis are sequestered into hydrides, hydroxides, and chlorides, and are themselves depleted from the photosphere (Lodders, 1999). The major Carbon-bearing molecule switches from CO to CH_4 at about 1300–1500 K, N_2 switches to NH_3 at around 700 K, and both H_2O and NH_3 condense out of the photosphere at roughly 350 and 200 K (Fegley & Lodders, 1996; Burrows & Sharp, 1999). Given a photospheric temperature/pressure profile, these transitions can be used as rough temperature estimators, as shown in Figure 1.8; indeed, this has been done for the L dwarfs by Kirkpatrick et al. (1999b, 2000, see §7.8.4).

Dust has been a particularly important topic in substellar atmospheres, not only in terms of elemental depletion but also as an opacity source. The role of condensibles in the opacity and evolution of brown dwarf atmospheres was first given attention by Lunine et al. (1989), who created

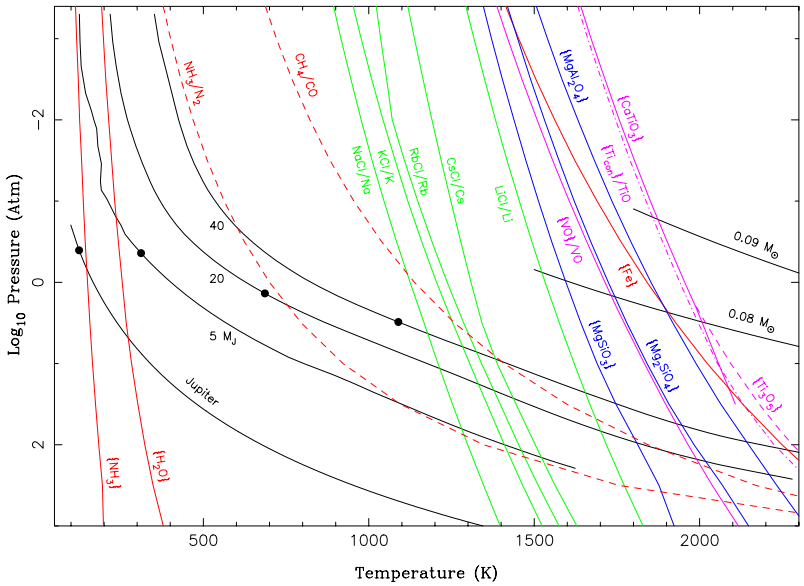

Figure 1.8: Chemical evolution and pressure/temperature profiles in the atmospheres of (from top to bottom) 1, 5, 10, 20, and 40 M_J brown dwarfs, and 0.08 and 0.09 $M_\odot$ stars. 50% depletion lines for chemical conversions and condensation (curly brackets) are indicated for a variety of atmospheric species (from Burrows, Marley, & Sharp 1999).

a basic upwelling model for grain formation. Tsuji et al. (1996) demonstrated the influence of dust on M dwarf spectral energy distributions, including reddening caused by thermal emission and shallowing of absorption bands (in particular H_2O) due to dissociative heating. These predictions were largely confirmed by Jones & Tsuji (1997). The treatment of grains is typically handled through Mie theory, and a grain size distribution must be assumed. There remains some controversy over the latter quantity, where atmospheric turbulence and convection can result in larger grain sizes than those seen in the ISM. Indeed, the plume models of Lunine et al. (1989) predict grain sizes of 10–100 μm, whereas the condensible grain size is only 1 μm (Burrows et al., 2001). The overall opacity is highly sensitive to the grain size distribution, and further work on a self-consistent theory of condensation, coagulation, and precipitation in dynamic atmospheres is clearly needed. Finally, the current dusty atmosphere models (Allard et al., 2001) do not take into account cloud formation or heterogeneous surface coverage, both of which are likely to be important in very cool brown dwarfs. As discussed in §7.8.5, new models by Ackerman & Marley (2001) have pursued this avenue with some success.

There is a great deal of literature available on the comparison of spectral models to empirical data, particularly in regards to the M and L dwarfs (Kirkpatrick et al., 1993, 1999a; Jones et al., 1995, 1996; Tsuji et al., 1996; Leggett et al., 1996, 2000b, 2001; Tinney et al., 1998; Leinert et al., 2000; Pavlenko, Zapatero Osorio, & Rebolo, 2000; Dawson & De Robertis, 2000; Schweitzer et al., 2001), as well as for Gliese 229B (Allard et al., 1996; Marley et al., 1996; Tsuji, Ohnaka, & Aoki, 1996a; Matthews et al., 1996; Burrows, Marley, & Sharp, 2000; Saumon et al., 2000). As the complexity of the underlying physics has grown in the theoretical models, the consistency between predicted and observed spectral energy distributions has improved. There remains some work do be done, however, particularly in the development of accurate line lists (Saumon et al., 2000), the treatment of dust and rainout, and disequilibrium chemistry (Griffith & Yelle, 1999; Saumon et

al., 2000). Many of the "fine-tuning" improvements to theoretical models have yielded substantial insight into the details of substellar atmospheres.

1.3 Searches for Brown Dwarfs

The observational search for brown dwarfs has had a long and checkered history, characterized early on by false alarms, upper limits, and general frustration. The tone of search campaigns prior to the mid-1990s is evident in the conference proceedings of Kafatos, Harrington, & Maran (1986) and Tinney (1995). The flood of brown dwarf discoveries starting in 1995 finally brought these efforts to fruition, and firmly put to rest doubts on the existence of substellar objects. Excellent reviews of brown dwarf searches can also be found in Oppenheimer, Kulkarni, & Stauffer (2000) and Basri (2000).

Early search efforts are summarized in Table 1.1, which basically fall into four categories: companion searches, cluster surveys, deep imaging surveys, and radial velocity monitoring. Because these objects were predicted to emit most of their light in the near-infrared, brown dwarf searches began in earnest soon after the development of infrared detectors and arrays. Early work by Probst & O'Connell (1982), Probst (1983a,b), and Jameson, Sherrington, & Giles (1983) failed to identify any faint companions around either white dwarfs or nearby stars. McCarthy, Probst, & Low (1985) reported the detection of a faint companion to VB 8B via speckle interferometry, and its faint magnitude firmly placed it in the substellar regime. Indeed, the first brown dwarf conference, held in Fairfax, Virginia in 1985 (Kafatos, Harrington, & Maran, 1986), largely centered around the analysis of this detection. However, both Perrier & Mariotti (1987) and Skrutskie, Forrest, & Shure (1987) failed to recover this object in followup investigation, and it is likely that the ill-fated VB 8B was merely an artifact[4]. Following this was a long period of non-detections in field and companion imaging surveys (Krishna Kumar, 1985, 1987; Boeshaar, Tyson, & Seitzer, 1986; Skrutskie, 1990), speckle interferometry (Henry & McCarthy, 1990, 1992), IRAS surveys (Shipman, 1986; Beichman, 1987), and searches for radio emission (Winglee, Dulk, & Bastian, 1986). Continuing the white dwarf companion efforts of Probst (1983b), Becklin & Zuckerman (1988) identified a faint companion to GD 165, whose unusual, cool spectrum (Kirkpatrick et al., 1993) made it one of the best brown dwarf candidates so far identified (see §1.4). Indeed, the substellarity of this object remains uncertain to this day (Kirkpatrick et al., 1999a). Skrutskie, Forrest, & Shure (1989) identified the cool companion object Gliese 569B (Forrest, Skrutskie, & Shure, 1988), which at the time appeared to be too luminous to be substellar, but has been recently identified as a double brown dwarf (Martín et al., 2000b) with a total system mass of 0.10-0.15 $M_{\odot}$ (Lane et al., 2001). Leinert et al. (1994) identified two low-luminosity, proper motion companions to LHS 1070, but follow-up investigation places them just above the HBMM (Leinert et al., 2000).

Deep imaging surveys of clusters began in force in the late 1980s, with the prospect of identifying brown dwarfs in their early, brighter phases. Early imaging surveys of the Hyades by Leggett & Hawkins (1988, 1989) turned up a number of very red, potentially cool objects; however, many were later identified as background protostars from parallax data (Harris et al., 1999). Bryja et al. (1992) also identified substellar candidates in the Hyades, but follow-up spectroscopy confined the faintest Hyades members to the stellar regime (Bryja, Humphreys, & Jones, 1994). An imaging survey of Taurus by Forrest et al. (1989) turned up a number of good candidates, but these were all identified as background stars by Stauffer et al. (1991). Skrutskie (1990) failed to identify any substellar companions in either Taurus or the Hyades. Jameson & Skillen (1989), Stauffer et al. (1989), and Stauffer, Hamilton, & Probst (1994) used deep red optical surveys to probe the Pleiades, turning up a number of candidates in this nearby cluster. However, there was ambiguity early on as to the

[4]Don McCarthy describes it as a seeing-induced differential airmass effect (J. D. Kirkpatrick, priv. comm.).

Table 1.1: Searches for Brown Dwarfs Prior to 1995.

Reference (1)	Type[a] (2)	Description (3)
Probst & O'Connell (1982)	C	NIR imaging around white dwarfs; no detections
Probst (1983a,b)	C	NIR imaging around white dwarfs; no detections
Jameson, Sherrington, & Giles (1983)	C	NIR imaging around nearby stars; no detections
McCarthy, Probst, & Low (1985)	C	NIR speckle interferometry around nearby stars; identified false source VB 8B
Krishna Kumar (1985, 1987)	C	NIR imaging around nearby stars; no detections
Boeshaar, Tyson, & Seitzer (1986)	D	B_J, R, I deep CCD survey; no detections
Shipman (1986)	C	IRAS search around white dwarfs; no detections
Winglee, Dulk, & Bastian (1986)	C	Radio search for cyclotron maser radiation; no detections
Beichman (1987)	D	IRAS survey; no detections
Becklin & Zuckerman (1988)	C	NIR imaging around white dwarfs; identified GD 165B
Campbell, Walker, & Yang (1988)	RV	No detections for 12 late-type dwarfs and 4 subgiants
Leggett & Hawkins (1988, 1989)	C	IR photometry of Hyades candidates; identified as background protostars
Forrest et al. (1989)	CL	Taurus imaging survey; BD candidates identified as background stars
Jameson & Skillen (1989)	CL	Pleiades I, R survey; 7 possible BDs
Latham et al. (1989)	RV	Detected HD 114762B
Skrutskie, Forrest, & Shure (1989)	C	NIR Imaging around nearby stars; identified Gliese 569B
Skrutskie (1990)	C,CL	NIR imaging of nearby by stars, Hyades, Taurus; no detections
Henry & McCarthy (1990)	C	NIR speckle interferometry around nearby M dwarfs; no detections
Rieke & Rieke (1990)	CL	ρ Oph imaging survey; 3 possible BDs identified
Barsony, Schombery, & Kis-Halas (1991)	CL	K-band imaging of Lk Hα 101; candidates but no followup
Bryja et al. (1992, 1994)	C	Proper motion Hyades candidates; no cluster members below 0.1 $M_\odot$
Henry & McCarthy (1992)	C	NIR speckle interferometry; no companions below 0.07 $M_\odot$
Simons & Becklin (1992)	CL	Pleiades I, K survey; BD candidates identified as background sources
Hambly, Hawkins, & Jameson (1993)	CL	Pleiades proper-motion survey; BDs candidates without Li
Murdoch, Hearnshaw, & Clark (1993)	RV	No detections for 29 solar-type and 10 giant stars
Leinert et al. (1994)	C	NIR speckle interferometry of M dwarfs; identified possible BD companions LHS 1070B and LHS 1070C
Stauffer, Hamilton, & Probst (1994)	CL	Pleiades I, V survey; 6 BD candidates

[a] C = companion search, CL = cluster survey, D = deep imaging surveys, RV = radial velocity monitoring.

contamination of red foreground stars (M dwarfs) in these samples. Hambly, Hawkins, & Jameson (1993) made a proper-motion survey of the Pleiades, revealing very cool members; however, follow-up optical spectroscopy failed to detect the 6708 Å Li line in any of these candidates (Marcy, Basri, & Graham, 1994; Martín et al., 1994). Rieke & Rieke (1990) and Barsony, Schombery, & Kis-Halas (1991) used imaging surveys of the young star-forming regions of ρ Ophiucus and Lk Hα 101 to identify substellar objects in their earliest phases, but follow-up spectroscopy of the former sample failed to detect M-type absorption features. The significant reddening of these young clusters results in significant ambiguity in determining the substellar nature of candidates.

Radial velocity surveys also began in earnest around this time, with the goal of detecting the reflex motion of close stellar and brown dwarf companions to nearby stars. Initial results by Campbell, Walker, & Yang (1988) and Murdoch, Hearnshaw, & Clark (1993) failed to detect any substellar companions. Latham et al. (1989) found significant radial velocity signatures in one of their radial velocity standards, HD 114762. A fit to the orbit yields a secondary mass $M \sin i = 11$ M_{Jup}, making it a likely brown dwarf; however, the uncertain inclination of this system curtailed wide acceptance of this object as substellar. Indeed, the state of the field in the early 1990s was one of great skepticism, as is plainly obvious in the proceedings of the next brown dwarf conference held in Garching, Germany in 1994 (Tinney, 1995).

The field changed dramatically in 1995, however, with the discovery of three *bona fide* brown dwarfs. Although there remains some controversy over the "first" brown dwarf detection (particularly given the radial velocity results of Latham et al. (1989) and ambiguous cluster candidates), the discovery of the ultracool companion Gliese 229B (Nakajima et al., 1995, §1.5), and the identification of the 6708 Å Li line in the Pleiades brown dwarfs PPl 15 (Basri, Marcy, & Graham, 1996, a Pleiades candidate identified by Stauffer et al., 1994) and Teide 1 (Rebolo et al., 1996), were the first widely-accepted positive results in the search for brown dwarfs. A subsequent conference held in Tenerife, Spain, in 1997 (Rebolo, Martín, & Zapatero Osorio, 1998) was filled with successful discoveries of brown dwarfs, and hundreds of brown dwarfs are now known in the field, in clusters, and as companions to nearby stars (Basri, 2000). So began the era of *observational* substellar astronomy.

1.4 L Dwarfs

One of the putative brown dwarf discoveries, GD 165B (Becklin & Zuckerman, 1988; Zuckerman & Becklin, 1992), turned out to be an interesting case. The first optical spectrum of this object obtained by Kirkpatrick et al. (1993, Figure 1.9) showed it to be quite distinct from other late-type M dwarfs known at that time, lacking the characteristic TiO bands at 8432 and 8859 Å. There was initially some concern raised over the possible pollution of this object by the evolved DA white dwarf primary during its asymptotic giant branch phase (Reid & Hawley, 2000). However, Kirkpatrick, Beichman, & Skrutskie (1997) soon identified a similar late-type dwarf in Two Micron All Sky Survey (Skrutskie et al., 1997, hereafter 2MASS) protocam data, 2MASP J0345432+254023, followed closely by the discovery of the field brown dwarf Kelu-1 (Ruiz, Leggett, & Allard, 1997) and three late-type objects by Delfosse et al. (1997) in data from the DEep Near-Infrared Survey (Epchtein et al., 1997, hereafter DENIS).

During the Tenerife conference, Kirkpatrick (1998) suggested that a new classification be introduced to encompass these discoveries, subsequently termed "L" by Martín et al. (1997). Both Kirkpatrick et al. (1999b) and Martín et al. (1999) have derived independent classification schemes for the first major addition to the MK system since its inception (Morgan, Keenan, & Kellman, 1943).

Figure 1.10 shows the late-M and L dwarf sequence of Kirkpatrick et al. (1999b) defined in the red optical (6300–10100 Å), showing nine distinct subclasses from L0 V to L8 V. By comparing to

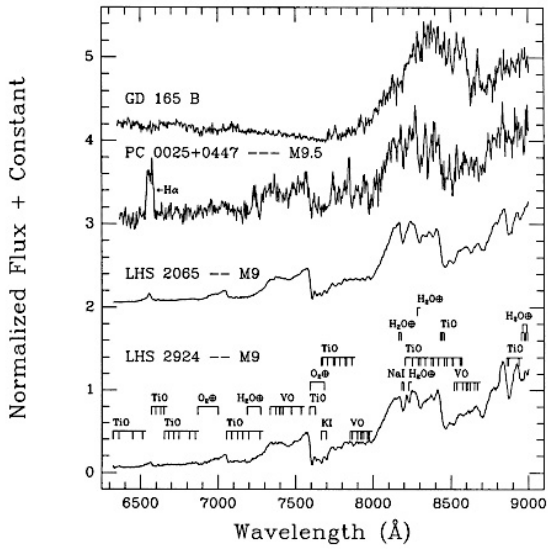

Figure 1.9: Early spectrum of GD 165B and three late M dwarfs LHS 2924 (M9 V), LHS 2065 (M9 V), and PC 0025+0447 (M9.5 V). Molecular, atomic, and telluric features are noted on the spectrum of LHS 2924 (from Kirkpatrick et al. 1993).

the features identified in Figure 1.11, we see that the evolution of this sequence is initially determined by the weakening of TiO (the defining feature of the M dwarfs, first identified by A. Fowler in 1904) and strengthening of VO in the early subtypes, followed by the subsequent weakening of the latter feature and strengthening of CrH and FeH, as well as strengthening resonance lines of K I, Rb I, and Cs I (Na I at 8183 and 8195 Å weakens throughout the sequence). There is a gradual increase in the slope from 7700 to 10000 Å in the mid- and late-L dwarfs, caused by the broadening of the K I doublet to over 100 Å in equivalent width, resulting in red optical/near-infrared colors (Figure 1.12). Finally, the CrH and FeH bands weaken, and H_2O strengthens, in the latest L subtypes.

In the near-infrared, L dwarfs are characterized by red J−K_s colors (see Figure 1.23), which have been generally attributed to photospheric dust opacity (Leggett, Allard, & Hauschildt, 1998). The reddest colors of L dwarfs identified by Kirkpatrick et al. (1999b, 2000) are around J−$K_s \approx 2.1$. Their near-infrared spectra are dominated by H_2O and CO absorption bands (Leggett et al., 2001; Reid et al., 2001a; Testi et al., 2001; Wilson et al., 2001c); while at J-band, a number of finer features attributed to K I, Na I, and FeH are found (McLean et al., 2000). At later types, these features generally weaken, while H_2O and CO bands both strengthen (Leggett et al., 2001; Reid et al., 2001a). Near-infrared colors also turn over slightly toward the blue from L6 V to L8 V (Kirkpatrick et al., 2000). Recently, Noll et al. (2000) have identified the fundamental 3.3 μm band of CH_4 in the latest-type L dwarfs. The majority of flux emitted from these objects comes out in the 1–2.5 μm range, which is why 2MASS and DENIS have had a great deal of success identifying this objects.

Kirkpatrick et al. (1999b, 2000) have used the behavior of the red optical features, along with the equilibrium calculations of Burrows & Sharp (1999), to derive an approximate effective temperature scale for the L dwarfs. They find a range of 2000 to $\sim$ 1300 K for types L0 V to L8 V, which is supported by the theoretical models of Pavlenko, Zapatero Osorio, & Rebolo (2000). Both Basri & Martín (1999a) and Stephens et al. (2001) find slightly higher temperatures of 2200–1600 K and 2220–1420 K, respectively. Similarly, Leggett et al. (2001) find a temperature scale of 2200–1400 K based on the structure models of Chabrier et al. (2000a). We discuss the temperatures of L dwarfs

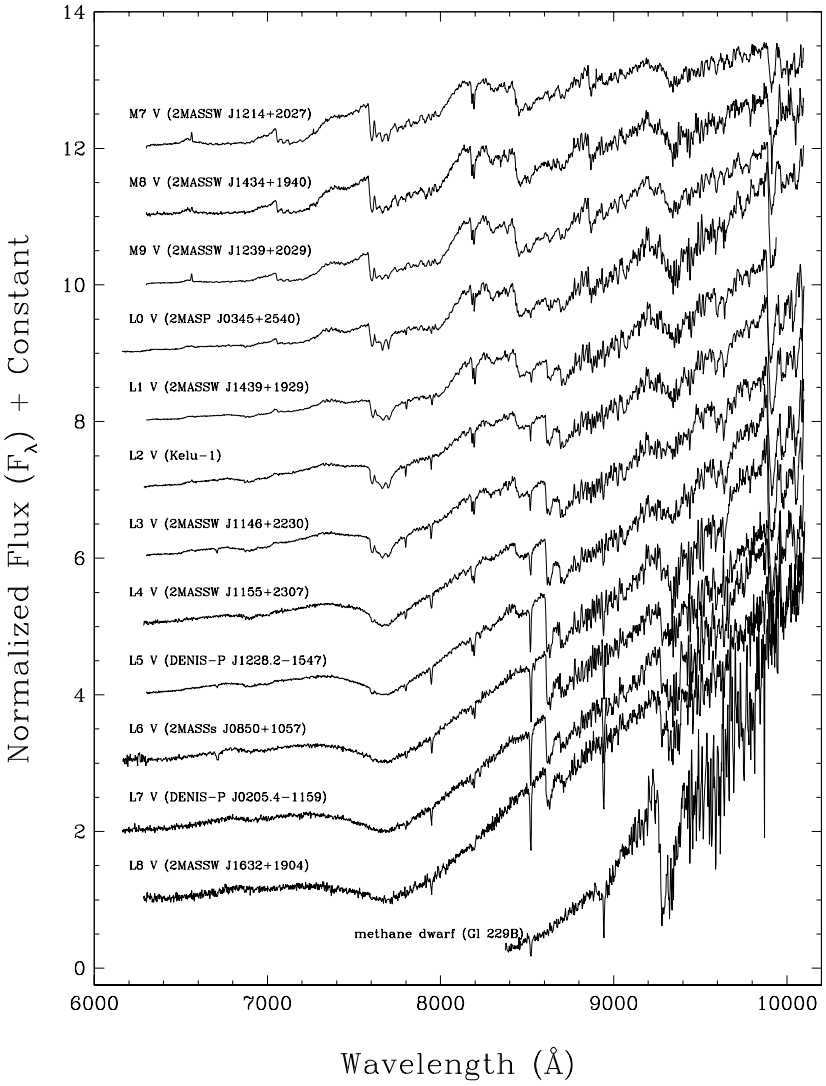

Figure 1.10: Spectral sequence of late-type dwarfs from M7 V to L8 V. Also shown are data for the prototype T dwarf Gliese 229B (from Kirkpatrick et al. 1999).

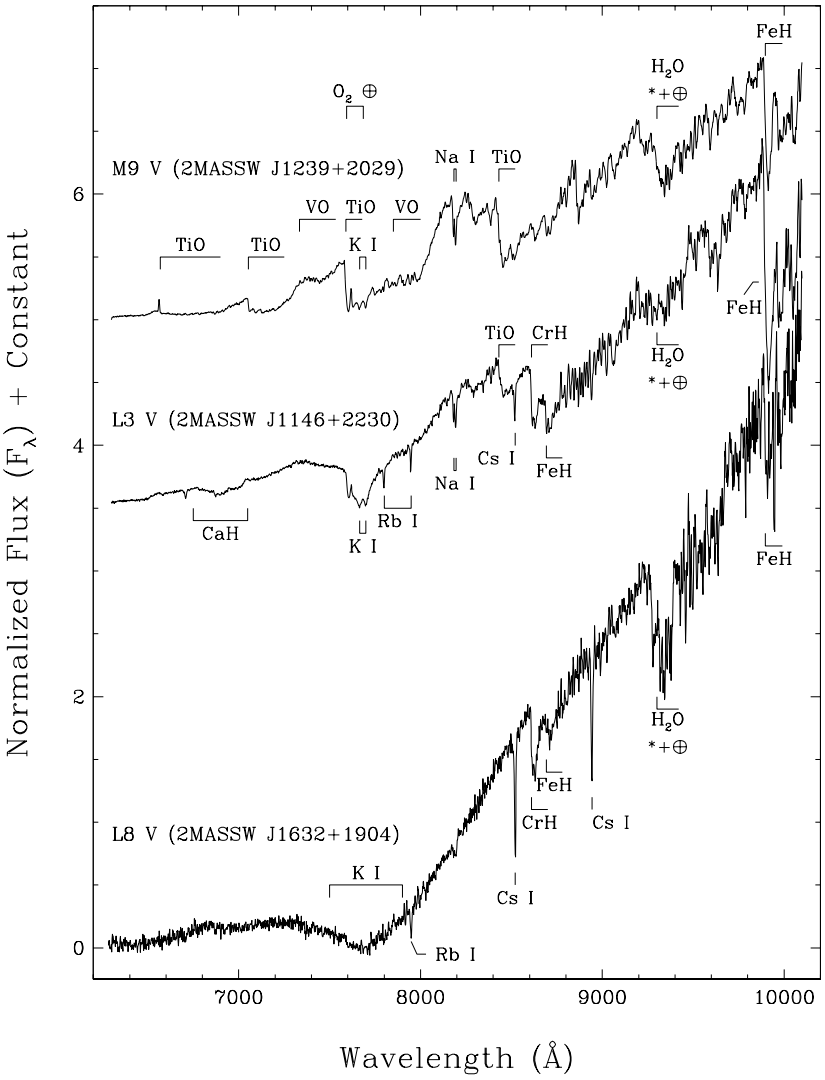

Figure 1.11: Spectral features in the 6300–10100 Å regime for late-M, early-L, and late-L dwarfs. Molecular, atomic and telluric (⊕) features are indicated (from Kirkpatrick et al. 1999).

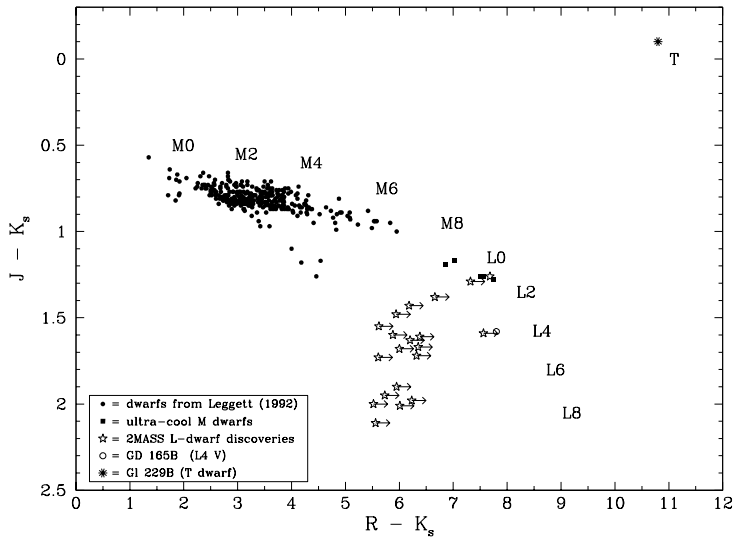

Figure 1.12: Optical/near-infrared colors of M and L dwarfs, showing a progressive reddening through the entire spectral sequence. The colors of Gliese 229B are indicated by the asterisk (from Kirkpatrick et al. 1999).

in more detail in §7.8.4. It should be noted, however, that these temperatures, convolved with the evolutionary models of Burrows et al. (1997) and Chabrier et al. (2000a), imply that all L dwarfs later than type $\sim$ L6 V are substellar. Indeed, Kirkpatrick et al. (1999b) estimate that roughly one-third of the L dwarfs in their sample are brown dwarfs based on the detection of the 6708 Å Li line (Figure 1.13).

With well over 100 L dwarfs identified to date, it is clear that GD 165B, rather than being an oddity influenced by the evolution of its white dwarf primary, is in fact the prototype for the well-established L dwarf class[5].

1.5 Gliese 229B: The Prototype T Dwarf

Another unusual object identified by brown dwarf searches was the ultracool Gliese 229B (Nakajima et al., 1995), a common proper motion companion 7.″8 from the M1 V Gliese 229A. This object was identified through a coronagraphic survey of the stars within 8 pc of the Sun and with $\delta > -35°$ (Nakajima et al., 1994; Oppenheimer et al., 2001). HST WFPC2 images of Gliese 229B from Golimowski et al. (1998) are shown in Figure 1.14.

This object gained rapid acceptance as a *bona fide* brown dwarf due to presence of CH_4 absorption in its near-infrared spectrum (Oppenheimer et al., 1995), reminiscent of the giant planets and Titan (Geballe et al., 1996). The CH_4 bands, along with H_2O and H_2 collision-induced absorption (CIA) (Saumon et al., 1994), produce blue near-infrared colors (J−K = −0.10±0.07; Leggett et al. 1999), quite unlike the L dwarfs. The red optical slope in this object is also quite pronounced, as can be seen at the bottom of Figure 1.10. The corresponding optical/near-infrared colors are thus quite large, with R−J $\approx$ 9.1 (Golimowski et al., 1998; Leggett et al., 1999, Figure 1.12). It was unclear early

[5]GD 165B is classified as L4 V, a mid-L dwarf.

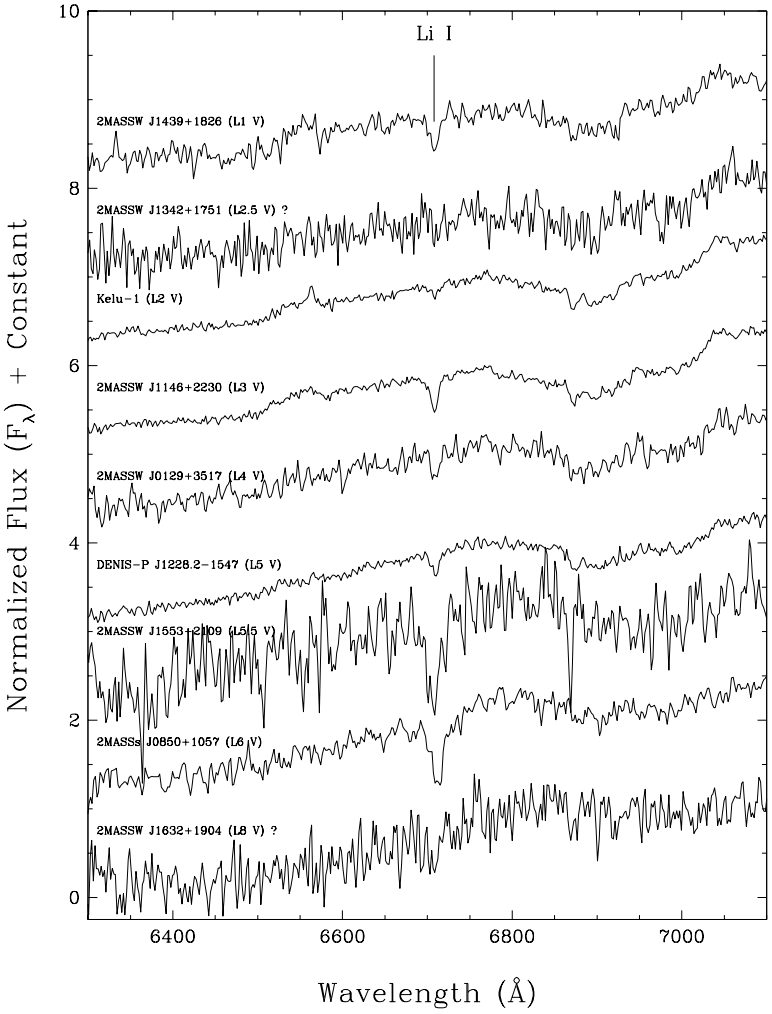

Figure 1.13: 6708 Å Li line in nine L dwarfs (from Kirkpatrick et al. 1999).

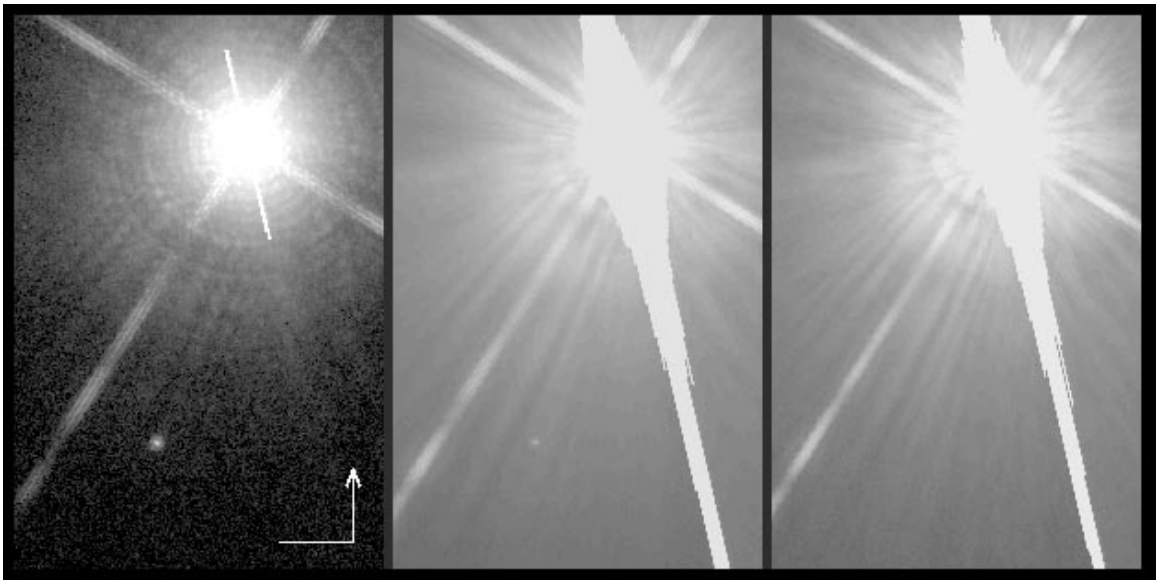

Figure 1.14: HST WFPC2 images of Gliese 229B (object at bottom of image) at F1042M (left), F814W (center), and F675W (right) (from Golimowski et al. 1998).

on as to what caused this steep drop in the red optical energy distribution, and various hypotheses including the retention of TiO and VO (Golimowski et al., 1998); photochemical haze particles (Griffith, Yelle, & Marley, 1998), analogous to tholins in the atmosphere of Titan (Khare & Sagan, 1984); and dust scattering (Tsuji, Ohnaka, & Aoki, 1999; Pavlenko, Zapatero Osorio, & Rebolo, 2000) were proposed. It is now clear that the 7665, 7699 Å K I doublet, which is seen to broaden in the L dwarfs (Figure 1.10), is largely responsible for this feature (Tsuji, Ohnaka, & Aoki, 1999; Liebert et al., 2000b; Burrows, Marley, & Sharp, 2000).

Oppenheimer et al. (1998) have investigated the spectrum of Gliese 229B in great detail, identifying major absorption features of Cs I, H_2O, CH_4, and CO from 0.8 to 5 μm (see Figure 6.7). CIA H_2 opacity is also important at K-band in this object. The coincident presence of strong Cs I lines and CO at 4.7 μm has been interpreted as arising from a detached convection zone in the upper photosphere (Oppenheimer et al., 1998). The abundance of CO, which was first detected in Gliese 229B by Noll, Geballe, & Marley (1997), is far in excess of its equilibrium value, implying that material is dredged up from deeper, hotter layers (Griffith & Yelle, 1999; Saumon et al., 2000).

The presence of CH_4 in Gliese 229B sets it apart from the L dwarfs, as noted by Kirkpatrick et al. (1999b, Figure 1.15). The K-band in L dwarfs is dominated by CO absorption at 2.3 μm, while CIA H_2 plays an important role in shaping the peak of this band (Tokunaga & Kobayashi, 1999). These differences led Kirkpatrick et al. (1999b) to propose a second new spectral type, T dwarf, in order to differentiate this object. Despite directed searches, however, Kirkpatrick et al. (1999b) found no analogues to Gliese 229B in 371 deg^2 of 2MASS data. Indeed, the first discoveries are some of those presented in this thesis. As is evident in the forthcoming chapters, it appears that, in analogy to GD 165B, Gliese 229B is no longer an oddity but the prototype of yet another new spectral class.

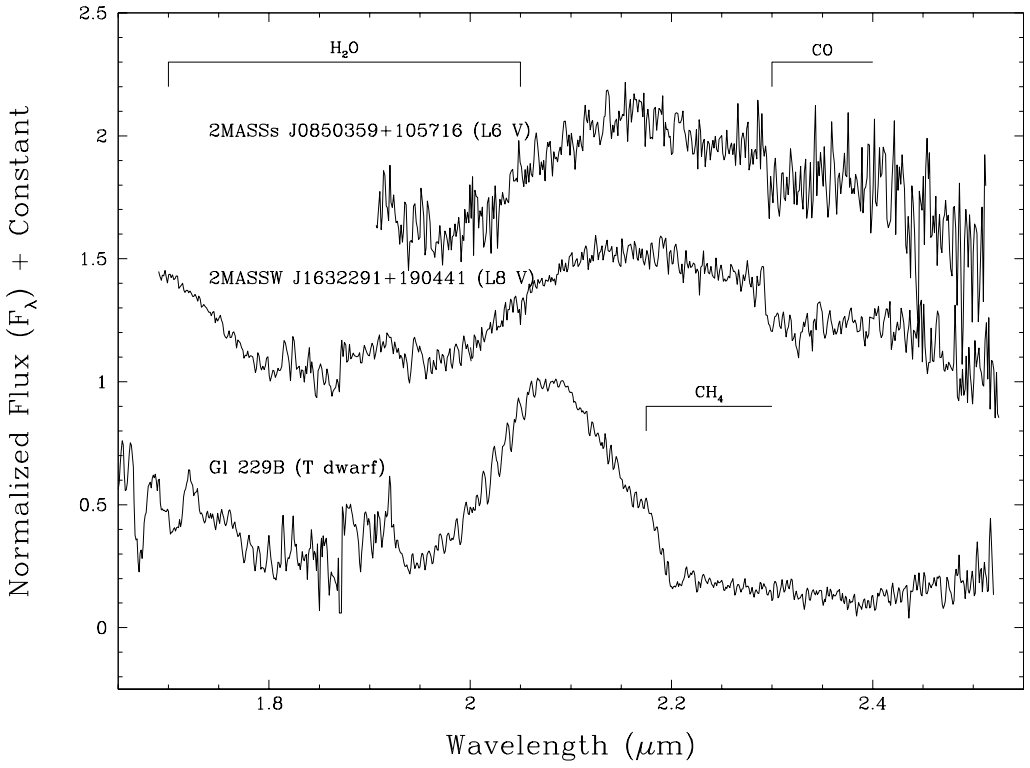

Figure 1.15: 1.7–2.5 μm spectra for two late-L dwarfs and Gliese 229B. Major absorption bands of H_2O, CH_4, and CO are indicated. Data for Gliese 229B are from Geballe et al. (1996) (from Kirkpatrick et al. 1999).

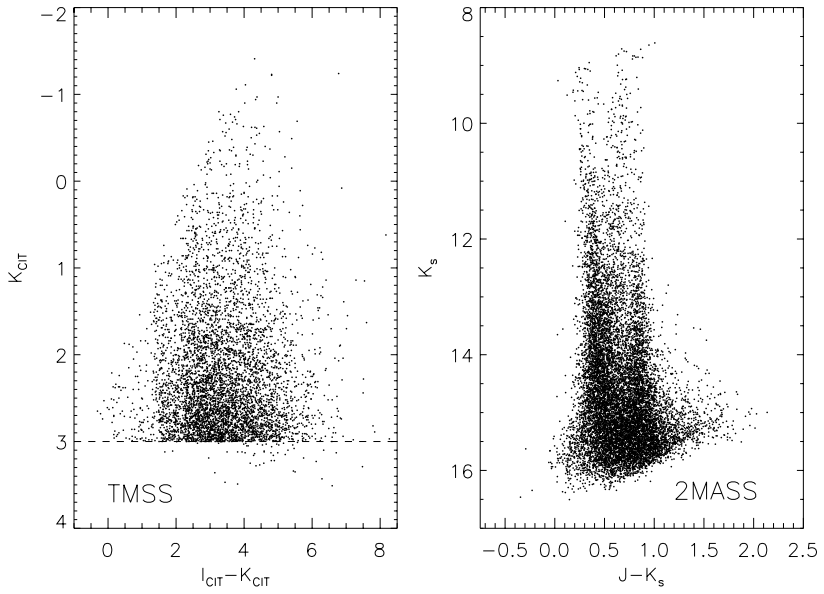

Figure 1.16: Color-magnitude plots for sources listed in the Two-Micron Sky Survey Preliminary Catalog (Neugebauer & Leighton, 1969) and those detected in all three bands by 2MASS in a 1° radius around 18^h R.A. and +40° decl. The $K_{CIT} < 3$ completeness limit in the TMSS catalog is indicated by a dashed line.

1.6 The 2MASS Survey and Point Source Catalog

[6]Our search for T dwarfs was conducted using the recently completed Two Micron All Sky Survey (Skrutskie et al., 1997, hereafter, 2MASS). This project is a joint venture of the University of Massachusetts and the Infrared Processing and Analysis Center (IPAC), headed by PI Michael F. Skrutskie (UMASS), Project Manager Rae Stiening (UMASS), and Project Scientist Roc M. Cutri (IPAC). The primary goals of 2MASS are (1) to uniformly map the mass distribution in the Local Universe out to 220 Mpc; (2) to uniformly map the distribution of stars, in order to find and measure large-scale structure, and provide a context for future studies; (3) to seek elusive or rare objects, such as brown dwarfs or red quasars; and (4) to support the next generation of space projects.

The 2MASS survey is a significant advancement over the earlier Two-Micron Sky Survey (Neugebauer & Leighton, 1969, hereafter, TMSS), carried out between 1965 January 30 (UT) and 1968 April 7 (UT) on the Mt. Wilson 60" telescope. Using cooled PbS photoconductive cells with a 2.0–2.4 μm interference filter, TMSS detected over 2×10^5 sources between $-33° < \delta < 81°$ in the magnitude range $-2.0 < K_{CIT} < 4.5$. Parallel observations made using a Si photovoltaic cell provided photometry at 0.84 μm (roughly I-band) in the range $2 < I_{CIT} < 10$. At the time of its undertaking, TMSS was a unique resource for infrared astronomers, providing the largest sky coverage for any near-infrared survey until the completion of 2MASS; however, the vast majority of sources it detected were previously identified stars (Neugebauer & Leighton, 1969; Bidelman, 1980).

[6]Much of the information provided in this section has been obtained from Cutri et al. (2001), Explanatory Supplement to the 2MASS Second Incremental Data Release, http://www.ipac.caltech.edu/2mass/releases/second/doc/explsup.html.

The development of infrared detector arrays since this earlier work has enabled 2MASS to produce a survey over 3×10^6 times more sensitive. Figure 1.16 shows a comparison between all 5612 sources in the TMSS Preliminary Catalog (Neugebauer & Leighton, 1969) and 12026 sources detected in all three bands in a 1° radius around 18^h R.A. and +40° decl. 2MASS is capable of detecting sources 13.5 mag fainter than the TMSS completeness limit of $K_{CIT} = 3$.

1.6.1 2MASS Operations

The 2MASS survey employs two highly-automated, equatorial-mount, 1.3m telescopes, one at Mt. Hopkins in Arizona, USA, and the other at Cerro Tololo in Chile. Each is equipped with a three-channel camera capable of simultaneous observations in the J (1.25 μm), H (1.65 μm), and K_s (2.17 μm) near-infrared bands, using three 256×256 HgCdTe NICMOS3 arrays. The pixel scale for each detector is roughly 2″ on the sky. Survey imaging operations begun in 1997 June 7 (UT) at Mt. Hopkins and 1998 March 19 (UT) at Cerro Tololo were completed on 2000 December 1 (UT) and 2001 February 15 (UT), respectively (J. D. Kirkpatrick, priv. comm.).

2MASS observations are obtained in a continuous scan-and-stare mode. Each telescope is driven at a rate of 57″ s^{-1} in declination, while the secondary mirror tracks the sky during each integration. Individual exposures are made in a "Reset-Read-Read" cycle, with an initial 51 ms READ1 followed by a 1.3 s READ2. These exposures are differenced to produce the final image frame, after correcting for image bias (dark frames) and pixel responsivity (twilight flat fields). Each area of the sky is imaged six times at different positions on the detectors for a total integration time of 7.8 s. The multiple dithered exposures are then coadded with subpixel offsets to produce a final tile image with substantially improved spatial resolution (1″ pixel scale). Tiles are acquired in a 6°×8.′5 strip, shifted 7.′65 in R.A. between scans to provide overlap.

Point sources are extracted from the 2MASS images by identifying local intensity maxima, and aperture photometry is initially obtained using a 4″ (2 pixel) aperture. Final photometric measurements are made using either a PSF-fitting algorithm or aperture photometry with a curve-of-growth correction. These values are calibrated to Persson et al. (1998) or UKIRT photometric standards (Casali & Hawarden, 1992; Hawarden et al., 2000), with secondary standards defined by 2MASS used to improve the final calibration; zero-point magnitudes are tracked repeatedly during each night through multiple observations of specified calibration fields. Photometry for bright sources that are saturated in the READ2 exposures (J $\lesssim$ 8.0, H $\lesssim$ 7.5, and $K_s \lesssim$ 7.0) are measured directly from the READ1 exposures; sources brighter than 4-5 mag are also saturated in the READ1 exposures. Objects not detected in any one band are assigned band-filled magnitudes, a 95% confidence, upper-limit estimate based on the background and noise levels in the area around the object's coordinates. Astrometry is tied to the International Celestial Reference System (Arias et al., 1995, ICRS), calibrated using the ACT Reference Catalog (Urban, Corbin, & Wycoff, 1998).

These observations have resulted in a catalog of photometrically calibrated point sources with nominal survey completeness limits (S/N = 10) of J=15.8, H=15.1, and K_s=14.3. Analysis of the 2MASS Second Incremental Data Release (IDR2), a subset of the final catalog covering an area of 19,641.8 sq. deg. (47.6% of the sky), indicates empirical 99% completeness limits down to J=15.8, H=15.4, and K_s=15.2. Astrometric dispersion of the 2MASS IDR2 was measured to be 0.″11 as compared to the ACT catalog and 0.″12 as compared to the UCAC1 catalog (Zacharias et al., 2000).

1.6.2 2MASS Near-Infrared Filters and Photometric System

In order to fully understand the photometric properties of 2MASS data, it is important to characterize the response characteristics of the optics and filters used in the survey cameras. The total

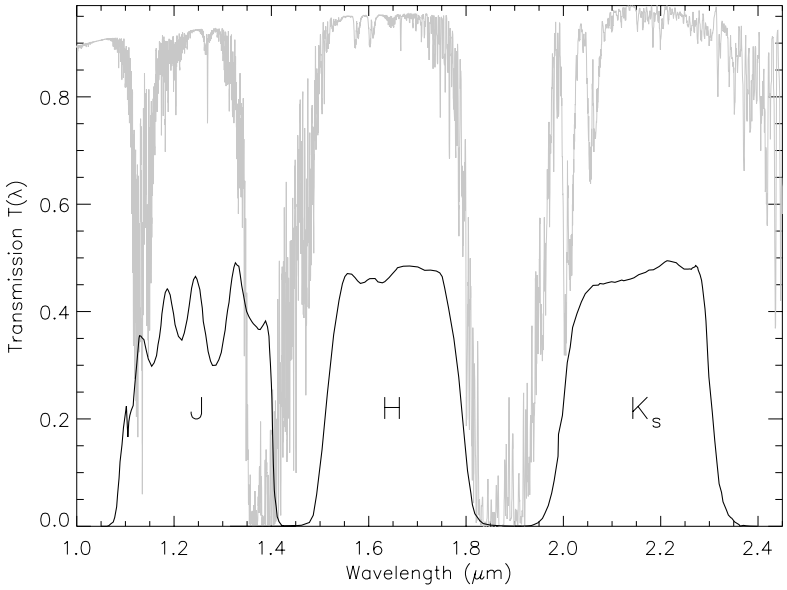

Figure 1.17: Total transmission curves, including telescope and instrumental response, for the 2MASS JHK$_s$ filters (thick solid lines). Gray lines plot the typical telluric transmission at Mt. Hopkins in this spectral range (USAF Plexus code; M. Cohen, priv. comm.).

throughput of the system, excluding atmospheric effects, can be computed from:

$$T(\lambda) = M^2 \times D_e \times L^7 \times \left\{ \begin{array}{l} J_{dr} \times J_f \\ J_{dt} \times H_{dr} \times H_f \\ J_{dt} \times H_{dt} \times K_{sf} \end{array} \right\} \times D_q, \tag{1.11}$$

where $M(\lambda)$ is the reflectivity of the primary and secondary mirrors ($\sim 0.96^2 = 0.92$), $D_e(\lambda)$ is the dewar window transmission (~ 0.95), $L(\lambda)$ is the lens coating transmission for the seven lenses in each camera lightpath ($\sim 0.98^7 = 0.87$), $J_{dr}(\lambda)$ and $H_{dr}(\lambda)$ are the J and H dichroic reflectivities and $J_{dt}(\lambda)$ and $H_{dt}(\lambda)$ the corresponding transmissivities, $J_f(\lambda)$, $H_f(\lambda)$, and $K_{sf}(\lambda)$ are the filter transmission curves, and $D_q(\lambda)$ is the quantum efficiency of the detectors (~ 0.62). Figure 1.17 plots the total transmission curves for the J-, H-, and K$_s$-bands; typical atmospheric transmission at the Mt. Hopkins sites is also shown, computed using the USAF PLEXUS code (M. Cohen, priv. comm.). The long wavelength cutoff of the 2MASS J filter falls within the telluric H_2O and CO_2 bands starting at 1.35 μm, and J-band photometry is thus subject to changes in atmospheric absorption. Indeed, zero-point variations of order 0.1 mag are seen at J-band over the course of a single 2MASS observing night (Cutri et al., 2001). The H-band is affected by OH airglow lines, which occasionally increase background and photometric noise levels. The K$_s$ filter, developed by M. Skrutskie, is slightly narrower than the standard K filter in order to reduce thermal background at ground-based sites (Persson et al., 1998).

The 2MASS filter set is similar to the LCO JHK$_s$ filters used by Persson et al. (1998) to define a suite of faint near-infrared standards. Table 1.2 lists the integrated flux densities for Vega (Bergeron, Wesemael, & Beauchamp, 1995) through these two filter sets and through the total 2MASS response

Table 1.2: Integrated Vega Flux Through JHK$_s$ Filters.

	LCO		2MASS filters		2MASS total response	
Band	Bandpass	f^{Vega}	Bandpass	f^{Vega}	Bandpass	f^{Vega}
(1)	(2)	(3)	(4)	(5)	(6)	(7)
J	1.12–1.35	6.410	1.10–1.40	6.937	1.11–1.40[a]	3.510
H	1.49–1.82	2.726	1.51–1.79	2.740	1.51–1.79	1.506
K$_s$	1.99–2.32	1.313	2.00–2.31	1.229	2.00–2.31	0.645

Note – Bandpasses measured in μm, flux (f^{Vega}) measured in units of 10^{-7} erg cm^{-2} s^{-1}
[a]Long wavelength cutoff is ~ 1.36 μm due to telluric absorption.

curves of Figure 1.17, computed from:

$$f^{Vega} = \int F_{\lambda}^{Vega}(\lambda')T(\lambda')d\lambda'. \tag{1.12}$$

The J and K$_s$ filters yield significantly different flux values, with 8% and 6% more flux coming through the 2MASS filters, respectively. The H filters differ by less than 1%.

Carpenter (2001) has recently compiled color transformations from the 2MASS photometric system to other near-infrared JHK systems. Table 1.3 summarizes the transformations into the AAO (Allen & Cragg, 1983; Elias et al., 1983), CIT (Elias et al., 1982, 1983), LCO (Persson et al., 1998), SAAO (Carter, 1990; Carter & Meadows, 1995), and UKIRT (Casali & Hawarden, 1992; Hawarden et al., 2000) systems, with the color ranges used for the transformations listed. Note that despite the broad range of colors sampled, these transformations may not be appropriate for L and T dwarfs, which have highly structured spectral morphologies and are therefore sensitive to the shape of the filter transmission function (Carpenter, 2001).

1.7 The Near-Infrared Sky

In any color-selected search for rare objects, it is essential to characterize the color properties of common, and therefore more numerous, contaminating sources. Figure 1.18 plots the near-infrared colors of 2MASS sources with J < 16, H < 15, and K$_s$ < 14.5, within a 1° radius of $(l, b) = (60°, 10°)$ (low galactic latitude sample) and (135°, −80°) (high galactic latitude sample). For reference, we plot the colors of Gliese 229B (grey triangle) from Leggett et al. (1999), the near-infrared reddening vector A$_V$ = 5 (Rieke & Lebofsky, 1985), and the Bessell & Brett (1988) giant (upper line) and dwarf (low line) tracks, the latter defined from a sample of bright main sequence stars. The low galactic latitude population (Figure 1.18a) appears be centralized around two points in color-color space, (H-K$_s$, J-H) $\approx$ (0.08, 0.33) and (0.14, 0.58), with some scatter about these points. There is some correlation with the Bessell & Brett (1988) tracks, and most objects lie along a fairly narrow range of colors. Nearly all of the low latitude sources are substantially redder than Gliese 229B. The high galactic latitude population (Figure 1.18b) shows a much greater correlation with the Bessell & Brett (1988) tracks, particularly along the reddest end of the dwarf track ($0.15 \lesssim$ H-K$_s$ $\lesssim 0.3$). The two density peaks seen in the low latitude population are not readily apparent here. Again, there appear to be few sources with near-infrared colors similar to Gliese 229B.

Table 1.3: 2MASS Color Transformations[a].

System (1)	Transformations (2)	J-K_s Range (3)
AAO	$(K_s)_{2MASS} = K_{AAO} - 0.021(J-K)_{AAO} - 0.032$	0.0 - 3.2
	$(J-H)_{2MASS} = 0.924(J-H)_{AAO} + 0.000$	
	$(J-K_s)_{2MASS} = 0.943(J-K)_{AAO} + 0.024$	
	$(H-K_s)_{2MASS} = 0.974(H-K)_{AAO} + 0.032$	
CIT	$(K_s)_{2MASS} = K_{CIT} + 0.000(J-K)_{CIT} - 0.024$	0.0 - 2.9
	$(J-H)_{2MASS} = 1.076(J-H)_{CIT} - 0.043$	
	$(J-K_s)_{2MASS} = 1.056(J-K)_{CIT} - 0.013$	
	$(H-K_s)_{2MASS} = 1.026(H-K)_{CIT} + 0.028$	
LCO	$(K_s)_{2MASS} = K_{LCO} - 0.001(J-K)_{LCO} - 0.006$	0.3 - 3.0
	$(K_s)_{2MASS} = (K_s)_{LCO} - 0.002(J-K_s)_{LCO} - 0.010$	
	$(J-H)_{2MASS} = 0.995(J-H)_{LCO} + 0.002$	
	$(J-K_s)_{2MASS} = 1.013(J-K)_{LCO} - 0.007$	
	$(J-K_s)_{2MASS} = 1.007(J-K_s)_{LCO} + 0.002$	
	$(H-K_s)_{2MASS} = 1.008(H-K)_{LCO} + 0.002$	
	$(H-K_s)_{2MASS} = 1.019(H-K_s)_{LCO} + 0.005$	
SAAO	$(K_s)_{2MASS} = K_{SAAO} + 0.020(J-K)_{LCO} - 0.025$	−0.1 - 2.8
	$(J-H)_{2MASS} = 0.949(J-H)_{SAAO} - 0.054$	
	$(J-K_s)_{2MASS} = 0.940(J-K)_{SAAO} - 0.011$	
	$(H-K_s)_{2MASS} = 0.961(H-K)_{SAAO} + 0.040$	
UKIRT	$(K_s)_{2MASS} = K_{UKIRT} + 0.004(J-K)_{UKIRT} + 0.002$	−0.2 - 3.8
	$(J-H)_{2MASS} = 1.069(J-H)_{UKIRT} - 0.027$	
	$(J-K_s)_{2MASS} = 1.069(J-K)_{UKIRT} - 0.012$	
	$(H-K_s)_{2MASS} = 1.062(H-K)_{UKIRT} + 0.017$	

[a] From Carpenter (2001).

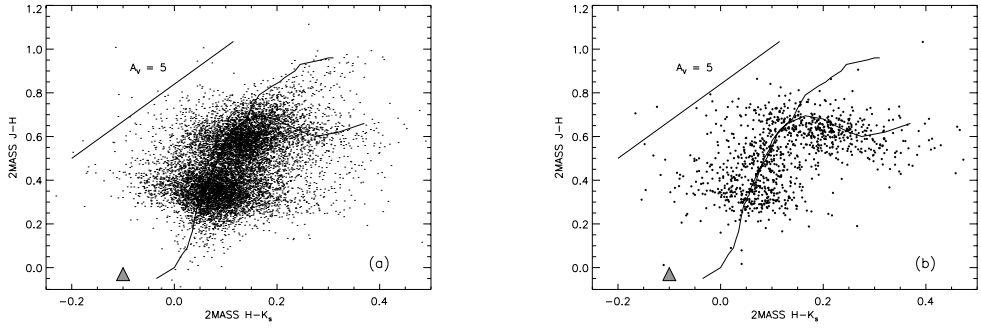

Figure 1.18: Near-infrared colors of 2MASS sources. Both plots show sources with J < 16, H < 15, and K_s < 14.5, lying within a 1° radius centered at (a) $(l, b) = (60°, 10°)$ and (b) (135°, −80°). The Bessell & Brett (1988) giant (upper line) and dwarf (lower line) tracks are shown, along with the reddening vector $A_V = 5$ (Rieke & Lebofsky, 1985) and the near-infrared colors of Gliese 229B (Leggett et al., 1999, grey triangle).

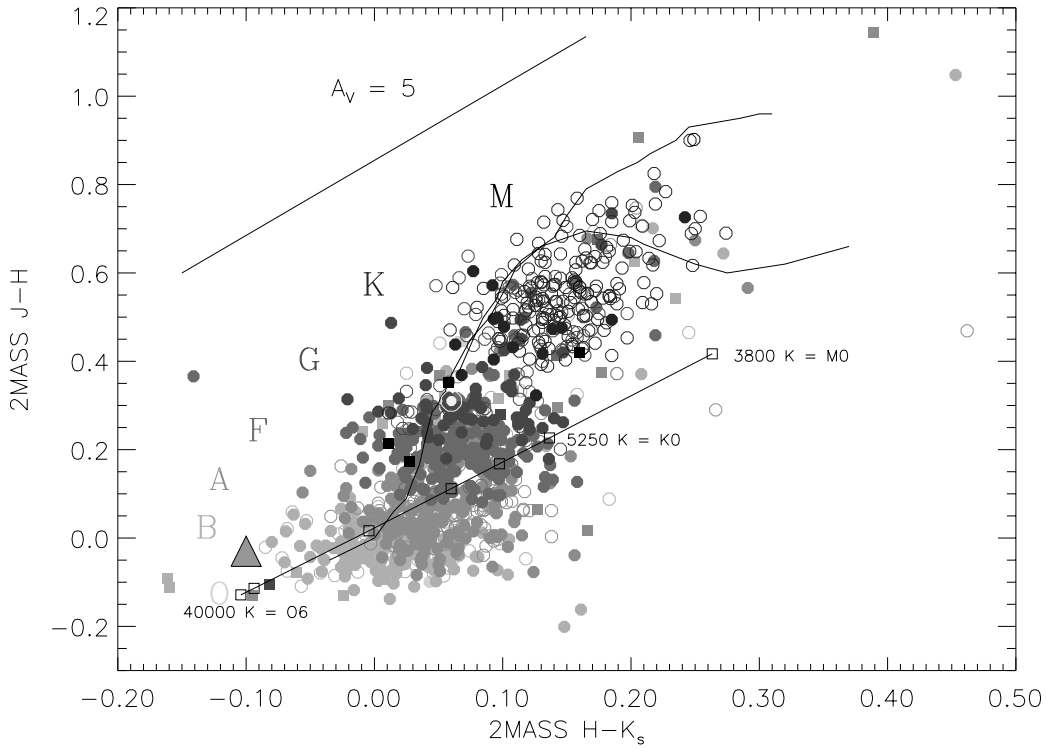

Figure 1.19: 2MASS colors of main sequence objects selected from SIMBAD. Spectral types are identified by shading from type O (light grey) to M (black). Solid circles are dwarf stars (luminosity class V), open circles are giants and subgiants (luminosity classes IV–II). Subdwarfs are plotted as filled squares. The colors of 40000, 30000, 10000, 7000, 5250, and 3800 K blackbodies, corresponding to spectral types O6, B0, A0, F0, G0, K0, and M0, are also indicated. Solar colors are plotted by the light grey $\odot$ symbol. The colors of Gliese 229B Leggett et al. (1999) are indicated by the grey triangle.

1.7.1 Main Sequence Stars

The distribution of main sequence stars in near-infrared color-color space is shown in Figure 1.19. Objects with well-defined spectral types were selected from the SIMBAD[7] database in an area between $6^h <$ RA $< 9^h$ and $-15° <$ decl. $< 0°$. We obtained 2MASS colors for these stars, restricting our sample to those with J < 16, H < 15, and $K_s < 14.5$. Note that the selection biases inherent to SIMBAD (highly dependent on the completeness of published spectral types), in addition to any color and/or magnitude biases that are difficult to quantify, implies that this sample is in no way complete, but we use it merely to illustrate the typical colors of main sequence objects. We have segregated our sample in Figure 1.19 into spectral classes O, B, A, F, G, K, and M by shading (light grey to black) and into the dwarf (V) and giant/subgiant (II–IV) luminosity classes by solid and open circles, respectively. 2MASS colors for subdwarfs selected from SIMBAD are also shown in Figure 1.19 as solid squares. For comparison, we overplot the 2MASS colors of 40000, 30000, 10000,

[7]http://simbad.harvard.edu/cgi-bin/WSimbad.pl.

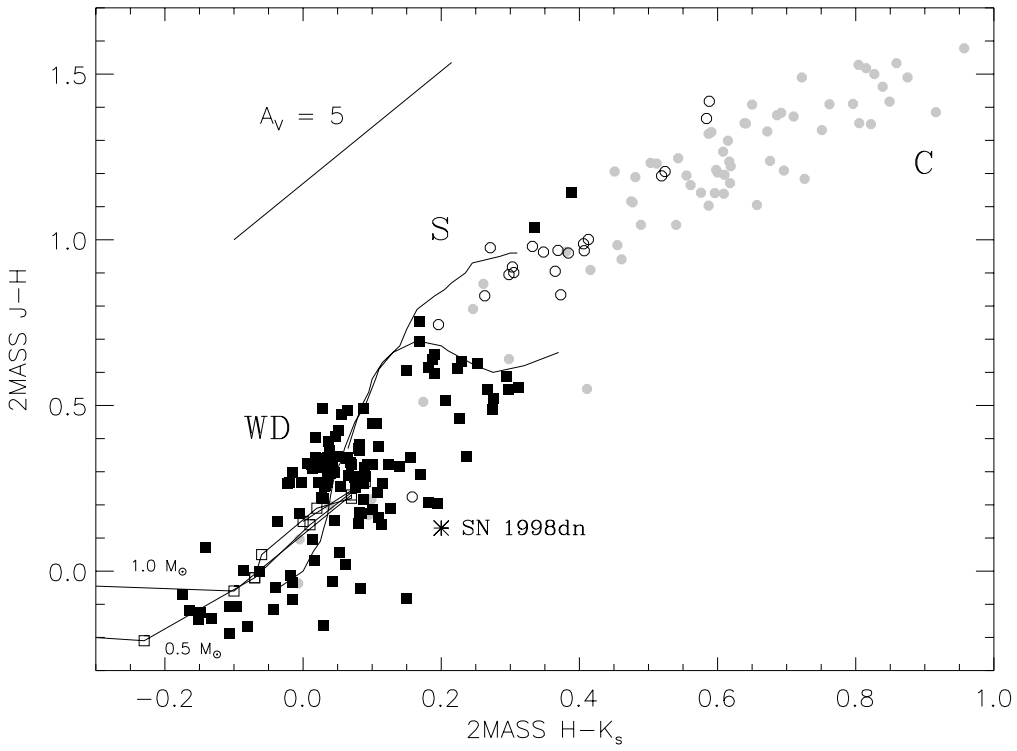

Figure 1.20: 2MASS colors of non-main sequence objects selected from SIMBAD. Colors for C-type (grey solid circles), S-type (open circles), and white dwarfs (black solid squares) are shown. The colors of SN 1998dn (Cao, 1998; Burgasser et al., 2001) are indicated by the asterisk.

7000, 5250, and 3800 K blackbodies, corresponding to spectral types O6, B0, A0, F0, G0, K0, and M0; and the near-infrared colors of the Sun (Tokunaga, 2000). We immediately perceive that the two density peaks seen in Figure 1.18a are comprised of the earliest-type dwarf (blue peak) and giant (red peak) stars, which dominate the sky toward the Galactic center. Note that the blackbody colors rapidly diverge from empirical stellar colors as early as types G–K; this is largely due to the effects of H^- absorption in the photospheres of late-type stars (Wing, 1991), as well as various molecular features that become particularly important in M stars.

1.7.2 Other Stellar Types

Figure 1.20 diagrams the color properties of C-type and S-type stars and white dwarfs. Both C-type and S-type stars are believed to be asymptotic giant branch (AGB) stars which have either dredged up enriched material from their cores or accreted this material from companion objects (Iben & Renzini, 1983; Wallerstein & Knapp, 1998). C-type, or Carbon stars, were first identified by Secchi (1868), and are distinguished by the presence of carbon-rich features such as CH, CN, and C_2, as well as lines of heavy metals including Tc. Like many AGB stars, C-type stars with high mass-loss rates are enshrouded by dusty envelopes, resulting in substantial thermal emission in the infrared. This reddening is plainly obvious in Figure 1.20, as C-type colors are much redder

than those of main sequence giants. Liebert et al. (2000a) have identified a number of Carbon stars in the 2MASS database with colors as red as J-K_s = 4.7, far redder than any currently known L dwarf (see §1.7.5). S-type stars are oxygen-rich AGBs showing significant enrichment of s-process nucleosynthesis elements, including Sr, Zr, Ba, La, and Tc (Wallerstein & Knapp, 1998). A defining feature of some S-type stars is the presence of ZrO and LaO bands replacing the TiO bands seen in M dwarfs. Like C-type stars, these objects undergo mass-loss and produce dusty outer shells, resulting in the near-infrared reddening seen in Figure 1.20.

Hot white dwarfs, on the other hand, have colors similar to blackbodies, and are thus primarily found in the vicinity of early-type dwarf stars in color-color space. As a white dwarf cools, H_2 collision-induced absorption becomes a dominant feature around M_J = 13–15 (T_{eff} = 9000–5000 K), depending on mass (Chabrier et al., 2000b). This absorption causes their near-infrared colors to become blue, as shown by the 0.5 and 1.0 $M_\odot$ evolutionary tracks from Chabrier et al. (2000b) plotted in Figure 1.20. The near-infrared colors of cool white dwarfs are thus quite similar to those of Gliese 229B, although the former objects are much brighter in the visual bands (R-J < 0; Chabrier et al. 2000b).

Finally, our search has uncovered one supernova detected by 2MASS, SN 1998dn (Cao, 1998; Burgasser et al., 2001, see §2.6.1), exhibiting blue near-infrared colors. The initial detection made on 1998 August 19 UT (2 months before the 2MASS observation) indicates that this event was a type II supernova observed well after maximum (Cao, 1998). Type II supernovae are blue in the near-infrared largely due to the presence of He I (1.0830 μm) and H I (1.0938 μm Pa γ, 1.1828 μm Pa β) emission lines at J-band (Gerardy et al., 2000).

1.7.3 Extragalactic Sources

Figure 1.21 shows the distribution of sources outside of the Galaxy. The colors of galaxies identified in the 2MASS IDR2 Extended Source Catalog, having J < 15, H < 14.5, and K_s < 14, are shown as small points. The distribution is generally constrained to a region 0.2 $\lesssim$ H-K_s $\lesssim$ 0.5 and 0.6 $\lesssim$ J-H $\lesssim$ 0.8, similar to the colors of M-type dwarfs (§1.7.5). This is not unexpected, as the infrared light of galaxies is dominated by emission from K and M dwarfs (Jarrett et al., 2000). Furthermore, galaxies with redshifts $z < 0.5$ will tend to transfer their brightness peaks into the K_s band, resulting in the so-called "K-correction," shown as solid black lines in Figure 1.21 (Bruzual & Charlot, 1993; Jarrett et al., 2000).

In addition to the (mostly) normal galaxies identified by 2MASS, we also plot the 2MASS colors of active galaxies (AGNs) selected from SIMBAD. Solid and open circles represent QSOs and Seyfert galaxies, respectively, while solid squares plot the colors of BL Lac and Liner objects. Starburst galaxies are indicated by asterisks. These objects show a great deal of scatter in their color distribution, although they are generally redder than the low-redshift galaxy distribution. Seyfert galaxies are typically redder than the other varieties of AGNs due to thermal dust emission, particularly in the narrow-line Seyfert I galaxies (Osterbock, 1989). Note that none of these objects, either normal galaxies or AGNs, have colors similar to Gliese 229B.

1.7.4 Sources in the Solar System

The colors of Solar System objects detected by 2MASS are shown in Figure 1.22. Point source detections matched to minor planet ephemerides generated by D. Tholen for the 2MASS project are indicated by small solid circles. These objects generally fall in the color region 0.0 $\lesssim$ H-K_s $\lesssim$ 0.25 and 0.3 $\lesssim$ J-H $\lesssim$ 0.45, although a number of objects are found to have much redder colors; these latter objects could be mismatched associations to reddened background stars, particularly at low galactic latitude (Sykes et al., 2000). Asteroids fall into different taxonomic classes based on surface

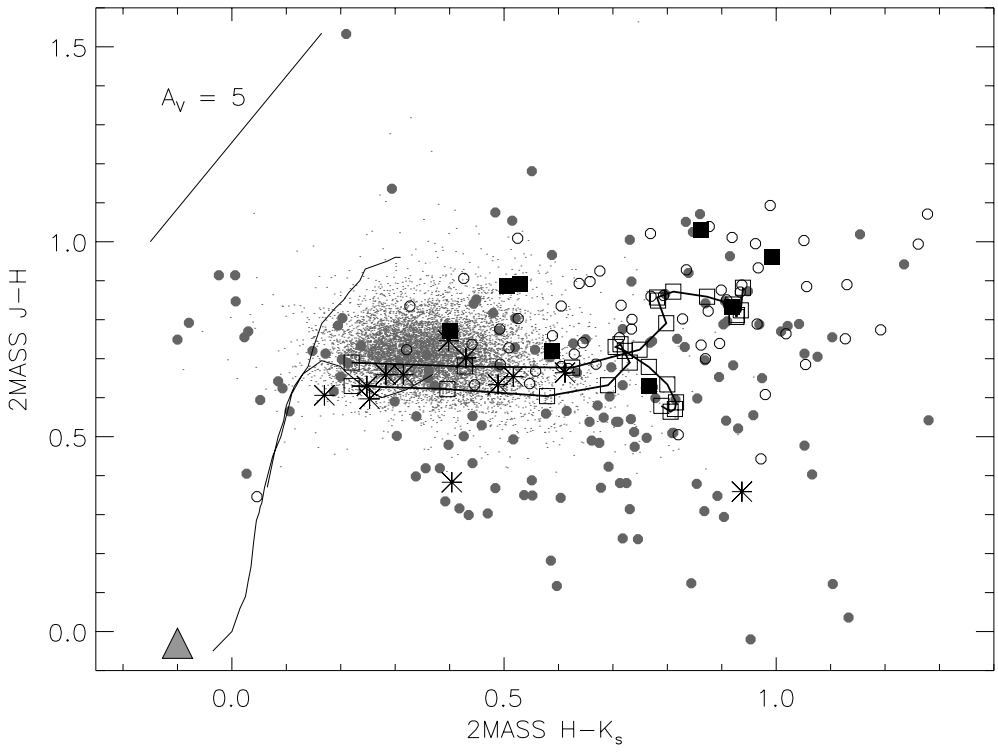

Figure 1.21: 2MASS colors of galaxies and extragalactic sources. The colors of galaxies selected from the 2MASS IDR2 Extended Source Catalog, with J < 15, H < 14.5, and K_s < 14, are plotted as small grey points. Solid and open circles indicate the 2MASS colors of SIMBAD-selected QSOs and Seyfert galaxies, respectively; BL Lac and Liner objects are indicated by black squares; and starburst galaxies are indicated by asterisks. K-corrections for elliptical (top) and spiral (bottom) galaxies are shown as thick lines extending off of the Bessell & Brett (1988) dwarf track (Bruzual & Charlot 1993; T. Jarrett, priv. comm.). The colors of Gliese 229B Leggett et al. (1999) are indicated by the grey triangle.

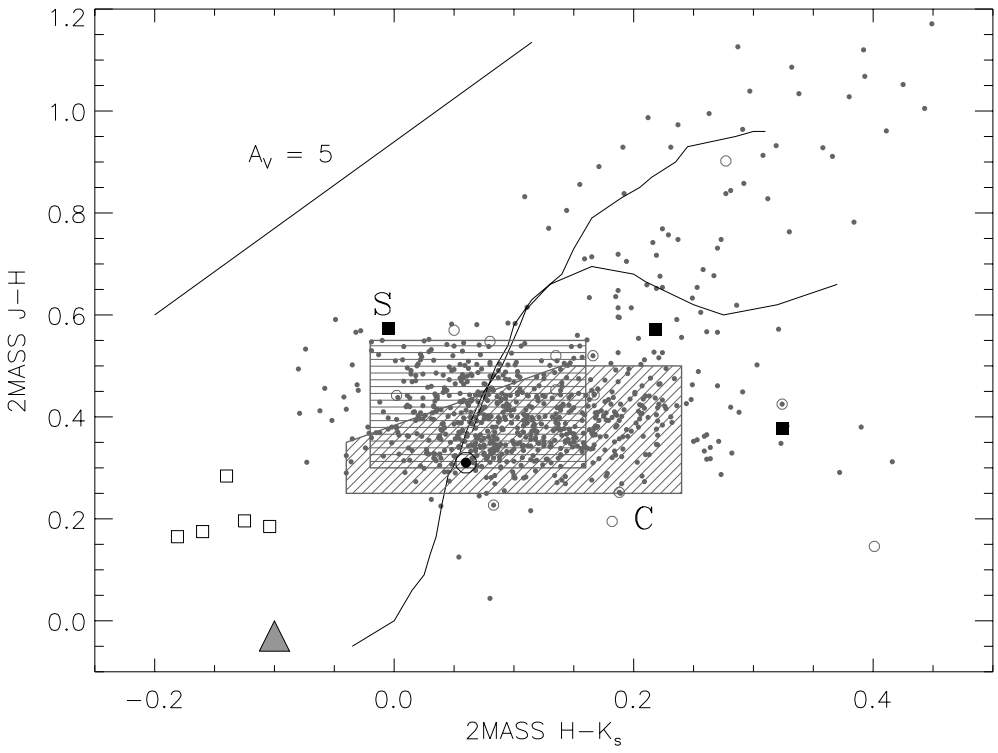

Figure 1.22: 2MASS colors of objects in the Solar System. Small solid circles are the colors of asteroids identified in the 2MASS IDR2 Point Source Catalog, with J < 15, H < 14.5, and K_s < 14. The typical loci of S- and C-type asteroids are indicated by hash-marked boxes (Sykes et al., 2000). Open circles plot identified comets (Cutri et al., 2001). The colors of the rocky Jovian satellites Elara, Pasiphae, Sinope, and Carme are shown as solid squares, while the icy Uranian satellites Ariel, Umbriel, Titania, and Oberon, and the Neptunian satellite Triton, are shown as open squares. The colors of Gliese 229B Leggett et al. (1999) are indicated by the grey triangle.

composition, and it has been shown that these classes can be partially resolved by near-infrared photometry (Leake, Gradie, & Morrison, 1978; Hahn & Lagerkvist, 1988; Smith et al., 1992; Veeder et al., 1995). Sykes et al. (2000) have identified the loci of specific asteroid classes in 2MASS color space, and the approximate boundaries of the more common S-type (igneous, concentrated in the inner main belt) and C-type (primitive, found in the central and outer main belt) classes (Lodders & Fegley, 1998) are shown in Figure 1.22. Comets detected by 2MASS (Cutri et al., 2001) appear to have near-infrared colors similar to asteroids.

2MASS has also detected some of the major satellites of Jupiter (Elara, Pasiphae, Sinope, and Carme), Uranus (Ariel, Umbriel, Titania, and Oberon), and Neptune (Triton); larger satellites, including the Galilean moons Io, Europa, Ganymede, and Callisto, are generally saturated in the 2MASS exposures. Figure 1.22 plots the colors of the above satellites, separated into the rocky Jovian satellites (filled squares) and icy Uranian and Neptunian satellites (open squares). The absorption features associated with the H_2O, CH_4, CO, and CO_2 ices generally cause the latter satellites to appear bluer than their rocky counterparts. Note that the both Uranus and Neptune were themselves detected by 2MASS (Jupiter was saturated). Point source photometry yield very blue near-infrared colors (J-K_s = -4.19 ± 0.09 and -1.99 ± 0.05, respectively) due to the presence of CH_4 and H_2 in their atmospheres.

1.7.5 Low Mass Dwarfs and Brown Dwarfs

The spectra of stars with the lowest effective temperatures, and those of warm brown dwarfs, are increasingly influenced by the presence of molecular absorption and dust opacity. This behavior is most clearly evident when we examine the near-infrared colors of objects of late-type dwarfs. Figure 1.23 plots the distribution of colors for M (solid squares) and L dwarfs (open triangles); 2MASS colors for objects identified by Kirkpatrick et al. (1999b, 2000) and Gizis et al. (2000) are shown, while colors from Leggett (1992) are plotted for early-type M dwarfs. M dwarfs are the primary constituents of the Bessell & Brett (1988) dwarf track after the giant/dwarf split at J-K_s $\sim$ 0.8, a divergence caused by the increasing importance of H^- absorption in the higher-gravity cool dwarfs. Late M dwarfs and L dwarfs become increasingly red due to the presence of warm photospheric dust (Tsuji, Ohnaka, & Aoki, 1996a), which weakens H_2O near-infrared bands and increases the thermal flux at longer wavelengths. Indeed, colors for late M and early L dwarfs begin to converge back onto the blackbody curve shown in Figure 1.23. Kirkpatrick et al. (1999b, 2000) have found that the colors of L dwarfs peak at J-K_s $\sim$ 2.1 around spectral type L6–L8 V. At this point, dust grains probably begin to settle out of the photosphere (Burrows, Marley, & Sharp, 2000; Ackerman & Marley, 2001), and molecular absorption regains its strength. This transition is also reflected in the decrease of CrH and FeH bandstrengths beyond roughly L5 V (Kirkpatrick et al., 1999b).

With the formation of CH_4 bands in the T dwarfs, near-infrared colors become significantly more blue, as is the case for Gliese 229B (Oppenheimer et al., 1995). This transition implies a clean distinction between objects of types L and T in near-infrared color-color space. However, while both types are also fairly distinct from other Galactic and extragalactic populations, the transition from L to T must occur through the densest region of color-color space. This fact places a critical constraint on our search criteria described in Chapter 2.

1.8 Summary

In this chapter, we have highlighted some of the major components of research upon which the following chapters are built. A great deal of work has been done in both the theoretical and observational

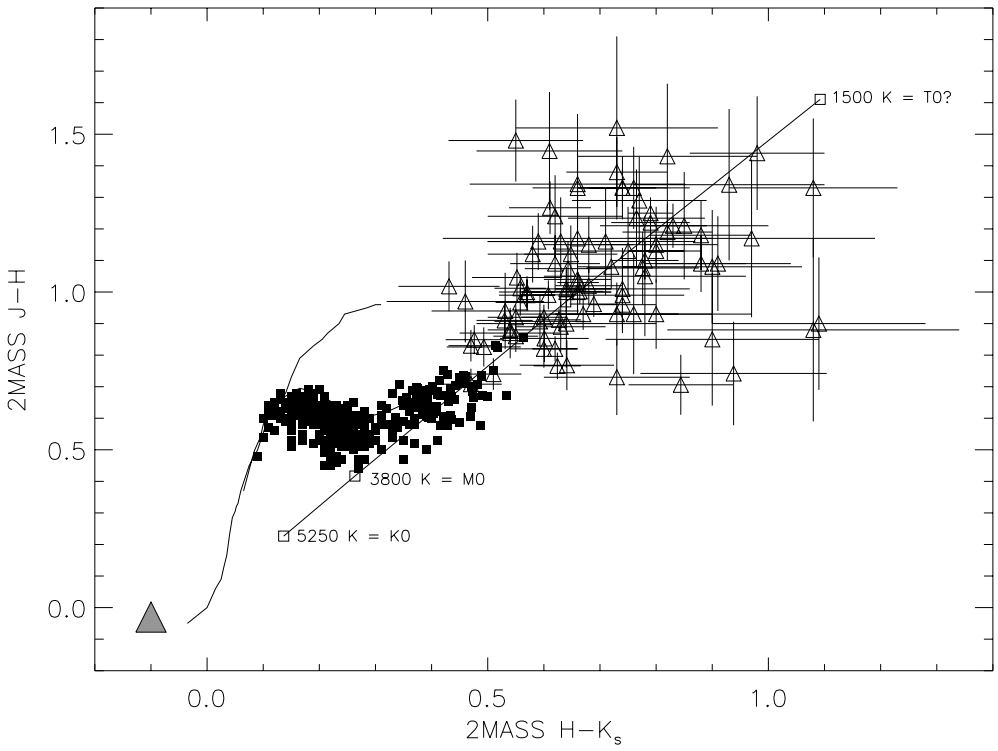

Figure 1.23: Near-infrared color-color diagram of low-mass stars and brown dwarfs detected by 2MASS. M (filled squares) and L (open triangles with error bars) dwarf colors are shown, based on 2MASS photometry (Kirkpatrick et al., 1999b, 2000; Gizis et al., 2000) and data from the literature (Leggett, 1992). The colors of Gliese 229B Leggett et al. (1999) are indicated by the grey triangle. The colors of 5250, 3800, 2200, and 1500 K blackbodies, corresponding to spectral types K0, M0, L0, and possibly T0 (Kirkpatrick et al., 1999b, 2000; Burgasser et al., 2001) are also indicated.

study of brown dwarfs over the past 40 years, and while we understand much about the internal physics, evolution, and energy distributions of these objects, there are many details and many more fundamental questions that remain unanswered. A small and incomplete list includes: the process of brown dwarf formation; the efficiency of star formation at low masses, including the "minimum" brown dwarf mass; the contribution of substellar matter to the Galactic mass budget; the nature of convection in the photospheres of cool brown dwarfs and its role in observed non-equilibrium abundances; substellar chromospheres; heterogeneous cloud formation and weather; duplicity and companionship; the formation of planetary systems; and the possible presence of a substellar companion to the Sun. Many of these issues were the motivators for early searches of brown dwarfs, and remain so today.

The early history of observational substellar astronomy is riddled with many wrong turns and infamous mistakes, but the discovery of Gliese 229B in 1995, and subsequent identifications of brown dwarfs in clusters, in the field, and around nearby stars, has galvanized the astronomical community toward the investigation of the true nature of our dark neighbors. These recent discoveries have also led to the first major addition to the stellar classification scheme in over 65 years, the L dwarf class. The smooth variation in spectral features (TiO, VO, FeH, CrH, H_2O, K I, and Na I) seen in red optical data provide a ready means of distinguishing these objects into 9 unique subtypes, L0 V through L8 V. The unique spectrum of Gliese 229B, however, warrants the definition of a new spectral class, the T class, for which we ultimately derive a classification scheme presented in Chapter 7. This object is the fundamental standard on which all of our subsequent investigation is based.

To identify Gliese 229B-like analogues, we used the 2MASS database, a full-sky, three-band, near-infrared survey, which improves upon previous work by over four orders of magnitude. 2MASS is capable of detecting sources down to 99% completeness magnitudes of J = 15.8, H = 15.4, and K_s = 15.2, with positional accuracy down to $0\farcs1$. The final catalog, which is likely to include over 10^9 point sources, will be a standard tool for astronomers for many decades to come.

Finally, we have examined the properties of various astronomical objects in the near-infrared sky, comparing sources within and without the Solar System, and within and without the Galaxy. We have shown the Gliese 229B is fairly unique when compared to the colors of most main sequence stars, and is much bluer in near-infrared colors than the L dwarfs. This bodes well for the search for analogues to this object in the massive 2MASS database, but we are not likely to find objects that transition from the latest L dwarfs to Gliese 229B. Nonetheless, by searching at the spectral energy peak of these cool brown dwarfs, we improve upon our chances of detecting a few T dwarfs given a large enough volume.

Date: Thu, 04 Jun 1998 11:20:21 -0700
From: Davy Kirkpatrick <davy@ipac.caltech.edu>
To: diver@cco.caltech.edu
Subject: 2MASS research?

Dear Adam:

Dave Koerner and I were recently chatting about research monies for students, and during the course of our conversation, I mentioned that I had funding for three years to support a student to work with data taken by 2MASS, the Two-Micron All-Sky Survey. As we continued to talk about this, I said that I'd been checking the attendance of recent IPAC talks to see if any "new" faces appeared from across the street. As I told Dave, there was a brown dwarf talk recently by Eduardo Martin, and in the audience were a couple of "new" people -- perhaps younger grad students from Caltech. To make a long story short, we discovered that one of those "new" faces was you (and thank you for having your picture up at your web site!).

I realize that you're working with Rich Terrile on some NICMOS images (fun, huh? Dave and I were NICMOS postdocs together) and have also done some science with Mike Brown. Dave says (and, yes, Dave says a lot! ;)) that you haven't chosen a thesis topic yet, and since you've just finished your course work and have shown at least some interest in brown dwarfs, I thought I'd throw out the 2MASS research idea to you. (Better yet, unlike most Caltech grad students YOU'VE ACTUALLY BEEN TO IPAC!)

So here's the scoop. We're sitting on a GOLD MINE of data here, over 6000 sq. deg. of JHKs data from both northern and southern hemispheres so far. The money I have is to support a student on 2MASS Core Project research related to finding "Rare Objects" in the resulting database. I've been using the data to find field dwarfs of type "L", but other possibilities include looking for field methane brown dwarfs, missing nearby stars, etc. (My personal opinion is that the 2MASS data will contain a star [or brown dwarf] closer to the sun than Proxima Centauri... we just gotta find it.) Thesis-style projects include (1) constructing the first ever field brown dwarf luminosity and mass functions, (2) determining the incompleteness of the nearby star census by using a survey unbiased by kinematic selections, (3) looking for planets around nearby, 2MASS-discovered M and L dwarfs, etc. The purpose of the Core Project is to verify that the data products we'll eventually be shipping to the community are solid, and the best way to verify those products is to try to extract some science from the data. Both Caltech and NASA have been giving me, Neill Reid, and Dave lots of Keck time for 2MASS follow-up using LRIS, HIRES, and NIRC. (TRANSLATION: Student gets free trips to Hawaii!) In fact, we've got 14 more nights of Keck time coming up between now and the end of January 1999 to pursue some of these ideas, so things are rocking and rolling.

Anyway, let me know if you'd be interested in any of this science. I think there are all kinds of possible thesis projects that can be done, and if you're interested, we'd also have to get a real faculty contact like Mike Brown involved as well. (I haven't run this idea by Mike yet, by the way. I figured I go directly to you first.) If you want to talk more about this, feel free to stop by my office (room 109 at IPAC), reply to this message, or just give me a call at 397-7002.

Take care! I hope to hear from you soon.

---Davy Kirkpatrick

P.S. -- If you're not interested and know of other first or second year grad students who might be, could you let me know who they are? Thanks, Adam.

Chapter 2 Search

Look for the stars, you'll say that there are none;
Look up a second time, and, one by one,
You mark them twinkling out with silvery light
And wonder how they could elude the sight.
William Wordsworth, *Calm is the Fragrant Air*

2.1 Introduction

[1]The discovery of the companion brown dwarf Gliese 229B (Nakajima et al., 1995) was a windfall to substellar astronomy, both in terms of it being the first *bona-fide* brown dwarf, and because of its highly unusual spectral energy distribution. In the four years following, many brown dwarfs were identified, in the field, in stellar clusters, and as companions to nearby stars (see Basri 2000 for a review), but none had the strong methane absorption bands (Oppenheimer et al., 1995) or cool effective temperature (Allard et al., 1996; Marley et al., 1996; Tsuji et al., 1996) of Gliese 229B. This is due in part to selection effects, as searches were typically made for the reddest near-infrared sources (i.e., the L dwarfs). Gliese 229B is also exceedingly faint, and even at its distance of 5.77 pc (Perryman et al., 1997) falls at the faintest detection limits of 2MASS. Nonetheless, as all brown dwarfs cool over their lifetimes, the presence of a substantial number of L-type brown dwarfs implies the certain existence of Gliese 229-like T dwarfs in the vicinity of the Sun. Furthermore, most of these are likely to be isolated, free-floating field objects. Our goal, therefore, was to seek out these low-luminosity neighbors.

Our search for T dwarfs was made using the 2MASS point source (working and release data) catalogs, incorporating additional optical data from the USNO-A2.0 catalog (Monet et al., 1998) and follow-up imaging and spectroscopy. In this chapter, we describe our selection criteria for these objects, starting with early samples and their results, and then going on to characterize our primary search samples. In §2.2, we describe and justify the color and magnitude constraints used to identify T dwarfs in 2MASS data. Early search samples and their results are presented in §2.3, while the properties of our three primary search samples are described in §2.4. Follow-up imaging observations made to eliminate uncatalogued minor planets, faint background stars, and proper motion stars from our search samples are described in §2.5. Finally, we summarize all of the T dwarf discoveries made in these searches in §2.6, as a prelude to their investigation in subsequent chapters. Results are summarized in §2.7.

2.2 Color and Magnitude Search Constraints

The 2MASS catalogs provide photometric and astrometric (typically single-epoch) data for over 10^9 near-infrared point sources. Hence, our search for T dwarfs is necessarily a color-selected and magnitude-limited one. As discussed in §1.7.5, there is quite a gap in color-color space between the coolest L dwarfs and Gliese 229B, occupied by the vast majority of detected 2MASS sources. Furthermore, the samples of Galactic and extragalactic sources investigated in §1.7 are generally

[1]Portions of this chapter have been previously published in Burgasser et al. (1999, 2000d, 2001).

made up of bright objects with well-defined photometry, and fainter sources (with magnitudes similar to those of our T dwarf candidates) will be scattered throughout the intervening color region. We have thus constrained our search efforts to identifying those T dwarfs which have sufficient H_2O and CH_4 absorption to push their near-infrared colors blueward of the majority of stars ($J-K_s \lesssim 0.6$), galaxies ($J-K_s < 0.8$) and minor planets ($H-K_s < 0.3$).

We can improve our chances of uncovering T dwarfs in the 2MASS database by taking advantage of their unusual optical/near-infrared color properties. Analysis of photometry for Gliese 229B (Matthews et al., 1996; Golimowski et al., 1998), confirmed by the colors of the first SDSS T dwarf discovery SDSS 1624+0029 (Strauss et al., 1999), show that low effective temperatures, broadened K I absorption (Burrows, Marley, & Sharp, 2000; Liebert et al., 2000b), and the possible presence of dust opacity (Tsuji, Ohnaka, & Aoki, 1999), make T dwarfs extremely red in the optical, with $R-J \gtrsim 9$ (Matthews et al., 1996). Thus, T dwarfs similar to Gliese 229B with $J \gtrsim 10$–12 (i.e., $d \gtrsim 2$ pc) would have been missed in earlier optical sky surveys (e.g., POSS-II; Reid et al. 1991), which have typical limiting magnitudes of $R \lesssim 19$–21. Based on this fact, we imposed an additional optical/near-infrared color cut by rejecting candidate objects with optical counterparts in either the USNO-A2.0 catalog or on Digital Sky Survey (DSS) R-band images, obtained using the Canadian Astronomy Data Centre's (CADC) DSS image server[2]. Objects in the USNO-A2.0 catalog are required to be detected on both the R- and B-band plates, so that faint red objects visible only on the R-band plates (such as very close T dwarfs or background M stars) generally remain in our candidate lists. We note that the Sloan Digital Sky Survey (York et al., 2000, hereafter SDSS) can directly take advantage of the red optical/near-infrared colors of late L and T dwarfs using i^*-z^* colors. As such, they more capable of finding objects in the L/T gap (Leggett et al., 2000b; Geballe et al., 2001b). The distinct advantage of 2MASS, however, is that it samples the brightest regions of the spectral energy distributions of these cool brown dwarfs, and is therefore better suited for identifying the coolest and faintest T dwarfs.

2.3 Early Search Efforts

Our initial search for T dwarfs in the 2MASS Working Database began as part of an ongoing investigation of late-type dwarfs by the 2MASS Rare Objects Team, starting with 2MASS Prototype Camera data (Kirkpatrick, Beichman, & Skrutskie, 1997) and continuing through to the current all-sky catalogs. Early efforts uncovered a number of late-M and L dwarfs (Kirkpatrick, Beichman, & Skrutskie, 1997; Kirkpatrick et al., 1999b), but failed to detect any objects similar to Gliese 229B with $J-K_s < 0.4$ in 371 deg^2 of 2MASS data (Kirkpatrick et al., 1999b). In this section, we describe the first directed searches for T dwarfs using the 2MASS catalogs. The samples presented here include initial Preliminary samples (§2.3.1) and the first "discovery" samples which successfully identified T dwarfs in 2MASS data (§2.3.2). These searches were generally small area investigations ($\sim$ 1500–4000 deg^2). Each effort, however, gave us a better understanding of the types of objects found in the color space occupied by T dwarfs, and allowed us to better tailor larger searches described in §2.4.

2.3.1 Preliminary Samples

Our initial magnitude-limited, color-selected sample made use of both 2MASS point source data and optical magnitudes derived from USNO in-house digital scans of the POSS-II (Reid et al., 1991; Monet et al., 1998) B_J ($\sim$ B-band), F ($\sim$ R-band), and N ($\sim$ I-band) photographic plates. All candidates were selected to have $J < 16$ or $K_s < 15$, either $F-K_s > 7$ ($R-K_s \gtrsim 6$) or $N-K_s > 5$

[2]http://cadcwww.dao.nrc.ca/cadcbin/getdss.

Table 2.1: Preliminary T Dwarf Search Subsamples.

Sample (1)	Color Cut (2)	Detection (3)
Blue	J-K_s < 0.7	J and either H or K_s
Green	0.7 ≤ J-K_s < 1.0	J and either H or K_s
Red	1.0 ≤ J-K_s < 1.3	K_s and either J or H
IR	1.3 ≤ J-K_s	K_s and either J or H
J-only	None	J only
K-only	None	K_s only

Note – These criteria are in addition to J < 16 or K_s < 15, F-K_s > 7 or N-K_s > 5, no B_J detection, and $|b| > 15°$.

(I-$K_s \gtrsim 4$), and no detection on the B_J plates. We also eliminated candidates with $|b| < 15°$ due to the high source density and corresponding source confusion in the Galactic plane. A number of subsamples were defined based on near-infrared color criteria and whether or not targets were detected at all 2MASS bands; these criteria are summarized in Table 2.1. In our search for T dwarfs, we made use of the Blue (J-K_s < 0.7), Green (0.7 ≤ J-K_s < 1.0), and J-only (no H or K_s detection) subsamples.

Initial investigation of 2MASS and DSS imaging data (Figure 2.1) indicated that a large percentage of our candidates were close double stars unresolved in the USNO digitized images; artifacts caused by bright stars, meteors, and image defects; or sources found in dense regions around galaxies or star clusters, such as the Magellanic Clouds and 47 Tuc. It became clear that candidates had to be visually examined in order to guarantee their reliability.

We proceeded to examine 2MASS near-infrared and DSS optical images for nearly 12000 T dwarf candidates by individual inspection, using software developed in the IDL environment. Statistics for this follow-up are given in Table 2.2. Over 97% of all candidates were rejected after visual inspection. Of these, nearly 80% were either blended doubles or faint optical sources not picked up in the USNO digitized scans. A number of candidates were also rejected after inspection of 2MASS images, including meteor streaks or other artifacts not removed from the working point source catalog[3]. The majority of J-only candidates (88.4%) were associated with some kind of image artifact, and there are probably very few clean sources present in this sample. Nonetheless, a total of 339 candidates were extracted: 177 Blue candidates from 5146 scans (4014 deg^2), 107 Green candidates from 2961 scans (2310 deg^2), and 55 J-only candidates from 4681 scans (3651 deg^2).

A total of 161 Blue, 99 Green, and 41 J-only candidates have been followed up with near-infrared and optical re-imaging since their identification (see §2.5). Initially, two interesting candidates were identified: 2MASSW J0326540+252015 and 2MASSW J0756048+234134[4]. POSS-II and J-band images of these objects are shown in Figure 2.2 and their photometric properties are summarized in Table 2.3. Both are located next to bright stars, SAO 75932 (G5, V=9.08) and HD 64704 (G0, V=7.34, π=15.9±0.9 marcs), respectively; this has prevented further spectroscopic follow-up and makes the 2MASS photometry relatively uncertain. Interestingly, both objects, despite being detected in follow-up imaging, are not rigorous 2MASS detections. 2MASS 0326+2520 is not detected in a second 2MASS scan of the field (Figure 2.2, upper right panel), despite having an

[3]These image artifacts are removed in the 2MASS Release Catalogs; Cutri et al. 2001.

[4]Source designations for 2MASS discoveries are given as "2MASSx Jhhmmss[.]s±ddmmss," where the "x" prefix varies depending upon which catalog the object originates, in this case "I" for 2MASS Release Data (i.e., IDR1 and IDR2) and "W" for the survey's working database. The suffix conforms to IAU nomenclature convention and is the sexigesimal R.A. and decl. at J2000 equinox.

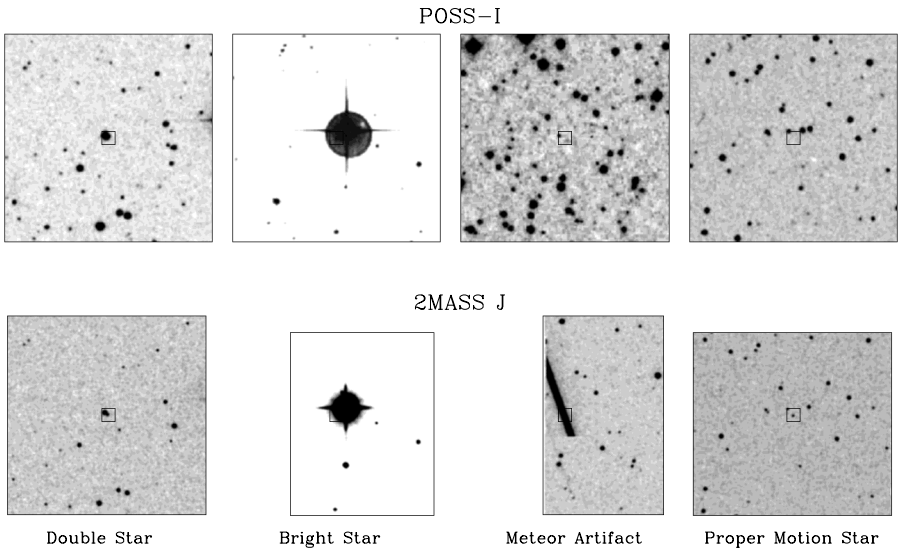

Figure 2.1: Examples of T dwarf candidates rejected by visual inspection. The top row shows POSS-I images taken from the CADC DSS server; 2MASS J-band images are shown at the bottom. Images are nominally $5' \times 5'$ with North up and East to the left. Candidate locations are indicated by a $20'' \times 20''$ box.

Table 2.2: Visual Inspection Statistics for Preliminary T Dwarf Candidates.

	Blue		Green		J-only		Total	
Identification	#	%	#	%	#	%	#	%
(1)	(2)	(3)	(4)	(5)	(6)	(7)	(8)	(9)
Double	6636	75.5	1838	81.1	8	0.8	8482	70.7
Faint OC[a]	911	10.4	92	4.1	12	1.3	1015	8.5
Bright star[b]	290	3.3	158	7.0	302	32.0	750	6.3
Galaxy	491	5.6	24	1.1	34	3.6	549	4.6
Meteor	215	2.4	12	0.5	291	30.9	518	4.3
Artifact	21	0.2	3	0.1	154	16.3	178	1.5
No source	25	0.3	4	0.2	87	9.2	116	1.0
PM star[c]	20	0.2	28	1.2	0	0.0	48	0.4
OK[d]	177	2.0	107	4.7	55	5.8	339	2.8
Total	8786		2266		943		11995	
No. of Scans	5146		2961		4681			
Area (deg^2)	4014		2310		3651			

[a]Faint optical counterpart seen in DSS images.

[b]Persistence artifact associated with a bright star.

[c]Proper motion star identified from multiple epoch imaging.

[d]Viable candidate based on appearance in 2MASS near-infrared images and lack of optical counterpart in DSS images.

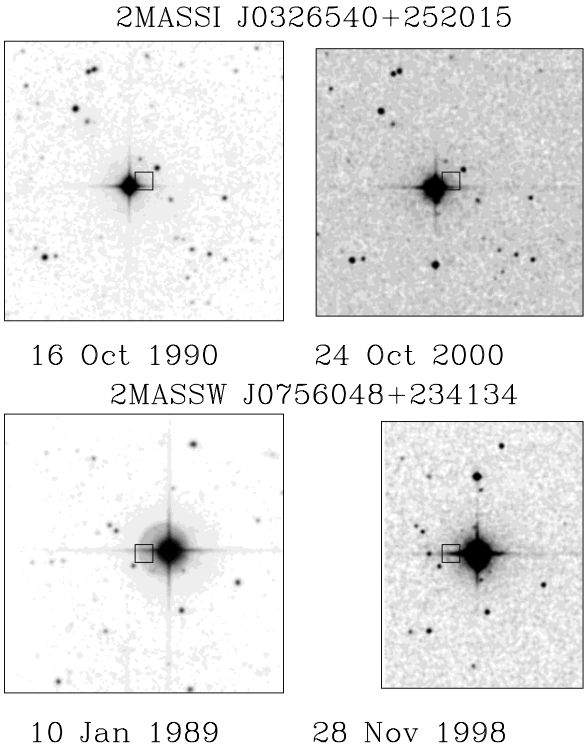

Figure 2.2: POSS-II R-band images (left) and 2MASS J-band images (right) for 2MASS 0326+2520 and 2MASS 0756+2341. Images are nominally $5' \times 5'$ with North up and East toward the left. A $20'' \times 20''$ box around each target position is shown.

initially measured J = 14.66±0.15. 2MASS 0756+2341 is not in the 2MASS IDR2, presumably because it lies along the diffraction spike of its bright neighbor. Optical photometry obtained with the Palomar 60" CCD Camera (see §2.5.2) indicate upper limits of r−J > 6.6 and 8.0 for 2MASS 0326+2520 and 2MASS 0756+2341, respectively, making them appear to be viable candidates. However, preliminary I-band photometry obtained using the Low Resolution Imaging Spectrograph (Oke et al., 1995) on 1999 March 3 (UT) yield detected I−J colors of only 5.6 and 2.8 (with errors of likely 0.1–0.3 mag), consistent with main sequence stars. These colors suggest that the two objects may simply be background stars with spurious photometry due to their close alignment with bright sources. Nonetheless, 2MASS 0326+2520 is blue enough in near-infrared colors, and red enough in optical/near-infrared colors, to make it an interesting source for further investigation. Efforts have thus far been inconclusive.

The Preliminary samples also identified two objects, 2MASSI J1225543-273947 and 2MASSI J0755480+221218, which were selected in subsequent samples, and have ultimately been confirmed as bona-fide T dwarfs (see §2.6). The latter object was initially rejected as a candidate due to the presence of a faint and fuzzy optical counterpart in LRIS images obtained on 1999 March 3 (UT). It was later determined that this counterpart is an aligned background galaxy at z = 0.18 (see §3.2.1). Thus far, these are the only confirmed T dwarfs from the Preliminary samples; however, many *bona-fide* candidates were re-extracted in subsequent samples described below, and no further

Table 2.3: Photometric Properties of 2MASS 0326+2520 and 2MASS 0756+2341.

Object (1)	Sample (2)	2MASS J (3)	J−K_s (4)	r−J (5)	LRIS I−J[a] (6)
2MASSI J0326540+252015	J-only	14.66±0.15	< -0.33[b]	> 6.6	5.6
2MASSW J0756048+234134	Blue	15.98±0.07	0.61±0.17	> 8.0	2.8

[a]Estimated from preliminary LRIS I-band photometry; errors are likely ±0.1-0.3 mag.
[b]Not detected at this band; magnitude is 2MASS 95% confidence upper limit.

effort has been made to complete follow-up of these early samples.

2.3.2 First Discovery Samples

2.3.2.1 Motivation

While individual examination of all T dwarf candidates over a relatively broad color range (including Green candidates) provided valuable information on the types of contaminants present, as well as the methods by which to eliminate these contaminants, the procedures followed for the Preliminary samples proved to be quite tedious and resulted in a large pool of poor prospects. We therefore selected new search samples with bluer color constraints (to eliminate faint background stars), and multiple-band detections (to eliminate artifacts), ultimately relaxing the requirements for rigorous completeness but increasing the likelihood of finding T dwarfs in the 2MASS database. This sample resulted in the first confirmed T dwarfs, and we hereafter refer to these as the "Discovery" samples.

2.3.2.2 Candidate Selection

The properties of the Discovery samples are summarized in Table 2.4. The first (Sample A) was taken from the 2MASS Spring 1999 Data Release (Cutri et al., 1999, hereafter IDR1), 2483 deg^2 of Northern hemisphere data containing approximately 2×10^7 point sources. Candidates were constrained to have detections at J- and H-bands with J < 16 (2MASS signal-to-noise ratio $\sim$ 10 limit), J-H < 0.3, H-K_s < 0.3, $|b| > 15^\circ$ (to eliminate source confusion in the plane), no minor planet correlations, and no optical counterparts within 5″ in the USNO-A2.0 catalog. We made an additional color cut to eliminate the large number of objects with colors J-$K_s \gtrsim 0.5$, most of which are likely to be background stars; objects were rejected if they had J-H > 0.15 *and* J-H > 0.2 - H-K_s (see Figure 2.5). J- and H-band detections were required to exclude artifacts, although a K_s-band detection was not required because of decreased sensitivity at these wavelengths[5].

The second set (Sample B) was taken from 3420 deg^2 ($\approx 2.8\times10^7$ point sources) of Northern and Southern hemisphere data obtained from the 2MASS working (pre-release) database, with search criteria of J-H < 0.2, H-K_s < 0.2, J < 16, $|b| > 20^\circ$, and no USNO-A2.0 optical counterpart. Again, sources were required to have J- and H-band detections but not required to have K_s-band detections.

These selection criteria identified 349 candidates from Sample A and 319 candidates from Sample B. Subsequent inspection of optical DSS images (see §2.4.2.1) and 2MASS near-infrared images to rule out faint optical sources (background stars), high proper motion stars, and image artifacts (primarily from sample B) eliminated all but 15 candidates from sample A and 10 from sample B. These objects are listed in Tables 2.5 and 2.6.

Figures 2.3 and 2.4 diagram the positional properties of these samples. The regions of the sky mapped in the 2MASS IDR1 are indicated in Figure 2.3 in grey. Most of the initial candidates in

[5]In this case the H-K_s limit is still required to be 0.3 mag.

Table 2.4: T Dwarf Discovery Search Samples.

	Sample A	Sample B
Database	IDR1	Working
Magnitude Cut	J < 16	J < 16
Color Cuts[a]	J-H < 0.3	J-H < 0.2
	H-K_s < 0.3	H-K_s < 0.2
Area (sq. deg.)	1770	3420
Candidates:		
Initial[b]	349	319
Final[c]	15	10
Confirmed[d]	3	3
T Dwarfs	2	3

[a]Candidates were also excluded from Sample A if they had J-H > 0.15 *and* J-H > 0.2 − H-K_s.
[b]Initial candidate pool from 2MASS catalogues.
[c]Candidates remaining after visual inspection of DSS images.
[d]Candidates remaining after near-infrared re-imaging observations.

Table 2.5: 2MASS T Dwarf Candidates: Sample A.

Object[a] (1)	J (2)	J-H (3)	H-K_s (4)	J-K_s (5)
2MASSI J0056583+151431	14.72±0.04	0.03±0.08	0.18±0.15	0.21±0.14
2MASSI J0112448+273803	15.46±0.06	0.14±0.13	0.10±0.21	0.24±0.21
2MASSI J0216465+304122	14.77±0.04	0.01±0.08	0.04±0.14	0.05±0.13
2MASSI J0252394+273244	15.12±0.05	0.14±0.09	0.09±0.13	0.25±0.11
2MASSI J0306308+244035	15.90±0.07	0.07±0.16	0.08±0.26	0.15±0.23
2MASSI J0312234+260936	15.56±0.06	0.18±0.12	−0.08±0.18	0.10±0.20
2MASSI J0333241+242720	15.92±0.09	0.25±0.17	$< -0.82^a$	$< -0.57^a$
2MASSI J0337320+290721	15.68±0.07	0.09±0.15	0.21±0.22	0.30±0.19
2MASSI J0400198+263753	15.59±0.07	0.22±0.12	−0.13±0.21	0.09±0.20
2MASSI J0436027+154753	15.09±0.10	−0.05±0.13	0.27±0.15	0.22±0.16
2MASSI J0727182+171001	15.55±0.07	−0.26±0.19	0.25±0.28	−0.01±0.22
2MASSI J0929245+230311	15.93±0.08	0.18±0.14	−0.13±0.22	0.05±0.21
2MASSI J1007406+180601	15.75±0.06	0.05±0.15	−0.07±0.28	−0.02±0.25
2MASSI J1047539+212423	15.82±0.06	0.03±0.13	$< -0.50^a$	$< -0.47^a$
2MASSI J1059440+183442	15.95±0.07	0.12±0.17	0.18±0.24	0.30±0.20

[a]Not detected at K_s band; colors are based on K_s 95% confidence magnitude lower (bright) limit.

Table 2.6: 2MASS T Dwarf Candidates: Sample B.

Object (1)	J (2)	J-H (3)	H-K_s (4)	J-K_s (5)
2MASSW J0035401−052008	15.89±0.06	−0.01±0.13	$< -0.09^a$	$< -0.10^a$
2MASSW J0036329+142255	15.72±0.07	0.08±0.14	−0.11±0.28	−0.03±0.26
2MASSW J0055164−015753	15.57±0.05	−0.11±0.14	0.13±0.24	0.02±0.21
2MASSW J0109011−045057	15.50±0.05	0.14±0.10	−0.36±0.24	−0.22±0.23
2MASSW J1217111−031113	15.85±0.07	0.06±0.14	$< -0.12^a$	$< -0.06^a$
2MASSW J1237392+652615	15.90±0.06	0.03±0.14	$< -0.03^a$	$< 0.00^a$
2MASSW J1346464−003150[b]	15.86±0.08	−0.19±0.22	$< 0.11^a$	$< -0.08^a$
2MASSW J2110230−285509	15.43±0.05	0.12±0.09	−0.03±0.17	0.09±0.16
2MASSW J2142333−035556	15.86±0.06	0.17±0.15	−0.04±0.28	0.13±0.25
2MASSW J2231365+245220	14.71±0.04	−0.98±0.15	0.22±0.24	−0.76±0.20

[a]Not detected at K_s band; colors are based on K_s 95% confidence magnitude lower (bright) limit.
[b]This object, also known as SDSSp J134646.45−003150.4, was previously identified by the Sloan Digital Sky Survey (Tsvetanov et al., 2000).

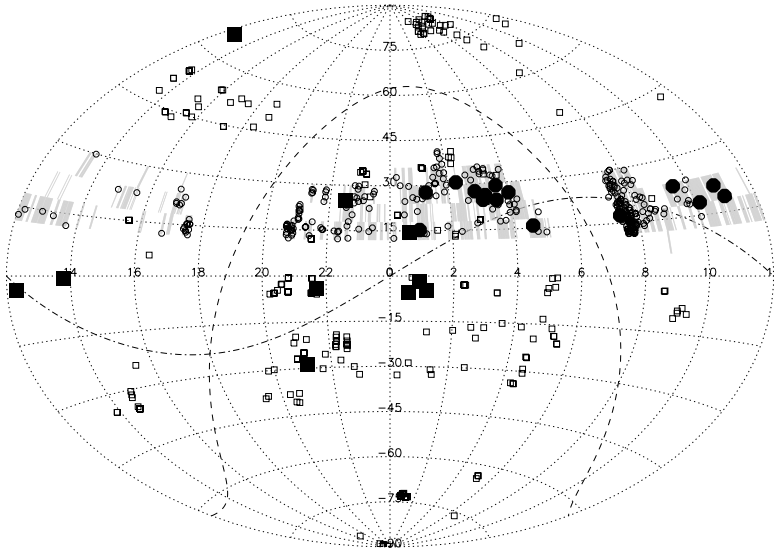

Figure 2.3: Positions of T dwarf Candidates. 349 initial (open circles) and 17 final (filled circles) candidates from Sample A, and 319 initial (open squares) and 11 final (filled squares) from Sample B are plotted. Galactic and Ecliptic equatorial planes are indicated as dashed and dot-dashed lines, respectively. Grey tiles delineate the areas present in the 2MASS IDR1 with $|b| > 15°$.

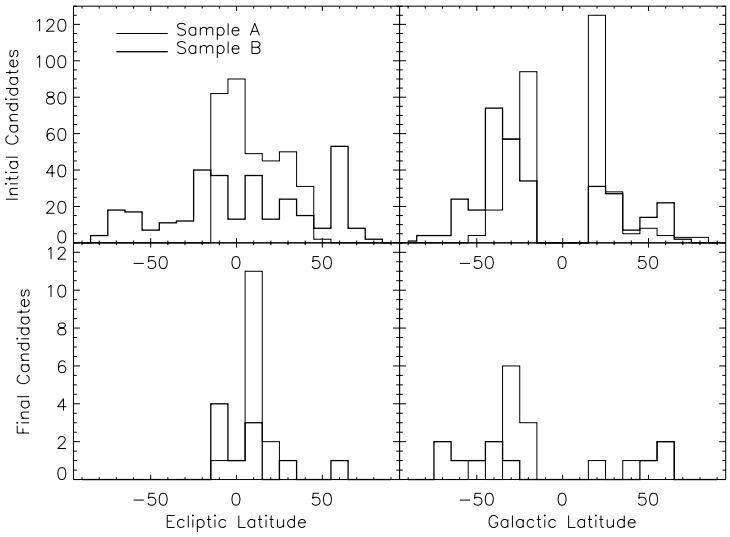

Figure 2.4: Ecliptic (left) and Galactic (right) latitude distributions of initial (top) and final (bottom) candidates from Samples A (thin line) and B (thick line). The absence of sources along the Galactic plane is due to our selection criteria for both samples.

both samples lie near the Galactic plane (note the absence of sources along the plane), reflecting contamination by background stars. The distribution of initial candidates in Sample A is quite peaked at the ecliptic plane, and final candidates from both samples also appear to lie preferentially near the ecliptic plane. This feature is due to contamination by minor planets, as discussed in §2.3.2.3.

Finally, Figure 2.5 plots the color distribution of candidates in each sample. Color cuts are indicated by dashed lines. Again, the density of sources near the high-mass end of the Bessell & Brett (1988) track suggests contamination by background stars; however, a number of final candidates have colors as blue or bluer than Gliese 229B, a good indication that a few of these targets may be bona fide T dwarfs.

2.3.2.3 Follow-up Imaging Observations

A log of follow-up observations for the Sample A and Sample B objects is given is Table 2.7. The most significant sources of contamination among our T dwarf candidates are uncatalogued minor planets, which have blue near-infrared colors (§1.7.4) and no optical counterpart due their motion between optical and 2MASS imaging epochs. While catalogued minor planets are flagged by the 2MASS processing pipeline in the IDR1, uncatalogued minor planets remain. Therefore, second epoch imaging is required to eliminate these contaminants from the candidate pool; note that minor planets are not identified in the Working database.

Initial imaging observations for two of our candidates, 2MASS 1217-0311 and 2MASS 1237+6526, were carried out on 1999 May 19 (UT) using the Tek2K CCD Camera mounted on the USNO K. Aa. Strand USNO 61" Astrometric Reflector. Eighty-minute exposures for both objects were obtained at z′ band (Fukugita et al., 1997). Reduced images for both objects are shown in Figure 2.6. Note that no flat-field correction was applied to these images, so significant fringing is present. Faint but

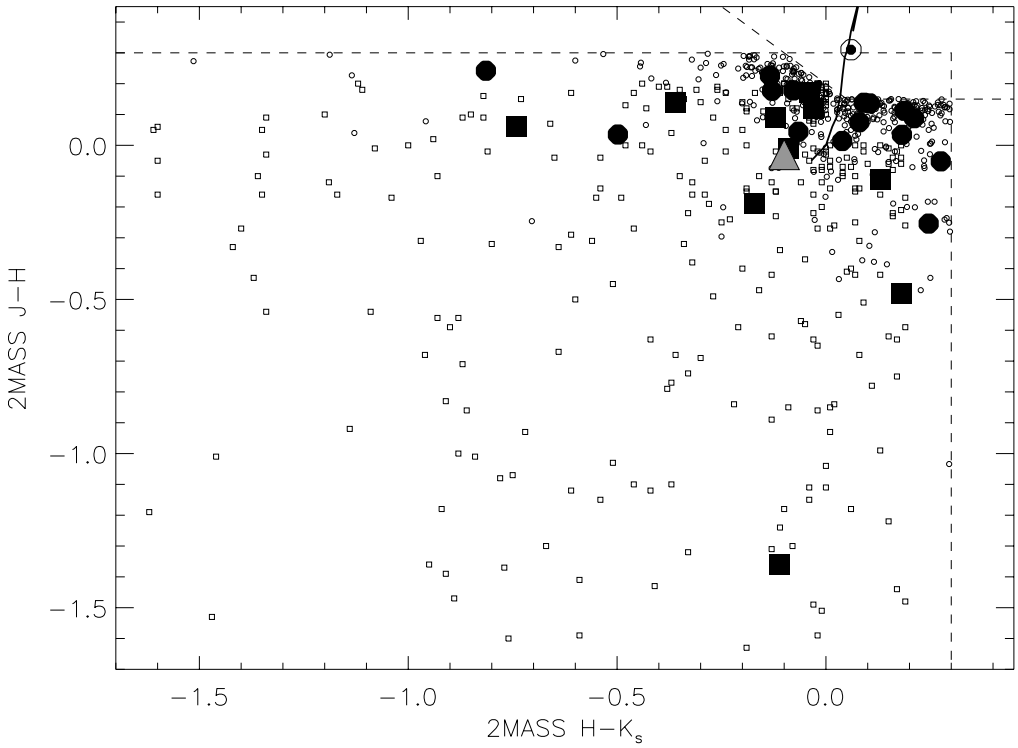

Figure 2.5: Colors of T dwarf Candidates. Symbols are repeated from Figure 2.3. Colors for Gliese 229B (Leggett et al., 1999) and the Sun (Tokunaga, 2000) are indicated by the grey triangle and $\odot$ symbol, respectively. The (bright) end of the Bessell & Brett (1988) dwarf track can be made out in the upper right corner. Dashed lines indicate the color cuts for Sample A.

Table 2.7: Follow-up of T Dwarf Candidates.

	Imaging		Spectroscopy		
Object	Instr.	UT Date	Instr.	UT Date	Notes
(1)	(2)	(3)	(4)	(5)	(6)
2MASS 0035−0520	P60 IRCam	1999 Jun 24			Not confirmed
2MASS 0036+1422	P60 IRCam	1999 Jun 24			Not confirmed
2MASS 0055−0157	P60 IRCam	1999 Jun 24			Not confirmed
2MASS 0056+1514	P60 IRCam	1998 Oct 6			Not confirmed
2MASS 0109−0450	P60 IRCam	1999 Jun 24			Not confirmed
2MASS 0112+2738	P60 IRCam	1998 Oct 6			Not confirmed
2MASS 0216+3041	CTIO CIRIM	1999 Jul 25			Not confirmed
2MASS 0252+2732	CTIO CIRIM	1999 Jul 25			Not confirmed
2MASS 0306+2440	P60 IRCam	1999 Feb 24			Not confirmed
2MASS 0312+2609	P60 IRCam	1999 Feb 23			Not confirmed
2MASS 0333+2427	P60 IRCam	1998 Oct 6			Not confirmed
2MASS 0337+2907	P60 IRCam	1998 Oct 6			Not confirmed
2MASS 0400+2637	P60 IRCam	1999 Sep 23			Not confirmed
2MASS 0436+1547	P60 IRCam	1999 Sep 23	P60 CorMass	1999 Oct 15	PM star
2MASS 0727+1710	CTIO CIRIM	1999 Dec 17	CTIO OSIRIS	1999 Dec 20	T dwarf
2MASS 0929+2303	CTIO CIRIM	1999 Dec 18			Not confirmed
2MASS 1007+1806	Keck NIRC	1999 May 27			Not confirmed
2MASS 1047+2124	Keck NIRC	1999 May 27	Keck NIRC	1999 May 28	T dwarf
2MASS 1059+1834	Keck NIRC	1999 May 27			Not confirmed
2MASS 1217−0311	USNO Tek2K	1999 May 19	Keck NIRC	1999 May 28	T dwarf
2MASS 1237+6526	USNO Tek2K	1999 May 19	Hale DBLSPEC	1999 May 24	T dwarf
			Keck NIRC	1999 May 28	
SDSS 1346−0031			Keck NIRC	1999 May 28	T dwarf
2MASS 2110−2855	P60 IRCam	1999 Jun 24			Not confirmed
2MASS 2142−0355	P60 IRCam	1999 Jun 24			Not confirmed
2MASS 2231+2452	P60 IRCam	1999 Jun 24			Not confirmed

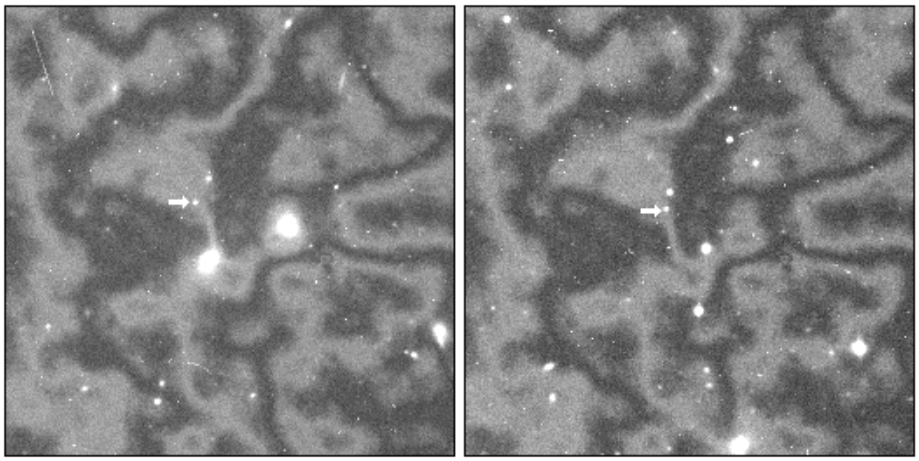

Figure 2.6: z′ Band images of 2MASS 1217-0311 (left) and 2MASS 1237+6526 (right), obtained using the USNO 61" Tek2K CCD Camera. Images are 2.′8×2.′8 with North oriented up and East to the left.

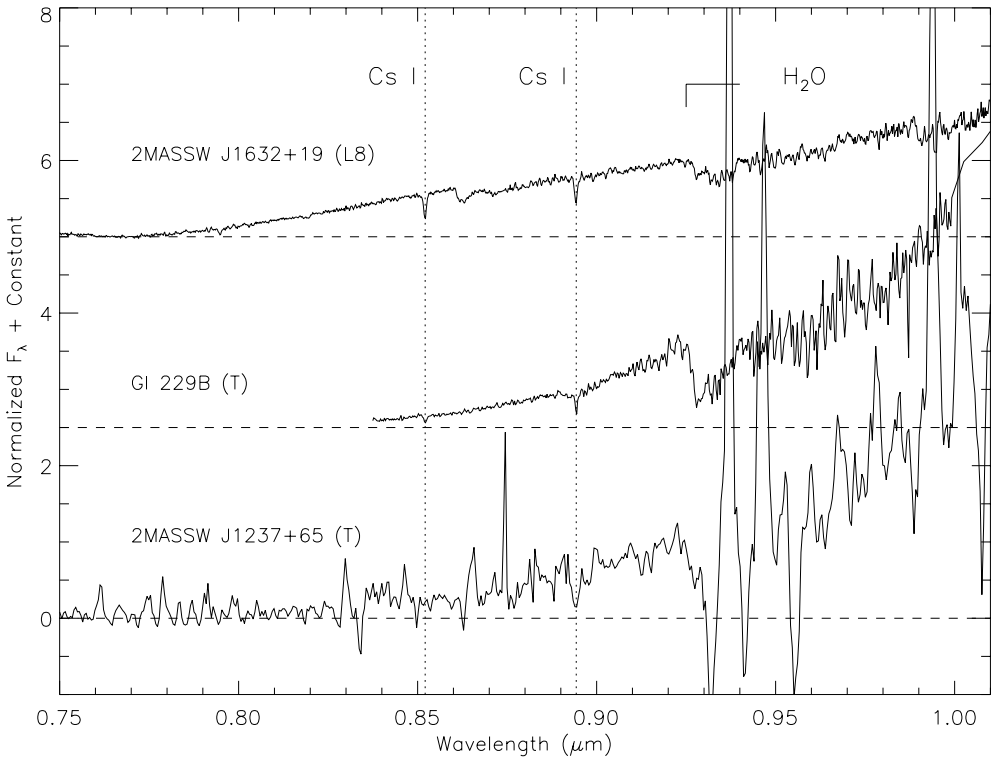

Figure 2.7: Optical spectrum (0.75 to 1.01 μm) of 2MASS 1237+6526 taken with the Double Spectrograph at the Hale 200-inch Telescope. Overlaid are optical spectra of Gliese 229B (T dwarf; Oppenheimer et al. 1998) and 2MASS 1632+1904 (L8V; Kirkpatrick et al. 1999). Spectra are normalized at 0.925 μm. Features redward of 0.93 μm in the 2MASS 1237+6526 spectrum are due to poor subtraction of telluric OH lines.

clear detections indicate that both objects have very red z-J colors.

The remaining targets were observed at J-band over various near-infrared re-imaging runs (see §2.5) made using the Palomar 60" Infrared Camera (Murphy et al., 1995, hereafter IRCam), the CTIO 1.5m CTIO Infrared Imager (hereafter, CIRIM), and the Keck 10m Near Infrared Camera (Matthews & Soifer, 1994, hereafter, NIRC). In total, 6 of 25 objects were confirmed at their expected positions, with the remaining objects presumed to be minor planets not flagged by the 2MASS databases.

2.3.2.4 Follow-up Optical and Near-Infrared Spectroscopy

The First Optical Spectrum of 2MASS 1237+6526 As an initial evaluation of the candidate sample, an optical (8000 to 11000 Å) spectrum of 2MASS 1237+6526 was taken on 1999 May 24 (UT) using the Hale 200" Double Spectrograph (Oke & Gunn, 1982) with a 1024×1024 CCD detector. Data were taken using the 158 lines mm^{-1} grating blazed at 7500 Å, yielding a dispersion of 4.8 Å pixel^{-1}. A 2″ slit was employed to guarantee acquisition of the object, resulting in $\sim$ 20 Å resolution. Because the target was invisible on the acquisition camera, offsets from a nearby visible

star were used to place the object on the slit. Three 50-minute exposures were taken. Standard IRAF[6] routines were used to reduce the data. Exposures were initially co-added, bias-subtracted, and flat-fielded. Corrections for telluric H_2O absorption were made by dividing the target spectrum by a normalized spectrum of the star PG1126+186[7] (Green, Schmidt, & Liebert, 1986). He-Ne-Ar-Hg lamps were used for wavelength calibration. Finally, flux calibration was done using the F5 subdwarf HD 84937 (Oke & Gunn, 1983).

The resulting reduced spectrum is shown in Figure 2.7, along with optical spectra of Gliese 229B (Oppenheimer et al., 1998) and the L8 dwarf 2MASSI J1632291+190441 (Kirkpatrick et al., 1999b). The redness of 2MASS 1237+6526 is quite obvious, as there is essentially no flux shortward of 8500 Å. There is a dip seen near 9400 Å which likely originates from broadened H_2O bands in the atmosphere of the target. A marginal Cs I detection at 8943 Å with an equivalent width of $\sim$ 20 Å is seen, while the 8549 Å line is undetectable due to lack of flux at these wavelengths. The weak CH_4 band at 8950 Å detected in Gliese 229B by Oppenheimer et al. (1998) is not evident in this spectrum. While many optical features are likely masked by poor signal-to-noise, the shape of the spectrum and presence of cool spectral features is a firm indication of its late spectral type.

Near-Infrared Spectra of Confirmed Candidates Four confirmed candidates, along with an additional 2MASS source 2MASS 1225-2739 (identified in the blue Preliminary sample; §2.3.1), were spectroscopically observed in the near-infrared using the Keck I NIRC grism on 1999 May 27-28 (UT). Observations of the two other confirmed candidates, 2MASS 0727+1710 and 2MASS 0436+1547, made using the CTIO 4m Ohio State InfraRed Imager/Spectrometer (Depoy et al., 1993, hereafter OSIRIS) and the Palomar 60" Cornell-Massachusetts Slit Spectrograph (Wilson et al., 2001a, hereafter CorMASS), are discussed in §§3.1.2 and 3.1.4, respectively. For the NIRC observations, we employed a 120 line mm^{-1} grism with the HK order sorting filter for first order resolution $\lambda/\Delta\lambda = 100$; wavelength resolution on the chip was 60 Å $pixel^{-1}$. Each target was first imaged with NIRC in camera mode and then placed into either a $0\farcs52$ (2MASS 1217-0311, 2MASS 1225-2739, and 2MASS 1237+6526) or $0\farcs38$ (2MASS 1047+2124 and SDSS 1346-0031) wide slit, depending on seeing conditions. Total integration times of 1000s were divided into five 200s exposures dithered $5''$ along the slit between exposures. The spectra were then pairwise subtracted to remove sky background, and each spectrum extracted separately. Flat-fielding was performed by obtaining a spectrum of a diffusely illuminated dome spot with identical instrumental settings. Each target spectrum was divided by the spectrum of a nearby SAO F star to correct for telluric absorption, and photometric standards were observed for flux calibrations. Individual exposures for each object were then averaged into a single, final spectrum.

Reduced spectra for the NIRC objects are shown in Figure 2.8, along with Gliese 229B (Geballe et al., 1996). All but one of the objects, 2MASS 1225-2739, were saturated at their H-band peaks, resulting in a false absorption feature at 1.58 μm. The region of saturation was at most 3 pixels wide. An extrapolation of each saturated H-band peak using the 2MASS 1225-2739 spectrum is indicated by a dotted line; each spectrum is normalized to this revised H-band peak. The 1.6 and 2.2 μm methane bands are quite obvious in all of the confirmed candidates, identifying them as T dwarfs. Broadened H_2O absorption bands shortward of 1.5 and 2.05 μm are also evident, consistent with those found in Gliese 299B (Oppenheimer et al., 1995). The 2.3 μm CO band seen in the L dwarfs (Jones et al., 1994; Delfosse et al., 1997) is either overwhelmed by CH_4 absorption or absent in the T dwarfs.

[6]IRAF is distributed by the National Optical Astronomy Observatories, which are operated by the Association of Universities for Research in Astronomy, Inc., under cooperative agreement with the National Science Foundation.

[7]Weak Ca, Mg, Fe, and other features are visible in the blue spectrum of this object, indicating it is not a DC8 white dwarf as initially typed by Green, Schmidt, & Liebert (1986), but rather a metal-poor subdwarf.

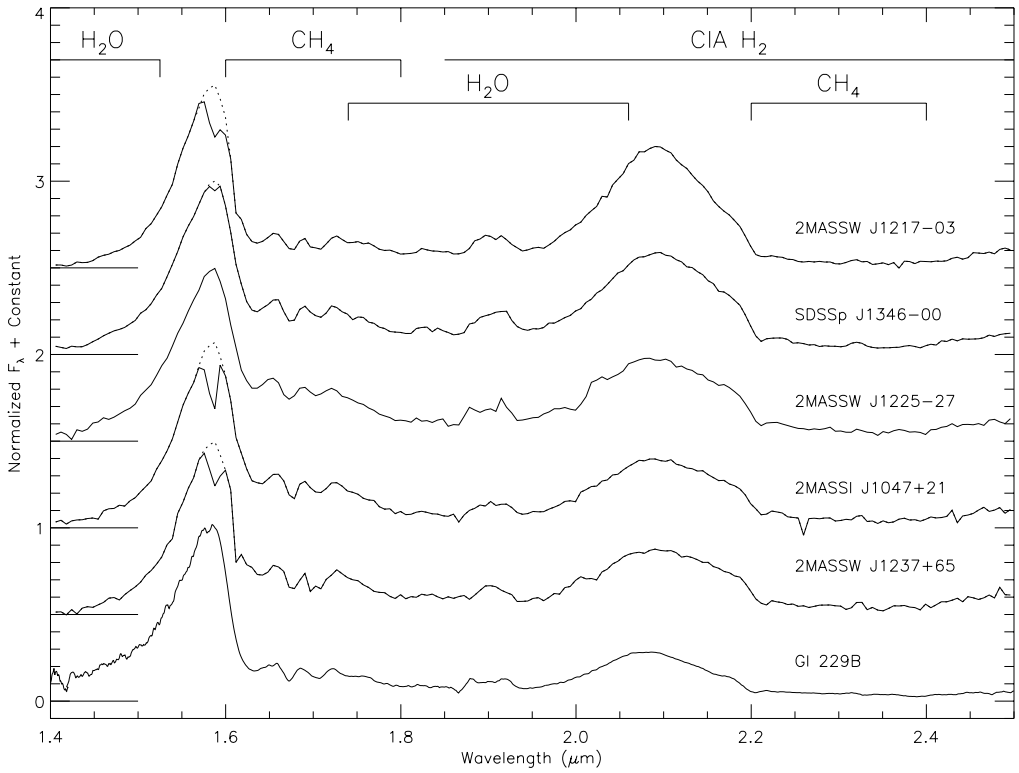

Figure 2.8: T dwarf near-infrared spectra (1.4 to 2.4 μm) taken with the Keck I NIRC grism, along with smoothed Gliese 229B spectral data from Geballe et al. (1996). Objects are displayed from top to bottom in a preliminary temperature sequence: 2MASS 1217-0311, SDSS 1346-0031, 2MASS 1225-2739, 2MASS 1047+2124, 2MASS 1237+6526, and Gliese 229B. Absorption bands for H_2, H_2O, and CH_4 are indicated. The "absorption features" seen at 1.58 μm for all but 2MASS 1225-2739 are due to saturation, and the dotted lines are extrapolations of the data in this region to fit to the 2MASS 1225-2739 H-band peak. Spectra are normalized to their H-band peak.

2.3.2.5 Initial Indications of a Spectral Sequence

The spectra in Figure 2.8 show significant variation in the ratio between the flux at 2.1 and 1.55 μm. The 2.1 μm peak appears to flatten from 2MASS 1217-0311 down to 2MASS 1237+6526. In contrast, there is an apparent steepening in the core of the 1.6 μm CH_4 band, which is flat for 2MASS 1217-0311, but decreases from 1.6 to 1.8 μm for 2MASS 1225-2739, 2MASS 1047+2124, and 2MASS 1237+6526.

According to Burrows et al. (1997), the dominant form of molecular carbon switches from CO to CH_4 at $T_{eff} \sim 1300$ K. H_2O vapor bands, which have a profound influence on the near-infrared spectra of M (Jones et al., 1994) and L (Delfosse et al., 1997) dwarfs, are also expected to be strong in T dwarfs. As Tokunaga & Kobayashi (1999) have shown, H_2 collision-induced absorption (CIA) has a marked influence on the latest L dwarfs, noticeably depressing the spectrum in a broad region around 2.2 μm. This has also been seen in the reflectance spectrum of Jupiter (Danielson, 1966). For the lower effective temperatures of T dwarfs, H_2 is expected to play a more dominant role (Saumon, Chabrier, & Van Horn, 1995).

Thus, for $T_{eff} \lesssim 1300$ K, the major absorbers in the near-infrared (JHK) spectra are CH_4, H_2O, and CIA H_2. Since the latter affects the K band more strongly than the H band, particularly toward lower temperatures, the ratio of the flux at H to that at K should increase with cooler effective temperatures. This reasoning was the basis for the sequence displayed in Figure 2.8, with the ordering: 2MASS 1217-0311, SDSS 1346-0031, 2MASS 1225-2739, 2MASS 1047+2124, 2MASS 1237+6526, and Gliese 229B. It must be stressed that this ordering was our first attempt toward a spectral sequence, using data saturated at 1.6 μm. However, many of the physical motivations for this temperature-based scheme were employed in the full derivation of a spectral classification system as described in Chapter 7.

2.3.2.6 Initial Estimates of the T Dwarf Space Density

Despite the rough color cuts made in these samples, it is possible to derive a preliminary estimate of the space density of Gliese 229B-like T dwarfs ($950 < T_{eff} < 1300$ K) with J-$K_s \lesssim 0.4$. Complete follow-up of all candidates has confirmed six objects, five of which were identified as T dwarfs. The remaining object, 2MASS 0436+1547, appears to be a faint proper motion star based on CorMASS data (J. Wilson, priv. comm.). Of the five identified T dwarfs, two (2MASS 0727+1710 and 2MASS 1047+2124) are from Sample A and three (2MASS 1217-0311, 2MASS 1237+6526, and SDSS 1346-0031) are from Sample B. These samples cover areas of 1770 and 3420 deg^2, respectively, implying surface densities of 1.1×10^{-3} and 8.8×10^{-4} T dwarfs deg^{-2}, or an average of 40 T dwarfs observable over the entire sky with J< 16. If we make the simplifying assumption that all five confirmed T dwarfs in our sample have the same luminosity as Gliese 229B, then our J-band limit corresponds to a distance limit of ~ 13 pc, and thus a mean space density of $\approx 4.5\times10^{-3}$ warm T dwarfs pc^{-3}. This is roughly half the value derived in Burgasser et al. (1999), based on the first discoveries made in 1999 May. It is nonetheless comparable to the L dwarf density of 7×10^{-3} L dwarfs pc^{-3} computed by Kirkpatrick et al. (1999b); comparison with the simulations of Reid et al. (1999b) suggests a mass function $\frac{dN}{dM} \propto M^{-1}$ in the T dwarf regime, comparable to the relation found for local late M dwarf stars (Reid et al., 1999b). T dwarf space densities are discussed in further detail in Chapter 8.

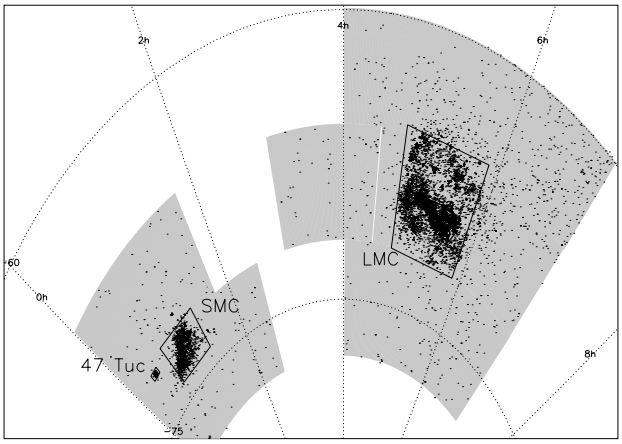

Figure 2.9: T dwarf candidates around the Magellenic Clouds and 47 Tuc. Tiles imaged by the 2MASS working database at the time of extraction of the wdb0699 candidates are shown in grey. Black lines delineate the areas removed from the search samples.

2.4 Primary T Dwarf Search Samples

2.4.1 Motivation

The T dwarfs identified in the samples above proved that these objects are readily detectable by 2MASS. However, the limited sky coverage of the early searches, coupled with awkward color constraints imposed by confusion with other sources at J-$K_s \sim 0.6$, makes it difficult to ascertain the reliability of our detection statistics. Characterizing the substellar mass function in the field requires an accurate determination of the space density of T dwarfs in the Solar Neighborhood; i.e., better statistics (see Chapter 8). Moreover, an expanded search can potentially unveil interesting objects, while a larger sample of T dwarfs enables us to characterize their properties as a population; e.g., absolute magnitudes, effective temperatures, duplicity, ages and masses, and metallicity distribution. With these scientific objectives in mind, we expanded our search both in sky coverage and color space.

2.4.2 Search Samples

We drew three new samples from the 2MASS point source catalogues in order to identify T dwarf candidates. The properties of these samples are summarized in Table 2.8. Initial candidates in all samples were required to have $|b| > 15°$ in order to avoid source confusion near the Galactic plane. We also eliminated candidates from high source density regions around the Magellanic Clouds and 47 Tuc (Figure 2.9); eliminating these regions reduced our areal coverage by only 45 deg^2 (0.3% of the wdb0699 sample), but removed up to 13059 background contaminants from our search samples. Initial candidates were also chosen to be single, unblended sources with no minor planet association (in the 2MASS Second Incremental Data Release, hereafter IDR2), and either having no optical counterpart in the USNO-A2.0 catalog or lying at least $10''$ from a nearby optical source. Finally, artifacts were eliminated by rejecting bright star glints or diffraction spikes (identified through the 2MASS database "purge flag"), and choosing sources with less than 50% probability of being bright star persistence.

Table 2.8: 2MASS T Dwarf Search Samples.

	wdb0699	rdb0400	rdb0600
Database	Working	IDR2	IDR2
Magnitude Cut	J < 16	J < 16	J ≤ 15
Required Detections	J & H	J, H, & K_s or J & H[a]	J, H, & K_s
Color Cuts	J-H < 0.3	J-H < 0.3	J-H < 0.4
	H-K_s < 0.3	H-K_s ≥ 0.3[a]	H-K_s ≤ 0.3
Area (deg^2)[b]	16620	15315	4735
Candidates:			
Initial	35280	15558	16560
Final[c]	404	272	138
Confirmed[d]	92	136	11
Unobserved	3	64	62
Followed up[e]	64	28	8
T Dwarfs	14	5	1

[a]Objects with no K_s detection did not have an H-K_s color constraint.
[b]Approximate area based on the number of imaging tiles; see §8.2.3 for a more thorough analysis of the wdb0699 sample.
[c]Number of candidates remaining after visual inspection of DSS images.
[d]Number of candidates remaining after near-infrared re-imaging observations.
[e]Number of confirmed candidates followed up with Gunn r-band imaging or near-infrared spectroscopy.

2.4.2.1 Visual Inspection

As with previous samples, we improved upon our USNO-A2.0 optical/near-infrared color cut by visually examining optical images for each candidate field. R-band imaging data 2.′5×2.′5 around each candidate coordinate, taken by the POSS-I (Wilson, 1952), POSS-II (Reid et al., 1991), ESO/SERC, and AAO SES (Morgan et al., 1992) surveys, were obtained from the CADC's DSS image server. Multiple epochs of each field were acquired whenever possible. The large number of initial candidates prompted us to look for automated techniques for rejecting optical counterparts, including the comparison of aggregate flux within 2″ of the source to the mean background, and variance limits. However, it was found that these methods suffered the same limitations as those incurred in the USNO-A2.0 Catalog; i.e., inability to recognize close doubles and faint optical sources. Hence, we printed the images *en masse* for individual visual inspection; a sample image sheet is shown in Figure 2.10. Candidates with obvious optical counterparts at their 2MASS coordinates were summarily rejected, with the majority of these contaminants being close optical doubles blended in the USNO-A2.0 catalog. Objects identified as proper motion stars based on multiple-epoch optical observations were also removed from candidate lists. Note that our criterion of no detection on the optical plates will tend to increase the number of false candidates in our search samples, rather than eliminate bona fide T dwarfs. Choosing low source density regions also reduced the possibility of throwing out good candidates due to source confusion. Nonetheless, 98.8% of the initial 2MASS-selected sources were eliminated after visual inspection, resulting in a substantially reduced search pool. As before, objects passing our visual inspection are hereafter referred to as "final" candidates.

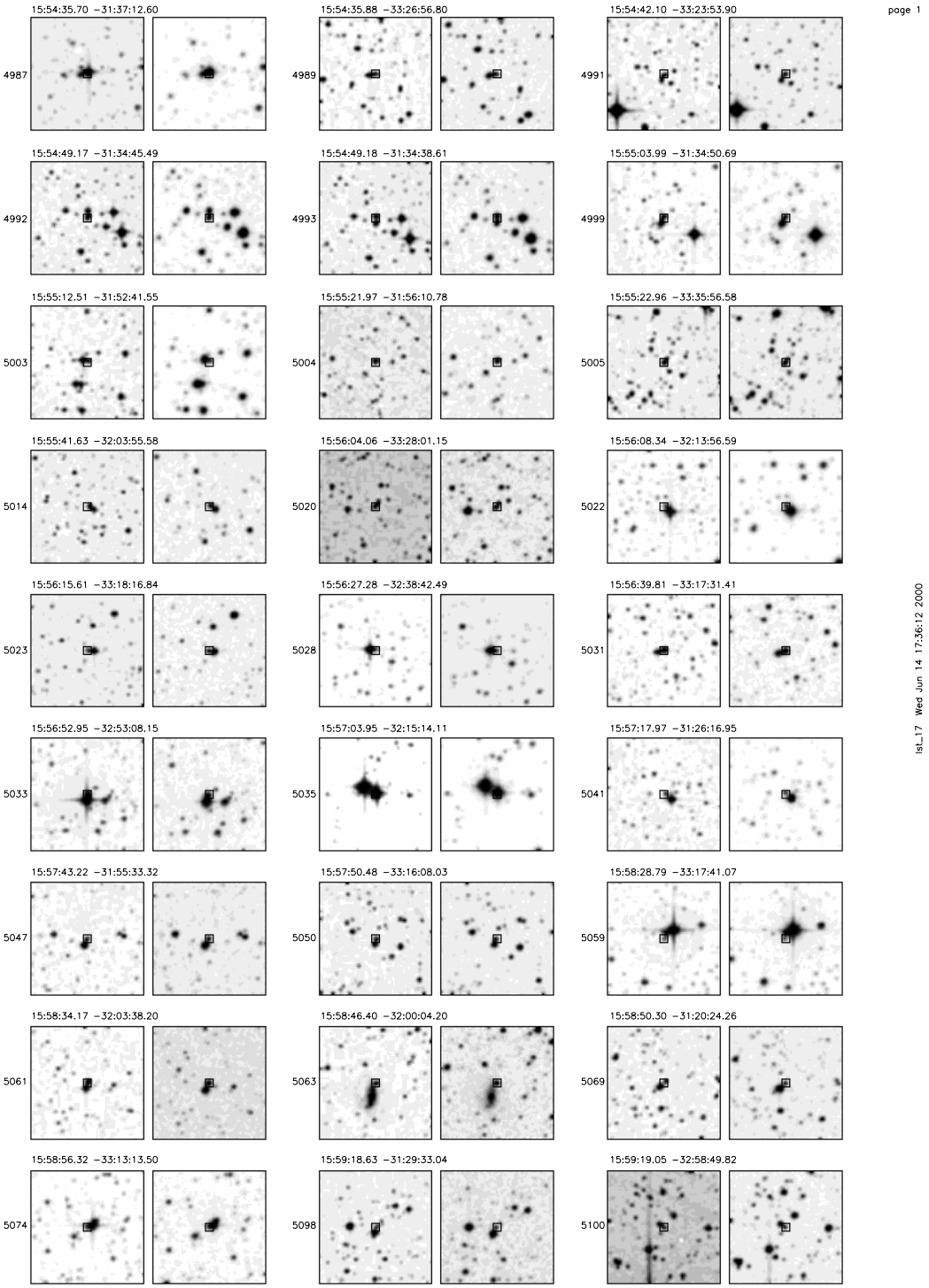

Figure 2.10: Sample image sheet from visual inspection.

2.4.2.2 Sample wdb0699

Our main search sample, wdb0699, was drawn from the 2MASS Working Database in 1999 June 22, at a time when 2MASS sky coverage was approximately 45% complete. Figure 2.11 displays a spatial map of the 35280 initial (points) and 404 final (filled circles) candidates from this sample, drawn from 16620 deg^2 of 2MASS data[8]. The final candidates are also listed in Table A.1. Grey boxes highlight tiles imaged by 2MASS at the time of candidate selection with $|b| > 15°$. Data from 23510 scans were used in this sample, 12556 from the northern hemisphere and 10954 from the southern hemisphere. These tiles cover 40.3% of the sky, or 54.4% of the sky with $|b| > 15°$, excluding the excised regions around the Magellenic Clouds and 47 Tuc. When the Ecliptic and Galactic latitude distributions of sources (thin lines) and scans (thick lines) are examined (Figure 2.12), we find an excess of initial candidates toward the Galactic plane, with 68.7% found between $15° < |b| < 30°$. This excess is largely due to contamination by the more numerous background stars at low Galactic latitudes. The expected distance limit for T dwarfs detected by 2MASS ($\sim$ 12.5 pc for Gliese 229B; Leggett et al. 1999) is significantly less than the Galactic scale height, so T dwarf discoveries should be isotropic. The final candidate latitude distribution (Figure 2.12d) is in closer agreement to the scan distribution. The Ecliptic latitude distribution of initial candidates (Figure 2.12a) is coincident with the scan distribution, but there is an excess of final candidates centered at the Ecliptic plane (Figure 2.12c). As noted in the Discovery samples, this excess represents the contamination of uncatalogued minor planets, which are absent in DSS images due to their motion.

Figures 2.13 and 2.14 diagram the color distributions of candidate objects. Initial candidates were required to have J- and H-band detections with J < 16, J-H < 0.3, and a measured color or limit of H-K_s < 0.3. The latter color cut is imposed regardless of whether or not the candidate was detected at K_s. Most of the initial and final candidates have colors near the sample limits (Figure 2.14), and based on the color distributions of stars and minor planets (§1.7), are likely dominated by faint background stars and uncatalogued asteroids. The fact that most of these candidates are also very faint (20.6% of initial and 55.0% of final candidates have 15.5 < J < 16) further suggests that they may be mostly comprised of faint background stars undetected in DSS images. Nonetheless, a number of blue candidates have been identified, with 55 final candidates having J-K_s < 0. Quite a few candidates have colors similar to Gliese 229B (grey triangle, Figure 2.13). Additional information for the wdb0699 candidates can be found in §A.1.

2.4.2.3 Sample rdb0400

The rdb0400 search sample was drawn from the 2MASS IDR2, and was used to investigate biases inherent to the color criteria of the primary wdb0699 sample. The rdb0400 sample reverses the wdb0699 H-K_s color cut in order to identify faint sources with large photometric errors, or sources without K_s detections, both populations having artificially red H-K_s colors. Objects with detections at J, H, and K_s were required to have H-$K_s \geq 0.3$, while objects without K_s detections had no H-K_s color constraint. All candidates were required to have J-H < 0.3. There is some overlap with the wdb0699 sample for objects not detected at K_s, although these candidates were selected from a different initial dataset.

A total of 15518 initial candidates were selected from 4.8×10^7 sources in 15315 deg^2 of IDR2 data with $|b| > 15°$. The 272 final candidates remaining after visual inspection are listed in Table A.6. Figure 2.15 shows the spatial distribution of both the initial and final candidates. Grey boxes in this diagram highlight the 21605 image tiles comprising this area, 10974 from the northern hemisphere and 10631 from the southern hemisphere. These scans comprise 37.7% of the entire sky, or 50.1% of

[8]Approximate area based on the number of imaging tiles; see §8.2.3 for a more thorough analysis of the search area.

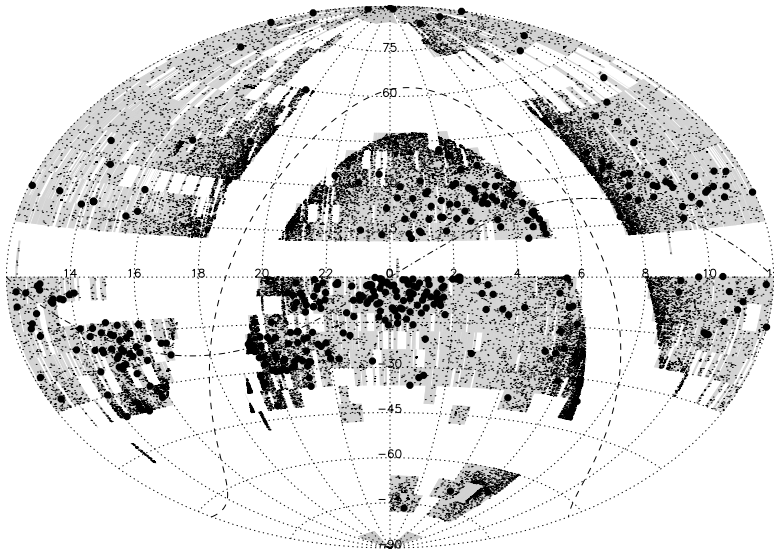

Figure 2.11: Positions of wdb0699 candidates. Small points and filled circles plot the positions of initial and final candidates, respectively. Grey area delineate the areas covered by the 2MASS survey at the time of the extraction of the wdb0699 sample. Galactic and Ecliptic equatorial planes are indicated as dashed and dot-dashed lines, respectively.

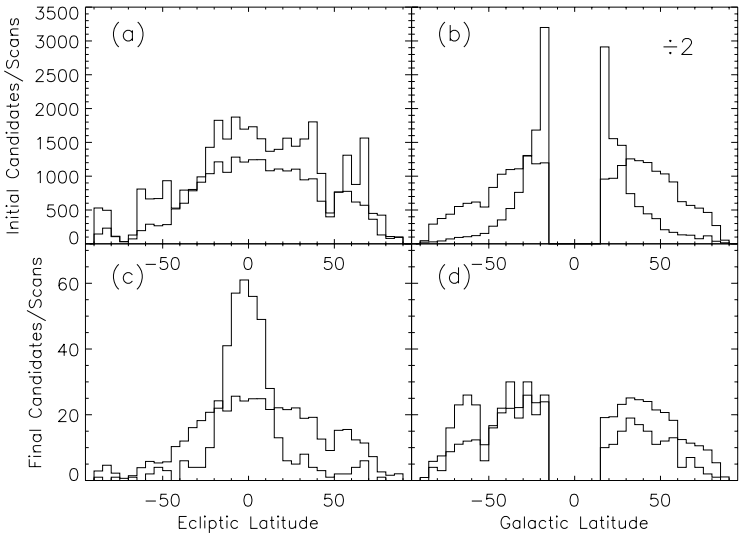

Figure 2.12: Ecliptic and Galactic latitude distributions of wdb0699 candidates. Candidate distributions are shown as thin lines, while the distribution of imaging tiles are shown as thick lines (scaled by a factor of 1/50 in (c) and (d)). The Galactic latitude distribution of initial candidates has been scaled by a factor of 1/2 in (b).

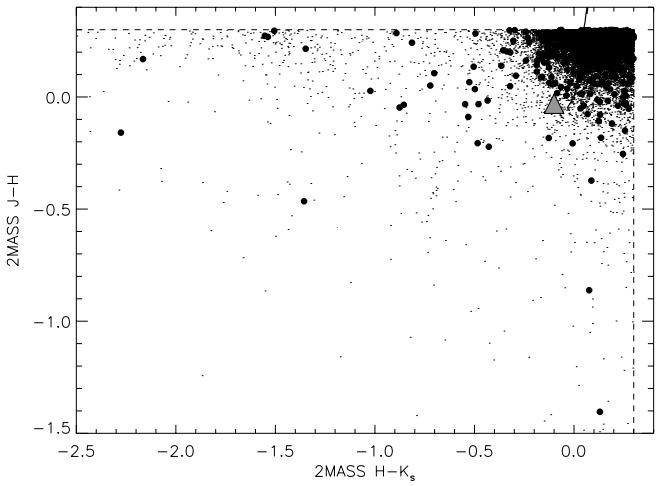

Figure 2.13: Color-color diagram of wdb0699 candidates. Symbols are those from Figure 2.11. Color constraints are delineated by the dashed lines, while the locus of Gliese 229B is indicated by the grey triangle (Leggett et al., 1999). The blue end of the Bessell & Brett (1988) dwarf track is shown as a thick black line.

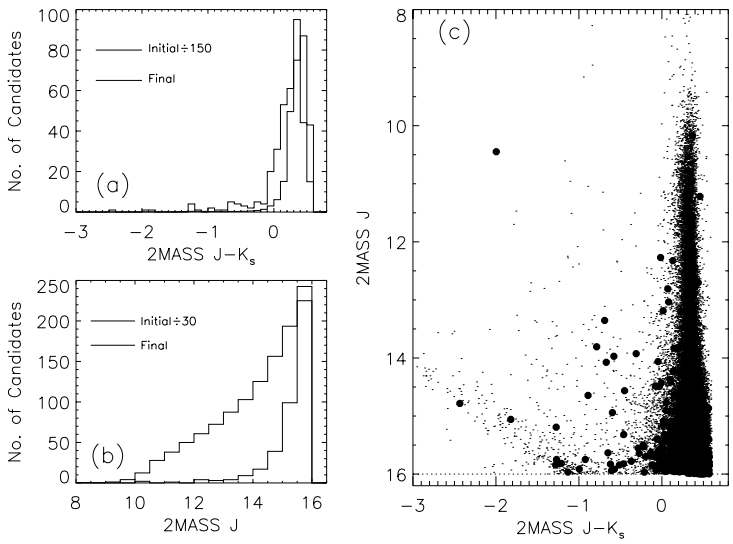

Figure 2.14: Colors and magnitudes of wdb0699 candidates. The left panels show color (*a*) and magnitude (*b*) histograms of initial (thin lines) and final (thick lines) candidates; initial candidate distributions have been scaled by factors of 1/150 and 1/30, respectively. Right panel (*c*) plots the color-apparent magnitude diagram of candidates; symbols are those from Figure 2.11.

the sky with $|b| > 15°$. Over 92% of these scans are rated quality 8 (out of 10) or higher. As shown in Figure 2.16b, the relative number of initial candidates close to the Galactic plane is less than that of the wdb0699 sample, although 56.6% of initial candidates have $15° < |b| < 30°$. The Ecliptic latitude distribution of final candidates (Figure 2.16c) is peaked at the Ecliptic plane, as was the case for the db0699 sample, although the rdb0400 distribution is significantly broader. Both the initial candidate Ecliptic latitude distribution (Figure 2.16a) and final candidate Galactic latitude distribution (Figure 2.16d) are consistent with the scan distributions.

Figures 2.17 and 2.18 plot the color distributions of the rdb0400 candidates. The majority of initial and final candidates lie to the right of the H-K_s = 0.3 line in Figure 2.17, and are therefore K_s-detected sources. Again, candidates with red J-H colors similar to stars and minor planets are more prevalent, although a number of final candidates have J-H colors as blue or bluer than Gliese 229B. The color histogram of Figure 2.18a shows a significant peak in both initial and final candidate distributions at J-K_s = 0.72–0.77. These colors are similar to those of early- and mid-M dwarfs, and indicates that the significant number of faint candidates (Figure 2.18b; 92.6% of final candidates have $15.5 < J < 16$) are likely comprised of late-type background stars too faint to be detected on DSS images. Additional information for the rdb0400 candidates can be found in §A.2.

2.4.2.4 Sample rdb0600

The rdb0600 sample extends the wdb0699 color constraints to J-H $\leq$ 0.4 and H-K_s $\leq$ 0.3, with detections in all three bands and J $\leq$ 15. These constraints imply some overlap with the wb0699 sample for brighter sources, but no overlap with the rdb0400 sample. The rdb0600 sample was used to identify T dwarfs with weaker CH_4 absorption, and was limited to the sky observable from the Southern Hemisphere during the months of June and July (R.A. $\geq 11^h$ or R.A. $\leq 1^h$, decl. $\leq 20°$). Figure 2.19 shows the spatial distribution of candidates and IDR2 images tiles extracted in this sample. A total of 16560 initial candidates were selected from $1.8{\times}10^7$ sources in 6417 scans (1139 in the northern hemisphere, 5278 in the southern hemisphere), comprising 4735 deg^2 of data, or 11.5% (15.5%) of the entire ($|b| > 15°$) sky. Note that despite the stricter magnitude limit and smaller search area of this sample, a large number of initial candidates was identified, emphasizing the difficulties caused by the high background source density in this region of color space. The 138 final candidates remaining after visual inspection are listed in Table A.11. The significant proportion of scans in this sample taken near the Ecliptic plane (62.0% have $|\beta| < 15°$) makes it difficult to ascertain any bias toward low Ecliptic latitude sources (i.e., minor planets) in either the initial (Figure 2.20a) or final (Figure 2.20c) candidate populations. However, a significant proportion of initial candidates were found close to the Galactic plane (Figure 2.20b; 63.0% with $15° < |b| < 30°$), and implies significant contamination from background sources. Indeed, 99.2% of the initial candidates were eliminated by visual inspection, resulting in a much flatter Galactic latitude distribution (Figure 2.20d).

Figure 2.21 shows the color-color plot of rdb0600 candidates. The broader color cut encompasses more objects with spectral types as late as G-K (Figure 1.19). Indeed, the source density peak seen at (H-K_s, J-H) $\approx$ (0.08, 0.33) in Figure 1.18a is almost fully sampled here. The stricter magnitude constraint eliminates many of the fainter background contaminants (late-type stars without DSS detections), and, as is seen in Figure 2.22b, there is relatively fewer faint stars in the final candidate pool as compared to the other samples (23.2% with $14.5 < J < 15$). The color distribution of both initial and final candidates (Figure 2.22a) peak around J-K_s = 0.41–0.42, corresponding to the early-type dwarf source density peak. Hence, many of the candidates may be brighter background stars (unrecognized proper motion stars and close doubles) and uncataloged minor planets, although a few objects have colors similar to Gliese 229B.

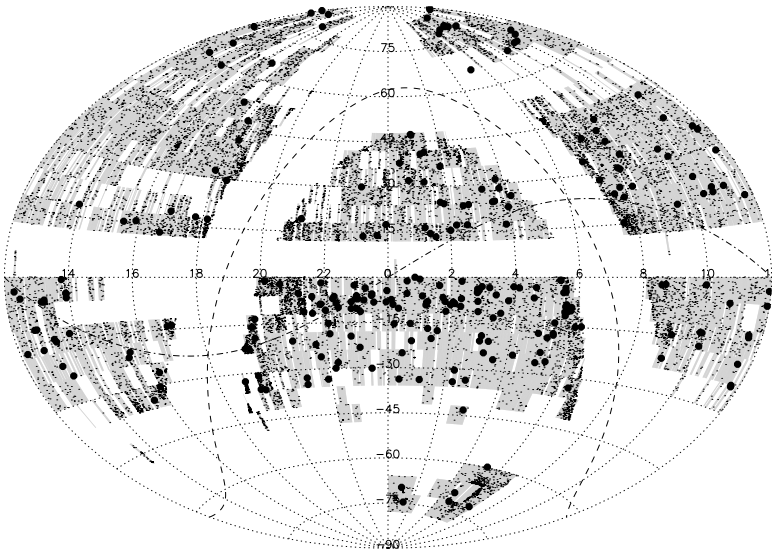

Figure 2.15: Positions of rdb0400 candidates. Symbols and lines are those of Figure 2.11. Grey areas delineate the imaging tiles present in the 2MASS IDR2 with $|b| > 15°$.

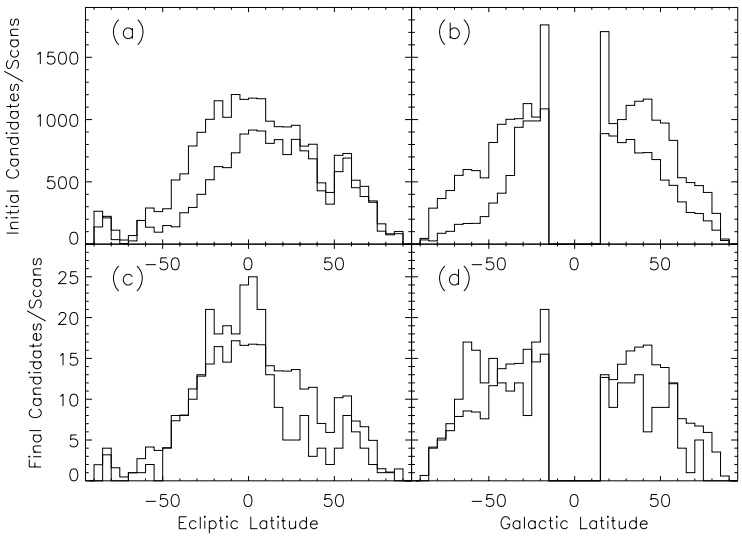

Figure 2.16: Ecliptic and Galactic latitude distributions of rdb0400 candidates. Lines are those of Figure 2.12. The distribution of imaging tiles from the 2MASS IDR2 are scaled by a factor of 1/70 in *c* and *d*.

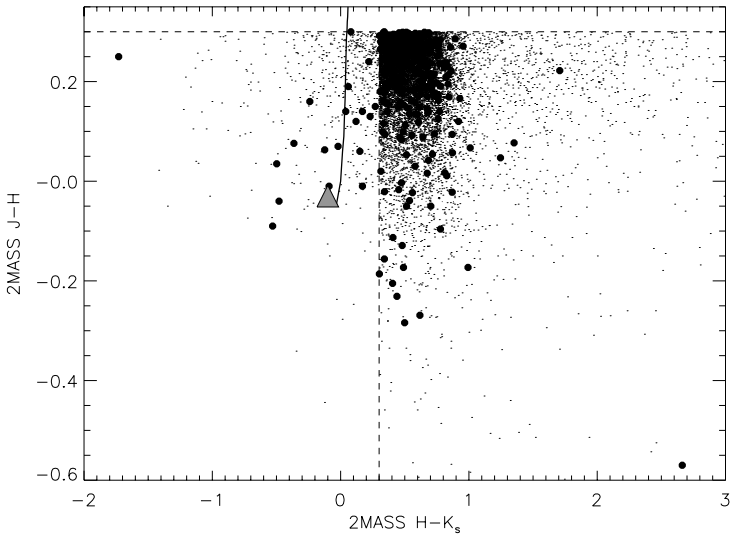

Figure 2.17: Color-color diagram of rdb0400 candidates. Symbols and lines are those from Figure 2.13.

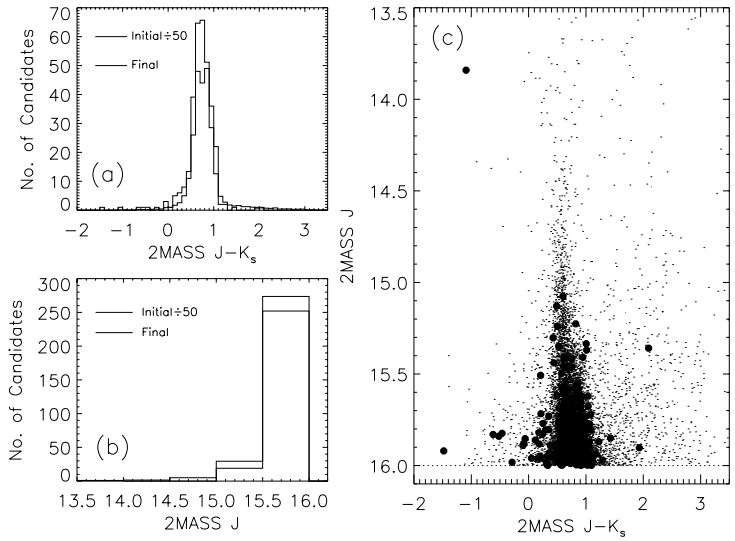

Figure 2.18: Colors and magnitudes of rdb0400 candidates. Symbols and lines are those from Figure 2.14. Initial candidate distributions in a and b have been scaled by a factor of 1/50.

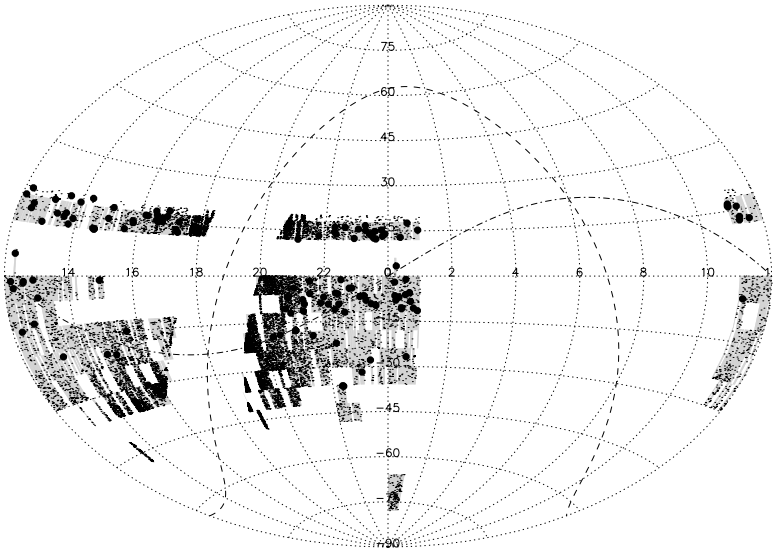

Figure 2.19: Positions of rdb0600 candidates. Symbols and lines are those of Figure 2.11. Grey areas delineate the imaging tiles present in the 2MASS IDR2 with $|b| > 15°$, R.A. $\geq 11^h$ or R.A. $\leq 1^h$, and $\delta \leq 20°$.

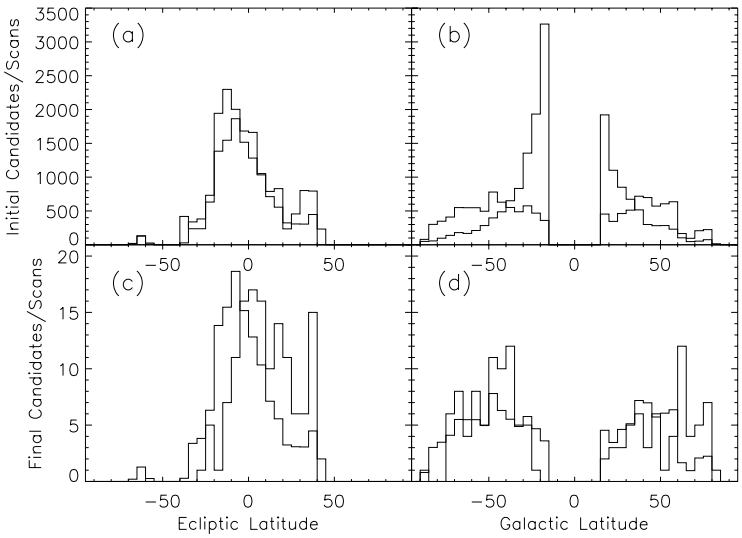

Figure 2.20: Ecliptic and Galactic latitude distributions of rdb0600 candidates. Lines are those of Figure 2.12. The distribution of imaging tiles are scaled by a factor of 2 in a and b and a factor of 1/50 in c and d.

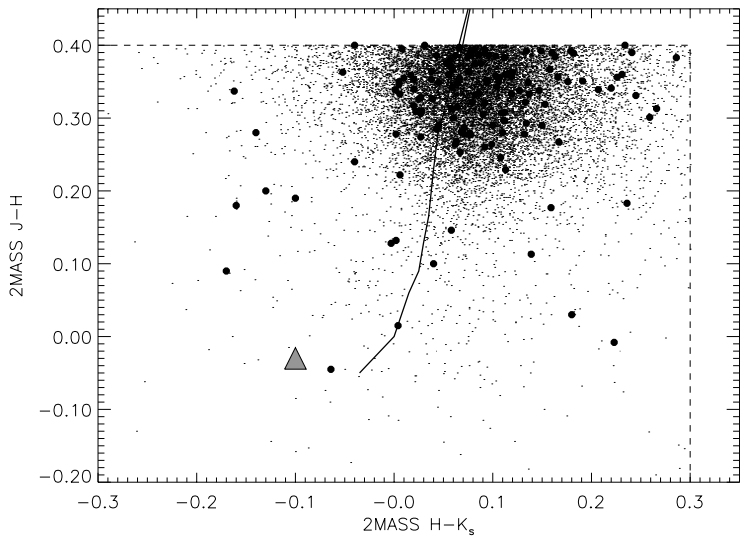

Figure 2.21: Color-color diagram of rdb0600 candidates. Symbols and lines are those from Figure 2.13.

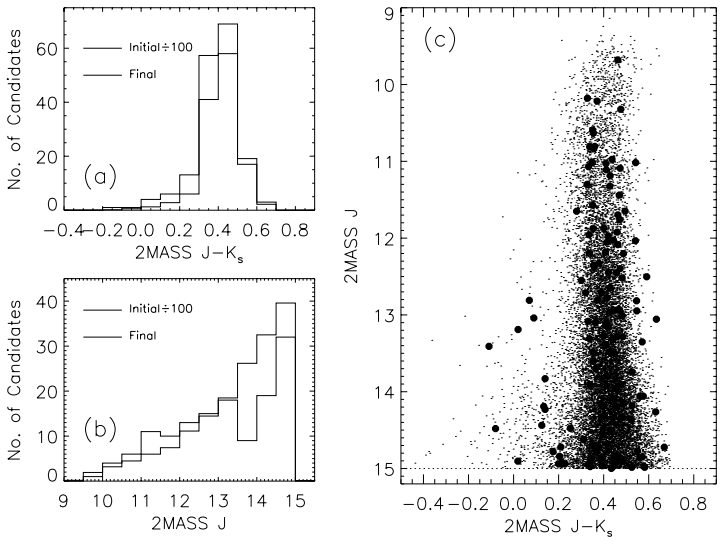

Figure 2.22: Colors and magnitudes of rdb0600 candidates. Symbols and lines are those from Figure 2.14. Initial candidate distributions in a and b have been scaled by a factor of 1/100.

2.5 Follow-up Imaging

Despite our near-infrared and effective optical/near-infrared color constraints, additional contaminants remain. As mentioned in §2.3.2.3, the most important of these are uncatalogued minor planets, which have near-infrared colors similar to T dwarfs (§1.7.4), and are absent in DSS images due to their motion. Other possible contaminants include the same image artifacts present in earlier samples (most likely to appear amongst the wdb0699 candidates), faint and red background stars that do not appear on DSS images, and proper motion stars unidentified in the visual inspection (due to large motion or absence of a second epoch optical image).

To remove these objects from our candidate pool, we have conducted two reimaging campaigns. The first was done in the near-infrared, using as our primary instruments the Palomar 60" IRCam, and both the CTIO 1.5m CIRIM and OSIRIS instruments. Additional observations were made using the Hale 5m D78 near-infrared camera and Keck NIRC. These observations are described in §2.5.1. We also obtained optical Gunn r-band images using the CCD Camera mounted on the Palomar 60" Telescope, described in §2.5.2.

2.5.1 Near-Infrared Reimaging

Near-infrared re-imaging observations of T candidates from our primary samples were made over 40 nights from 1998 October through 2001 January. Table 2.9 summarizes these observations. The early runs included objects also selected in the Preliminary and Discovery samples. Imaging data were obtained at J-band in paired, dithered exposures, with integration times ranging from 30 sec (around bright stars) to 45 sec (faint targets or poor observing conditions). In some case, observations of faint, detected targets were also made at K-band to verify their near-infrared colors.

Initial examination of the pairwise subtracted images at the telescope provided confirmation of the candidate objects. Because these observations were obtained at similar-sized facilities and with longer integration times than 2MASS observations, this first check was considered to be adequate for tailoring our candidate pool; i.e., rejecting candidates not seen. Overall, second epoch imaging eliminated nearly 80% of the final T dwarf candidates in our primary samples with J-K_s < 0.5. We have completed confirmation reimaging of 99%, 76%, and 54% of our wdb0699, rdb0400, and rdb0600 final candidates, respectively.

Tables A.2, A.7, and A.12 list all of the candidates that were not confirmed in near-infrared reimaging for the wdb0699, rdb0400, and rdb0600 samples, respectively. These objects comprise 76.8%, 34.1%, and 88.0% of the re-observed candidates from these samples, suggesting significant contamination by minor planets. We can examine the nature of these unconfirmed candidates by investigating their spatial distribution. Figure 2.23 shows the ecliptic latitude distribution of 144 unconfirmed targets from our wdb0699 sample present in the 2MASS IDR2 and not associated with a known asteroid in Table A.2. We compared this to the distribution of 288 flagged minor planets in the 2MASS IDR2 having the same color and magnitude properties as the wdb0699 sample, and 25 unconfirmed wdb0699 candidates that were found to be widely separated (within $25''$) from a known asteroid. Both populations peak near the ecliptic plane, making it likely that the vast majority of our unconfirmed candidates are in fact uncatalogued minor planets. The distribution of the unconfirmed candidates is distinctly broader, however. We cannot rule out that a few of these transient sources may be faint variable stars, infrared counterparts to bursting sources, or, in at least one confirmed case, supernovae[9]. Nonetheless, it is highly unlikely that any are missed T dwarfs.

[9]2MASSI J0101271-073636 is the near-infrared counterpart to SN 1998DN (Cao, 1998).

Table 2.9: Log of Confirmation Imaging Observations for Primary Sample Candidates.

UT Date (1)	Instrument (2)	# Observed All / (J-K_s < 0.5) (3)	% Confirmed All / (J-K_s < 0.5) (4)	Conditions (5)
1998 Oct 7–9	Palomar 60" IRCam	11 (10)	0.0 (0.0)	thin cirrus to clear
1999 Feb 23–27	Palomar 60" IRCam	6 (6)	16.7 (16.7)	clear to scattered clouds
1999 May 3	Palomar 60" IRCam	4 (2)	50.0 (0.0)	cirrus and fog
1999 May 27	Keck 10m NIRC	4 (4)	50.0 (50.0)	clear
1999 Jul 23–25	CTIO 1.5m CIRIM	194 (176)	7.2 (6.3)	clear to hazy
1999 Sep 22–25	Palomar 60" IRCam	83 (70)	37.3 (37.1)	fog to hazy
1999 Nov 19–21	Palomar 60" IRCam	4 (3)	0.0 (0.0)	thin clouds to cloudy
1999 Dec 17–19	CTIO 1.5m CIRIM	28 (22)	50.0 (36.4)	hazy to scattered clouds
2000 Jan 23–24	Keck 10m NIRC	5 (5)	0.0 (0.0)	clear and windy
2000 Apr 14–15	Palomar 60" IRCam	54 (45)	55.6 (57.8)	clear to low clouds and wind
2000 May 18–20	Palomar 60" IRCam	83 (8)	80.7 (25.0)	clear to fog and haze
2000 Jun 21–23	CTIO 1.5m OSIRIS	104 (45)	35.6 (15.6)	cloudy to clear
2000 Aug 18–20	CTIO 1.5m OSIRIS	26 (6)	53.8 (16.7)	light cirrus
2000 Oct 11–13	Palomar 60" IRCam	27 (5)	63.0 (40.0)	clear, high humidity
2001 Jan 5	Palomar 5m D78	1 (1)	100.0 (100.0)	cloudy
TOTAL		634 (408)	36.3 (21.3)	

Table 2.10: Log of Optical Imaging Observations for Primary Sample Candidates.

UT Date (1)	# Observed All / (J-K_s > 0.3) (2)	% Detected All / (J-K_s > 0.3) (3)	Conditions (4)
1999 Sep 10–11	7 (4)	85.7 (100.0)	variable clouds to haze/smoke; seeing 1.″4–1.″6
2000 May 4–5	3 (0)	0.0 (–)	clear and photometric; seeing 1.″2–1.″5
2000 Jul 1–2	23 (18)	78.3 (88.9)	windy/clear to light cirrus; seeing 1.″8–2.″0
2000 Dec 27–28	35 (27)	88.6 (92.6)	windy/clear to cirrus/clouds; seeing 1.″8–2.″7
TOTAL	68 (49)	80.9 (91.8)	

2.5.2 R-band Imaging

Additional imaging observations were made using the Palomar 60" CCD Camera with the CCD13 detector and Gunn r broad band filter (Wade et al., 1979). The purpose of these observations was to identify faint background stars and close optical doubles, in order to eliminate these objects from our candidate pool. Based on the observed red colors of late-type L dwarfs (Figure 1.12) and the F675W−J = 9.1±0.2 color of Gliese 229B (Golimowski et al., 1998; Leggett et al., 1999), we can effectively throw out any detection as a probable background star, as our typical (blank sky) limiting magnitude of r ∼ 22–23 in 300s implies detected r-J < 6–7, equivalent to spectral type M6 to M8.

2.5.2.1 Observations and Data Reduction

Observations were made in nine nights over four runs, as summarized in Table 2.10. Conditions during 1999 September 9–11 and 2000 December 28 (UT) were plagued by cloudy weather, the latter night also afflicted with poor seeing. Photometry obtained on these nights are particularly suspect. Poor seeing (2–3″) was also a problem during 2000 July 1–2 and 2000 December 27 (UT). Our best photometric observations were made during 2000 May 4–5 (UT), in clear conditions and 1.″2–1.″5 seeing. All runs generally occurred during dark time.

Confirmed candidates were generally exposed for 3–300s at r-band, depending on the proximity of a nearby sources (see §2.5.2.2). At least one or two photometric standards selected from Kent (1985) were observed each night, with multiple dithered exposures made on the same frame. In addition to the target and standard observations, we imaged a flat-field lamp reflected off of the interior dome in each band used over the course of a run, and short dark (closed shutter) exposures were also made for each run to determine the bias level. Longer dark exposures (∼ 100 s) showed no significant light leakage in the instrument. For observations during 2000 December 27–28 (UT), we also obtained exposures of the interior dome without the flat field lamp, as we have found that using this procedure in the near-infrared produces higher-quality flats. We also attempted to observe twilight flats during our 2000 May 4–5 (UT) run, but the paucity of successful exposures made limited their use.

The resulting raw data were initially trimmed to the central 512×512 pixel region of the chip to improve computing efficiency. For each observing run we created a master bias image by median-combining all of our short dark exposures. We then created flats for each filter by median-combining the appropriate lamp exposures (rejecting deviant images), subtracting the bias, and normalizing to the median value. For our 2000 December 27–28 (UT) observations, we median-combined the appropriate lamp-off exposures and used this as the bias frame for the lamp-on exposures. A mask of deviant pixels was constructed from the bias and flat-field images for each run. The science data were then bias-subtracted, divided by the normalized flat-field, and corrected for bad pixels by interpolation. The resulting image was then reflected about the y-axis of the chip to properly orient the field.

We measured the flux from our science targets by aperture photometry. First, the precise location of the object was determined by summing the rows and columns in an encompassing 7×7 pixel box, and fitting the point spread function (PSF) distributions to a Gaussian. The seeing, S, was estimated from these fits and from those of other single stars in the frame. We then centered an aperture and sky annulus on the source, with the radii for a standard star fixed at 6S and 12S–18S, respectively; and 4S and 8S–12S for the science target. Apertures for the science targets were allowed to vary to compensate for nearby bright sources, but in general we chose reasonably large aperture sizes to sample the entire PSF.

For each measurement, we first computed the RMS scatter in the sky annulus (δ_{sky}), and then determined the mean sky after rejecting the 30% lowest and 30% highest values (to eliminate background stars, cosmic rays, and bad pixels). This value was subtracted from each pixel in the flux aperture, and the pixel flux values summed and divided by the exposure time to yield the instrumental count rate (f_{obj}). Formal uncertainties were calculated as

$$\sigma^2_{f_{obj}} = f_{obj} + N\delta^2_{sky}, \tag{2.1}$$

where N is the total number of pixels in the aperture. For standard stars, this process was repeated for each exposure on the frame, and we computed a mean count rate and formal uncertainty from these values. The scatter in the individual count rates, which was typically larger than the formal uncertainty, was added in quadrature to derive a final error estimate.

2.5.2.2 Measuring Photometry for Candidates Close to Bright Stars

Candidates close to bright sources are typically hidden by the glare produced by these stars, as exemplified for 2MASS 2203+3327 in Figure 2.24. This object lies 8″ from the V=9.68 star GSC 02724-01948, whose PSF extends over roughly 20″ in the image. To resolve the source, we subtracted off a reflection of the image across a vertical axis centered on the bright star. The position of this axis was chosen manually in order to obtain the best subtraction. As shown in the right panel, this procedure significantly reduces the glare in the wings of the bright source and allows us (in this case) to recover the candidate. Aperture photometry was then done, excluding the region encompassing the bright star from our sky annulus. A smaller aperture was used to exclude residual glare. This technique was quite successful in both identifying close background sources and measuring their flux, and we implemented this procedure for all of our candidate sources close to bright stars.

2.5.2.3 Calibration and Results

Calibration from instrumental to apparent magnitudes was done through our standard observations, but the procedure used varied according to the quality of the observing conditions. For our 2000 May 4–5 and 2000 July 1–2 (UT) observations, we determined an airmass (z) correction by a linear fit to the calculated zeropoints,

$$ZP = m_{std} + 2.5 \log f_{std}, \tag{2.2}$$

where f_{std} is the instrumental flux of the standard star and m_{std} its published magnitude. For our 2000 May 4 and 5 observations we derived (Figure 2.25)

$$\begin{aligned} ZP &= (23.99\pm0.02) - (0.05\pm0.02)z \\ ZP &= (24.10\pm0.02) - (0.17\pm0.02)z. \end{aligned} \tag{2.3}$$

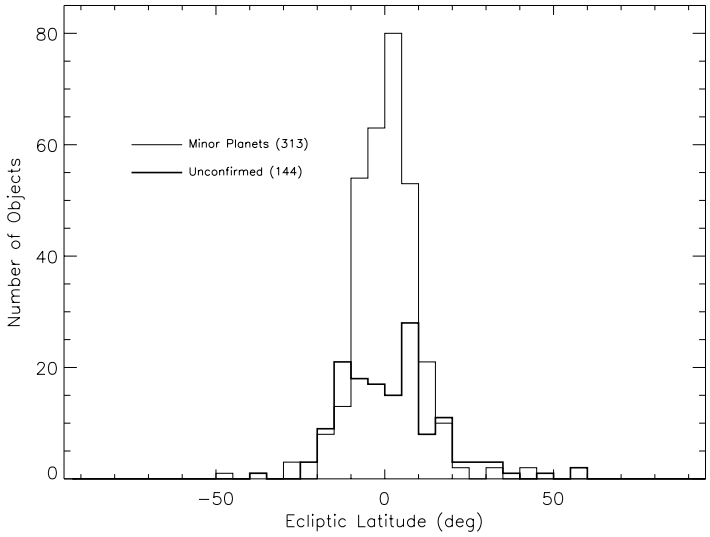

Figure 2.23: Ecliptic latitude distribution of 144 unconfirmed wdb0699 candidates found in the 2MASS IDR2 and not associated with a known minor planet. We compare this to the distribution of 288 identified asteroids (with the same color properties) and 25 missed associations (from our search).

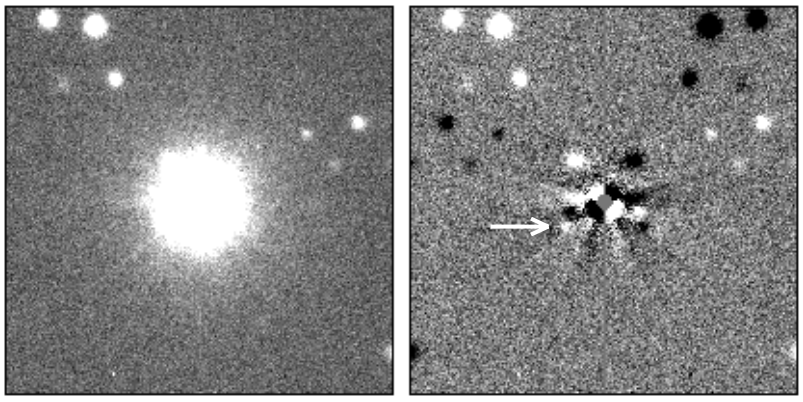

Figure 2.24: Demonstration of reflection technique for resolving background stars close to bright optical sources. The left panel shows the raw CCD image at r-band, while the right panel shows the same image reflected about a vertical axis centered on the bright star. The candidate object is clearly seen just below and to the left of the star (arrow). Images are $1\farcm2 \times 1\farcm2$ in size.

The differences in slope may have been due to low-lying smog present on the night of May 5. For 2000 July 1 and 2 we derived (Figure 2.26)

$$\begin{aligned} ZP &= (24.31\pm0.07) - (0.06\pm0.06)z \\ ZP &= (24.42\pm0.06) - (0.16\pm0.06)z. \end{aligned} \tag{2.4}$$

Note that a different standard was used for these two runs, Feige 34 and BD +35°3659, respectively. For our 1999 September and 2000 December, the conditions were not good enough to warrant accurate photometry, so we used the mean zeropoints with no airmass correction: ZP = 24.0 and 23.9 for 1999 September 10 and 11, and 23.7 for December 27–28. Note that Equations 2.3 and 2.4 imply at least a 0.05–0.17 mag bias in our derived photometry without airmass correction, but systematics due to the conditions (variable weather, patchy clouds, etc.) likely outweigh these corrections.

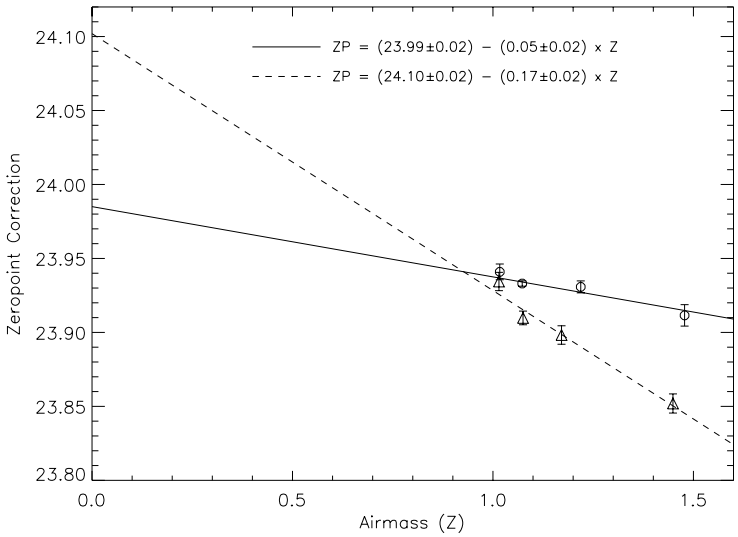

Figure 2.25: Zeropoint corrections for our 2000 May 4–5 (UT) r-band observations. Linear fits to airmass for May 4 (circles) and May 5 (triangles) data are indicated by solid and dashed lines, respectively.

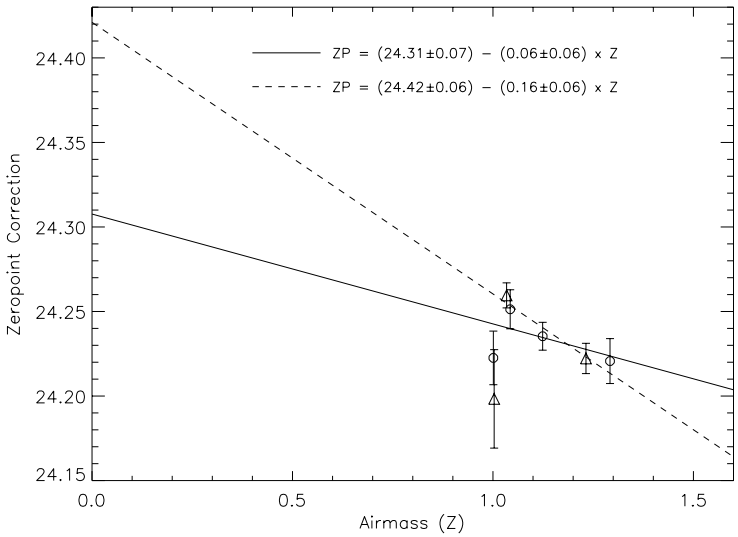

Figure 2.26: Zeropoint corrections for our 2000 July 1–2 (UT) r-band observations. Linear fits to airmass for July 1 (circles) and July 2 (triangles) data are indicated by solid and dashed lines, respectively.

Table 2.11: Optical Photometry of T Dwarf Candidates.

		2MASS Photometry		Optical Photometry					
Object (1)	Sample (2)	J (3)	J−K_s (4)	Date (5)	r (6)	i (7)	z (8)	r-J (9)	Note (10)
0007035-104322	db0699	14.06±0.29	-0.05±0.31	1999 Sep 10	18.06±0.06			4.00±0.30	Optical Source
0009242-085956	db0400	15.96±0.08	0.45±0.24	2000 Dec 27	20.34±0.13		17.94±0.25	4.38±0.15	Optical Source
0031314-135546	db0699	15.82±0.07	0.41±0.20	1999 Sep 10	20.14±0.09			4.32±0.11	Optical Source
0044126-154751	db0699	15.98±0.09	0.55±0.21	2000 Dec 27	19.84±0.11			3.86±0.14	Optical Source
0101091-331701	db0699	15.56±0.06	0.50±0.16	1999 Sep 10	19.91±0.09			4.35±0.11	Other
0108363-100941	db0699	15.48±0.37	0.26±0.61	2000 Dec 27	> 18.76			> 3.28	Confirmed
0109117-202923	db0699	15.83±0.07	0.54±0.18	2000 Dec 27	19.67±0.10		17.78±0.25	3.84±0.12	Optical Source
0110425-323016	db0699	15.92±0.09	0.49±0.28	1999 Sep 10	19.25±0.03			3.33±0.09	Optical Source
0140496-063634	db0699	15.40±0.39	-0.05±1.07	2000 Dec 27	> 14.45			> -0.95	Confirmed
0218571-011723	db0400	15.77±0.07	0.59±0.15	2000 Dec 27	20.62±0.18		18.33±0.29	4.85±0.19	Optical Source
0256553-030043	db0400	15.86±0.07	0.66±0.17	2000 Dec 27	20.89±0.34		> 20.26	5.03±0.35	Optical Source
0314092-053236	db0699	15.99±0.08	0.53±0.22	2000 Dec 27	20.28±0.14		18.22±0.28	4.29±0.16	Optical Source
0324424+885645	db0699	15.93±0.09	0.52±0.22	2000 Dec 27					Optical Source
0333311+160825	db0699	15.64±0.23	0.37±0.49	2000 Dec 27	> 18.86		19.37±0.49	> 3.22	Confirmed
0356399-025959	db0400	15.95±0.08	0.57±0.20	2000 Dec 27	> 22.51		19.06±0.33	> 6.56	M dwarf
0455317+150457	db0699	15.75±0.20	0.47±0.29	2000 Dec 27	21.39±0.19			5.64±0.28	Optical Source
0514048+655916	db0400	15.80±0.08	< 0.34	2000 Dec 27	> 23.24		> 21.57	> 7.44	Confirmed
0519427-045221	db0699	12.70±0.03	0.43±0.04	2000 Dec 27	14.27±0.03			1.57±0.04	Optical Source
0530385-044010	db0400	13.84±0.03	-1.09±0.14	2000 Dec 27	20.92±0.16		18.29±0.27	7.08±0.16	Optical Source
0532000-001657	db0699	14.83±0.35	0.53±0.40	2000 Dec 27	15.44±0.04			0.61±0.35	Optical Source
0539068-091024	db0699	14.49±0.32	-0.03±0.34	2000 Dec 27	19.55±0.13			5.06±0.35	Optical Source
0544509-213912	db0699	15.63±0.08	0.37±0.20	2000 Dec 27	17.38±0.04			1.75±0.09	Optical Source
0559191-140448	db0699	13.83±0.03	0.22±0.06	2000 Dec 27			17.75±0.06		T dwarf
0644261+791008	db0400	15.95±0.08	0.63±0.19	2000 Dec 27	21.19±0.18		18.17±0.27	5.24±0.20	Optical Source
0812028+210731	db0699	15.64±0.08	0.52±0.17	2000 Dec 27	20.58±0.10		17.93±0.25	4.94±0.13	Optical Source
0844312+212402	db0699	15.56±0.24	0.40±0.36	2000 Dec 27	19.58±0.15			4.02±0.28	Optical Source
0900472+661612	db0699	15.25±0.06	0.39±0.17	2000 Dec 27	18.70±0.04		16.78±0.24	3.45±0.07	Optical Source
0903132-035438	db0699	15.75±0.07	0.47±0.19	2000 Dec 27	20.64±0.04			4.89±0.08	Optical Source
0924576+815205	db0699	15.87±0.11	< 0.05	2000 Dec 27	20.27±0.13		19.48±0.35	4.40±0.17	Optical Source
0927346+240816	db0699	16.00±0.10	0.49±0.26	2000 Dec 27	19.66±0.07		17.90±0.25	3.66±0.12	Optical Source
0928401+184114	db0400	15.99±0.08	0.31±0.19	2000 Dec 27	16.98±0.03		17.22±0.24	0.99±0.09	Optical Source
0937347+293142	db0699	14.65±0.04	-0.89±0.24	2000 May 04	> 24.50	22.02±0.37	18.50±0.09	> 9.85	T dwarf
0958432+303626	db0400	15.85±0.08	0.64±0.16	2000 Dec 27	20.95±0.13		18.12±0.25	5.10±0.15	Optical Source
1004064-133823	db0699	15.95±0.08	< 0.42	2000 Dec 27	20.91±0.13		17.64±0.25	4.96±0.15	Optical Source
1009128-140056	db0699	15.99±0.10	0.34±0.27	2000 Dec 27	19.54±0.05		17.84±0.26	3.55±0.11	Optical Source
1028103+202838	db0699	15.98±0.09	0.49±0.23	2000 Dec 27	20.18±0.07		18.02±0.25	4.20±0.11	Optical Source
1029231+521954	db0699	15.97±0.11	< -1.13	2000 Dec 27	20.45±0.11		17.84±0.26	4.48±0.16	Optical Source

Table 2.11: Optical Photometry, Cont.

		2MASS Photometry		Optical Photometry					
Object	Sample	J	J−K_s	Date	r	i	z	r-J	Note
(1)	(2)	(3)	(4)	(5)	(6)	(7)	(8)	(9)	(10)
1034135+205405	db0699	15.76±0.06	0.53±0.15	2000 Dec 27	19.42±0.05		17.56±0.25	3.66±0.08	Optical Source
1036593+681529	db0699	15.82±0.08	< -1.21	2000 Dec 27	20.50±0.11		17.85±0.26	4.68±0.14	Optical Source
1047539+212423	db0699	15.82±0.06	< -0.47	2000 May 05		> 23.83	19.94±0.17		T dwarf
1146257-013636	db0699	15.53±0.06	0.34±0.18	2000 Dec 27	16.49±0.03			0.96±0.07	Optical Source
1217111-031113	db0699	15.85±0.07	< -0.06	2000 Dec 27		> 22.82	21.69±1.24		T dwarf
1225543-273947	db0699	15.22±0.05	0.16±0.16	2000 May 05		> 22.95	19.00±0.19		T dwarf
1346464-003150	db0400	15.86±0.08	< 0.11	2000 May 04	> 24.40	> 23.44	20.20±0.22	> 8.54	T dwarf
1444206-201922	db0600	12.50±0.03	0.59±0.04	2000 Jul 02	18.15±0.15		14.69±0.08	5.65±0.15	Optical Source
1457150-212148	db0699	15.33±0.05	0.06±0.18	2000 May 05	> 24.16	> 23.58	19.72±0.20	> 8.83	T dwarf
1524334-213944	db0400	15.93±0.09	< 0.70	2000 Jul 02	20.37±0.24		17.95±0.11	4.44±0.26	Optical Source
1529506+150501	db0400	15.83±0.07	0.68±0.16	2000 Jul 02	20.53±0.19		18.12±0.10	4.70±0.20	Optical Source
1553023+153237	db0400	15.81±0.08	0.30±0.21	2000 Jul 01	> 23.32		19.38±0.22	> 7.51	T dwarf
1626203+392519	db0699	14.43±0.03	-0.01±0.09	2000 Jul 01	19.80±0.11			5.37±0.11	Optical Source
1653543+184437	db0600	14.85±0.05	0.57±0.09	2000 Jul 02	18.76±0.14			3.91±0.15	Optical Source
1718515+525634	db0400	15.78±0.07	< 0.66	2000 Jul 02	21.02±0.24			5.24±0.25	Optical Source
1758230+141738	db0600	14.95±0.05	0.33±0.09	2000 Jul 02	16.22±0.11			1.27±0.12	Optical Source
1809036+173428	db0400	15.96±0.13	0.62±0.33	2000 Jul 02	20.97±0.11		18.63±0.07	5.01±0.17	Optical Source
1824434+293713	db0699	15.93±0.09	< 0.36	2000 Jul 01	21.09±0.14		18.25±0.46	5.16±0.17	Optical Source
1940236-141011	db0699	15.58±0.35	0.18±0.42	1999 Sep 10					Optical Source
2029352-185315	db0600	14.68±0.29	0.42±0.30	2000 Jul 02	17.93±0.11			3.25±0.31	Optical Source
2036340-021111	db0400	15.91±0.10	0.65±0.18	2000 Jul 01	21.60±0.21		18.44±0.21	5.69±0.23	Optical Source
2047412-050230	db0699	15.53±1.26	-0.21±1.57	2000 Jul 01	> 18.89			> 3.36	Confirmed
2103161-014956	db0699	15.97±0.07	0.43±0.21	2000 Jul 01	19.71±0.12		17.90±0.07	3.74±0.14	Optical Source
2114321-055550	db0699	15.96±0.10	0.47±0.26	2000 Jul 01	19.53±0.13			3.57±0.16	Optical Source
2118006-274204	db0699	15.85±0.15	-0.03±0.43	1999 Sep 10	20.96±0.09			5.11±0.17	M dwarf
2132452-014148	db0600	14.72±0.04	0.67±0.07	2000 Jul 02	18.30±0.10			3.58±0.11	Optical Source
2203168+332721	db0699	13.81±0.53	-0.78±0.54	2000 Jul 01	19.62±0.10			5.81±0.54	Optical Source
2212321-295538	db0400	16.00±0.09	0.57±0.22	2000 Jul 01	20.41±0.36			4.41±0.37	Optical Source
2217435+160729	db0600	15.00±0.06	0.44±0.13	2000 Jul 02	16.12±0.09		15.89±0.06	1.12±0.11	Optical Source
2218247-280316	db0400	15.79±0.08	0.69±0.17	2000 Jul 02	20.66±1.60			4.87±1.60	Confirmed
2254188+312349	db0699	15.28±0.05	0.45±0.15	2000 Jul 01	> 23.69		19.66±0.36	> 8.41	T dwarf
2312077+133603	db0400	15.96±0.08	0.65±0.20	2000 Jul 01	21.28±0.11			5.32±0.14	Optical Source
2316211-084336	db0699	15.91±0.08	0.48±0.20	1999 Sep 10	20.16±0.14			4.25±0.16	Optical Source
2336354+341116	db0699	15.77±0.08	0.53±0.18	2000 Dec 28	20.52±0.30		17.62±0.24	4.75±0.31	Optical Source
2339101+135230	db0400	15.88±0.08	0.18±0.29	2000 Jul 01	> 23.16		19.49±0.19	> 7.28	T dwarf
2344211+140616	db0699	13.20±0.44	0.23±0.45	2000 Dec 27	17.15±0.03			3.95±0.44	Optical Source
2356548-155311	db0699	15.80±0.06	-0.03±0.21	1999 Sep 11	> 25.16	21.88±0.14	19.80±0.16	> 9.36	T dwarf

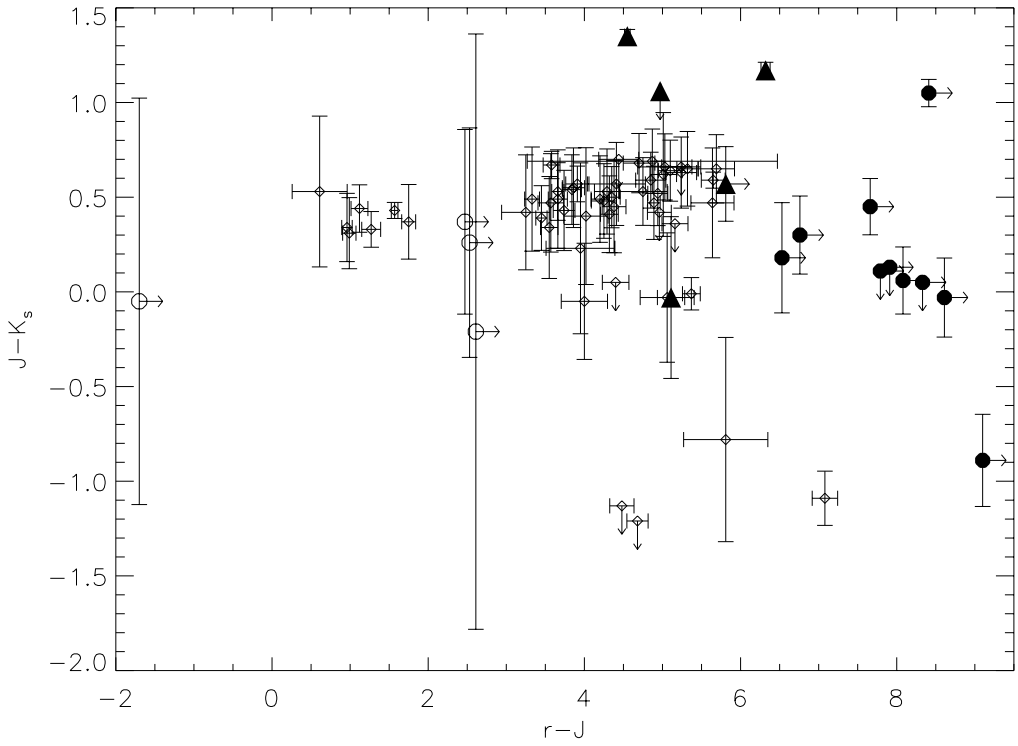

Figure 2.27: r−J versus J−K$_s$ for T dwarf candidates from the primary samples. Detected candidates are plotted as diamonds, undetected candidates as open circles, known (or spectroscopically identified) M dwarfs as solid triangles, and identified T dwarfs as solid circles. Upper limits on colors are indicated by arrows.

Using these zeropoints, we derived r-band magnitudes for our candidate targets, as listed in Table 2.11. Figure 2.27 plots J−K$_s$ versus r−J for detected candidates, undetected candidates, known M dwarfs, and known T dwarfs observed using the CCD Camera. Note that none of the T dwarfs were detected in these observations at r-band, despite longer integration times than the candidate sources (1200–1800s versus 300s). Nearly all of the detected sources have r−J < 6, implying that they are all earlier than mid-M. Indeed, most have J−K$_s$ ~ 0.5, only slightly bluer than the known M dwarfs shown here. The one very unusual detection, 2MASS 0530-0440, with J−K$_s$ $= -1.09\pm0.14$ and r−J $= 7.08\pm0.16$, has colors quite unlike any cool dwarf currently known, and may be an interesting source for spectroscopic follow-up. Excluding the T dwarfs, the sources that were undetected at r were all close to bright stars, as is evident in their large J−K$_s$ uncertainties. None have limits that exceed r−J $= 3$, and it is likely that they are also background sources.

Overall, of the 68 sources observed by follow-up imaging, 80% have r−J < 6, with one detected source having r−J $= 7.08\pm0.16$. If we consider only the sources with J−K$_s$ > 0.3, this percentage increases to 92%. Hence, it is likely that most of the red candidates found in all three primary samples are background stars, although a few T dwarfs may be hidden in this part of color space as well.

Table 2.12: T Dwarfs Identified in the 2MASS Catalog.

2MASS Designation (1)	Primary Sample[a] (2)	2MASS J (3)	2MASS H (4)	2MASS K_s (5)
2MASSI J0243137−245329	wdb0699	15.40±0.05	15.15±0.10	15.21±0.17
2MASSI J0415195−093506	wdb0699	15.71±0.06	15.57±0.12	15.45±0.20
2MASSI J0559191−140448	wdb0699	13.83±0.03	13.68±0.04	13.61±0.05
2MASSI J0727182+171001	wdb0699	15.55±0.07	15.82±0.18	15.56±0.21
2MASSI J0755480+221218	wdb0699	15.72±0.07	15.66±0.14	15.77±0.21
2MASSI J0937347+293142	wdb0699	14.65±0.04	14.68±0.07	15.54±0.24
2MASSI J1047539+212423	wdb0699	15.82±0.06	15.79±0.12	$> 16.29^b$
2MASSI J1217111−031113	wdb0699	15.85±0.07	15.79±0.12	$> 15.91^b$
2MASSI J1225543−273947	wdb0699	15.23±0.05	15.10±0.08	15.06±0.15
2MASSI J1237392+652615	Sample B	16.03±0.09	15.72±0.16	$> 15.90^b$
SDSS 1346464−003159	rdb0400	15.86±0.08	16.05±0.21	$> 15.75^b$
Gliese 570D[c]	wdb0699	15.33±0.05	15.28±0.09	15.27±0.17
2MASSI J1534498−295227	wdb0699	14.90±0.04	14.89±0.09	14.89±0.11
2MASSI J1546271−332511	wdb0699	15.60±0.05	15.44±0.09	15.42±0.17
2MASSI J1553022+153236	rdb0400	15.81±0.08	15.92±0.17	15.51±0.19
2MASSI J2254188+312349	wdb0699	15.28±0.05	15.04±0.09	14.83±0.14
2MASSI J2339101+135230	rdb0400	15.88±0.08	16.04±0.17	15.70±0.28
2MASSI J2356547−155310	wdb0699	15.80±0.06	15.64±0.10	15.83±0.19

[a]Some objects found in multiple samples due to overlapping search criteria.
[b]Not detected at K_s band; given magnitude is the 2MASS 95% confidence magnitude limit based on background flux.
[c]Also known as 2MASSI J1457150-212148.

2.6 T Dwarf Discoveries

Candidates that are confirmed and do not have optical detections are then spectroscopically observed in the near-infrared. Chapter 3 describes the acquisition and reduction of this spectral data, and the characterization of the observed candidates. Spectroscopic follow-up has been completed for 40%, 7%, and 22% of the confirmed candidates in the primary wdb0699, rdb0400, and rdb0600 samples, respectively, so that 70%, 26%, and 89% of confirmed candidates have been followed up in some manner (i.e., through spectroscopy or optical imaging), as listed in Tables A.3, A.8, and A.13.

Table 2.12 lists the 18 T dwarfs identified to date in both the Discovery and Primary samples. Only one object, 2MASS 1237+6526, has not been recovered by the Primary samples, as its revised J-band magnitude, 16.03±0.09, puts it below the faint magnitude limit for these samples. Figure 2.28 shows an updated version of the color-color plot in Figure 1.23 which includes the identified T dwarfs. Because most of these objects have been identified in the wdb0699 sample (14 of 18), they generally have J−H and H−K_s < 0.3, with the bluest object being 2MASS 0937+2931, with J−K_s = −0.89±0.24 (see §7.7). Two objects, 2MASS 1553+1532 and 2MASS 2339+1352, are from the rdb0400 sample and have H−K_s > 0.3, although both are faint sources whose colors may have scattered into this region. No objects have yet been identified with J−H > 0.3. The incompleteness of the rdb0400 and rdb0600 samples prevents us from drawing any firm conclusions from these color distributions, but it is likely that most Gliese 229B-like T dwarfs have colors that fall within the wdb0699 sample.

Since the wdb0699 sample is nearly completely characterized, we can use this sample to again make a rough estimate of the T dwarf space density. Adopting a search area of 16620 deg^2 and limiting distance of 12.5 pc (distance at which Gliese 229B has J = 16; Leggett et al. 1999), the 14 T dwarfs identified in this sample yield a surface density of 8.4×10^{-4} deg^{-2} and a space density of 4.2×10^{-3} pc^{-3}. This is very close to the estimate made from the Discovery samples (§2.3.2.6),

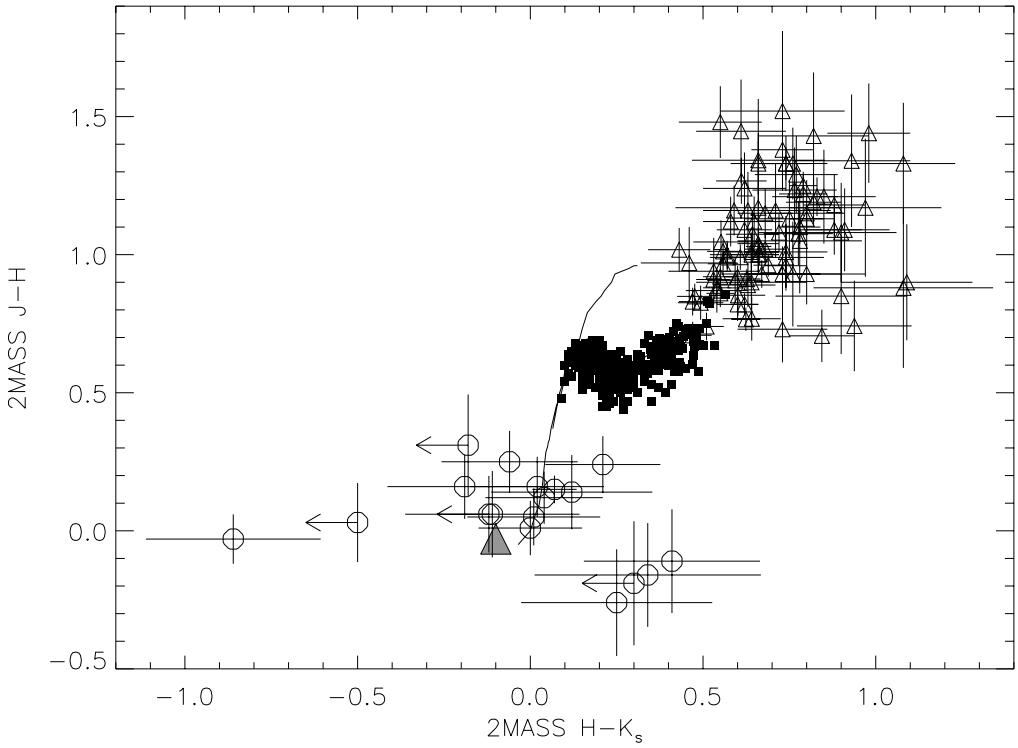

Figure 2.28: Near-infrared colors for M, L, and T dwarfs, where symbols are from Figure 1.23, except for the 18 T dwarfs identified in the search samples, which are plotted as open circles. Upper limits on H−K$_s$ color are shown as arrows.

although both numbers have not been corrected for selection biases. A more rigorous derivation of the T dwarf space density is made in Chapter 8. These estimates predict that 30–40 T dwarfs can be identified in the complete 2MASS database with these selection criteria, all of which will be important new additions to the nearby stellar (and substellar) census.

2.7 Summary

In this chapter, we have described the search criteria and methodology used to identify T dwarfs in the 2MASS database. We have generally constrained our search to the identification of cool T dwarfs with blue near-infrared colors in order to avoid the congestion of background and foreground objects in the near-infrared color space between the latest L dwarfs and Gliese 229B. Three sets of samples have been extracted over the course of this work: the early Preliminary samples, which used both $J-K_s$ and optical/near-infrared color constraints, the latter derived from USNO scans of the POSS-II survey plates; the Discovery samples, extracted from the 2MASS working database and IDR1 and compared against DSS optical images, which provided our first complete sample with identified T dwarfs; and finally, the larger-scale Primary samples, extracted from the working database and IDR2 and compared against both first-epoch and second-epoch DSS images. Examination of DSS images in both the Discovery and Primary samples has been extremely effective in curtailing our candidate lists, eliminating upwards of 99% of our 2MASS-selected source, and reducing follow-up from tens of thousands of candidates down to hundreds. Clearly, this is a critical step in the identification of these optically faint objects.

We have also described near-infrared confirmation imaging observations made to eliminate minor planets and spurious sources from our candidate samples. These observations have systematically rejected an additional 80% of our candidate pool, and analysis of the ecliptic latitude distribution of these objects indicates that they are likely comprised of uncatalogued asteroids. We have also made optical imaging observations to further curtail our lists, identifying faint background (probably M-type) stars and candidates lying close to bright optical sources. These observations have eliminated an additional 80% of our (primarily red) confirmed sources. The final stage of candidate identification, spectroscopy, is described in Chapter 3.

These observations have ultimately identified 18 T dwarfs from both the Discovery and Primary samples, as listed in Table 2.12. In the following chapters, we will examine these discoveries in detail, analyzing photometric, spectroscopic, and astrometric observations, to ultimately constrain the contribution of Gliese 229B-like T dwarfs to the substellar mass of the Galaxy.

MEDIA RELATIONS OFFICE
JET PROPULSION LABORATORY
CALIFORNIA INSTITUTE OF TECHNOLOGY
NATIONAL AERONAUTICS AND SPACE ADMINISTRATION
PASADENA, CALIF. 91109 TELEPHONE (818) 354-5011
http://www.jpl.nasa.gov

Contact: Jane Platt (818) 354-0880

FOR IMMEDIATE RELEASE June 1, 1999

ASTRONOMERS FIND SUN'S COOLEST NEIGHBORS

A pair of near-infrared telescopes sponsored by NASA and the National Science Foundation has detected the coolest brown dwarfs ever seen -- celestial objects that are neither fish nor fowl, or in this case, neither planet nor star.

Brown dwarfs are often thought of as "stellar wannabes." They are failed stars that never got hot enough to ignite the nuclear fusion process that makes stars shine brightly. On the other hand, they tend to be more massive than planets and do not form around a star, as the planets in our solar system did.

"These latest discoveries are merging the fields of stellar astronomy and planetary science," said Adam Burgasser, physics graduate student at the California Institute of Technology, Pasadena, CA. He is leading the hunt for these objects along with Dr. Davy Kirkpatrick, senior staff scientist at the JPL/Caltech Infrared Processing and Analysis Center.

After sorting through millions of celestial objects, Burgasser discovered four brown dwarfs in images taken by a pair of 1.3-meter (51-inch) telescopes near Tucson, AZ, and at Cerro Tololo, Chile. The telescopes, used for the Two-Micron All Sky Survey (2MASS), study near-infrared wavelengths that can't be seen by the naked eye. They sense heat and thus detect heat-emitting objects like stars and galaxies normally hidden by curtains of cold dust. In this case, the brown dwarfs are too cold to be seen in visible wavelengths, but 2MASS was able to detect the small amounts of heat they emit.

Armed with this information, Michael Brown, Caltech assistant professor of planetary astronomy, studied the objects using the Keck Telescope atop Mauna Kea, HI, to look for the presence of methane, a telltale chemical fingerprint of very cool brown dwarfs.

"Methane forms only in objects cooler than 900 degrees Celsius (1,652 Fahrenheit)," Burgasser said. "That's only four times hotter than the maximum setting on a conventional kitchen oven."

"We think these brown dwarfs are only 30 light years away," said Kirkpatrick. "Because our telescopes can only see the closest examples, this means the Milky Way must be brimming with objects like these." The newly discovered brown dwarfs are located in the constellations of Ursa Major (the Big Dipper), Leo, Virgo, and Corvus.

The 2MASS telescopes are in the midst of a 3-1/2-year survey

of the entire sky. The survey is designed to catalog one million galaxies, 300 million stars, and other celestial objects throughout our Milky Way galaxy. The 2MASS telescopes actually discovered five methane brown dwarfs, but one of them had been found previously by the Sloan Digital Sky Survey, also supported by NASA and the National Science Foundation.

The 2MASS project is based at the University of Massachusetts, Amherst, where its principal investigator Dr. Michael Skrutskie is a physics and astronomy professor. The JPL/Caltech Infrared Processing and Analysis Center combines and processes 2MASS images into usable data.

As part of NASA's Origins Program, 2MASS is funded by NASA's Office of Space Science and the National Science Foundation. Results from 2MASS will benefit future Origins missions, including Space Infrared Telescope Facility and the Next Generation Space Telescope. JPL manages the program for NASA's Office of Space Science, Washington, DC. JPL is a division of the California Institute of Technology, Pasadena, CA.

The current images, and additional 2MASS information and images are available at: http://www.ipac.caltech.edu/2mass.

2MASS information and images are also available at: http://pegasus.phast.umass.edu.

Chapter 3 Spectroscopy

I procured me a Triangular glass-Prisme,
to try therewith the celebrated Phaenomena of Colours.
Isaac Newton (1672)

Spectroscopy is a key component in the search and characterization of a new astronomical population. For this work, near-infrared spectroscopy provides final confirmation of a candidate object (Chapter 2) as a T dwarf through the identification of CH_4 absorption bands. Analysis of spectral morphology for a group of T dwarfs enables the development of a classification system (see Chapter 7); finally, spectra provide detailed information on the temperatures, gravities, and abundances of T dwarf photospheres, to far greater detail than photometric colors alone.

In this chapter, we describe the acquisition, data reduction, basic morphology, and features of T dwarf spectra. Near-infrared spectra are presented in §3.1, including 1–2.5 μm data obtained using the NIRC (on the Keck 10m), OSIRIS (on the CTIO Blanco 4m), and D78 (on the Palomar Hale 5m) instruments; and 3.0–4.6 μm data obtained for 2MASS 0559-1404 using the Keck NIRC instrument. Red optical spectra (6000–10000 Å), obtained using the Keck LRIS instrument, are presented in §3.2, along with blue optical (3800–8650 Å) data for 2MASS 1237+6526.

3.1 Near-Infrared Spectroscopy

Near-infrared spectra are essential for the identification of T dwarf discoveries, particularly given the ambiguity of near-infrared colors with other background objects (proper-motion stars, faint M dwarfs, etc.; see §1.7). As such, we have observed many of the 2MASS T dwarf candidates in this spectral region, along with other known M, L, and T dwarfs for comparison. In this section, we discuss the acquisition, reduction, and properties of the 1–2.5 μm spectra of these objects obtained using four different instruments. Observations made using the Near Infrared Camera (Matthews & Soifer, 1994, hereafter NIRC) mounted on the Keck I 10m, including 3.0–4.6 μm observations of 2MASS 0559-1404, are discussed in §3.1.1; observations made using the Ohio State InfraRed Imager/Spectrometer (Depoy et al., 1993, hereafter OSIRIS), mounted on the CTIO 4m Blanco Telescope, are discussed in §3.1.2; and observations made using D78, an instrument similar in construction to NIRC mounted on the Palomar 5m Hale Telescope, are discussed in §3.1.3. Additional observations made by J. Wilson (Cornell) using the Palomar 60" Cornell-Massachusetts Slit Spectrograph (Wilson et al., 2001a, hereafter CorMASS), as described in §3.1.4. The features identified in the near-infrared spectra are described in §3.1.5. Finally, we examine the accuracy of the NIRC and OSIRIS datasets in §3.1.6 by comparison with each other and to previously published data.

3.1.1 NIRC Observations

The NIRC instrument is comprised of a 256×256 InSb array camera mounted on the f/25 Forward Cassegrain focus of the Keck I 10m Telescope. Filters and grisms permit low-resolution ($\lambda/\Delta\lambda \sim$ 60–120) spectroscopy from 1–2.5 μm in two settings: 1–1.6 μm, using the 150 lines mm^{-1} grating blazed at 1.7 μm and JH order blocking filter; and 1.4–2.5 μm, using the 120 lines mm^{-1} grating blazed at 2.1 μm and HK order blocking filter. Spectral resolutions on the $0\farcs15$ pixel^{-1} chip are 49 Å pixel^{-1} and 59 Å pixel^{-1}, respectively. Spectra from 3.0–4.6 μm can also be obtained using the

Table 3.1: Log of 1–2.5 μm NIRC Observations.

Object (1)	Type (2)	UT Date (3)	t_{int} (s) (4)	Airmass (5)	$\lambda\lambda$ (μm) (6)	Calibrator (7)	Cal. Type[a] (8)
2MASS 0144−1221	mid M	1999 Nov 18	540	1.27	1.0–1.6	HD 990	F5 V
2MASS 0243−2453	T	2000 Jan 24	1080	1.41	1.0–2.5	HD 19378	G0 V
2MASS 0332+2001	early M	1999 Nov 18	540	1.22	1.4–2.5	HD 990	F5 V
2MASS 0333−1016	mid M	1999 Nov 18	540	1.22	1.0–1.6	HD 990	F5 V
2MASS 0415−0935	T	1999 Nov 18	1080	1.21	1.0–2.5	SAO 150589	G5 V
		2000 Jan 24	1080	1.35	1.0–2.5	HD 22855	G3 V
2MASS 0559−1404	T	2000 Jan 23	1080	1.21	1.0–2.5	HD 41083	G2/3 V
		2000 Jan 24	1080	1.26	1.0–2.5	HD 41083	G2/3 V
2MASS 0727+1710	T	2000 Jan 23	1080	1.00	1.0–2.5	SAO 96796	G5 V
2MASS 0825+2115[b]	L7.5 V	2000 Jan 23	1080	1.00	1.0–2.5	SAO 96796	G5 V
2MASS 0920+3517[b]	L6.5 V	2000 Jan 24	1080	1.04	1.0–2.5	HD 73617	F5 V
2MASS 0937+2931	T	2000 Jan 23	1080	1.01	1.0–2.5	HD 76332	G2 V
		2000 Jan 24	1080	1.03	1.0–2.5	HD 76332	G2 V
2MASS 1047+2124	T	2000 Jan 23	1080	1.00	1.0–2.5	HD 98562	G2 V
		2000 Jan 24	1080	1.00	1.0–2.5	HD 98562	G2 V
2MASS 1217−0311	T	2000 Jan 23	1080	1.09	1.0–2.5	HD 108754	G7 V
2MASS 1237+6526	T	2000 Jan 24	1080	1.42	1.0–2.5	HD 110276	G0 Vw
SDSS 1346−0031	T	2000 Jan 23	1080	1.07	1.0–2.5	HD 127913	G2 V
Gliese 570D	T	2000 Jan 24	1080	1.39	1.0–2.5	HD 126253	G0 V
2MASS 1553+1532	T	2000 Jul 22	900	1.15	1.0–2.5	HD 146759	G5 V
2MASS 2254+3123	T	2000 Jul 22	900	1.08	1.0–2.5	HD 219213	G5 V
2MASS 2339+1352	T	2000 Jul 22	900	1.08	1.0–2.5	HD 219213	G5 V
2MASS 2356−1553	T	1999 Nov 18	1080	1.28	1.0–2.5	HD 990	F5 V

[a]Spectral types obtained from the SIMBAD database.
[b]Previously identified L dwarfs observed for spectral comparision.

60 lines mm^{-1} grating blazed at 4.2 μm and LM order blocking filter. Spectral resolution in this configuration is 129 Å pixel^{-1}.

3.1.1.1 Acquisition of 1–2.5 μm Spectra

A log of observations, taken over four nights, is given in Table 3.1. Conditions on 1999 November 18 (UT) were clear with good seeing ($\sim 0\farcs4$); observations made on 2000 January 23-24 (UT) were done in clear but windy weather, with seeing ranging from $0\farcs7$ to $1\farcs3$; finally, conditions on 2000 July 22 (UT) were plagued by light to heavy cirrus, although seeing was $0\farcs4$. Early spectral data were also obtained on 1999 May 27-28 (UT), as discussed in §2.3.2.4 (see Figure 2.8) and presented in Burgasser et al. (1999); however, these data were subject to saturation problems and are not discussed here.

Targets were initially acquired in imaging mode and placed into a $0\farcs525$ (3.5 pixel) slit. Multiple sets of three exposures dithered $5''$ along the slit were made for each object at the JH and/or HK settings. F and G dwarf standards close to the target objects, chosen for their weak hydrogen lines, were observed using the same instrumental setup. Finally, spectral lamps reflected off of the interior dome were observed in order to calibrate pixel response.

3.1.1.2 Data Reduction

Procedures for data reduction are summarized schematically in Figure 3.1. Science images were initially pairwise subtracted to remove dark current and sky background, then divided by a median-combined, dark-subtracted, normalized dome flat image to correct for pixel-to-pixel spectral response variations. Bad pixels were removed by interpolation using a mask constructed from dark and flat

field frames. Curvature of the dispersion along the chip was corrected by tracing OH sky lines. Spectra were then optimally extracted using a smoothed weighting function.

The extracted spectra were then roughly corrected for "bleeding," an effect inherent to the NIRC instrument in which flux detected in a particular pixel is carried over into every fourth pixel as the instrument reads out[1]. The excess flux F_{excess} at pixel P1 caused by the flux F_{P2} at pixel P2 (a multiple of four pixels away along the horizontal axis of the chip) can be parameterized by (M. Liu, priv. comm.):

$$F_{excess} = 0.002655 \times F_{P2} e^{-\frac{P1-P2}{4 \times 16.353}}. \tag{3.1}$$

Corrections were made after the spectral extraction, i.e., using one-dimensional data, while a more rigorous procedure would have been to make this correction on the raw data frame. However, we have found that this correction typically amounts to no more than 1-3% of the flux value at any particular pixel in our spectral data, so no further iteration on this reduction procedure was done.

The low resolution of the grism data (blending telluric OH lines) and lack of internal emission lamps prevented an empirical determination of the wavelength dispersion; hence wavelength calibration was computed using coefficients listed in the NIRC instrument manual[2]:

$$\lambda(JH) = 1.715 + 0.004912(x - x_{slit}) - 4.45 \times 10^{-7}(x - x_{slit})^2 \tag{3.2}$$

$$\lambda(HK) = 2.118 + 0.005916(x - x_{slit}) - 3.52 \times 10^{-7}(x - x_{slit})^2, \tag{3.3}$$

where x is the pixel column from the left side of the chip, and x_{slit} is the position of the slit, set to column 180. Individual target spectra were ratioed with the standard spectra at each dispersion position for flux calibration, and then multiplied by a blackbody appropriate to the standard star (Tokunaga, 2000). The resulting flux-calibrated data for each grism setting were then median-combined after scaling the individual spectra and rejecting those with excessive noise.

3.1.1.3 Photometric Calibration

Spectra from 1.0–1.6 μm and 1.4–2.5 μm were then combined and flux calibrated. First, we scaled the HK spectra by a multiplicative factor to match the overlap region from 1.4–1.6 μm. Then, using data for Vega (Bergeron, Wesemael, & Beauchamp, 1995) and 2MASS photometry, we calculated flux corrections by integrating the 2MASS filter response curves (see §1.6.2) over calibrator and object spectra, using the relation

$$F_{obj}^{(corr)}(\lambda) = F_{obj}^{(uncorr)}(\lambda) \times 10^{-0.4 m_b} \times \frac{\int F_{Vega}(\lambda') T_b(\lambda') d\lambda'}{\int F_{obj}^{(uncorr)}(\lambda') T_b(\lambda') d\lambda'}, \tag{3.4}$$

where $F_{obj}^{(corr)}(\lambda)$ and $F_{obj}^{(uncorr)}(\lambda)$ are the corrected and uncorrected flux densities of the object spectrum, $F_{Vega}(\lambda)$ is the flux density of Vega, m_b is the magnitude of the object through filter b, and $T_b(\lambda)$ is the filter transmission function. For this calibration, we chose to use b = J-band magnitudes, as T dwarfs tend to be brightest at this band, reducing photometric errors.

To test our flux calibration, we measured spectrophotometric colors for all of the calibrated spectra in the 2MASS near-infrared bands for confirmed L and T dwarfs, and compared these to 2MASS photometric colors. Results are given in Table 3.2. Residuals ($\delta \equiv$ photometry minus spectrophotometry) are typically on the order of 0.1 to 0.3 mag, slightly larger than the 2MASS photometric errors, with some colors discrepant by more than 0.6 mag. Nonetheless, the mean of these residuals,

[1] This feature is noted by Liu, Graham, & Wright (1996), and a brief description of the effect and its correction are given in http://astron.berkeley.edu/~mliu/nirc/bleeding.html.

[2] http://www2.keck.hawaii.edu:3636/realpublic/inst/nirc/manual/Manual.html.

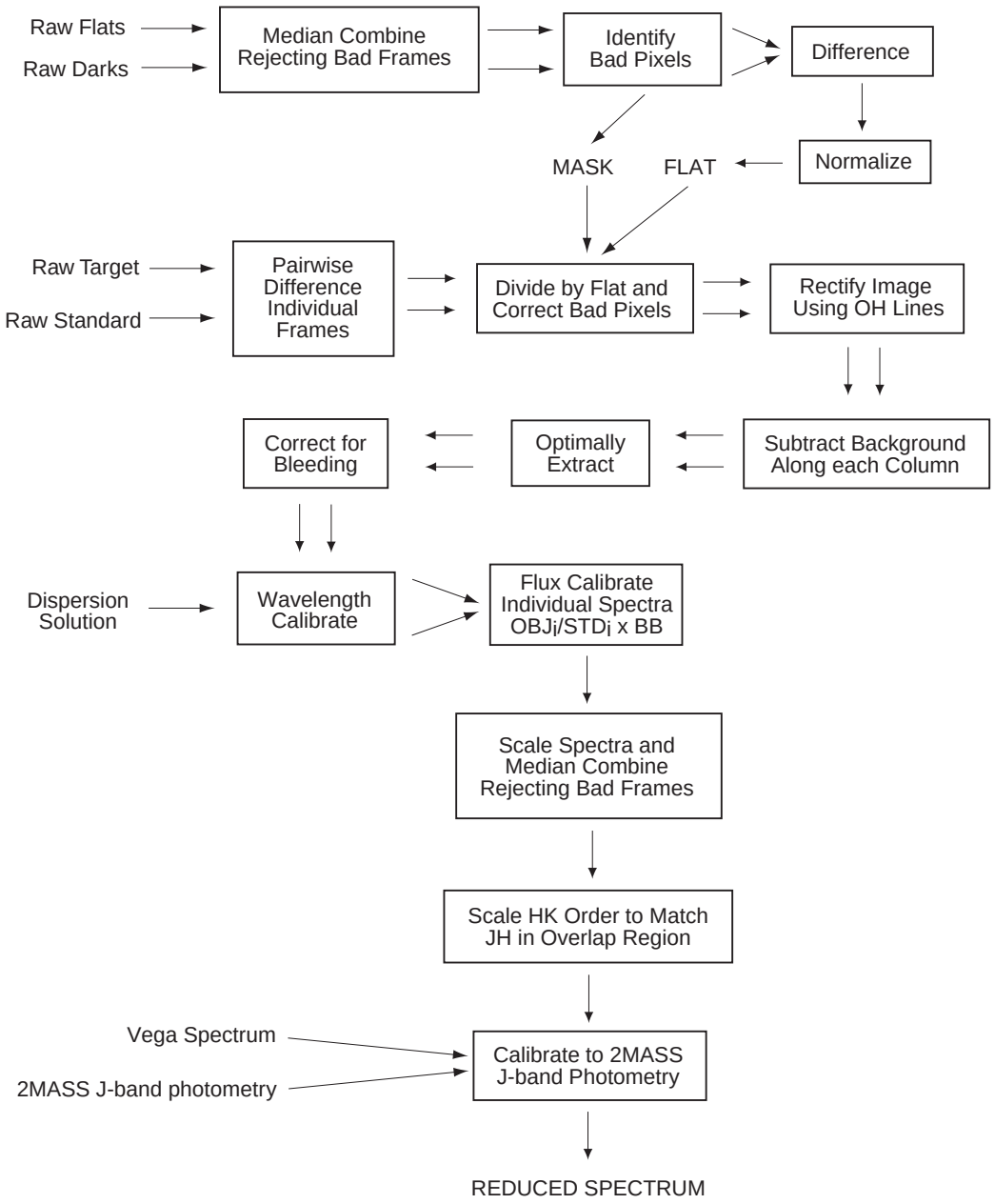

Figure 3.1: A flowchart diagramming the procedures for NIRC spectral data reduction. This algorithm was implemented in the IDL environment.

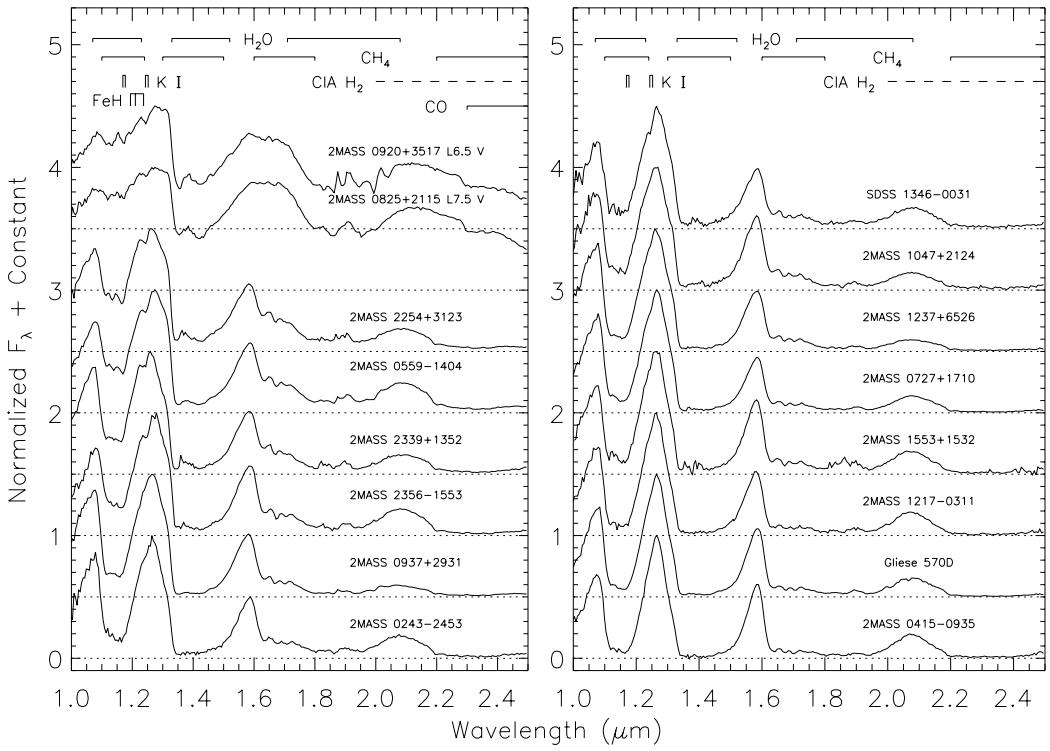

Figure 3.2: 1–2.5 μm spectra of T dwarfs observed using the Keck I NIRC instrument. Spectra are normalized at their J-band peaks, offset by a constant (dotted lines), and ordered by increasing 1.15 and 1.6 μm absorption. Major H_2O, CH_4, CO, and FeH absorption bands are indicated, as are lines of K I (1.169, 1.177, 1.243, and 1.252 μm) and the region of strongest CIA H_2 absorption. The L dwarfs 2MASS 0920+3517 (L6.5 V) and 2MASS 0825+2115 (L7.5 V) are shown for comparison.

$\langle\delta_{J-H}\rangle = -0.18\pm0.19$, $\langle\delta_{H-K_s}\rangle = 0.15\pm0.29$, and $\langle\delta_{J-K_s}\rangle = 0.01\pm0.28$, imply overall consistency in the relative calibration. Significant color differences may be due to the effects of cirrus during our 2000 July 22 observations (affecting data for 2MASS 1553+1532, 2MASS 2254+3123, and 2MASS 2339+1352), or possibly low signal-to-noise photometry (i.e., flux overestimation) of objects barely detected by 2MASS at K_s (e.g., 2MASS 0937+2931). Regardless, the flux calibration appears to be adequate to characterize gross spectral morphology.

3.1.1.4 Results

Final NIRC spectra for confirmed T dwarfs are shown in Figure 3.2, along with data for the L6.5 V 2MASS 0920+3517 and the L7.5 V 2MASS 0825+2115 (Kirkpatrick et al., 2000). Spectra are normalized at their J-band peak, offset (dotted line), and ordered by increasing 1.1 and 1.6 μm absorption. Major absorption bands of H_2O, CH_4, CO, FeH (1.19, 1.21, and 1.237 μm), and CIA H_2 are indicated, as are atomic lines of K I (1.169, 1.177, 1.243, and 1.252 μm). The strong CH_4 absorption bands at 1.6 and 2.2 μm seen in all of the objects (excluding the two late L dwarfs) readily identify them as T dwarfs.

Table 3.2: Comparison of NIRC Spectrophotometric Colors to 2MASS Photometry.

	2MASS J-H			2MASS H-K_s			2MASS J-K_s		
Object	Phot.	Spec.	δ^a	Phot.	Spec.	δ^a	Phot.	Spec.	δ^a
(1)	(2)	(3)	(4)	(5)	(6)	(7)	(8)	(9)	(10)
2MASS 0243−2453	0.25±0.11	0.10	0.15	−0.06±0.20	0.15	−0.21	0.19±0.18	0.25	−0.06
2MASS 0415−0935[b]	0.14±0.13	0.12	0.02	0.12±0.23	−0.04	0.16	0.26±0.21	0.08	0.18
	0.14±0.13	0.12	0.02	0.12±0.23	0.21	−0.09	0.26±0.21	0.33	−0.07
2MASS 0559−1404[c]	0.14±0.05	0.25	−0.11	0.07±0.06	0.18	−0.11	0.21±0.06	0.43	−0.22
	0.14±0.05	0.26	−0.12	0.07±0.06	0.34	−0.27	0.21±0.06	0.60	−0.39
2MASS 0727+1710	−0.27±0.19	−0.15	−0.12	0.26±0.28	0.05	0.21	−0.01±0.22	−0.10	0.09
2MASS 0825+2115	1.33±0.06	0.98	0.35	0.74±0.06	0.77	−0.03	2.07±0.06	1.75	0.32
2MASS 0920+3517	0.93±0.10	0.85	0.08	0.73±0.11	0.68	0.05	1.66±0.11	1.52	0.14
2MASS 0937+2931[c]	−0.03±0.08	0.15	−0.18	−0.86±0.25	−0.30	−0.56	−0.89±0.24	−0.16	−0.73
	−0.03±0.08	0.02	−0.05	−0.86±0.25	−0.49	−0.37	−0.89±0.24	−0.48	−0.41
2MASS 1047+2124[c]	0.03±0.13	0.15	−0.12	< -0.50	−0.22	–	< -0.47	−0.06	–
	0.03±0.13	0.19	−0.16	< -0.50	−0.22	–	< -0.47	−0.02	–
2MASS 1217−0311	0.06±0.14	0.01	0.05	< -0.12	0.23	–	< -0.06	0.24	–
2MASS 1237+6526	0.31±0.18	0.00	0.31	< -0.18	−0.41	–	$<$ 0.13	−0.41	–
SDSS 1346−0031	−0.19±0.22	0.02	−0.21	$<$ 0.30	0.15	–	$<$ 0.11	0.17	–
Gliese 570D	0.05±0.10	0.09	−0.04	0.01±0.19	−0.01	0.02	0.06±0.18	0.07	−0.01
2MASS 1553+1532	−0.11±0.19	0.14	−0.25	0.41±0.25	0.05	0.36	0.30±0.21	0.19	0.11
2MASS 2254+3123	0.24±0.10	0.20	0.04	0.21±0.17	−0.09	0.30	0.45±0.15	0.11	0.34
2MASS 2339+1352	−0.16±0.19	0.12	−0.28	0.34±0.33	−0.08	0.42	0.18±0.29	0.04	0.14
2MASS 2356−1553	0.16±0.12	0.18	−0.02	−0.19±0.21	0.12	−0.31	−0.03±0.20	0.30	−0.33

[a] $\delta \equiv$ photometry minus spectrophotometry.
[b] Separate observations obtained on 1999 November 18 and 2000 January 24 (UT).
[c] Separate observations obtained on 2000 January 23 and 24 (UT).

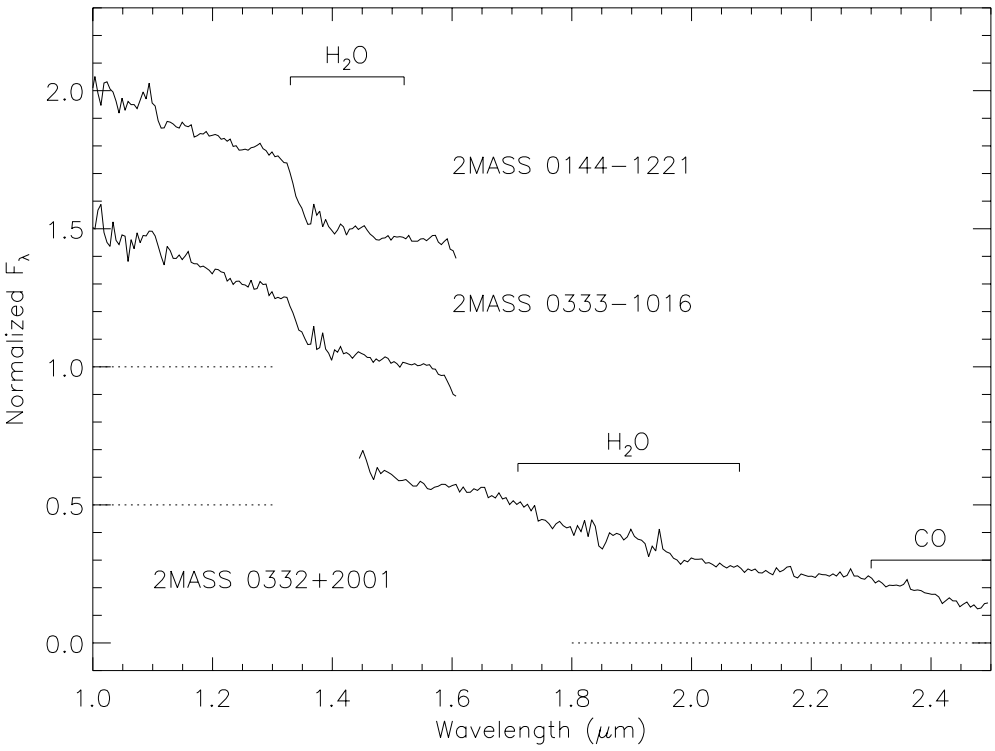

Figure 3.3: 1–2.5 μm spectra of 2MASS 0144-1221, 2MASS 0333-1016, and 2MASS 0332+2001. Spectra are normalized at their individual flux peaks and offset (dotted lines). These objects have weak signatures of H_2O and no CH_4, and are likely background M dwarfs.

In contrast, Figure 3.3 plots spectral data for T dwarf candidates 2MASS 0144-1221, 2MASS 0332+2001, and 2MASS 0333-1016. These objects do not exhibit the telltale CH_4 bands, and the presence of H_2O absorption bands suggests that they are instead background M dwarfs. Indeed, 2MASS 0144-1221 and 2MASS 0333-1016 have a fairly prominent absorption band at 1.33 μm consistent with the $2(\nu_1,\nu_3)$ H_2O band and are likely mid- or late-type M dwarfs. 2MASS 0332+2001 has only a marginal indication of H_2O around 1.8 μm and no obvious CO bandhead, but its spectral slope is consistent with a 3000–4000 K blackbody, and is likely an early- or mid-M dwarf or giant. The near-infrared colors of these objects (J-K_s = 0.42±0.23, 0.41±0.20, and 0.36±0.22) are consistent with early- to mid-type M dwarfs within the estimated uncertainties.

3.1.1.5 3.0–4.6 μm Observations of 2MASS 0559-1404

In addition to the 1.0–2.5 μm spectra obtained for the objects above, we also obtained 3.0–4.6 μm spectra for 2MASS 0559-1404 on 18 November 1999 (UT). Observations are summarized in Table 3.3. Data were acquired using the 60 lines mm^{-1} grating blazed at 4.2 μm and LM order blocking filter. 2MASS 0559-1404 was observed using the 2.5 pixel (0.″375) slit, while the F0 V calibrator star HD 46169 was observed using the 3.5 pixel (0.″525) slit. Because of the high thermal background at these wavelengths, observations were made in rapid chopping mode, with a two position chop

Table 3.3: Log of 3.0–4.6 μm NIRC Observations on 18 November 1999 (UT).

Object (1)	Type (2)	UT Time (3)	Airmass (4)	No. Chops (5)	Total t_{int} (s) (6)
2MASS 0559-1404	T	13:24:05	1.24	1000	360
		13:32:29	1.25	4000	1440
HD 46169	F0 V	14:15:34	1.26	100	36
		14:17:22	1.26	100	36

separated by 16 pixels (2.″4) along the slit, triggered at 5 Hz. Individual integration times of 18 msec (times 10 coadds) at each position permit accurate background subtraction, and the detector was sub-arrayed to 256×32 pixels for faster readout. Cycles of 100 chops were used for the standard star observation, and 1000 to 4000 chops were coadded for the spectra of 2MASS 0559-1404 to boost its signal-to-noise.

Science data were reduced by first differencing the separate nod images, eliminating (to first order) bias and sky background. Flat field frames were not obtained for these observation, but corrections were assumed to be small enough ($\lesssim 10\%$) to be adequately divided out by the standard star. Wavelength calibration was determined by matching spectral features in the standard observation to telluric absorptions (Figure 3.4a); in particular, the deep atmospheric CO_2 and H_2O feature at 4.2 μm, as well as telluric H_2O and CH_4 features in the 3.0–3.5 μm range. Note that the feature from 3.35–3.50 μm in the standard spectrum is due in part to resin found on the grism filter. The short wavelength cutoff of the LM filter at 2.95 μm provided another fixed wavelength point. This comparison resulted in the dispersion solution:

$$\lambda(LM) = 4.20 + 0.01023(x - x_{slit}) \tag{3.5}$$

with $x_{slit} = 210$. Note that these coefficients are not those listed in the NIRC instrument manual. Final spectral calibration was done by ratioing the target and standard spectra and multiplying by a 7020 K blackbody (Tokunaga, 2000).

Reduced data for 2MASS 0559-1404 is shown in Figure 3.4b (thin line), which is compared to the 3.0–4.85 μm spectrum of Gliese 229B (Oppenheimer et al., 1998). Both spectra are normalized at 4.0 μm. CH_4 is clearly the prime source of opacity in this region, as the Gliese 229B spectrum drops to nearly zero flux at the center of the 3.3 μm fundamental band. Note, however, that flux is detected at the base of this band in 2MASS 0559-1404, and is generally less broad than the absorption in Gliese 229B. This is consistent with the interpretation that 2MASS 0559-1404 is a warmer T dwarf (Chapter 6). The 4.7 μm 1-0 $X^1\Sigma^+$-$X^1\Sigma^+$ CO band is also an important feature, detected in the spectrum of Gliese 229B (Noll, Geballe, & Marley, 1997; Oppenheimer et al., 1998). Our spectral range partially samples this band, and the greater suppression of flux between 4.5 and 4.7 μm in 2MASS 0559-1404 is likely due to stronger CO absorption (see §6.3.2)

3.1.2 OSIRIS Observations

The OSIRIS instrument is a near-infrared imager/spectrometer mounted on the f/14.5 Cassegrain focus of the CTIO 4m Blanco Telescope. It is equipped with a 1024×1024 HgCdTe HAWAII array with 18.5 μm pixels, sampling the entire illuminated field. Use of the single diffraction grating blazed at 6.6 μm with the 120 lines mm^{-1} grating and f/2.8 camera provides simultaneous, cross-dispersed, moderate resolution ($\lambda/\Delta\lambda \sim 1200$) spectroscopy from 1.2–2.35 μm in four orders: J (5^{rd} and 6^{th}),

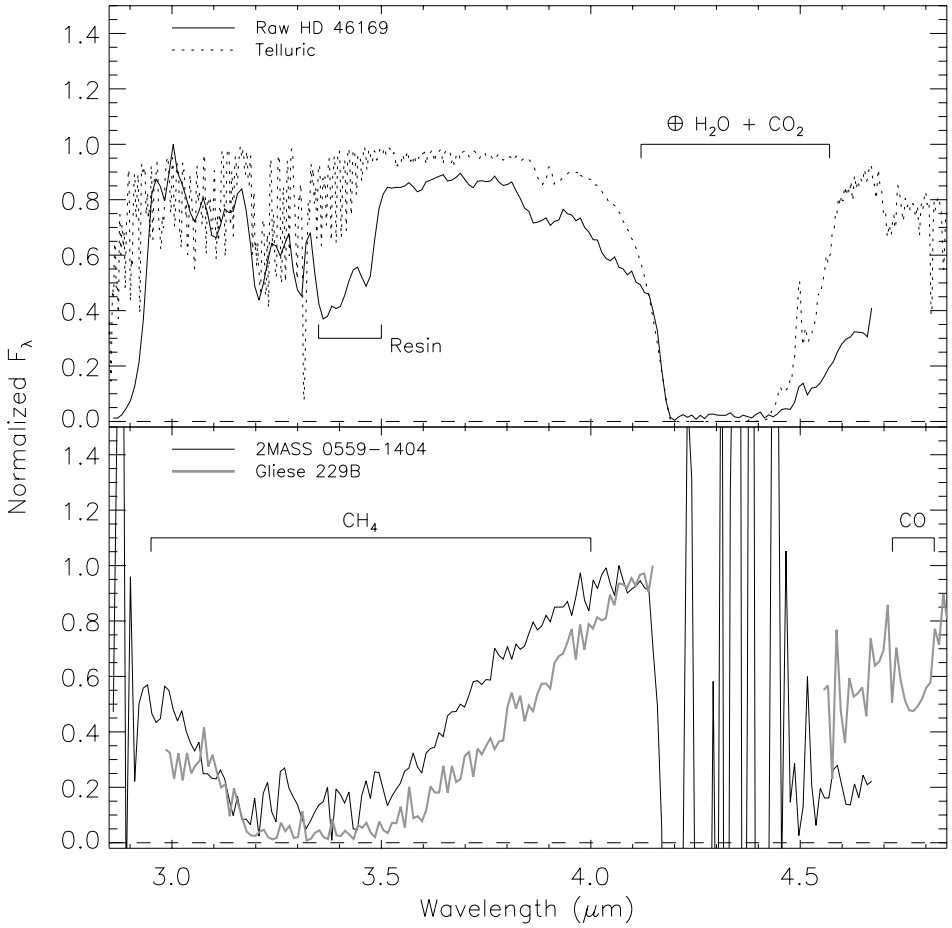

Figure 3.4: 3.0–4.6 μm spectrum of 2MASS 0559-1404. (top panel) Raw extracted spectrum of the F0 V standard HD 46169, showing the alignment of stellar features (solid line) with telluric absorption (dotted line; from the UKIRT homepage). Features of resin from the grism filter are also seen between 3.35 and 3.50 μm. (bottom panel) Final calibrated spectrum of 2MASS 0559-1404 (thin line) compared to that of Gliese 229B (thick gray line). CH_4 and CO bands are indicated.

H (4^{th}), and K (3^{th}). Resolution on the $0\farcs403$ pixel^{-1} chip ranges from 4.4 to 8.8 Å pixel^{-1}.

3.1.2.1 Data Acquisition

Table 3.4 summarizes our OSIRIS observations. Data obtained during 1999 July 26-29 (UT) were taken in weather conditions ranging from light cirrus to obscuring clouds, with seeing around $0\farcs8$-$1\farcs0$, except on July 29 when windy conditions led to the $\sim 2''$ seeing; data obtained during 1999 December 20-22 (UT) were taken in clear to hazy conditions, with seeing ranging from $0\farcs6$ to $1\farcs0$; finally, observations made in 2000 July 15-19 (UT) were taken in conditions ranging from clear to cloudy, and seeing ranged from $0\farcs6$ to $1\farcs8$. Note that many of the confirmed T dwarfs from our 1999 July 26-29 (UT) run were reobserved at later dates to higher signal-to-noise, and the early data are generally not included in subsequent discussion.

A total of 28 T dwarf candidates were observed using OSIRIS, along with a number of M and L dwarfs for comparison. Targets were acquired in imaging mode and placed into a $1\farcs2 \times 30''$ slit. Observations were made in sets of 5–7 exposures dithered 4–5″ along the slit, with individual integrations ranging from 15 to 250 sec per exposure. A-type SAO standards, chosen for their lack of metal lines at moderate resolution, were observed near the target objects for flux calibration and telluric corrections. Spectral lamps reflected off of the 4m dome spot were observed each night for pixel response calibration.

3.1.2.2 Data Reduction

Data reduction procedures are summarized schematically in Figure 3.5. Science images were initially trimmed to eliminate vignetted columns, divided by a median-combined, dark-subtracted flat field, and corrected for bad pixels by interpolation, using a mask created from flat-field and dark exposures. Images were then pairwise subtracted to eliminate sky background and dark current. Curvature of the dispersion lines was determined by tracing the spectra of the standard stars, and this trace was used as a template for the target spectra. Both standard and object spectra were optimally extracted using a smoothed weighting function, after subtracting off the median background along each row. Individual spectra from each order were then scaled by a multiplicative factor and combined by averaging, rejecting 3σ outliers in each spectral bin.

Wavelength calibration was done using OH line identifications from Olivia & Origlia (1992), yielding dispersions for our 2000 July observations:

$$\lambda(6^{th}) = 1.353 - 0.0004417y - 4.852\times10^{-9}y^2 \tag{3.6}$$

$$\lambda(5^{th}) = 1.624 - 0.0005381y + 2.532\times10^{-9}y^2 \tag{3.7}$$

$$\lambda(4^{th}) = 2.040 - 0.0007039y + 2.138\times10^{-8}y^2 \tag{3.8}$$

$$\lambda(3^{rd}) = 2.700 - 0.0008849y - 7.668\times10^{-9}y^2, \tag{3.9}$$

where y is the pixel row measured from the bottom of the chip. A telluric correction was computed for each target/standard pair by interpolating over H_2O absorption features in the standard star spectra and ratioing this with the uncorrected standard spectra. A smoothed flux correction was then calculated by interpolating over hydrogen Paschen and Brackett lines in the telluric-corrected standard spectra and multiplying by the appropriate blackbody. Finally, the resulting flux-calibrated spectral orders were combined by first scaling each order to match overlap regions (typically 1.29–1.31, 1.53–1.57, and 1.96–1.98 μm), and then correcting the combined spectra to 2MASS H-band magnitudes (not J, due to the short wavelength cutoff) using Equation 3.4. Note that the overlap

Table 3.4: Log of OSIRIS Observations.

Object (1)	Type (2)	UT Date (3)	t_{int} (s) (4)	Airmass (5)	Calibrator (6)	Cal. Type[a] (7)
2MASS 0036+1821[b]	L3.5 V	1999 Jul 29	1400	1.53–1.56	HD 5641	A2 V
2MASS 0058−0651[b]	L0 V	1999 Jul 28	2100	1.10–1.15	HD 6530	A1 V
2MASS 0101−3317	other	1999 Dec 22	600	1.09	HD 6619	A1 V
2MASS 0122−7635	other	2000 Jul 19	2500	1.46–1.47	HD 8783	Ap
DENIS J0205−1159AB[b]	L7 V	2000 Jul 19	1250	1.07	HD 13406	A3 Vm
DENIS J0225−4700[b]	L8 V	1999 Jul 29	1120	1.05	HD 17864	A0 V
2MASS 0243−2453	T	1999 Dec 20	3600	1.04–1.15	HD 17168	A1 V
		1999 Dec 21	4200	1.01–1.09	HD 17168	A1 V
2MASS 0302−1028	other	1999 Dec 22	600	1.07	HD 22243	A2 V
2MASS 0333−1016	other	1999 Dec 22	600	1.07	HD 22243	A2 V
GJ 1062[b]	M2 V	1999 Dec 22	600	1.10	HD 22243	A2 V
		1999 Dec 24	1200	1.07–1.08	HD 22243	A2 V
2MASS 0508−2253	other	1999 Dec 21	600	1.13	HD 36187	A1 V
2MASS 0530−2314	other	1999 Dec 21	600	1.02	HD 36187	A1 V
2MASS 0546−0845	other	1999 Dec 21	600	1.09	HD 36187	A1 V
2MASS 0559−1404	T	1999 Dec 20	2400	1.05–1.09	HD 40972	A0 V
2MASS 0636−3027	other	1999 Dec 21	600	1.02	HD 36187	A1 V
2MASS 0727+1710	T	1999 Dec 20	3600	1.52–1.72	HD 60275	A1 V
2MASS 0937+2931	T	1999 Dec 21	3000	1.98–2.00	HD 79248	A2 V
2MASS 1225−2739	T	2000 Jul 18	2500	1.16–1.24	HD 109142	A3 Vm
SDSS 1254-0122	T	2000 Jul 16	4500	1.21–1.54	HD 112846	A3 V
2MASS 1321−0546	other	2000 Jul 19	2500	1.20–1.27	HD 116831	A7 III
Gliese 570D	T	1999 Jul 27	5880	1.05–1.37	HD 136334	A1 V
		2000 Jul 16	4500	1.09–1.30	HD 131992	A2/3 V
SDSS 1624+0029	T	1999 Jul 27	1680	1.56–1.68	HD 145788	A1 V
		2000 Jul 15	3450	1.49–2.07	HD 148207	A0 V
2MASS 1507−1627[b]	L5 V	1999 Jul 28	1200	1.03–1.04	HD 132230	A1 V
2MASS 1534−2952	T	1999 Jul 28	6300	1.02–1.29	HD 137015	A2 V
		2000 Jul 18	2500	1.19–1.28	HD 139202	A1 Vm
2MASS 1546−3325	T	1999 Jul 29	5880	1.00–1.19	HD 137015	A2 V
		2000 Jul 19	3750	1.04–1.13	HD 140442	A1 V
2MASS 1553+1532	T	2000 Jul 17	3750	1.43–1.53	HD 143936	A0 V
		2000 Jul 18	2500	1.46–1.51	HD 143936	A0 V
2MASS 1924−2239	other	2000 Jul 17	2500	1.03–1.06	HD 183091	A2 IV/V
2MASS 1937−1539	other	2000 Jul 16	2500	1.06–1.10	HD 185533	A0 V
2MASS 1940−1410	other	1999 Jul 29	840	1.04	HD 182678	A0 V
2MASS 1945−2149	other	1999 Jul 28	980	1.01–1.02	HD 175892	A1 V
		1999 Jul 29	840	1.01	HD 182678	A0 V
HB 2115−4518[b]	M8.5 V	2000 Jul 19	750	1.04	HD 203725	A0 III
2MASS 2118-2742	other	1999 Jul 27	840	1.01	HD 207155	A2 V
HB 2124−4268[b]	M7.5 V	2000 Jul 19	750	1.02	HD 203725	A0 III
LHS 511AB[b]	M4.5 V	2000 Jul 19	75	1.08	HD 205178	A0 V
2MASS 2206−4217[b]	L2 V	1999 Jul 28	3500	1.02–1.05	HD 210739	A3 V
		1999 Jul 29	3360	1.02–1.04	HD 210739	A3 V

Table 3.4: OSIRIS Observations, Cont.

Object (1)	Type (2)	UT Date (3)	Int. (s) (4)	Airmass (5)	Calibrator (6)	Cal. Type[a] (7)
2MASS 2224−0158[b]	L4.5 V	1999 Jul 28	1680	1.17–1.23	HD 217186	A1 V
		1999 Jul 29	2520	1.16–1.21	HD 217186	A1 V
		2000 Jul 19	1250	1.15	HD 212417	A3 V
2MASS 2254+3123	T	2000 Jul 16	3750	2.10–2.20	HD 216716	A0 V
2MASS 2339+1352	T	2000 Jul 16	2500	1.44–1.51	HD 222250	A3 V
2MASS 2356−1553	T	1999 Jul 26	6720	1.03–1.17	HD 223466	A3 V
		1999 Jul 27	3360	1.08–1.18	HD 223466	A3 V
		1999 Dec 20	1800	1.27–1.37	HD 4065	A0 V
		2000 Jul 17	5000	1.04–1.15	HD 223785	A1 V

[a]Spectral types obtained from the SIMBAD database.
[b]Previously identified M and L dwarfs observed for spectral comparison.

between the H- and K-band orders falls within the 1.9 μm H_2O band; because of this, we applied the same scaling corrections to both orders.

3.1.2.3 Results

Resulting spectra for confirmed T dwarfs are shown in Figures 3.6 and 3.7, along with OSIRIS data obtained for the M4.5 V LHS 511AB (Luyten, 1979), M8.5 V HB 2124-4228 (Hawkins & Bessell, 1988), L4.5 V 2MASS 2224-0158 (Kirkpatrick et al., 2000), and L7 V DENIS 0205-1159AB (Delfosse et al., 1997). Spectra are normalized, offset, and ordered as in Figure 3.2. Bands of H_2O, CH_4, CO, FeH, and CIA H_2 are indicated, as are lines of K I (1.25 and 1.52 μm doublets), Na I (2.21 μm doublet), and Ca I (1.314, 1.98, and 2.26 μm triplets). The 1.52 μm K I doublet and Ca I lines, prominent in M dwarfs (Jones et al., 1994) are only detectable in the M4.5 V LHS 511AB. Regions of increased noise are due to telluric H_2O opacity; note, however, that higher-energy H_2O transitions originating from the target objects extend well into the J, H, and K telluric windows.

The remaining objects listed in Table 3.4 did not show the characteristic CH_4 bands expected for T dwarfs. Examination of second-epoch optical plates reveal very faint optical counterparts for some of the objects, consistent with a faint background M stars that have colors scattered into our selection criteria. In general, the low signal-to-noise spectra obtained for these objects were not adequate for spectral typing, but clearly ruled them out as T dwarfs.

3.1.3 D78 Observations

Additional low-resolution observations were made on 2001 January 4-5 (UT) using the D78 near-infrared camera, mounted at the f/70 Cassegrain focus of the Palomar 5m Hale Telescope. This instrument is similar in construction to NIRC, providing grism spectroscopy from 1–2.5 μm in three orders (3^{rd}, 4^{th}, and 5^{th}) with $\lambda/\Delta\lambda \sim 100$. Resolution on the $0.125''$ pixel^{-1} chip ranges from 23 to 37 Å pixel^{-1}.

3.1.3.1 Data Acquisition

A log for the D78 observations is given in Table 3.5. Weather was generally clear on 2001 January 4 with good seeing ($0\farcs7$); however, conditions on 2001 January 5 were poor, with clouds frequently obscuring observations. Candidate objects were acquired in imaging mode and placed into a $0\farcs71$ slit.

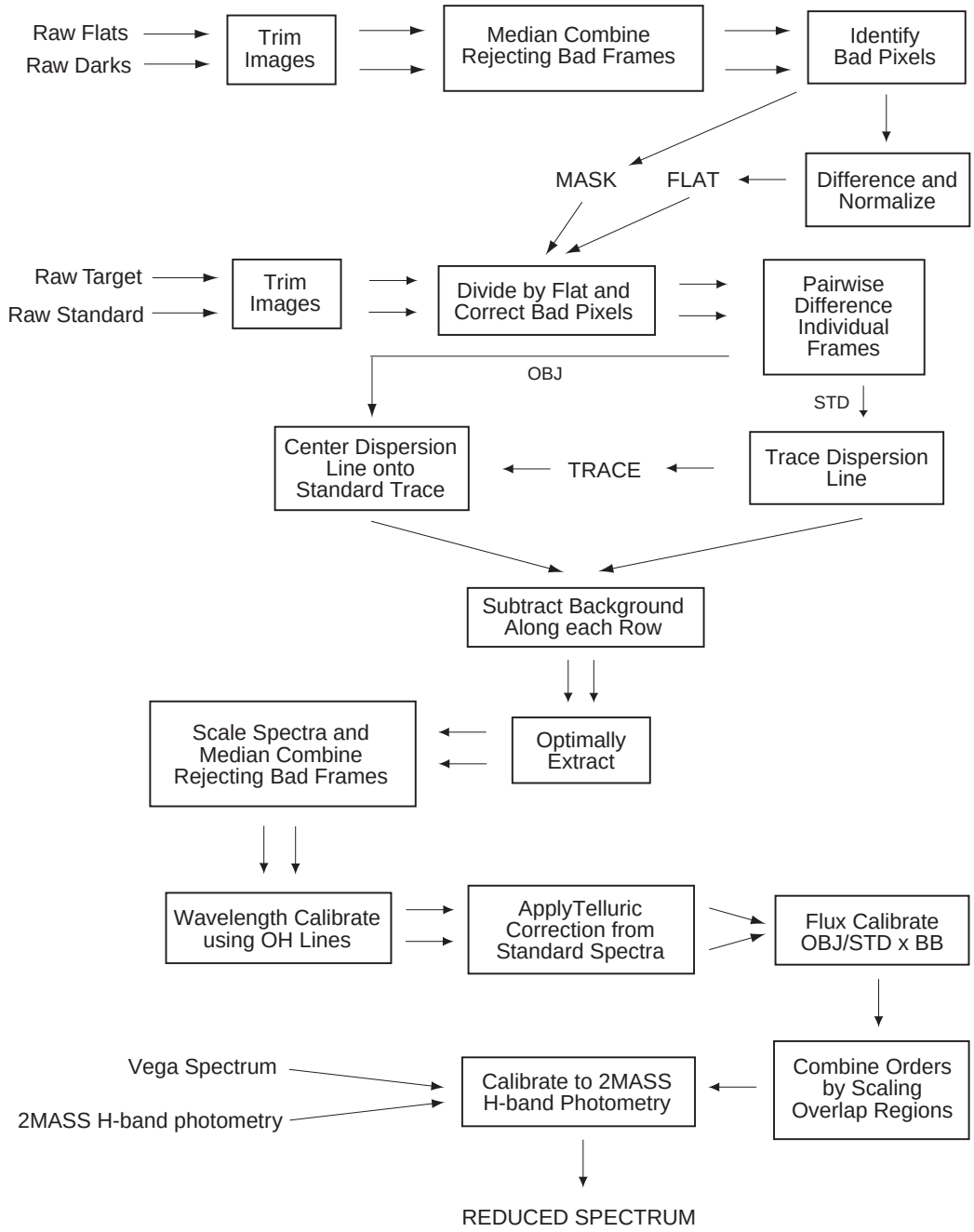

Figure 3.5: A flowchart diagramming the procedures for OSIRIS spectral data reduction. This algorithm was implemented in the IDL environment.

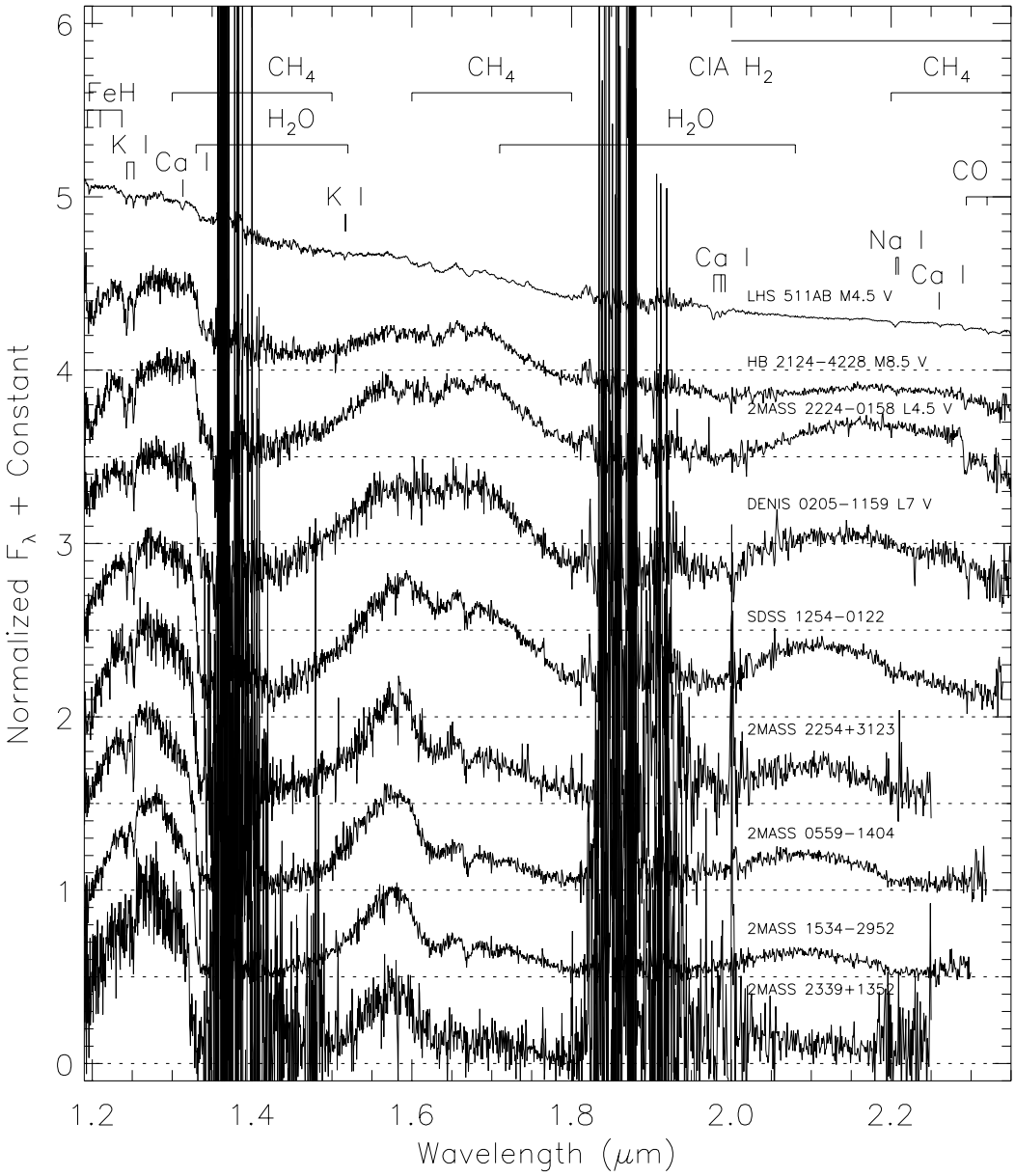

Figure 3.6: 1–2.3 μm spectra of objects observed using the CTIO 4m OSIRIS instrument. Data are normalized at 1.27 μm, offset by a constant (dotted lines), and sorted as in Figure 3.2. Bands of H_2O, CH_4, CO, FeH, and CIA H_2 are indicated, as are lines of K I (1.25 μm doublet) and Na I (2.2 μm doublet). Ca I (1.314, 2.26, and 1.98 μm triplets) and the 1.52 μm K I doublet present in the spectrum of the M4.5 V LHS 511AB are also noted. Noisy regions around 1.4 and 1.9 μm are due to telluric H_2O absorption.

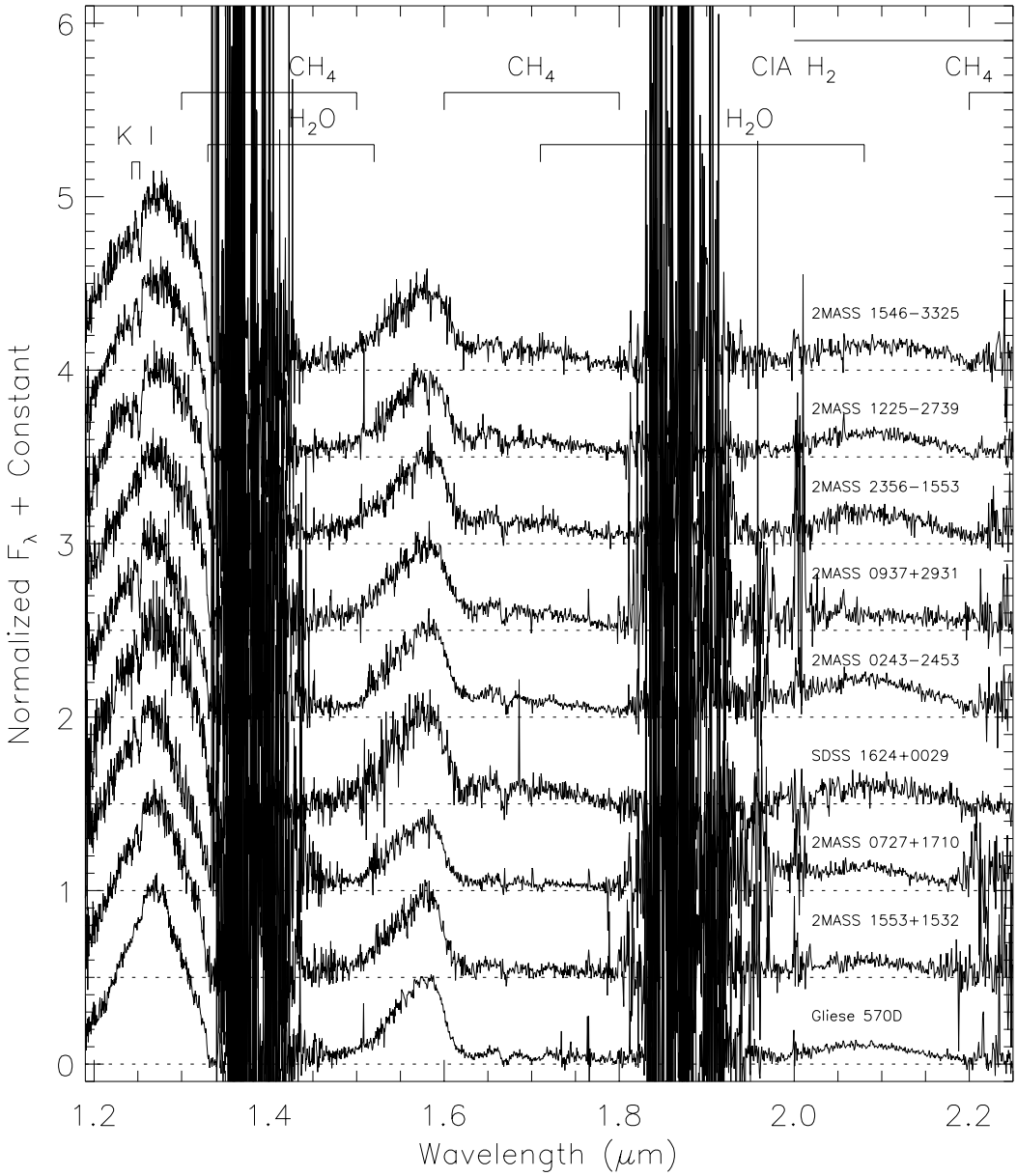

Figure 3.7: Continuation of Figure 3.6.

Table 3.5: Log of D78 Observations.

Object (1)	Type (2)	UT Date (3)	t_{int} (s) (4)	$\lambda\lambda$ (μm) (5)	Airmass (6)	Calibrator (7)	Type (8)
2MASS 0055−1127	F-K/WD[a]	2001 Jan 5	900	1.2–1.9	1.47–1.51	HD 25069	G9 V
2MASS 0356−0228	M	2001 Jan 4	900	1.2–1.9	1.35–1.40	HD 25069	G9 V
2MASS 0510−1838	M	2001 Jan 5	900	1.2–1.5	1.02–1.06	HD 25069	G9 V
2MASS 0738+2405	M	2001 Jan 5	900	1.4–1.9	1.11–1.15	HD 25069	G9 V
2MASS 0755+2212	T	2001 Jan 5	1500	1.2–1.9	1.02–1.06	HD 25069	G9 V
		2001 Jan 5	750	1.9–2.3	1.02–1.06	HD 67767	G7 V
2MASS 1026+2012	M	2001 Jan 5	750	1.4–1.9	1.02–1.03	HD 25069	G9 V
		2001 Jan 5	750	1.9–2.5	1.02–1.03	HD 101501	G8 V
2MASS 1111+2107	late M	2001 Jan 5	750	1.4–1.9	1.02–1.03	HD 25069	G9 V
		2001 Jan 5	750	1.9–2.5	1.02–1.03	HD 101501	G8 V
2MASS 1154+7914	A/WD[a]	2001 Jan 5	750	1.4–1.9	1.42–1.44	HD 25069	G9 V
		2001 Jan 5	500	1.9–2.5	1.42–1.44	HD 101501	G8 V

[a]Proper motion star identified from DSS and 2MASS images.

Three exposures dithered 10″ were obtained at each setting. Pixel response and flux calibrations at J- and H-bands were simultaneously made using observations of the G9 V standard HD 25069 taken on January 4; the calibrator spectrum was smeared along the slit by driving the tip-tilt secondary with a 20 Hz, 40″ (peak-to-peak amplitude) triangle wave. Corresponding sky frames were also obtained. Observations made at K-band were calibrated using data for the G7 V HD 67767 (= ψ Cnc) and the G8 V HD 101501, both obtained on January 5.

3.1.3.2 Data Reduction

Data reduction procedures are roughly similar to those used for the NIRC spectra (Figure 3.1). Science images at the J- and H-band grism settings were initially divided by the sky-subtracted and normalized observations of HD 25069, and then pairwise differenced to remove dark current and sky background. K-band standard observations (STD) were made without a corresponding sky exposure, so a calibrator frame (CAL) for these data was constructed by median combining the target observations (TARG) and using a 1 sec dark frame (DARK) obtained on January 4:

$$CAL = STD - DARK - \frac{t_{std}}{N t_{targ}} \sum_{i=1}^{N} TARG_i; \tag{3.10}$$

here, t_{std} and t_{targ} are the integration times for the standard and N target observations, respectively. K-band science images were then pairwise differenced after dividing by the normalized CAL frame. Note that while this procedure provides only a rough calibration at best, the quality of the observing conditions did not require further iteration. The resulting images were shifted and coadded to boost signal-to-noise, after correcting for dispersion curvature along the slit. Spectra were then extracted from the combined images.

Wavelength calibration was done using the dispersion solutions (K. Matthews, priv. comm.):

$$\lambda(J) = 1.178 + 0.00232\times(x - x_0) \tag{3.11}$$

$$\lambda(H) = 1.458 + 0.00288\times(x - x_0) \tag{3.12}$$

$$\lambda(K) = 1.925 + 0.00371\times(x - x_0), \tag{3.13}$$

where x is the pixel column measured from the left side of the chip, and $x_0 = 43.3$ is the offset column, determined from observations of the 1.2818 Paβ emission line in NGC 2392 (Rudy et al., 1992) obtained on January 5. Finally, spectral orders were multiplied by the appropriate blackbody and combined. No attempt was made to scale the individual orders or compute flux corrections, nor could rigorous telluric corrections be made (other than those incurred by dividing out the calibrator star) due to the variable weather.

3.1.3.3 Results

Spectra for all of the observed targets are shown in Figure 3.8; the poor observing conditions are evident in the significant amount of noise present in the data. Strong H_2O and CH_4 bands (outside of the telluric features) are noticeably absent in all of the targets except 2MASS 0755+2212, ruling them out as T dwarfs; weak H_2O absorption may be present in the J- and H-band wings of some of the spectra, however. We narrowed down the identification of these objects by re-examining optical and near-infrared images, shown in Figures 3.9 and 3.10. 2MASS 0356-0259, 2MASS 0510-1838, 2MASS 0738+2405, 2MASS 1036+2012, and 2MASS 1111+2107 all have faint R-band detections in second epoch plates[3] (SERC R and POSS-II). Assuming detection thresholds of roughly 21 mags at R (Reid et al., 1991), these objects have R-J $\sim$ 5, and are thus M dwarfs. 2MASS 1111+2017 also shows CO absorption, so it is probably a later-type M dwarf. 2MASS 0055-1127 and 2MASS 1154+7914, on the other hand, are earlier-type proper motion stars. The former is most likely the near-infrared counterpart to U0750_00221931 from the USNO-A2.0 catalog (Monet et al., 1998), and its optical brightness (R = 15.0) implies R-J = 0.5, making it a late-type (F-K) main sequence star or a cool white dwarf. The latter is likely U1650_01554300 with R-J = 0; i.e., an A-star or (more likely) a 10,000 K white dwarf.

Figure 3.11 shows the reduced spectrum of the only identified T dwarf in these observations, 2MASS 0755+2212. H_2O absorption is quite prominent at 1.2, 1.35, and 1.9 μm, and CH_4 bandheads at 1.6 and 2.2 μm can be readily identified. 2MASS 0755+2212 was originally selected as a 2MASS T candidate in the Preliminary samples (see §2.3.1), but was initially rejected from the candidate list due to the presence of a faint and extended optical counterpart seen in I-band images obtained using the Keck 10m Low Resolution Imaging Spectrograph (Oke et al., 1995, hereafter, LRIS) on 1999 March 3 (UT). Based on subsequent spectroscopic observations obtained with LRIS on 2001 February 20 (UT), it appears that this counterpart is in fact a background galaxy at z=0.18 coincident with the T dwarf (see §3.2.1).

3.1.4 CorMASS Observations

Additional observations of T dwarf candidates were made by J. Wilson using the Cornell-Massachusetts Slit Spectrograph (Wilson et al., 2001a, hereafter CorMASS). Acquisition and reduction procedures for CorMASS data are described in §6.2.2. Table 3.6 lists the objects observed over 4 nights during 1999 October 25–26 and 2000 May 12–13 (UT). Only one of these objects was identified as a T dwarf, 2MASS 0559-1404; its spectrum is discussed in §6.2.2. The remaining objects appear to be background stars, exemplified by the r-J = 5.37±0.11 color of 2MASS 1626+3925 (§2.5.2). One object, 2MASS 0211+3955, was identified as the proper-motion DA white dwarf LHS 151.

[3]Generally only single epoch (e.g., POSS-I) or blue plates were available during the initial candidate selection; see §2.4.2.1.

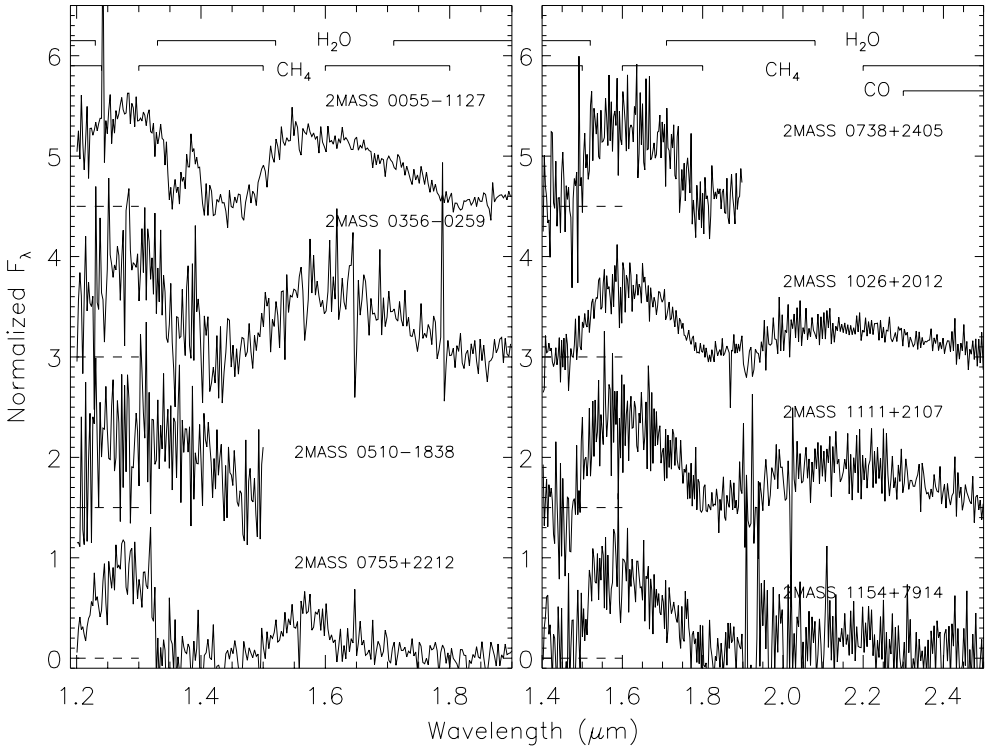

Figure 3.8: Near-infrared spectra of objects obtained using the Palomar Hale 5m D78 near-infrared camera. Spectra have been normalized and offset (dashed lines) for clarity. Major absorption bands of H_2O, CH_4, and CO found in M, L, and T dwarfs are indicated. Note the change in wavelength range between the left and right panels.

Table 3.6: Log of CorMASS Observations.

Object (1)	Type (2)	UT Date (3)	t_{int} (s) (4)	Airmass (5)	Calibrator (6)	Type (7)
2MASS 0211+3955	WD[a]	1999 Oct 25	1200	1.03	HD 18881	A0
2MASS 0436+1547	other	1999 Oct 26	1800	1.05	HD 77281	A2
2MASS 0532+8246	other	1999 Oct 26	1200	1.56	HD 44612	A0
2MASS 0559-1404	T	1999 Oct 25	1800	1.48	HD 77281	A2
		1999 Oct 26	1200	1.48	HD 77281	A2
2MASS 1416+1902	other	2000 May 13	2000	1.04	HD 124625	G
2MASS 1626+3925	other	2000 May 12	5600	1.11	HD 148491	G0

[a]Also known as LHS 151.

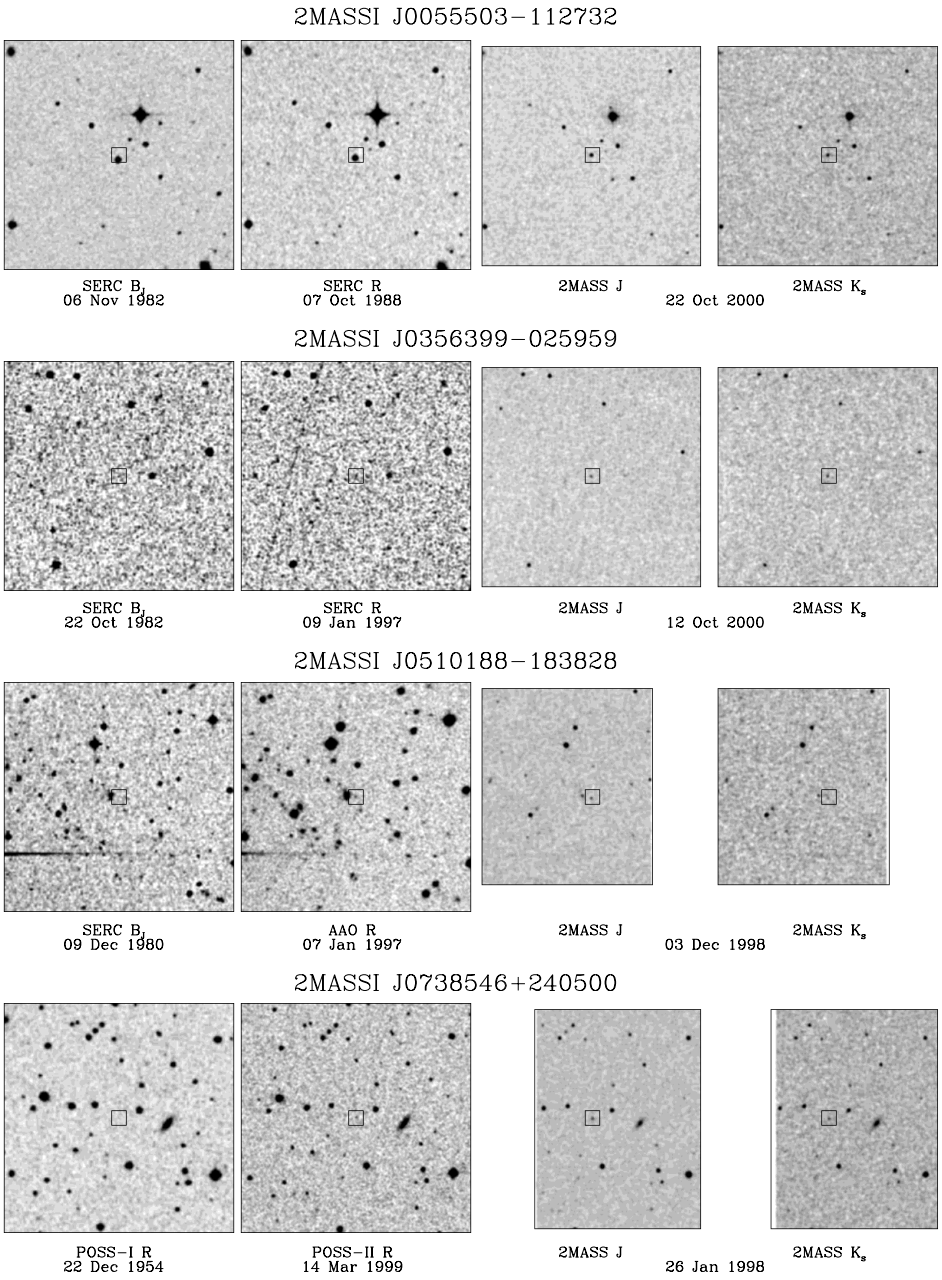

Figure 3.9: DSS (POSS-I R, SERC B_J), XDSS (POSS-II R, SERC R, AAO R), 2MASS J, and 2MASS K_s images of objects observed by D78. Fields are nominally $5'\times5'$ with North up and East toward the left. A $10''\times10''$ box around each target position is shown.

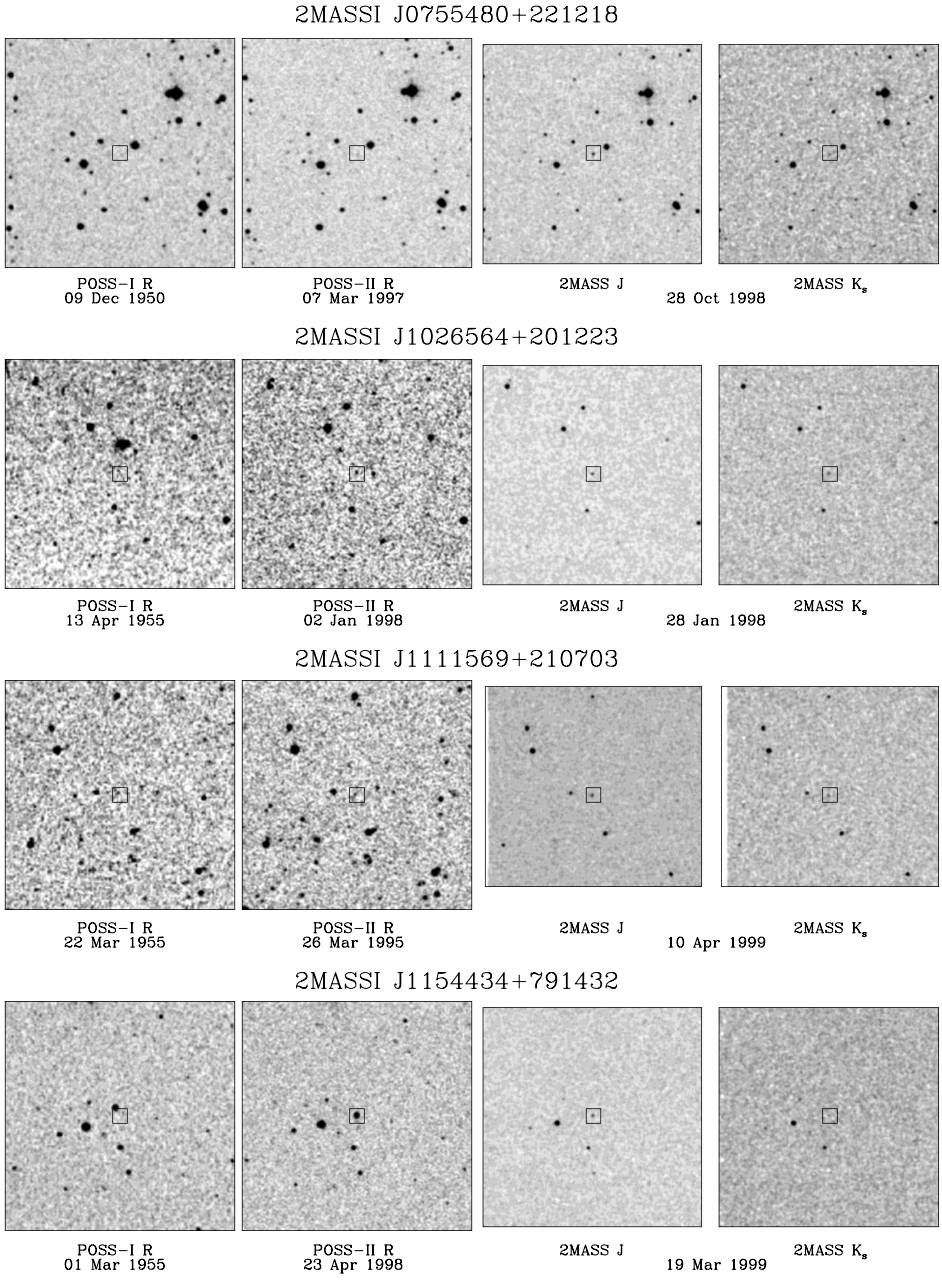

Figure 3.10: Cont.

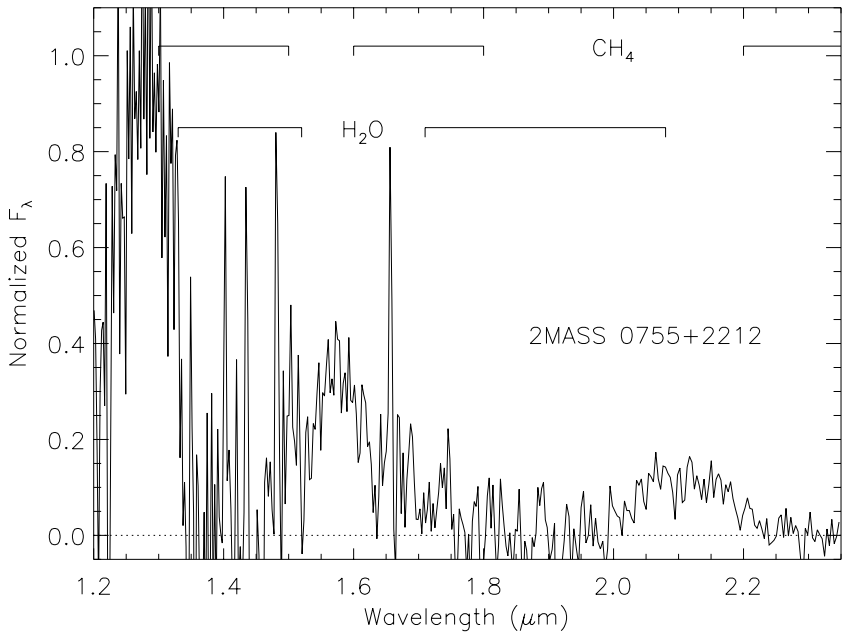

Figure 3.11: D78 1.2–2.3 μm spectrum of 2MASS 0755+2212. Data are normalized at 1.27 μm. Identifying H_2O and CH_4 absorption bands are indicated.

Table 3.7: 0.9–2.5 μm Features in T Dwarfs.

Feature (1)	λ (μm) (2)	Transition[a] (3)	Ref. (4)
K I	0.7665[b]	4s $^2S_{1/2}$ − 4p $^2P_{3/2,1/2}$	1,2,3
K I	0.7699[b]	4s $^2S_{1/2}$ − 4p $^2P_{3/2,1/2}$	1,2,3
H_2O	0.925–0.940	3(ν_1,ν_3)	4
H_2O	0.945–0.980	2(ν_1,ν_3) + 2ν_2	4
CH_4[c]	0.960–0.102	3(ν_1,ν_3) + 1(ν_2,ν_4)	5
FeH	0.9896 bandhead	0-0 band of $A^4\Delta$-$X^4\Delta$	6
H_2O	1.07–1.11	3(ν_1,ν_3) - ν_2	4
CH_4	1.10–1.24	3(ν_1,ν_3)	7,8
H_2O	1.11–1.16	2(ν_1,ν_3) + ν_2	4
H_2O	1.16–1.23	1(ν_1,ν_3) + 3ν_2	4
K I	1.1690	4p $^2P_0$ − 3d ^2D	1
K I	1.1773	4p $^2P_0$ − 3d ^2D	1
H_2[c]	centered at 1.20	2-0 Quadrupole (CIA)	9
K I	1.2432	4p $^2P_0$ − 5s ^2S	1
K I	1.2522	4p $^2P_0$ − 5s ^2S	1
CH_4	1.30–1.50	2(ν_1,ν_3) + 1(ν_2,ν_4)	7,8
H_2O	1.33–1.43	2(ν_1,ν_3)	4
H_2O	1.43–1.52	1(ν_1,ν_3) + 2ν_2	4
CH_4	1.60–1.80	2(ν_1,ν_3)	7,8
H_2O	1.71–1.80	2(ν_1,ν_3) - ν_2	4
H_2O	1.80–2.08	1(ν_1,ν_3) + ν_2	4
CH_4	2.20–2.60	1(ν_1,ν_3) + 1(ν_2,ν_4)	7,8
CO	2.294 bandhead	2-0 $X^1\Sigma^+$-$X^1\Sigma^+$	10
CO[c]	2.323 bandhead	3-1 $X^1\Sigma^+$-$X^1\Sigma^+$	10
H_2	centered at 2.35	1-0 Quadrupole (CIA)	9

[a]Nomenclature for H_2O and CH_4 bands are X(ν_i,ν_j), where bands are formed from the set of X ν_i and ν_j transitions. For example, 2(ν_1,ν_3) covers the transitions $\Delta\nu = 2\nu_1$, $\nu_1+\nu_3$, and $2\nu_3$.
[b]Pressure-broadened out to 1 μm (Burrows, Marley, & Sharp, 2000).
[c]Not yet detected but suspected to exist.
Refs – (1) Wiese, Smith, & Glennon (1966); (2) Tsuji, Ohnaka, & Aoki (1999); (3) Burrows, Marley, & Sharp (2000); (4) Auman (1967); (5) Dick & Fink (1977); (6) Phillips et al. (1987); (7) Danielson (1966); (8) Fink & Larson (1979); (9) Lenzuni, Chernoff, & Salpeter (1991); (10) Krotov, Wang, & Scoville (1980).

3.1.5 Near-infrared Spectral Features

3.1.5.1 Band Features

Table 3.7 summarizes the spectral features present in T dwarf near-infrared spectra. Figures 3.2, 3.6, and 3.7 show that H_2O and ultimately CH_4 absorption are the dominant features shaping the spectra of objects cooler than late M dwarfs. The H_2O bands centered at 1.15, 1.4, and 1.9 μm segregate the spectral energy distributions into distinct z-, J-, H-, and K-band peaks as early as L6.5 V, while the addition of CH_4 bands beginning at 1.05, 1.3, 1.6, and 2.2 μm further confine the emitted flux into narrow peaks centered at 1.08, 1.27, 1.59, and 2.07 μm. Note that CH_4 is necessary to produce the strong absorption at 1.15 μm, a feature also seen in the spectra of giant planets and in laboratory data (Fink & Larson, 1979). In addition, the gradually developing slope between the 1.27 μm peak and the 1.4 μm H_2O band is also caused by CH_4 at 1.3 μm.

In addition to H_2O and CH_4 absorptions, the K-band spectral region is shaped by 2.3 μm CO in M and L dwarfs, a feature that has been detected in the early T dwarfs as well (Leggett et al., 2000b). The distinct bandheads seen in LHS 511AB strengthen through L4.5 V, but appear to weaken beyond this, as they are barely detectable in our spectrum of SDSS 1254-0122. None of

the 2MASS T dwarfs show CO absorption. The other important molecular absorber at K-band is CIA H_2, which has no distinct bandhead but likely suppresses flux throughout the 2–2.5 μm region[4] starting in the latest L dwarfs (see §7). With the presence of H_2O, CH_4, CO, and CIA H_2 absorption features, the K-band peak undergoes a substantial evolution. Starting from a flat slope with CO bandheads in mid-M dwarfs, the K-band becomes a plateau girded by CO and H_2O absorptions in the L dwarfs; it then develops from a double plateau with the dual presence of CH_4 and CO in the early T dwarf SDSS 1254-0122, to an increasingly suppressed and rounded hump centered at 2.11 μm in the earliest 2MASS T dwarfs; finally, we see a smooth triangular peak centered at 2.07 μm in the latest T dwarfs (those exhibiting the strongest CH_4 and H_2O absorption).

3.1.5.2 Atomic Lines

Finer features of FeH and K I have been identified in the J-band spectra of M and L dwarfs by McLean et al. (2000), and these features are also indicated in Figures 3.2, 3.6, and 3.7. The resolution of the NIRC data is generally insufficient to resolve these lines, although the 1.25 μm K I doublet can be seen as a notch in the blue wing of the J-band peak of the T dwarf spectra. OSIRIS data can resolve this doublet, however. Figure 3.12 shows a close-up of the 1.19–1.34 μm spectral region for the OSIRIS data; spectra are normalized and offset as in Figures 3.6 and 3.7. In general, the K I lines are present as early as M4.5 V, and appear to remain strong from the latest M dwarfs through most of the T dwarfs, but are weak in Gliese 570D. This behavior is mimicked in the evolution of the notch feature in the NIRC spectra.

To make a more quantitative assessment of this behavior, we have measured the pseudo-equivalent widths (PEWs) of the K I lines by integrating over their line profiles. In this case,

$$PEW = \frac{\int [C(\lambda) - f(\lambda)] d\lambda}{C(\lambda_c)}, \tag{3.14}$$

where $C(\lambda)$ is the neighboring pseudo-continuum and λ_c the transition wavelength, measured at the minimum flux point in the spectral line. Errors are computed from the scatter in the neighboring pseudo-continuum. Results for OSIRIS data are given in Table 3.8, which lists the central wavelength and PEW for each transition. We have made similar measurements on the spectra of M, L, and T dwarfs obtained from the literature (Geballe et al., 1996; Strauss et al., 1999; Tsvetanov et al., 2000; Leggett et al., 2000b, 2001; Reid et al., 2001a, hereafter CGS4 data). These values are given in Table 3.9. Figure 3.13 plots the K I PEWs versus spectral type, with OSIRIS data shown as triangles and CGS4 data as squares. T dwarf spectral types are from Chapter 7. We immediately discern an apparent strengthening of the 1.2432 μm line from the mid-M dwarfs to the mid-L dwarfs, which is present but more subtle at 1.2522 μm. The growth of the 1.2432 μm line is likely influenced by contamination of FeH at 1.237 μm; however, the gradual strengthening of both lines mimic that of the 0.77 μm K I resonance doublet in red optical data (Kirkpatrick et al., 1999b, also §3.2). There is a significant drop in the PEWs of the 1.2432 μm line between L5 V and L7 V, likely due to the disappearance of the FeH lines (McLean et al., 2000), although a subtle dip may be present in the 1.2522 μm line strengths. Both lines appear to peak up slightly in the mid-T dwarfs (e.g., 2MASS 0559-1404), and then, as seen in Figure 3.7, drop toward Gliese 570D. The 1.2522 μm line appears to be stronger than the 1.2432 μm line in the T dwarfs, in contrast to the relative strengthen of the latter in the early- and mid-L dwarfs. This asymmetry was originally noted by Leggett et al. (2001) in the late L7 V DENIS 0205-1159AB, and is a consequence of intrusion by the FeH line in the L dwarfs.

[4]CIA H_2 absorption also peaks around 1.2 μm (Lenzuni, Chernoff, & Salpeter, 1991, 2-0 Quadrapole) but is 100 times weaker.

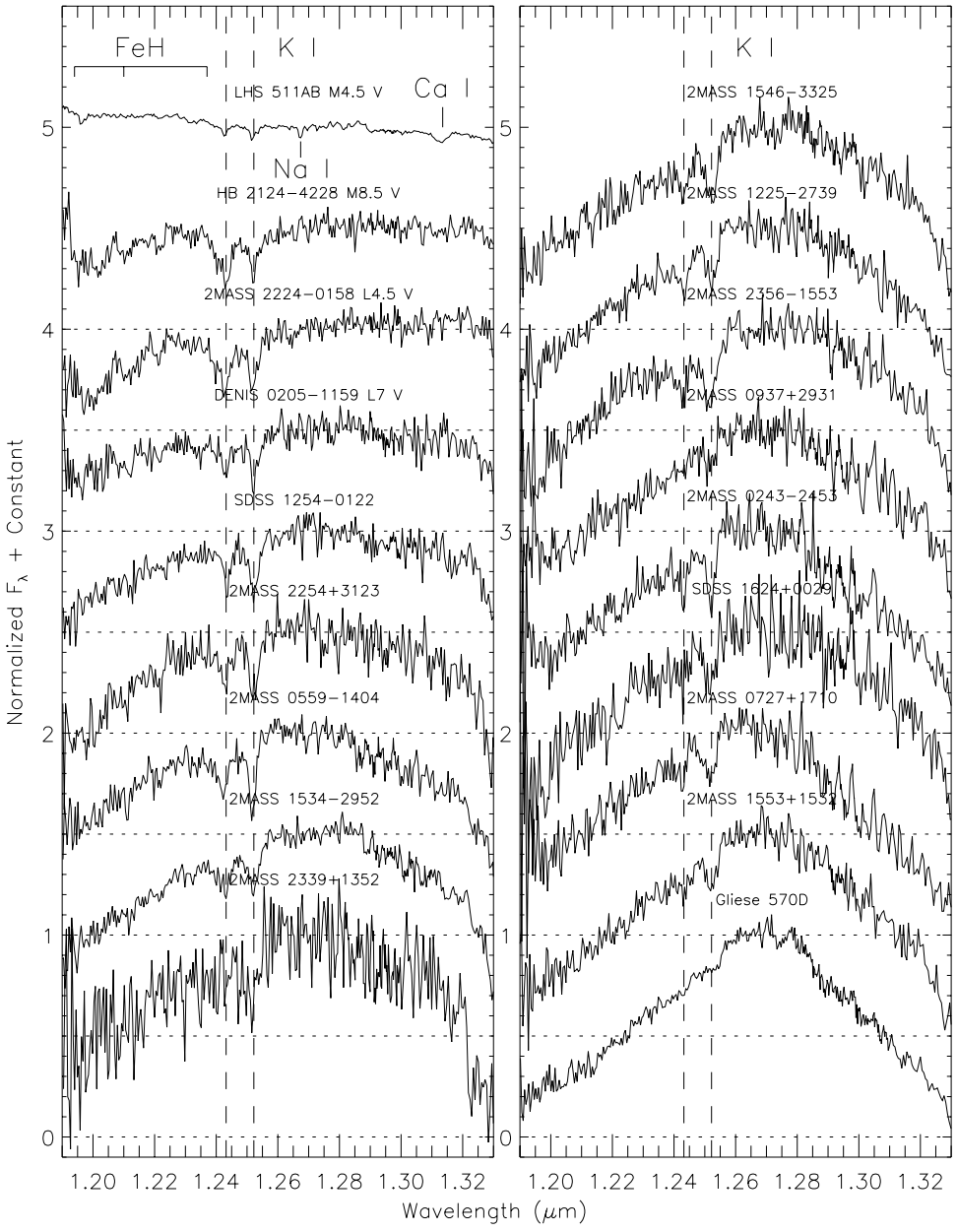

Figure 3.12: OSIRIS data from 1.19 to 1.33 μm. Spectra are scaled and offset as in Figures 3.6 and 3.7. The 1.25 μm K I doublet is indicated by dashed lines, and FeH features at 1.194, 1.21, and 1.237 μm, Na I at 1.2679 μm, and the Ca I triplet at 1.314 μm (the latter two features present only in LHS 511AB) are noted.

Table 3.8: K I Pseudo-equivalent Widths - OSIRIS Data.

		1.2432 μm			1.2522 μm	
Object	Type	λ_c (μm)	PEW (Å)		λ_c (μm)	PEW (Å)
(1)	(2)	(3)	(4)		(5)	(6)
LHS 511AB	M4.5 V	1.2425	1.50±0.15	1.2514	1.50±0.12	
HB 2115−4518	M7.5 V	1.2433	8.1±0.7		1.2518	4.3±0.7
HB 2124−4228	M8.5 V	1.2429	9.2±0.7		1.2518	5.6±0.8
2MASS 2224−0158	L4.5 V	1.2425	8.6±0.9		1.2513	6.9±0.9
DENIS 0205−1159	L7 V	1.2433	3.3±0.8		1.2522	6.2±0.7
SDSS 1254−0122	T2 V	1.2433	5.5±0.9		1.2521	9.1±0.9
2MASS 2254+3123	T5 V	1.2434	7.5±1.4		1.2527	10.6±1.3
2MASS 0559−1404	T5 V	1.2423	6.4±1.0		1.2515	9.3±0.9
2MASS 1534−2952	T5.5 V	1.2432	5.9±0.6		1.2521	7.7±0.6
2MASS 2339+1352	T5.5 V	1.2405	< 3.2		1.2516	7.4±3.5
2MASS 1546−3325	T5.5 V	1.2427	5.9±1.3		1.2528	11.1±1.2
2MASS 2356−1553	T6 V	1.2427	4.1±1.4		1.2506	11.7±1.1
2MASS 0243−2453	T6 V	1.2430	4.2±1.0		1.2523	8.9±1.2
2MASS 0937+2931	T6 V	1.2407	< 1.3		1.2508	2.5±1.2
2MASS 1225−2739	T6 V	1.2436	6.6±1.1		1.2524	7.8±0.6
SDSS 1624+0029	T6 V	1.2429	3.4±1.8		1.2517	9.8±1.8
2MASS 0727+1710	T7 V	1.2428	1.9±1.2		1.2516	6.8±1.0
2MASS 1553+1532	T7 V	1.2430	2.9±1.0		1.2519	5.8±0.9
2MASS 1553+1532	T7 V	1.2425	1.5±1.1		1.2522	5.7±1.1
Gliese 570D	T8 V	1.2411	3.7±0.7		1.2491	3.0±0.5

Table 3.9: K I Pseudo-equivalent Widths - Data from the Literature.

		1.2432 μm			1.2522 μm		
Object	Type	λ_c (μm)	PEW (Å)		λ_c (μm)	PEW (Å)	Ref.
(1)	(2)	(3)		(4)	(5)	(6)	(7)
LHS 3406	M5.5 V	1.2416	5.1±0.9		1.2503	4.2±0.2	1
LHS 2930	M6.5 V	1.2404	4.5±1.1		1.2503	2.9±0.5	1
LHS 3003	M7 V	1.2404	4.2±0.9		1.2503	2.0±0.4	1
LHS 429	M7 V	1.2404	4.0±0.7		1.2503	1.8±0.4	1
LHD 94	M7 V	1.2434	5.4±0.6		1.2519	4.3±0.7	2
2MASS 0320+1854	M8 V	1.2438	7.2±0.3		1.2524	4.3±0.4	2
TVLM 513−46546	M8.5 V	1.2436	9.0±0.4		1.2528	6.2±0.3	1
BRI 0021−0214	M9.5 V	1.2432	9.0±0.6		1.2525	5.2±0.5	1
2MASS 0345+2540	L0 V	1.2435	8.0±0.5		1.2522	6.1±0.3	1
2MASS 0345+2540	L0 V	1.2438	8.0±0.6		1.2525	6.2±0.5	2
2MASS 0746+2000	L0.5 V	1.2436	9.3±0.4		1.2522	6.8±0.3	2
2MASS 0829+1456	L2 V	1.2431	11.2±1.8		1.2518	6.9±0.6	2
Kelu 1	L2 V	1.2435	9.8±0.5		1.2527	6.6±0.3	1
2MASS 1029+1626	L2.5 V	1.2422	8.2±1.5		1.2513	5.0±0.8	2
DENIS 1058−1548	L3 V	1.2434	11.6±0.5		1.2521	8.4±0.6	1
2MASS 0036+1821	L3.5 V	1.2435	10.1±0.5		1.2522	9.4±0.4	2
GD 165B	L4 V	1.2436	12.5±0.7		1.2522	6.3±0.4	1
2MASS 1112+3548	L4.5 V	1.2439	9.2±1.0		1.2518	5.2±1.2	2
DENIS 1228−1547	L5 V	1.2431	9.4±0.9		1.2525	7.8±0.8	1
SDSS 0539−0059	L5 V	1.2440	8.1±0.6		1.2527	7.3±0.5	3
DENIS 0205−1159	L7 V	1.2435	4.9±1.0		1.2529	5.3±0.4	1
DENIS 0205−1159	L7 V	1.2435	< 1.0		1.2516	6.2±1.7	2
2MASS 0825+2115	L7.5 V	1.2424	4.1±1.9		1.2522	4.6±1.0	2
2MASS 0310+1648	L8 V	1.2439	< 1.8		1.2532	7.1±1.5	2
SDSS 0837−0000	T1 V	1.2430	3.4±1.2		1.2517	3.2±1.4	3
SDSS 1254−0122	T2 V	1.2460	3.5±0.5		1.2517	7.2±0.6	3
SDSS 1021−0304	T3 V	1.2430	4.7±0.5		1.2517	7.8±0.4	3
SDSS 1346−0031	T6 V	1.2429	2.9±1.1		1.2516	9.1±0.9	4
SDSS 1624+0029	T6 V	1.2425	1.9±0.4		1.2513	5.1±0.7	5
Gliese 229B	T6.5 V	1.2410	1.3±0.6		1.2520	4.3±0.5	6

Refs – (1) Leggett et al. (2001); (2) Reid et al. (2001); (3) Leggett et al. (2000); (4) Tsvetanov et al. (2000); (5) Strauss et al. 1999; (6) Geballe et al. (1996).

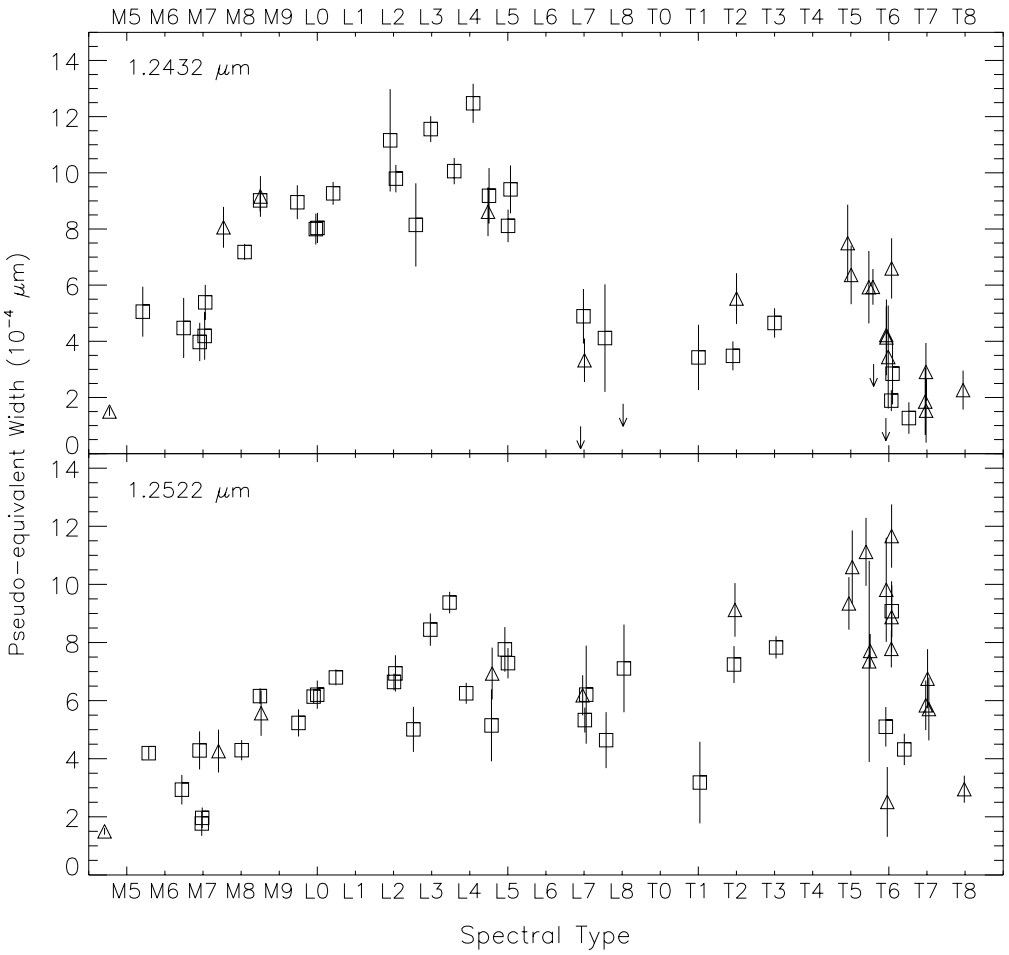

Figure 3.13: 1.2432 and 1.2522 μm K I pseudo-equivalent width (PEW) measurements for late-M, L, and T dwarfs. OSIRIS data are indicated with triangles; CGS4 data from the literature are indicated by squares.

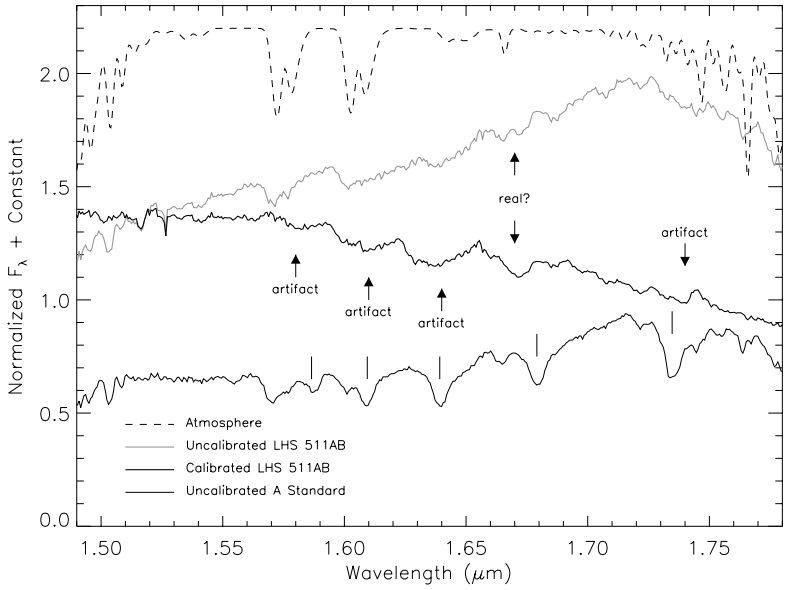

Figure 3.14: Close examination of the weak H-band features. Uncalibrated (thick gray line) and calibrated (thick black line) spectra of LHS 511AB are shown, along with a telluric absorption spectrum (dashed line; from the UKIRT webpage) and the uncalibrated spectrum of the A0 V standard HD 205178 (thin line) features are indicated with arrows. Hydrogen recombination lines in the A star are indicated by dashes.

Lines of Na I (1.138, 1.141 μm) and Rb I (1.323 μm) noted by McLean et al. (2000) are also likely present in the L dwarf spectra, but are weakened by overlying H_2O opacity; we do not see these features in our data. We also note a Na I doublet at 1.2679 μm and Ca I triplet at 1.314 μm that are present in the spectrum of LHS 511AB but not in any of the other objects.

3.1.5.3 Unidentified Features at H-band

Finally, we note that several weak absorption features are seen in the H-band peaks of our M and L dwarf spectra, near 1.58, 1.61, 1.64, 1.67, and 1.74 μm. Reid et al. (2001a) have also detected these features in their spectral data. The absorptions are fairly close to the Brackett hydrogen lines (1.5885, 1.6114, 1.6412, 1.6811, and 1.7367 μm), which are strong in the spectra of our A-type standards, with little continuum between the lines. We believe that these features may be artifacts produced in the reduction process, as they are not obviously present in the data prior to flux calibration. Figure 3.14 demonstrates this in the reduction of LHS 511AB. The thick gray line is the uncalibrated spectrum, which has telluric H_2O features present (dashed line); the thick black line is the flux-calibrated spectrum. Note that the observed features are generally not seen in the uncalibrated spectrum, coincide with telluric features, and lie close to the hydrogen lines in the A-star calibrator (thin line). Most of the features are probably artifacts, with the possible exception of the 1.67 μm dip which is seen in the uncalibrated spectrum (however, note the difference in morphology between uncalibrated and calibrated data). Recalibrating the data using later-type standards may help to pin down the origin of these weak features. For the time being we ignore

these probable artifacts, as their presence does not effect further analysis.

3.1.6 Comparing Data Sets

Data from NIRC and OSIRIS observations comprise our primary spectral sample. Because the instrumental setup, resolution, standards, and reduction procedures were slightly different between these two datasets, we have observed several objects with both instruments to identify any inherent biases. Figure 3.15 plots OSIRIS (light gray) and NIRC (black) data for 2MASS 2254+3123, 2MASS 0559-1404, 2MASS 2356-1553, 2MASS 0937+2931, 2MASS 1553+1532, and Gliese 570D. In general, wavelength and overall flux levels agree well, but there are some differences seen in the individual flux peaks. This is most striking at H- and K-bands, where the NIRC data are generally brighter, although differences can also be seen at J-band at the 10–15% level as well. Spectral data for 2MASS 0559-1404 are the most discrepant, with NIRC observations as much as 35% brighter at K; there is also a difference in slope seen in the 1.6 μm CH_4 band. The discrepancies at K may be due to the difficulty in determining overlap between the OSIRIS H- and K-band spectral orders (see §3.1.2). A similar problem may be present in the spectrum of 2MASS 1553+1532. However, spectral differences generally do not exceed 10–15%, similar to the differences seen between the 2MASS photometry and NIRC spectrophotometry (§3.1.1.3).

Figure 3.16 shows OSIRIS and NIRC data (light gray) compared to data from the literature for DENIS 0205-1159AB (Leggett et al., 2001), SDSS 1254-0122 (Leggett et al., 2000b), 2MASS 0559-1404 (Burgasser et al., 2000c), Gliese 570D (Geballe et al., 2001a), SDSS 1346-0031 (Tsvetanov et al., 2000), and SDSS 1624+0029 (Strauss et al., 1999). Again, overall wavelength calibration and flux levels appear to be consistent, and band morphologies are generally coincident. Most discrepant are data for 2MASS 0559-1404, which is roughly $\sim$ 50% brighter at K-band in the NIRC spectrum (left panel). Data from Burgasser et al. (2000c) were obtained with the Palomar 60" Cornell-Massachusetts Slit Spectrograph (Wilson et al., 2001a); this instrument has no overlap between the H- and K-bands, and it is possible that the K-band segment of these data was improperly scaled, particularly given the overall agreement from 1–2 μm. CGS4 data for Gliese 570D are roughly 25% brighter than corresponding NIRC data at the z- and J-band peaks; it is unclear as to whether this may be a scaling problem between the JH and HK portions of the NIRC data. The spectra of the other objects agree quite well with published results, and small offsets may simply be due to differences in resolution or signal-to-noise. In general, we find that typical discrepancies do not exceed 10–15%, although differences as large as 25% are present.

3.2 Optical Spectroscopy

While T dwarfs are brightest in the near-infrared and show a number of features sensitive to temperature, gravity, and metallicity, red optical (defined here as the 6300–10100 Å spectral region) spectroscopy also reveals a great deal about the physics of these objects. The broadened Na I (5890 and 5896 Å) and K I (7665 and 7699 Å) doublet lines that are seen in the spectra of mid- and late-type L dwarfs (Kirkpatrick et al., 1999b; Reid et al., 2000) dominate this spectral region in T dwarfs and are sensitive to both temperature and gravity (Liebert et al., 2000b; Burrows, Marley, & Sharp, 2000). Other atomic and molecular features, useful as temperature diagnostics and classification, are present as well. In order to investigate the optical properties of these objects, we have obtained 6300–10100 Å spectral data for most of the T dwarfs discovered in this work and by SDSS (Strauss et al., 1999; Tsvetanov et al., 2000; Leggett et al., 2000b) using the Low Resolution Imaging Spectrograph (Oke et al., 1995, hereafter LRIS). These observations are described in §3.2.1, along with 3800–8650Å data for 2MASS 1237+6526, also obtained using LRIS. The red optical spectral

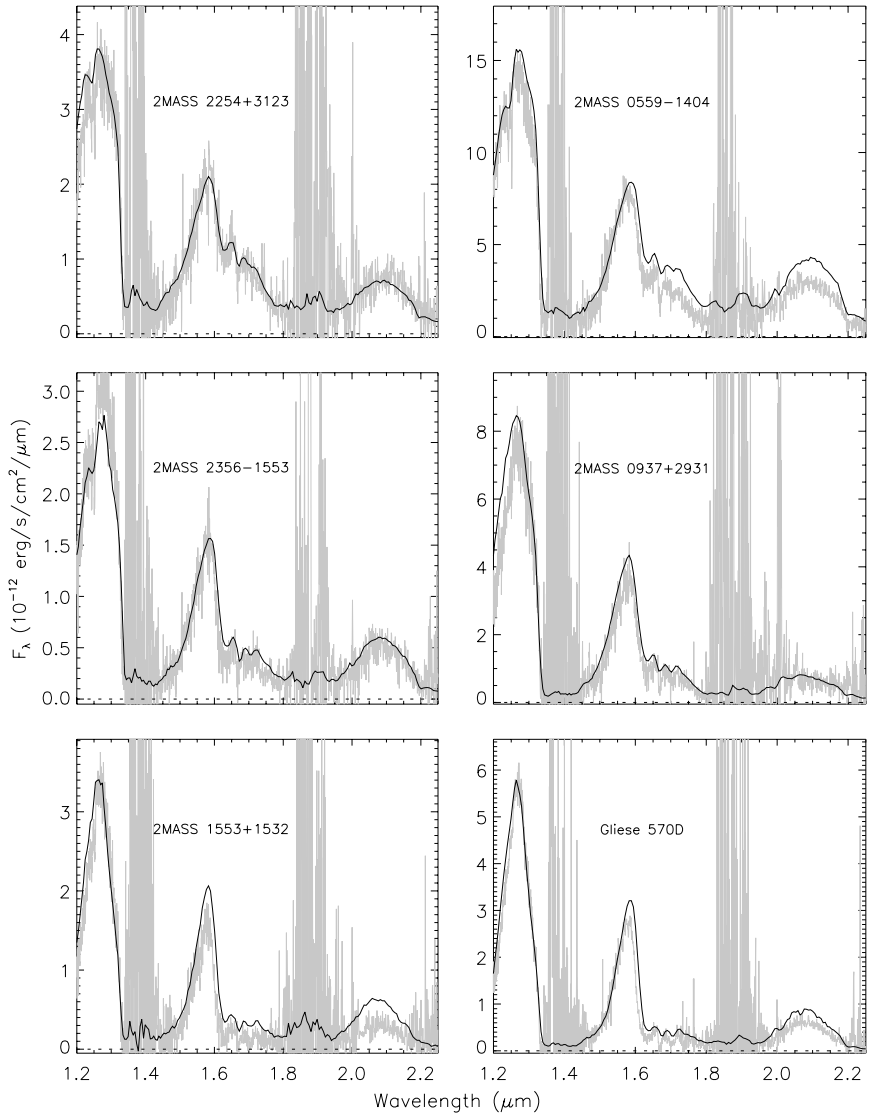

Figure 3.15: Comparison between NIRC (black lines) and OSIRIS data (gray lines) for the T dwarfs 2MASS 2254+3123, 2MASS 0559-1404, 2MASS 2356-1553, 2MASS 0937+2931, 2MASS 1553+1532, and Gliese 570D.

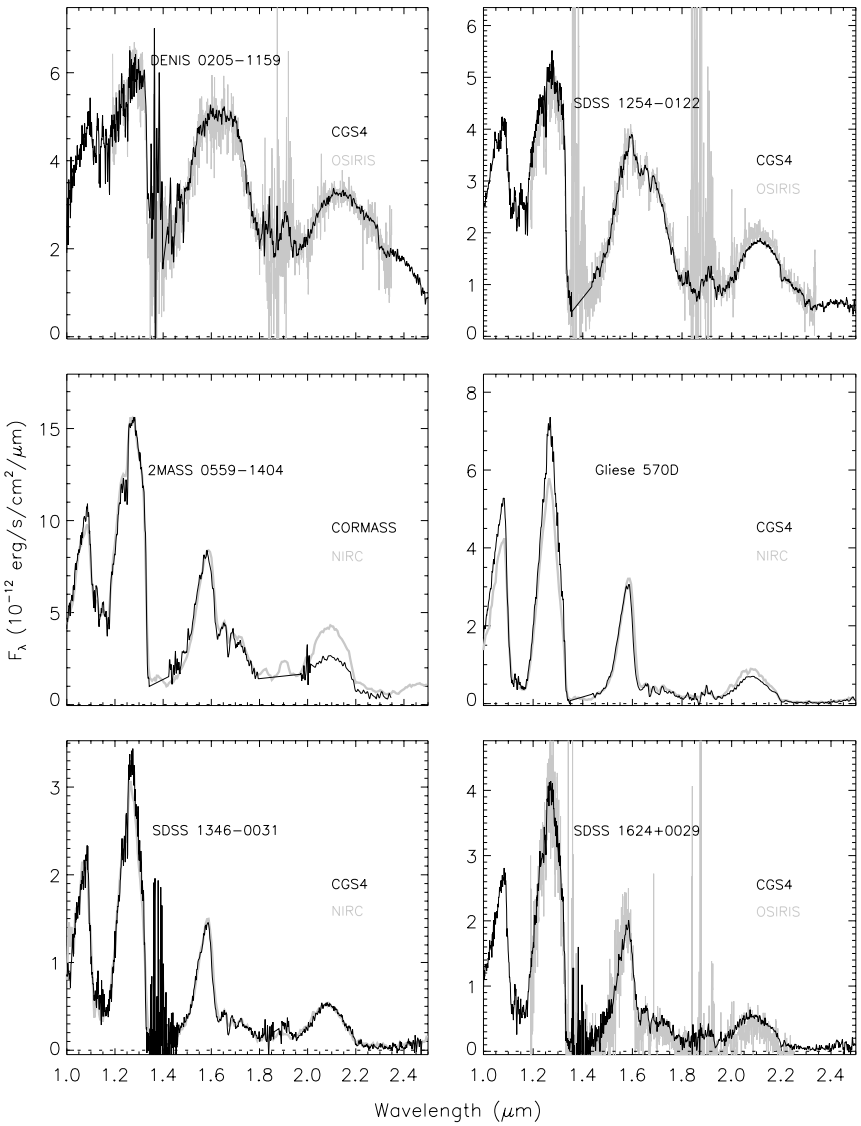

Figure 3.16: Comparison between NIRC/OSIRIS data (gray lines) and data from the literature (black lines) for DENIS 0205-1159AB (L7 V) and the T dwarfs SDSS 1254-0122, 2MASS 0559-1404, Gliese 570D, SDSS 1346-0031, and SDSS 1624+0029.

properties of T dwarfs are discussed in §3.2.2.

3.2.1 LRIS Observations

LRIS is a dual spectrograph mounted at the Cassegrain focus of the Keck 10m Telescope. This instrument is similar in design to the Palomar Hale 5m Double Spectrograph (Oke & Gunn, 1982), as light entering the instrument is nominally passed through a 5500 Å dichroic mirror into two channels, blue and red. Since the blue channel has only recently been implemented (semester 2000B), data presented here are taken using only the red channel with a mirror bypassing the dichroic. Each channel is imaged onto a back-illuminated TEK 2048×2048 CCD with 24 μm pixels. Resolution on the sky is $0\farcs21$ pixel^{-1}. Spectra from 6300–10100 Å at 9 Å resolution can be acquired using the 400 lines mm^{-1} grating blazed at 8500 Å. Blue optical spectral data over 3800–8650 Å can also be acquired at 12 Å resolution using the 300 lines mm^{-1} grating blazed at 5000 Å. Pixel resolutions on the chip are 2.4 and 1.9 Å pixel $^{-1}$ for blue and red optical spectra, respectively.

3.2.1.1 Data Acquisition

An observing log for T dwarf observations is given in Table 3.10. Conditions during our 1999 July 16-18 (UT) observations were generally clear with sub-arcsecond seeing, although seeing was variable during the night of July 18; observations made on 2000 March 5 and 2000 December 26 (UT) were both taken in clear weather with seeing $\lesssim 1''$; finally, our 2001 February 20 (UT) data were obtained in light clouds with roughly $1''$ seeing. All red optical observations were made using the 400 lines mm^{-1} grating blazed at 8500 Å and a $1''$ (4.7 pixels) slit. We also used the OG570 order blocking filter to reduce higher-order light.

Targets were nominally acquired using the facility guide camera; however, some objects were not seen on the guider because of their optical faintness (R $\gtrsim$ 26 for a J = 16 T dwarf; Matthews et al. 1996, Burgasser et al. 1999). These objects were placed into the slit by blind offset from a nearby optical source using offset values determined from 2MASS coordinates. Occasionally an object did not fall into the slit (likely due to its proper motion), and in such cases small offsets were made until sufficient signal could be detected in the 9000-10100 Å region. Individual exposures ranged from 1200 to 1800 sec, with up to four observations obtained on a particular night. Observations of the B1 V Hiltner 600 and DB3 LTT 9491 flux standards (Hamuy et al., 1994; Bessell, 1999) were obtained for flux calibration using the same instrumental configuration. We also observed white dwarf and late-F/early-G stars close to the target objects during our 2000 March 5, 2000 December 26–28, and 2001 February 20 (UT) runs to correct for telluric absorption.

3.2.1.2 Data Reduction

Reduction procedures for LRIS data are diagrammed in Figure 3.17. Science data were reduced using standard IRAF[5] routines. First, a series of one-second dark exposures was median-combined and subtracted from the science data and flat-field exposures to eliminate detector bias. Images were then trimmed and divided by median-combined, bias-subtracted, and normalized quartz-lamp flat-field exposures (reflected off of the interior dome) to correct for detector response. Spectra were then extracted using the APEXTRACT package. Curvature of the dispersion line was determined from either the telluric or flux standard star exposures and used as a template for the target extractions. Telluric standards were preferred in order to reduce the effects of instrument flexure between the

[5]Image Reduction and Analysis Facility (IRAF) is distributed by the National Optical Astronomy Observatories, which are operated by the Association of Universities for Research in Astronomy, Inc., under cooperative agreement with the National Science Foundation.

Table 3.10: Log of LRIS Observations.

Object (1)	UT Date (2)	t_{int} (s) (3)	Airmass (4)	Flux Cal. (5)	Type[a] (6)	Telluric Cal. (7)	Type[b] (8)
2MASS 0415−0935	2001 Feb 20	6000	1.20–1.38	Hiltner 600	B1 V	Gl 166B	DA4
	2000 Dec 26	3600	1.15–1.16	Hiltner 600	B1 V	SAO 131064	G0 V
2MASS 0559−1404	2000 Mar 5	3600	1.20–1.22	Hiltner 600	B1 V	LHS 32	DZ9
2MASS 0727+1710	2000 Mar 5	1800	1.00	Hiltner 600	B1 V	GJ 1102A	DC9 (K2 V?[c])
2MASS 0755+2212	2001 Feb 20	2400	1.13–1.19	Hiltner 600	B1 V	SAO 79820	G0 V
SDSS 0837−0000	2000 Dec 26	7200	1.07–1.23	Hiltner 600	B1 V	SAO 116950	G0 V
	2000 Dec 27[d]	3600	1.23–1.40	Hiltner 600	B1 V	SAO 116950	G0 V
	2000 Dec 28[d]	3600	1.32–1.58	Hiltner 600	B1 V	SAO 116950	G0 V
2MASS 0937+2931	2000 Mar 5	3600	1.01	Hiltner 600	B1 V	WD 0924+199	DC
SDSS 1021−0304	2000 Dec 26	2400	1.09	Hiltner 600	B1 V	HD 89526	F8 V
2MASS 1047+2124	2001 Feb 20	4800	1.06–1.22	Hiltner 600	B1 V	HD 93583	G0 V
2MASS 1217−0311	2000 Mar 5	1800	1.11–1.16	Hiltner 600	B1 V	WD 1225-079	DZA
2MASS 1225−2739	2000 Mar 5	3600	1.48–1.50	Hiltner 600	B1 V	WD 1225-079	DZA
2MASS 1237+6526	1999 Jul 16	4800	1.87–1.91	LTT 9491	DB3		
	1999 Jul 17	1800	2.21	LTT 9491	DB3		
	1999 Jul 18[e]	1800	1.79	LTT 9491	DB3		
	2000 Mar 5	1800	1.46	Hiltner 600	B1 V		
	2001 Feb 20	2400	1.49–1.52	Hiltner 600	B1 V	SAO 15828	F8 V
SDSS 1254−0122	2000 Dec 26	2400	1.24	Hiltner 600	B1 V	HD 111942	G0 V
	2001 Feb 20	3600	1.08–1.13	Hiltner 600	B1 V	HD 111942	G0 V
SDSS 1346−0031	1999 Jul 17	2700	1.35–1.45	LTT 9491	DB3		
Gliese 570D	2000 Mar 5	3600	1.33–1.36	Hiltner 600	B1 V	GJ 3866	DC9 (DA4 + K V?[c])
	2001 Feb 20	4800	1.08–1.13	Hiltner 600	B1 V	HD 131878	G0 V
2MASS 1534−2952	2001 Feb 20	2400	1.58–1.63	Hiltner 600	B1 V	HD 138874	F7 V
SDSS 1624+0029	1999 Jul 16	3600	1.12–1.18	LTT 9491	DB3		

[a]Spectral types for Hiltner 600 and LTT 9491 from Bessell (1999).
[b]Telluric calibrator spectral types from McCook & Sion (1999) and SIMBAD.
[c]Possible revised spectral type based on LRIS observations (see §3.2.1.2).
[d]Observation made by J. Carpenter and L. Hillenbrand.
[e]Blue optical data (3800–8650 Å) obtained using the 300 lines mm^{-1} grating blazed at 5000 Å.

observations. All spectral data were optimally extracted with a cleaning algorithm to eliminate cosmic rays and spurious pixels. Wavelength calibration was done using Ne-Ar arc lamp exposures taken after the target observations.

We then computed a telluric correction from the telluric calibrator spectra by interpolating over atmospheric O_2 (6850–6900 Å B-band, 7600–7700 Å A-band) and H_2O (7150–7300, 8100–8350, and 9300–9650 Å) bands, and then dividing through by the original standard spectrum. This correction was applied to both the flux standards and target spectra. White dwarfs (DC and DZ) and late-F/early-G stars were chosen as telluric calibrators for their lack of features in this spectral region. However, a number of our white dwarf calibrators from 2000 March 5 (UT) appear to have been mistyped in the literature, as shown in the flux-calibrated spectra of Figure 3.18. GJ 1102A, typed as a DC9 by McCook & Sion (1999), has weak Hα absorption and, more importantly, strong Ca II triplet lines (8498, 8542, & 8662 Å) and a Ba II line at 6497 Å; this object is likely a K-type dwarf. GJ 3866, designated DC9 by Liebert, Dahn, & Monet (1988), has a broad Hα line, a 10000±2000 K blackbody, and Ca II lines. This object may be a DA4/K-dwarf binary, given its moderately red V-J = 1.5, J-K_s = 0.26 colors (McCook & Sion, 1999, 2MASS). The spectra in Figure 3.18 also highlight a few features inherent to LRIS data, including fringing at long wavelengths and a dead column at roughly 6720 Å. The additional features seen in these spectra did not affect our ability to compute adequate telluric corrections.

Finally, flux calibration was done by correcting our Hiltner 600 and LTT 9491 observations to the spectrophotometric data given by Hamuy et al. (1994), being careful to interpolate over telluric features and the Balmer Hα line. This correction was then applied to the T dwarf data to produce the final calibrated spectra. If multiple spectra were obtained on a particular night, these were scaled and coadded to further improve signal-to-noise.

3.2.1.3 Results

Reduced spectral data for all observed T dwarfs are shown in Figures 3.19 and 3.20. Flux is normalized at 9250 Å and offset for clarity. Features present in the spectra are noted, including Cs I at 8521 and 8943 Å; Rb I at 7800 and 7948 Å; the heavily broadened wings of the Na I 5890, 5896 Å doublet and K I 7665, 7699 Å doublet; FeH bands at 8692 and 9896 Å; CrH bands at 8611 and 9969 Å; H_2O and 9250 Å; the weak CH_4 band centered at 8950 Å; and finally Hα at 6563 Å, detected in 2MASS 1237+6526 and SDSS 1254-0122. We address these identifications further in § 3.2.2.

3.2.1.4 3800–8650 Å Spectrum of 2MASS 1237+6526

During our 1999 July 16-18 (UT) LRIS observing run, we obtained a blue optical (3800–8650 Å) spectrum of 2MASS 1237+6526. The purpose of this observation was to look for continuum flux shortward of 6300 Å as well as search for Hβ emission. Using the 300 lines mm^{-1} grating blazed at 5000 Å, we obtained a single 1800 sec exposure of 2MASS 1237+6526 on 1999 July 18 (UT). A 1″ slit was employed with no order blocking filter. Observations of an Hg-Ne-Ar arc lamp were observed after the target exposure for wavelength calibration, and the DB3 LTT 9491 (Hamuy et al., 1994; Bessell, 1999) was observed for flux calibration.

Data were reduced as diagrammed in Figure 3.17 with no telluric correction. The final calibrated spectrum is shown in Figure 3.21. We failed to detect any significant continuum below 8000 Å, although there may be some positive flux around 4400 Å; it is unclear as to whether the latter is an artifact of flat-fielding, however). Hα was clearly detected but not Hβ. A number of spikes are also seen at 5569, 6295, 7746, and 7849 Å; it is likely that all four of these spikes are spurious, particularly given that their pixel widths are half that of the Hα line.

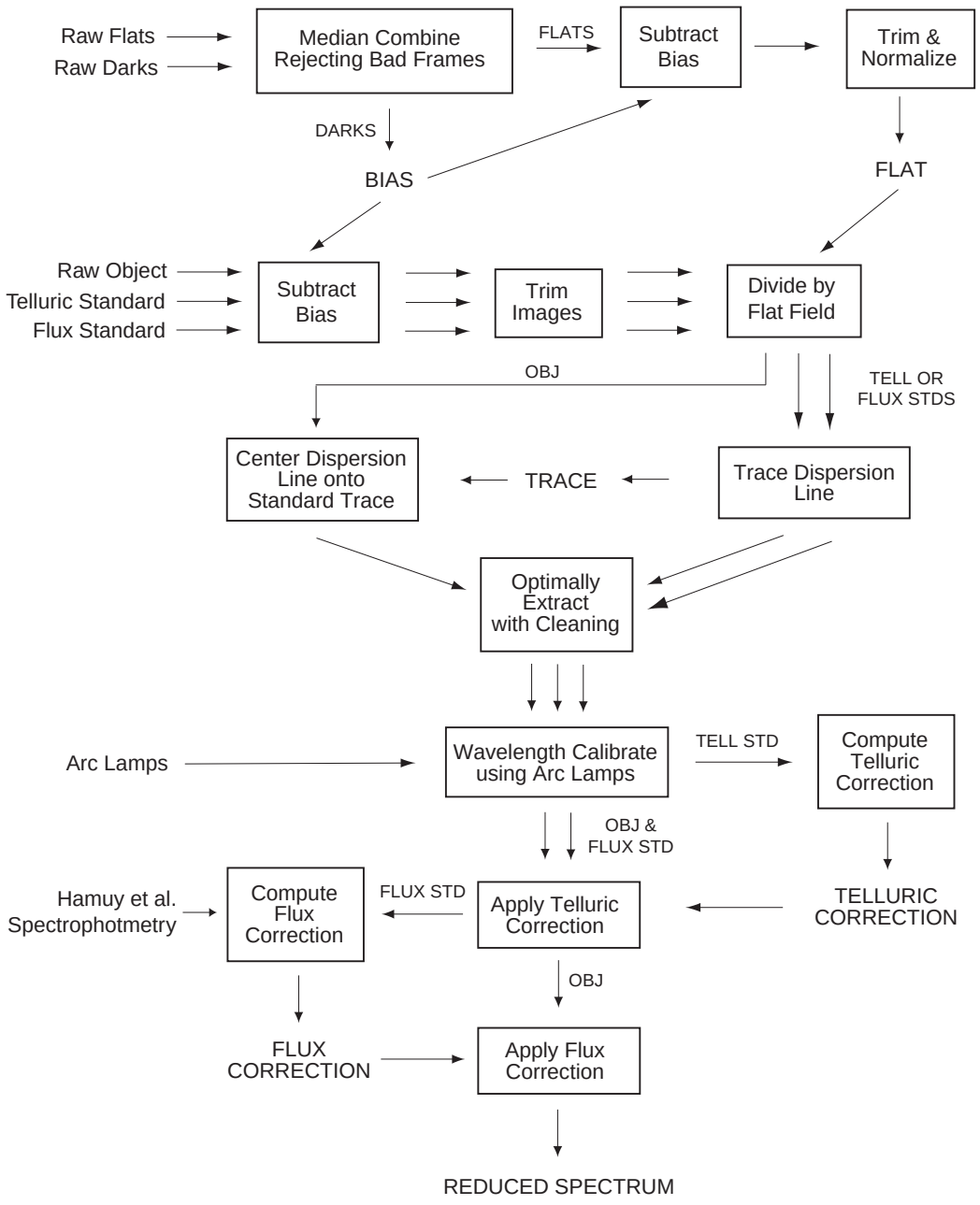

Figure 3.17: A flowchart diagramming the procedures for LRIS spectral data reduction. This algorithm was implemented in the IRAF environment using the APEXTRACT package.

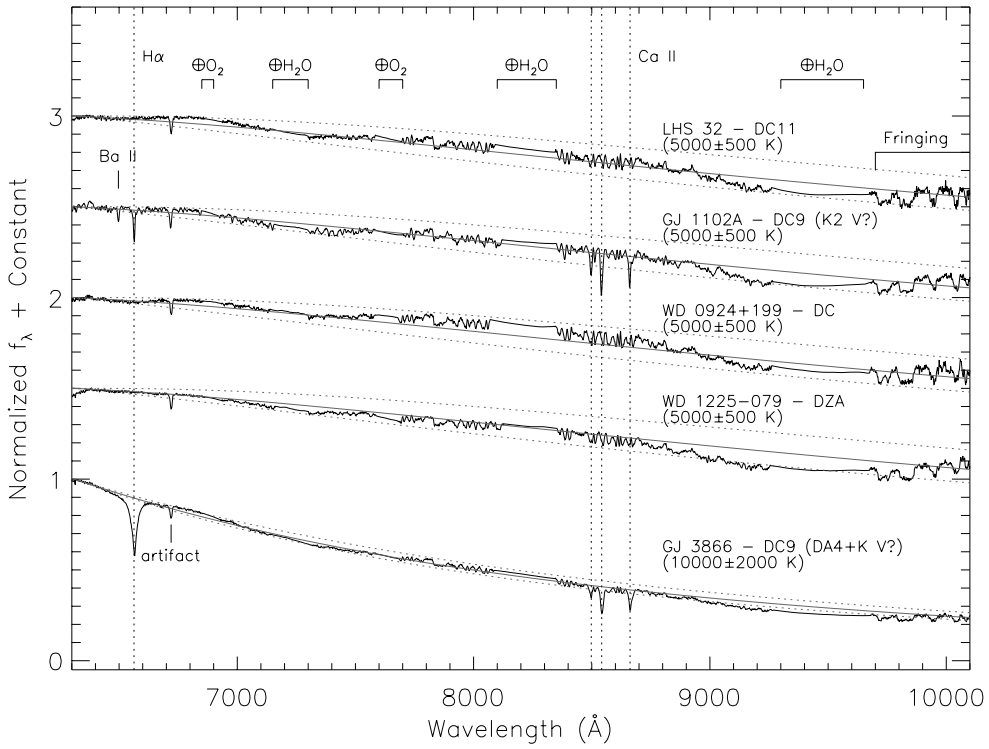

Figure 3.18: Telluric standards used during our 2000 March 5 (UT) observations. Spectra are normalized at their flux peaks and offset. Regions of telluric absorption (interpolated over the spectra) are indicated. Blackbody fits (solid and dashed lines) are overlaid. Hα (seen in white dwarfs) is noted, as are the effects of fringing (at long wavelengths) and the dead column at 6720 Å. Note the presence of Ba II (6497 Å blend) in GJ 1102A, and the Ca II triplets (8498, 8542, & 8662 Å) in both GJ 1102A and GJ 3866; the former is likely a K2 V (not a DC9), while the latter may be a white-dwarf/K-dwarf binary (not a DC9).

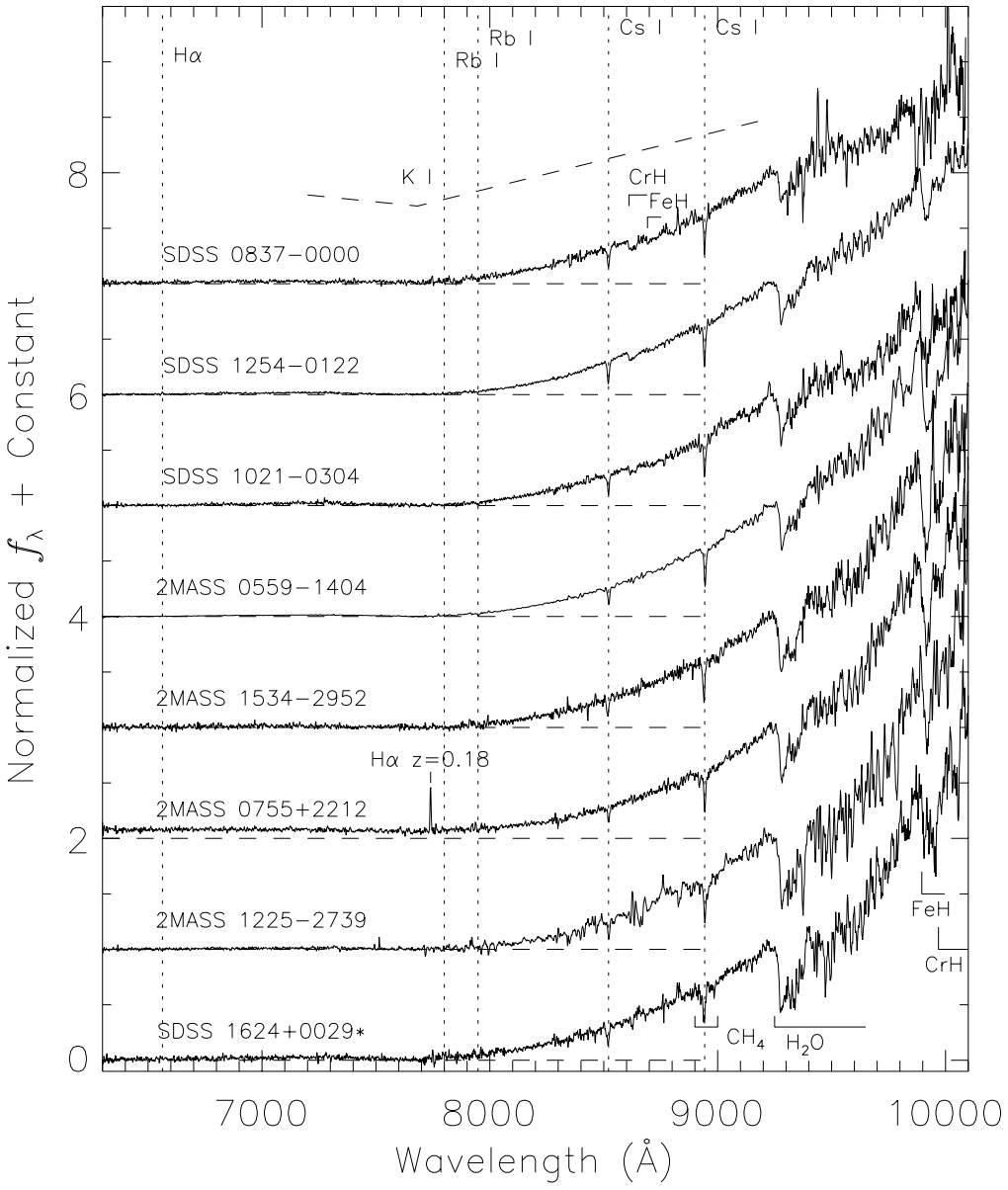

Figure 3.19: Red optical (6300–10100 Å) spectra of T dwarfs. Data are normalized at 9250 Å and offset (dashed lines). Atomic and molecular absorption features are indicated. Objects noted by an asterisk are not corrected for telluric absorption. Note that the possible Hα line in 0755+2212 at a redshift z = 0.18 and continuum flux shortward of 8000 Å originates from an aligned background galaxy.

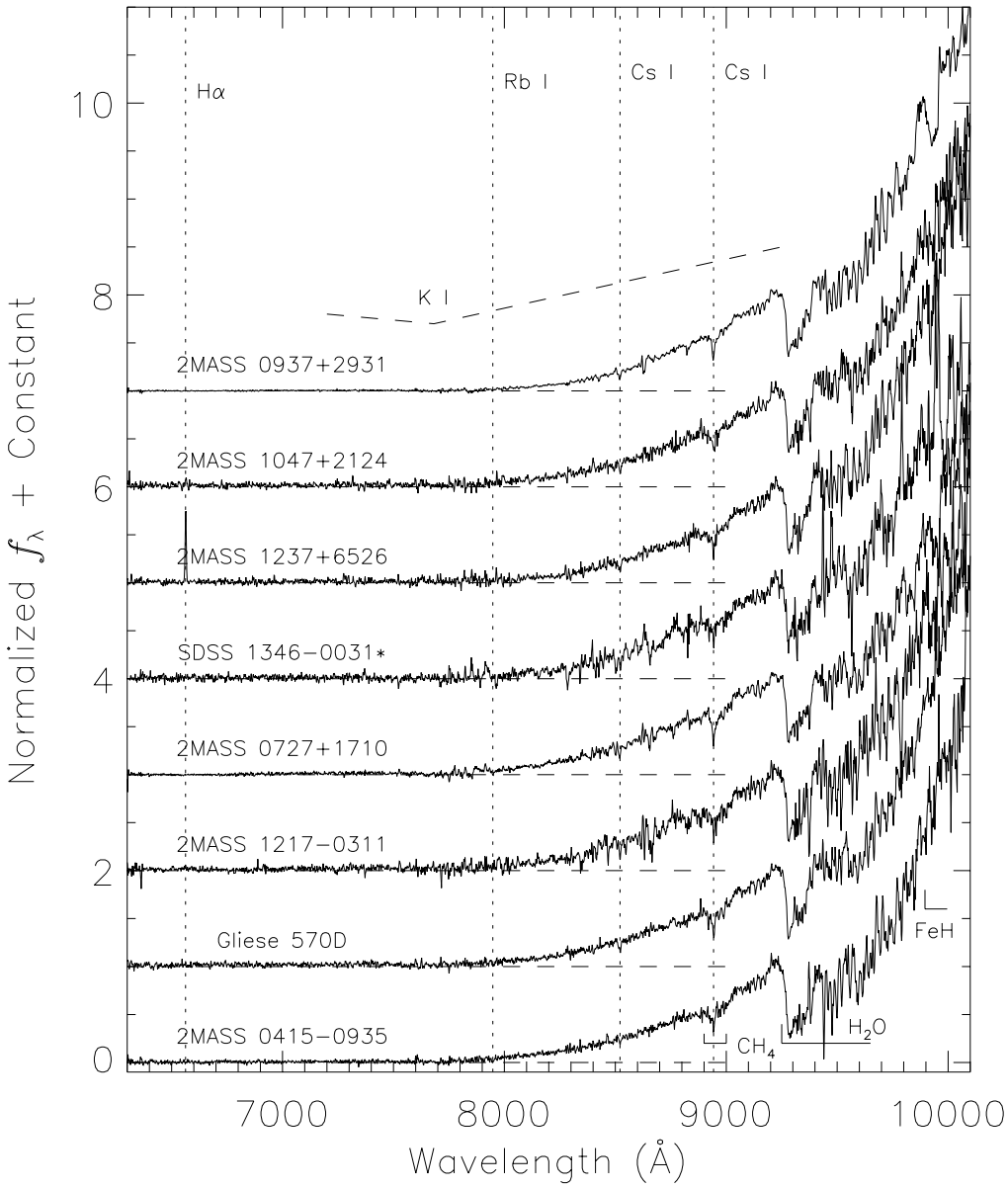

Figure 3.20: Continuation of Figure 3.19.

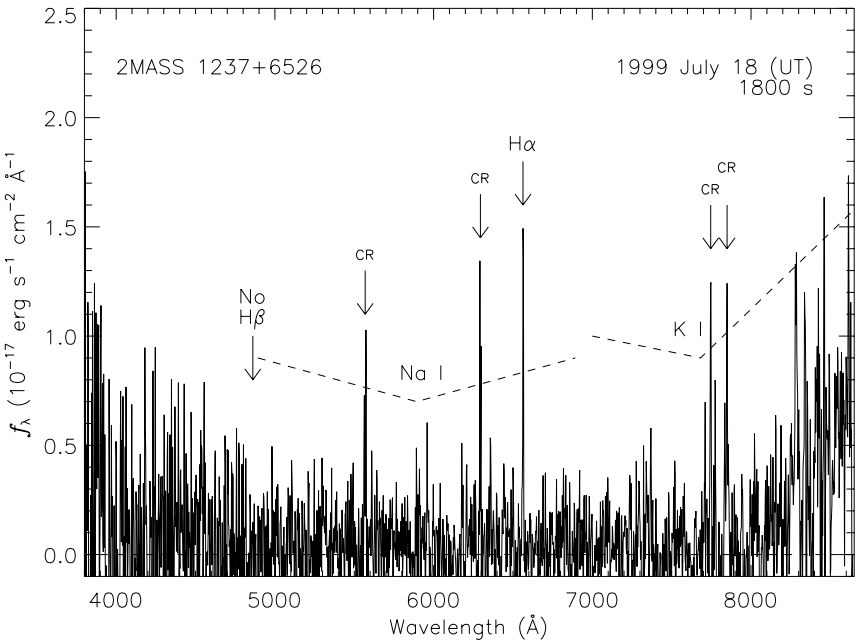

Figure 3.21: 3800–8650 Å spectrum of 2MASS 1237+6526, taken on 1999 July 18 (UT) using LRIS. The positions of the Hα (detected) and Hβ (not detected) lines are indicated, as are five other lines not identified with any common atomic transition. Regions likely affected by the broadened Na I and K I absorption doublet lines are also indicated.

Table 3.11: Red Optical μm Features in T Dwarfs.

Feature (1)	λ (μm) (2)	Transition[a] (3)	Ref. (4)
Na I	5890[a]	3s $^2S_{1/2}$ − 3p $^2P_{3/2}$	1,2,3
Na I	5896[a]	3s $^2S_{1/2}$ − 3p $^2P_{1/2}$	1,2,3
Hα	6563	3d $^2D_{5/2}$ − 2p $^2P_{3/2}$	1
Li I[b]	6708	2s $^2S_{1/2}$ − 2p $^2P_{3/2,1/2}$	1
CaH	6750–7050	0-0 band of $A^2\Pi$-$X^2\Sigma$	4
CH_4[b]	7000–7400	5(ν_1,ν_3)	5
K I	7665[a]	4s $^2S_{1/2}$ − 4p $^2P_{3/2}$	1,2,6
K I	7699[a]	4s $^2S_{1/2}$ − 4p $^2P_{1/2}$	1,2,6
CH_4[b]	7700–8200	4(ν_1,ν_3) + 1(ν_2,ν_4)	5
Rb I	7800	5s $^2S_{1/2}$ − 5p $^2P_{3/2,1/2}$	1
Rb I	7948	5s $^2S_{1/2}$ − 5p $^2P_{3/2,1/2}$	1
CH_4	8800–9200	4(ν_1,ν_3)	5
Cs I	8521	6s $^2S_{1/2}$ − 6p $^2P_{3/2}$	1
CrH	8611 bandhead	0-0 band of $A^6\Sigma^+$-$X^6\Sigma^+$	4
FeH	8692 bandhead	1-0 band of $A^4\Delta$-$X^4\Delta$	4
Cs I	8943	6s $^2S_{1/2}$ − 6p $^2P_{1/2}$	1
H_2O	9250–9400	3(ν_1,ν_3)	7
H_2O	9450–9800	2(ν_1,ν_3) + 2ν_2	7
CH_4[b]	9600–10200	3(ν_1,ν_3) + 1(ν_2,ν_4)	5
FeH	9896 bandhead	0-0 band of $A^4\Delta$-$X^4\Delta$	8
CrH	9969 bandhead	0-1 band of $A^6\Sigma^+$-$X^6\Sigma^+$	4

[a]Pressure-broadened over $>$ 1000 Å (Burrows, Marley, & Sharp, 2000).
[b]Not yet detected but expected to exist in cooler T dwarfs.
Refs – (1) Wiese, Smith, & Glennon (1966); (2) Burrows, Marley, & Sharp (2000); (3) Reid et al. (2000); (4) Kirkpatrick et al. (1999b); (5) Dick & Fink (1977); (6) Tsuji, Ohnaka, & Aoki (1999); (7) Auman (1967); (8) Phillips et al. (1987).

3.2.2 Red Optical Spectral Features

As shown in Figures 3.19 and 3.20, there are a number of atomic and molecular features present in the red optical spectra of T dwarfs, listed in Table 3.11. Most obvious are the atomic lines of Cs I at 8521 and 8943 Å ($6s^2S_{1/2}$→$6p^2P_{3/2,1/2}$) and the much weaker Rb I doublet at 7800 and 7948 Å ($5s^2S_{1/2}$→$5p^2P_{3/2,1/2}$). These lines are first seen in the L dwarfs as the TiO features dominant in M dwarfs disappear (Kirkpatrick et al., 1999b). The Cs I lines appear to be fairly strong through 2MASS 1225-2739, but are nearly gone by 2MASS 0415-0935. The Rb I lines are only seen in the highest signal-to-noise spectra, and are generally weak, as they are in the late-L dwarfs. Note that Li I at 6708 Å ($2s^2S_{1/2}$→$2p^2P_{3/2,1/2}$) is not detected in any of the T dwarf spectra.

The most dominant feature in these spectra is also an alkali line doublet, the strongly pressure-broadened K I resonance doublet ($4s^2S_{1/2}$→$4p^2P_{3/2,1/2}$), centered at 7665 and 7699 Å but extending over most of the red optical spectral regime. Liebert et al. (2000b) and Burrows, Marley, & Sharp (2000) have shown that the red wing of the K I doublet, which clearly strengthens in the mid- and late-L dwarfs (Kirkpatrick et al., 1999b), produces the steep slope seen from 8000–10000 Å in the spectrum of SDSS 1624+0029, and this feature is likely responsible for shaping the red optical spectrum of all of the objects. This slope becomes greater from SDSS 0837-0000 through 2MASS 0415-0935, with the latter object having four times more flux (1.5 mag) at 10100 Å as compared to 9250 Å. The K I red wing is largely responsible for the extremely red optical/near-infrared colors of

late-L and T dwarfs.

Figure 3.22 shows a close-up of the 6300–8250 Å spectral region for SDSS 1254-0122, 2MASS 0559-1404, SDSS 1624+0029, 2MASS 0937+2931, and 2MASS 0415-0935. The recovery of flux between the K I doublet and the even more strongly broadened Na I doublet at 5890 and 5896 Å ($3s^2S_{1/2}\rightarrow 3p^2P_{3/2,1/2}$) is seen clearly in the first three T dwarfs, but is not readily obvious in the spectra of 2MASS 0937+2931 and 2MASS 0415-0935. The absence of this so-called "blue bump" (Liebert et al., 2000b) in the latter objects may be due to stronger K I/Na I absorption or reduced continuum emission from a cooler photosphere. Note that the possible rise in flux at 4400 Å in 2MASS 1237+6526 (Figure 3.21) may be part of the blue wing of the broadened Na I doublet. A weak signature of CaH around 6750–7150 Å (0-0 band of A $^2\Pi$ - X $^2\Sigma$), seen in M and L dwarfs, also appears to be present but weak in SDSS 1254-0122, 2MASS 0559-1404, and SDSS 1624+0029 (although the latter uncorrected spectrum may be affected by residual telluric absorption).

The most prominent molecular features in the red optical spectra of T dwarfs are the $3(\nu_1,\nu_3)$ and $2(\nu_1,\nu_3)+2\nu_2$ H_2O bands starting at 9250 and 9450 Å, respectively (Auman, 1967). These bands strengthen considerably from SDSS 0837-0000 to 2MASS 0415-0935, but are generally weaker than their near-infrared counterparts. An FeH bandhead at 9896 Å (0-0 band of A $^4\Delta$ - X $^4\Delta$) is also seen quite clearly in some of the spectra of Figure 3.19, and is strongest in 2MASS 1534-2952; beyond 2MASS 0937+2931, however, this band appears to be weak or absent. Its higher-order counterpart, the 1-0 band of A $^4\Delta$ - X $^4\Delta$ at 8692 Å, is clearly seen in SDSS 0837-0000 and possibly in SDSS 1254-0122, but is absent in the remaining spectra. CrH at 8611 Å (0-0 band of A $^6\Sigma^+$ - X $^6\Sigma^+$) also fades beyond SDSS 1021-0304, although the 1-0 band of A $^6\Sigma^+$ - X $^6\Sigma^+$ at 9969 Å appears to be present up to 2MASS 0755+2212. FeH and CrH absorption are prominent features in the spectra of L dwarfs.

While CH_4 is ubiquitous in the near-infrared spectra of T dwarfs, only the weak $4(\nu_1,\nu_3)$ CH_4 band centered at 8950 Å (Dick & Fink, 1977), tentatively "detected" by Oppenheimer et al. (1998) in Gliese 229B, is seen in objects later than 2MASS 0727+1710, and even then it is ambiguous as to whether the observed feature is CH_4 or broadened Cs I at 8943 Å. Three other CH_4 features seen in planetary and laboratory spectra, the $5(\nu_1,\nu_3)$ complex centered at 7300 Å, the $4(\nu_1,\nu_3)+1(\nu_2,\nu_4)$ complex centered at 8000 Å, and the $3(\nu_1,\nu_3)+1(\nu_2,\nu_4)$ complex centered at 10000 Å (Dick & Fink, 1977), are weaker than the 8950 Å band and are not seen in the spectral data. These bands may be masked by K I absorption.

Finally, Hα is also seen in the spectrum of 2MASS 1237+6526, and is further discussed in §5.2; SDSS 1254-0122 shows a much weaker line, evident in Figure 3.22. A redshifted line, likely Hα at z = 0.18, is seen in 2MASS 0755+2212, which originates in an aligned background galaxy. This background source also contributes continuum flux in the blue portion of the spectrum. None of the other T dwarf spectra show emission features.

3.3 Summary

In this chapter, we have presented near-infrared and red optical spectra for a number of T dwarf candidates, confirmed T dwarfs, and late-M and L dwarfs. In general, near-infrared spectra is far more easily acquired given that the peak of the T dwarf spectral energy distribution lies in the 1–2.5 μm region. Optical spectroscopy is much more difficult to obtain, as the cool temperatures of these objects, coupled with the deep and broad Na I and K I doublets, allow little flux to be emitted in this spectral region. This is most obvious in the lack of signal in the blue optical spectrum of 2MASS 1237+6526 (Figure 3.21), although most of the T dwarfs were not detected shortward of 8000 Å.

Both near-infrared and red optical spectral regions show a number of atomic and molecular features, summarized in Tables 3.7 and 3.11. These features appear to vary in a regular way, a fact

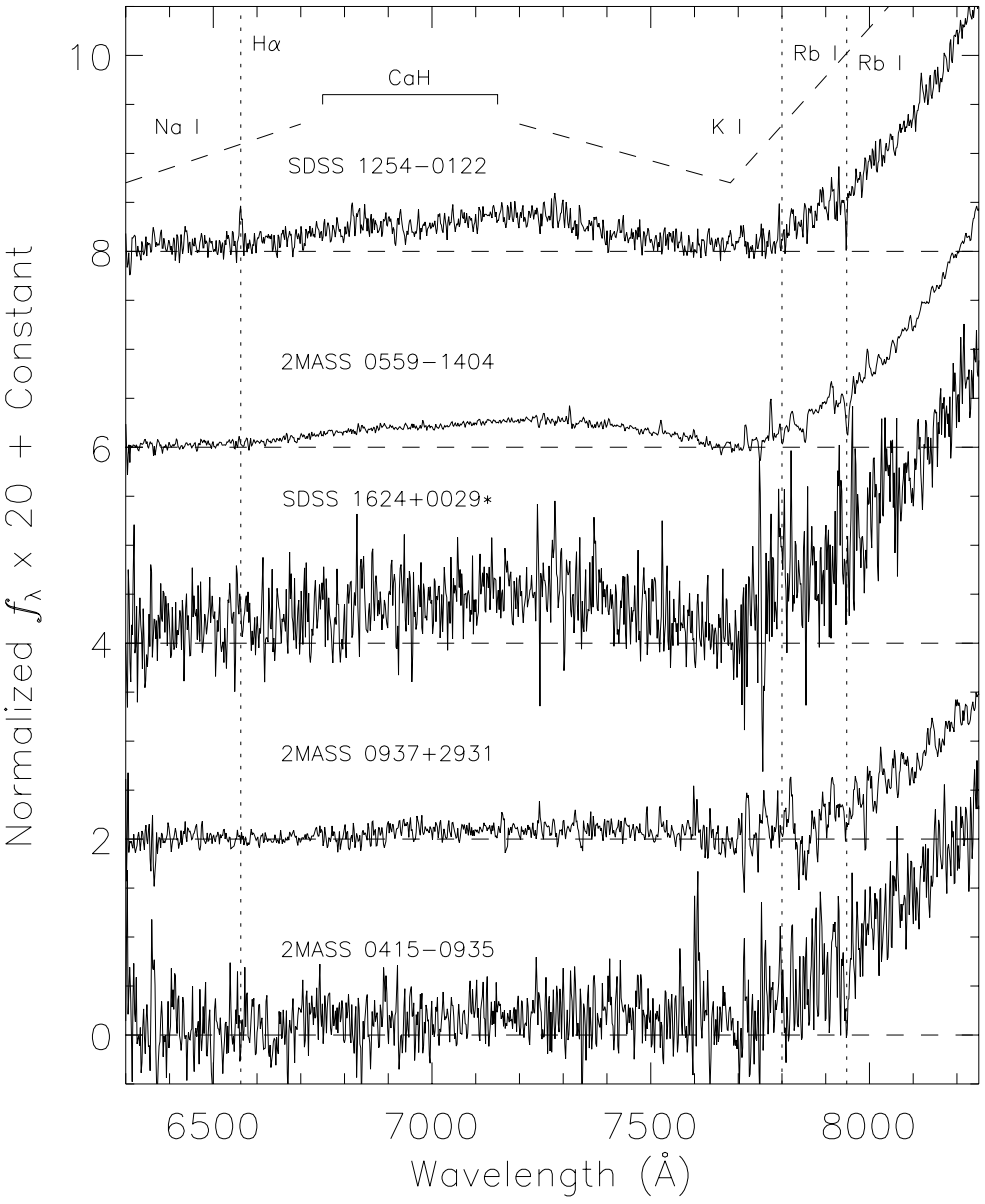

Figure 3.22: Close up of the 6300–8250 Å spectral region for SDSS 1254-0122, 2MASS 0559-1404, SDSS 1624+0029, 2MASS 0937+2931, and 2MASS 0415-0935. Data are normalized at 9250 Å, multiplied by a factor of 20, and offset (dashed line). Flux is detected between the broadened Na I and K I doublets in the first three objects but not the latter two. Note the weak Hα emission in SDSS 1254-0122. Data for SDSS 1624+0029 have not been corrected for telluric absorption

we capitalize on in deriving a spectral classification in Chapter 5. Atomic lines are most prevalent in the red optical region, where the alkalis form both narrow (Cs I and Rb I) and very broad (Na I and K I) spectral features. The cool, high-gravity environments of T dwarf photospheres clearly produce emergent spectra with unique and rich morphologies.

Chapter 4 Gliese 570D

Nerissa: When the Moon shines, we do not see the candle.
Portia: So doth the greater glory dim the less...

- William Shakespeare, *The Merchant of Venice*

Prior to the 2MASS L and T dwarf searches, only two *bona fide* brown dwarf companions had been directly detected, Gliese 229B (Nakajima et al., 1995) and the young L-type brown dwarf G 196-3B (Rebolo et al., 1998)[1]. Most of the early searches for brown dwarf companions were confined to a narrow field of view around the primary (typically 10-60″). Hence, widely-separated companions[2] would have been missed. Indeed, both G 196-3B and Gliese 229B are less than 20″ from their primaries. Field surveys overcome this limitation.

In this chapter we present the discovery of a second T dwarf companion, Gliese 570D, identified as part of our field T dwarf search. In §4.1 we describe the identification of this object as a T dwarf by follow-up imaging and spectroscopy, and establish its companionship to the Gliese 570 system in §4.2. In §4.3 we estimate some of the physical properties of Gliese 570D based on properties of the primary and brown dwarf structure models. Finally, we place Gliese 570D in context with other brown dwarf companions in §4.4. We summarize our results in §4.5.

4.1 Identification

Gliese 570D was initially identified as the field T dwarf candidate 2MASSW J1457150-212148 in the wdb0699 search sample (see §2.4.2.2). Optical images of the Gliese 570D field indicate no optical counterpart and hence R-J $\gtrsim$ 5.5 (Figure 4.1). Follow-up near-infrared imaging carried out using the CTIO 1.5m Infrared Imager (CIRIM) on 1999 July 23 (UT) confirmed this object as a bona-fide T dwarf candidate (see §2.5).

Near-infrared spectroscopy was then obtained using the Ohio State InfraRed Imager/Spectrometer (Depoy et al., 1993, hereafter OSIRIS) at the CTIO Blanco 4m Telescope on 1999 July 27 UT (see §3.1.2); data are shown in Figure 4.2 (bottom), along with OSIRIS data obtained for SDSS 1624+0029 (Strauss et al., 1999) on the same night (top) and a comparison spectrum of Gliese 229B (Geballe et al., 1996, black line). The identifying features of CH_4 and H_2O are readily apparent, confirming this object as a T dwarf. Furthermore, the 1.4 μm H_2O and 1.6 μm CH_4 bands appear to be deeper in Gliese 570D, while there is more flux in the 1.3 μm CH_4 band in SDSS 1624+0029. As H_2O and CH_4 bands are expected to strengthen with decreasing temperatures (Burrows et al., 1997), these features suggest that Gliese 570D is cooler than SDSS 1624+0029.

4.2 Association with the Gliese 570ABC System

In the lower left corner of Figure 4.1 lies the Gliese 570ABC system, comprised of a K4 V primary and a M1.5 V-M3 V close binary (Duquennoy & Mayor, 1988; Mariotti et al., 1990; Forveille et al.,

[1]The companion object GD 165B (Becklin & Zuckerman, 1988) may also be a brown dwarf, although its status remains uncertain (Kirkpatrick et al., 1999a).

[2]We adopt an observational definition for "widely-separated" as angular separation greater than 100″; see Fischer & Marcy (1992).

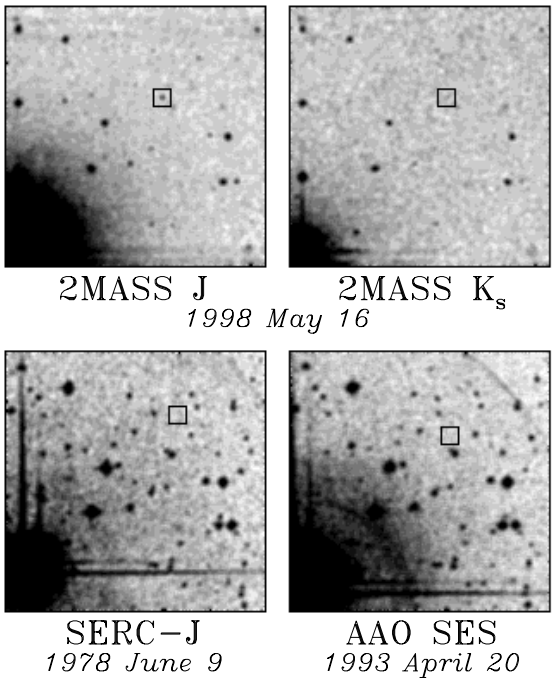

Figure 4.1: 2MASS J- and K_s-band images of Gliese 570D, along with optical images from SERC-J and AAO-SES at two different epochs. Each field is $5' \times 5'$ with North up and East to the left. The Gliese 570ABC triple is seen in the lower left corner (the BC binary is unresolved). Gliese 570D is indicated in the 2MASS images by a $10'' \times 10''$ box, while its projected location due to motion is indicated in each optical image.

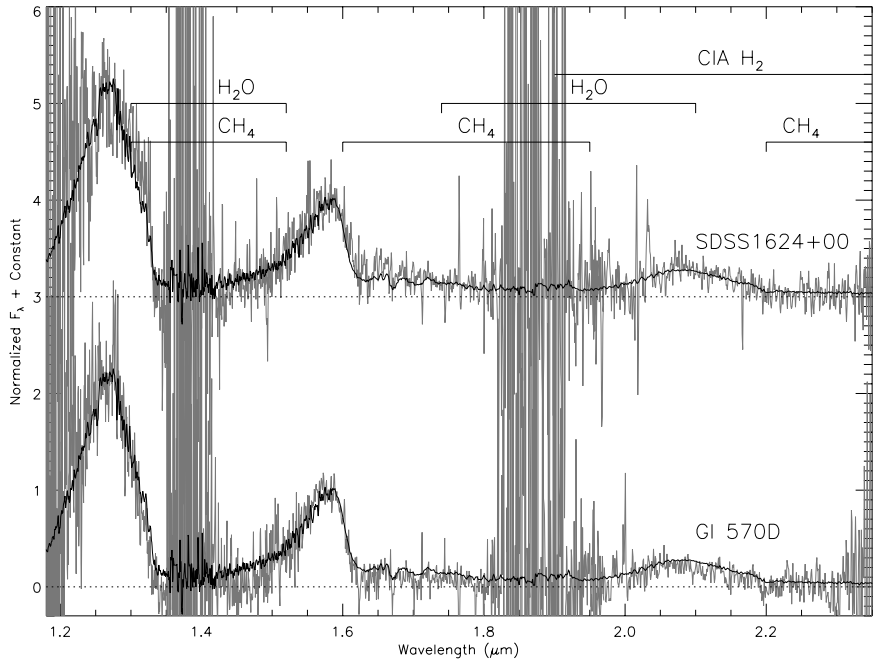

Figure 4.2: Near-infrared spectral data for Gliese 570D (bottom) and SDSS 1624+0029 (top). Both are normalized at 1.55 μm with spectral data for Gliese 229B overlaid for comparison (Geballe et al., 1996, dark line). Spectra are offset for clarity (dashed lines). CH_4 bands at 1.3, 1.6, and 2.2 μm, and H_2O bands at 1.3 and 1.9 μm, are indicated, as is H_2 collision-induced absorption (CIA) longward of about 1.9 μm.

Table 4.1: 2MASS Observations of Gliese 570ABCD.

	1998 May 16 (UT)		1999 July 29 (UT)		Difference	
	RA[a] (1)	Decl. (2)	RA (3)	Decl. (4)	$''$ (5)	$^\circ$ (6)
A[b]	$14^h\ 57'\ 27\farcs87$	$-21^\circ\ 24'\ 52\farcs72$	$14^h\ 57'\ 27\farcs93$	$-21^\circ\ 24'\ 54\farcs87$	2.3±0.4	159±8
BC	$14^h\ 57'\ 26\farcs42$	$-21^\circ\ 24'\ 38\farcs54$	$14^h\ 57'\ 26\farcs49$	$-21^\circ\ 24'\ 40\farcs77$	2.4±0.4	156±7
D	$14^h\ 57'\ 14\farcs96$	$-21^\circ\ 21'\ 47\farcs79$	$14^h\ 57'\ 15\farcs04$	$-21^\circ\ 21'\ 49\farcs82$	2.3±0.4	151±8
J[c]	15.33±0.05		15.07±0.06		0.26±0.08	
H	15.28±0.09		15.37±0.14		−0.09±0.17	
K_s	15.27±0.17		15.26±0.18		0.01±0.24	

[a] All coordinates are equinox J2000.0, with formal uncertainties of $0\farcs15$.
[b] Astrometry for components A, BC, and D.
[c] Photometry for Gliese 570D.

1999) at a distance of 5.91±0.06 pc (Perryman et al., 1997). The T dwarf lies $258\farcs3\pm0\farcs4$ from the primary of this system, a projected separation of 1525±15 AU at the distance of Gliese 570A. The proximity of this object to the Gliese 570 system, in conjunction with its expected distance (d ∼ 11 pc, assuming $M_J = M_J^{(Gl229B)} = 15.52\pm0.09$; Leggett et al. 1999), provide compelling evidence that it is a fourth member of the system. More rigorous proof, however, is found in common proper motion.

4.2.1 Confirming Common Proper Motion

Fortunately, the Gliese 570 system has a relatively large proper motion of $2\farcs012\pm0\farcs002$ yr^{-1} (Perryman et al., 1997), apparent in the two optical images of Figure 4.1; this, coupled with the astrometric accuracy of 2MASS, enabled us to measure the motion of this system with reasonable precision in a one-year time scale. The original 2MASS scan of the Gliese 570D field was taken on 1998 May 16 (UT); a second scan was obtained on 1999 July 29 (UT). Table 4.1 summarizes the resulting astrometric and photometric data. All components have have a common sky motion of $2\farcs3\pm0\farcs4$ at position angle 155±8°, confirming common proper motion and hence association for Gliese 570D. Note the significant difference in J-band magnitudes for this object between the two epochs, ΔJ = 0.26±0.08.

We determined the statistical significance of common proper motion by examining the mean motion of other sources in the two 2MASS scans. We selected objects from the 2MASS Working Database from both scans with detections in all three bands, J < 16, and probabilities of persistence $P_{pers} < 0.5$; we also eliminated sources that were potentially blended (2MASS "blend" flags = 1) or were poorly fit by a typical stellar point spread function. A total of 2069 objects were matched between these fields within a $10''$ radius. Results are shown in Figure 4.3, with Δ ≡ epoch 2 - epoch 1. Gaussian fits to the astrometric separations yield 1σ values of $\langle\Delta\text{R.A.}\rangle = 0\farcs03\pm0\farcs14$ and $\langle\Delta\text{Decl.}\rangle = 0\farcs01\pm0\farcs14$, clearly less than the motion seen in the Gliese 570 system. The separations of Gliese 570A and BC between these two scans are indicated in the lower left plot by open circles; only one object, Gliese 570D, is found to have a similar separation.

We also examined the difference in the observed J magnitude for Gliese 570D between these two epochs. Figure 4.4 shows the shift in J, H, and K_s magnitudes for matched objects in the Gliese 570D field. As expected, deviations between the two epochs are greatest for the faintest objects, reaching ±0.1 mag around J ∼ 15.3. There appears to be a constant offset in the J-band magnitudes of $m_2 - m_1 \sim -0.05$ mag, likely due to differences in telluric absorption between the observations (see

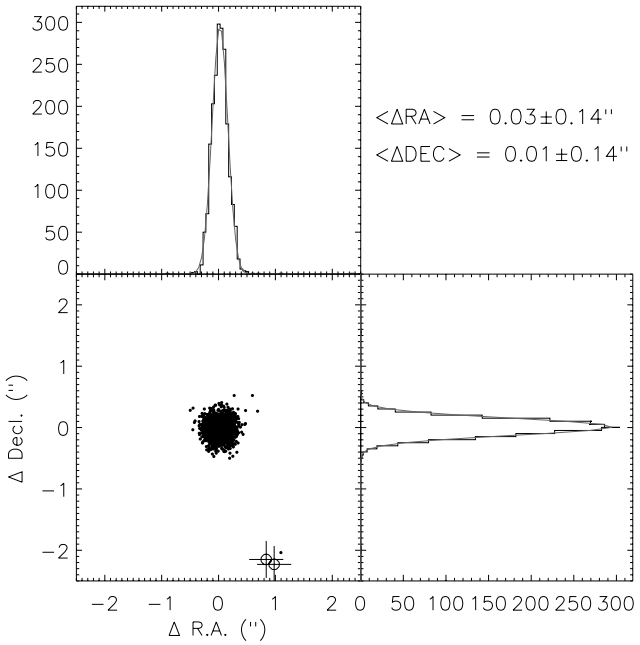

Figure 4.3: Comparison of positions for 2069 sources matched within 10″ between the 1998 May 16 and 1999 July 29 (UT) observations of the Gliese 570D field. Values are computed as $\Delta \equiv$ epoch 2 - epoch 1. The motion of Gliese 570A and BC as measured from this data are indicated as open circles in the lower left plot. Gaussian fits to the astrometric deviations yield 1σ values of $\langle \Delta$R.A.$\rangle$ = 0.″03±0.″14 and $\langle \Delta$Decl.$\rangle$ = 0.″01±0.″14.

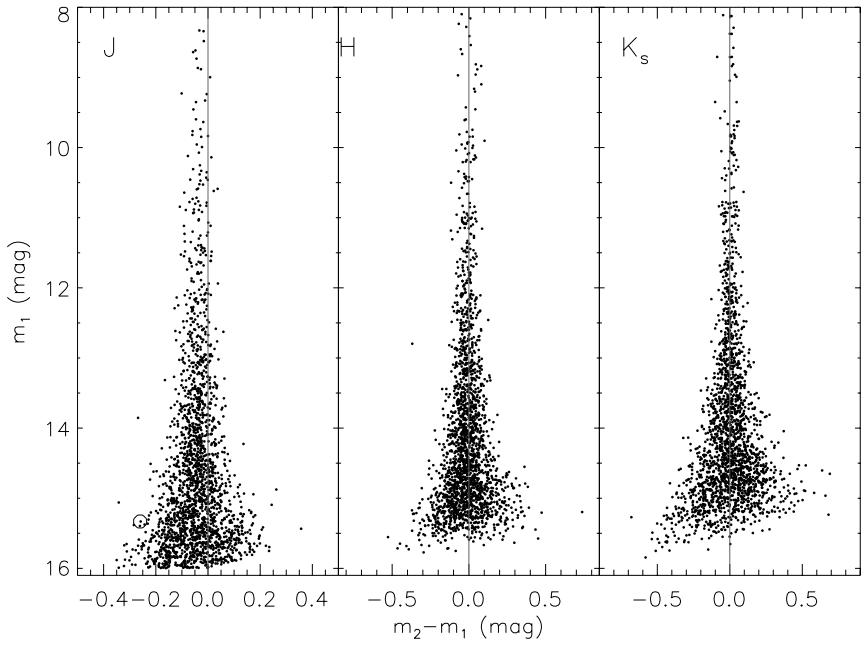

Figure 4.4: Deviations in 2MASS J, H, and K_s photometry between the 1998 May 16 (epoch 1) and 1999 July 29 (epoch 2) for objects in the Gliese 570D field. Zero offsets are indicated by vertical lines. Gliese 570D is indicated in the J panel by an open circle.

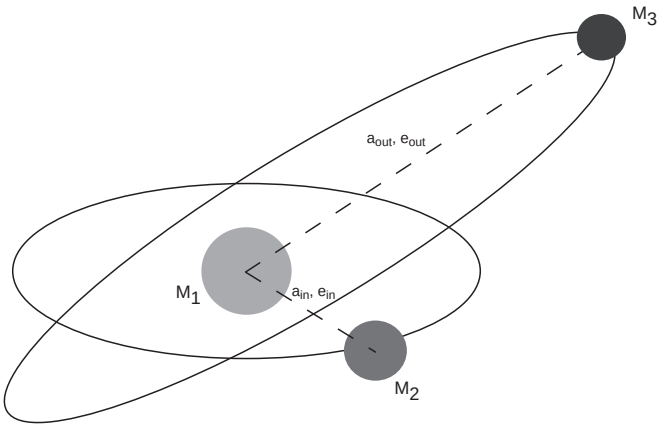

Figure 4.5: Schematic drawing of a triple system defining the variables for the Eggleton & Kiseleva (1995) formalism.

§1.6.2). Such offsets are expected to be corrected in the final reprocessing of the 2MASS database. Gliese 570D is indicated in the J-band panel by an open circle, and while it is clearly separated from the mean scatter in ΔJ, it is not an extreme deviation, approximately 2σ after correcting for the mean offset. Hence the difference in J magnitudes may not be intrinsic to the source; however, monitoring observations would be required to confirm that this is the case. Because the 1998 May 16 (UT) data are included in the 2MASS IDR2, we consider photometry from this epoch to be accurate.

4.2.2 Stability in the Gliese 570ABCD System

The separation of Gliese 570D from its K4 V primary is an order of magnitude larger than the A-BC separation ($24\farcs7\pm0\farcs4$) and over four orders of magnitude larger than the B-C separation of $0\farcs1507\pm0\farcs0007$ (Forveille et al., 1999). We addressed the dynamic stability of this system using the results of Eggleton & Kiseleva (1995). By their formalism (Figure 4.5), stability in a triple system with masses M_1, M_2, and M_3; semimajor axes a_{in} and a_{out}; and eccentricities e_{in} and e_{out}; is met when the ratio of outermost peristron to innermost apestron,

$$Y = \frac{a_{out}(1-e_{out})}{a_{in}(1+e_{in})}, \tag{4.1}$$

is greater than the critical value:

$$Y^{min} = 1 + \frac{3.7}{q_{out}^{1/3}} + \frac{2.2}{q_{out}^{1/3}+1} + \frac{1.4}{q_{in}^{1/3}}\frac{q_{out}^{1/3}-1}{q_{out}^{1/3}+1}, \tag{4.2}$$

where $q_{in} = \frac{M_1}{M_2} > 1$ and $q_{out} = \frac{M_1+M_2}{M_3}$ are the inner and outer mass ratios.

This criterion is clearly met for the Gliese 570ABC sub-system. Adopting $M_1 = 0.586\pm0.007$ $M_\odot$ and $M_2 = 0.390\pm0.005$ $M_\odot$ for the masses of the M dwarf binary (Forveille et al., 1999), M_3

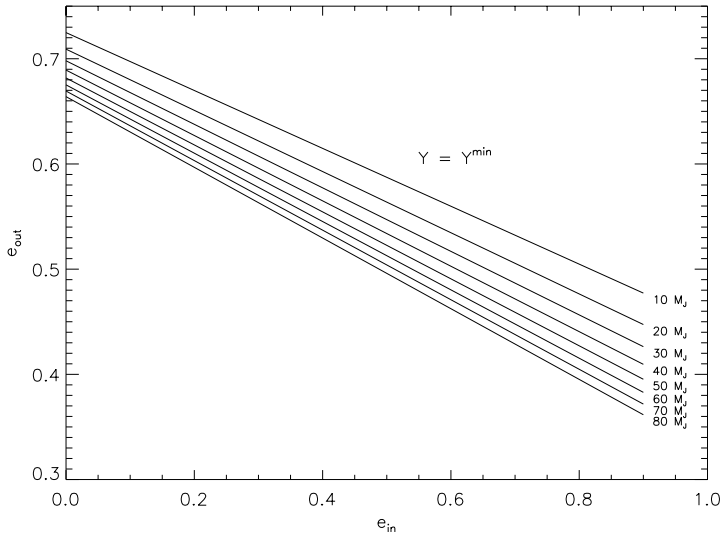

Figure 4.6: Critical values of e_{out} below which the Gliese 570D orbit can be considered stable as a function of e_{in} and M_3 (of Gliese 570D).

= 0.7 $M_\odot$ for Gliese 570A (estimated from the measured mass of the M0Ve eclipsing binary YY Gem; Bopp 1974), a_{in} = 0.″1507±0.″0007 (Forveille et al., 1999), a_{out} = 24.″7±0.″4 (from 2MASS observations), and e_{in} = 0.7559±0.0002 (Forveille et al., 1999), we find that $Y_{BCA} = 93.3(1 - e_{out}) > Y_{BCA}^{min} = 5.97$ for $e_{out} < 0.94$. The Gliese 570ABC triple is clearly a stable system.

To examine the stability of the orbit of Gliese 570D, we consider Gliese 570BC to be a single star with M_1 = 0.976±0.009 $M_\odot$, and use a_{out} = 258.″3±0.″4. Adopting a range of masses for Gliese 570D, 0.01 ≤ M_3 ≤ 0.08 $M_\odot$, and a range of inner orbit eccentricities, 0.0 ≤ e_{in} ≤ 0.9, we calculated the critical e_{out} below which the Gliese 570D orbit can be considered stable. Figure 4.6 diagrams the results. The worst case scenario (high mass secondary, eccentric inner orbit) has a limit of $e_{out} <$ 0.36; more moderate values of e_{in} = 0.4 and M_3 = 0.05 $M_\odot$ yield $e_{out} < 0.58$. The size of the Gliese 570D orbit allows for large values of e_{out}; hence, we cannot state with absolute confidence that the Gliese 570D orbit is stable over many periods. A more rigorous analysis using measured orbital parameters is unfortunately restricted by the roughly 40,000-year orbit of Gliese 570D around the Gliese 570ABC barycenter.

4.3 Estimates of the Physical Properties of Gliese 570D

The known distance of Gliese 570D enables us to determine its physical properties — luminosity, effective temperature, and mass — based on the properties of the Gliese 570A primary and theoretical structure models. A rough estimate of the first two quantities can be made by comparing Gliese 570D to the well-studied T dwarf companion Gliese 229B, and using basic properties of brown dwarfs. Gliese 570D has M_J = 16.47±0.07, M_H = 16.42±0.10, and M_{Ks} = 16.41±0.18, nearly a magnitude fainter than Gliese 229B at all three near-infrared bands (Leggett et al., 1999). If we assume a Gliese 229B J-band bolometric correction of 2.19±0.10 (Leggett et al., 1999) and a radius of (7.0±0.5)×10^9 cm ≈ 1 Jupiter radius (Burrows & Liebert, 1993), we derive L = (2.8±0.3)×10^{-6} $L_\odot$ and T_{eff} =

Table 4.2: Age Diagnostics for Gliese 570A = HD 131977 = HR 5568.

Diagnostic (1)	Measurement (2)	Ref. (3)	Age Estimate (4)
SpT	K4 V	Keenan & McNeil (1989)	
	M1.5 V (BC)	Keenan & McNeil (1989)	
B−V	1.024±0.015	Henry et al. (1996)	
$[Fe/H]$	$+0.16^{-0.02}_{+0.00}$	Allende Prieto & Lambert (2000)	$\tau < 6.5$ Gyr
	0.08±0.05	Thoren & Feltzing (2000)	
	0.00±0.12	Feltzing & Gustafsson (1998)	
W_{Li} (mÅ)	< 3	Strassmeier et al. (2000)	$\tau > 0.3$ Gyr
log R'$_{HK}$	−4.21	Strassmeier et al. (2000)	$0.01 < \tau < 0.80$ Gyr
	−4.484	Henry et al. (1996)	
log L_X (erg s^{-1})	27.54±0.04	Hünsch et al. (1999)	$0.60 < \tau << 4.5$ Gyr
	27.72	Fleming, Schmitt & Giampapa (1995)	
	28.11	Bookbinder (1985)	
	27.34	Harris & Johnson (1985)	
	28.90±0.22	Walter et al. (1980)	
U,V,W (km s^{-1})	+43.2,-19.9,-37.6	Strassmeier et al. (2000)	$2 < \tau < 10$ Gyr[a]
P_{rot} (days)	40	Cumming, Marcy, & Butler (1999)	$6 < \tau < 9$ Gyr
	44.6[c]	Saar & Osten (1997)	

[a]Old disk kinematic group (Eggen, 1989; Leggett, 1992).
[b]Luminosity in the wavelength range 0.1–2.4 (Hünsch et al., 1999; Fleming, Schmitt & Giampapa, 1995, ROSAT), 0.2–4 (Bookbinder, 1985, EINSTEIN), 0.15–0.4 (Harris & Johnson, 1985), and 0.15–0.3 keV (Walter et al., 1980). Results from Bookbinder (1985) are reported in Mathiondakis & Doyle (1989).
[c]Estimated from $v \sin i$.

750±50 K. This temperature is roughly 200 K cooler than Gliese 229B, making Gliese 570D the least luminous and coolest brown dwarf so far detected.

4.3.1 Characterizing the Gliese 570 System

Determining the mass of Gliese 570D can be done using brown dwarf evolutionary models, but only if we can constrain its age (τ). To do this, we examined age diagnostics for the brighter K and M dwarf components, and assumed coeval formation[3]. Lachaume et al. (1999) have recently compiled a number of age-dating techniques for main sequence stars. Table 4.2 summarizes the various measures used by these techniques, which generally fall into three categories: composition, activity, and kinematics. Note that another method described by Lachaume et al. (1999), isochrone dating, is generally useful for early-type stars (B9 – G5), but inadequate for Gliese 570A, a K4 V.

4.3.1.1 Composition

Through stellar processing, the metallicity of the Galaxy increases with time, so that stars formed at early times are generally metal-poor as compared to stars formed more recently. This implies that the composition of a star, generally traced through the [Fe/H] ratio, can be used to date that star. In general, however, this practice is fairly inaccurate except for the most extreme metallicities, given the spread of abundances seen in coeval cluster stars due to chemical inhomogeneity (Carraro, Ng, & Portinari, 1998), and general uncertainties in determining abundances from photospheric compositions (Lachaume et al., 1999). Figure 4.7 plots the metallicities of F and G stars in moving

[3]This assumption may not be accurate if Gliese 570D were somehow captured into its current configuration. However, given the lack of orbital information for this object, the simplest case is a coeval multiple system.

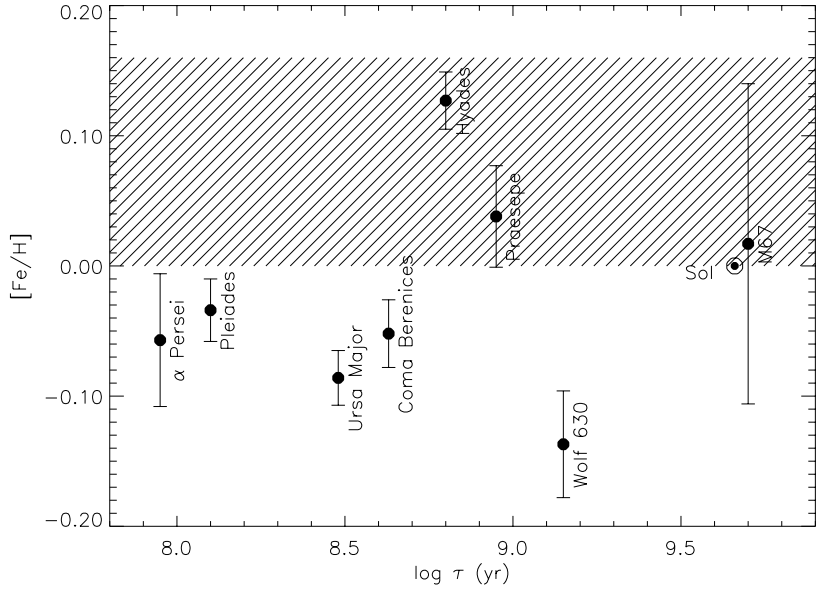

Figure 4.7: Metallicities of F and G dwarfs in moving groups as a function of age. [Fe/H] values are from Friel & Boesgaard (1992); ages are from Friel & Boesgaard (1992); Hambly et al. (1995); Perryman et al. (1998); Stauffer, Schultz, & Kirkpatrick (1998); Stauffer et al. (1999). The range in [Fe/H] measurements for Gliese 570A are indicated by the hatched region (Allende Prieto & Lambert, 2000; Thoren & Feltzing, 2000; Feltzing & Gustafsson, 1998).

groups with known ages (Boesgaard, 1989; Boesgaard & Friel, 1990; Friel & Boesgaard, 1992), with the spread in values of [Fe/H] for Gliese 570A (Allende Prieto & Lambert, 2000; Thoren & Feltzing, 2000; Feltzing & Gustafsson, 1998) indicated by the hatched area. While the slightly super-solar composition of Gliese 570A suggests an older age (e.g., at least as old as the Hyades), the scatter in cluster values makes this measure quite uncertain. Age limits from Lachaume et al. (1999) yield a range of $-\infty < \tau < 6.5$ Gyr, fairly unrestrictive.

Lithium, which is destroyed in the core of a star by the thermonuclear reaction

$$^7Li + p \longrightarrow ^4He + ^4He (Q = 17.347 MeV), \tag{4.3}$$

is generally a better tracer of age, particularly in F and G dwarfs (Boesgaard, 1991). K dwarfs, which have fully convective interiors, destroy Li in relatively short time scales. Figure 4.8 shows the Li 6708 Å equivalent width (W_{Li}) as a function of B-V color for a number of clusters with well-defined ages (Stauffer et al., 1989; Soderblom et al., 1993a,b,c). Strassmeier et al. (2000) have determined an upper limit of $W_{Li} < 3$ mÅ for Gliese 570A, less than the equivalent widths of K dwarfs in the Pleiades (125 Myr), but equivalent to upper limits for K dwarfs in Ursa Major (300 Myr) and Praesepe (660 Myr). Hence, this limit indicates a minimum age $\tau \gtrsim 0.3$ Gyr.

4.3.1.2 Activity

Activity has long been used as an age indicator because of the observed correlation between magnetic field strength and rotation speed (Noyes et al., 1984), which is expected to decrease over time due

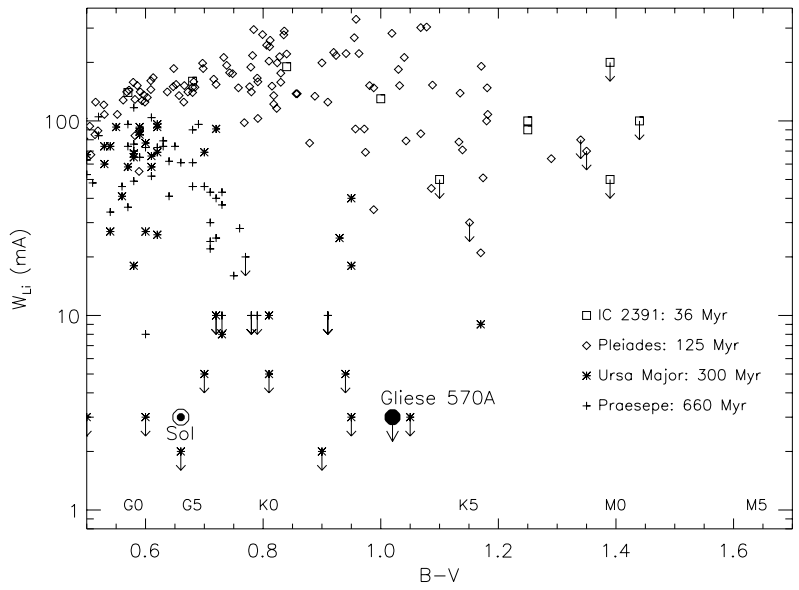

Figure 4.8: 6708 Å Li equivalent width (W_{Li}) versus B-V color for the moving groups IC 2391 (Stauffer et al., 1989, squares), Pleiades (Soderblom et al., 1993b, diamonds), Ursa Major (Soderblom et al., 1993c, asterisks), and Praesepe (Soderblom et al., 1993a, pluses). Upper limits are indicated with downward arrows. An upper limit measure $W_{Li} < 3$ mÅ for Gliese 570A as measured by Strassmeier et al. (2000) is indicated by the solid circle. Rough spectral type calibrations from Drilling & Landolt (2000) are listed along the bottom.

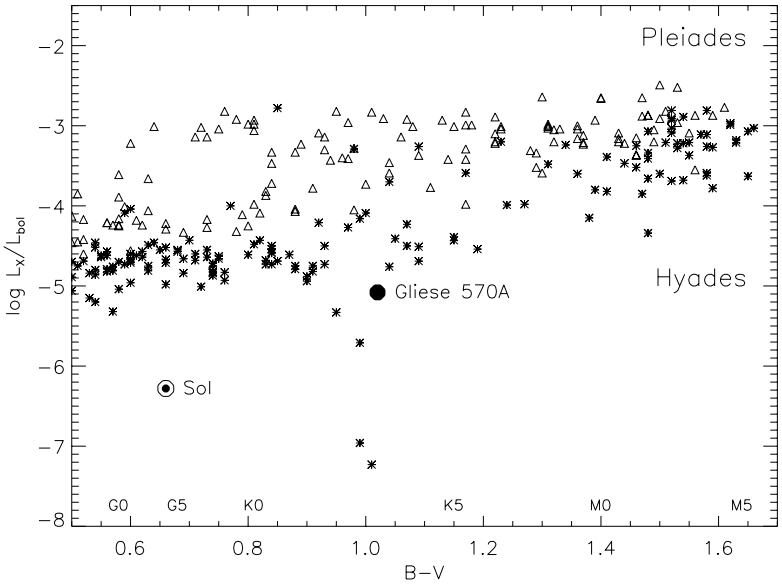

Figure 4.9: Relative X-ray luminosity, $\log L_X/L_{bol}$, versus B-V color for objects in the Pleiades (Krishnamurthi, 1998; Micella et al., 1999, triangles) and Hyades (Stern, Schmitt, & Kahabka, 1995; Hemplemann et al., 1995, asterisks). Measures for Gliese 570A (Fleming, Schmitt & Giampapa, 1995) and the Sun (Maggio et al., 1987) are indicated. Rough spectral type calibrations from Drilling & Landolt (2000) are listed along the bottom.

to angular momentum loss (Skumanich, 1972; Walter & Barry, 1991). Activity in F-K dwarfs can be measured in either X-ray luminosity (L_X) or emission in the Ca II H and K lines. The former quantity has been measured for Gliese 570A by a variety of instruments (Walter et al., 1980; Harris & Johnson, 1985; Bookbinder, 1985; Fleming, Schmitt & Giampapa, 1995), most recently by the ROSAT instrument (Hünsch et al., 1999), resulting in $L_X = (3.5\pm0.3)\times10^{27}$ erg s^{-1} (Hünsch et al., 1999), implying a relative X-ray luminosity of $\log L_X/L_{bol} = -5.08$ (Fleming, Schmitt & Giampapa, 1995). Figure 4.9 compares the emission of this object to those of G and K dwarfs in the Pleiades (Krishnamurthi, 1998; Micella et al., 1999), Hyades (Stern, Schmitt, & Kahabka, 1995; Hemplemann et al., 1995), and the Sun (Maggio et al., 1987). The X-ray luminosity of Gliese 570A is only slightly less than that of K dwarfs in the Hyades, suggesting a minimum age of 625 Myr (Perryman et al., 1998). Its relative brightness compared to the Sun implies that this object is much younger than 4.5 Gyr.

Ca II H and K emission is typically quantified by the parameter R'_{HK}, which measures the ratio of emission to photospheric flux, defined as (Noyes et al., 1984):

$$R'_{HK} = \frac{F_{HK} - F_{phot}}{\sigma T_{eff}^4}, \tag{4.4}$$

where F_{HK} and F_{phot} are the total fluxes in the H and K lines and photosphere, respectively, measured at the stellar surface. Soderblom, Duncan, & Johnson (1991) have demonstrated that ratio is correlated with age in main sequence stars. Measurements for Gliese 570A (Henry et al.,

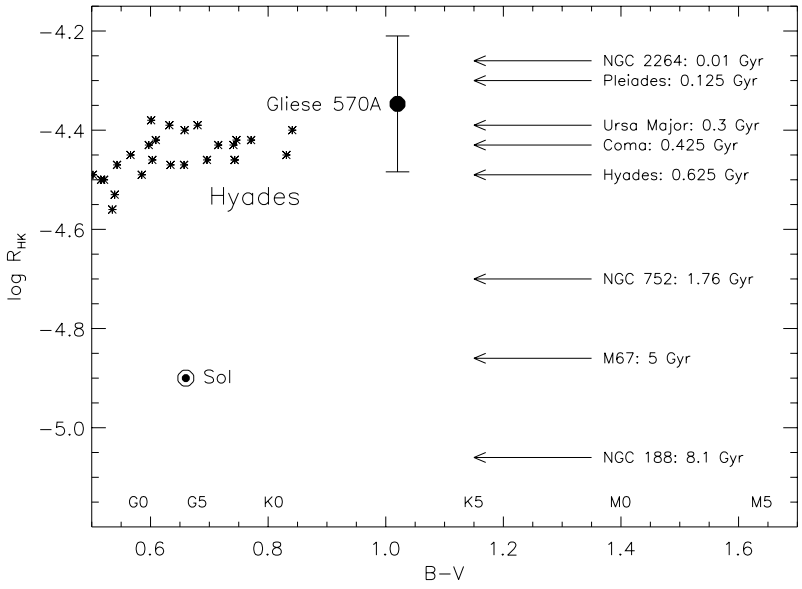

Figure 4.10: Ca II HK emission in main sequence stars of the Hyades (Duncan et al., 1984); the Sun (Baliunas, Sokoloff, & Soon, 1996); and mean values for G and K dwarfs in NGC 2264 (10 Myr), Pleiades (125 Myr), Ursa Major (300 Myr), Coma Bernices (425 Myr), Hyades (625 Myr), NGC 752 (1.76 Gyr), M67 (5 Gyr), and NGC 188 (8.1 Gyr) from Soderblom, Duncan, & Johnson (1991). The mean value for Gliese 570A, $\log R'_{HK} = -4.35 \pm 0.14$ (Henry et al., 1996; Strassmeier et al., 2000) is indicated by the solid circle. Rough spectral type calibrations from Drilling & Landolt (2000) are listed along the bottom.

1996; Strassmeier et al., 2000) yield $\log R'_{HK} = -4.35 \pm 0.14$. We compare this value to measurements of objects in the Hyades (Duncan et al., 1984); the Sun (Baliunas, Sokoloff, & Soon, 1996); and mean values for G and K dwarfs in NGC 2264 (10 Myr), Pleiades (125 Myr), Ursa Major (300 Myr), Coma Bernices (425 Myr), Hyades (625 Myr), NGC 752 (1.76 Gyr), M67 (5 Gyr), and NGC 188 (8.1 Gyr) from Soderblom, Duncan, & Johnson (1991). Again, Gliese 570A appears to be at least as active as early K dwarfs in the Hyades, and the range in R'_{HK} implies an age of 10-625 Myr.

Because HK emission appears to be an accurate age indicator, a number of analytical expressions have been derived using the R'_{HK} index. Rocha-Pinto & Maciel (1998), extending the relation derived by Soderblom, Duncan, & Johnson (1991) to include metallicity terms, define the relation (valid for $\log R'_{HK} > -4.75$ and -1.2 < [Fe/H] < 0.4):

$$\log \tau(Gyr) = -6.943 - 1.5 \log R'_{HK} - 1.382[Fe/H] - 0.213[Fe/H]^2 + 0.270[Fe/H]^3, \quad (4.5)$$

which yields a range of $140 < \tau_{CE} < 600$ Myr. The activity-age relation of Lachaume et al. (1999) for $\log R'_{HK} > -4.6$,

$$\log \tau(Gyr) = -22.64 - 5 \log R'_{HK}, \quad (4.6)$$

yields a chromospheric age of 25–600 Myr. Finally, the emission relation of Donahue (1993, given in Henry et al. 1996),

$$\log \tau(Gyr) = 1.725 - 1.334R_5 + 0.4085R_5^2 - 0.0522R_5^3, \quad (4.7)$$

where $R_5 = 10^5 \times R'_{HK}$, gives a chromospheric age of 0.6–800 Myr. Hence, activity relations generally indicate a young age for the Gliese 570 system, roughly 0.01–0.80 Gyr.

4.3.1.3 Kinematics

The kinematics of Gliese 570A presents a different story, however. The U, V, W space motions of this object place it into the "old disk" population (Eggen, 1989; Leggett, 1992, 2–10 Gyr), and the total velocity, $|v| = 64$ km s^{-1}, is clearly more consistent with an older population of stars. The minimum statistical age based on the random walk analysis of Lachaume et al. (1999)[4],

$$\tau_{min} = max \left\{ 0, \frac{|v^2| + B^2}{A} \right\}, \quad (4.8)$$

ranges from 0.6 to 3.3 Gyr, significantly larger than the minimum ages estimated from activity diagnostics.

Gliese 570A also has a long rotation period, 40–45 days (Saar & Osten, 1997; Cumming, Marcy, & Butler, 1999). This is consistent with a longer lifetime due to the expected spin-down of a star over time, scaling approximately as $P_{rot} \propto \tau^{\alpha}$, where $1/e \lesssim \alpha \lesssim 1/2$ (Skumanich, 1972; Walter & Barry, 1991). As shown in Figure 4.11, the period of Gliese 570A is significantly longer than those of K dwarfs in both the Pleiades (Hemplemann et al., 1995; Krishnamurthi, 1998) and Hyades (Hemplemann et al., 1995; Stern, Schmitt, & Kahabka, 1995), as well as the Sun (Howard, 2000). Lachaume et al. (1999) gives a functional form for main-sequence stellar spin-down as

$$\log \tau(Gyr) = 2.667 \log P(days) - 0.994(B - V) - 0.309[Fe/H] - 3.530, \quad (4.9)$$

which yields $6 < \tau < 9$ Gyr for Gliese 570A.

[4]Extending the classical results of Wielen (1977).

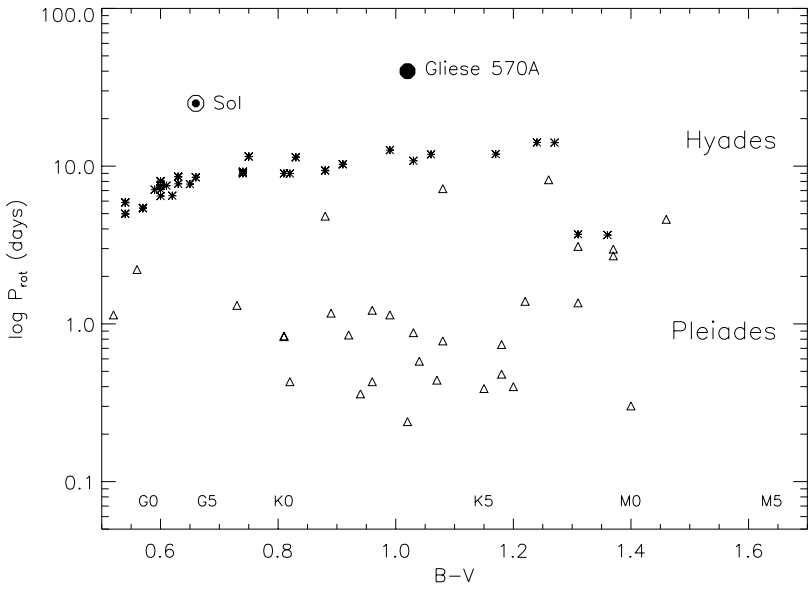

Figure 4.11: Rotation periods for objects in the Pleiades (Hemplemann et al., 1995; Krishnamurthi, 1998) and Hyades (Hemplemann et al., 1995; Stern, Schmitt, & Kahabka, 1995), as compared to the rotation period of Gliese 570A (Saar & Osten, 1997; Cumming, Marcy, & Butler, 1999) and the Sun (Howard, 2000). Rough spectral type calibrations from Drilling & Landolt (2000) are listed along the bottom.

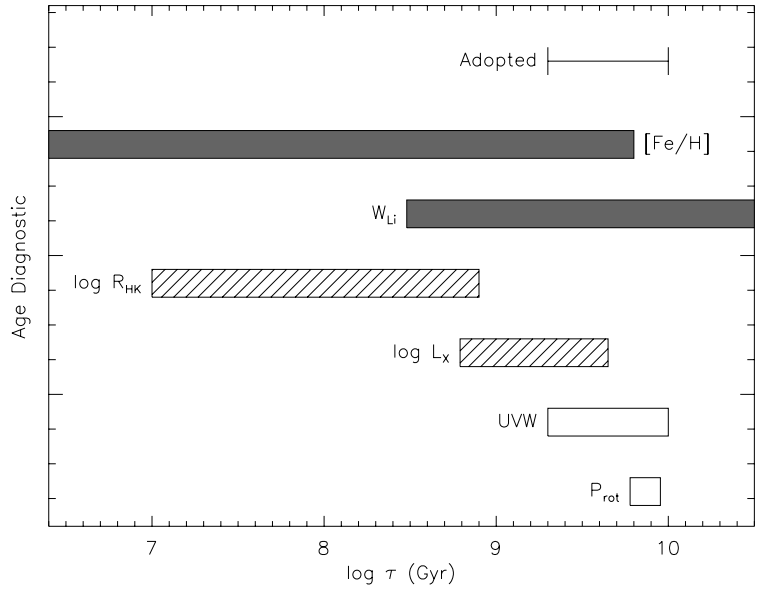

Figure 4.12: Age estimates for Gliese 570A from Table 4.2. The adopted age of 2–10 Gyr is indicated.

4.3.1.4 The Age of the Gliese 570 System

Age estimates from the diagnostics described above are diagrammed in Figure 4.12. Activity age estimates generally indicate ages coeval with the Hyades (625 Myr), while kinematic ages are significantly older. Lithium abundance generally supports the older kinematic ages but is consistent with the X-ray age. Recently, Gaidos, Henry, & Henry (2000) have identified an object with similar activity and kinematic properties, the K0 V star HD 10780, which has a rotation period and Li abundance consistent with solar age (4.5 Gyr), but exhibits enhanced X-ray and Ca II emission, over a magnitude stronger than that of the Sun. The low $v \sin i \sim 0.6$ km s^{-1} for this object (Fekel, 1997) appears to be consistent with high inclination (Gaidos, Henry, & Henry, 2000), and increased Ca II activity may result from direct observation of the magnetic poles. Gliese 570A also has a low $v \sin i \sim 1.2$ km s^{-1} (Fekel, 1997), and may lie in the same viewing geometry, with similarly enhanced activity compared to its kinematic age. Assuming this to be the case, we give precedence to the kinematic diagnostics and adopt an age of 2–10 Gyr for the Gliese 570 system. Note that this is roughly consistent with the estimates of Geballe et al. (2001a), who assign an age of 2–5 Gyr.

4.3.2 The Mass of Gliese 570D

Using the evolutionary models of Burrows et al. (1997) and assuming an age $\tau = 6\pm4$ Gyr and L $= (2.8\pm0.3)\times10^{-6}$ L$_\odot$, we derive values of T$_{eff}$ = 810±45 K and M = 52±16 M$_{Jup}$. The effective temperature is consistent with the brightness estimate above, and is significantly lower than that of Gliese 229B. For comparison, Geballe et al. (2001a) derive $\log L/L_\odot = -5.53\pm0.01$, T$_{eff}$ = 804±20 K, and M = 43±9 M$_{Jup}$, assuming an age of 2–5 Gyr and using synthetic bolometric corrections and evolutionary models from Burrows et al. (1997).

Table 4.3: Comparison of Gliese 229B and Gliese 570D.

	Gliese 229B[a] (1)	Gliese 570D (2)
J	14.33±0.05	15.33±0.05
H	14.35±0.05	15.28±0.09
K_s	14.42±0.05	15.27±0.17
J-H	−0.02±0.07	0.05±0.11
H-K_s	−0.07±0.07	0.01±0.11
J-K_s	−0.09±0.07	0.06±0.23
d (pc)	5.77±0.04	5.91±0.06
M−m	1.19±0.07	1.14±0.05
M_J	15.52±0.06	16.47±0.07
ρ, P.A. ($''$, °)	7.8±0.1, 163	258.3±0.4, 316 (A-D)
		234.1±0.4, 317 (BC-D)
ρ (AU)	44.9±0.6	1525±15 (A-D)
		1385±15 (BC-D)
$[Fe/H]$[c]	−0.6–0.4	0.00–0.16
τ (Gyr)	0.5–1.0	2–10[d]
$\log L/L_\odot$	−5.18±0.04	−5.56±0.05[d]
T_{eff} (K)	960±70	810±45[d]
$\log g$ (cm s^{-2})	5.12±0.22	5.25±0.21[d]
M (M_{Jup})	43±12	52±16[d]

[a]Data from Nakajima et al. (1995); Marley et al. (1996); Leggett et al. (1999).
[b]Parallax data from Perryman et al. (1997).
[c]Metallicity of primary; ranges for Gliese 229A from Schiavon, Barbuy, & Singh (1997), while those for Gliese 570D are from Table 4.2.
[d]Geballe et al. (2001a) give values of $\log L/L_\odot = -5.53\pm0.01$, $T_{eff} = 804\pm20$ K, $\log g = 5.14\pm0.14$ cm s^{-2}, and M = 43±9 M_{Jup} for $2 < \tau < 5$ Gyr.

4.4 Comparison to Other Brown Dwarf Companions

Companion brown dwarfs, through their association with brighter, well-studied primaries, comprise a useful sample for examining the evolution and physics of substellar objects. In the past few years, a number of brown dwarf companions have been identified through imaging campaigns, including a number of widely-separated companions identified by 2MASS. It is compelling, therefore, to examine how Gliese 570D, the least luminous substellar companion so far identified, compares with its contemporaries.

4.4.1 Gliese 570D versus Gliese 229B

One obvious object to compare against Gliese 570D is the first T dwarf companion identified, Gliese 229B. Parameters for these two objects are listed in Table 4.3. As previously mentioned, Gliese 570D is roughly one mag fainter than Gliese 229B at all bands, which is reflected in its diminished luminosity and effective temperature. The greater age of Gliese 570D implies that, despite being cooler, it may actually be more massive than Gliese 229B. This possibility accentuates the difficulty of basing comparisons of brown dwarfs on brightness and/or temperature alone, and the importance of age determinations in deriving the physical properties of substellar objects.

The initial spectrum of Gliese 570D (Figure 4.2) indicated deeper bands of H_2O and CH_4 in

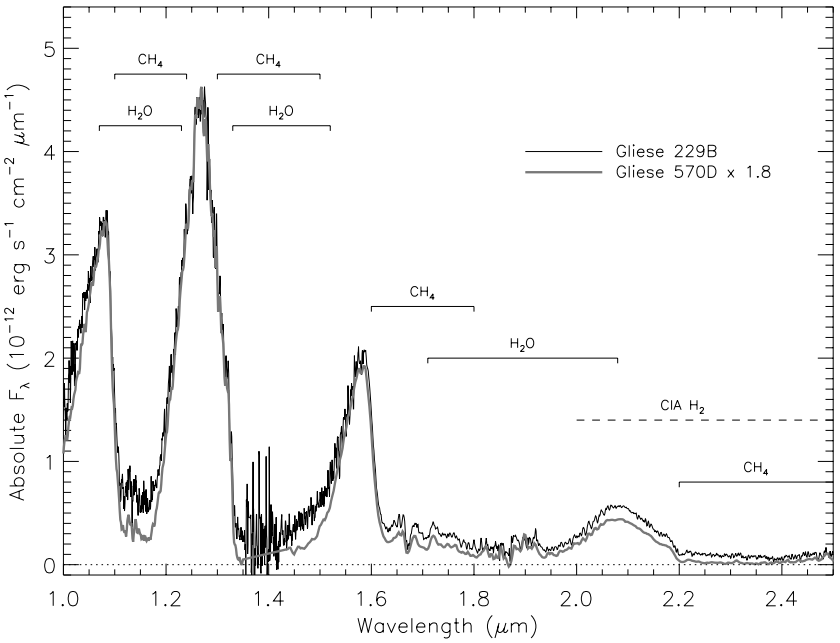

Figure 4.13: Near-infrared spectral data for Gliese 570D (Geballe et al., 2001a, thick grey line) compared to that of Gliese 229B (Geballe et al., 1996, black line). Spectra are in absolute flux units, with data for Gliese 570D scaled by a factor of 1.8. H_2O, CH_4, and CIA H_2 absorption features are indicated.

Gliese 570D as compared to SDSS 1624+0029. When we compare the spectrum of Gliese 570D (Geballe et al., 2001a) to that of Gliese 229B (Geballe et al., 1996), we find similiar differences in band strengths (Figure 4.13). Both H_2O and CH_4 bands are stronger in Gliese 570D, and the K-band peak is more suppressed relative to J and H. The similarity in metallicities (roughly solar) and gravities between the two objects confirms that these differences are temperature-dependent effects. We will exploit this fact in Chapter 7 in the derivation of a spectral sequence.

4.4.2 Other Brown Dwarf Companions

Besides Gliese 570D and Gliese 229B, a number of brown dwarf companions to stars have been identified in the past few years, including several widely-separated companions discovered by 2MASS (Gizis, Kirkpatrick, & Wilson, 2001; Kirkpatrick et al., 2001a,b; Wilson et al., 2001b). The properties of the 2MASS objects are summarized in Table 4.4, while Table 4.5 lists the data for other brown dwarf companions recently identified (Becklin & Zuckerman, 1988; Henry & Kirkpatrick, 1990; Nakajima et al., 1995; Rebolo et al., 1998; Goldman et al., 1999; Lowrance et al., 1999, 2000; Martín et al., 2000b). As diagrammed in Figure 4.14, these objects span a broad range in age (6 Myr to $\sim$ 10 Gyr), T_{eff} (750 to 2800 K), and mass (20 M_J to the Hydrogen-burning mass limit). The association of these objects with (generally) well-studied primaries make them useful tracers of substellar evolution. In particular, companions with moderately wide separations (seven objects have $a \gtrsim 30''$) are well-suited for detailed observational investigation. Closely-separated objects (e.g., Gliese 229B) may provide dynamic mass measurements and orbital parameters over the next few decades. One brown dwarf companion, Gliese 569 Bab, has been resolved as a double itself (Martín et al., 2000b), and mass measurements for this pair have provided the first empirical constraints for brown dwarf structure models (Kenworthy et al., 2001; Lane et al., 2001).

The detection of many widely-separated companions is at odds with the observed dirth in closely-separated substellar secondaries to nearby main sequence stars, what has come to be known as the "brown dwarf desert" (Halbwachs et al., 2000; Marcy & Butler, 2000). Radial-velocity studies indicate that less than 0.5% of F-M dwarfs have substellar companions down to 10 M_J within 3 AU, a rigorous result given the unambiguous radial velocity signature such an object would produce. A survey of 107 stellar systems in the northern hemisphere within 8 pc by Oppenheimer et al. (2001) resulted in only one brown dwarf detection between 40 and 100 AU, Gliese 229B (Nakajima et al., 1995). These detection rates are in contrast to the 13.3% of G dwarfs which have stellar companions in these separation ranges (Duquennoy & Mayor, 1991). Gizis et al. (2001a) have shown statistically that the absence of closely-separated brown dwarfs does not carry out to wider distances (d > 1000 AU), where the frequencies of stellar and substellar companions are nearly equal. These authors predict more than four times as many widely-separated brown dwarf companions than closely-separated, unlike the roughly equal numbers of stellar secondaries in the same separation bins.

These preliminary results (based on only three widely-separated substellar companions identified at that time) provide tantalizing clues into the origins of brown dwarf secondaries versus planets, and may indicate that brown dwarfs (say $M > 13\ M_{Jup}$) cannot form in the vicinity of a stellar disk. Interestingly enough, none of the companions discovered to date have masses below the deuterium burning limit (Chabrier & Baraffe, 2000, $M \sim 0.013\ M_\odot$), which Shu, Adams, & Lizano (1987) propose as a minimum mass for isolated (i.e., star-like) formation. Cluster surveys are currently pushing down to these masses (Zapatero Osorio et al., 1999, 2000; Lucas & Roche, 2000; Najita, Tiede, & Carr, 2000), but convincing detections of objects well below the deuterium limit have yet to be made. Hence, a brown dwarf "mass desert" may exist, yielding substantial insight into the formation of planetary and substellar objects.

Table 4.4: 2MASS Brown Dwarf Companions.

	G216-7B[a] (1)	HD 89744B (2)	GJ 1048B (3)	Gliese 618.1B (4)	Gliese 417B (5)	Gliese 584C (6)	Gliese 337C (7)	Gliese 570D (8)
Type	M9.5 V	L0 V	L1 V	L2.5 V	L4.5 V	L8 V	L8 V	T8 V
Primary	M0 V	F7 V/IV	K2 V	M0 V	G0 V	G1 V+G3 V	G8 V+K1 V	K4 V+M1.5 V+M3 V
J	13.35±0.03	14.89±0.04	13.67±0.12	15.31±0.05	14.57±0.04	16.32±0.11	15.70±0.08	15.33±0.05
H	12.68±0.03	14.04±0.05	12.98±0.10	14.32±0.05	13.47±0.04	15.00±0.07	14.59±0.08	15.28±0.09
K_s	12.15±0.03	13.62±0.05	12.32±0.08	13.59±0.04	12.69±0.05	14.24±0.07	14.02±0.06	15.27±0.17
d (pc)[b]	18.9±0.7	39.0±1.1	21.3±0.5	30.3±2.4	21.7±0.4	18.6±0.4	20.5±0.4	5.91±0.06
M−m	−1.38±0.08	−2.96±0.06	−1.64±0.05	−2.41±0.17	−1.68±0.04	−1.35±0.05	−1.56±0.04	1.14±0.02
ρ ($''$)	$33.''6$	$63.''1$	$11.''9$±$0.''4$	$35.''9$	90	194	43	$258.''3$±$0.''4$
ρ (AU)	635	2460	250±10	1090	2000	3600	880	1525±15
P.A. ($^\circ$)			252		245	136		316
T_{eff}	1950–2200	2000–2200	1900–2200	1800–1950	1650–1950	1300–1600	1300–1600	750–820
τ (Gyr)	> 0.6	1.5–3.0	0.6–1.0	0.5–1.2	0.08–0.3	1.0–2.5	0.6–3.4	2–5
Mass ($M_\odot$)	0.06–0.08	0.07–0.08	0.055–0.075	0.06–0.08	0.02–0.05	0.045–0.075	0.04–0.07	0.035–0.070
Li I EW(Å)[c]			< 1		11.5	7.4		–
CPM?	Yes			Yes	Yes	Yes	Yes	Yes
q[d]	0.10–0.13	0.05–0.06	0.09–0.11	0.08–0.10	0.02–0.05	0.05–0.08	0.02-0.04	0.05–0.10
Ref.	1	2	3	2	4	4	2	5,6

[a]Kirkpatrick et al. (2001b) hypothesize that the primary of this system may be an unresolved binary.
[b]Parallax measurements of primaries from Perryman et al. (1997).
[c]Indicator of substellarity (Rebolo, Martín, & Magazzu, 1992).
[d]Companion mass ratio, q = M_{sec}/M_{prim}, where primary masses have been estimated from Drilling & Landolt (2000).
REFS – (1) Kirkpatrick et al. (2001b); (2) Wilson et al. (2001b); (3) Gizis, Kirkpatrick, & Wilson (2001); (4) Kirkpatrick et al. (2001a); (5) Burgasser et al. (2000b); (6) Geballe et al. (2001a).

Table 4.5: Other Brown Dwarf Companions.

	HR 7329B (1)	Gliese 569 Bab[a] (2)	TWA-5B (3)	G 196-3B (4)	GD 165B (5)	GJ 1001B (6)	Gliese 229B (7)
Type	M7/8 V	M8.5 V+M9 V	M8.5/9 V	L2 V	L4 V	L5 V	T6.5 V
Primary	A0 V	M2.5 V	M1.5 T-Tauri	M2.5 V	DA4	M4 V	M1 V
J		10.61±0.05[b]		14.90±0.05	15.55±0.06	13.10±0.03	14.32±0.05[c]
H	11.93±0.06[d]		12.14±0.06[d]	13.67±0.07	14.55±0.09	12.05±0.02	14.35±0.05[c]
K_s		9.45±0.05[b]		12.81±0.13	14.06±0.07	11.40±0.03	14.42±0.05[c]
d (pc)[e]	47.4±1.5	9.81±0.16	55±16	20±6[f]	31.5±2.5	9.55±0.10	5.77±0.04
M−m	−3.39±0.07	0.04±0.04	−3.7±0.6	−1.5±0.7	−2.49±0.17	0.10±0.02	1.19±0.02
ρ ($''$)	$4\farcs2$	$5\farcs0$	$2\farcs0$	$16\farcs2$	$3\farcs7$	$18\farcs6$	$7\farcs8\pm0\farcs1$
ρ (AU)	190	50	110	320	120	180	44.9±0.6
P.A. (°)	169	17	2	210	191	258	163
T_{eff}	2400–2800	2075–2225	2400–2700	1600–2000	1700–2000	1600–1900	890–1030
τ (Gyr)	0.02–0.03	0.12–1.0	0.006–0.018	0.02–0.3	1.2–5.5	> 1	0.6–5.0
Mass ($M_\odot$)	0.03–0.05	0.101–0.150	0.015–0.040	0.02–0.05	0.07–0.08	0.06–0.08	0.02–0.06
Li I EW(Å)[g]				6	< 0.7	< 0.2	–
CPM?	Yes	Yes	Yes	Yes	Yes	Yes	Yes
q[h]	0.01–0.02	0.2–0.3	0.03–0.08	0.04–0.10	0.12–0.13	0.15–0.20	0.03–0.10
Ref.	1,2	3,4,5,6	7,8	9,10	11,12	13	14,15

[a] This double system separated by $0\farcs101\pm0\farcs002$ (Martín et al., 2000b) has an orbital period of 892±25 days (Lane et al., 2001). Values given are for the combined pair, including the total measured mass (Lane et al., 2001).
[b] JK photometry from Lane et al. (2001).
[c] JHK photometry from Leggett et al. (1999).
[d] F160W photometry from Lowrance et al. (1999, 2000).
[e] Parallax measurements of primaries from Perryman et al. (1997) except for TWA-5B (Lowrance et al., 1999) and GD 165B (Kirkpatrick et al., 2001a).
[f] Photometric parallax from Kirkpatrick et al. (2001a).
[g] Indicator of substellarity (Rebolo, Martín, & Magazzu, 1992).
[h] Companion mass ratio, $q = M_{sec}/M_{prim}$, where primary masses have been estimated from Drilling & Landolt (2000).
Refs – (1) Lowrance et al. (2000); (2) Guenther et al. (2000); (3) Henry & Kirkpatrick (1990); (4) Martín et al. (2000b); (5) Kenworthy et al. (2001); (6) Lane et al. (2001); (7) Lowrance et al. (1999); (8) Neuhäuser et al. (2000); (9) Rebolo et al. (1998); (10) Kirkpatrick et al. (2001a); (11) Becklin & Zuckerman (1988); (12) Kirkpatrick et al. (1999a); (13) Goldman et al. (1999); (14) Nakajima et al. (1995); (15) Marley et al. (1996).

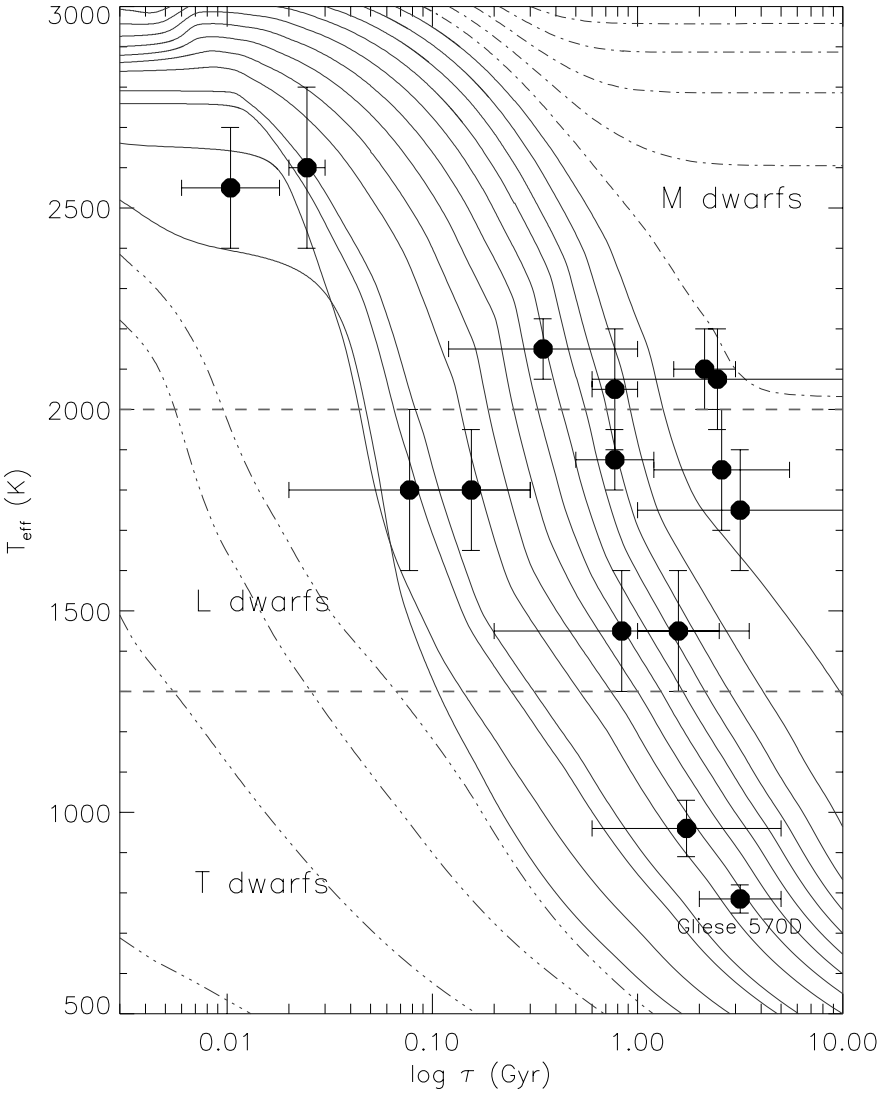

Figure 4.14: Age and T_{eff} estimates for identified brown dwarf companions listed in Tables 4.4 and 4.5. Evolutionary models from Burrows et al. (1997) for masses below the deuterium-burning limit (0.001, 0.005, 0.01, 0.125 $M_{\odot}$; dot-dot-dot-dashed lines), deuterium-burning brown dwarfs (0.015, 0.02, 0.025, 0.03, 0.035, 0.04, 0.045, 0.05, 0.055, 0.06, 0.065, 0.07, 0.075 $M_{\odot}$; solid lines), and Hydrogen-burning stars (0.08, 0.085, 0.09, 0.095, 0.10 $M_{\odot}$; dot-dashed lines) are indicated. The approximate temperature ranges for M, L, and T dwarfs are shown by horizontal dashed lines (Kirkpatrick et al., 1999b, 2000).

4.5 Summary

In this chapter we have presented the discovery and characterization of Gliese 570D, a widely-separated (a = 258.″3±0.″4) T dwarf companion to the low-mass triple system Gliese 570ABC. This object is a full magnitude fainter than Gliese 229B, and is indeed the intrinsically faintest object imaged outside of the Solar System to date. Analysis of age diagnostics for Gliese 570A, structure models from Burrows et al. (1997), and empirical constraints from Gliese 229B allow us to determine the physical properties of this object: $\tau = 6\pm4$ Gyr, L = $(2.8\pm0.3)\times10^{-6}$ $L_{\odot}$, $T_{eff} = 810\pm45$ K, and M = 52±16 M_{Jup}. Comparison of this spectrum of Gliese 570D to that of Gliese 229B indicates that several temperature diagnostics exist in the near-infrared, including the deepening of CH_4 and H_2O bands, and the suppression of the 2.1 μm peak by CIA H_2. Gliese 570D is one example of a growing list of widely-separated brown dwarf companions to stars identified by 2MASS. Collectively, these and other substellar companions comprise a useful sample for investigating brown dwarf formation and evolution.

MEDIA RELATIONS OFFICE
JET PROPULSION LABORATORY
CALIFORNIA INSTITUTE OF TECHNOLOGY
NATIONAL AERONAUTICS AND SPACE ADMINISTRATION
PASADENA, CALIF. 91109 TELEPHONE (818) 354-5011
http://www.jpl.nasa.gov

Contact: Michelle Viotti (818) 354-8774

FOR RELEASE: 9:20 a.m. EST, January 15, 2000

ASTRONOMERS REVEAL COOLEST SOLAR NEIGHBOR EVER IMAGED

Today astronomers announced that they have reached an all-time low -- low temperatures, that is. Adam Burgasser and Davy Kirkpatrick at the California Institute of Technology in Pasadena, CA, have identified the coolest body ever imaged outside of the solar system, a brown dwarf that lies only 19 light years from the Earth.

"Brown dwarfs are essentially failed stars," explains Burgasser, a Caltech physics graduate student who is heading up the investigation of these objects as his doctoral thesis project. "They are too small to ignite nuclear reactions in their cores, so they simply fade with time."

This newest brown dwarf discovery was imaged by the Two Micron All Sky Survey (2MASS), a project whose goal is to image the entire sky at near-infrared wavelengths. 2MASS is a collaborative effort between the University of Massachusetts and Caltech's Infrared Processing and Analysis Center (IPAC). Optical photographs obtained as part of the first-generation Palomar Observatory Sky Survey (POSS-I) were converted into digitial form at the U. S. Naval Observatory in Flagstaff, Arizona, and compared against the 2MASS data. This comparison revealed that the object had no associated optical counterpart, implying that it was most likely a very cool object shining primarily at near-infrared wavelengths. Burgasser confirmed the object's status as a brown dwarf by taking its spectral "fingerprint" using a spectrograph constructed by The Ohio State University at the National Science Foundation's 4-meter (160-inch) Victor M. Blanco telescope. This telescope is located at the Cerro Tololo Interamerican Observatory (CTIO) outside of La Serena, Chile.

The 2MASS discovery image, taken in 1998 during routine survey operations from the 2MASS southern observatory also located at Cerro Tololo, Chile, showed that the brown dwarf lay in close proximity to a nearby triple star system called Gliese 570ABC, located in the constellation Libra. A second 2MASS image taken 14 months later confirmed that the brown dwarf was in fact a previously undetected fourth member of this system. "Gliese 570ABC moves across the sky very slightly every year, undetectable with the naked eye but detectable with a telescope. The triple star and the brown dwarf moved the same distance and in the same direction, which means that they are part of the same stellar family," said Burgasser.

Using the known distance to Gliese 570ABC and the brightness of the brown dwarf itself, Burgasser and Kirkpatrick, senior staff scientist at IPAC and a member of the 2MASS team, computed that the object's temperature must be only 500 degrees Celsius (900 degrees Fahrenheit), or just one and a half times warmer than the maximum setting on a conventional kitchen oven. "This makes it the coolest star-like object ever imaged beyond our Solar System," says Kirkpatrick.

The spectral "fingerprint" that Burgasser obtained shows that the brown dwarf contains methane as well, a trait also shared by planets such as Jupiter and Saturn but not by stars. Although the new discovery, now dubbed Gliese

570D, shows methane and is believed to be roughly the same size as Jupiter itself, it is believed to be roughly 50 times more massive. "The dividing line between planets and stars was once obvious," says Burgasser, "but we are now finding objects that really blur that distinction."

The 2MASS telescopes are in the midst of a 3-1/2-year survey of the entire sky. IPAC's processing of the 20 terabytes of raw survey data will create a publicly accessible catalog of 300 million stars and over one million galaxies. Already, 6% of the sky -- more than 20 million objects -- has been released to the public. Nearly one-half of the sky -- almost 200 million objects -- will be publicly available early in 2000. The 2MASS project is based at the University of Massachusetts, Amherst. The JPL/Caltech Infrared Processing and Analysis Center combines and processes 2MASS images into usable data and serves those catalogs and images to the public.

As part of NASA's Origins Program, 2MASS is funded by NASA's Office of Space Science and the National Science Foundation. Results from 2MASS will benefit future Origins missions, including Space Infrared Telescope Facility and the Next Generation Space Telescope. JPL manages the program for NASA's Office of Space Science, Washington, DC. JPL is a division of the California Institute of Technology, Pasadena, CA.

CTIO is a division of the National Optical Astronomy Observatories (NOAO). NOAO is operated by the Association of Universities for Research in Astronomy (AURA), Inc., under co-operative agreement with the National Science Foundation.

Additional 2MASS information and images are available at
http://www.ipac.caltech.edu/2mass

2MASS information and images are also available at
http://pegasus.phast.umass.edu

For more information:
Mr. Adam Burgasser (626-397-7014, diver@its.caltech.edu)
Dr. Davy Kirkpatrick (626-397-7002, davy@ipac.caltech.edu)

Chapter 5 2MASS 1237+6526

Doubt me, my dim companion!
Emily Dickinson, *Complete Poems, III.5*

5.1 Introduction

Activity is an important parameter in the study of stellar populations. Numerous investigations of late-type (F-M) stars have shown correlations between emission (e.g., Ca II H & K, Mg II h & k, Balmer series, X-ray, etc.) and fundamental parameters such as age, rotation, and metallicity (Wilson, 1963; Kraft, 1967; Skumanich, 1972; Powell, 1972; Pallavicini et al., 1981; Noyes et al., 1984). It is generally believed that the majority of optical emission occurs in the chromosphere via collisional heating by ions and electrons along magnetic field lines. Indeed, this hypothesis is supported by the observed correlation of activity and rotation in late-type stars, which is expected if magnetic fields are generated by an internal dynamo (Parker, 1955, e.g., α-Ω dynamo). The observed decrease in activity as stars age can be attributed to spin-down due to angular momentum loss in stellar winds (Stauffer & Hartmann, 1986).

As we examine cooler M and L dwarfs, however, these relations begin to break down. As stars become fully convective (~ 0.3 M$_\odot$), the α-Ω dynamo mechanism becomes ineffective, as it requires a low-buoyancy, radiative/convective boundary to anchor flux lines (Spiegel & Weiss, 1980). However, the observed activity level remains roughly constant around this transition point (Hawley, Gizis, & Reid, 1996), suggesting a turbulent dynamo as an alternate magnetic field source (Durney, De Young, & Roxburgh, 1993). Indeed, flaring activity, which is magnetically driven, is seen in objects as late as M9.5 V (Liebert et al., 1999; Reid et al., 1999a; Martín, Zapatero Osorio, & Lehto, 2001), supporting the existence of substantial magnetic fields beyond the convective cut-off. Alternately, acoustic heating could sufficiently heat the chromosphere (Schrijver, 1987; Mathioudakis & Doyle, 1992) to produce a "basal flux" of Hα emission. In either case, Gizis et al. (2000) have shown that the fraction of objects with measurable emission rises to 100% at spectral type M7 V, then rapidly declines, so that no emission is seen in types L5 V or later (Kirkpatrick et al., 2000). The decrease in (steady) activity even encompasses objects with rapid rotation (Basri & Marcy, 1995; Tinney & Reid, 1998), at odds with trends in hotter stars. Whether this drop in emission is due to ineffective chromospheric heating, decreased magnetic activity, or some other mechanism is unclear, but the end of the main sequence appears to signal a clear change in activity.

Based on the results of Gizis et al. (2000), we would not expect significant activity in T dwarfs. Nonetheless, we have observed Hα in emission in 2MASS 1237+6526. In §5.2, we discuss the detection and persistent emission of this line, and place it in context with other cool dwarfs. In §5.3, we discuss possible mechanisms for the observed emission, and present our hypothesis of an interacting brown dwarf binary. We discuss follow-up photometric monitoring observations to test the binary hypothesis in §5.4, and discuss the constraint imposed by the lack of detected variability. Finally, in §5.5 we compare 2MASS 1237+6526 to the unusually active M9.5 Ve PC 0025+0447 (Schneider et al., 1991). We summarize our results in §5.6.

5.2 Hα in 2MASS 1237+6526

5.2.1 Initial Detection

Hα in 2MASS 1237+6526 was initially detected in red optical (6300–10100 Å) spectra obtained on 1999 July 16–18 (UT) using the Low Resolution Imaging Spectrograph (Oke et al., 1995, hereafter LRIS) mounted on the Keck 10m Telescope[1] (see §3.2). Figure 5.1 shows the reduced data for 2MASS 1237+6526, SDSS 1346-0031 (Tsvetanov et al., 2000), and SDSS 1624+0029 (Strauss et al., 1999), all obtained during this observing run. Some of the features listed in Table 3.11 are indicated, including H_2O absorption from 9250–9800 Å, a possible weak band of CH_4 centered at 8950 Å, Cs I lines at 8521 and 8943 Å, and FeH at 9896 Å detected in the spectrum of SDSS 1624+0029. The pressure-broadened resonant K I doublet at 7665 and 7699 Å, which is prominent in the spectra of L dwarfs (Kirkpatrick et al., 1999b), is masking most of the flux between 7300 and 8100 Å in all three objects (Liebert et al., 2000b). Note that no telluric correction was applied to these data, so residual atmospheric bands of H_2O and O_2 remain.

Hα emission at 6563 Å is clearly seen in the spectrum of 2MASS 1237+6526, and is quite unexpected given the cool nature of this object. Great care was taken to verify its presence over three nights of observation. The emission spike was clearly seen in the raw data and is not spatially extended, ruling out the possibility of a background HI region or possibly telluric emission. Hα was detected in five observations and two different instrument settings spanning the nights of 1999 July 16–18 (UT), with the emission full-width at half-maximum equivalent to the instrumental resolution ($\sim$ 5 pixels). Hence, we can safely rule out the possibility of a chance cosmic ray. Finally, since no emission at 6563 Å is seen in the other T dwarfs, which were reduced using the same bias and flat-field exposures, we can rule out detector features or reduction artifacts. The Hα emission line is thus quite real.

Figure 5.2 shows a close-up of the spectral region around the Hα line for these three objects. Four sets of observations for 2MASS 1237+6526 are shown, excluding data from July 17 in which the object appears to have been improperly placed on the slit, resulting in a poor signal-to-noise spectrum. Not only is the emission persistent between July 16 and 18, but it also remains steady to within 35%. Table 5.1 lists the Hα line flux for each spectrum, which were obtained by integrating the data within 20 Å of the emission peak after subtracting off the neighboring pseudo-continuum, the scatter of which was used to estimate uncertainties. The mean line flux for the July 16 observations is $\langle f_{H\alpha} \rangle = (6.6 \pm 0.6) \times 10^{-17}$ erg cm^{-2} s^{-1}.

We then computed the relative Hα luminosity for each spectrum, $\log L_{H\alpha}/L_{bol} = \log f_{H\alpha}/f_{bol}$, where

$$\log f_{bol} = -0.4 m_{bol} - 4.61 \tag{5.1}$$

in units of erg cm^{-2} s^{-1} (Drilling & Landolt, 2000), and $m_{bol} = m_J + \mathrm{BC}_J$ is the apparent bolometric magnitude. Using the 2MASS J-band magnitude for 2MASS 1237+6526 and $\mathrm{BC}_J = 2.09 \pm 0.10$ (Leggett et al., 1999, determined from measurements of Gliese 229B[2]), we derive $m_{bol} = 18.12 \pm 0.14$ and a mean $\log L_{H\alpha}/L_{bol} = -4.3$.

Spectral data from 1999 July 18 (UT) were obtained using the 300 lines mm^{-1} grating blazed at 5000 Å, and covered the wavelength range 3800–8650 Å (see §3.2.1.4). Reduced data are shown in Figure 3.21. This region samples the Hβ line at 4861 Å, which was undetected at the limit $f_{H\beta} < 2 \times 10^{-17}$ erg cm^{-2} s^{-1}. The resulting Balmer emission ratio on 1999 July 18 (UT) was $f_{H\beta}/f_{H\alpha} < 0.24$.

[1] Earlier data obtained using the Palomar 200" Double Spectrograph (Oke & Gunn, 1982) had insufficient signal-to-noise at these wavelengths to unambiguously detect the emission line (see §2.3.2.4).

[2] Gliese 229B and 2MASS 1237+6526 have the same spectral type, T6.5 V (Table 7.7); hence, differences in the bolometric correction should be negligible.

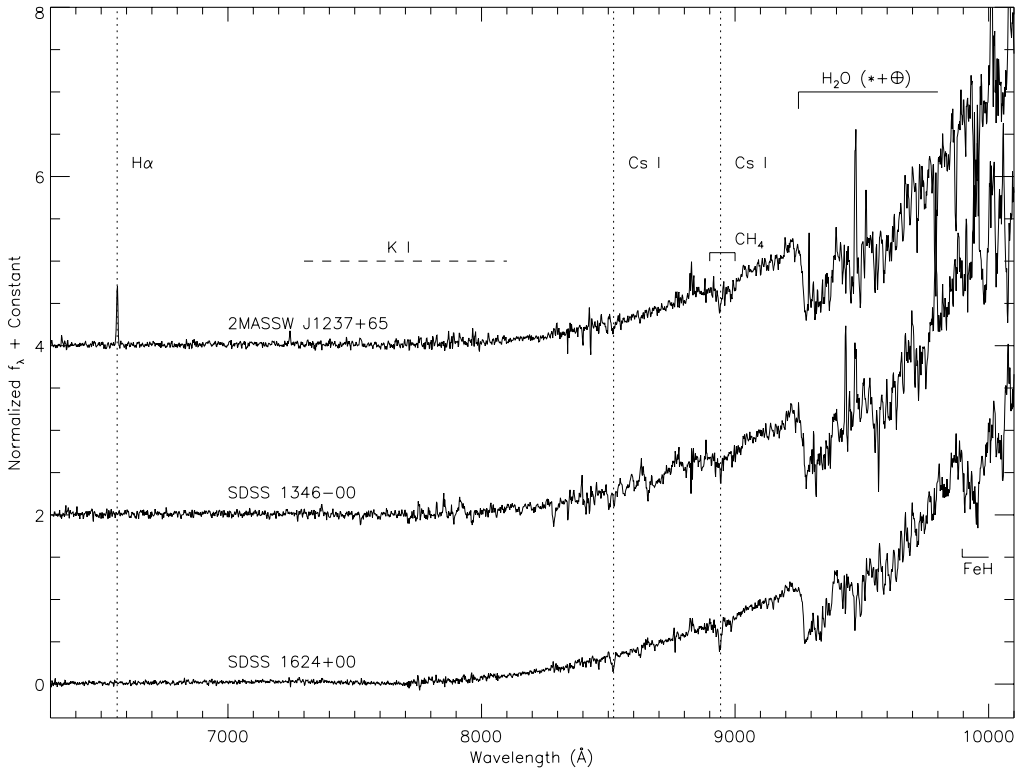

Figure 5.1: LRIS optical spectra of 2MASS 1237+6526, SDSS 1346-0031, and SDSS 1624+0029, obtained on 1999 July 16–18 (UT). Spectra are normalized at 9200 Å, with data for SDSS 1346-0031 and 2MASS 1237+6526 vertically offset by constants of 2 and 4, respectively. Common features — the K I resonant doublet (broadened to $\sim$ 7300-8100 Å), Cs I (8521 and 8943 Å), CH_4 (8950 Å), and H_2O (9250 Å, stellar and telluric) — are indicated, as is the 0-0 band of FeH (9896 Å) in SDSS 1624+0029. Spectra are not corrected for telluric absorption. Hα at 6563 Å is unambiguously seen in 2MASS 1237+6526.

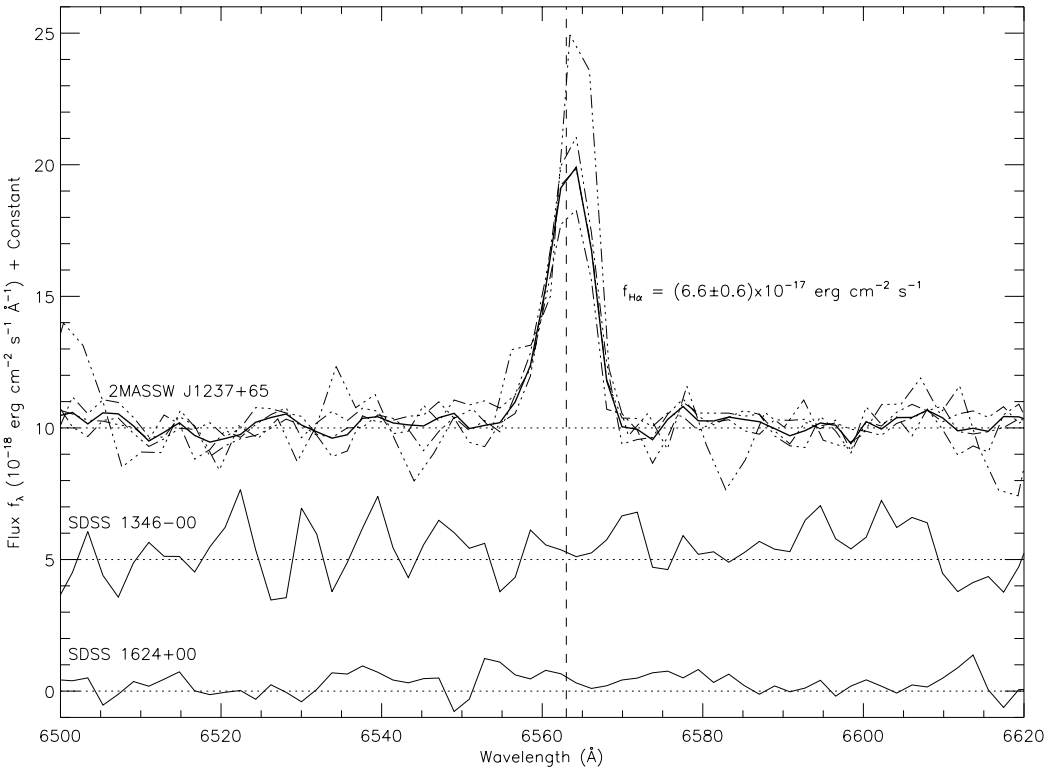

Figure 5.2: A close-up of the Hα feature in 2MASS 1237+6526. Four sets of observations are shown for this object by dash-dotted lines, while the mean from the 1999 July 16 (UT) data is indicated by a solid thick line. The spectra of SDSS 1346-0031 and SDSS 1624+0029 are also shown for comparison. Zero levels are indicated by dotted lines.

Table 5.1: Emission Measurements for Three T dwarfs.

	Observation (UT)					
Object	Date/Time	t_{int} (s)	$f_{H\alpha}$ [a]	$\log(L_{H\alpha}/L_{bol})$ [b]	$f_{H\beta}$ [a]	$\log(L_{H\beta}/L_{bol})$ [b]
(1)	(2)	(3)	(4)	(5)	(6)	(7)
2MASS 1237+6526	1999 July 16 06:21	1200	5.95±0.13	−4.4	–	–
2MASS 1237+6526	1999 July 16 06:40	1800	7.06±0.09	−4.3	–	–
2MASS 1237+6526	1999 July 16 07:15	1800	6.76±0.04	−4.3	–	–
SDSS 1624+0029	1999 July 16 08:27	3600	<0.4 [d]	<−5.8	–	–
SDSS 1346−0031	1999 July 17 07:00	2700	<0.7 [d]	<−5.4	–	–
2MASS 1237+6526 [c]	1999 July 17 07:56	1800	1.68±0.08	−4.9	–	–
2MASS 1237+6526	1999 July 18 11:07	1800	8.50±0.30	−4.2	<2.0 [d]	<−4.8

[a] In units of 10^{-17} erg cm^{-2} s^{-1}.
[b] Assuming BC_J = 2.09±0.10 (Leggett et al., 1999).
[c] The object appears to have been improperly placed in the slit for this observation, so that the entire spectrum is depressed by a factor of ≈ 2. Data are included only to show detection of Hα.
[d] Upper limits based on the continuum noise and spectral resolution of 9 Å (Hα) and 12 Å (Hβ).

Table 5.2: Hα Line Strengths.

Observation (UT)		Uncorrected	Corrected	Corrected	
Date/Time (1)	t_{int} (s) (2)	λ_c[a] (3)	$f_{H\alpha}$[b] (4)	$f_{H\alpha}$[b] (5)	$\log L_{H\alpha}/L_{bol}$ (6)
1999 July 16 06:21[c]	4800	6563.6	6.9±0.3	6.9±0.3	−4.3
1999 July 17 07:56	1800	6565.3	1.6±0.5	3.4±1.0	−4.6
1999 July 18 06:39[d]	1800	6564.4	8.4±1.4	6.8±1.1	−4.3
2000 March 5 13:54	1800	6560.4	2.9±0.3	7.4±0.6	−4.3
2001 February 20 11:07	2400	6563.6	10.6±0.3	7.9±0.2	−4.2

[a]In units of Å, assuming 0.5 Å uncertainty.
[b]In units of 10^{-17} erg cm^{-2} s^{-1}.
[c]Measured from the combined spectrum from 1999 July 16 (UT), as opposed to the average value listed in §5.2.1.
[d]Data obtained in the 3800–8600 Å regime.

5.2.2 Persistent Emission

One feasible explanation for the emission in 2MASS 1237+6526 is the presence of a flare. We examined this possibility by monitoring the Hα line, obtaining additional spectra using LRIS on 2000 March 5 and 2001 February 20 (UT). Data acquisition and reduction procedures (including telluric corrections) are described in §3.2.1.2. Reduced data are shown in Figure 5.3. Full spectra with flux plotted on a logarithmic scale are shown in the right panel, while a close up of the Hα line on a linear scale is shown on the left. A combined spectrum from our 1999 July 16 (UT) observations is also plotted for comparison. The 2000 March spectrum is roughly 2.6 times fainter than our 1999 July observations, likely the result of poor targeting onto the slit due to the proper motion of 2MASS 1237+6526 (first observed by 2MASS on 1999 March 13 UT). The 2001 February spectrum, on the other hand, is brighter by a factor of 1.3; seeing conditions on this night were excellent, and the target was visible on the facility guide camera enabling proper slit placement. It is likely, therefore, that our 2000 March 5 observations suffered the same slit placement problems as our 1999 July 17 observations. Again features listed in Table 3.11 are noted.

Hα emission at 6563 Å is clearly seen in all of the spectra of Figure 5.3, and its presence in our recent data suggests that emission is persistent in 2MASS 1237+6526 over a period of at least 1.6 years. We have investigated the temporal behavior of Hα emission by measuring the line flux in all of our spectra to date, as described above. In this case, corrections have also been computed to compensate for slit losses, by scaling the individual spectra to match data from 1999 July 16 (UT) in the 8000–9500 Å region. The initial and corrected line fluxes are listed in Table 5.2.

Figure 5.4 plots these line fluxes versus UT time. All of the corrected values are in excellent agreement with the mean line flux from our 1999 July 16 and 18 (UT) observations, $(7.0\pm0.5)\times10^{-17}$ erg cm^{-2} s^{-1}, with the exception of data taken on 1999 July 17 (UT). As mentioned above, these data were of extremely low signal-to-noise, and it is likely that the formal errors are too low. Excepting this data point, we find that the Hα emission in 2MASS 1237+6526 is quite stable and persists for at least 1.6 years. The weighted mean value over all observations is $f_{H\alpha} = (7.44\pm0.08)\times10^{-17}$ erg cm^{-2} s^{-1}, corresponding to $\log L_{H\alpha}/L_{bol} = -4.3$, and is consistent with the earlier results.

Closer examination of Figure 5.3 shows an apparent wavelength shift in the peak of the Hα line. We examined the reality of this shift by comparing telluric emission lines in the 2000 March 5 and 2001 February 20 (UT) data; these were consistent to within 0.5 Å around 6563 Å. We also visually inspected the images to confirm that cosmic rays or bad pixels were not responsible for the 3.2 Å Hα line shift, which is nearly two pixels along the chip; this is indeed the case. Furthermore, the shift

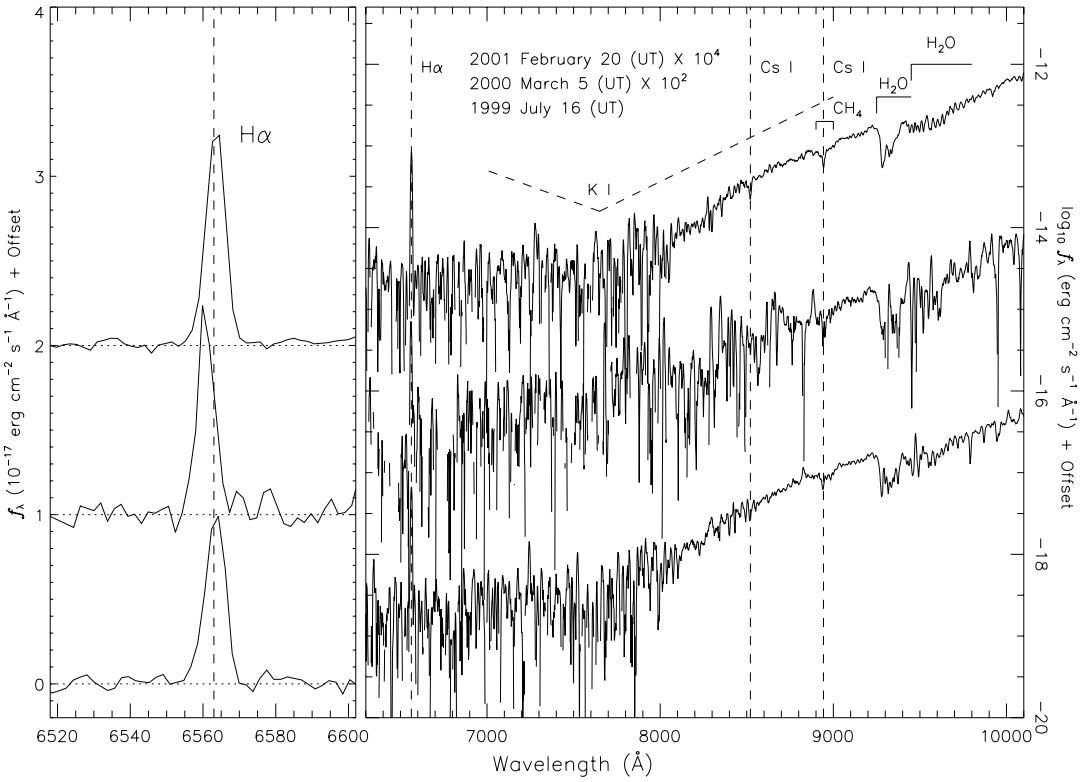

Figure 5.3: Optical spectra of 2MASS 1237+6526 obtained using LRIS. Observations from 1999 July 16, 2000 March 5, and 2001 February 20 (UT) are shown, and are scaled by correction factors as described in the text. The right panel shows full red optical spectra from 6300–10100 Å, with flux plotted on a logarithmic scale to enhance features; spectra are offset by a constant factor. Observed bands of H_2O and CH_4, and lines of Cs I and Hα are labeled, along with the pressure-broadened K I doublet. The left panel shows a closeup of the Hα line on a linear scale, with data offset by an additive constant (dotted lines).

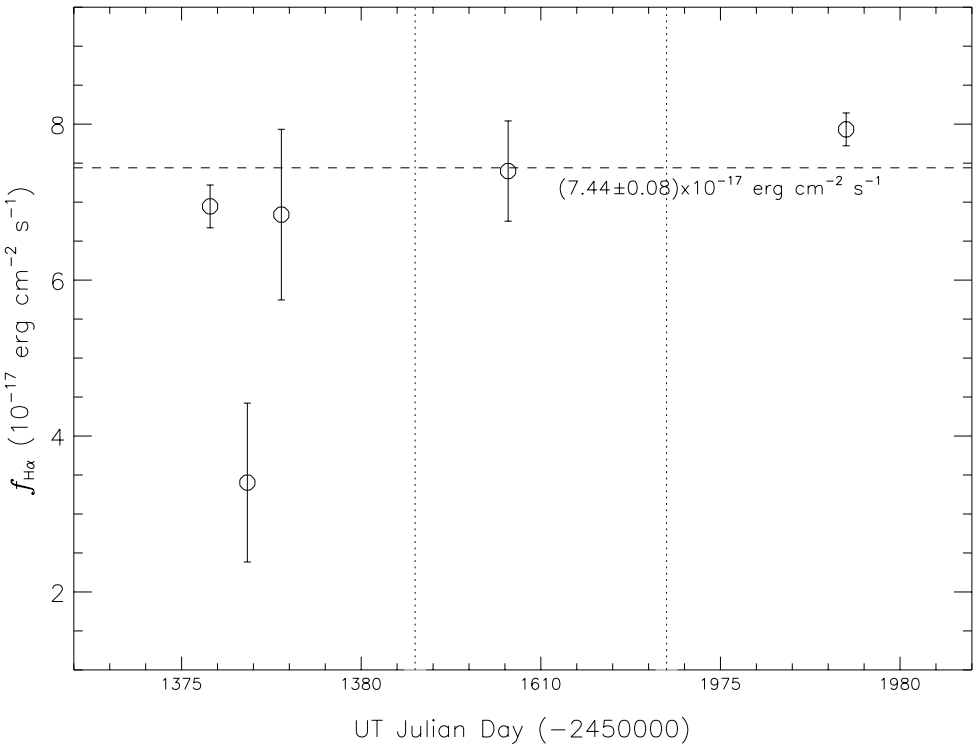

Figure 5.4: Emitted Hα flux from 2MASS 1237+6526 versus UT time. Circles plot corrected line flux values, scaled by matching flux data in the 8000-9500 Å region to observations made on 1999 July 16 (UT). The mean emission strength of $(7.44\pm0.08)\times10^{-17}$ erg cm^{-2} s^{-1} is indicated by the dashed line.

is consistent in each pair of observations taken on those two nights. There is a possiblity, however, that an overall wavelength shift in the spectrum of 5 March 2000 (UT) is due to poor placement on the 1″ slit in that night's sub-arcsecond seeing conditions. If we assume that the wavelength shift is a real, than the maximum shift corresponds to a velocity of 146±23 km s^{-1}. This large motion could be indicative of extreme atmospheric dynamics (escape velocity from a 60 M_{Jup} brown dwarf is roughly 330 km s^{-1}) or orbital motion incurred by a relatively massive companion (e.g., an edge-on, equal-mass double with component masses of 60 M_{Jup} and separation 10 R_{Jup}). Confirmation of the reality and characterization of the behavior of the Hα line requires higher resolution observations; it is nonetheless an intriguing indication of unique dynamics in this object.

5.2.3 Unique Emission

To gauge how the strength of Hα emission in 2MASS 1237+6526 compares to other active, cool dwarfs, we computed the relative Hα luminosity for late-M, L, and T dwarfs using spectral data from Kirkpatrick et al. (1999b, 2000, 2002) and §3.2.1. Hα line fluxes were measured directly from the spectra as described above, with bolometric fluxes for late-M and L dwarfs computed from 2MASS J-band photometry and BC_J values from Reid et al. (2001a). For T dwarfs, we used 2MASS J-band photometry and $BC_J = 2.09$, yielding an upper limit to the true bolometric correction for the early- and mid-T dwarfs (Burgasser, 2001, §7.8.2), and hence a lower limit to the bolometric flux; i.e., overestimating the relative Hα luminosity.

Results are shown in Figure 5.5, where detections are plotted as open symbols and upper limits (determined from pseudocontinuum noise levels) by downward arrows. For comparison, we have included M and L dwarf samples from Hawley, Gizis, & Reid (1996, crosses) and Gizis et al. (2000, diamonds). The trend of decreasing activity beyond M5–M7 V reported by Gizis et al. (2000) is readily apparent in this plot, and appears to continue well into the T dwarf regime. Indeed, only two objects have reliable detections beyond spectral type L5 V, the T2 V SDSS 1254-0122 (Leggett et al., 2000b), with $\log L_{H\alpha}/L_{bol} = -5.7$ (Kirkpatrick et al., 2001b), and 2MASS 1237+6526. SDSS 1254-0122 is over 25 times less luminous in Hα than 2MASS 1237+6526, and upper limits for the other T dwarfs do not exceed $\log L_{H\alpha}/L_{bol} = -5.2$. Hence, the emission in 2MASS 1237+6526 is truly unique amongst cool brown dwarfs.

5.3 Emission Mechanisms

Having ascertained the presence and persistence of Hα emission in 2MASS 1237+6526, we turn now to possible mechanisms for this feature. Activity in cool dwarf stars is commonly attributed to the interaction of magnetic field lines with the upper atmosphere. Measurement of magnetic field strengths in M dwarfs yield values of 2500–4000 Gauss (Johns-Krull & Valenti, 1996), comparable in strength to the Solar umbrae (Muller, 2000). These fields are just as strong above the fully convective mass limit (M $\sim$ 0.25, roughly spectral type M4 V) as below (Reid & Hawley, 2000), implying a turbulent dynamo is sufficient to maintain signficant magnetic fields (Durney, De Young, & Roxburgh, 1993). As we progress to even cooler L and T dwarfs, however, there is a clear drop in magnetic activity, as shown in Figure 5.5. So what could be powering the emission in 2MASS 1237+6526?

5.3.1 Flaring

While sustained activity may appear to diminish toward later spectral types, flaring does not. A good example of this is BRI 0021-0214, a rapid M9.5 V rotator (Basri & Marcy, 1995) which in

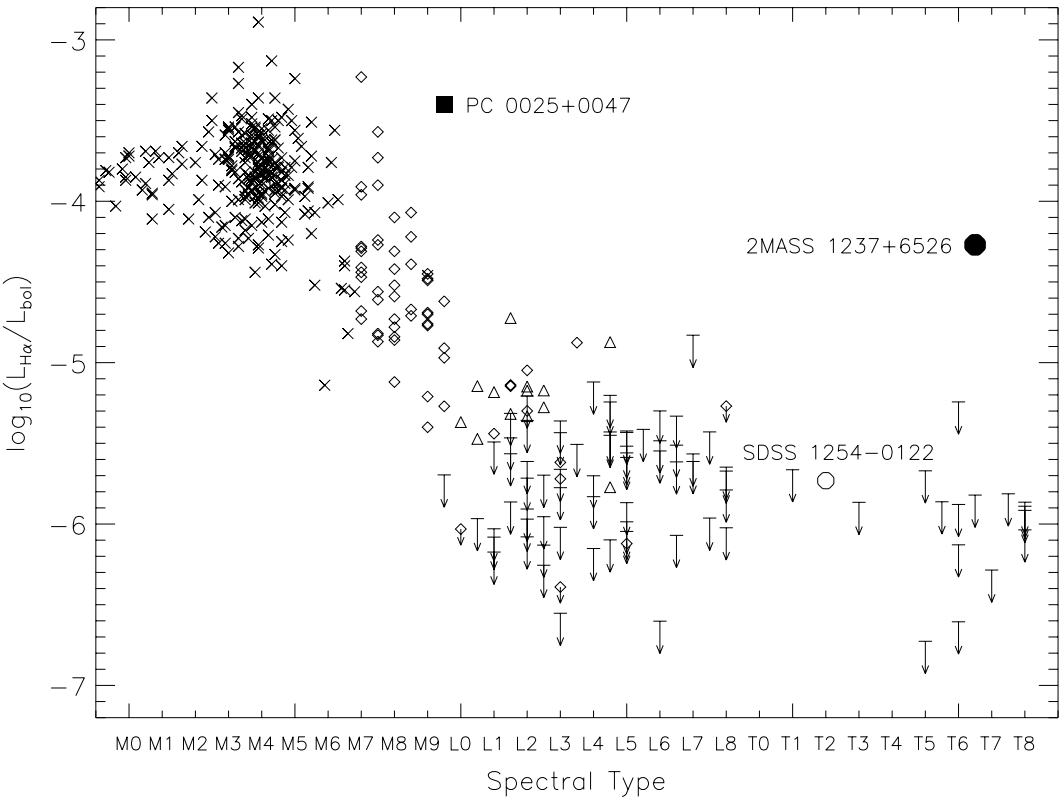

Figure 5.5: Relative Hα luminosity versus spectral type for cool dwarfs. The mean relative luminosity for 2MASS 1237+6526 is indicated by the solid circle, while values calculated from late-M, L, and T dwarf spectra (Kirkpatrick et al., 1999b, 2000, 2002, §3.2.1) are shown as open symbols (detected) or arrows (nondetection upper limits). Data for M and L dwarfs from Hawley, Gizis, & Reid (1996, crosses) and Gizis et al. (2000, diamonds), and for PC 0025+0047 (Schneider et al., 1991, solid square) are also plotted. T spectral types are from Chapter 7.

quiescence shows little or no Hα emission (Basri & Marcy, 1995; Tinney, Delfosse, & Forveille, 1997; Tinney & Reid, 1998), yet was seen to flare by Reid et al. (1999a) with $\log(L_{H\alpha}/L_{bol}) = -4.2$, similar in strength to 2MASS 1237+6526. The BRI 0021-0214 flare also showed no continuum emission, which is quite unlike the flare of 2MASS 0149+2956 (Liebert et al., 1999), an active (i.e., emission in quiesence) M9.5 Ve that produced both line and blue continuum emission (see Figure 5.6). Late M dwarfs have been observed in flare from radio to X-ray wavelengths (Fleming, Giampapa & Schmitt, 2000; Rutledge et al., 2000; Berger et al., 2001). While flaring has not yet been observed in L dwarfs, the occurrence of flares in the latest M dwarfs suggests we simply have not yet caught one out of quiescence.

The persistence of the Hα line in 2MASS 1237+6526, however, lends serious doubt to the possibility that arises from either a single prolonged flare or multiple flare events. Most strong M-dwarf flares persist only a few hours (Hawley & Petterson, 1991; Favata et al., 2000), while smaller flares (which would show weaker continuum emission) have time scales on the order of minutes (Nelson et al., 1986) down to seconds (Gershberg, 1989). Short-period emission is clearly not seen in 2MASS 1237+6526, as it persists over at least three days (1999 July 16–18 UT), if not the entire 1.6 years of observation. Furthermore, a massive flare (that may be able to sustain itself longer) is ruled out by the lack of blue continuum emission in this object. We can see this by comparing a spectrum of 2MASS 1237+6526 (2001 February data) to a similar object, 2MASS 1047+2124[3], as shown in Figure 5.7. While flux blueward of the 7665, 7699 Å K I doublet is marginally detected in both objects, there is no discernible difference in the flux levels between them. This behavior is analogous to the unaffected continuum in the BRI 0021-0214 flare, although substantial emission in that object was only seen once (Reid et al., 1999b). Hence, it is highly unlikely that the observed emission is the result of one major, continuous flaring event.

Another possibility is that we are witnessing repeated flaring in this object. We can compute the probability of observing multiple flare events repeatedly over a given period assuming an underlying flare duty cycle, f. If we examine the frequency of flaring on a daily time scale (i.e., longer than a typical flare lifetime), we can assume that randomly occurring flares will be detected on fN_{tot} days over a period of N_{tot} days. We can then determine the probability, $P(f|N_{obs}, N_{tot})$, of observing a flare on each of N_{obs} dates during the same period assuming a value of f:

$$\begin{aligned} P(f|N_{obs}, N_{tot}) &= \frac{\begin{array}{c}\text{\# of combinations of consistent flare} \\ \text{detections with sampling rate } \mathrm{N_{obs}/N_{tot}}\end{array}}{\begin{array}{c}\text{\# of combinations of flare events} \\ \text{over } \mathrm{N_{tot}} \text{ periods}\end{array}} \\ &= \left(\begin{array}{c} N_{per} - N_{obs} \\ N_{per}(1-f) \end{array} \right) \Bigg/ \left(\begin{array}{c} N_{per} \\ fN_{per} \end{array} \right) \\ &= \frac{(fN_{tot})\times(fN_{tot}-1)\times\cdots\times(fN_{tot}-N_{obs}+1)}{(N_{tot})\times(N_{tot}-1)\times\cdots\times(N_{tot}-N_{obs}+1)} \end{aligned} \tag{5.2}$$

In this case, we adopt $N_{tot} = 584$ days as the total number of days between the first and last observation of 2MASS 1237+6526 (see Table 5.2), and plot $P(f|N_{obs}, N_{tot})$ for various values of N_{obs} in Figure 5.8. The probability of consistent detection is a steep function of f, particularly as the number of observations increases. For $N_{obs} = 5$, we can rule out $f < 40\%$ with 99% confidence. Compared to the 7% duty cycle of BRI 0021-0214 estimated by Reid et al. (1999a), this limit effectively rules out repeated flaring as a viable mechanism.

[3]Both objects have the same spectral classification, T6.5 V, as discussed in Chapter 7.

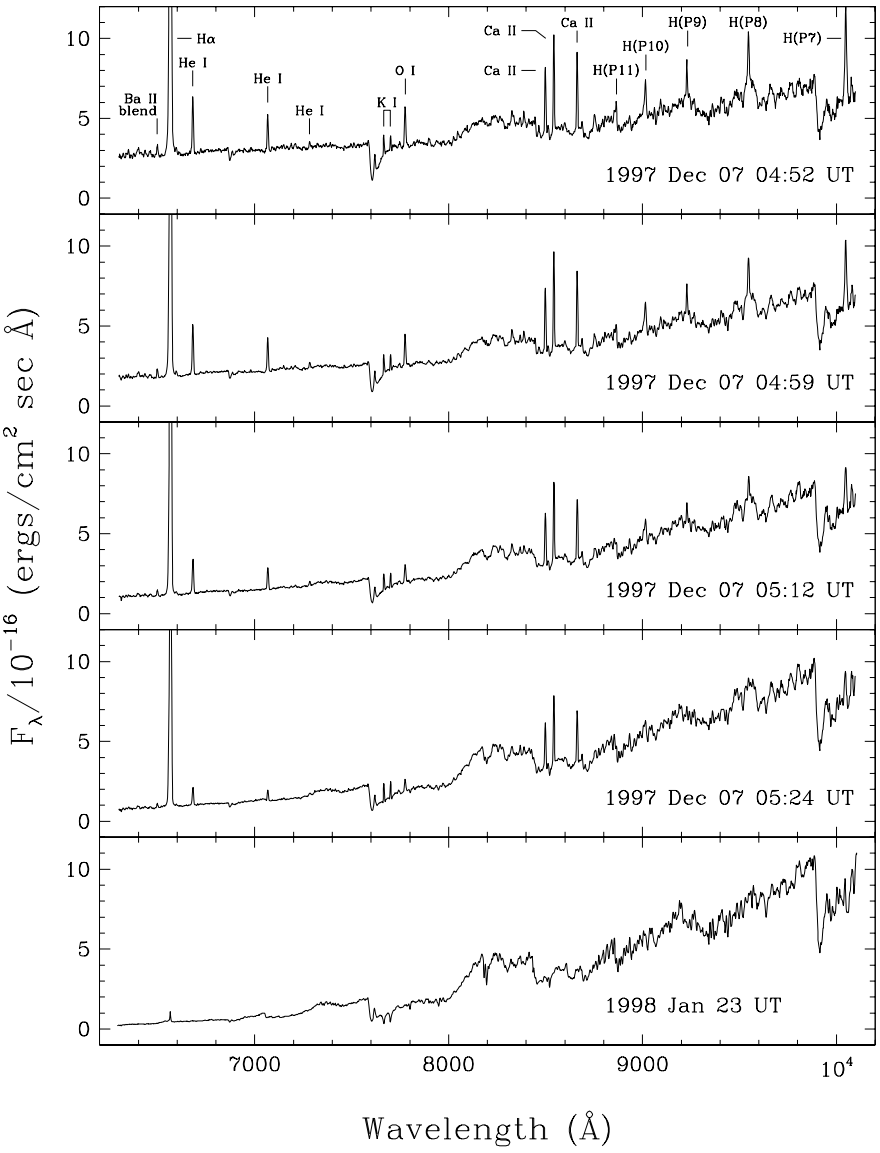

Figure 5.6: Time sequence of an optical flare seen in 2MASS 0149+2956 on 1997 December 7 (UT). Various emission lines seen in spectra on that night are indicated, and appear to fade from 04:52 to 05:24 UT. There is also considerable veiling of molecular features, which can be seen in comparison to the quiescent spectrum at the bottom (from Liebert et al. 1999).

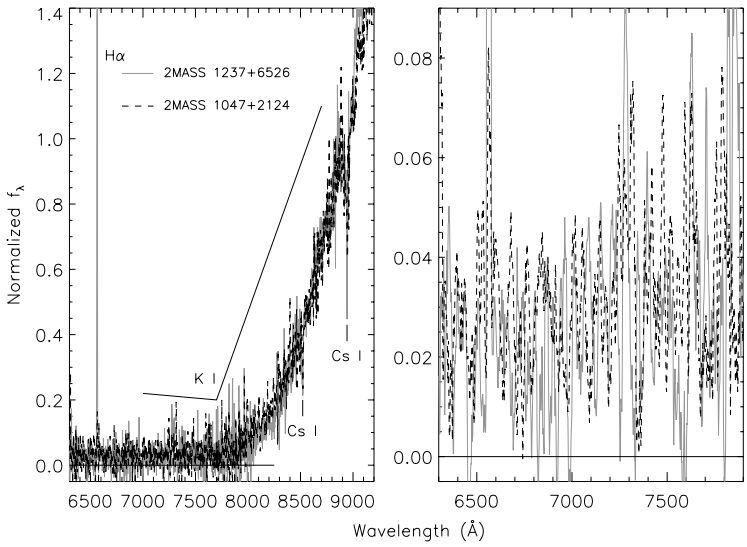

Figure 5.7: Optical spectra of 2MASS 1237+6526 (grey line) and 2MASS 1047+2124 (dashed line), overlaid for comparison. Spectra are normalized at 9000 Å, with zeropoints indicated by the black lines. The left panel shows the 6300–9200 Å spectra with alkali features and Hα emission in 2MASS 1237+6526 indicated. The right panel shows the 6300–7900 Å spectra, where positive flux is detected in both objects at similar levels.

5.3.2 Acoustic Flux

Schrijver (1987) first pointed out that a minimum "basal flux" seen in late-type stars, which is independent of both magnetic field strength and rotation, could be attributed to chromospheric heating from acoustic waves. These disturbances, generated by turbulent convective flow in the interior, rise and shock-heat the chromosphere to temperatures exceeding 10^5 K (Buchholz, Ulmschneider, & Cuntz, 1998), sufficient to cause low-level Ca II and Mg II emission in cool M dwarfs (Mathioudakis & Doyle, 1992). The fact that brown dwarfs are fully convective suggests that this could be a viable mechanism for the emission in 2MASS 1237+6526.

We can estimate the amount of acoustic flux for 2MASS 1237+6526 by comparing to the models of Ulmschneider et al. (1996), which improved on pivotal work done by Bohn (1984). These models extend down to effective temperatures of 2000 K, where the surface acoustic flux $F_{acoustic}$ scales roughly as $T_{eff}{}^{19}$. Figure 5.9 plots the predicted $\log L_{acoustic}/L_{bol}$ as a function of T_{eff} for various gravities ($\log g$ = 4, 5, 6 cm s^{-2}) and mixing-length parameters (α = 1.0, 1.5, 2.0), where we have used bolometric luminosities and radius estimates from Leggett et al. (2001) and Drilling & Landolt (2000). The steep drop off in acoustic energy toward cooler temperatures is readily apparent. Estimating $T_{eff} \approx 950$ K and log g(cm s^{-2}) ≈ 5, we estimate a surface flux $F_{acoustic} \approx 7 \times 10^{-8}$ erg cm^{-2} s^{-1}. Assuming a radius of $R = R_{Jup} = 7.15{\times}10^9$ cm and $L_{bol} = L_{bol}^{Gl229B} = 6.6{\times}10^{-6}$ $L_\odot$ (Leggett et al., 1999), this flux translates into $\log(L_{acoustic}/L_{bol}) \approx -15$, well below the observed activity level. Hence, acoustic energy is not likely the source of activity in 2MASS 1237+6526. This is not, in fact, surprising since acoustic heating should occur in most T dwarfs if any due to their convective interiors. The uniqueness of the strong emission in 2MASS 1237+6526 necessarily rules out any mechanism common to all T dwarfs.

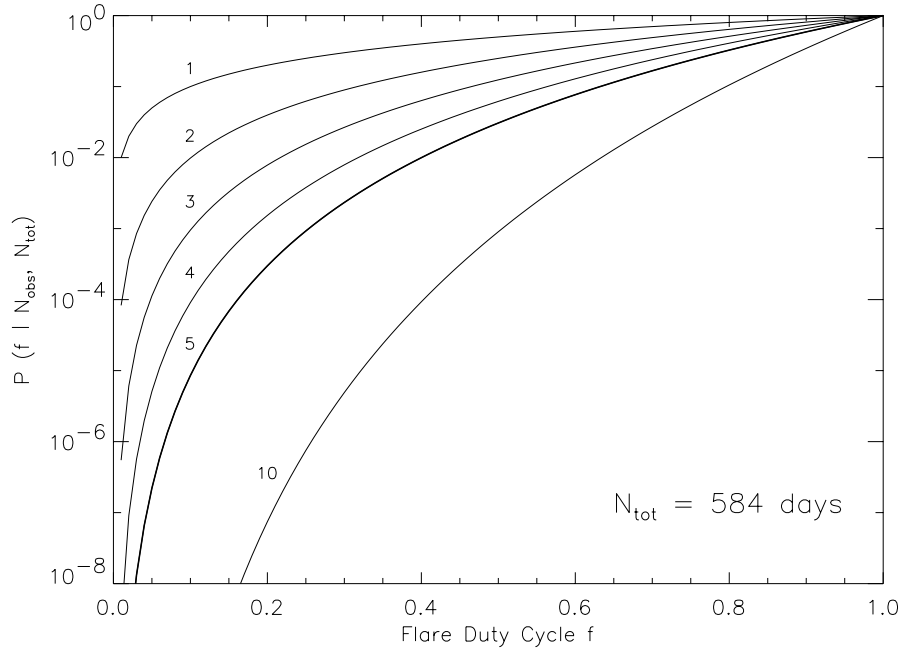

Figure 5.8: Probability, $P(f|N_{obs}, N_{tot})$, of observing a flare on each of N_{obs} days over N_{tot} total days given an underlying duty cycle f. To match to the 2MASS 1237+6526 observations, we have chosen $N_{tot} = 584$ days. Curves correspond to $N_{obs} = 1$, 2, 3, 4, 5, and 10 days (top to bottom).

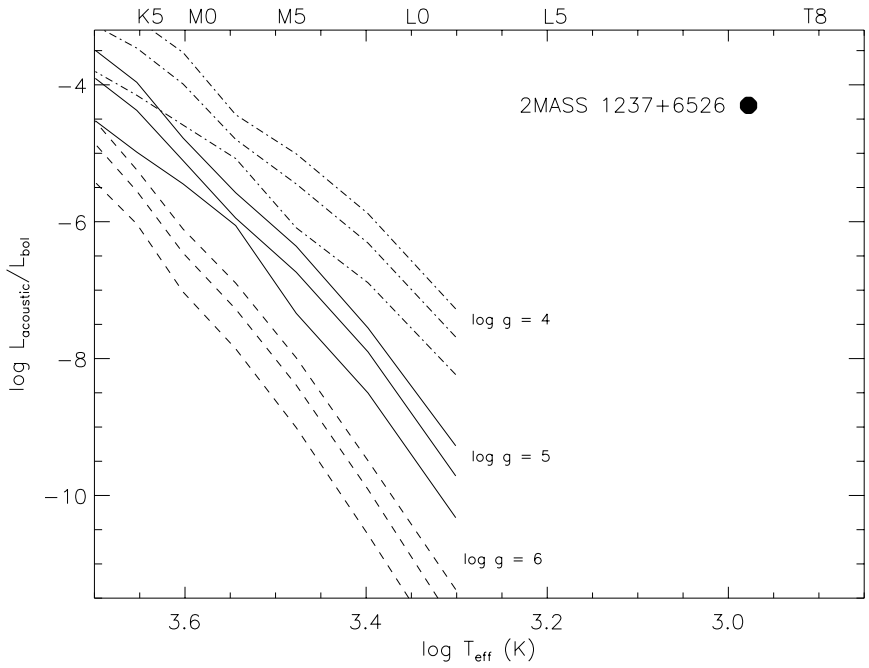

Figure 5.9: Relative acoustic luminosity, as a function of effective temperature. Acoustic flux values from Ulmschneider et al. (1996) for gravities $\log g$ of 4 (dot-dashed line), 5 (solid lines), and 6 cm s^{-2} and mixing-length parameters (top to bottom) $\alpha = 1.0$, 1.5, and 2.0 have been transformed to $\log L_{acoustic}/L_{bol}$ using bolometric luminosities and radii estimates from Leggett et al. (2001) and Drilling & Landolt (2000). The relative Hα luminosity of 2MASS 1237+6526 is indicated by the solid circle.

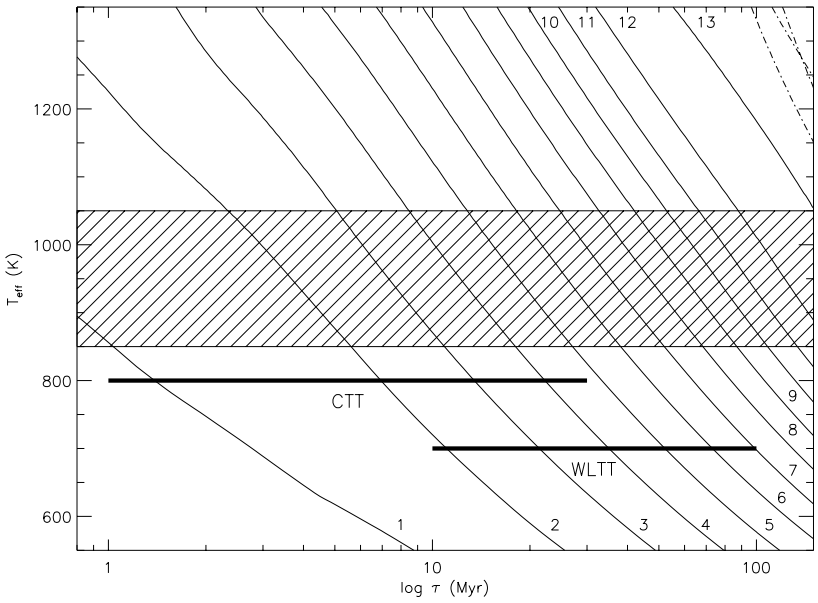

Figure 5.10: Evolutionary trajectories from Burrows et al. (1997) for a T_{eff} = 950±100 K brown dwarf with an age in the T Tauri regime. Tracks are shown for masses 1–13 M_{Jup} in 1 M_{Jup} increments. The range of ages of classical (CTT) and weak-lined (WLTT) T Tauri stars are indicated (Stahler & Walter, 1993).

5.3.3 Youth

Activity has long been heralded as a sign of youth in late-type stars, due either to accretion-driven energetics in pre-main sequence and T Tauri stars (Ulrich, 1976; Hartmann, 1990) or magnetic activity in a rapidly-spinning, zero-age main sequence star (i.e., the age-rotation-activity relation; Noyes et al. 1984). Weak-lined T-Tauri (WLTT) stars, in particular, show strong line emission but little continuum veiling, attributed to the loss of an optically thick disk and/or active accretion (Appenzeller & Mundt, 1989; Stahler & Walter, 1993). Periodic variability is also a common trait amongst WLTTs (Stahler & Walter, 1993). Such objects are probably older than 10–30 Myr, and may be as old as $\sim$ 100 Myr (Hartmann, Kenyon, & Hartigan, 1993). Recently, the low-mass member of a quadrupole T-Tauri system, GG Tau Bb, was identified as a substellar WLTT, with strong Hα emission, no optical veiling, and spectral signatures of low gravity (White et al., 1999). Comparison to the evolutionary models of Baraffe et al. (1998) yield a mass of M_{Bb} = 0.044±0.006 $M_{\odot}$ and age $\tau \approx$ 10 Myr (Prato et al., 2001).

It is possible, given its emission characteristics and apparent lack of continuum emission, that 2MASS 1237+6526 could also be a young WLTT. However, this implies an extremely small mass. Figure 5.10 diagrams Burrows et al. (1997) evolutionary tracks in the young, low-temperature regime. Assuming an effective temperature of 950±100 K (Marley et al., 1996, i.e., similar to Gliese 229B), a WLTT brown dwarf ($10 < \tau < 100$ Myr) has a mass range of 3–12 M_{Jup}, below the Deuterium-burning limit. While it is entirely conceivable that a brown dwarf with as low a mass as this could exist, there are a number of problems with this interpretation. First, 2MASS 1237+6526 is an isolated object, and there are no known active star-forming regions within 20 pc; it is, however,

Table 5.3: L dwarf Binaries.

Object	Type	Separation		f_B/f_A[a]	Filter	Ref.
		$''$	AU			
(1)	(2)	(3)	(4)	(5)	(6)	(7)
DENIS 0205−1159AB	L7 V	0.″51	9.2	1.0	K	1
		0.″35	6.3	1.0	JHKL'	2
2MASS 0746+2000AB	L0.5 V	0.″22	2.7	0.56	F814W	3
2MASS 0850+1057AB	L6 V	0.″16	4.4	0.29	F814W	3
2MASS 0920+3517AB	L6.5 V	0.″07	1.6	0.67	F814W	3
2MASS 1146+2230AB	L3 V	0.″29	7.6	0.75	F814W	3
		0.″29	7.6	1.0	K	1
DENIS 1228−1159AB	L5 V	0.″28	5.0	0.82	F110M	4
		0.″27	4.9	0.91	K	1

[a]Flux ratio of secondary to primary.
Refs – (1) Koerner et al. (1999); (2) Leggett et al. (2001); (3) Reid et al. (2001b); (4) Martín, Brandner & Basri (1999).

possible that it could be an ejected object. Second, cluster surveys, which have recently probed down to very low masses (Zapatero Osorio et al., 1999, 2000; Lucas & Roche, 2000; Najita, Tiede, & Carr, 2000), have yet to make a convincing detection below the Deuterium burning limit. It is possible that 2MASS 1237+6526 could be slightly older, as the decrease in activity with age appears to be less pronounced for low-mass stars (Gizis et al., 2000). An age of 400–800 Myr (i.e., roughly the age of the Hyades) and T_{eff} = 950±100 K would imply a very reasonable mass of 25±5 M_{Jup} (Burrows et al., 1997).

5.3.4 An Interacting Brown Dwarf Binary

One possible mechanism that deserves special attention is that of an interacting brown dwarf binary. The binarity of brown dwarfs is now well established (Martín, Brandner & Basri, 1999; Basri & Martín, 1999a; Koerner et al., 1999; Leggett et al., 2001; Reid et al., 2001b, Table 5.3), and the binary fraction for L dwarfs is around 20% (Koerner et al., 1999; Reid et al., 2001b), slightly less than the binary fraction of late-type main sequence stars (∼ 35%; Fischer & Marcy 1992; Henry & McCarthy 1993). Furthermore, all of the brown dwarf binaries identified to date are closely separated, with $a \sim 0.''1$ to $0.''5$. There is a good possibility, therefore, that 2MASS 1237+6526 could itself be double, as this angular scale is finer than the resolution of 2MASS.

A unique feature of brown dwarf binaries is the possibility of sustained Roche lobe overflow. For this discussion, we normalize masses to M_{Jup} and distances to R_{Jup}, and assume a circular orbit and negligible angular momentum loss (e.g., to gravitational radiation). The negative mass-radius relation of degenerate brown dwarfs, $d\log R/d\log M \approx -\frac{1}{3}$ (Burrows & Liebert, 1993), implies that if a brown dwarf loses mass on a dynamical timescale ($\tau \sim (\frac{R^3}{GM})^{\frac{1}{2}} \sim 1$ hr), its radius will increase if its mass lies in the range 5 - 70 M_{Jup}. Sustained mass transfer can then occur if the lower-mass companion fills its Roche lobe, while the corresponding change in the Roche lobe radius (R_L) as the interacting pair evolves satisfies (assuming angular momentum conservation):

$$\frac{dlnR_L}{dlnM_2} = \frac{8}{3}q - \frac{4}{3} - (q+1)\frac{0.4q^{\frac{2}{3}} + \frac{1}{3}q^{\frac{1}{3}}(1+q^{\frac{1}{3}})^{-1}}{0.6q^{\frac{2}{3}} + ln(1+q^{\frac{1}{3}})} < -\frac{1}{3}, \tag{5.3}$$

Table 5.4: Parameters for Interacting Brown Dwarf Binary Model.

τ (Gyr) (1)	α_1 [a] (2)	α_2 [a] (3)	M_1 [a] (M_{Jup}) (4)	a [b] (M_{Jup}) (5)	p [b] (hours) (6)	Max. v_{rad} [b] (km s^{-1}) (7)
0.5	1.50	2.10	23	3.2–4.4	2.7–5.2	19–56
1.0	1.43	2.00	30	3.0–4.7	2.2–5.0	17–65
5.0	1.32	1.85	60	2.6–5.5	1.2–4.7	11–100

[a]Input parameters matched to the structure models of Burrows et al. (1997).
[b]Range of possible values for $q < 0.63$ and $M_2 > 5$ M_{Jup}.

where $q \equiv \frac{M_2}{M_1}$ is the mass fraction, M_1 and M_2 the primary and secondary masses, and R_L is given by Eggleton (1983)

$$R_L = a\frac{0.49q^{\frac{2}{3}}}{0.6q^{\frac{2}{3}} + ln(1+q^{\frac{1}{3}})} \equiv af_1(q). \tag{5.4}$$

Here, a is the binary separation. Equation 5.3 is satisfied when $q < q_{crit} = 0.63$.

Degenerate brown dwarf radii can be analytically approximated at late ages by the relation (Zapolsky & Salpeter, 1969; Stevenson, 1991):

$$R = \alpha_1 \frac{\pi M^{-\frac{1}{3}}}{(1+\alpha_2 M^{-\frac{1}{2}})^{\frac{4}{3}}} = f_2(M), \tag{5.5}$$

where α_1 and α_2 are age-dependent scale factors chosen to match the interior models of Burrows et al. (1997). Table 5.4 lists the optimal values for α_1 and α_2 for ages $\tau = 0.5$, 1.0 and 5.0 Gyr. As shown in Figure 5.11, this expression is quite accurate for old ($\tau \sim 5$ Gyr) brown dwarfs, deviating by no more than 2% from 5–70 M_{Jup}. However, younger objects, which have residual heating from late deuterium or hydrogen burning, will not be fully degenerate, and their radii can deviate from Equation 5.5 by as much as 3% ($M \sim 45$ M_{Jup}) to 12% ($M \sim 75$ M_{Jup}). For now, we will ignore these errors because of the utility of an analytical expression in investigating the binary model. Moreover, the hypothetical secondary in a 2MASS 1237+6526 interacting system must have a mass $M_2 < 35$ M_{Jup} for $\tau < 5$ Gyr, given the value of q_{crit} (see below). This is well into the regime where errors are less than 3% for all ages in consideration. Nevertheless, we advocate caution in the interpretation of our results for the youngest ages.

Setting $R_2 = R_L$, we derive an expression for the binary separation:

$$a = \frac{f_2(M_2)}{f_1(q)} = a(M_1, q); \tag{5.6}$$

i.e, a is only function of the primary mass and the binary mass ratio, so that these two parameters define the dynamics of this (simplified) system. The period, p (in hours), is determined from the standard Keplerian relation,

$$p^2 = 4\pi^2 \frac{a^3}{G(M_1+M_2)} = 8.79\frac{a^3}{M_1(1+q)}, \tag{5.7}$$

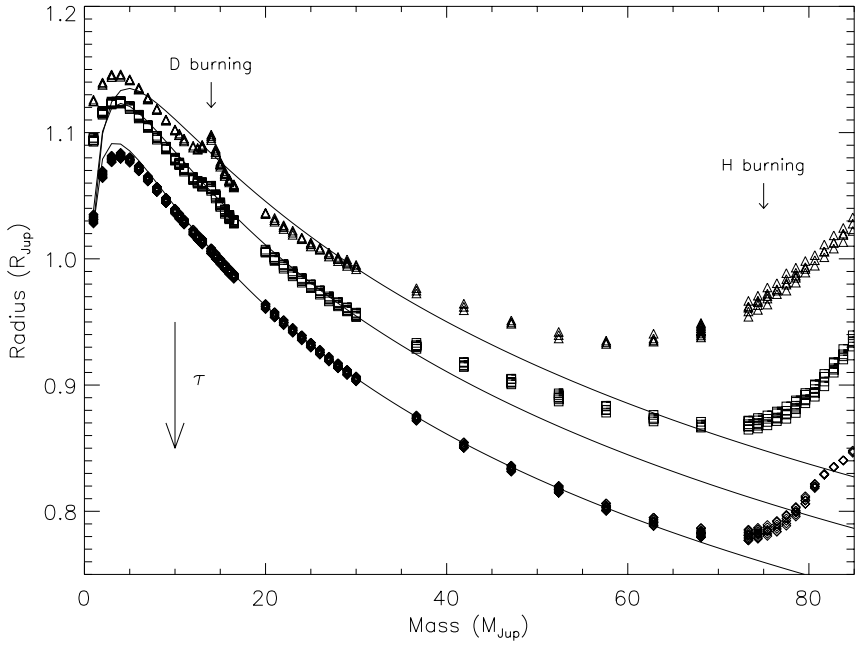

Figure 5.11: Radius versus mass for brown dwarfs and low-mass stars for ages 0.5 (triangles), 1.0 (squares), and 5.0 Gyr (diamonds), from Burrows et al. (1997). An analytical fit to these points using Equation 5.5 and the parameters listed in Table 5.4 is shown for each age. Mass regions where late deuterium or residual hydrogen burning occurs at early times are noted.

while the maximum radial velocity of the primary, v_{rad} (in km s^{-1}), is given by

$$v_{rad} = \sqrt{\frac{GM_1}{a}\frac{q^2}{1+q}} = 42.1\sqrt{\frac{M_1}{a}\frac{q^2}{1+q}}. \quad (5.8)$$

Figure 5.12 plots these values for a 2MASS 1237+6526 interacting system as a function of q. Based on the models of Burrows et al. (1997), we have adopted primary masses M_1 = 23, 30, and 60 M_{Jup} for ages of τ = 0.5, 1.0, and 5.0 Gyr, assuming T_{eff} = 950 K (i.e., similar to Gliese 229B; Marley et al. 1996). This rough model shows that sustained outflow is possible in systems with separations of $2.5 < a < 5.5$ R_{Jup} and periods of $1.2 < p < 5.2$ hours. The close separation required may seem problematic; however, as mentioned above, brown dwarf binaries have already been seen in close separation systems with $a \sim$ 2–10 AU, while the brown dwarf spectroscopic binary PPl 15 has been shown to have an orbital separation of about 60 R_{Jup} (Basri & Martín, 1999a). The radial velocity of the primary can approach 100 km s^{-1} for systems with the highest total mass, consistent with the possible line shift observed in our LRIS data (§5.2.2).

The emission mechanism from overflow accretion is uncertain, as a hot accretion disk is ruled out by the lack of thermal continuum. Ionization along a shock front or magnetic streaming onto the primary's pole are possibilities. Nonetheless, we find this an intriguing and, more importantly, observationally constrainable hypothesis. While resolving the pair may be beyond our current capabilities[4], the presence of the secondary may reveal itself by its added light contribution or radial velocity modulation (fully detectable by NIRSPEC in echelle mode). Another possible indicator, transit events, is the focus of our next section.

5.4 Searching for Photometric Variability

One possible means of testing the interacting binary hypothesis is to search for transit events. The separation of the hypothetical system is only a few times larger than the component radii, so partial eclipsing can occur for inclinations as low as $i \sim 60°$. To examine this possibility, we monitored 2MASS 1237+6526 at J-band over two nights, 2000 May 19–20 (UT), using the Palomar 60" Infrared Camera (Murphy et al., 1995, hereafter IRCam). In §5.4.1 we describe the observations and data reduction, and discuss the construction of a relative magnitude time series in §5.4.2. In §5.4.3 we analyze the results of this time series, including a search for periodic trends. In §5.4.4 we discuss the constraints these observations make on the binary hypothesis.

5.4.1 Observations and Data Reduction

The Palomar 60" IRCam is comprised of a 256×256 NICMOS3 HgCdTe array, with 0.″619 pixels and a 158″ field-of-view, and a series of broad-band and narrow-band near-infrared filters. Observations were made on the nights of 2000 May 19–20 (UT) using the J-band filter. Conditions during these nights were generally hazy but clear, with average seeing of 1.″2 to 1.″8; some scattered cirrus was present during the observations of May 20. Data were acquired in sets of five 45s exposures dithered by 10″ on May 19 and 15″ on May 20 in a square pattern. A total of 155 and 165 images were obtained, spanning periods of 2.50 and 2.57 hours on May 19 and 20, respectively. Airmasses ranged from 1.19 to 1.60.

[4] Assuming a distance of 12.7 pc (based on $M_J = M_J^{Gl229B} = 15.51$, Leggett et al. 1999), $a \sim$ 0.1–0.2 milliarcseconds. The best ground-based, diffraction-limited observations can achieve $\lambda/D \sim 20$ milliarcseconds for $\lambda = 1$ μm and D = 10m.

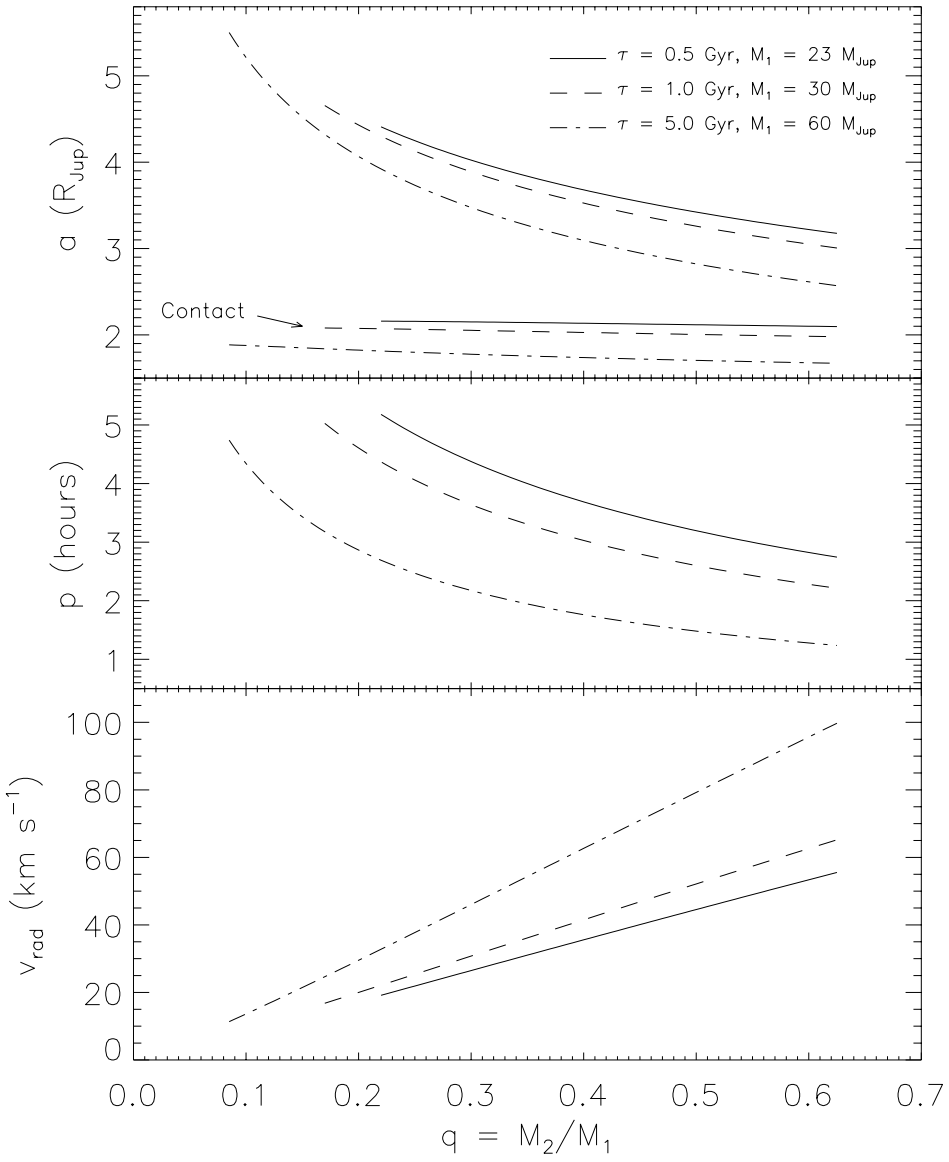

Figure 5.12: Orbital separation, period, and maximum primary radial velocities as a function of q for a 2MASS 1237+6526 interacting brown dwarf binary model. Lines trace out parameters for ages τ = 0.5 (solid), 1.0 (dashed), and 5.0 Gyr (dot-dashed), corresponding to primary masses M_1 = 23, 30, and 60 M_{Jup}. The contact limit ($a = R_1 + R_2$) is shown in the top panel.

Table 5.5: Log of Imaging Observations.

UT Date (1)	UT Time (2)	Airmass (3)	Total t (hr) (4)	No. Images (5)	Conditions (6)
19 May 2000	05:31 – 08:02	1.19–1.39	2.51	155	hazy and clear
20 May 2000	06:36 – 09:13	1.25–1.60	2.62	165	hazy with some scattered cirrus

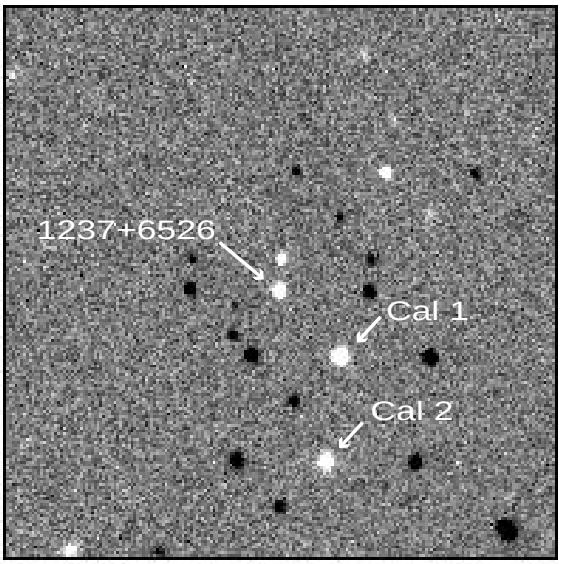

Figure 5.13: Combination of five, 45 sec J-band images of the 2MASS 1237+6526 field obtained on 2000 May 19 (UT). 2MASS 1237+6526 is indicated, as are the two comparison stars Cal 1 and Cal 2. The field shown is $2\farcm5 \times 2\farcm5$ oriented with North up and East toward the left.

Science data were initially pairwise differenced to eliminate bias and sky background, and then divided by a normalized flat-field image, constructed by differencing median-combined sets of lamp-on and lamp-off dome observations made on May 19. Bad pixels were identified in the flat-field image and corrected in the science images by interpolation. The four separate readouts of the IRCam NICMOS-3 HgCdTe array occasionally introduced additive quadrant biases that we removed by subtracting off the median from each quadrant. Finally, individual images in each set were shifted and coadded to produce a final reduced image (Figure 5.13).

5.4.2 Differential Photometry and Analysis of the Time Series

For each image, we computed aperture photometry (f_i) for 2MASS 1237+6526 and other sources in the field. Flux within a $2\farcs5$ (4.04 pixel) radius aperture was integrated after subtracting the mean background measured in a 6 to $12''$ annulus around each object. Uncertainty estimates of the photometry included contributions by shot noise in the source and variations in the sky. Instrumental magnitudes, $m_i = -2.5\log_{10} f_i$, were then computed with corresponding uncertainties. The scatter in instrumental magnitudes for 2MASS 1237+6526 was roughly 0.03 mag on May 19 and 0.01 mag on May 20, with formal photometric uncertainties of ± 0.025 mag.

To compute a relative magnitude light curve, we first examined sources in the field for variability, using the procedure outlined in Bailer-Jones & Mundt (1999, 2001). We first determined relative magnitudes for each j^{th} source,

$$\hat{m}_i^{(j)} = m_i^{(k)} - \sum_{k \neq j}^{K} m_i^{(k)} \tag{5.9}$$

$$\hat{\sigma}_i^{(j)^2} = \sigma_i^{(j)^2} + \sum_{k \neq j}^{K} \sigma_i^{(k)^2}, \tag{5.10}$$

summing over the $k = 1$ through K other sources in the field. After subtracting off the mean relative magnitude, we computed the reduced χ^2 for each source to determine if photometric variations were significant:

$$\chi_r^2 = \frac{1}{n-1} \sum_{i}^{n} (\frac{\hat{m}_i - \langle \hat{m}_i \rangle}{\hat{\sigma}_i})^2; \tag{5.11}$$

here, n is the total number of images. We constrained calibrator sources to have $\chi_r^2 \lesssim 0.5$, corresponding to a probability of variability $P \leq 1\%$ for $n = 30$. Two calibrators present in images from both nights passed this constraint, 2MASSI J1237367+652600 (Calibrator 1) and 2MASSI J1237372+652536 (Calibrator 2). These sources have 2MASS J magnitudes of 15.07±0.05 and 15.34±0.06, respectively, and are indicated on Figure 5.13. Relative magnitudes were then computed for 2MASS 1237+6526 using these two calibrator stars.

5.4.3 Results and Analysis

The resulting time series is shown for both nights in Figure 5.14. The mean relative magnitude has been subtracted off in both datasets. Time series for the differenced calibrator magnitudes ($m_i^{(1)} - m_i^{(2)}$) are also shown (offset) for comparison. Scatter in the relative magnitudes of 2MASS 1237+6526 was 0.020 and 0.014 mag on May 19 and 20, respectively, less than the formal photometric uncertainties. As shown in Figure 5.15, these values are not above the expected magnitude scatter for an object of its magnitude. Corresponding χ_r^2 values are 0.505 and 0.314, which are greater than those of the calibrator stars (0.271 and 0.237, respectively), but nevertheless reject variability (at levels above our detection threshold) at the $> 99\%$ confidence level.

To examine the possibility of a modulated signal (e.g., multiple eclipsing events or geometric modulation), we constructed periodograms for each night's data using the formalism of Lomb (1976) and Scargle (1982) as summarized in Press et al. (1992). Given the duration of the observations, we are sensitive to periodicities ranging from roughly 0.1–1.3 hr on each night. The computed periodograms (oversampled by a factor of 10) for both 2MASS 1237+6526 (black lines) and calibrator stars (grey lines) are shown in Figure 6. May 19 and 20 data are identified by solid and dashed lines, respectively. None of the peaks in the 2MASS 1237+6526 periodograms are significant, as they do not exceed the 50% false alarm probability level and are roughly equal in magnitude to insignificant peaks seen in the calibrator periodograms.

Variability over two nights also appears to be absent. There is a 0.024 mag offset in the mean relative magnitudes between the two nights; this is greater than the difference between the mean calibrator values (0.003 mag), but comparable to the photometric uncertainties. We compute χ_r^2 = 0.593 over both nights, again rejecting variability at the $> 99\%$ confidence level. Because of the large temporal gap in the time series data, periodicity analysis requires more sophisticated algorithms (e.g., the CLEAN algorithm; Roberts, Léhar, & Dreher 1987); however, given the lack of statistical evidence for variability, further analysis appears to be unnecessary.

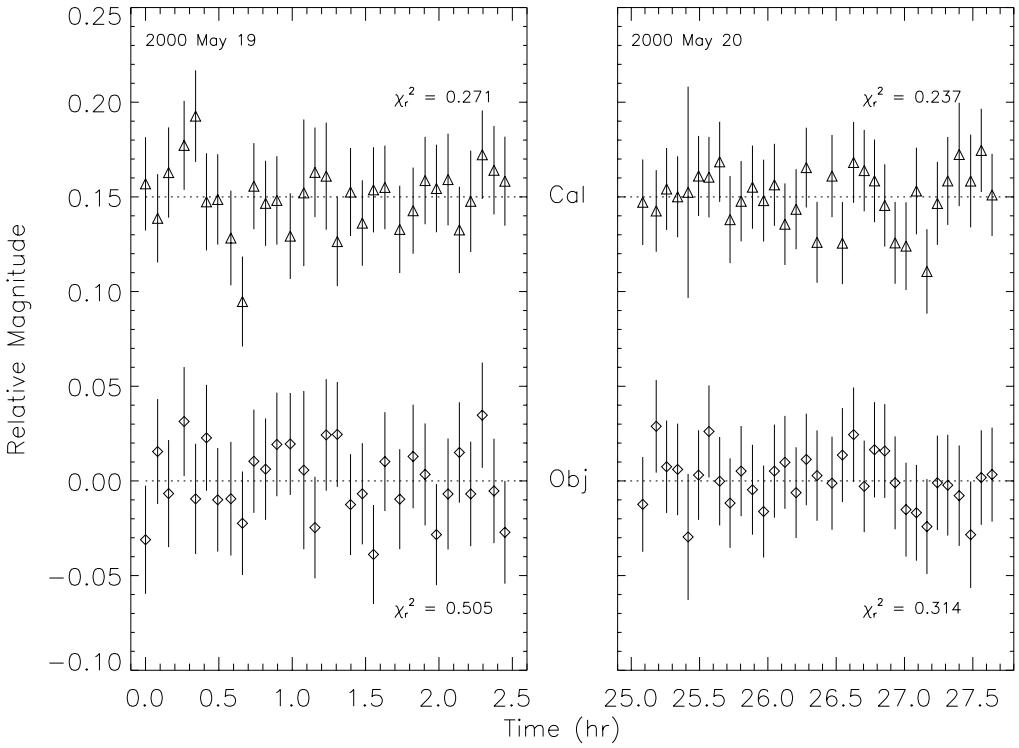

Figure 5.14: Relative magnitude time series for 2MASS 1237+6526 (diamonds) and comparison stars (triangles). Data for 2000 May 19 and 20 (UT) are shown separately. The mean relative magnitudes for each night have been subtracted, with datasets within a night offset for clarity.

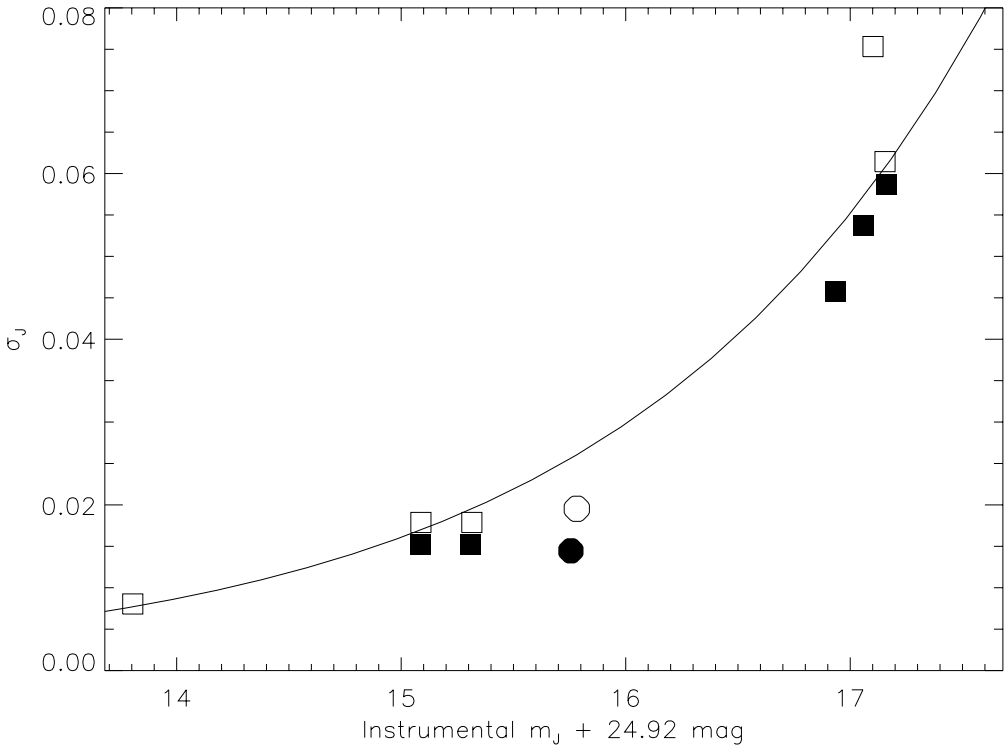

Figure 5.15: Scatter in relative magnitude versus instrumental magnitude, corrected to photometric magnitudes by a constant 24.92 mag. Data for 2MASS 1237+6526 are plotted as circles, while field sources are shown as squares. Open and filled symbols identify observations from 2000 May 19 and 20 (UT), respectively. An exponential fit to the field sources is plotted for clarity.

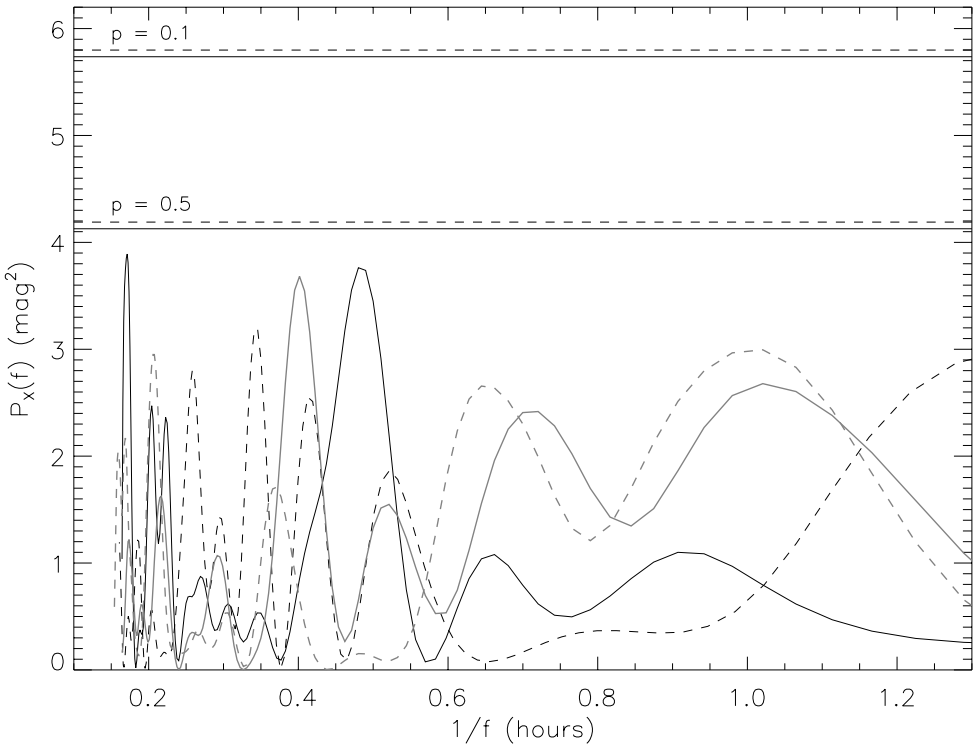

Figure 5.16: Periodogram of time series data for each observing night. Black and grey lines trace the periodograms of 2MASS 1237+6526 and comparison stars, respectively, while solid and dashed lines identify data from 2000 May 19 and 20 (UT). False alarm probability limits of 50% and 10% are indicated.

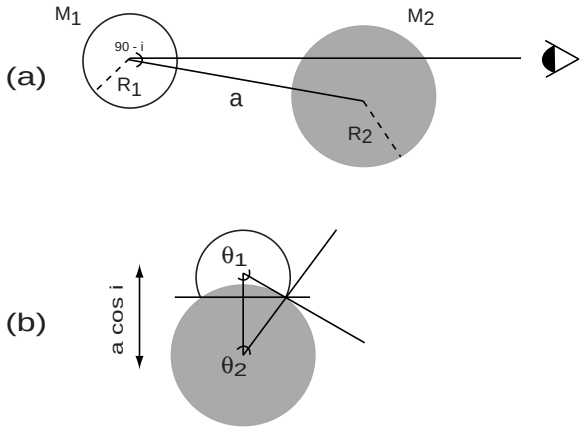

Figure 5.17: Geometry of the binary eclipse model. (a) Orientation along the line-of-sight; a is the binary separation, i the inclination, M_1 and M_2 the masses of the primary and secondary, and R_1 and R_2 their respective radii. (b) Face-on orientation, showing the relevant angles, θ_1 and θ_2, used to compute the obscured area of the primary.

Given the null results from these statistical tests, we conclude that there is no short-term variability in 2MASS 1237+6526 at the ± 0.025 mag level over periods of 0.1–2.5 hours and no evidence of periodicity for periods of up to 1.3 hours. There also appears to be no compelling indication of variability at this level for periods of up to $\sim$ 14 hours.

5.4.4 Constraints on the Binary Hypothesis

In order to define what constraints our null variability results impose on the interacting binary hypothesis, we must first determine the expected change in brightness at J band for a full or partial eclipse. Our observables are (1) a period limit from the duration of monitoring observations, (2) a magnitude limit at which we are sensitive to variability, and (3) the properties of the primary. We therefore seek to derive a relation $\Delta \mathrm{J} = f(p, i; M_1)$.

We assumed a simple geometry of overlapping spheres along the line of sight, as diagrammed in Figure 5.17. In general, the lower-mass secondary has a larger radius ($R_2 > R_1$) for $M_2 > 5$ M$_{Jup}$. The relative area of the primary, A, obscured by the secondary during maximal eclipse is

$$\pi A = \theta_1 - 0.5 \sin 2\theta_1 + (\frac{R_2}{R_1})^2 (\theta_2 - 0.5 \sin 2\theta_2) \tag{5.12}$$

where

$$R_1 \sin\theta_1 = R_2 \sin\theta_2 \tag{5.13}$$

$$R_1 \cos\theta_1 + R_2 \cos\theta_2 = a \cos i, \tag{5.14}$$

with θ_1 and θ_2 defined in Figure 5.17. These equations allow us to uniquely determine A in terms of M_1, q, and i. Note that no eclipse occurs when $\cos i > (R_1 + R_2)/a$, while a complete eclipse occurs for $\cos i < (R_2 - R_1)/a$.

The observed magnitude difference at maximal eclipse is then

$$\begin{aligned} \Delta J &= -2.5 \log \left(\frac{F_1(1-A)+F_2}{F_1+F_2} \right) \\ &= -2.5 \log \left(1 - \frac{A}{1+\beta}\right), \end{aligned} \tag{5.15}$$

where $\beta = F_2/F_1$ is the flux ratio of the secondary to primary at J-band. We can determine the change in the J-band magnitude of a brown dwarf as a function of T_{eff} empirically from the two known companion T dwarfs, Gliese 229B (Nakajima et al., 1995; Oppenheimer et al., 1995) and Gliese 570D (Burgasser et al., 2000b). The former object has $M_J = 15.51 \pm 0.08$ (Leggett et al., 1999) and $T_{eff} \sim 950$ K (Allard et al., 1996; Marley et al., 1996; Tsuji et al., 1996), while the latter has $M_J = 16.47 \pm 0.07$ (Burgasser et al., 2000b) and $T_{eff} \sim 800$ K (Geballe et al., 2001a). These values yield the approximate relation dJ/dT $= -0.0064$ mag/K, which may be accurate over only a limited T_{eff} range. Interior models from Burrows et al. (1997) show a power law relation between T_{eff} and mass which is roughly dependent on age (τ). A fit to the models yields the relations:

$$\frac{dT}{dM} = \begin{cases} 88.7 M^{-0.43} & \tau = 0.5\ Gyr \\ 73.4 M^{-0.44} & \tau = 1.0\ Gyr \\ 45.4 M^{-0.44} & \tau = 5.0\ Gyr \end{cases} \quad K/M_{Jup}. \tag{5.16}$$

Combining Equation 5.16 with the expression for dJ/dT yields the secondary flux ratio:

$$\begin{aligned} -2.5 \log \beta &= \frac{dJ}{dT} \frac{dT}{dM} \Delta M \\ &= \frac{dJ}{dT} \frac{dT}{dM} M_1 (q-1) \\ &= \alpha_\beta \times (1-q) \end{aligned} \tag{5.17}$$

where α_β is a constant essentially dependent on age.

Using the above equations, we have calculated the expected magnitude drop (ΔJ_{ecl}) for an eclipsing, interacting brown dwarf binary with $q < 0.63$, $M_2 > 5$ M_{Jup}, and $40^\circ \leq i \leq 90^\circ$. We have again assumed that 2MASS 1237+6526 has $T_{eff} \sim 950$ K and hence M = 23, 30, and 60 M_{Jup} for $\tau = 0.5$, 1.0, and 5.0 Gyr, respectively. Results are shown in Figure 5.18. Significant drops in the observed flux are predicted by this model, particularly for $i \geq 80^\circ$, where fluxes at maximum eclipse can be 0.7 mag fainter than the nominal brightness over the full range of periods shown. These flux deviations are due primarily to the substantial brightness ratio between the secondary and primary, which is particularly important at high inclination angles when obscuration is complete. At lower inclination angles, the limiting factor is the orbital separation, which is larger for lower mass secondaries. No eclipse variations are predicted to occur for $i \lesssim 50^\circ$ over the range of ages examined. Significant systematic uncertainties may be present for the lowest mass ratios (i.e., low secondary T_{eff}) due to the rough estimate of β in Equation 5.17; however, our observations generally sample only the highest mass ratios due to the period cutoff.

The predicted ΔJ_{ecl} from these models are generally much larger than our observational limits (indicated by the hatched region in Figure 5.18). The constraints imposed by the non-detection of variability are summarized in Table 5.6 for $i > 60^\circ$; in this case, $q > 0.72$, 0.53, and 0.37, corresponding to secondary masses $M_2 > 16$, 16, and 22 M_{Jup} for $\tau = 0.5$, 1.0, and 5.0 Gyr, respectively. Note that for the 0.5 Gyr case, our mass ratio limit exceeds the minimum q required to sustain mass loss, so that we cannot constrain any parameter space for an interacting binary in this case. The lowest inclination angle eclipses that could have been detected by our observations for $\tau = 1.0$ and 5.0 Gyr is $i_{min} = 54^\circ$, with corresponding minimum secondary masses of 18 and 38 M_{Jup}, respectively.

Based on the results of the monitoring observations, we can confidently rule out an interacting

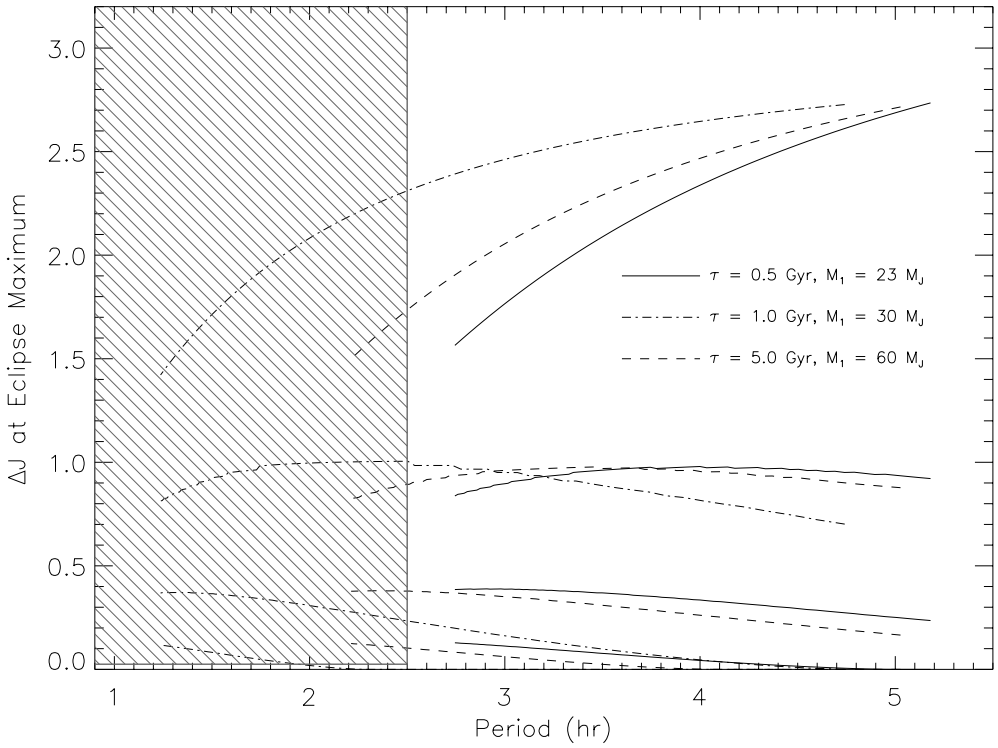

Figure 5.18: Constraints on the binary hypothesis. Predicted ΔJ_{ecl} during maximal eclipse is plotted versus period for $q < 0.63$; $M_2 > 5$ M_{Jup}; and $\tau = 0.5$ (solid line), 1.0 (dot-dashed line), and 5.0 (dashed line) Gyr; and (from top to bottom) $i = 90°$, 80°, 70°, and 60°. The hatched area covers the parameter space probed by the J-band monitoring observations.

Table 5.6: Parameters for the Eclipse Model.

τ (Gyr) (1)	M_1 (M_{Jup})[a] (2)	α_β (mag)[a] (3)	q_{max}[b] (4)	$M_{2,max}$ (M_{Jup})[b] (5)	i_{min} (°) (6)
0.5	23	3.39	0.72[c]	16	–
1.0	30	3.16	0.53	16	54
5.0	55	2.88	0.37	22	54

[a]Model parameters determined by matching to structure models from Burrows et al. (1997). See also Table 5.4.
[b]Maximum values permitted by non-detection of variability for $i > 60$ °.
[c]This value is greater than the maximum $q = 0.63$ required to sustain mass loss.

binary system for 2MASS 1237+6526 for $i > 60°$ and $M_2 > 22$ M_{Jup}. There are additional problems with this mechanism for 2MASS 1237+6526 as well. The stability of the Hα emission does not fit with accretion of material onto the primary, which is likely to be a stochastic process reflected in emission variability (c.f., flickering in cataclysmic variables). Inasmuch as an interacting binary could be expected to be a rare phenomenon, the detection of an apparently stable Hα line (albeit at significantly lower levels) in the spectrum of SDSS 1254-0122 no longer makes 2MASS 1237+6526 unique in this sense.

The observations presented here do not unambiguously rule out the presence of an unseen companion, but they do provide fairly stringent constraints on the geometry and membership of such a system. Monitoring observations of up to 5.5 hours with an accuracy of ± 0.01 mag would be required to fully eliminate the possibility that 2MASS 1237+6526 is an eclipsing system with $i > 70°$. Alternate observational checks include the measurement of a parallax for this object, in order to compare its brightness to similar T dwarfs such as Gliese 229B. Radial velocity monitoring using NIRSPEC could further constrain the geometry or reality of this mechanism. Space motion measurements may provide additional clues into the age of this object, as it is fully conceivable that 2MASS 1237+6526 is simply an old, active, low-mass brown dwarf (see §5.3.3). In any case, the steady and luminous Hα emission of 2MASS 1237+6526 remains an enigma.

5.5 PC 0025+0447: An Analogue?

There is another low-mass object that shows significant, sustained Hα emission; the M9.5 Ve PC 0025+0447. This object was identified by Schneider et al. (1991) in a search for high redshift quasars due to its unusually strong Balmer line emission (Figure 5.19). PC 0025+0447 has $\log L_{H\alpha}/L_{bol} = -3.4$ (Schneider et al., 1991), nearly an order of magnitude stronger than 2MASS 1237+6526, as well as other M9.5 V dwarfs in emission (Figure 5.5, square), and shows a full complement of Balmer lines out to H9 at 3836 Å (Mould et al., 1994). Furthermore, the activity in this object appears to be persistent over an 8-year timescale (Schneider et al., 1991; Mould et al., 1994; Martín, Basri, & Zapatero Osorio, 1999), with minor fluctuations in the emission strength of a factor of four seen on timescales of months to years (Martín, Basri, & Zapatero Osorio, 1999). The latter authors also detect occasional He I and O I emission, but no Ca II HK emission has yet been seen (Mould et al., 1994).

Both Schneider et al. (1991) and Martín, Basri, & Zapatero Osorio (1999) argue that PC 0025+0447 is a young ($\tau \lesssim 600$ Myr) brown dwarf, the latter basing their claim on the object's small radial ($v_r = 6 \pm 3$ km s^{-1}) and rotational ($v \sin i = 13 \pm 3$ km s^{-1}) velocities and possible (although controversial) detection of the 6708 Å Li line. Reid, Tinney, & Mould (1994) measure a correspondingly small space motion for this object of $v_{tot} = 10 \pm 28$ km s^{-1}. Martín, Basri, & Zapatero Osorio (1999) also detect signatures of optical veiling (weakening of TiO and VO bands) during periods of higher excitation; i.e, with He I and O I in emission. These signatures are consistent with flaring (c.f., 2MASS 0149+2956 in Figure 5.6; Liebert et al. 1999), or accretion, but fails to explain the steady emission.

If PC 0025+0447 is a brown dwarf, it is possible that 2MASS 1237+6526 could be an evolved or lower-mass analog. Note, however, that Mould et al. (1994) argue against PC 0025+0447 being a brown dwarf based on significant Li depletion, and propose rather that it is a Hyades-age ($\tau \gtrsim 625$ Myr) main sequence star with normal photospheric thermal emission. This scenario is consistent with the trignometric parallax and color-magnitude models (Martín, Basri, & Zapatero Osorio, 1999).

The strong emission in this object, like 2MASS 1237+6526, could originate from an interacting brown dwarf secondary. In this case, the primary can either be a low-mass star ($\tau \gtrsim 900$ Myr)

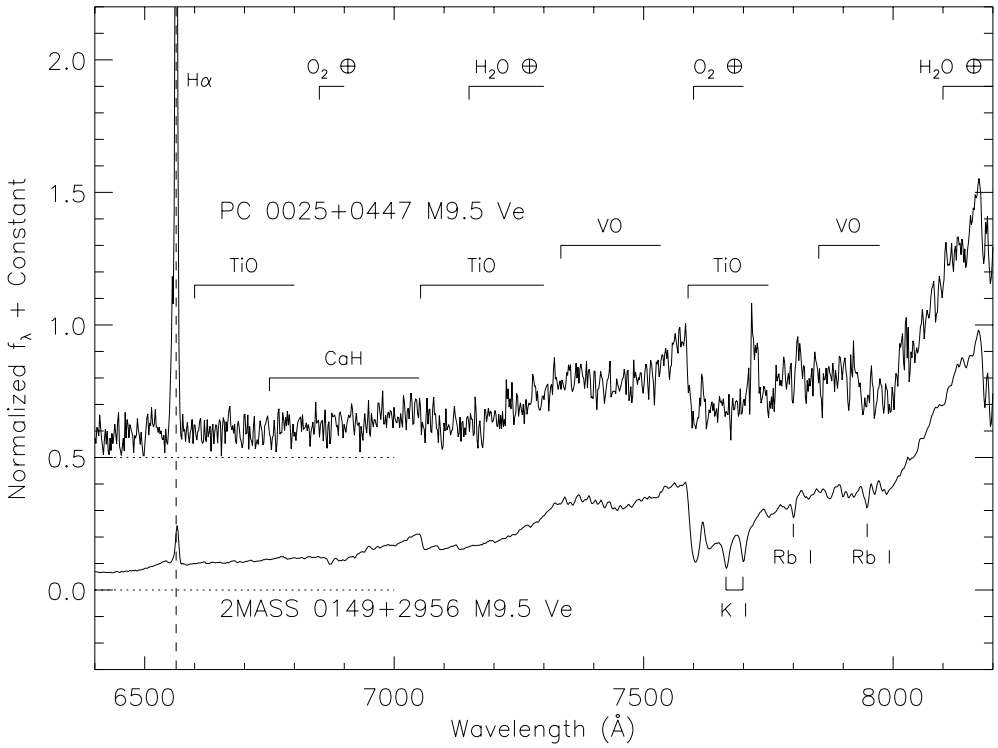

Figure 5.19: Optical spectrum of the M9.5 Ve PC 0025+0447 (I. N. Reid, priv. comm.), compared to the (quiescent) spectrum of the M9.5 Ve 2MASS 0149+2956 (Liebert et al., 1999). M dwarf features listed in Kirkpatrick et al. (1999b) are noted.

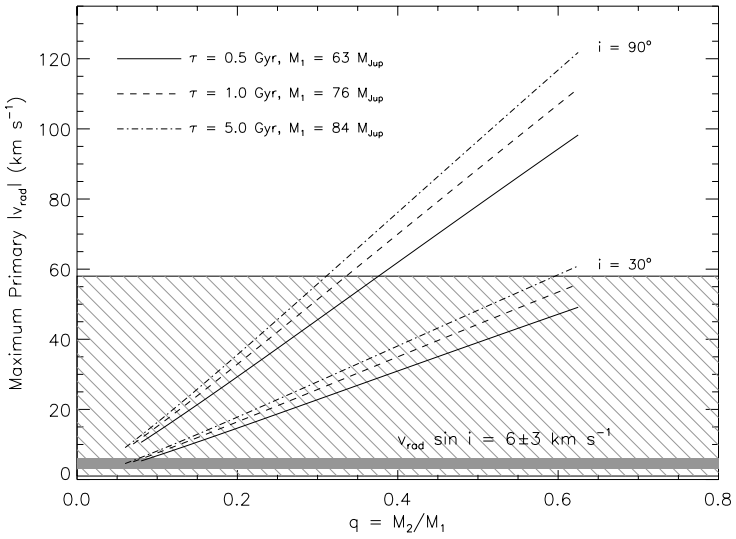

Figure 5.20: Predicted maximum $|v_{rad}|$ of the primary in an interacting binary PC 0025+0447 system. Shown are vaues for $\tau = 0.5$, 1.0, and 5.0 Gyr, corresponding to primary masses of 64, 76, and 84 M_{Jup} assuming $T_{eff} = 2100\pm100$ K, and $i = 90°$ and 30°. Observational constraints from Martín, Basri, & Zapatero Osorio (1999) are indicated by the hatched (range of values) and solid (best estimate) regions.

or a brown dwarf itself ($\tau \lesssim 900$ Myr), while the secondary must have $M_2 < 70$ M_{Jup}. For ages of $\tau = 0.5$, 1.0, and 5.0 Gyr, the typical temperature of an M9.5 V (2100±100 K, Kirkpatrick et al. 1999) corresponds to primary masses of 63, 76, and 84 M_{Jup}, respectively (Burrows et al., 1997). The observed constraints on this hypothetical system are (1) $1 \lesssim |v_{rad} \sin i| \lesssim 58$ km s^{-1} (from Table 2 in Martín, Basri, & Zapatero Osorio 1999a) and (2) $v_{rot} \sin i = 13\pm3$ (Martín, Basri, & Zapatero Osorio, 1999). Figure 5.21 plots the predicted maximum $|v_{rad}|$ for the primary in an interacting system as a function of q (see §5.3.4) with the parameters listed above and in Table 5.4. The $|v_{rad} \sin i|$ constraints are indicated by the hatched region, as well as the mean value reported by Martín, Basri, & Zapatero Osorio (1999). This latter value effectively rules out in an interacting system unless $i \lesssim 50°$ and q is very small (e.g., $q < 0.30$ for $i = 20°$). It is possible that this value of $v_{rad} \sin i$ was measured when the primary and secondary were at maximum projected separation (i.e., minimum orbital $v_{rad} \sin i$). The range of observed values (all made at low resolution using LRIS) is not as restrictive, although errors on these measurements exceed 20 km s^{-1}.

A better constraint is the $v_{rot} \sin i$ measurement. Assuming that the binary components are sufficiently close as to be tidally locked[5], the equatorial velocity of the primary will be

$$v_{rot} = \frac{2\pi R_1}{p}. \tag{5.18}$$

Comparing the observations to the predicted values (Figure 5.21) again require $i \lesssim 40°$ and small q (e.g., $q \lesssim 0.28$ for $i = 20°$). It is therefore highly unlikely that PC 0025+0447 is an interacting

[5]Note that tidal dissipation prior to tidal lock would remove angular momentum from the system, implying a slightly lower critical q during this phase.

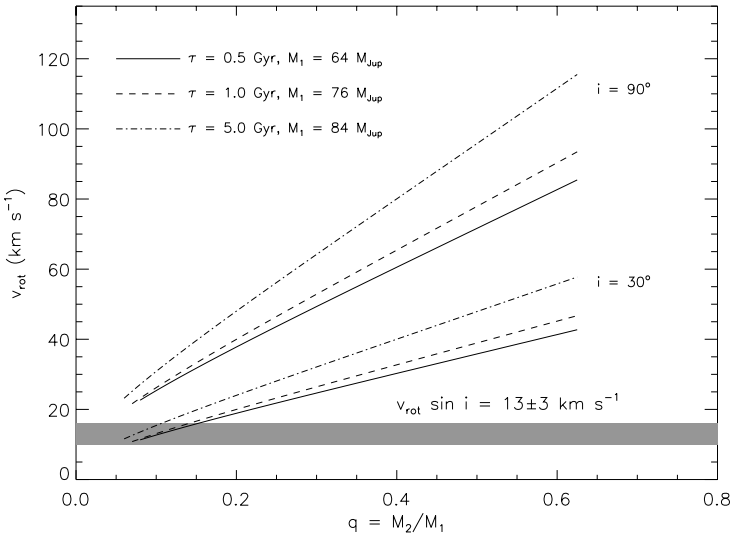

Figure 5.21: Predicted v_{rot} of the primary in an interacting binary PC 0025+0447 system assuming tidal lock. Curves are those of Figure 5.20. A measurement of $v_{rot} \sin i = 13 \pm 3$ from Martín, Basri, & Zapatero Osorio (1999) is indicated by the solid region.

binary system.

With the similarity in unique, strong, and persistent emission in these two objects, it is difficult to ignore the possibility that their activity is in some way related. However, the mechanism for both of these objects remains unclear. The most likely scenario for PC 0025+0447 (and possibly also for 2MASS 1237+6526), is that of a young, post-T Tauri, active brown dwarf or low-mass star. Substellarity does not require the presence of Li I, since a 400-500 Myr old object (i.e., younger than the Hyades) would have a mass of around 60 M_{Jup}; i.e., at the Lithium burning limit. The extremity in emission for both objects could be a combination of both youth and viewing angle if magnetic fields are the source (Buzasi, 1997). Whatever the underlying mechanism, PC 0025+0447 and 2MASS 1237+6526 are clearly exceptions and not the rule, and are therefore interesting objects for further investigation.

5.6 Summary

In this chapter, we have examined the properties of 2MASS 1237+6526, a faint T dwarf showing Hα in emission. Spectroscopic observations over 1.6 years indicate that this emission is both persistent and steady, and the relative luminosity of the line, $\log L_{H\alpha}/L_{bol} = -4.3$, is significantly greater than that of other active L and T dwarfs. This stands in bold contrast to the apparent decrease in emission frequency and luminosity for objects later than M7 V, as investigated by Gizis et al. (2000). The persistence of the emission in 2MASS 1237+6526 effectively rules out classical flaring as a possible mechanism, although some unique continuous or rapidly-repeating flare cycle could be responsible. Heating by acoustic waves cannot provide sufficient energy to power this emission. It is possible that the activity is a sign of extreme youth, although this requires 2MASS 1237+6526 to have a very low mass.

We have examined in detail the possibility that 2MASS 1237+6526 could be an interacting brown dwarf binary, with emission resulting from accretion of material from a faint, close secondary. Comparison to near-infrared monitoring observations made over two days rules out this scenario for $i > 60^\circ$ and $M_2 > 22$ M_{Jup}, placing stringent constraints on the geometry and membership of such a system.

Finally, we have compared this object to a similarly unique active dwarf, the M9.5 Ve PC 0025+0447 (Schneider et al., 1991), which has had steady Hα emission over eight years at a level around $\log L_{H\alpha}/L_{bol} = -3.4$ (Schneider et al., 1991; Mould et al., 1994; Martín, Basri, & Zapatero Osorio, 1999). Kinematic observations of this object generally reject the possibility that this object is itself an interacting binary, and a more likely explanation is that it is a young, low-mass star or high-mass brown dwarf. It is possible, in fact, that both objects are simply young, active, substellar objects which have recently evolved out of the classical T-Tauri phase. Future studies may be aimed at identifying features of low-gravity, excess luminosity, or (in the case of 2MASS 1237+6526) space motion. Regardless, 2MASS 1237+6526 is either a benchmark or black sheep in the activity characteristics of cool brown dwarfs.

Chapter 6 2MASS 0559-1404

How far that little candle throws his beams!
So shines a good deed in a naughty world.
William Shakespeare *Merchant of Venice, V:1*

6.1 Introduction

[1]The characterization of astronomical populations is commonly traced through its brightest members. Such objects permit detailed observational investigation at higher resolution and typically over a broader wavelength scale. In low-mass stellar studies, bright objects are quite often nearby, enabling the measurement of space motion and parallax. Identifying proximate low-mass stars and brown dwarfs also improves our census of the Solar Neighborhood, a sample by which many of the properties of the Galaxy and extragalactic systems are anchored.

Our search for T dwarfs has identified one particularly bright example, 2MASS 0559-1404. This object has J = 13.83±0.03, roughly half a magnitude brighter than the closest known T dwarf, Gliese 229B. As such, 2MASS 0559-1404 is an excellent target for detailed investigation. In this chapter, we describe the spectral and photometric properties of this object and consider its place amongst other T dwarfs identified by 2MASS. In §6.2, we describe the initial discovery and characterization of 2MASS 0559-1404, identified from spectral data obtained with the Palomar 60" Cornell-Massachusetts Slit Spectrograph (Wilson et al., 2001a, hereafter CorMASS). We present further observations in §6.3, including a complete spectrum from 0.6–4.7 μm. In §6.4, we address the possibility that 2MASS 0559-1404 could be a double brown dwarf, drawing on parallax observations made through the USNO parallax program (see §7.8.1) and imaging observations made with HST. We summarize our results in §6.5.

6.2 Identification

6.2.1 Selection and Confirmation

2MASS 0559-1404 was initially selected as a T dwarf candidate from the wdb0699 search sample (see §2.4.2.2). This object was successfully reimaged on 23 September 1999 (UT) at J-band using the Palomar 60-inch Infrared Camera (Murphy et al., 1995) confirming it as a bona-fide T dwarf candidate (i.e., not a minor planet or artifact; see §2.5). 2MASS 0559-1404 is the brightest 2MASS T dwarf candidate confirmed to date, with J = 13.83±0.03, H = 13.68±0.04, and K_s = 13.61±0.05. It is also one of the reddest 2MASS T dwarf candidates, with J−K_s = 0.22±0.06. Optical SERC-EJ (Morgan et al., 1992) and J-band 2MASS images of the 2MASS 0559-1404 field are shown in Figure 6.1; no optical counterpart is seen to $B_J \sim 23$, implying $B_J -$ J > 9. Non-detection on SERC-ER R-band plates implies R−J > 8.

[1]This chapter is based partially on results presented in Burgasser et al. (2000c); Burgasser (2001).

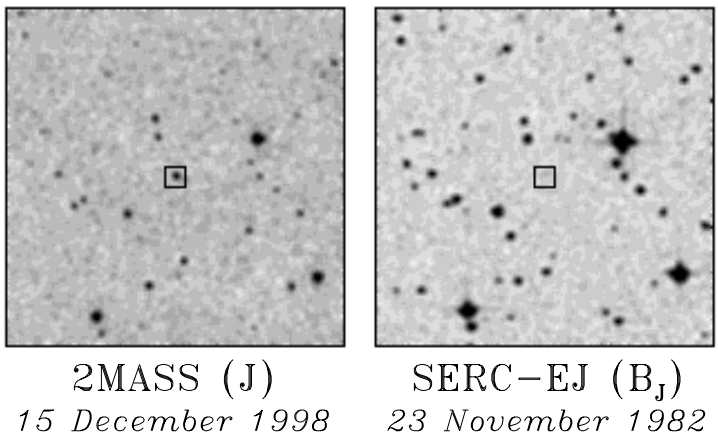

Figure 6.1: SERC-EJ B_J-band and 2MASS J-band images of the 2MASS 0559-1404 field. Images are $5' \times 5'$ with North up and East to the left. A $20'' \times 20''$ box is drawn around the location of the T dwarf in both images.

6.2.2 CorMASS Spectrum

Low-resolution near-infrared spectral data of 2MASS 0559-1404 were obtained on 24 October 1999 (UT) using CorMASS. This newly commissioned instrument is an R $\sim$ 300 prism cross-dispersed near-infrared spectrograph, with a 256×256 NICMOS3 array and a 40 lines mm^{-1} grating, blazed at 4.8 μm. CorMASS was designed primarily for the spectral classification of candidate low-mass objects color-selected from the 2MASS database. The instrument's echelle format provides simultaneous coverage of the zJHK bands, for $0.8 \lesssim \lambda \lesssim 2.5$ μm. The fixed slit has a width of $2''$ and a length of $15''$. Further details on this instrument can be found in Wilson et al. (2001a).

6.2.2.1 Observations and Data Reduction

Conditions during the CorMASS observations on 24 October 1999 (UT) were not photometric, and estimated seeing was $\sim 1\farcs5$, with variable thin cirrus throughout the night. 2MASS 0559-1404 was initially acquired in imaging mode at K_s-band and placed into the slit. Total on-source time was 2400 seconds divided into sets of 300-second integrations, nodding $\sim 5''$ along the slit between exposures. The A2 V standard HD 77821 (Elias et al., 1982) was observed immediately after the target exposure for flux calibration.

Spectra were reduced using standard IRAF routines. After correction for bad pixels, flat field and flux calibration images were corrected for NICMOS3 reset-decay bias (also known as shading) as follows: a quadratic was fit to a row-by-row clipped median of the top quarter of the array, the portion unused by the spectrograph. The fit was extrapolated to 128 rows for the top two quadrants, duplicated for the bottom two quadrants, and subtracted row-by-row from all pixels. All images were flat-fielded with a pixel responsivity solution from the APFLATTEN task using dome flats from all five nights of the run summed together. Nodded image pairs for the science object were subtracted from each other to remove sky background and reset-decay bias. The APALL task was used for spectral extraction. Wavelength calibration was accomplished using spectral observations

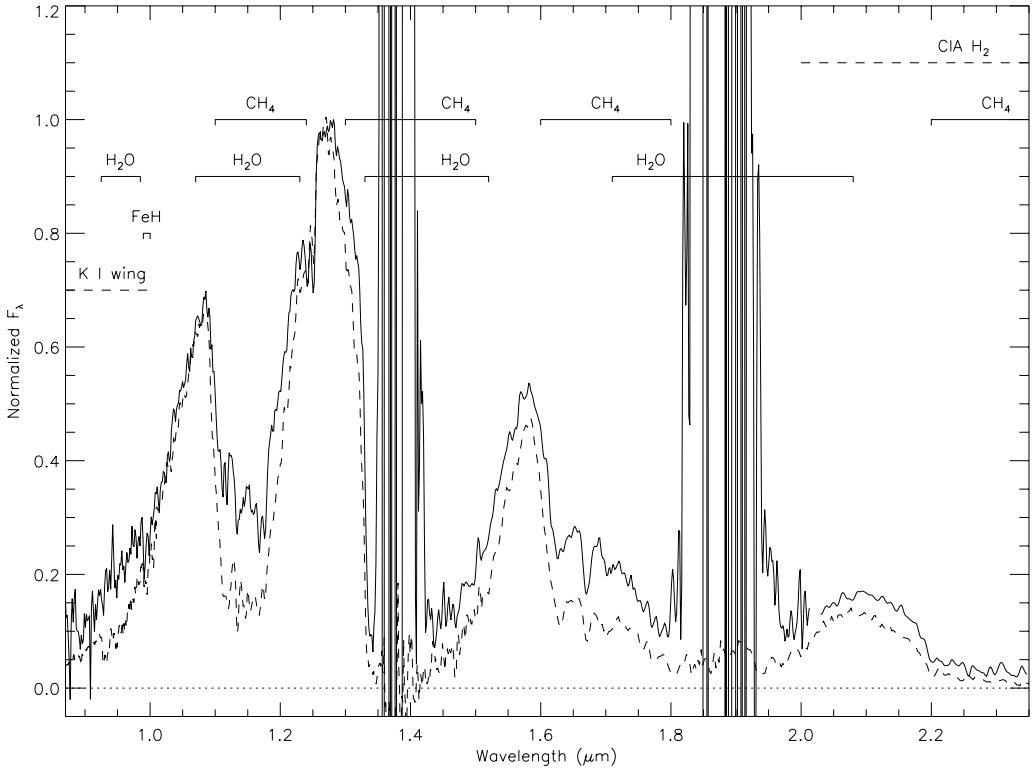

Figure 6.2: Near-infrared spectrum of 2MASS 0559-1404 (solid line) obtained by CorMASS. Overlaid are SDSS 1624+0029 data from Burgasser et al. (2000a, §3.2) and from Strauss et al. (1999) for the 0.87–1.0 μm and 1.0–2.35 μm regions, respectively (dashed line). Both spectra are normalized to one at the 1.27 μm peak. Prominent molecular bands of H_2O, CH_4, and H_2 (collision-induced absorption) are indicated, as is the FeH band at 0.9896 μm and the K I wing at z-band.

of the planetary nebula NGC 7027 obtained on 25 October 1999 (UT). Flux calibration was done by dividing by the reduced spectrum of the standard star, which was hand corrected for stellar H Paschen and Brackett recombination lines. That ratio was then multiplied by a 8810 K (Tokunaga, 2000) blackbody to complete the flux calibration. Finally, all 300-second observations for each order were weighted by the spectra mean and combined with the SCOMBINE task using a trimmed average. Orders were stitched together with SCOMBINE after hand deletion of noisy data at the ends of the orders.

6.2.2.2 The Near-infrared Spectrum of 2MASS 0559-1404

The spectrum of 2MASS 0559-1404 is shown in Figure 6.2, along with optical (0.87–1.0 μm; Burgasser et al. 2000b) and near-infrared (1.0–2.35 μm; Strauss et al. 1999) data for SDSS 1624+0029. The combined SDSS 1624+0029 spectrum was smoothed to the resolution of CorMASS. Spectra for both objects are normalized to one at 1.27 μm (J-band peak). Detailed views of 0.88–1.01 and 1.15–1.345 μm are shown in Figure 6.3.

Absorption features listed in Tables 3.7 and 3.11 are identified in these figures. The characteristic

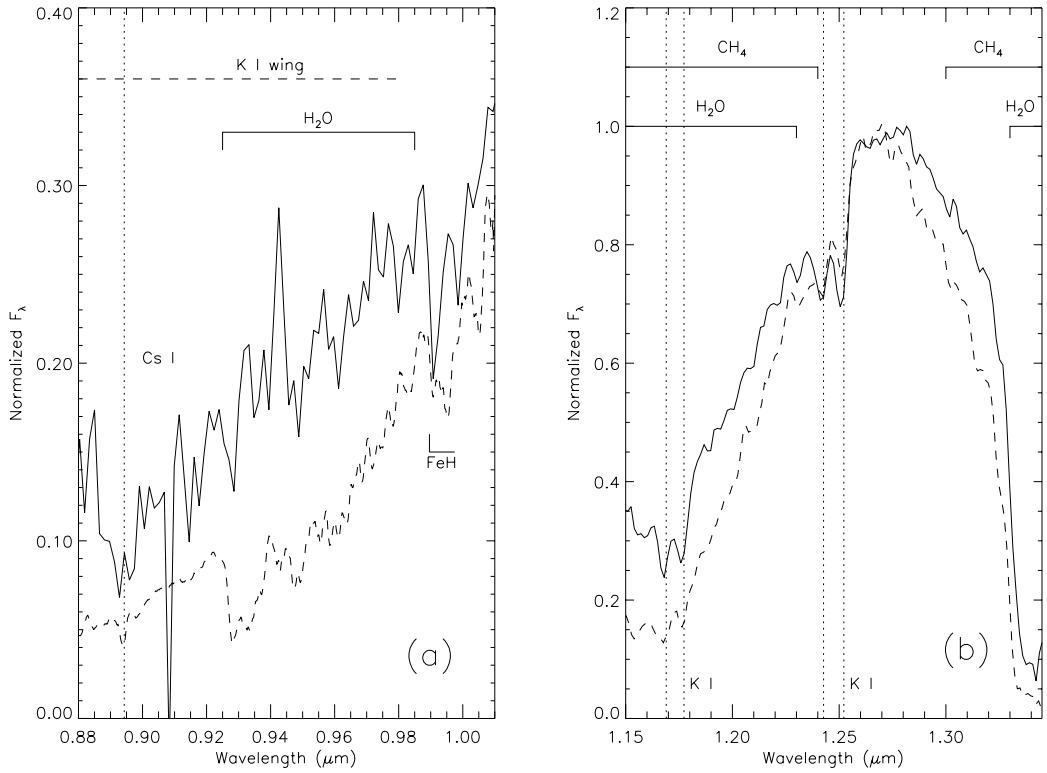

Figure 6.3: Two detailed regions of Figure 6.2 showing the (a) 0.88–1.01 μm and (b) 1.15–1.345 μm regions. Spectra are normalized at 1.27 μm. Features of FeH (0.9896 μm), K I (1.1690, 1.1773, 1.2432, 1.2522 μm), and Cs I (0.8943 μm) are indicated, as are H_2O and CH_4 bands.

CH_4 bands at 1.6 and 2.2 μm are present, as are bands at 1.1 and 1.3 μm identified from laboratory data (Fink & Larson, 1979), which are blended with H_2O bands at the same wavelengths. An FeH feature is seen at 0.9896 μm (0-0 band of $A^4\Delta$-$X^4\Delta$) which has also been identified in SDSS 1624+0029 (Burgasser et al., 2000a, §3.2.2). We do not detect the higher order 0-1 FeH band at 1.191 μm, which is known to weaken in the latest L dwarfs (McLean et al., 2000). Two sets of K I doublets are noted at 1.1690 & 1.1773 μm (4p $^2P_0$ − 3d ^2D) and 1.2432 & 1.2522 μm (4p $^2P_0$ − 5s ^2S), as is Cs I at 0.8943 μm (6s $^2S_{1/2}$ − 6p $^2P_{1/2}$). We do not detect the 2-0 $X^1\Sigma^+$-$X^1\Sigma^+$ band of CO at 2.3 μm.

Comparison between 2MASS 0559-1404 and SDSS 1624+0029 reveals significant differences in spectral morphology. In Figure 6.3a, it is apparent that the slope between 0.9 and 1.05 μm is shallower in 2MASS 0559-1404, possibly due to decreased absorption by the pressure-broadened K I doublet at 0.7665 and 0.7699 μm (Liebert et al., 2000b). CH_4 and H_2O features are generally weaker in 2MASS 0559-1404, exemplified by the significantly weakened 1.1–1.2 μm trough between z- and J-band peaks. The decreased CH_4 opacity noticeably affects the shape of the J-band peak near 1.27 μm, as the weak CH_4 wings at 1.24 and 1.30 μm carve out less flux on either side of the peak. In Figure 6.2, a significant flux offset is seen at the base of the 1.6 μm CH_4 band in 2MASS 0559-1404, and relative enhancement of flux at both H- and K-bands in this object is almost certainly due to decreased H_2 CIA (1-0 Quadrupole), H_2O, and CH_4 opacity.

6.2.3 Interpreting 2MASS 0559-1404 as a Warm T dwarf

The weak CH_4 bands seen in 2MASS 0559-1404 can be most readily explained by this object being warmer than other T dwarfs identified by 2MASS. At higher effective temperatures, the dominant carbon-bearing species changes from CO to CH_4 at smaller optical depths (higher above the photosphere), so that the CH_4 column density will be less than that of cooler T dwarfs, and observed band strengths correspondingly weaker. Increased thermal flux will also be seen at the base of these bands, particularly at 1.6 μm, which is unaffected by H_2O absorption. The lower CH_4 column density directly affects the H_2O column density, via the reaction CO + 3 H_2 → CH_4 + H_2O, leading to shallower bands at 1.1 and 1.45 μm. Water can also be heated and dissociated by dust layers deep in the photosphere (Leggett, Allard, & Hauschildt, 1998). Finally, decreased H_2 CIA opacity at K-band, congruous with reduced CH_4 and H_2O opacity, will result in redder J-K_s colors with warmer T_{eff}. These features are observed in 2MASS 0559-1404.

The warm temperature of this object is independently supported by the detection of the 0.9896 μm FeH band, which is present but weakening in the latest L dwarfs (Kirkpatrick et al., 1999b). A similar argument has been made for SDSS 1624+0029 by Burgasser et al. (2000a), which was one of only three T dwarfs in that particular sample to show this feature (see Figure 5.1). SDSS 1624+0029 also exhibits optical flux between broadened Na I and K I features (Liebert et al., 2000b), and Nakajima et al. (2000) have argued that this object is both warmer and dustier than Gliese 229B based on its shallower CH_4 and H_2O bands. By analogy, 2MASS 0559-1404 should be warmer still. Finally, the detection of excited K I lines at J-band, which are seen to weaken in the latest L dwarfs (McLean et al., 2000), is further evidence of the relative warmth of this object.

6.2.4 The Photometric Distance of 2MASS 0559-1404

The relative brightness of 2MASS 0559-1404 as compared to other T dwarfs suggests that it may be a nearby brown dwarf. Ignoring for the moment parallax observations of this object (§7.8.1), we can estimate its photometric distance using simple scaling arguments. A lower limit is obtained by assuming 2MASS 0559-1404 has the same intrinsic brightness as Gliese 229B, $M_J = 15.51 \pm 0.09$

(Leggett et al., 1999), so that

$$d(pc) = 10^{0.2(J-M_J)+1} \tag{6.1}$$

yields d $\gtrsim$ 4.6 pc. However, if 2MASS 0559-1404 is warmer than Gliese 229B, it is also more luminous (due to the roughly constant radii of brown dwarfs). The latest-type L dwarfs have M_J $\sim$ 14.9 (Kirkpatrick et al., 2000); hence, assuming that these objects are intrinsically brighter at this band than 2MASS 0559-1404, Equation 6.1 yields d $\lesssim$ 6.1 pc. A corresponding range from K_s-band magnitudes yields 4 < d < 14 pc, the larger limit coming from the significant difference in color between late L dwarfs (J$-$K$_s$ $\sim$ 2) and 2MASS 0559-1404. Therefore, barring multiplicity, the photometric distance of 2MASS 0559-1404 is roughly 4–8 pc, within the 8 pc nearby star sample defined by Reid & Gizis (1997). However, as we shall see in §7.8.1, this distance is too small, due to the possible duplicity of 2MASS 0559-1404 (§6.4) and/or redistribution of flux as dust clouds settle out of the photospheres of post-L dwarfs.

6.3 Follow-up Observations

Following our initial detection and characterization of 2MASS 0559-1404, we obtained additional spectra in to order to investigate features over a broader wavelength range. For example, observations long-ward of 2.5 μm sample the strong fundamental bands of H_2O (2.7 μm), NH_3 (3.0 μm), CH_4 (3.3 μm), H_2S (3.75 μm), and CO (4.7 μm). The latter 1-0 $X^1\Sigma^+$-$X^1\Sigma^+$ band of CO can aid in constraining the atmospheric abundance of this molecule in 2MASS 0559-1404, which is sensitive to convective mixing (Noll, Geballe, & Marley, 1997; Oppenheimer et al., 1998; Griffith & Yelle, 1999) and transparency (Lodders, 1999) in T dwarf atmospheres. At shorter wavelengths lie the broad K I and Na I features, as well as a host of other atomic and molecular absorptions prominent in late L and early T dwarfs including the fading hydrides FeH, CrH, and CaH. The presence or absence of these bands in 2MASS 0559-1404 could potentially constrain the temperature range of the L/T transition, which is likely to be less than 350 K (Kirkpatrick et al., 2000).

In this section, we focus on two spectral regions, the red optical (§6.3.1) and 3.0–4.7 μm (§6.3.2). A complete spectrum of 2MASS 0559-1404 from 0.6 to 4.7 μm is presented in §6.3.3 and compared to that of Gliese 229B (Oppenheimer et al., 1998). Additional 1–2.5 μm spectra obtained for 2MASS 0559-1404 are described in §3.1.1 and §3.1.2.

6.3.1 Red Optical Spectrum

Red optical (6300–10100 Å) spectra were obtained for 2MASS 0559-1404 on 2000 March 5 (UT) using the Low Resolution Imaging Spectrograph (Oke et al., 1995, hereafter LRIS) mounted on the Keck 10m Telescope. Observation and data reduction procedures are described in §3.2. The reduced red optical spectrum of 2MASS 0559-1404 is shown in Figure 6.4, along with data for the L dwarfs 2MASS 1507-1627 (L5 V), 2MASS 0920+3517 (L6.5 V), and Gliese 337C (L8 V) (Kirkpatrick et al., 1999b, 2000; Wilson et al., 2001b); for Gliese 229B (Oppenheimer et al., 1998); and for SDSS 1254-0122 and Gliese 570D (§3.2). Spectra are displayed on a log scale and offset vertically in order to highlight features. Note that spectral data for the L dwarfs and Gliese 229B have not been corrected for telluric absorption features. The brightness of 2MASS 0559-1404 has enabled us to obtain a high signal-to-noise spectrum over much of the 6300–10100 Å range, so that accurate comparisons to earlier spectral types can be made.

If we examine the L dwarf features of CrH (8611 and 9969 Å) and FeH (8692 and 9896 Å), we see that the fading of these bands observed in the late L dwarfs (Kirkpatrick et al., 1999b) continues into the T dwarf regime, with only a weak 8611 Å CrH feature seen in SDSS 1254-0122 and not seen in 2MASS 0559-1404; and a weak 9896 Å FeH absorption seen in 2MASS 0559-1404. In fact,

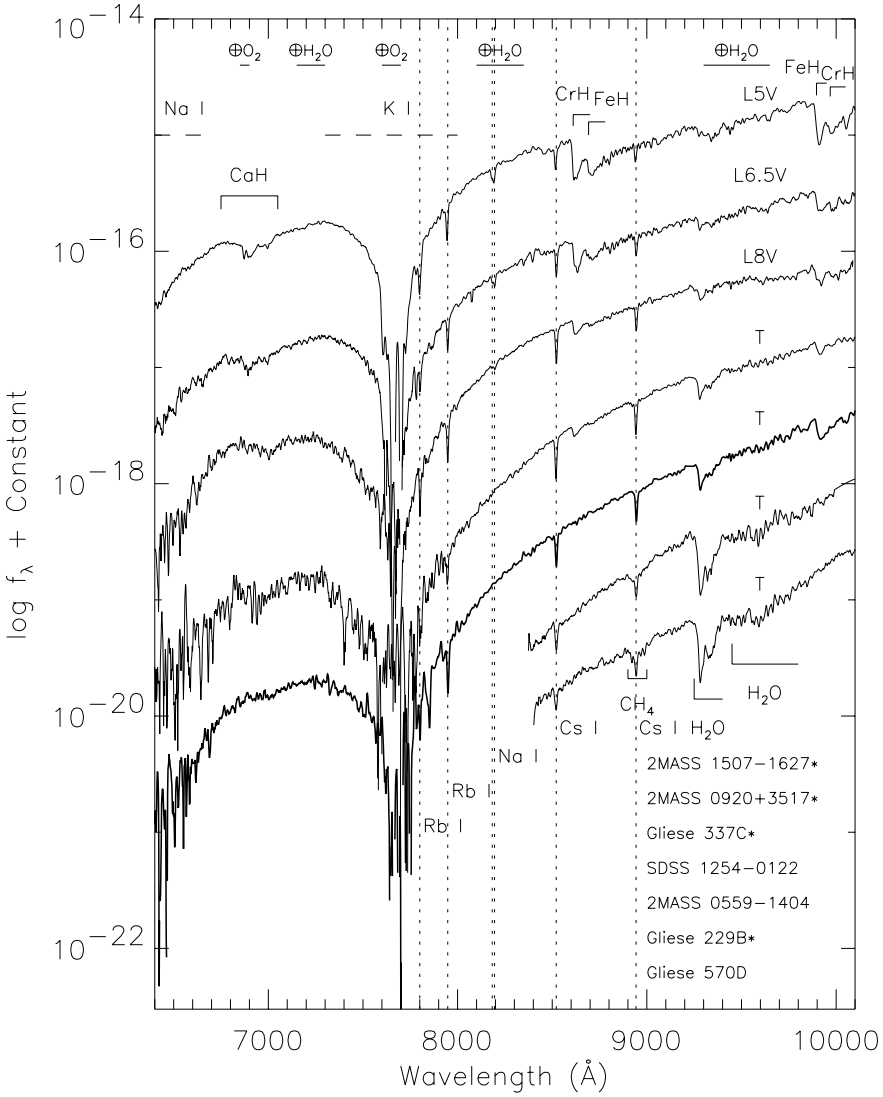

Figure 6.4: Red optical spectra of late L dwarfs 2MASS 1507-1627 (L5 V), 2MASS 0920+3517 (L6.5 V), Gliese 337C (L8 V) (Kirkpatrick et al., 1999b, 2000; Wilson et al., 2001b); and T dwarfs SDSS 1254-0122, 2MASS 0559-1404, Gliese 229B (Oppenheimer et al., 1998), and Gliese 570D. Spectra are displayed on a log scale and offset by a constant factor. Objects noted by an asterisk have spectra which are not corrected for telluric features, listed along the top. Features listed in Table 3.11 and from Kirkpatrick et al. (1999b) are noted.

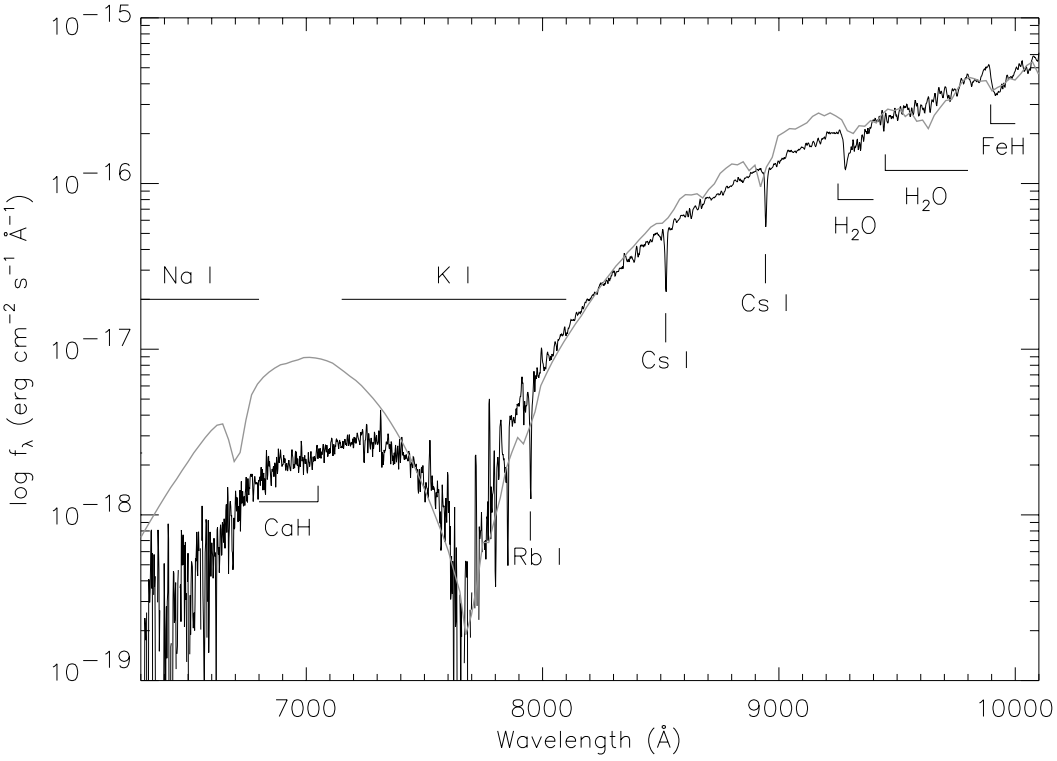

Figure 6.5: Red optical spectrum of 2MASS 0559-1404 (thin black line) along with an exploratory theoretical model from A. Burrows (priv. comm.). Features listed in Table 3.11 are indicated.

the latter feature appears to be stronger in 2MASS 0559-1404 than in the early T dwarf SDSS 1254-0122 and the L8 V Gliese 337C. The higher-order Na I lines at 8183 and 8195 Å are absent in both SDSS 1254-0122 and 2MASS 0559-1404, and the slope of these objects from 8000 to 10000 Å is significantly greater than that of the L dwarfs. Therefore, there appears to be a clear morphological break between the spectrum of 2MASS 0559-1404 and those of the late L dwarfs, implying that the effective temperature of this object is probably cooler than $\sim$ 1300 K (Kirkpatrick et al., 2000). On the other hand, the much stronger 9250 Å H_2O absorption seen in Gliese 229B and Gliese 570D, and the disappearance of the 9896 Å FeH band in these objects, implies that 2MASS 0559-1404 is likely to be warmer than $\sim$ 1000 K (Marley et al., 1996). Splitting the difference (and assuming these effects are temperature-dependent), we estimate the effective temperature of 2MASS 0559-1404 to be roughly 1150$\pm$150 K, with SDSS 1254-0122 slightly warmer due to the presence of CrH in its spectrum.

The most prominent feature in the spectra of Figure 6.4 is the broadened K I doublet centered at 7665 and 7699 Å. This absorption is unique to cool brown dwarfs, as it is the culmination of a highly transparent, high-gravity photosphere where alkalis have persisted over more refractory, dust-producing molecular species. The depth of this feature is largely the result of the substantial column depth through which K I is observed, while its breadth is caused by K–H_2 collisional broadening deep in the atmosphere, resulting in wide wings that extend over thousands of angstroms (Burrows,

Marley, & Sharp, 2000). Liebert et al. (2000b) have shown that this feature is almost entirely responsible for the strong ramp-up in flux from 8000 to 10000 Å in SDSS 1624+0029, as well as a peak-up in flux between the blue wing of the K I transition and the red wing of the even more heavily broadened Na I D lines at 5890 and 5896 Å[2] (i.e., the "blue bump"). Figure 6.5 plots the red optical spectrum of 2MASS 0559-1404 with an exploratory model from A. Burrows (priv. comm.), in which K I is largely responsible for the 7000–9000 Å opacity. The similarity between the model and data is strongly suggestive that K I is the dominant absorber in this spectral region for 2MASS 0559-1404 as well.

The brightness of 2MASS 0559-1404 allows us to examine the spectral region between the Na I and K I features with far greater detail than was possible for SDSS 1624+0029. Here, there appears to be a very weak band of CaH present, centered at 6900 Å. This feature is seen in L dwarf spectra (Kirkpatrick et al., 1999b, Figure 6.4). The presence of this band is peculiar, as Ca is predicted to be depleted around 1700–1900 K by the formation of dust species such as perovskite ($CaTiO_3$), hibonite ($CaAl_{12}O_{19}$), grossite ($CaAl_2O_4$), and gehlenite ($Ca_2Al_2SiO_7$) (Lodders, 1999). It may be that Ca has in fact not been depleted, and residual dust species may exist in the photosphere or are convectively mixed upward from deeper levels. Dust in the lower atmosphere of Gliese 229B has been invoked to explain weakened near-infrared H_2O bands in this object (Tsuji, Ohnaka, & Aoki, 1999). It is also possible that the apparent CaH band is actually the very red end of the 5890/5896 Å Na I doublet, whose line shape is not yet well understood (Burrows, Marley, & Sharp, 2000). We also note the absence of the 6708 Å Li I line in 2MASS 0559-1404. This has two possible interpretations: either 2MASS 0559-1404 is an old brown dwarf, with $\tau > 3.5$ Gyr and $M > 0.06$ $M_\odot$ for $T_{eff} = 1150$ K (Burrows et al., 1997), which has depleted all of its primordial Li via thermonuclear fusion (Chabrier, Baraffe, & Plez, 1996); or, Li could be depleted from the photosphere chemically by the formation of LiCl and LiOH (Burrows & Sharp, 1999; Lodders, 1999). The formation of these molecules is predicted to occur below 1300–1600 K (Burrows & Sharp, 1999), although dynamical mixing may dredge up atomic Li from warmer layers (c.f., Cs I in Gliese 229B; Oppenheimer et al. 1998). All of the alkalis are expected to survive in atomic form down to temperatures of $T \lesssim 1300$ K if dust species do not rain out of the photosphere, but can survive to $T \lesssim 1000$ K if dust species are removed (Burrows, Marley, & Sharp, 2000). The clear presence of the resonant doublet lines of Na I, K I, Rb I, and Cs I in the red optical spectrum of 2MASS 0559-1404 provides evidence that rain-out does indeed occur.

6.3.2 3.0–4.7 μm Spectrum

The 3–5 μm spectral region is primarily dominated by the fundamental bands of H_2O, CH_4, NH_3, and CO. This is also a region of significant telluric absorption and thermal emission from the Earth's atmosphere, making observations of faint L and T dwarfs particularly difficult. 2MASS 0559-1404, however, is sufficiently bright to be observed at these wavelengths.

We obtained a 3–4.7 μm spectrum of 2MASS 0559-1404 on 18 November 1999 (UT) using the Keck I Near Infrared Camera (Matthews & Soifer, 1994, hereafter, NIRC). Observations and data reduction are described in §3.1.1.5, with a fully reduced spectrum shown in Figure 3.4. As discussed in that section, the strong 3.3 μm fundamental band of CH_4 completely dominates this spectral region, suppressing most of the flux between 3–4 μm. This band is noticeably weaker in 2MASS 0559-1404 when compared to Gliese 229B (Oppenheimer et al., 1998), however, consistent with the interpretation that the former object is warmer.

There are other features of interest in this region, including the 4.7 μm CO band, which was

[2]The solar abundance of Na is 15.2 times greater than that of K (Anders & Grevesse, 1989), implying a 230-fold increase in the relative column density.

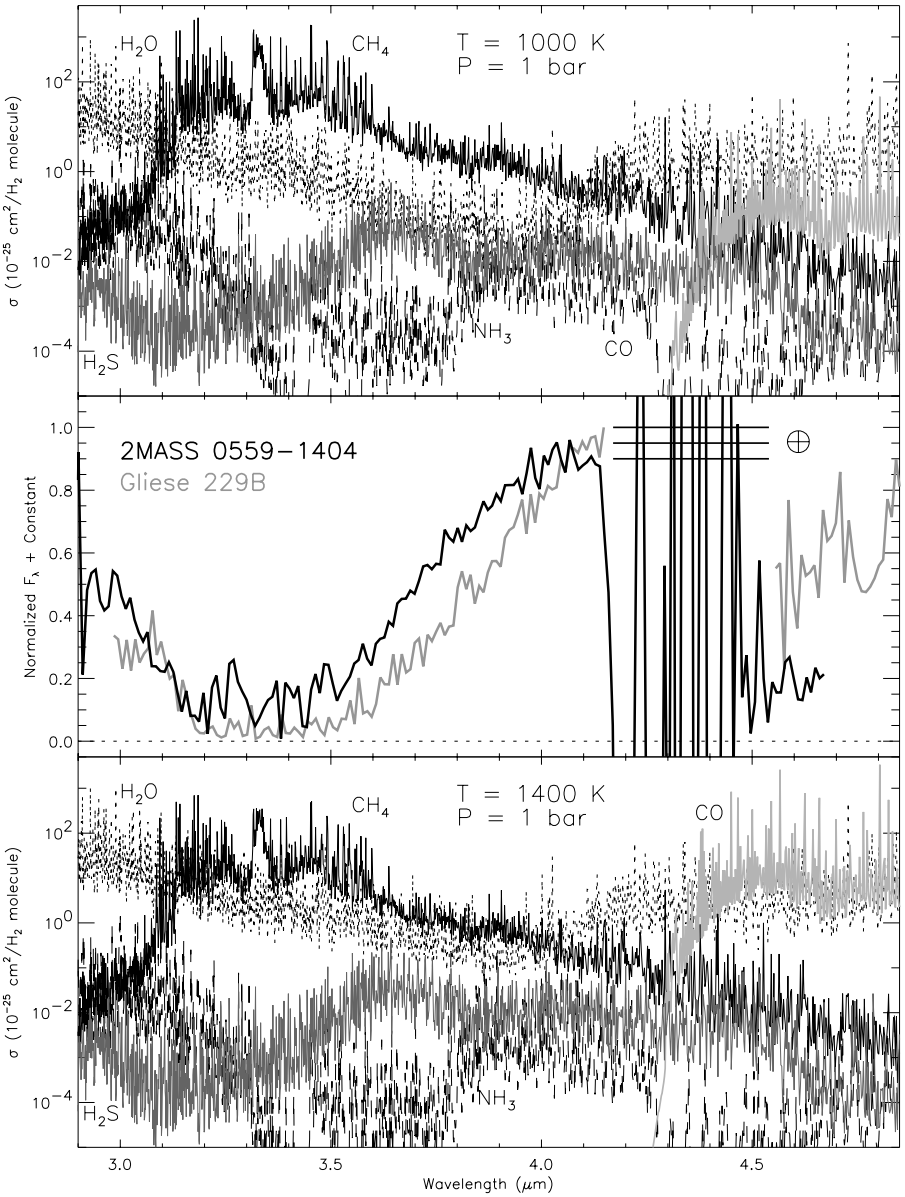

Figure 6.6: 3–4.7 μm spectra of 2MASS 0559-1404 (black line) and Gliese 229B (grey line; middle panel), the latter data from Oppenheimer et al. (1998). The top and bottom panels are opacity spectra from A. Burrows (priv. comm.), showing the relative opacities of CH_4 (thin black line), H_2O (dotted line), CO (light grey line), NH_3 (dashed line), and H_2S (dark grey line) for pressures of 1 bar and temperatures 1000 K (top) and 1400 K (bottom). Opacity spectra have been scaled by chemical equilibrium number densities as given by Burrows & Sharp (1999).

detected in Gliese 229B at higher concentrations than predicted by chemical equilibrium (Noll, Geballe, & Marley, 1997; Oppenheimer et al., 1998). The presence of this band can be explained by convective mixing of material from hotter regions below the photosphere (Prinn & Barshay, 1977; Griffith & Yelle, 1999). In Figure 6.6 we again plot the 3–4.7 μm spectra of 2MASS 0559-1404 and Gliese 229B (Oppenheimer et al., 1998), along with opacity spectra of H_2O, CH_4, NH_3, CO, and H_2S at P = 1 bar and T = 1000 K (top panel) and 1400 K (bottom panel). These data have been kindly provided by A. Burrows (priv. comm.). We have scaled the opacities by their chemical equilibrium abundances relative to H_2 using the calculations of Burrows & Sharp (1999). The temperatures and pressures chosen for the opacity spectra are meant to conservatively represent the conditions in the photosphere of Gliese 229B and 2MASS 0559-1404, respectively[3]. The most prominent absorbers in this region are H_2O and CH_4, although CO is as strong or stronger than H_2O from 4.4–4.9 μm at T = 1400 K. Because its abundance increases with higher temperature (Burrows & Sharp, 1999), the CO feature is likely to be prominent in 2MASS 0559-1404. Indeed, although our observations do not extend to the distinct 4.7 μm band seen in Gliese 229B, the relative suppression of flux from 4.5–4.65 μm in 2MASS 0559-1404 is likely due to CO absorption, particularly if the relative abundance of this species is enhanced by convective mixing.

The NH_3 molecule is a more elusive species in brown dwarf spectra (e.g., Saumon et al. 2000), and its abundance is greatly sensitive to both temperature and pressure (and thereby gravity). At chemical equilibrium, the contribution of this molecule to the overall opacity is far weaker than H_2O and CH_4. Even at the fundamental 3 μm band, NH_3 has an opacity that is roughly 100 times weaker than that of H_2O at T = 1000 K, and is even weaker at warmer temperatures. Hence direct detection of this molecule in these (comparatively) warm objects is unlikely. However, we note that the 3.0–3.1 μm spectrum of Gliese 229B is noticeably flatter than that of 2MASS 0559-1404. This is contrary to the behavior of the CH_4 and H_2O opacities, since H_2O is relatively weaker in these region at 1000 K, implying a steeper ramp-up in flux for the cooler object. It is possible that NH_3 could be responsible for the flux cutoff in Gliese 229B if its equilibrium abundance were enhanced by a similar factor as CO ($\sim 1600\times$; Noll, Geballe, & Marley 1997). However, since NH_3 abundance decreases with increasing temperature from 600 to 1300 K, and only moderately increases from 1300 to 2500 K (Burrows & Sharp, 1999), it is unlikely that significant material can be dredged up from warmer levels below the photosphere. Hence, NH_3 absorption is not likely to have any affect on the 3–5 μm spectra of either object. Detailed study of even cooler T dwarfs, such as Gliese 570D (Chapter 4) may ultimately provide unambiguous confirmation of this elusive molecule.

The sulfide reservoir H_2S is also relatively abundant in the photospheres of cool brown dwarfs, with an equilibrium abundance $\log N_{H_2S}/N_{H_2} \approx -4.5$ from 700–2500 K at 1 bar (Burrows & Sharp, 1999). The molecule has a particularly strong band at 3.75 μm which is along the red wing of the 3.3 μm CH_4 fundamental band. The far greater strength of the latter feature, however, generally overwhelms H_2S opacity by a factor of roughly 100 at T = 1000 K, and both CH_4 and H_2O opacities are stronger than H_2S at warmer temperatures. Again, convective mixing is not likely to be helpful due to its relatively fixed abundance over a broad range of temperatures (Burrows & Sharp, 1999). Both NH_3 and H_2S may be more readily resolved at mid-infrared wavelengths.

6.3.3 Characterizing the Full Spectrum

In Figure 6.7, we plot the culmination of our spectral observations of 2MASS 0559-1404, a complete spectrum from 0.6–4.7 μm, plotted in absolute F_ν in mJy (see §7.8.1). The spectrum has been stitched together using data obtained with LRIS (0.6–1.0 μm) and NIRC (1.0–4.7 μm), where the

[3]Noll, Geballe, & Marley (1997) estimate that unity optical depth for Gliese 229B at 4 μm occurs at P $\leq$ 1.3 bar and T $\leq$ 800 K, and it is likely that the photosphere temperature for 2MASS 0559-1404 at this wavelength is cooler than 1400 K. Hence, our temperature estimates are probably too high by 100–200 K.

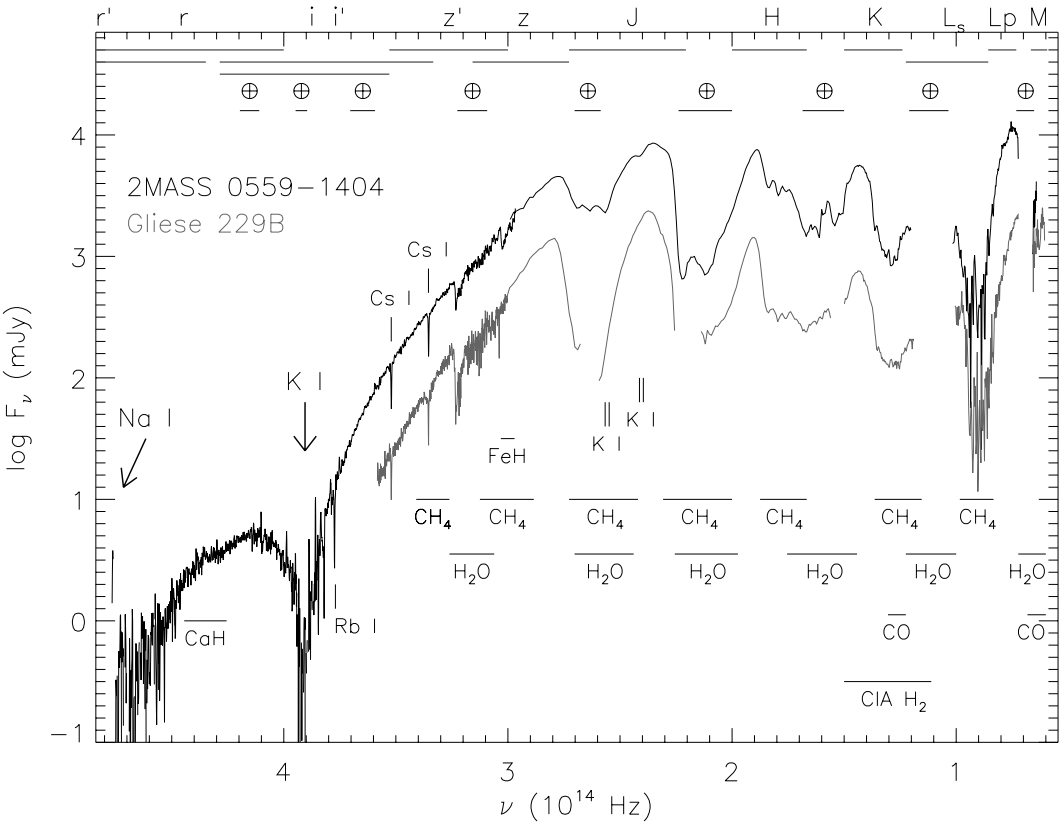

Figure 6.7: Combined optical and near-infrared spectra of 2MASS 0559-1404 (black) and Gliese 229B, the latter data from Oppenheimer et al. (1998). Spectra are plotted as $\log F_\nu$ in mJy versus frequency. The 2MASS 0559-1404 spectrum is a combination of LRIS data from 0.63–1.0 μm with NIRC data from 1.0–4.8 μm. Major absorption features of H_2O, CH_4, CO, FeH, CaH, Na I, K I, and Cs I are indicated, as well as regions of telluric absorption. The central wavelengths of standard photometric bands are indicated along the top.

3–4.7 μm flux has been calibrated using $K-L_p \approx 2.2$ from Stephens et al. (2001). For comparison, we have included data for Gliese 229B from Oppenheimer et al. (1998), also obtained using LRIS and NIRC. Major absorption bands and lines listed in Tables 3.7 and 3.11 are indicated, along with regions of telluric absorption ($\oplus$) and the wavelength coverage of standard photometric filters (Wade et al., 1979; Schneider, Gunn, & Hoessel, 1983; Bessell & Brett, 1988; Fukugita et al., 1997).

A few general conclusions can be made from this figure. First, it is interesting to note that the strongest absorption features are not the prevalent H_2O and CH_4 bands in the near-infrared, but rather the Na I and K I atomic features in the optical. This is a unique property of cool brown dwarf spectra, and enables searches done with i- and z-band colors (e.g., with SDSS) to readily distinguish these objects from other Galactic sources. We also see that while the 1–2.5 μm regime covers a significant portion of the total luminosity ($\sim$ 75%; Burrows et al. 1997[4]), the flux density

[4]See http://astro.NMSU.Edu/~exowww/planet/.

Table 6.1: Apparent Bolometric Magnitude of 2MASS 0559-1404.

λ (μm) (1)	Instrument (2)	Integrated Flux[a] (3)	% of Total (4)
0.0–0.6	Extrapolated	0.0005	0.007
0.6–1.0	LRIS	0.34	4.3
1.0–2.5	NIRC	5.87	75.5
2.5–2.95[b]	Extrapolated	0.27	3.5
2.95–4.7	NIRC	1.10	14.1
4.7–∞	Blackbody	0.20	2.5
f_{bol}		7.8$\pm$0.4[c]	
m_{bol}		16.26$\pm$0.06[c]	

[a]In units of 10^{-12} erg s^{-1} cm^{-2}.
[b]Flux estimate in this region is likely overestimated due to the presence of H_2O absorption.
[c]Assuming 5% error.

continues to rise to 5 μm. 2MASS 0559-1404 is an excellent candidate for spectroscopic observations in the mid-infrared, where the vibration-rotation bands of alkali chlorides and sulfides are strongest, particularly as their atomic counterparts become depleted (Lodders, 1999). This region also contains the strong fundamental ν_2 band of NH_3 (10.5 μm) and various silicate features. The SIRTF and SOFIA missions may provide our first glimpse at these features in brown dwarf spectra.

We can also make some comparisons between 2MASS 0559-1404 and Gliese 229B based on their spectra. In general, the H_2O and CH_4 bands are stronger in Gliese 229B, while FeH and CO bands are weaker. CIA H_2 may also be stronger in Gliese 229B given the greater relative suppression of flux at K-band in this object. Cs I lines appear to remain unchanged in strength, while K I doublets at 1.17 and 1.25 μm are only detected in 2MASS 0559-1404. The Oppenheimer et al. (1998) optical spectrum of Gliese 229B does not extend into the core of the 7700 Å K I feature, but does appear to have a shallower slope from 8500–10000 Å as compared to 2MASS 0559-1404. The weakening of both of these K I features may indicate the onset of depletion in the cooler T dwarf (Lodders, 1999). With the chemical equilibrium calculations of Burrows & Sharp (1999) as our guide, these features are all consistent with 2MASS 0559-1404 being a warmer and hence more luminous T dwarf.

Finally, the broad spectrum of 2MASS 0559-1404 allows us to make an estimate of its bolometric luminosity. To do this, we have followed the prescription of Leggett et al. (2001), integrating the observed spectrum (extrapolating over the 2.7 and 4.3 μm telluric breaks), extrapolating the short wavelength flux linearly to zero at zero wavelength, and using a 1150 K blackbody beyond 5 μm, scaled to match the flux values at our longest measured wavelengths. Table 6.1 summarizes the various contributions to the total bolometric flux, over 75% of which eminates from 1–2.5 μm, while 14% is emitted at 2.9–4.7 μm, even with the presence of the strong 3.3 μm fundamental band. Uncertainties are dominated by extrapolation errors at long wavelengths, including the likely overestimation of flux in the 2.5–2.9 μm region (containing a strong H_2O band coincident with telluric absorption), which cannot exceed 3.5% of the total luminosity; and offsets beyond 4.7 μm due to molecular absorption (overestimate) and the predicted peak in flux at 5 μm (underestimate), which are not likely to be more than 2.5–5% of the total luminosity. Hence, we estimate our uncertainties at 5%, and derive an apparent bolometric flux $f_{bol} = (7.8\pm0.4)\times10^{12}$ erg s^{-1} cm^{-2}. Using $f^0_{bol} = 2.48\times10^5$ erg s^{-1} cm^{-2} for $m_{bol} = 0$ (Drilling & Landolt, 2000), we derive $m_{bol} = 16.26\pm0.06$ for 2MASS 0559-1404. Note that this implies a J-band bolometric correction $BC_J = 2.43\pm0.07$, 0.24 mag greater than that for Gliese 229B (Leggett et al., 1999, 2.19$\pm$0.10) and 0.80 mag greater than that for the latest L dwarfs (Reid et al., 2001a, see §7.8.4).

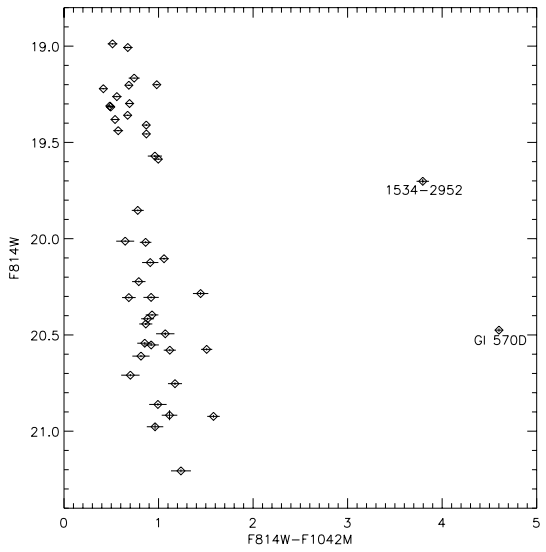

Figure 6.8: F814W−F1042M versus apparent F814W magnitude for sources in the PC chip field of 2MASS 1534-2952 and Gliese 570D. All background sources have F814W−F1042M ¡ 2, while the T dwarfs are redder than 3, allowing excellent segregation of background sources and target objects.

6.4 Is 2MASS 0559-1404 a Double?

The photometric distance of 4–8 pc derived in §6.2.4 suggests that 2MASS 0559-1404 may be one of the closest brown dwarfs to the Sun. However, parallax observations carried out through the USNO parallax program (see §7.8.1) is in fact 10 pc distant, implying $M_J = 13.80 \pm 0.04$, which is 0.62 mag brighter at J-band than the presumably warmer 2MASS 1254-0122. Furthermore, using our derived apparent bolometric magnitude (Table 6.1) and Equations 7.18 and 7.24 (see §7.8), we find $T_{eff} = 1350 \pm 80$ K, which is warmer than the estimated effective temperatures of L8 dwarfs (Kirkpatrick et al., 2000). On the other hand, if 2MASS 0559-1404 is an equal-magnitude binary, its temperature lowers to 1130±70 K, consistent with our spectroscopic estimate in §6.3.1. Hence, there is compelling evidence that 2MASS 0559-1404 is a double brown dwarf.

To address this possibility, we have examined HST images of 2MASS 0559-1404, obtained as part of a broader program to examine duplicity in T dwarfs. We have used the HST Wide Field/Planetary Camera 2 (Biretta et al., 2000, hereafter WFPC2) to image ten T dwarfs at high spatial resolution, using the F814W and F1042M broadband filters. The choice of WFPC2 and the two filters (essentially i and z) enables segregation of bona-fide T dwarf companions and background stars. As shown in Figure 6.8, we can clearly distinguish these two populations by color alone, foregoing the need for common proper motion confirmation. Observations (conducted during Cycle 9) have recently been completed and analysis is currently underway.

The observations of 2MASS 0559-1404 were made on 6 September 2000 (UT). Pairs of 1200s and 1300s observations were made at F814W and F1042M, respectively. Standard pipeline reduction images were used for our analysis. The double exposures were required to eliminate cosmic rays in the images, which are abundant in our long exposures. Cosmic ray rejection was done using software provided by C. Miskey (priv. comm.). Figure 6.9 shows a $10'' \times 10''$ section of the reduced F814W

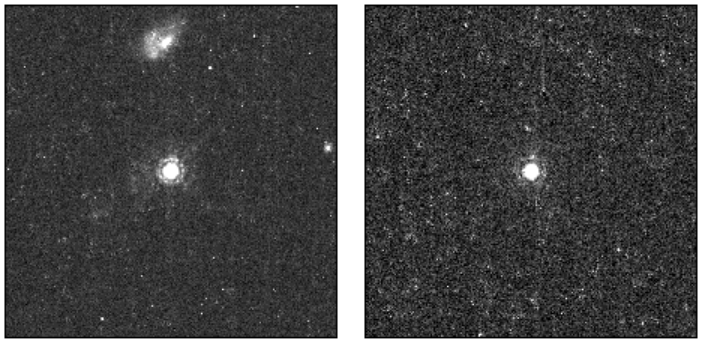

Figure 6.9: F814W and F1042M WFPC2 images of 2MASS 0559-1404. The field of view is $10''\times10''$, with North oriented 55° counterclockwise from vertical.

and F1042M images around 2MASS 0559-1404. We immediately discern the utility of our choice of two bands, as the nebulosity seen above 2MASS 0559-1404 in the F814W image is absent in the F1042M image. Indeed, few stars were seen at F1042M except for the target objects.

Initial examination of the images indicates that 2MASS 0559-1404 is unresolved. We can quantify this by comparing the point spread function (PSF) profile of 2MASS 0559-1404 to an apparently single reference star in the F814W frame, as shown in Figure 6.10. PSF profiles along the (image) x- and y-axes were computed by summing the rows and columns, respectively, of a 30×30 pixel box around the target. Both object profiles and that of the F814W reference star are similar, with a full-width at half-maximum (FWHM) of 0.″11, roughly the diffraction limit of HST at 0.8 μm. There appears to be a slight asymmetry in the PSF column profile at F1042M, with a subtle bump extending 0.″1–0.″2 from the center of the PSF profile; however, no secondary could be resolved by PSF fitting using the XPHOT task (D. Koerner, priv. comm.). We therefore conclude that 2MASS 0559-1404 is single within the resolution of our images, roughly 0.″05.

The HST and photometry data lead us to three possible conclusions for 2MASS 0559-1404. First, it could be a single object with an unusual spectral energy distribution, in which flux is redistributed toward 1 μm. This scenario would require much greater opacity beyond 5 μm as compared to SDSS 1254-0122. Second, 2MASS 0559-1404 could be a close binary system. At its distance, the physical separation of the hypothetical pair would be $\lesssim$ 0.5 A.U., implying an orbital period of roughly 1 year for two equal-mass 50 M_{Jup} objects. Of course, the orientation of the system could be such that it is not currently at maximal separation, which leads to a third possibility: 2MASS 0559-1404 could be a wider binary close to alignment. The latter two cases require high-resolution, follow-up imaging over the next few years to determine either an upper-limit on the separation or possibly the orbital parameters for this potential binary system.

6.5 Summary

In this chapter, we have discussed the identification and characterization of the brightest T dwarf identified to date, 2MASS 0559-1404. Various spectral indicators, including FeH at 9896 Å; strong K I lines at 1.25 μm; weak CH_4 at 1.3, 1.6, 2.2, and 3.3 μm; strong CO at 4.7 μm; and reduced suppression of flux at K-band, along with redder near-infrared colors, all suggest that this object is a

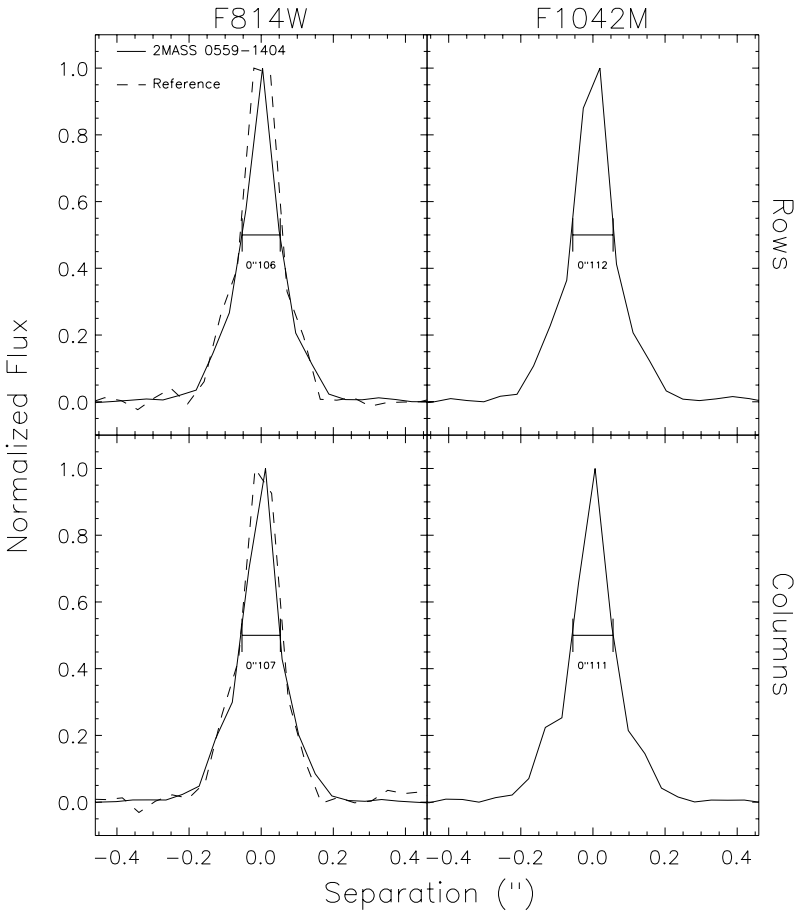

Figure 6.10: Row and column profiles of 2MASS 0559-1404 (solid lines) and a reference star in the F814W PC image (dashed lines) for the F814W and F1042M images in Figure 6.9. Profiles were derived by summing 30 rows or columns in the cross direction. A Gaussian fit to the PSF core yields the FWHM separations indicated in the panels.

relatively warm T dwarf. Its brightness has enabled a detailed investigation over a broad wavelength range, and has allowed us to examine the presence and strength of key diagnostic features, including the opacity window between the strongly broadened Na I and K I optical doublets, Li at 6708 Å (a tracer of mass through thermonuclear depletion, or temperature through chemical depletion onto LiCl and LiOH), CaH at 6750 Å (a tracer of dust rain-out), CH_4 at 3.3 μm (a measure of temperature), and CO at 4.7 μm (a tracer of convective mixing in the photosphere). This object is a prime target for longer wavelength observations in the upcoming mid-infrared missions SIRTF and SOFIA.

Using spectral data from 0.6 to 4.7 μm, along with parallax measurements made by the USNO Parallax Program, we have measured a total luminosity for this object of M_{bol} = 16.23±0.07, or L = (2.54±0.03)×10^{-5} $L_\odot$, corresponding to an effective temperature of 1340±80 K if it is single, or 1130±70 K if it is an equal-magnitude double. The question of duplicity is important for this object, as it is likely to be in a late stage of dust depletion, and as such is a benchmark for the investigation of this process occurring between the latest L dwarfs and the T dwarfs. 2MASS 0559-1404 is unresolved in HST imaging, however; if it is a close binary system, it could have an orbital period on the order of one year, enabling a dynamical mass measurement in a very short timeframe. This measurement would require either high-resolution spectroscopic monitoring (e.g., with NIRSPEC in echelle mode) if it is a closely-separated system, or additional HST or AO (with laser guide star) observations if it is more widely separated. Clearly, 2MASS 0559-1404 is an important target for future observational and theoretical study, as its brightness and potential duplicity may reveal new insight into the temperatures, masses, photospheric compositions, and atmospheric dynamics of brown dwarfs as they evolve from dusty L dwarfs to dust-free T dwarfs.

Chapter 7 Spectral Classification

...one is forced to wonder, where it will all lead to,
if everyone who works on stellar spectra
also introduces a new classification...
Nils C. Duner (1899)

7.1 Motivation

[1]Classification is an important first step in the characterization of any astronomical population. It enables one to study the global properties of a group of similar objects and generalize to larger, and perhaps undetected, members. A fundamental property of astronomical classification is that it is based on observations; i.e., the way objects appear morphologically, photometrically, or spectroscopically. Stellar spectral classification has been in practice for nearly 150 years, and calibration of spectral classes against temperature and luminosity has provided crucial insight into the internal physics of stars, their history and evolution, and the properties of the Galaxy and extragalactic systems.

The stellar sequence of Morgan, Keenan, & Kellman (1943), the most widely accepted classification scheme, originates from the temperature-based sequence first used in the Henry Draper catalog (Pickering, 1890) and luminosity discriminants initially identified by Maury & Pickering (1897). It extends the main sequence from hot O-type stars to cool M dwarfs, the latter of which were until recently the coolest and faintest stars known. With the advent of more sensitive optical and near-infrared detectors and large-scale surveys, including 2MASS, SDSS, and DENIS, cooler stars and brown dwarfs have now been identified. As a result, two new spectral classes have been introduced, the L and T classes (Kirkpatrick et al., 1999b), which are extensions of the MK spectral sequence into the brown dwarf regime. Classification schemes for L dwarfs in the red optical have been defined by Kirkpatrick et al. (1999b) and Martín et al. (1999).

In this chapter, we define a near-infrared classification scheme for T dwarfs based on the strengths of near-infrared CH_4 and H_2O absorption bands, using spectra presented in Chapter 3 and data from the literature. In doing this, we have followed the philosophy of the MK system, basing our classification criteria exclusively on the observed spectral features, without presumption of the actual physical properties of these objects (i.e., T_{eff}, gravity, or metallicity). This is an important point, as models of cool brown dwarfs, although greatly improved over earlier work, do not yet adequately predict all of the features seen in T dwarf spectra (Leggett et al., 2001). It is, in our opinion, better to classify an object on its actual appearance rather than on possibly incorrect physical interpretations.

In §7.2, we address the question of what wavelength regime T classification should be defined in, and justify our choice of the near-infrared (1–2.5 μm). In §7.3, we define the subtypes and identify spectral standards. Classification indices are defined and discussed in §7.4, and a recipe for subtyping T dwarfs using these indices is presented. We also examine the behavior of defined near-infrared M and L dwarf spectral indices in the T dwarf regime. We re-address the topic of classification in the red optical (6300–10100 Å) in §7.5, examining the behavior of spectral indices and how they relate to the near-infrared subtypes. The breadth of the L/T transition is discussed in §7.6, focusing on the possible formation of weak CH_4 features in the spectrum of the L7 V DENIS 0205-1159AB

[1]This chapter is based on results presented in Burgasser, Kirkpatrick, & Brown (2001); Burgasser et al. (2001).

(Delfosse et al., 1997). We also address the properties of the only peculiar T dwarf in this scheme, 2MASS 0937+2931, in §7.7. Finally, in §7.8, we address the effective temperature scale of L and T dwarf spectral classes, and speculate that the temperature range between the latest L dwarfs and T dwarfs such as 2MASS 0559-1404 is quite narrow, perhaps only 200–300 K. We summarize our results in §7.9.

7.2 Near-Infrared or Optical Classification?

A classification scheme for T dwarfs should be able to distinguish these objects from each other and from the warmer L dwarfs. One might expect to do this at red optical wavelengths, where both the Kirkpatrick et al. (1999b) and Martín et al. (1999) L dwarf classification schemes are defined. Kirkpatrick et al. (2002) have shown that T dwarfs can be segregated from L dwarfs in this spectral regime, and features useful for classification are described in §5.8. However, T dwarfs are exceedingly faint shortward of 1 μm, (i^*-J $\gtrsim$ 7.5; Leggett et al. 2000), and data are difficult to obtain using even the largest ground-based telescopes.

In the near-infrared, however, T dwarfs are significantly brighter, and large samples can be observed using only moderate-sized (4m-class) telescopes. This facilitates a T classification scheme based on 1–2.5 μm spectroscopy. Corresponding classification schemes for L dwarfs in this spectral regime have also recently been proposed. Preliminary efforts were made by Tokunaga & Kobayashi (1999) using indices that measure H_2O and H_2 features at K-band. Reid et al. (2001a) have mapped the Kirkpatrick et al. (1999b) L dwarf scheme onto near-infrared spectra using the strengths of the 1.4 and 1.9 μm H_2O bands. Testi et al. (2001) find similar correlations using their own H_2O and color indices. Other near-infrared investigations are currently underway by McLean et al. (2001), Gizis et al. (2001b), and Wilson et al. (2001c).

Therefore, in order to gauge how well our classification system segregates L and T dwarfs in the near-infrared, we have augmented our T dwarf spectral sample with NIRC and OSIRIS observations of known M and L dwarfs. We have also included near-infrared spectra for M, L, and T dwarfs obtained from the literature (Geballe et al., 1996, 2001b; Strauss et al., 1999; Tsvetanov et al., 2000; Leggett et al., 2000b, 2001; Reid et al., 2001a, hereafter CGS4 data). Note that no attempt is made to define a near-infrared L classification scheme; our purpose is simply to examine how our T classification (in particular, spectral indices, §7.4) sets these objects apart from other spectral types. We examine how L dwarf near-infrared schemes may carry into the T dwarf regime in §7.4.4.

7.3 Defining the Subtypes

The first step toward classification is to determine groupings, or subtypes. Numerous techniques for identifying spectral subtypes in the MK system have been proposed (Morgan, 1950; Bailer-Jones, 2001). We have chosen to define T subclasses by the following procedure: First, we visually compared the spectra, normalized at their J-band peaks, with OSIRIS and CGS4 data smoothed with a Gaussian filter to match the resolution of the NIRC data. These spectra were then sorted into a morphological order based on the strengths of the 1.6 and 2.2 μm CH_4 bands, the 1.15 μm H_2O/CH_4 band, and the overall appearance of the J, H, and K-band peaks, similar to the ordering used in Figures 3.2, 3.6, and 3.7. The CH_4 absorption bands are expected to strengthen with decreasing effective temperature (Burrows et al., 1997), so that a classification scheme based on these features should adequately represent an underlying temperature sequence. The spectra were then grouped into subtypes of similar morphology, with the number of subtypes chosen to represent evenly the spectral variations seen.

This process was repeated until a consistent system developed, resulting in seven groups we have labeled T1 V, T2 V, T3 V, T5 V, T6 V, T7 V, and T8 V. Our two subtype omissions, T0 V and T4 V, are based on apparent gaps in the photometric colors and spectral morphologies of the T dwarf population as it was known in 2001 May. The earliest T dwarf identified at that time, SDSS 0837-0000, is considerably bluer in J-K_s color than the latest L8 dwarfs, suggesting the presence of an additional (earlier) subtype with weaker methane features. We have also omitted a class between the latest of the early Sloan T dwarfs, SDSS 1021-0304, and the reddest T dwarf from our search, 2MASS 2254+3123, again based on the significant near-infrared color differences, as well substantial relative suppression of the H- and K-band peaks in the spectrum of the latter object. Note that all of the 2MASS discoveries fall exclusively in the latter four groups, due to the color criteria discussed in Chapter 2.

Representative bright standards for each subtype were then chosen. Low resolution spectra of these standards are shown in Figure 7.1, along with data for the L7 V DENIS 0205-1159AB (Leggett et al., 2001). Spectra are normalized at their J-band peaks with zero point offsets indicated by dashed lines. Data from Leggett et al. (2000b, 2001) have been degraded to NIRC resolution using a Gaussian filter. The spectral properties of these subtypes are summarized in Table 7.1. The progressive strengthening of the H_2O and CH_4 bands throughout the sequence is readily apparent. Early types are distinguishable from L dwarfs by the presence of weak CH_4 absorption at 1.6 and 2.2 μm, the latter of which appears in conjunction with CO at 2.3 μm in types T1 V, T2 V, and T3 V. Other important features include the strengthening 1.15 μm H_2O/CH_4 band, weakening 1.25 μm K I doublets, suppression of H- and K-band flux relative to J (significant between T3 V and T5 V), and narrowing of the 1.08, 1.27, 1.59, and 2.07 μm peaks through T8 V. The K-band peak of the later subtypes evolves from a rounded hump centered at 2.11 μm (T5 V), to a sloped, asymmetric peak notched at 2.17 μm (T7 V), and finally into a sharper, symmetric peak centered at 2.07 μm (T8 V).

7.4 T Dwarf Spectral Indices

7.4.1 Defining the Indices

T dwarfs can be classified, to first order, by a simple visual comparison against the standard sequence plotted in Figure 7.1. A more quantitative approach is to use spectral indices, ratios of fluxes in spectral regions which measure specific morphological features, such as the CH_4 and H_2O bands and the changing appearance of the K-band peak. Based on the subtype properties listed in Table 7.1, we have defined a suite of spectral indices, listed in Table 7.2 and diagrammed in Figure 7.2. For each index, flux regions were chosen to sample the feature of interest and a nearby pseudo-continuum point (typically the flux peaks at J, H, or K), and the mean of the data in these regions were ratioed. The H_2O, CH_4, and CO indices measure the relative depths of their respective bands, while the color indices H/J, K/J, and K/H are approximate measures of color around the 1.25, 1.6, and 2.1 μm flux peaks. Both the 2.11/2.07 and K shape indices measure the change in the K-band peak, influenced by the molecular absorbers H_2O, CH_4, CO, and CIA H_2.

The behavior of these indices was examined for the T dwarf standards, and a subset of indices showing obvious trends were chosen for use in spectral typing. These include the H_2O-A, H_2O-B, CH_4-A, CH_4-B, and CH_4-C band indices; the H/J and K/J color indices; and the 2.11/2.07 K-band ratio. Values of these indices measured for late-L (Kirkpatrick et al., 1999b) and T dwarf standards are listed in Table 7.3. CGS4 data were used to compute the standard ratios for types L5 V through T3 V, while NIRC data were used for types T5 V through T8 V.

Using the standard values as benchmarks, we then computed spectral types for the remaining

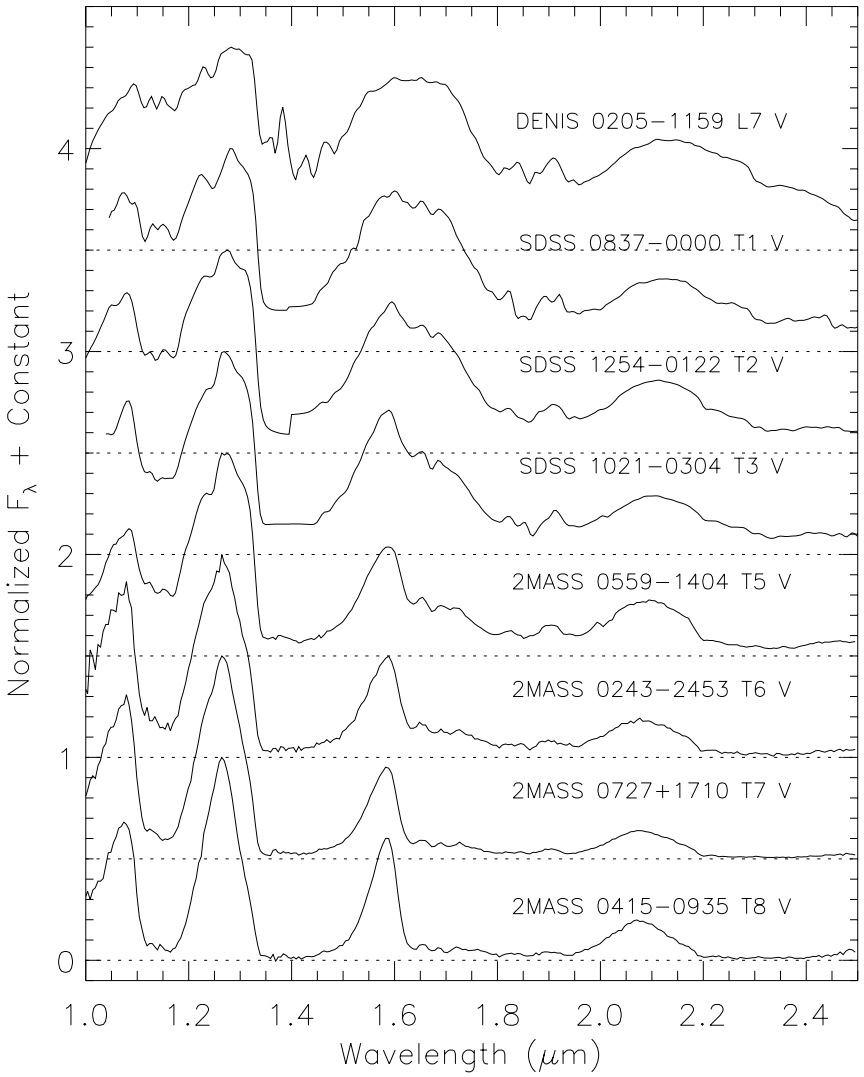

Figure 7.1: Low resolution spectra of T dwarf standards and the L7 V DENIS 0205-1159AB. Data are normalized at their J-band peaks, and zero point offsets are indicated by dotted lines. Data for DENIS 0205-1159AB (Leggett et al., 2001), SDSS 0837-0000, SDSS 1254-0122, and SDSS 1021-0304 (Leggett et al., 2000b) have been degraded to the resolution of the NIRC spectra using a Gaussian filter.

Table 7.1: Near-Infrared Spectral Properties of T Dwarf Subtypes.

Type (1)	Description (2)	Example (3)
T1 V	Weak CH_4 bands seen at 1.3, 1.6, and 2.2 μm	SDSS 0837-0000
	Distinct 1.07 and 1.27 μm peaks separated by 1.15 μm H_2O/CH_4 feature	
	K-band peak noticeably depressed relative to J and H	
	CH_4 and CO bands at K equal in strength	
	K I lines at 1.25 μm strong	
T2 V	CH_4 bands strengthening	SDSS 1254-0122
	Flux at 1.15 μm feature roughly 50% J-band peak	
	K-band CH_4 stronger than CO	
	K-band peak rounded	
T3 V	Flux at 1.15 μm feature roughly 40% J-band peak	SDSS 1021-0304
	Flux at 1.6 μm feature roughly 60% H-band peak	
	CO barely visible at K-band	
T5 V	Flux at 1.6 μm trough roughly 50% H-band peak	2MASS 0559-1404
	No CO present	
	H-band suppressed relative to J and K	
	K I lines at 1.25 μm peak in strength	
T6 V	Flux at 1.15 μm feature roughly 20% J-band peak	2MASS 0243-2453
	Flux at 1.6 μm feature roughly 30% H-band peak	
	1.25 μm K I lines beginning to weaken	
	1.3 μm CH_4 band blended with 1.4 μm H_2O	
	2.2 μm CH_4 absorption nearly saturated	
	K-band beginning to flatten, asymmetric peak centered at 2.11 μm	
T7 V	Flux at 1.15 μm feature roughly 10% J-band peak	2MASS 0727+1710
	Flux at 1.6 μm feature roughly 10% H-band peak	
	1.25 μm K I lines barely discernible	
	H- and K-band peaks maximally suppressed relative to J	
	J-band peak increasingly narrow	
T8 V	Flux at 1.15 μm feature nearly saturated	2MASS 0415-0935
	Flux at 1.6 μm feature nearly saturated	
	No 1.25 μm K I lines present	
	Slight increase in H- and K-band peaks relative to J	
	K-band peak more sharply peaked and symmetric about 2.07 μm	

Table 7.2: Ratios Used as T Dwarf Spectral Diagnostics.

Diagnostic (1)	Numerator (μm) (2)	Denominator (μm) (3)	Feature Measured (4)
H_2O-A[a]	$\langle F_{1.12-1.17} \rangle$	$\langle F_{1.25-1.28} \rangle$	1.15 μm H_2O/CH_4
H_2O-B[a]	$\langle F_{1.505-1.525} \rangle$	$\langle F_{1.575-1.595} \rangle$	1.4 μm H_2O
H_2O-C	$\langle F_{2.00-2.04} \rangle$	$\langle F_{2.09-2.13} \rangle$	1.9 μm H_2O
CH_4-A[a]	$\langle F_{1.295-1.325} \rangle$	$\langle F_{1.25-1.28} \rangle$	1.3 μm CH_4
CH_4-B[a]	$\langle F_{1.64-1.70} \rangle$	$\langle F_{1.575-1.595} \rangle$	1.6 μm CH_4
CH_4-C[a]	$\langle F_{2.225-2.275} \rangle$	$\langle F_{2.09-2.13} \rangle$	2.2 μm CH_4
H/J[a]	$\langle F_{1.50-1.75} \rangle$	$\langle F_{1.20-1.325} \rangle$	NIR color
K/J[a]	$\langle F_{2.00-2.30} \rangle$	$\langle F_{1.20-1.325} \rangle$	NIR color
K/H	$\langle F_{2.00-2.30} \rangle$	$\langle F_{1.50-1.75} \rangle$	NIR color
CO	$\langle F_{2.325-2.375} \rangle$	$\langle F_{2.225-2.275} \rangle$	2.3 μm CO
2.11/2.07[a]	$\langle F_{2.10-2.12} \rangle$	$\langle F_{2.06-2.08} \rangle$	K-band shape/CIA H_2
K shape	$\langle F_{2.12-2.13} \rangle$ - $\langle F_{2.15-2.16} \rangle$	$\langle F_{2.17-2.18} \rangle$ - $\langle F_{2.19-2.20} \rangle$	K-band shape/CIA H_2

[a]Spectral ratio used as a classification diagnostic.

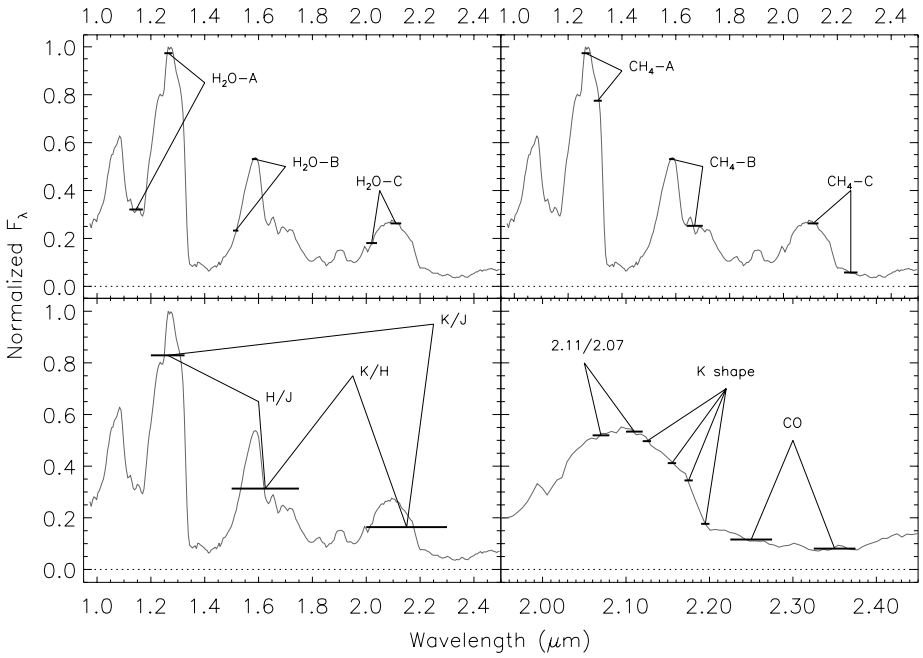

Figure 7.2: The locations of flux regions sampled for the various near-infrared indices listed in Table 7.2. Indices are shown on the NIRC spectrum of 2MASS 0559-1404, normalized at the J-band peak.

Table 7.3: Spectral Diagnostics for L and T Dwarf Standards.

Object (1)	Type (2)	H_2O-A (3)	H_2O-B (4)	CH_4-A (5)	CH_4-B (6)	CH_4-C (7)	H/J (8)	K/J (9)	2.11/2.07 (10)
DENIS 1228−1547	L5 V	0.765	0.771	1.044	1.035	0.938	0.891	0.575	1.102
DENIS 0205−1159	L7 V	0.764	0.760	1.026	1.010	0.841	0.837	0.524	1.079
SDSS 0837−0000	T1 V	0.669	0.637	0.991	0.920	0.662	0.746	0.326	1.061
SDSS 1254−0122	T2 V	0.501	0.569	0.910	0.832	0.527	0.637	0.299	1.081
SDSS 1021−0304	T3 V	0.393	0.518	0.864	0.657	0.498	0.581	0.250	1.068
2MASS 0559−1404[a]	T5 V	0.351	0.450	0.786	0.464	0.210	0.380	0.185	0.999
2MASS 0243−2453	T6 V	0.174	0.353	0.555	0.292	0.139	0.310	0.136	0.902
2MASS 0727+1710	T7 V	0.117	0.296	0.498	0.176	0.087	0.241	0.097	0.864
2MASS 0415−0935[a]	T8 V	0.062	0.228	0.407	0.102	0.071	0.301	0.127	0.825

[a]Indices averaged from multiple spectra.

T dwarfs by directly comparing the individual indices. Tables 7.4–7.6 list the index values and corresponding subtypes derived from NIRC and D78, OSIRIS, and literature data, respectively. Only measurable indices are listed in each set; for example, the spectral limits of the OSIRIS and D78 data, and significant K-band noise, restrict the use of the H_2O-A, CH_4-C, and 2.11/2.07 indices. We note that the CH_4-C, H/J, and K/J indices appear to saturate in the latest subtype standards, obviating their use in distinguishing between types T7 V and T8 V; in addition, the 2.07/2.11 index shows a consistent trend only for types T3 V through T8 V.

Individual subtypes were then averaged into a decimal classification after rejecting the single highest and lowest values; these are listed in the last column of each table. Uncertainties were determined from the scatter of the index subtypes, which in no case exceeded ± 0.9 subclasses. Finally, the decimal classifications were rounded off to the nearest 0.5 subclass to provide the final subtypes listed in Table 7.7. In general, preference was given to classifications derived from NIRC and CGS4 data, as these samples were used to derive the standard ratios. Nonetheless, differences between the various datasets for common objects did not exceed ± 1.0 subclasses. Note that final subtypes for 2MASS 0755+2212 and NTTDF 1205-0744 are assigned tentative (uncertain) values due to the poor quality of their spectral data. Excepting these two objects, comparison between the datasets indicates that the derived subtypes have typical uncertainties of ± 0.5 subclasses.

We also list in Table 7.7 the T subtypes assigned by Geballe et al. (2001b), who derive an independent classification scheme based on CGS4 spectral data. The assigned subtypes are identical except for Gliese 229B, which differs by only 0.5 subclass. The similarity of the types is not surprising, since both systems are tied to the strengths of H_2O and CH_4 bands. Nevertheless, the convergence of these systems intimates a natural order in the T dwarf class.

7.4.2 Spectral Index Relations

The behavior of our derived spectral indices as compared to spectral type allows us to ascertain the usefulness of these indices for classification, while also probing the evolution of spectral features. Figures 7.3–7.6 plot these ratios for objects with types M4.5 V through T8 V, measured from the NIRC (diamonds), OSIRIS (triangles), and CGS4 (squares) datasets. Filled circles indicate spectral standard values; T spectral types are those listed in Table 7.7. Note that we have ended the L sequence in this (and subsequent) diagrams at L8 V; motivation for this choice is discussed in §7.6.

The H_2O indices (Figure 7.3) are seen to decrease monotonically over the entire sequence, except for the H_2O-C index, which increases from T2 V to T8 V. Decreasing indices imply strengthening bands, which can be easily seen in the spectral data of Figures 3.2, 3.6, and 3.7. The slopes are greater in the T dwarfs, reflecting either increased band contrast with the loss of higher-energy (and hence higher temperature) wing transitions; increased H_2O photospheric abundance with the formation of CH_4:

$$CO + 3H_2 \rightarrow CH_4 + H_2O; \tag{7.1}$$

or increased transparency due to the settling of dust cloud layers (Ackerman & Marley, 2001; Burrows et al., 2001). The sharper increase in slope for the H_2O-A index is due to the additional contribution of CH_4 absorption in this feature. Note that the H_2O-C index has a great deal of scatter in the T dwarf regime, and its behavior is likely affected by both CH_4 and CIA H_2 absorption at K-band.

The CH_4 indices (Figure 7.4) are generally flat for most of the M and L dwarfs earlier than type L5 V, but rapidly decrease starting around L5 V to T1 V. Note that this behavior makes the CH_4 indices particularly useful in distinguishing T dwarfs from other late-type objects, as is expected. The CH_4-A and CH_4-B indices start to decrease around L8 V to T1 V, while CH_4-C decreases as early as L3 V to L5 V. The latter downturn is likely due to absorption by CIA H_2 in the late-L and T dwarfs, although we cannot rule out the early influence of CH_4 as a minor absorber.

Table 7.4: T Dwarf Spectral Indices: NIRC and D78 Data.

Object (1)	H_2O-A (2)	H_2O-B (3)	CH_4-A (4)	CH_4-B (5)	CH_4-C[a] (6)	H/J[a] (7)	K/J[a] (8)	2.11/2.07 (9)	Dec. Type (10)
2MASS 2254+3123	0.442(2–3)	0.496(3–5)	0.721(5)	0.513(5)	0.243(5)	0.378(5)	0.133(6)	0.965(5)	4.8±0.4
2MASS 0559−1404[b]	0.351(5)	0.450(5)	0.786(5)	0.464(5)	0.210(5)	0.380(5)	0.185(5)	0.999(5)	5.0±0.0
2MASS 2339+1352	0.300(5)	0.418(5)	0.547(6)	0.388(5–6)	0.182(5)	0.337(6)	0.119(6–7)	0.990(5)	5.4±0.5
2MASS 0755+2212	...	0.548(2–3)	0.758(5)	0.450(5)	...	0.327(6)	0.159(5–6)	...	5.2:[c]
2MASS 2356−1553	0.261(5–6)	0.389(6)	0.720(5)	0.322(6)	0.140(6)	0.351(5–6)	0.150(6)	0.946(6)	5.8±0.4
2MASS 0937+2931[b]	0.185(6)	0.410(5–6)	0.602(6)	0.287(6)	0.199(5)	0.314(6)	0.082(7)	0.920(6)	5.9±0.2
2MASS 0243−2453	0.174(6)	0.353(6)	0.555(6)	0.292(6)	0.139(6)	0.310(6)	0.136(6)	0.902(6)	6.0±0.0
SDSS 1346−0031	0.157(6)	0.354(6)	0.561(6)	0.240(6–7)	0.145(6)	0.286(6)	0.125(6)	0.900(6)	6.0±0.0
2MASS 1047+2124[b]	0.166(6)	0.345(6)	0.524(7)	0.235(6–7)	0.170(6)	0.339(6)	0.105(7)	0.884(6–7)	6.3±0.4
2MASS 1237+6526	0.127(7)	0.328(6–7)	0.511(7)	0.221(7)	0.144(6)	0.284(6)	0.073(7)	0.902(6)	6.6±0.5
2MASS 0727+1710	0.117(7)	0.296(7)	0.498(7)	0.176(7)	0.087(≥7)	0.241(≥7)	0.097(≥7)	0.864(7)	7.0±0.0
2MASS 1553+1532	0.130(7)	0.311(7)	0.444(8)	0.175(7)	0.078(≥7)	0.317(≥7)	0.128(≥7)	0.864(7)	7.0±0.0
2MASS 1217−0311	0.091(7–8)	0.292(7)	0.412(8)	0.138(7–8)	0.074(≥7)	0.276(≥7)	0.132(≥7)	0.817(8)	7.7±0.2
Gliese 570D	0.080(8)	0.242(8)	0.441(8)	0.135(7–8)	0.063(≥7)	0.293(≥7)	0.110(≥7)	0.938(6)	7.8±0.3
2MASS 0415−0935[b]	0.062(8)	0.228(8)	0.407(8)	0.102(8)	0.071(≥7)	0.301(≥7)	0.127(≥7)	0.825(8)	8.0±0.0

[a]Index ambiguous for subtypes T7 V through T8 V.
[b]Indices averaged from multiple spectra.
[c]Spectral type uncertain due to poor quality of D78 spectrum.

Table 7.5: T Dwarf Spectral Indices: OSIRIS Data.

Object (1)	H_2O-B (2)	CH_4-A (3)	CH_4-B (4)	H/J[a] (5)	K/J[a] (6)	Dec. Type (7)
SDSS 1254−0122	0.558(2)	0.943(2)	0.825(2)	0.680(2)	0.344(1)	2.0±0.0
2MASS 2254+3123	0.469(5)	0.886(2–3)	0.484(5)	0.410(5)	0.184(5)	5.0±0.0
2MASS 0559−1404	0.456(5)	0.811(5)	0.383(5–6)	0.337(5–6)	0.153(5–6)	5.3±0.3
2MASS 2339+1352	0.456(5)	0.756(5)	0.344(6)	0.266(7)	0.176(5)	5.3:[b]
2MASS 1534−2952	0.441(5)	0.824(3–5)	0.380(5–6)	0.305(6)	0.103(7)	5.5±0.4
2MASS 1546−3325	0.418(5)	0.788(5)	0.283(6)	0.297(6)	0.134(6)	5.7±0.6
2MASS 2356−1553	0.409(5–6)	0.795(5)	0.254(6)	0.297(6)	0.153(6)	5.8±0.3
2MASS 0937+2931	0.388(6)	0.710(5)	0.246(6)	0.282(6)	0.147(6)	6.0±0.0
2MASS 0243−2453	0.328(6)	0.605(6)	0.225(7)	0.277(6)	0.205(5)	6.0±0.0
2MASS 1225−2739	0.403(5–6)	0.745(5)	0.262(6)	0.264(7)	0.110(7)	6.2±0.8
SDSS 1624+0029	0.230(8)	0.739(5)	0.188(7)	0.235(7)	0.057(7)	7.0:[b]
2MASS 0727+1710	0.332(6)	0.511(7)	0.133(8)	0.183(7)	0.137(≥7)	7.0±0.0
2MASS 1553+1532[c]	0.300(7)	0.601(6)	0.114(8)	0.250(7)	0.109(≥7)	7.0±0.0
Gliese 570D	0.294(7)	0.537(6)	0.106(8)	0.261(7)	0.111(≥7)	7.0±0.0

[a]Index ambiguous for subtypes T7 V through T8 V.
[b]Spectral type uncertain due to poor quality spectrum.
[c]Indices averaged from multiple spectra.

Table 7.6: T Dwarf Spectral Indices: Data from Literature.

Object (1)	Ref. (2)	H_2O-A (3)	H_2O-B (4)	CH_4-A (5)	CH_4-B (6)	CH_4-C (7)	H/J[b] (8)	K/J[b] (9)	2.11/2.07[a] (10)	Dec. Type (11)
SDSS 0837−0000	1	0.669(1)	0.637(1)	0.991(1)	0.920(1)	0.662(1)	0.746(1)	0.326(1)	1.061($\leq$3)	1.0±0.0
SDSS 1254−0122	1	0.501(2)	0.569(2)	0.910(2)	0.832(2)	0.527(2)	0.637(2)	0.299(2)	1.081($\leq$3)	2.0±0.0
SDSS 1021−0304	1	0.393(3)	0.518(3)	0.864(3)	0.657(3)	0.498(3)	0.581(3)	0.250(3)	1.068($\leq$3)	3.0±0.0
2MASS 0559−1404	2	0.350(5)	0.494(3–5)	0.862(3)	0.470(5)	0.232(6–7)	0.377(6)	0.127(7)	1.001(5)	5.3±0.9
SDSS 1624+0029	3	0.167(6)	0.371(6)	0.703(5)	0.280(6)	0.150(6)	0.279(6–7)	0.099(7)	0.937(6)	6.1±0.2
SDSS 1346−0031	5	0.175(6)	0.352(6)	0.635(6)	0.247(6)	0.094(7)	0.261(7)	0.113(6–7)	0.937(6)	6.3±0.4
NTTDF 1205−0744	4	0.087(7–8)	0.289(7)	0.723(5)	0.229(6–7)	0.261(5)	0.279(6–7)	0.117(6–7)	0.913(6)	6.3:[c]
Gliese 229B[d]	6,7	0.114(7)	0.425(5–6)	0.485(7)	0.200(7)	0.195(5)	0.277(6–7)	0.100(7)	0.926(6)	6.5±0.6
Gliese 570D	8	0.074(8)	0.284(7)	0.519(7)	0.126(8)	0.060(8)	0.222($\geq$7)	0.071($\geq$7)	0.881(6–7)	7.5±0.6

[a]Index ambiguous for subtypes T1 V through T3 V.
[b]Index ambiguous for subtypes T7 V through T8 V.
[c]Spectral type uncertain due to poor quality spectrum.
[d]Indices averaged from multiple spectra.
Refs – (1) Leggett et al. (2000b); (2) Burgasser et al. (2000c); (3) Strauss et al. (1999); (4) Cuby et al. (1999); (5) Tsvetanov et al. (2000); (6) Geballe et al. (1996); (7) Oppenheimer et al. (1998); (8) Geballe et al. (2001a)

Table 7.7: Classified T Dwarfs.

	Individual Subtypes				
Object	NIRC/D78	OSIRIS	Literature	Final Type	SDSS Type[a]
(1)	(2)	(3)	(4)	(5)	(6)
2MASS 0243−2453	T6 V	T6 V	...	T6 V	...
2MASS 0415−0935	T8 V	...	...	T8 V	...
2MASS 0559−1404	T5 V	T5.5 V	T5.5 V	T5 V	T4.5 V
Gliese 229B	...	...	T6.5 V	T6.5 V	T6 V
2MASS 0727+1710	T7 V	T7 V	...	T7 V	...
2MASS 0755+2212	T5 V:	...	...	T5 V:	...
SDSS 0837−0000	...	...	T1 V	T1 V	T0.5 V
2MASS 0937+2931	T6 V	T6 V	...	T6 Vp	...
SDSS 1021−0304	...	...	T3 V	T3 V	T3 V
2MASS 1047+2124	T6.5 V	...	...	T6.5 V	T6.5 V
NTTDF 1205-0744	...	...	...	T6 V:	...
2MASS 1217−0311	T7.5 V	...	...	T7.5 V	T8 V
2MASS 1225−2739	...	T6 V	...	T6 V	T6 V
2MASS 1237+6526	T6.5 V	...	...	T6.5 V	...
SDSS 1254−0122	...	T2 V	T2 V	T2 V	T2 V
SDSS 1346−0031	T6 V	...	T6.5 V	T6 V	T6 V
Gliese 570D	T8 V	T7 V	T7.5	T8 V	T8 V
2MASS 1534−2952	...	T5.5 V	...	T5.5 V	...
2MASS 1546−3325	...	T5.5 V	...	T5.5 V	...
2MASS 1553+1532	T7 V	T7 V	...	T7 V	...
SDSS 1624+0029	...	T7 V:	T6 V	T6 V	T6 V
2MASS 2254+3123	T5 V	T5 V	...	T5 V	...
2MASS 2339+1352	T5.5 V	T5.5 V:	...	T5.5 V	...
2MASS 2356−1553	T6 V	T6 V	...	T6 V	...

[a]From Geballe et al. (2001b).

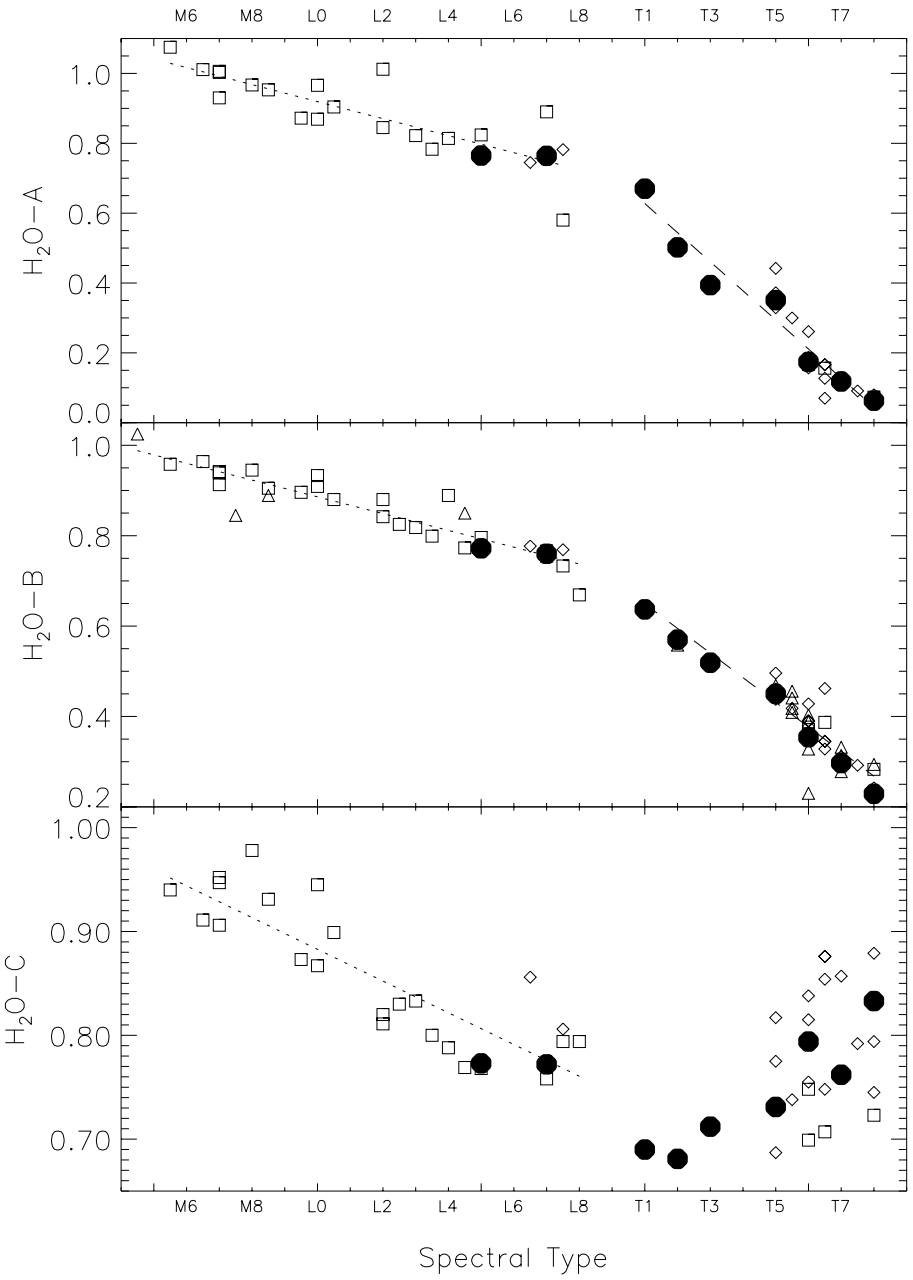

Figure 7.3: H_2O Near-infrared spectral indices for M, L, and T dwarfs versus spectral type. NIRC data are represented by diamonds, OSIRIS data by triangles, and CGS4 literature data by squares. Filled circles indicate measures for late-L and T dwarf standards. Long-dashed and short-dashed lines trace linear fits to indices in the T and late-M and L dwarf regimes, respectively.

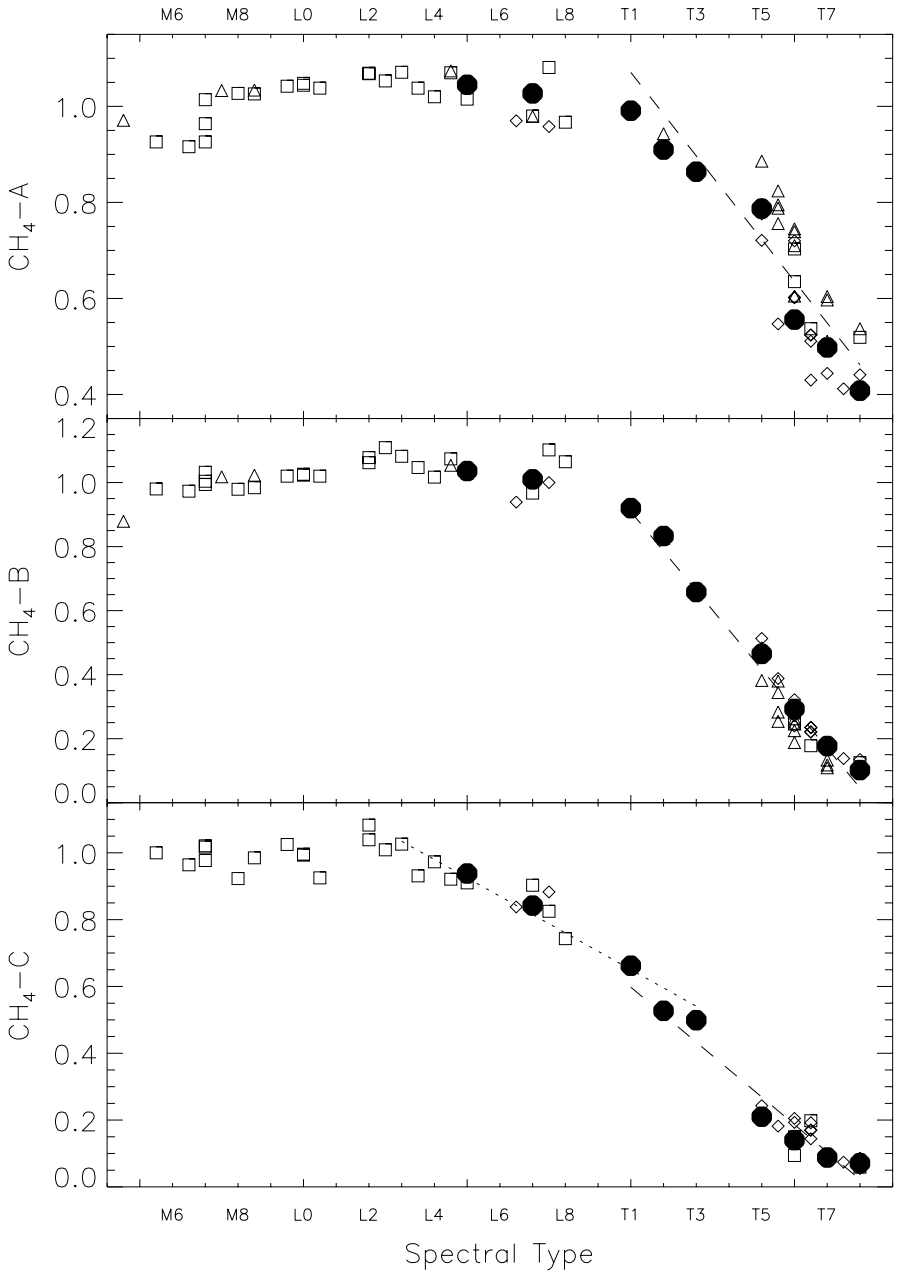

Figure 7.4: Same as Figure 7.3 for CH_4 indices.

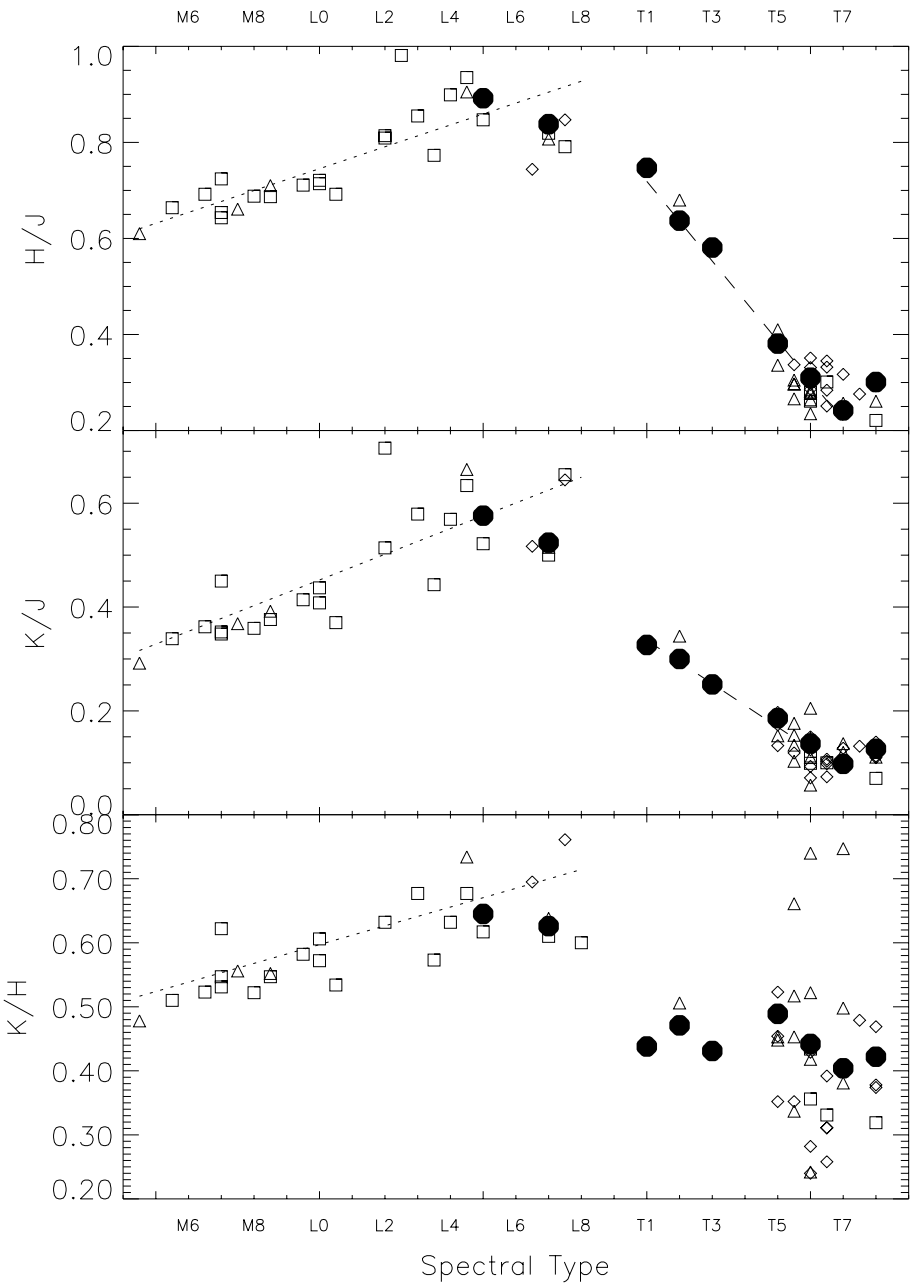

Figure 7.5: Same as Figure 7.3 for color indices.

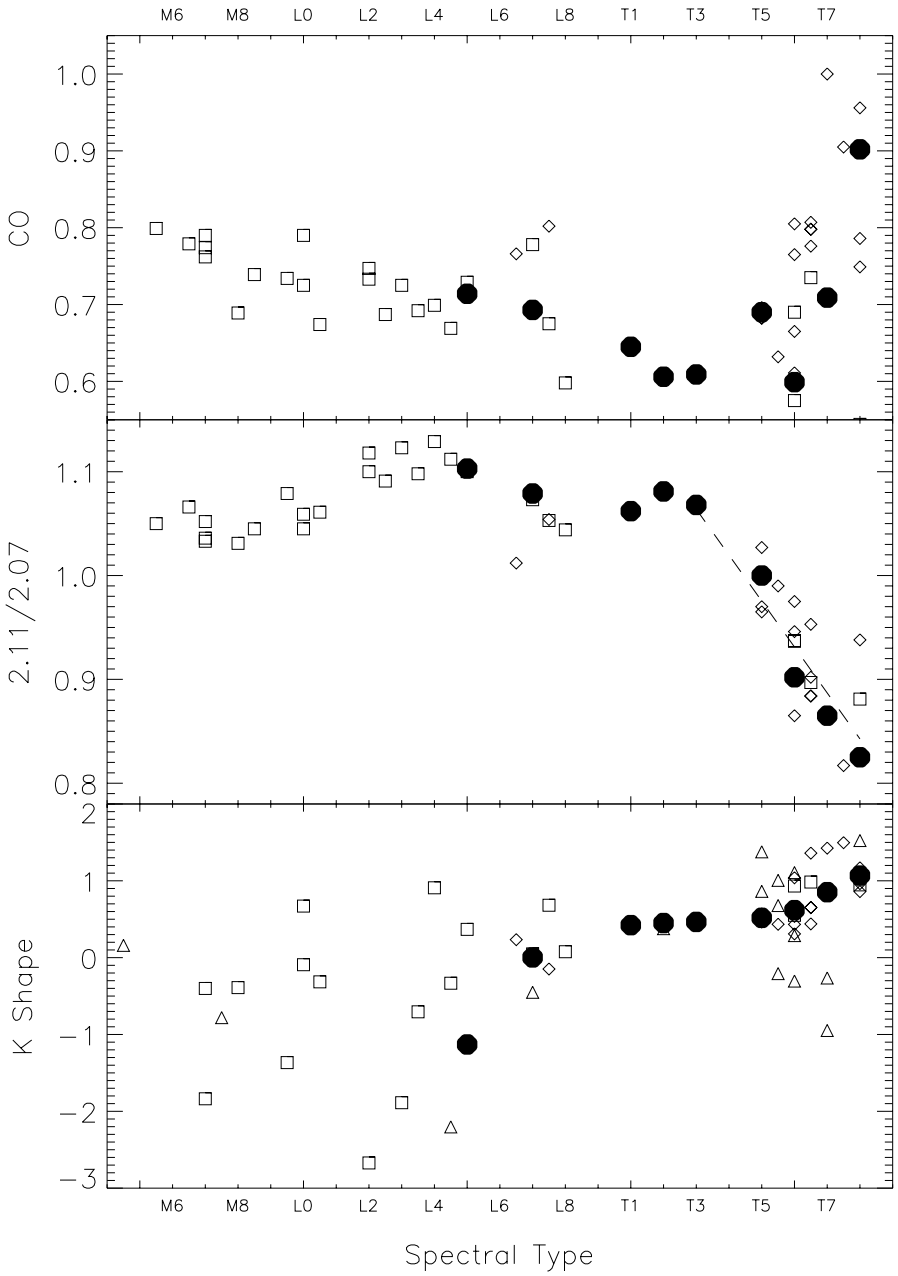

Figure 7.6: Same as Figure 7.3 for CO, 2.11/2.07, and K shape indices.

Table 7.8: Linear Fits to Spectral Indices: T Dwarfs[a].

Index (1)	c0 (2)	c1 (3)	Range (4)	RMS Error (SpT)[b] (5)
H_2O-A[c]	8.5±2.7	−12.0±0.9	T1 V – T8 V	0.6
H_2O-B	12.9±3.1	−18.4±1.4	T1 V – T8 V	0.7
CH_4-A	13.3±3.9	−11.5±1.1	T1 V – T8 V	0.9
CH_4-B	8.4±1.5	−8.1±0.3	T1 V – T8 V	0.4
CH_4-C[c]	8.3±2.4	−12.2±0.8	T1 V – T8 V	0.5
H/J	9.7±2.3	−12.0±0.7	T1 V – T7 V	0.5
K/J	9.0±3.4	−23.9±2.2	T1 V – T7 V	0.7
2.11/2.07[c]	27.0±7.9	−22.6±3.4	T3 V – T8 V	0.8

[a]Coefficients are for linear fit SpT = c0 + c1×Index, where SpT(T1) = 1, SpT(T5) = 5, etc.
[b]RMS of SpT minus adopted spectral type, the latter quantity listed in Table 7.7.
[c]Does not include values for OSIRIS data.

The color indices (Figure 7.5) reflect the well-known trend in increasingly red colors seen from mid-M through late-L dwarfs, but shows that there is a smooth transition to bluer colors in the T dwarf regime. All three of these indices peak around L5 V, at which point colors become steadily bluer, with late T dwarf values below those of mid-M dwarfs. It is interesting to note that both H/J and K/J turn over at the same spectral type, but that CIA H_2 likely affects only the latter index. Kirkpatrick et al. (1999b) see a similar downturn in FeH and CrH bandstrengths in the red optical around L4 V to L5 V, and it is possible that these trends are in some way correlated, possibly through the precipitation of photospheric dust (Burrows, Marley, & Sharp, 2000; Ackerman & Marley, 2001). Both the H/J and K/J indices appear to saturate and possibly reverse their downward trends between types T7 V and T8 V. The K/H index shows more scatter and is less useful than the other color indices.

The remaining indices (Figure 7.6) are generally not useful for spectral classification over the full range of spectral types shown. The CO index shows a gradual decline from mid-M to early-T (implying increasing band strength), but is predominantly scatter for most of the T dwarfs due to 2.2 μm CH_4 absorption and lack of a CO bandhead. The 2.11/2.07 index is generally constant from mid-M to early-T, but shows a downturn beyond T3 V. Despite the significant scatter, this index appears to separate mid- and late-T dwarfs from warmer objects, reflecting changes in the relative strengths of absorbers at K-band beyond T5 V. Finally, the K-shape index appears to show no real trends over the entire range of subtypes.

Overlaid on these plots are linear fits to select indices over discrete subtype ranges. Linear fits to T dwarfs are indicated by long-dashed lines, while fits to M and L dwarfs are indicated by short-dashed lines. Coefficients for these lines are given in Tables 7.8 and 7.9, with values for the root mean square (RMS) deviations over the subtype ranges used. These relations yield spectral types accurate to within ±0.4–0.9 subclasses for the T dwarfs, with greater scatter seen in the linear fits to the M and L dwarfs.

7.4.3 A Recipe for Spectral Classification

Based on the discussion above, we outline a procedure for determining the spectral types of T dwarfs using near-infrared data:

Table 7.9: Linear Fits to Spectral Indices: M and L Dwarfs[a].

Index (1)	c0 (2)	c1 (3)	Range (4)	RMS Error (SpT)[b] (5)
H_2O-A[c]	37.7±7.0	−41.0±5.8	M5 V – L7 V	2.5
H_2O-B	47.7±4.6	−53.9±4.2	M5 V – L7 V	1.7
H_2O-C[c]	57.8±8.1	−65.5±7.7	M5 V – L7 V	2.2
CH_4-C[c]	21.9±3.3	−18.2±1.7	L3 V – T3 V	0.9
H/J	−32.7±4.6	43.9±7.8	M5 V – L7 V	3.9
K/J	−18.3±2.5	40.4±6.8	M5 V – L7 V	3.6
K/H	−30.7±8.0	68.2±16.4	M5 V – L7 V	5.3

[a]Coefficients are for linear fit SpT = c0 + c1×Index, where SpT(L0) = 0, SpT(L5) = 5, SpT(M5) = -5, etc.
[b]RMS of SpT minus adopted spectral type, the latter quantity from the literature.
[c]Does not include values for OSIRIS data.

1. Measure the H_2O-A, H_2O-B, CH_4-A, CH_4-B, CH_4-C, H/J, K/J, and 2.11/2.07 indices as defined in Table 7.2. A subset of these indices can be used when spectral data do not extend into the required spectral regions.

2. Compare each index with standard values, either from Table 7.3 or (preferably) from measurements of standards using the same instrumental setup. Compute spectral types for each index.

3. Average the derived subtypes, rejecting the single high and low values, to determine a mean decimal spectral type. This decimal value rounded off to the nearest 0.5 subclass yields the final discrete subtype.

The linear relations given in Table 7.8 can be used to derive individual spectral types in step 2, although trends in the indices are not necessarily linear and direct comparison to standard values is generally preferable. Spectral types should be computed using as many of the indices listed in step 1 as possible, in order to reduce any biases due to differences in instrumentation (resolution or response characteristics) or observing conditions. Nonetheless, we find that this procedure yields consistent results for data with low to moderate resolutions to better than ±1.0 subclasses. By the procedure outlined here, we have assigned spectral types to the observed T dwarfs as listed in Table 7.7.

7.4.4 Comparison to L Dwarf Classification Indices

A number of spectral indices have been defined to classify M and L dwarfs in the near-infrared, and it is useful to examine the behavior of these indices in the T dwarf regime.

7.4.4.1 Jones et al. (1994) Indices

Jones et al. (1994) examined the near-infrared spectral properties of a small sample of late-type M dwarfs, and derived three spectral indices:

$$1.34\mu\text{m}\ \ H_2O = \frac{\langle F_{1.286-1.303}\rangle}{\langle F_{1.338-1.356}\rangle} \tag{7.2}$$

$$2.294\mu\text{m } CO = \frac{\langle F_{2.22-2.28}\rangle}{\langle F_{2.30-2.36}\rangle} \tag{7.3}$$

$$2.05/2.15 \text{ } Gradient = \frac{1}{0.1\mu\text{m}} \times \frac{\langle F_{2.04-2.06}\rangle - \langle F_{2.14-2.16}\rangle}{0.5(\langle F_{2.04-2.06}\rangle + \langle F_{2.14-2.16}\rangle)} \tag{7.4}$$

based on the strengths of H_2O and CO bands. By examining their behavior from M2 V to M9.5+ V (GD 165B, later classified as an L4 V by Kirkpatrick et al. 1999), the authors concluded that these indices were excellent temperature diagnostics for M dwarfs.

Figure 7.7 plots the values of these indices for M, L, and T dwarfs using NIRC (diamonds) and CGS4 (squares) data. L and T dwarf standards are plotted as solid circles. The H_2O index shows a clear break between L8 V and the T dwarfs, as values increasing quite dramatically beyond T3 V. However, beyond T6 V there is a great deal of scatter, as this index samples a region of nearly zero flux in most of the spectra. There are also problems with telluric contamination, as noted by Jones et al. (1994). The 2.294 μm CO band index behaves almost identically to the CO index defined in §7.4 (inverted due to the different definitions), slightly increasing from M5 V to T2 V, then decreasing as CH_4 absorption overwhelms the pseudo-continuum. Finally, the 2.05/2.15 μm gradient shows a slight increase from M5 V to L2/4 V as noted by Jones et al. (1994), then rapidly becomes negative as first CIA H_2 absorption and then CH_4 suppresses flux on the 2.15 μm side of the K-band peak. Despite being defined for much warmer M dwarfs, both the H_2O and 2.05/2.15 gradient indices nevertheless show clear trends in objects as late as type T8 V.

7.4.4.2 Tokunaga & Kobayashi (1999) Indices

Tokunaga & Kobayashi (1999) have defined two indices at K-band to measure the strengths of the 1.9 μm H_2O and CIA H_2:

$$K1 = \frac{\langle F_{2.10-2.18}\rangle - \langle F_{1.96-2.04}\rangle}{0.5(\langle F_{2.10-2.18}\rangle + \langle F_{1.96-2.04}\rangle)} \tag{7.5}$$

$$K2 = \frac{\langle F_{2.20-2.28}\rangle - \langle F_{2.10-2.18}\rangle}{0.5(\langle F_{2.20-2.28}\rangle + \langle F_{2.10-2.18}\rangle)}, \tag{7.6}$$

the latter of which is also sensitive to CH_4 in the T dwarfs. Figure 7.8 is an extension of Figure 4 from Tokunaga & Kobayashi (1999), comparing these indices for types M (triangles), L (squares), and T (circles) from the NIRC (open symbols) and CGS4 (filled symbols) datasets. Representative M, L, and T dwarfs are labeled by their spectral types. The $K1$ index appears to peak in the early T dwarfs, then decreases toward later subtypes, similar to what is seen in our H_2O-C index. $K2$ decreases from late L through late T, reflecting increased CH_4 and CIA H_2 toward cooler temperatures. Despite significant scatter in the T dwarf regime, these indices, defined for M and L dwarfs, do show trends in objects as late as T8 V.

7.4.4.3 Reid et al. (2001a) Indices

Reid et al. (2001a) have defined two indices for L dwarfs that measure the blue and red wing of the 1.4 μm H_2O band:

$$H_2O^A = \frac{\langle F_{1.33-1.35}\rangle}{\langle F_{1.28-1.30}\rangle} \tag{7.7}$$

$$H_2O^B = \frac{\langle F_{1.47-1.49}\rangle}{\langle F_{1.59-1.61}\rangle}. \tag{7.8}$$

We plot these indices versus spectral type in Figure 7.9, using NIRC (diamonds) and CGS4 (squares)

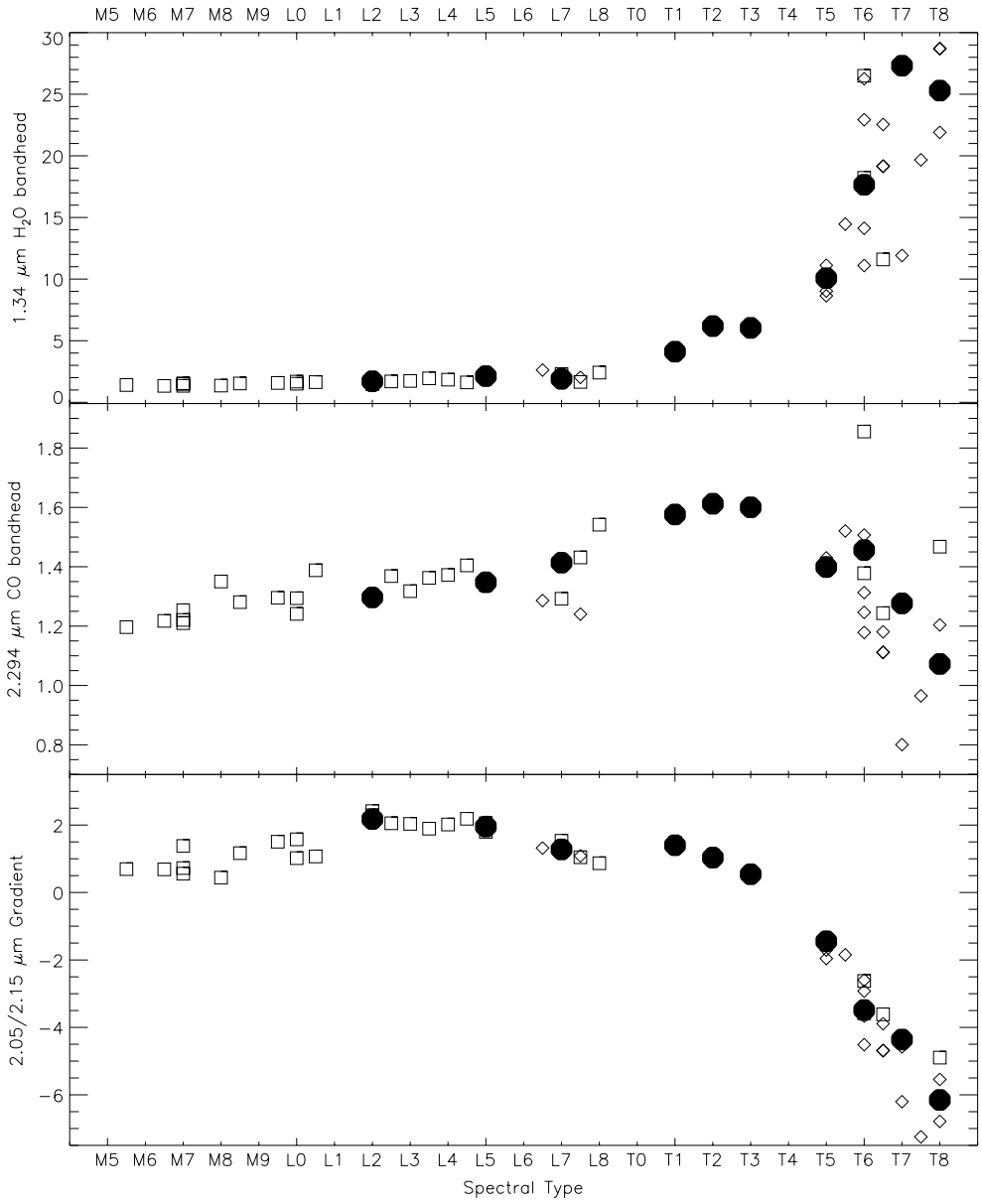

Figure 7.7: Values for the 1.34 μm H_2O bandhead, 2.294 μm CO bandhead, and 2.05/2.15 μm Gradient indices from Jones et al. (1994) versus spectral type. Symbols are those used in Figure 7.3.

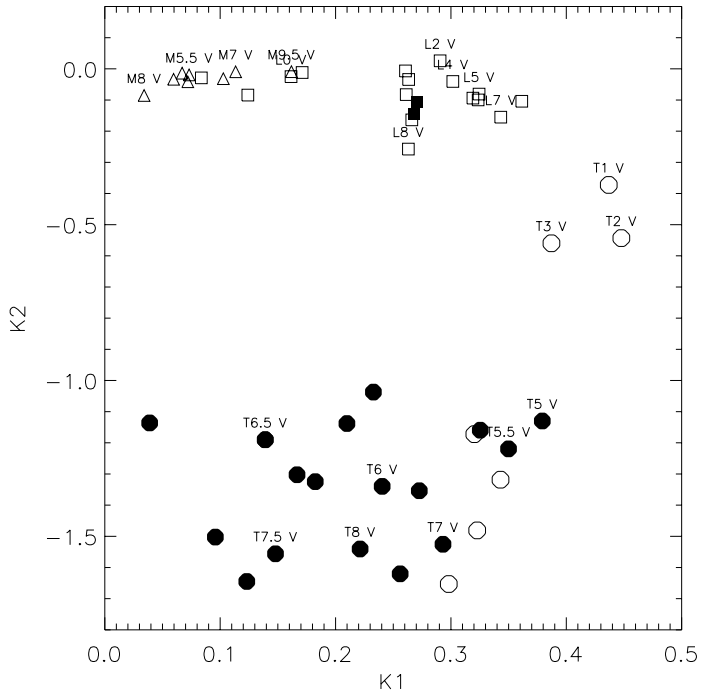

Figure 7.8: Comparison of K1 and K2 indices from Tokunaga & Kobayashi (1999) for M (triangles), L (squares), and T dwarfs (circles). Filled symbols are data taken from NIRC, open symbols are CGS4 data from the literature. Representative M, L, and T dwarfs are labeled by their subtypes.

Table 7.10: Testi et al. Spectral Indices.

Index (1)	Definition (2)	Feature Measured (3)
sHJ	$\frac{\langle F_{1.265-1.305}\rangle - \langle F_{1.60-1.70}\rangle}{0.5(\langle F_{1.265-1.305}\rangle + \langle F_{1.60-1.70}\rangle)}$	Spectral Slope
sKJ	$\frac{\langle F_{1.265-1.305}\rangle - \langle F_{2.12-2.16}\rangle}{0.5(\langle F_{1.265-1.305}\rangle + \langle F_{2.12-2.16}\rangle)}$	Spectral Slope
sH_2O^J	$\frac{\langle F_{1.265-1.305}\rangle - \langle F_{1.09-1.13}\rangle}{0.5(\langle F_{1.265-1.305}\rangle + \langle F_{1.09-1.13}\rangle)}$	1.15 μm H_2O
sH_2O^{H1}	$\frac{\langle F_{1.60-1.70}\rangle - \langle F_{1.45-1.48}\rangle}{0.5(\langle F_{1.60-1.70}\rangle + \langle F_{1.45-1.48}\rangle)}$	1.4 μm H_2O
sH_2O^{H2}	$\frac{\langle F_{1.60-1.70}\rangle - \langle F_{1.77-1.81}\rangle}{0.5(\langle F_{1.60-1.70}\rangle + \langle F_{1.77-1.81}\rangle)}$	1.9 μm H_2O
sH_2O^K	$\frac{\langle F_{2.12-2.16}\rangle - \langle F_{1.96-1.99}\rangle}{0.5(\langle F_{2.12-2.16}\rangle + \langle F_{1.96-1.99}\rangle)}$	1.9 μm H_2O

data; filled circles denote values for late-L and T dwarf spectral standards. The index-spectral type relations from Reid et al. (2001a), defined over the range M8 V to L8 V, are plotted as short-dashed lines, and are extended into the T dwarf region for comparison. The H_2O^A index does not track linearly into the T regime, due to contamination by the 1.3 μm CH_4 band. The H_2O^B index is remarkably linear, however, over the entire subtype range shown. A fit to this index over types M5 V through T8 V yields (long-dashed line):

$$SpT = (12.6\pm0.9) - (26.7\pm0.6)\times[H_2O^B], \tag{7.9}$$

with an RMS scatter of 1.2 subtypes, where SpT(T0 V) = 0, SpT(T5 V) = 5, SpT(L5 V) = -4, etc. This relation is consistent with that derived by Reid et al. (2001a), Thus, the H_2O^B index is quite useful for classification over a broad range of late-type dwarfs.

7.4.4.4 Testi et al. (2001) Indices

Testi et al. (2001) have recently defined a suite of near-infrared indices for classifying late-M and L dwarfs, using low-resolution spectral data (R $\sim$ 100) obtained using the Near Infrared Camera and Spectograph (Baffa et al., 2000) mounted on the 3.5m Telescopio Nazionale Galileo. They define six indices (Table 7.10) measuring spectral slope and H_2O band strengths, and determine linear fits to these indices in the subtype range L0 V to L6 V.

Figure 7.10 plots the sHJ, sKJ, and sH_2O^J Testi et al. indices measured for NIRC (diamonds) and CGS4 (squares) datasets; measures for late-L and T dwarf standards are indicated by filled circles. The linear relations for these indices derived by Testi et al. (2001) are shown as short-dashed lines. The sHJ and sKJ indices are similar to the H/J and K/J indices defined in Table 7.2 but are defined over a narrower spectral window. This results in an apparently smaller dispersion in their values versus spectral type, although the same general trends are apparent. Both indices decrease until type L5 V to L7 V (the reddest objects), and then increase through the T dwarfs, with a saturation and possible reversal between T7 V and T8 V. The sH_2O^J index, similar to our H_2O-A, shows a general, although not linear, increase from M5 V through T8 V. The deviation in linearity through the L/T transition region may be caused by dust loss effecting H_2O band strengths.

The remaining Testi et al. H_2O indices (Figure 7.11) all show the same roughly linear trends from mid-M to late-T as seen in the Reid et al. (2001a) indices and our H_2O-A and H_2O-B indices. sH_2O^{H1} appears to saturate around L8 V, due to contamination of CH_4 between 1.60–1.70 μm. This contamination is not as apparent in the sH_2O^{H2} indices, although there is considerably more scatter at a particular subtype. Finally, sH_2O^K also appears to saturate slightly around T3 V to T5 V, in

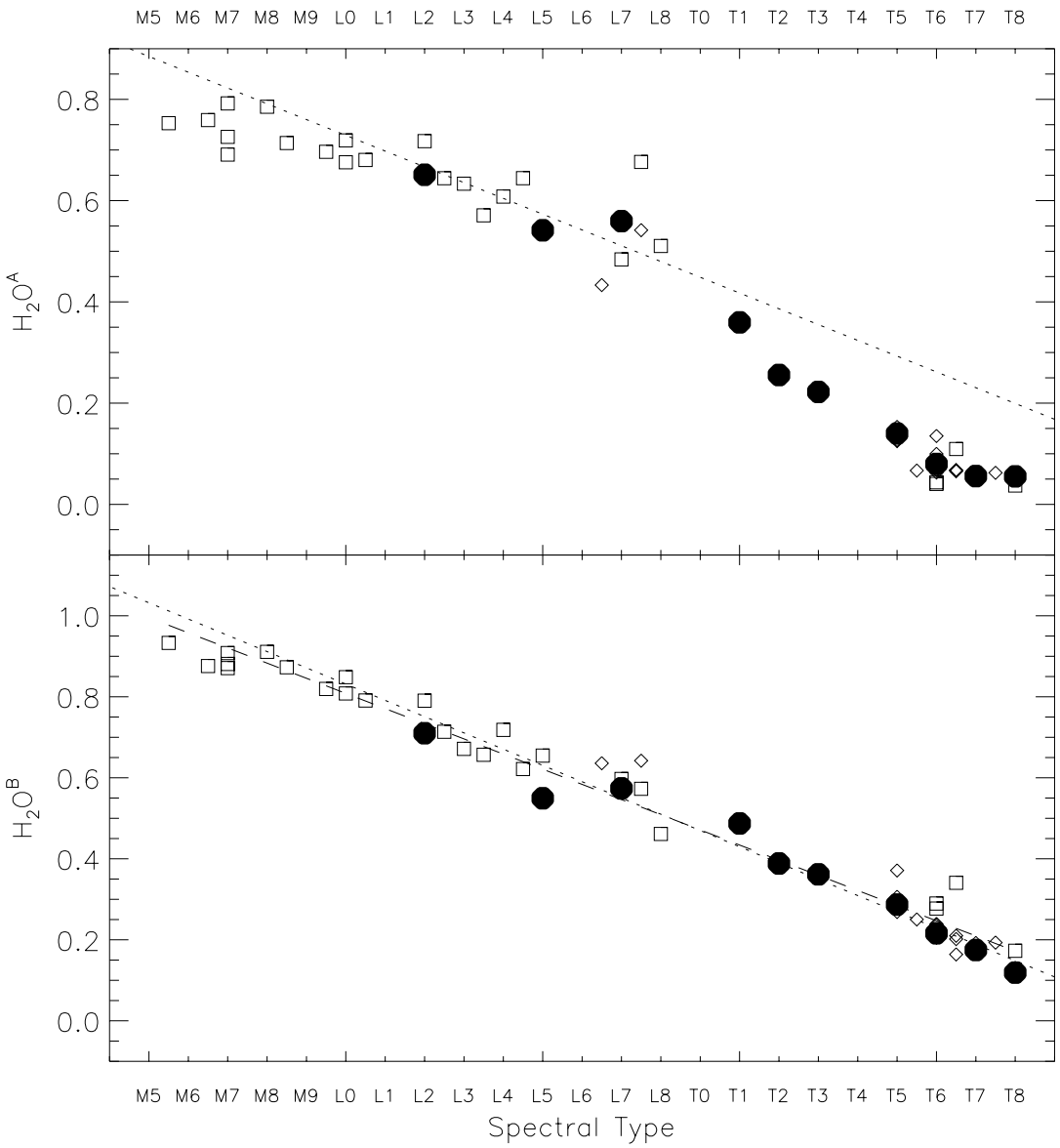

Figure 7.9: Values for H_2O^A and H_2O^B indices from Reid et al. (2001a) versus spectral type. Symbols are those used in Figure 7.3. Short-dashed lines are the index/spectral type relations determined by Reid et al. (2001a) for spectral types M8 V through L8 V, extended over the spectral range shown. The long-dashed line traces a linear fit to the H_2O^B indices for types M5 V through T8 V.

this case due to the suppression of the K-band peak by CH_4 and CIA H_2. All three of these indices show increased scatter with spectral type (particularly in the T dwarfs) due to contamination of absorption not present or weaker in the early- and mid-L dwarfs.

The general success of L dwarf spectral indices in separating T subclasses should not be surprising, since the strengthening of H_2O bands is continuous from type M through T, and near-infrared color changes clearly segregate the red L dwarfs from blue T dwarfs. It is clear from our H_2O-B and the Reid et al. H_2O^B indices that the 1.4 μm H_2O feature is useful for continuous classification for late-M, L, and T dwarfs. The Testi et al. sH_2O^{H1}, which measures the same feature, is less effective due to the contamination of 1.6 μm CH_4. The sHJ and sKJ indices of Testi et al., however, appear to show less scatter than our corresponding color indices H/J and K/J. The difference is in the size of the index spectral window; in this case, our color indices are broader and lead to increased contamination by a multiple absorption features. Clearly, indices defined over narrow spectral windows are more suitable for the classification of these complex spectra. Regardless, examination of these indices supports the overall agreement of color, H_2O, and (for the T dwarfs) CH_4 features in segregating L and T dwarfs.

7.5 T Dwarf Classification in the Red Optical

With the definition of a T dwarf classification scheme in the near-infrared, we now examine spectra in the red optical (6300–10100 Å), where L dwarfs have been classified by Kirkpatrick et al. (1999b) and Martín et al. (1999). In this section, we identify features, and thereby spectral indices, useful for classification at these wavelengths. Our purpose is not to redefine the near-infrared classification, but rather examine the feasibility of subtyping objects in this regime. In §7.5.1 we trace the progression of spectral features through the subtypes defined in §7.3, and define and characterize spectral indices derived from these features in §7.5.2. Finally, in §7.5.3 we examine how the L dwarf indices defined by Kirkpatrick et al. (1999b) and Martín et al. (1999) behave in the T dwarf regime.

7.5.1 Red Optical Features

In §3.2.1, we described the acquisition and morphology of red optical spectra for T dwarfs obtained using the Keck LRIS instrument (Oke et al., 1995). Important features in this spectral regime are listed in Table 3.11. We plot the spectral data for representative L8 V (Gliese 337C; Wilson et al., 2001b), T1 V (SDSS 0837-0000), T2 V (SDSS 1254-0122), T3 V (SDSS 1021-0304), T5 V (2MASS 0559-1404), T6 V (SDSS 1624+0029), T7 V (2MASS 0727+1710), and T8 V (2MASS 0415-0935) objects in Figures 7.12 (linear scale) and 7.13 (logarithmic scale). These two plots allow different features to be highlighted. Identified lines and bands are labeled.

A few general trends in the T dwarf spectra are readily apparent. Most obvious is the increasingly steep spectral slope from 7700–10000 Å, a feature attributed to pressure broadened K I at 7665 and 7699 Å (Tsuji, Ohnaka, & Aoki, 1999; Liebert et al., 2000b; Burrows, Marley, & Sharp, 2000). The presence of the doublet is clearly evident in Figure 7.13, and the rise in flux between the K I and more heavily broadened Na I D lines (5890, 5896 Å) can be discerned in all of the objects except the faint T7 V and T8 V. A drop in flux shortward of 6600 Å (clearly seen in the 2MASS 0559-1404) is due to the red wing of Na I (Reid et al., 1999b). Higher order Na I lines at 8183 and 8195 Å are seen to weaken in the late L dwarfs and are not evident in the T dwarf spectra. Other alkali lines present in this spectral region include Rb I (7800, 7948 Å), seen only in the highest signal-to-noise spectra; and Cs I (8521, 8943 Å), which are strong through most of the T sequence but begin to weaken at T6 V.

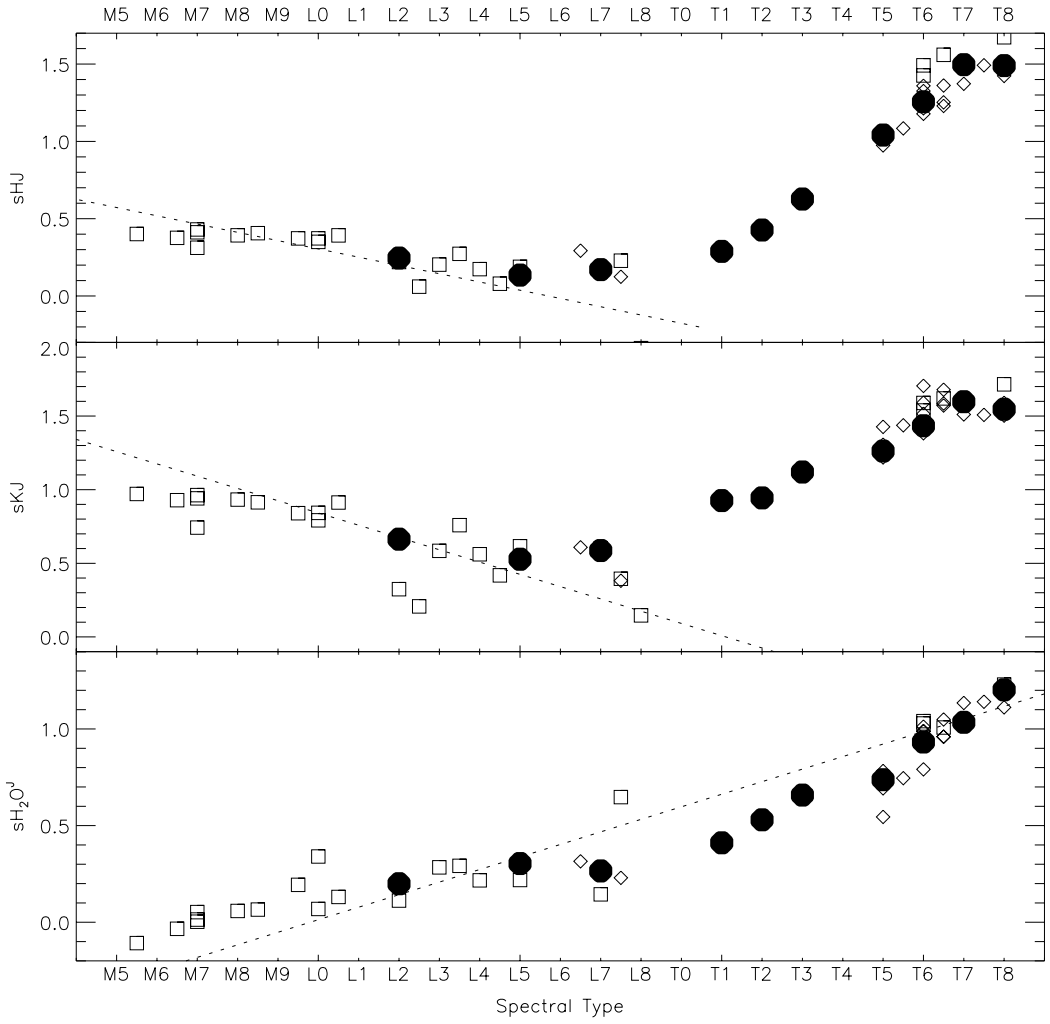

Figure 7.10: Values for sHJ, sKJ, and sH_2O^J indices from Testi et al. (2001) versus spectral type. Symbols are those used in Figure 7.3. Short-dashed lines are the index/spectral type relations determined by Testi et al. (2001) for spectral types L0 V through L6 V.

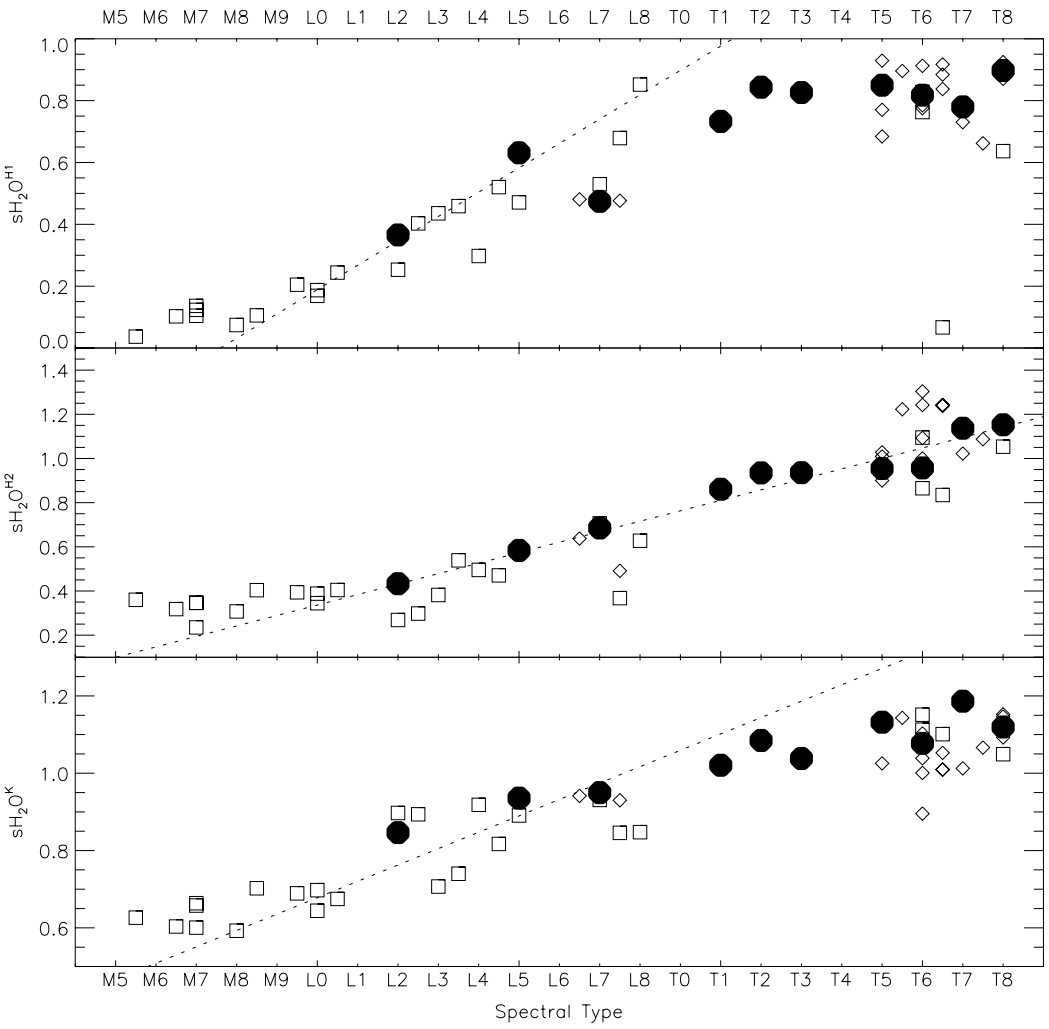

Figure 7.11: Same as Figure 7.10 with the sH_2O^{H1}, sH_2O^{H2}, sH_2O^{K} indices.

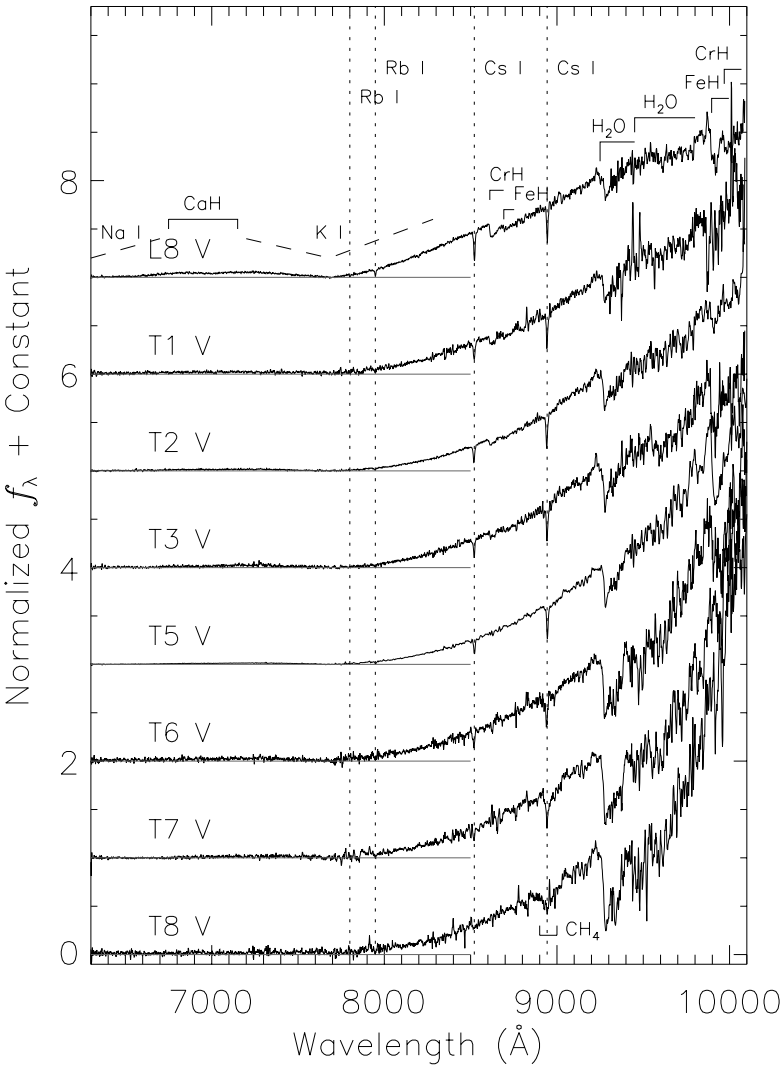

Figure 7.12: LRIS red optical spectra of T dwarf standards and the L8 V Gliese 337C (Wilson et al., 2001b). Major absorption features are noted.

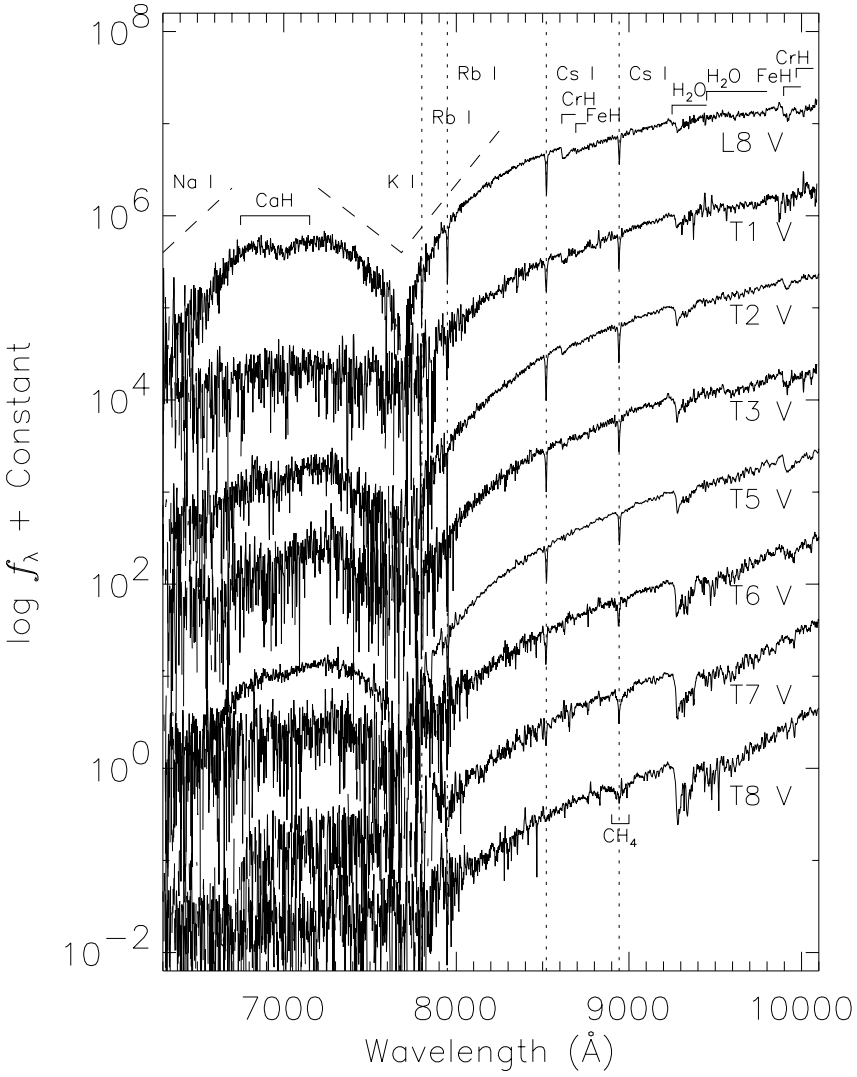

Figure 7.13: Same as Figure 7.12 on a logarithmic scale.

Table 7.11: T Dwarf Spectral Ratios in the Red Optical.

Diagnostic (1)	Numerator (Å) (2)	Denominator (Å) (3)	Feature Measured (4)
K I	$\langle F_{7100.0-7300.0} \rangle$	$\langle F_{7600.0-7800.0} \rangle$	7665, 7699 Å K I
Cs-a[a,b]	$0.5(\langle F_{8496.1-8506.1} \rangle + \langle F_{8536.1-8546.1} \rangle)$	$\langle F_{8516.1-8526.1} \rangle$	8521 Å Cs I
Cs-b[b]	$0.5(\langle F_{8918.5-8928.5} \rangle + \langle F_{8958.3-8968.3} \rangle)$	$\langle F_{8938.5-8948.3} \rangle$	8943 Å Cs I
H_2O[a,c]	$\langle F_{9225.0-9250.0} \rangle$	$\langle F_{9275.0-9300.0} \rangle$	9250 Å H_2O
FeH-a[b]	$\langle F_{8660.0-8680.0} \rangle$	$\langle F_{8700.0-8720.0} \rangle$	8692 Å FeH
FeH-b[a,b]	$\langle F_{9863.0-9883.0} \rangle$	$\langle F_{9908.0-9928.0} \rangle$	9896 Å FeH
CrH-a[b]	$\langle F_{8580.0-8600.0} \rangle$	$\langle F_{8621.0-8641.0} \rangle$	8611 Å CrH
CrH-b[b]	$\langle F_{9940.0-9960.0} \rangle$	$\langle F_{9970.0-9990.0} \rangle$	9969 Å CrH
Color-c[b]	$\langle F_{9800.0-9850.0} \rangle$	$\langle F_{8100.0-8150.0} \rangle$	Spectral Slope
Color-d[b]	$\langle F_{9675.0-9875.0} \rangle$	$\langle F_{7350.0-7550.0} \rangle$	Spectral Slope
Color-e[c]	$\langle F_{9210.0-9250.0} \rangle$	$\langle F_{8540.0-8580.0} \rangle$	Spectral Slope
Color-f[a,c]	$\langle F_{10000.0-10040.0} \rangle$	$\langle F_{9210.0-9250.0} \rangle$	Spectral Slope

[a]Spectral ratio useful as a classification diagnostic.
[b]Defined by (Kirkpatrick et al., 1999b).
[c]Not reliable in non-telluric corrected spectra.

Molecular features include H_2O absorptions at 9250 and 9450 Å which strengthen throughout the T sequence, the former producing the strongest bandhead in the T8 V 2MASS 0415-0935. CrH (8611 Å) and FeH (8692 Å) features weaken through the latest L dwarfs, but persist up through T3 V. The FeH band at 9896 Å also weakens from mid- to late-L, and continues this trend through T2 V. However, there is a deepening of this band in SDSS 1021-0304 and 2MASS 0559-1404, followed by a subsequent decline and disappearance by T8 V. A weak CH_4 band centered at 8950 Å (blended with the 8943 Å Cs I line) appears to be evident as a shallow feature in the T6 V, T7 V, and T8 V spectra, with possible strengthening toward the latest object. Finally, CaH (6750 Å) is detected in the spectra with the highest signal-to-noise (L8 V, T2 V, and T5 V), and appears to be weaker in 2MASS 0559-1404 than in the L8 V Gliese 337C.

7.5.2 Spectral Indices

It is clear that there are definite variations in the optical features of the T dwarfs that make them distinguishable. To explore these differences quantitatively, we have examined a suite of spectral indices, listed in Table 7.11. These indices were chosen to sample the most prominent features in the T dwarf spectra, including the CrH, FeH, and H_2O bands; the Cs I lines; and the K I doublet and its effect on the 8000–10000 Å spectral slope. A number of the indices were chosen from those defined by Kirkpatrick et al. (1999b) for the L dwarfs; note that the CrH-b and Color-d indices are used by Kirkpatrick et al. (1999b) as primary L classification indices. The various Color indices we list in Table 7.11 were chosen to sample different continuum points along the red slope in order to avoid low signal-to-noise regions around the K I doublet. We diagram the regions sampled by our red optical indices in Figure 7.14.

Figures 7.15 and 7.16 plot the values of these indices measured on L (Kirkpatrick et al., 1999b, 2000, triangles) and T (circles) dwarf spectra. The Cs-a and Cs-b indices show similar trends, strengthening from L3/L4 V to T3/T5 V, then weakening toward T8 V; these trends reflect the behavior seen in the spectra of Figures 7.12 and 7.13. Note that Cs-b is also influenced by the

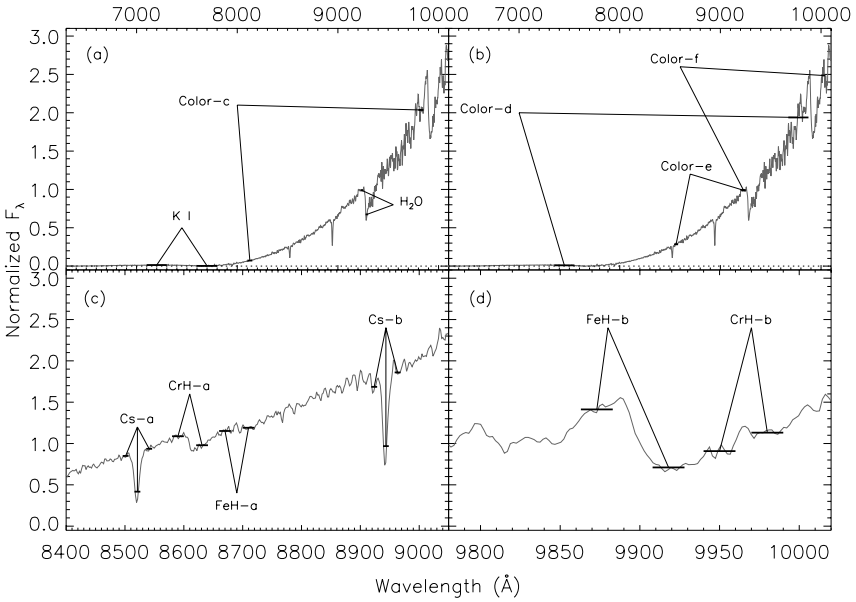

Figure 7.14: Red optical spectral indices mapped onto the spectra of 2MASS 0559-1404 (a, b, and d) and SDSS 1254-0122 (c). Indices are defined in Table 7.11.

weak 8950 Å CH_4 band, particularly in the latest T dwarfs. FeH-a decreases from L3 V to T3 V, and values beyond this subtype likely sample only spectral slope due to the disappearance of the band. FeH-b also decreases from L1/L2 V to T1 V, but then appears to increase from T1 V to T3/T5 V, followed by another sharp decrease to T8 V. Again, this behavior reflects that seen in the representative spectra. CrH-a (Figure 7.17) shows similar behavior as FeH-a, while CrH-b is essentially scatter with no obvious trends[2]. H_2O shows a dramatic increase through the T dwarf regime, and values for T8 V are nearly three times larger than those for the latest L dwarfs. Note, however, that this index is influenced by telluric absorption, and L dwarf data from Kirkpatrick et al. (1999b, 2000) have not been corrected for this absorption. Hence, some care must be taken in interpreting the behavior of this index between the L and T classes. K I is essentially a measure of the "blue bump" (Liebert et al., 2000b) between the K I and Na I doublets, and appears to increase from L0 V to T6 V, albeit with substantial scatter. The faintness of late-L and T dwarfs at wavelengths shortward of 7700 Å generally makes this ratio difficult to measure with high accuracy.

The color indices all show similar trends, with rapid increases beyond L8 V and generally greater scatter in the late T dwarfs. Color-d, in particular (Figure 7.17), samples a region near the K I doublet, and shows the most scatter of all the color indices. This is likely due to the lack of measurable flux around the K I absorption. Both Color-c and Color-e (the latter of which measures the spectral slope shortward of the 9250 Å H_2O band) show similar behaviors, rapidly increasing between L8 V and T2 V, then appearing to flatten off around values of 27 and 3.5, respectively. Note that the latter index has a slight decrease from L0 to L4/5 V, as it is affected by TiO and VO absorption around 8500–8600 Å (Kirkpatrick, Henry, & McCarthy, 1991). Color-f, which samples the spectral slope from the 9250 Å H_2O band to 1 μm, shows the most consistent, monotonic trend

[2]This feature resides in the wings of the 9896 Å FeH band, and is affected by both fringing and low quantum efficiency in the detector.

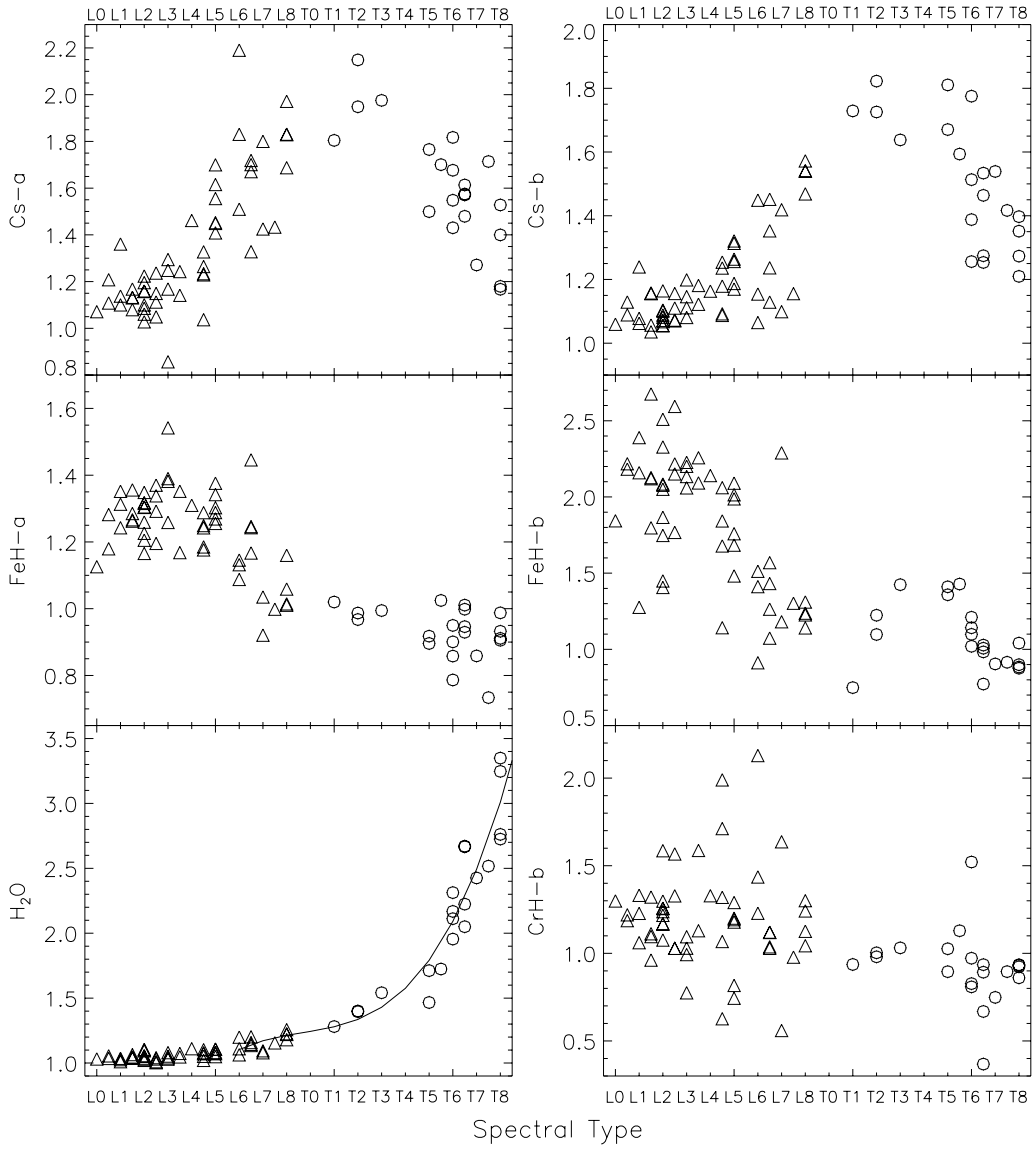

Figure 7.15: Values for the Cs-a, Cs-b, FeH-a, FeH-b, H_2O, and CrH-b red optical spectral indices for L (triangles) and T (circles) dwarfs.

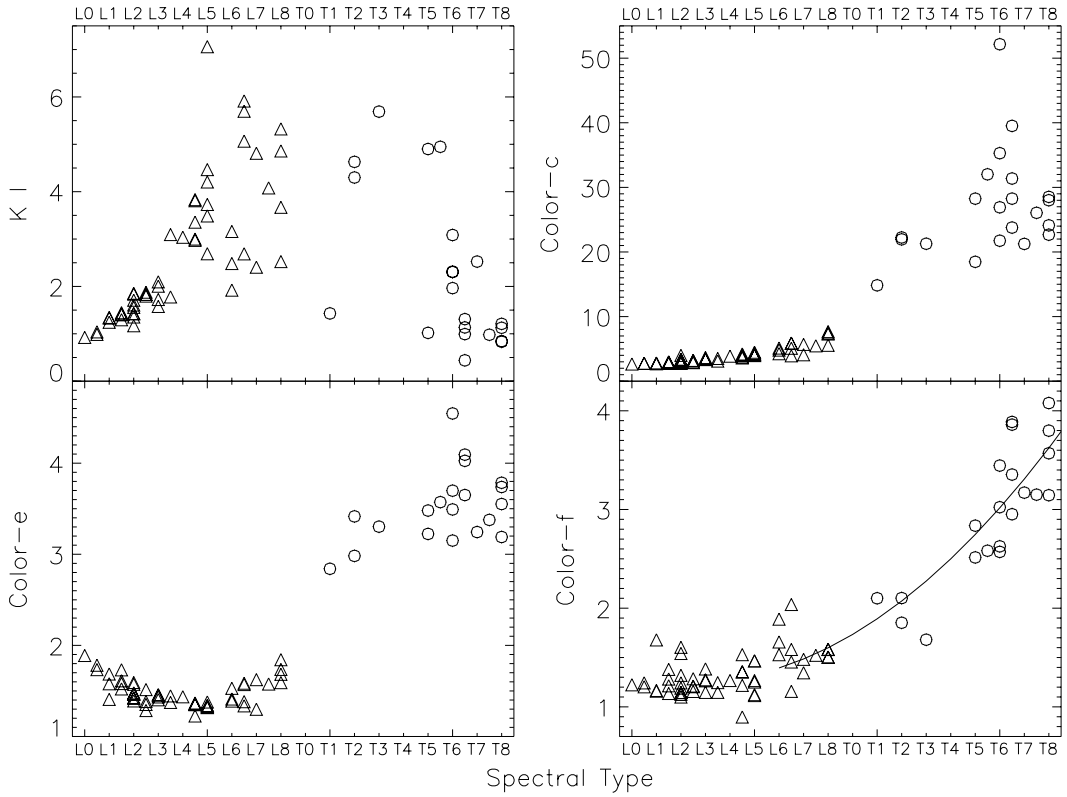

Figure 7.16: Values for the K I, Color-c, Color-e, and Color-f red optical spectral indices for L (triangles) and T (circles) dwarfs.

of the Color indices, increasing from roughly L7 V to T8 V; note, however, the apparent decrease in this index from T1 V to T3 V. Again, care must be taken in the interpretation of both the Color-e and Color-f indices between telluric corrected and non-telluric corrected data.

Of these indices, Cs-a, Cs-b, FeH-b, H_2O, and Color-f show the most consistent trends in the T dwarf regime. Values for these indices for T dwarfs are listed in Table 7.12. The first three indices are clearly non-monotonic across the T class, and are thus not particularly useful for classification except, for instance, to segregate early (T1 V - T5 V) from later (T6 V - T8 V) subtypes. The H_2O and Color-f indices do show monotonic trends, and we have fit these to third- and second-order polynomials (solid lines in Figures 7.15 and 7.16), respectively, yielding:

$$SpT = -(41.4\pm5.2) + (56.1\pm8.2)\times[H_2O] - (21.3\pm4.0)\times[H_2O]^2 + (2.7\pm0.6)\times[H_2O]^3, \quad (7.10)$$

$$SpT = -(19.5\pm1.9) + (14.1\pm1.9)\times[Colorf] - (1.7\pm0.4)\times[Colorf]^2 \quad (7.11)$$

where SpT(T1) = 1, SpT(T5) = 5, etc. These relations were fit from L5 V – T8 V, with RMS dispersions of 2.0 and 0.9 subclasses. Using these relations, we computed subtypes for the T dwarfs, as listed in Table 7.12. Deviations in classification in the T dwarf regime were typically 0.7 and 1.5 subclasses for the H_2O and Color-f indices, respectively, although differences as high as 2.4 and 4.8 subclasses occurred. Greater consistency was seen in the later subtypes (0.5 and 1.0 RMS deviations, respectively), likely due to the larger number of later-type objects constraining the fits. An average of these indices yielded typical differences of 0.9 subclasses, although again a computed type could be off by as much as 2.2 subclasses (e.g., SDSS 1021-0304).

While these classification uncertainties are generally larger than those for the near-infrared spectra, it is clear that red optical spectra can be used to subtype a T dwarf to within a ±1.0 subclasses. Note that the uncertain type of T5 V assigned to 2MASS 0755+2212 based on D78 near-infrared data (Table 7.7) appears to be confirmed by the red optical data.

7.5.3 Comparison to L Dwarf Classification Indices

7.5.3.1 Kirkpatrick et al. (1999b) Indices

In their prescription for spectral classification of L dwarfs in the red optical, Kirkpatrick et al. (1999b) identified four spectral indices useful for determining spectral type: Color-d, CrH-a, Rb-b/TiO-b, and Cs-a/VO-b. The first two are defined in Table 7.11, the latter two are defined as

$$\frac{\mathrm{Rb-b}}{\mathrm{TiO-b}} = \frac{0.5(\langle F_{7775.2-7785.2}\rangle + \langle F_{7815.2-7825.2}\rangle)}{\langle F_{7795.2-7805.2}\rangle} \times \frac{\langle F_{8435.0-8470.0}\rangle}{\langle F_{8400.0-8415.0}\rangle} \quad (7.12)$$

$$\frac{\mathrm{Cs-a}}{\mathrm{VO-b}} = \frac{0.5(\langle F_{8496.1-8506.1}\rangle + \langle F_{8536.1-8546.1}\rangle)}{\langle F_{8516.1-8526.1}\rangle} \times \frac{\langle F_{7960.0-8000.0}\rangle}{\langle F_{7860.0-7880.0}\rangle + \langle F_{8080.0-8100.0}\rangle}. \quad (7.13)$$

The behavior of these indices for L (triangles) and T (circles) dwarfs are shown in Figure 7.17; values for L dwarf standards from Kirkpatrick et al. (1999b) are shown as solid triangles. CrH-a and Color-d are described above. Both Rb-b/TiO-b and Cs-a/VO-b encompass molecular features that are important in late-M to mid-L dwarfs, but fade in the late-L dwarfs. Hence, both indices are not particularly useful in the T dwarf regime. The Rb-b/TiO-b ratio in particular becomes more sensitive to spectral slope in the T dwarfs rather than specific features, and is sensitive to noise near the K I doublet, as is the Color-d index. The 7912 Å VO band measured by Cs-a/VO-b is also fairly close to this flux minimum in T dwarf spectra, resulting in significant scatter in the latest T dwarfs. Note, however, that Cs-a shows a fairly unambiguous trend in Figure 7.15. Nonetheless, the primary indices defined by Kirkpatrick et al. (1999b) for the L dwarfs are not particularly useful for

Table 7.12: T Dwarf Red Optical Spectral Indices.

							Computed Type		
Object	Type	Cs-a	Cs-b	FeH-b	H_2O	Color-f	H_2O	Color-f	Ave.
(1)	(2)	(3)	(4)	(5)	(6)	(7)	(8)	(9)	(10)
SDSS 0837-0000	T1 V	1.804	1.729	0.749	1.281	2.100	0.2	1.4	0.8
SDSS 1254-0122[a]	T2 V	2.149	1.822	1.224	1.401	2.102	1.8	1.4	1.6
		1.948	1.726	1.097	1.395	1.852	1.7	−0.4	0.7
SDSS 1021-0304	T3 V	1.976	1.638	1.424	1.542	1.681	3.4	−1.8	0.8
2MASS 0559-1404	T5 V	1.765	1.670	1.410	1.466	2.514	2.6	3.9	3.2
2MASS 0755+2212	T5 V	1.499	1.811	1.358	1.712	2.836	4.8	5.4	5.1
2MASS 1534-2952	T5.5 V	1.700	1.594	1.428	1.724	2.582	4.8	4.2	4.5
2MASS 1225-2739	T6 V	1.817	1.775	1.210	2.112	2.570	6.5	4.2	5.3
SDSS 1624+0029	T6 V	1.676	1.388	1.141	1.955	2.626	6.0	4.5	5.2
SDSS 1346-0031	T6 V	1.430	1.256	1.020	2.168	3.023	6.6	6.1	6.4
2MASS 0937+2931	T6 V	1.548	1.513	1.099	2.313	3.445	6.9	7.3	7.1
2MASS 1237+6526[a]	T6.5 V	1.571	1.534	0.983	2.670	3.887	7.0	7.9	7.5
		1.575	1.464	1.028	2.666	3.860	7.0	7.9	7.5
		1.614	1.253	0.772	2.050	2.952	6.4	5.9	6.1
2MASS 1047+2124	T6.5 V	1.479	1.274	1.007	2.224	3.354	6.7	7.1	6.9
2MASS 0727+1710	T7 V	1.271	1.539	0.904	2.426	3.171	6.9	6.6	6.8
2MASS 1217-0311	T7.5 V	1.714	1.417	0.915	2.517	3.150	7.0	6.6	6.8
Gliese 570D[a]	T8 V	1.528	1.397	0.884	2.761	3.799	7.1	7.8	7.4
		1.400	1.273	0.876	2.725	4.078	7.0	7.9	7.5
2MASS 0415-0935[a]	T8 V	1.167	1.352	0.899	3.247	3.144	7.9	6.5	7.2
		1.180	1.210	1.041	3.349	3.570	8.3	7.5	7.9

[a]Values measured for multiple spectra.

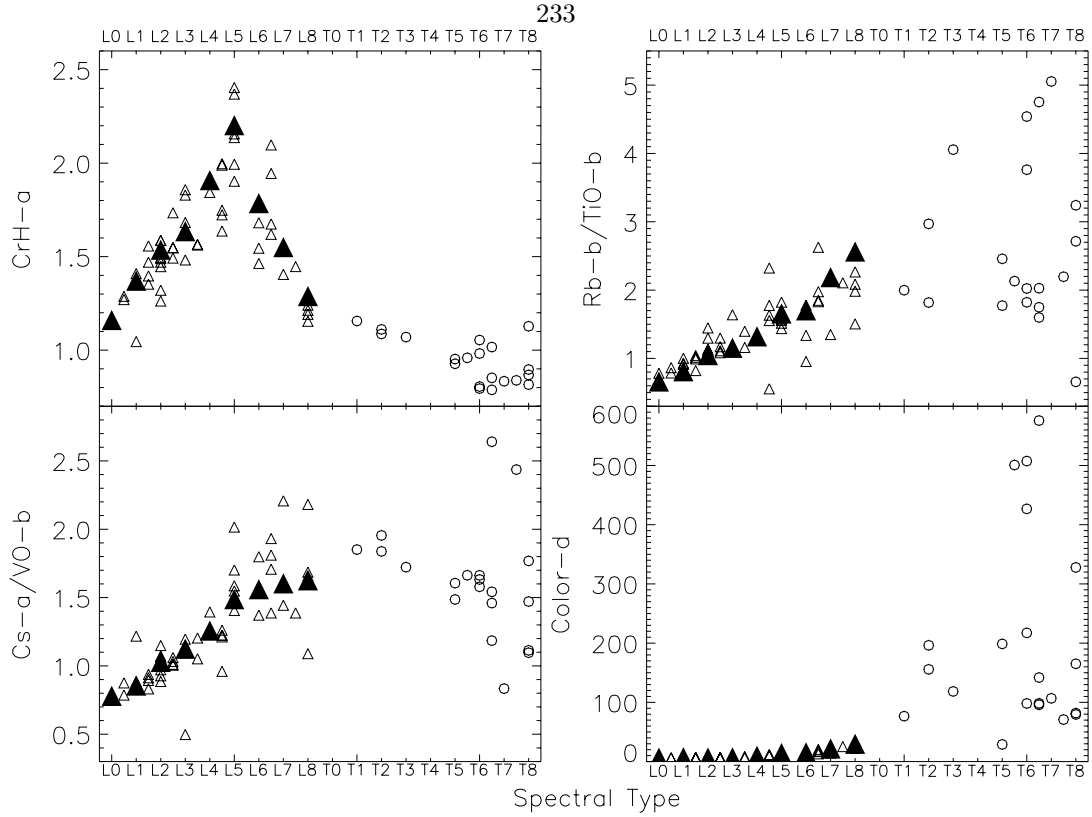

Figure 7.17: Kirkpatrick et al. (1999b) CrH-a, Rb-b/TiO-b, Cs-a/VO-b, and Color-d indices measured for L (triangles) and T (circles) dwarf LRIS spectra. Standard values from Kirkpatrick et al. (1999b) are indicated by solid triangles.

the T dwarfs in the red optical.

7.5.3.2 Martín et al. (1999) Indices

Martín et al. (1999) have quantified their spectral classification of L dwarfs using pseudo-continuum indices, similar to the Color indices of Kirkpatrick et al. (1999b) and those defined in Table 7.12. In particular, they define two indices for use in the red optical region:

$$PC3 = \frac{\langle F_{8230.0-8270.0} \rangle}{\langle F_{7540.0-7580.0} \rangle} \tag{7.14}$$

$$PC6 = \frac{\langle F_{9090.0-9130.0} \rangle}{\langle F_{6500.0-6540.0} \rangle}. \tag{7.15}$$

Figure 7.18 plots these indices for the spectra of L (triangles) and T (circles) dwarfs. The average values of the PC3 index for their spectral types L1 V to L6 V (converted here to L1 V to L8 V on the Kirkpatrick et al. scale using corrections from Martín et al. 1999) are indicated by solid triangles, which Martín et al. (1999) find yield a typing accuracy of ±0.5 subclasses. Both indices suffer from the same difficulty in the T dwarf regime, however, in that they sample the lowest flux regions in

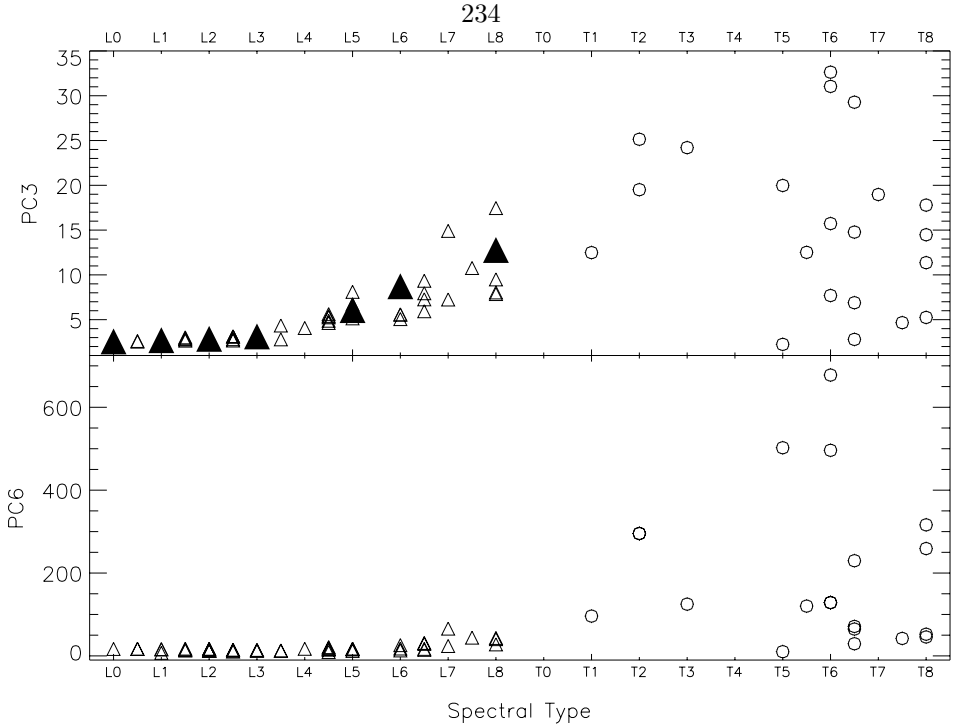

Figure 7.18: PC3 and PC6 L dwarf indices defined by Martín et al. (1999) measured for L (triangles) and T (circles) dwarf LRIS spectra. Average values for the PC3 index for Martín et al. (1999) types L0 V through L6 V (converted to Kirkpatrick et al. (1999b) subtypes) are indicated by solid triangles.

the spectra of that class, and hence behave similarly to the Kirkpatrick et al. (1999b) Color-d index, showing significant scatter beyond L8–T3 V.

Hence, unlike their counterparts in the near-infrared indices, indices defined for L dwarfs in the red optical are not as applicable to T dwarfs, due primarily to the disappearance of key L dwarf spectral features (e.g., TiO, CO, CrH, etc.) and the heavily suppressed flux around the Na I and K I doublets. Indices measured in Table 7.12 are clearly more adequate for separating the T dwarf subclasses. Nevertheless, the insufficiency of the L dwarf indices in the red optical attests to the significant differences between L and T dwarf spectral morphologies, and shows that these classes can truly be distinguished in this regime.

7.6 DENIS 0205-1159AB and the L/T Transition

The behavior of spectral indices and colors between the latest L dwarfs and early T dwarfs shows a small morphological gap between L8 V and T1 V. The recent detection of the fundamental band of CH_4 at 3.3 μm in objects as early as L5 V (Noll et al., 2000) and the lack of objects later than L8 V in 2MASS L dwarf searches (Kirkpatrick et al., 2000) both suggest that the separation in temperature between these two classes is also not large. To investigate the L/T transition, we examined the near-infrared spectrum of the L7 V DENIS 0205-1159AB, a bright, well-studied, equal-magnitude binary (Koerner et al., 1999; Leggett et al., 2001), 17.5 pc from the Sun (Kirkpatrick et al., 2000). Delfosse et al. (1997) discovered this object in DENIS survey data, and identified a feature at 2.22 μm that

they attributed to weak CH_4 absorption. Tokunaga & Kobayashi (1999) rejected this hypothesis, however, favoring CIA H_2 absorption based on the spectral models of Tsuji, Ohnaka, & Aoki (1999).

Figure 7.19 plots spectral data from 2.01 to 2.35 μm for DENIS 0205-1159AB obtained from Delfosse et al. (1997), Tokunaga & Kobayashi (1999), Leggett et al. (2001), and Reid et al. (2001a). Near-infrared spectral data for SDSS 0539-0059 (L5 V) and SDSS 1254-0122 (T2 V) from Leggett et al. (2000b) are also shown for comparison. Spectra are normalized at their K-band peaks (short-dashed lines) and offset for comparison. Above these data are opacity spectra for CIA H_2 (thick line), CH_4 (thin line), H_2O (dashed line), and CO (dot-dashed line) at T = 1400 K and P = 1 bar (see references in Burrows et al. 1997). This combination of temperature and pressure is expected to represent the typical photospheric conditions for a 1 Gyr, T_{eff} = 1500 K brown dwarf (Burrows et al., 1997; Ackerman & Marley, 2001). Opacity data for CH_4, H_2O, and CO have been scaled by their number densities relative to H_2 using the chemical equilibrium models of Burrows & Sharp (1999).

The opacity spectra indicate that the broad absorption feature seen from 2.18 to 2.29 μm is a combination of CIA H_2, CH_4, and H_2O, with CIA H_2 being the strongest contributor beyond 2.1 μm. In addition, there is a weak absorption feature at 2.20 μm (arrows) present in all of the DENIS 0205-1159AB spectra except that of Leggett et al. (2001) that closely corresponds to a sharp feature in the CH_4 opacity spectrum. This absorption is only slightly offset from the 2.2056/2.2084 μm Na I doublet (4s ^{2}S $\rightarrow$ 4p $^2P_0$), indicated by vertical lines in Figure 18. The high-energy Na I lines form 3.2 eV above the ground state and appear to weaken over types late-M to mid-L (Reid et al., 2001a). It is likely, therefore, that Na I is not responsible for this feature in DENIS 0205-1159AB.

Does the weak 2.20 μm feature constitute a clear detection of CH_4 at K-band in the latest L dwarfs? In our opinion it does not, due to the weakness and occasional non-detection of the absorption. Its apparent variability in the spectra of Figure 18 may be intrinsic to the source, as a number of L- and T-type brown dwarfs have recently been shown to be variable, both photometrically (Bailer-Jones & Mundt, 1999, 2001) and spectroscopically (Nakajima et al., 2000; Kirkpatrick et al., 2001a), likely due to patchy clouds of dust in the photosphere (Ackerman & Marley, 2001). Differences in instrumental resolution and observing conditions, however, make this interpretation ambiguous, and the weakness of this feature may lend doubt to its reality. Higher resolution, higher signal-to-noise, and time-resolved data are required to confirm its authenticity and possible variable nature.

Nonetheless, the opacity spectra in Figure 18 do suggest that CH_4 is an important minor absorber at these temperatures, and its emergence as an identifiable feature likely occurs in objects only slightly cooler than DENIS 0205-1159AB. This suggests that the earliest T dwarfs (i.e., those with clear CH_4 bands) are probably not significantly cooler than the latest L dwarfs currently known. In that case, L8 V may be the last subtype of the L spectral class, with cooler objects showing obvious CH_4 absorption features at K-band, classifying them as T dwarfs. In order to verify this hypothesis, it is necessary to identify more of the so-called "L/T transition" objects and determine at what point the detection of CH_4 becomes unambiguous at J-, H-, and K-bands. Note that even if the 2.20 μm CH_4 feature is confirmed in DENIS 0205-1159AB or in other L7/L8 dwarfs, it does not necessitate a reclassification of these objects, much as the 3.3 μm absorption seen in mid- and late-L dwarfs reclassify them as T dwarfs (Noll et al., 2000), or the presence of TiO bands in bright K5 and K7 dwarfs (Reid, Hawley, & Gizis, 1995) reclassify them as M dwarfs. The weak feature described here may indicate that the latest-type L dwarfs known are close to the L/T boundary, but not that they have traversed it.

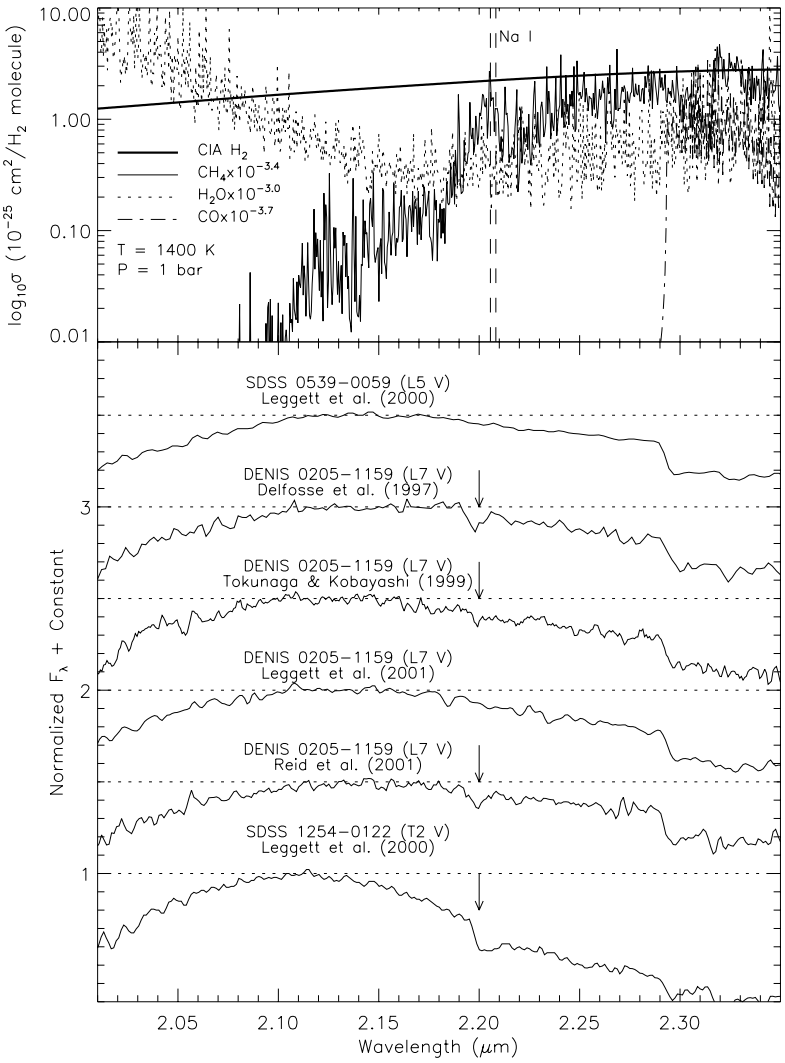

Figure 7.19: The K-band spectrum of DENIS 0205-1159AB. Top panel shows opacity spectra of CH_4 (solid line), H_2O (dotted line), CO (dot-dashed line) and CIA H_2 (thick solid line) at T = 1400 K and P = 1 bar. Data for CH_4, H_2O, and CO have been scaled to their relative chemical equilibrium number densities at this temperature and pressure (Burrows & Sharp, 1999). The location of the 2.2 μm Na I doublet is also indicated. Bottom panel shows spectra of DENIS 0205-1159AB from Delfosse et al. (1997); Tokunaga & Kobayashi (1999); Leggett et al. (2001); and Reid et al. (2001a). Data for SDSS 0539-0059 (L5 V) and SDSS 1254-0122 (T2 V) from Leggett et al. (2000b) are also shown for comparison. Spectra are normalized at 2.15 μm (dotted lines) and offset. Arrows identify a possible weak CH_4 feature at 2.20 μm.

7.7 The Peculiar T Dwarf 2MASS 0937+2931

One T dwarf that deserves special attention is the T6 Vp 2MASS 0937+2931, designated peculiar because of its highly suppressed K-band peak. Indeed, this object's near-infrared colors are significantly bluer that any other T dwarf so far identified. As can be seen in Figure 3.7, 2MASS 0937+2931 also has very weak or absent 1.25 μm K I absorption, weaker even than the T8 V Gliese 570D.

To identify the source of this anomalous absorption, we again examined the individual contributors to the photospheric opacity in this object. Figure 7.20 plots 1.9–2.3 μm NIRC data for 2MASS 0937+2931 (solid line) along with data for the T6 V standard 2MASS 0243-2453. Both spectra are normalized at their J-band peaks and match very well from 1–1.8 μm; however, 2MASS 0937+2931 is nearly 50% fainter at K-band. Plotted above this are opacity spectra for CIA H_2 (thick solid line), CH_4 (solid line), and H_2O (dotted line) at T = 1000 K and P = 1 bar, with CH_4 and H_2O scaled to their chemical equilibrium relative number densities (Burrows & Sharp, 1999). H_2O and CH_4 are clearly more important at cooler temperatures, as CIA H_2 at 1 bar is only a minor absorber outside of the 2.1 μm window. However, because H_2 features form via collisional processes, they strengthen with increasing pressure, scaling roughly as $\sigma \propto P$. This effect can be seen in the increased opacity of CIA H_2 for P = 10 bar (thick dashed line). The corresponding opacities of H_2O and CH_4 are generally unaffected by changes in pressure; and at or below T $\sim$ 1000 K, number densities at equilibrium remain essentially unchanged (Burrows & Sharp, 1999). Thus, CIA H_2 is the only major molecular absorber sensitive to local pressure in T dwarf atmospheres.

Photospheric pressure is directly related to specific gravity by hydrostatic equilibrium:

$$\frac{dP}{d\tau} \sim \frac{P}{\tau} = \frac{g}{\kappa_R} \propto \frac{M}{R^2 \kappa_R}. \tag{7.16}$$

Because brown dwarf radii are roughly constant, this implies the (simplistic) relation $P_{phot} \propto M$ for constant κ_R. Thus, at a given T_{eff} and composition, an older, more massive object will tend to have a higher photospheric pressure than a younger, less massive object, and hence stronger CIA H_2 absorption. If we assume that most T dwarfs identified to date have masses between 40 to 60 M_{Jup} (assuming $800 < T_{eff} < 1200$ and $1 < \tau < 5$ Gyr), then CIA H_2 absorption should be 1.5 times stronger in 2MASS 0937+2931 if it were a 75 M_{Jup} object. The structure models of (Burrows et al., 1997) predict a factor of 1.75 increase in specific gravity due to the increased contraction of the older, more massive object. Thus, significant differences in photospheric pressures are possible. However, a 75 M_{Jup} brown dwarf with T_{eff} = 1000 K would also have to be older than 11.5 Gyr (Burrows et al., 1997).

An alternate hypothesis capable of explaining the strong K-band absorption in 2MASS 0937+2931 is decreased metallicity. Zero-metallicity brown dwarf spectral models are dominated by CIA H_2 opacity and peak shortward of 1 μm; when molecular absorption is included, the suppression of flux at shorter wavelengths increases the relative luminosity at K-band by roughly a factor of two (Saumon, Chabrier, & Van Horn, 1995). If the metallicity of a brown dwarf atmosphere were decreased from $Z = Z_\odot$ to 0.1 $Z_\odot$, the number densities of CH_4 and H_2O and (in an approximate sense) their relative opacities would also decrease roughly by a factor of 10. Decreased metallicity would not significantly affect the amount of photospheric H_2 present, although it may slightly alter the opacity spectrum. Assuming photospheric pressure remained constant, one might expect the same relative opacity contributions in this scenario as in the $Z = Z_\odot$, P = 10 bar case. Decreased metallicity would also explain the deficit of K I absorption seen at J-band. Note that because of the reduced opacity and corresponding increased luminosity, brown dwarfs with subsolar metallicity cool more rapidly (Chabrier & Baraffe, 1997). Thus, a metal-poor model for 2MASS 0937+2931 is

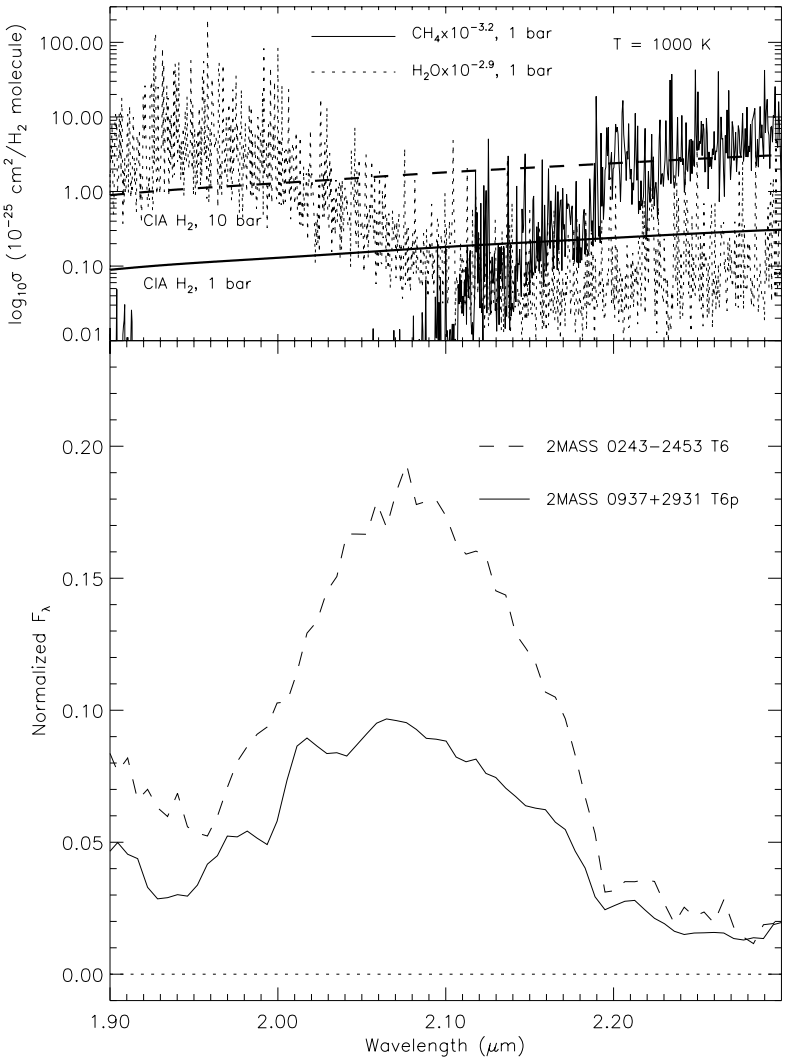

Figure 7.20: The K-band spectrum of 2MASS 0937+2931. Top panel shows opacity spectra of CH_4 (solid line) and H_2O (dotted line) at T = 1000 K and P = 1 bar, and CIA H_2 opacity at T = 1000 K and P = 1 bar (thick solid line) and 10 bar (thick dashed line). CH_4 and H_2O data have been scaled as in Figure 7.19. Bottom panel shows spectra of 2MASS 0937+2931 (solid line) and the T6 V standard 2MASS 0243-2453 (dashed line). Both spectra have been normalized at their J-band peaks.

either younger (same mass) or more massive (same age) than its solar metallicity, T_{eff} = 1000 K counterpart, while a high-pressure model must be both older and more massive.

These arguments are based on very simple scaling laws of abundance and opacity, and disentangling the effects of T_{eff}, specific gravity, and metallicity on the emergent spectrum of 2MASS 0937+2931 requires more extensive modeling. It is clear, however, that CIA H_2 plays an important role in shaping the spectra of both L and T dwarfs, and its sensitivity to the ambient pressure makes it an excellent tracer of surface gravity and hence mass. Diagnostics that measure the relative contributions of CIA H_2, CH_4, and H_2O may allow us to extract the physical characteristics of these constantly evolving objects.

7.8 An Empirical Effective Temperature Scale

One of the most important quantities that can be derived from a classification scheme is the mapping of spectral types to effective temperatures. Spectral types in the MK system generally coincide with an underlying temperature (or more accurately, ionization) scale, while separate luminosity classes yield radius/surface gravity information. In this section we examine the temperature scale for L dwarfs and speculate on the temperatures of T dwarfs, which is made ambiguous by both the paucity of distance and luminosity measurements for these objects, as well as the significant evolution of spectral features across the L/T boundary.

For this discussion, we use the fundamental definition of effective temperature,

$$\sigma T_{eff}^4 = \frac{L}{4\pi R^2}; \tag{7.17}$$

i.e., that it is essentially a measure of the surface flux. As we have seen in Chapter 3, the actual temperature observed is a strong function of wavelength, as variations in opacity imply flux is emitted from different thermal layers. However, the aggregate flux from an object (barring magnetospheric or accretion emission) is determined by the fundamental parameters of mass, age, and metallicity. As such, Equation 7.17 provides an overall measure of the evolutionary state of a brown dwarf without the details of its complex atmospheric properties.

7.8.1 Absolute Brightness Measurements

The first step in determining the effective temperature of an object is to measure its total luminosity. For this we require both absolute brightness (parallax) measurements and bolometric corrections, since

$$\log \frac{L}{L_\odot} = -0.4(m_b + BC_b + 5\log\pi + 5 - M_{bol,\odot}) = -0.4M_{bol} + 1.896. \tag{7.18}$$

For the former, we have worked in collaboration with the USNO Parallax Program (Monet et al., 1992), which, since the mid-1980s, has been obtaining parallaxes for low-mass stars, subdwarfs, and brown dwarfs in the Solar Neighborhood, using the USNO K. Aa. Strand USNO 61" Astrometric Reflector. Many of the recent results from this program come from observations initiated in February 1992 using the Tek2K Camera, a 2048×2048 pixel, thinned, back-illuminated CCD with $0\farcs33$ pixels and an $11' \times 11'$ field of view (Dahn, 1997). Faint (R > 12) stars are imaged using a variety of filters (V, R, I_C, z′) to simultaneously provide photometric and astrometric data over an extended observing period (usually greater than 1.5 years). Astrometric accuracy better than ±1.0 milliarcseconds has been typically obtained in this program, with many results in the ±0.3–0.5 mas uncertainty range. Late-L and T dwarfs are typically observed at z′ (Fukugita et al., 1997) due to their optical faintness, with up to 90-minute exposures obtained per observation. Recently, the near-infrared ASTROCAM

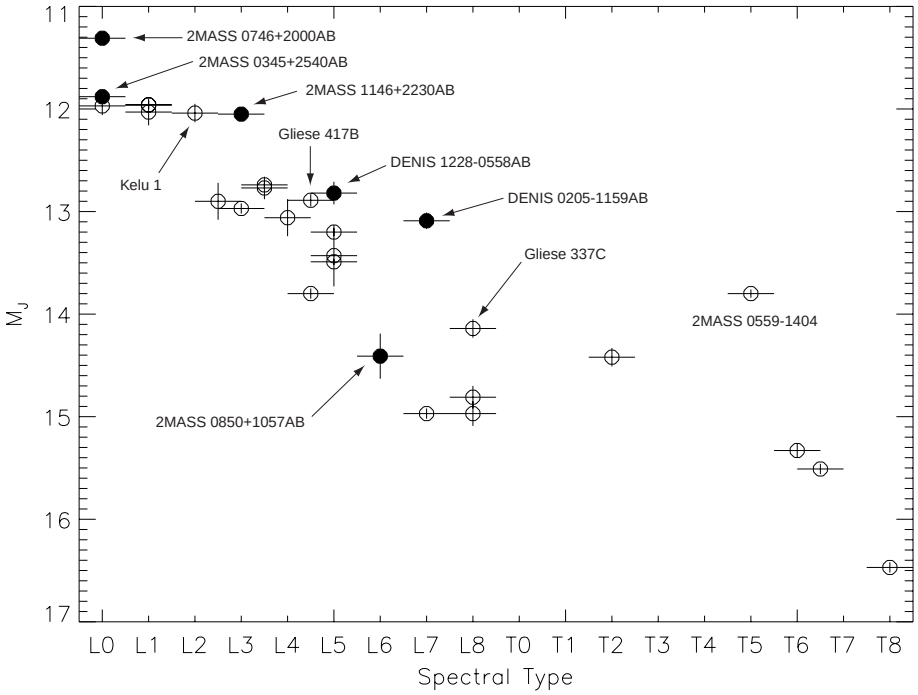

Figure 7.21: M_J versus spectral type for objects in Table 7.13. Open circles plot values for apparently single objects, while the solid circles indicate over-luminous objects. Known or suspected doubles are labeled. T dwarf spectral types are from Chapter 7.

camera has been installed to improve the detection of faint, late-type dwarfs. This instrument is comprised of a 2048×2048 ALADDIN array with 0.″37 pixels and a 7.′4×7.′4 field of view. First results from the ASTROCAM program are expected within the next year or two (C. Dahn, priv. comm.).

Table 7.13 lists the parallaxes, space motions, and absolute magnitudes for 20 L and T dwarfs measured by the USNO program (Kirkpatrick et al., 1999b, 2000, C. Dahn priv. comm.), including R- and I-band photometry for a handful of L dwarfs (C. Dahn priv. comm.). We also include ten L and T dwarf companions whose astrometric data are derived from their primaries (Becklin & Zuckerman, 1988; Nakajima et al., 1995; Goldman et al., 1999; Burgasser et al., 2000b; Gizis, Kirkpatrick, & Wilson, 2001; Kirkpatrick et al., 2001a; Wilson et al., 2001b, Tables 4.4 and 4.5). These objects sample the entire L dwarf range and include a diverse set of T dwarfs.

Figures 7.21 and 7.22 plot M_J and M_{K_s} for the objects listed in Table 7.13 as a function of spectral type. One of the immediate results from these data is the identification of over-luminous dwarfs with respect to their assigned spectral types. Because L- and T-type objects are all dwarf stars and brown dwarfs (Kirkpatrick et al., 1999b), their radii do not vary by more than 10–15% (Burrows & Liebert, 1993, see §§1.2.2 and 7.8.3), corresponding to a magnitude scatter of ±0.15 mag, all other variables being equal. Hence, over-luminosity must be due to duplicity. Indeed, the known doubles (Table 5.3) 2MASS 0746+2000AB (Reid et al., 2001b), 2MASS 1146+2230AB (Koerner et al., 1999; Reid et al., 2001b), DENIS 1228−0558AB (Koerner et al., 1999; Martín, Brandner & Basri,

Table 7.13: Parallax Measurements for L and T Dwarfs.

		Astrometry			Photometry[a]				
Object (1)	Type[b] (2)	M−m (mag) (3)	μ (mas yr^{-1}) (4)	P.A. (°) (5)	M_R (mag) (6)	M_I (mag) (7)	M_J (mag) (8)	M_{Ks} (mag) (9)	Ref. (10)
HD 89744B	L0 V	−0.38±0.08	183.4±0.7	220	–	–	11.97±0.09	10.77±0.09	3,4
2MASS 0345+2540[c]	L0 V	−0.15±0.03	102.4±0.3	249.6±0.2	17.45±0.05	15.21±0.03	11.88±0.05	10.55±0.06	1,5
2MASS 0746+2000AB[d]	L0.5 V	−0.43±0.01	378.5±0.3	261.2±0.1	16.97±0.01	14.68±0.01	11.31±0.03	10.06±0.03	1,2
2MASS 1439+1929	L1 V	−0.80±0.02	1294.6±0.3	288.3±0.1	17.72±0.02	15.32±0.02	11.96±0.04	10.78±0.04	1,5
2MASS 1658+7027	L1 V	−0.35±0.03	344.8±1.7	204.8±0.2	–	–	11.96±0.04	10.57±0.04	1,2
GJ 1048B	L1 V	−0.64±0.05	85.5±1.3	81	–	–	12.03±0.13	10.68±0.09	4,6
Kelu 1[d]	L2 V	−0.34±0.08	285.8±1.2	271.8±0.2	17.76±0.09	15.60±0.08	12.04±0.09	10.47±0.09	1,2,5
Gliese 618.1B	L2.5 V	−0.41±0.17	418±3	267	–	–	12.90±0.18	11.18±0.17	3,4
DENIS 1058−0548	L3 V	−0.21±0.04	255.9±0.5	279.2±0.2	–	–	12.97±0.05	11.32±0.05	2,5
2MASS 1146+2230AB[d]	L3 V	−0.18±0.05	96.1±0.5	19.6±0.3	17.96±0.06	15.67±0.05	12.05±0.06	10.45±0.06	1,2,5
2MASS 0036+1821	L3.5 V	0.30±0.02	907.8±0.7	82.4±0.1	18.65±0.03	16.41±0.02	12.74±0.04	11.33±0.04	1,2
2MASS 0326+2950	L3.5 V	−0.66±0.10	68.7±1.1	341.5±0.9	–	–	12.77±0.11	11.17±0.12	2,5
GD 165B	L4 V	−0.49±0.17	256	240	–	–	13.06±0.18	11.57±0.18	5,7
2MASS 2224−0158	L4.5 V	−0.25±0.04	984.4±1.4	152.3±0.1	–	–	13.80±0.05	11.77±0.05	1,2
Gliese 417B[d]	L4.5 V	−0.68±0.04	291.0±1.0	239	–	–	12.89±0.06	11.01±0.06	4,8
2MASS 1507−0627	L5 V	0.67±0.01	902.5±0.7	190.3±0.1	19.71±0.03	17.32±0.03	13.49±0.03	11.97±0.03	1,2
GJ 1001B	L5 V	0.10±0.24	1618	154	–	–	13.20±0.04	11.50±0.04	7,8
DENIS 1228−0558AB[d]	L5 V	−0.56±0.10	226.0±1.5	143.5±0.4	–	–	12.82±0.11	11.25±0.10	2,5
2MASS 1328+2114	L5 V	−0.61±0.28	480.9±2.3	152.9±0.3	–	–	13.43±0.30	11.64±0.30	2,5
2MASS 0850+1057AB	L6 V	−0.04±0.19	144.7±2.0	267.0±0.9	–	–	14.41±0.22	12.42±0.20	2,5
DENIS 0205−0159AB[d]	L7 V	−0.46±0.07	439.5±1.0	82.7±0.1	–	–	13.09±0.08	11.53±0.08	5
2MASS 0825+2115	L7.5 V	−0.15±0.03	584.1±1.8	240.8±0.2	–	–	14.97±0.05	12.90±0.05	1,2
2MASS 1632+1904	L8 V	−0.05±0.09	300.9±1.5	100.9±0.3	–	–	14.81±0.11	12.93±0.10	2,5
Gliese 584C	L8 V	−0.35±0.05	216.7±1.0	145	–	–	14.97±0.12	12.89±0.09	4,8
Gliese 337C[d]	L8 V	−0.56±0.04	578.9±1.1	295	–	–	14.14±0.09	12.46±0.07	3,4
SDSS 1254−0122	T2 V	−0.46±0.08	492.4±3.1	285.3±0.6	–	–	14.42±0.09	13.37±0.10	1,9
2MASS 0559−0404	T5 V	−0.03±0.03	665.4±2.0	121.5±0.2	–	–	13.80±0.04	13.58±0.06	1,10
SDSS 1624+0029	T6 V	−0.20±0.06	382.5±2.6	268.5±0.7	–	–	15.33±0.07[e]	15.50±0.08[e]	1,11
Gliese 229B	T6.5 V	1.19±0.02	727.1±1.1	191	–	–	15.51±0.05[e]	15.61±0.05[e]	4,12
Gliese 570D	T8 V	1.14±0.02	2011.6±2.2	149	–	–	16.47±0.05	16.41±0.17	4,13

[a] JK_s photometry from 2MASS unless otherwise noted; photometry for doubles are for combined pair.
[b] T Classifications are discussed in Chapter 7.
[c] Suspected spectroscopic binary (Reid et al., 1999b).
[d] Object appears to be over-luminous.
[e] JK photometry from Strauss et al. (1999) and Leggett et al. (1999).
Refs – (1) C. Dahn, priv. comm.; (2) Kirkpatrick et al. (2000); (3) Wilson et al. (2001b); (4) Perryman et al. (1997); (5) Kirkpatrick et al. (1999b); (6) Gizis, Kirkpatrick, & Wilson (2001); (7) van Altena, Lee, & Hoffleit (1995); (8) Kirkpatrick et al. (2001a); (9) Burgasser (2001); (10) Burgasser et al. (2000c); (11) Strauss et al. (1999); (12) Leggett et al. (1999); (13) Burgasser et al. (2000b)

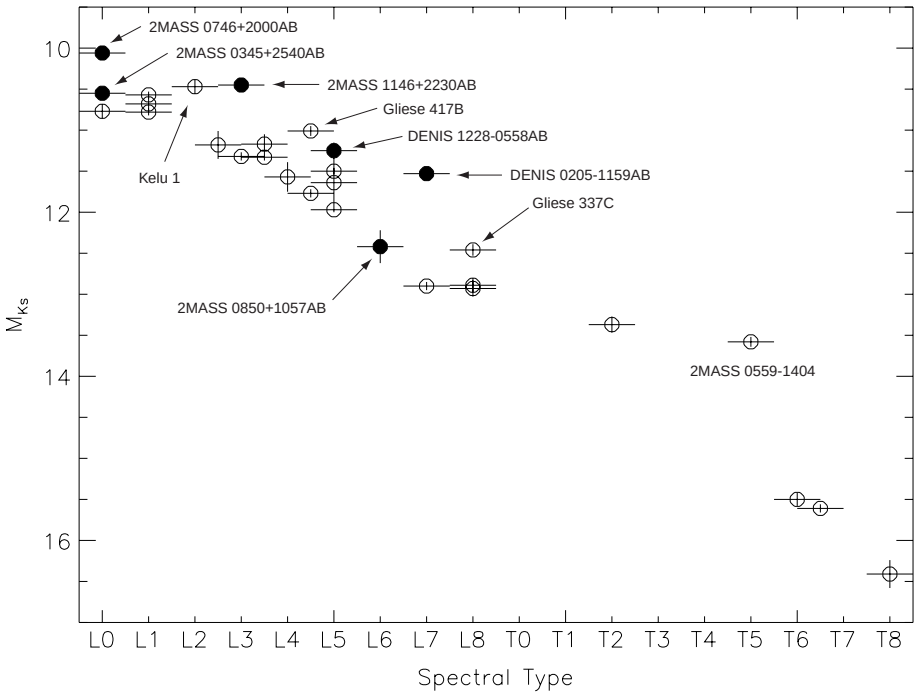

Figure 7.22: Same as Figure 7.21 for M_{K_s}.

1999), and DENIS 0205−1159AB (Koerner et al., 1999; Leggett et al., 2001) all stand out in this respect in both M_J and M_{K_s}. The visual binary 2MASS 0850+1057AB (Reid et al., 2001b) does not appear to be particularly over-luminous, however; this is likely due to the fact that the secondary in this system is only 30% as bright as the primary at F814W (Table 5.3). Similarly, the spectroscopic binary 2MASS 0345+2540AB (Reid et al., 1999b) is not noticeably over-luminous as compared to other L0 V and L1 V objects, implying that its companion may also be less massive (or more evolved if this is a star/brown dwarf pair). We see that Kelu 1 (Ruiz, Leggett, & Allard, 1997), Gliese 417B (Kirkpatrick et al., 2001a), and Gliese 337C (Wilson et al., 2001b) also appear to be over-luminous at M_{K_s}, although only Gliese 337C is also obviously over-luminous at M_J. Koerner et al. (1999) have examined Kelu 1 and find it to be unresolved to $\lesssim 0\farcs25$; the other two objects have not yet been observed at high spatial resolution, but are intriguing candidates as they are companions to nearby bright stars. Finally, 2MASS 0559-1404 is significantly brighter at J-band than any of the other T dwarfs so far observed, and is only marginally fainter than the T2 V SDSS 1254-0122 at K_S. As discussed in §6.4, this object is also likely to be a double brown dwarf, with both component contributing to the J band flux. Despite the uncertainties associated with duplicity, these measures provide a starting point for determining the effective temperature scale.

7.8.2 Bolometric Corrections

Luminosities for a number of late-M and L dwarfs have recently been compiled by Leggett et al. (2001) and Reid et al. (2001a). These authors calculate bolometric corrections by extrapolating near-infrared spectral and photometric data to shorter (linear) and longer (Rayleigh-Jeans tail) wavelengths. Date from Reid et al. (2001a) show a roughly linear relationship between BC_J and spectral type for types M8 V through L8 V (Figure 7.23):

$$BC_J = (1.92\pm0.03) - (0.037\pm0.008)\times SpT, \tag{7.19}$$

where SpT(L0) = 0 SpT(L5) = 5, SpT(M5) = −5, etc.

For the T dwarfs, three objects currently have BC_J estimates: 2.43±0.07 for the T5 V 2MASS 0559-1404 (Table 6.1), 2.19±0.10 for the T6.5 V Gliese 229B (Leggett et al., 1999), and 2.09±0.10 for the T8 V Gliese 570D (Burgasser et al., 2000b; Geballe et al., 2001a). SDSS 1624+0029 is a T6 V, and we can estimate a bolometric correction for this object by linear interpolation over the values for the previous three objects:

$$BC_J = (3.00 \pm 0.24) - (0.12\pm0.04)SpT, \tag{7.20}$$

where in this case, SpT(T0) = 0, SpT(T5) = 5, etc. Hence BC_J(SDSS 1624+0029) = 2.28±0.34, with the uncertainty largely due to the limited available data. SDSS 1254-0122 is a different case entirely, as it lies in the L/T transition region, where the settling of dust and cloud formation result in a significant evolution in spectral energy distributions. An upper limit on BC_J for this object can be made by adopting the value of 2MASS 0559-1404. Earlier T dwarfs should have smaller values of BC_J, however, due to weaker CH_4, H_2O, and CIA H_2 absorption beyond 1.4 μm, since from Equation 7.18 we see that

$$BC_J \propto \log \frac{F_J}{F_{bol}}. \tag{7.21}$$

If the true BC_J is less than that of 2MASS 0559-1404, we will underestimate F_{bol} and thereby T_{eff}. In the late-L dwarfs, thermal dust emission and lack of CH_4 absorption does indeed result in smaller values of BC_J. We can therefore set a lower limit to this value for SDSS 1254-0122 as the mean for L dwarfs later than L2 V, 1.73±0.13 (Reid et al., 2001a, Figure 7.23). Note that a too low of a

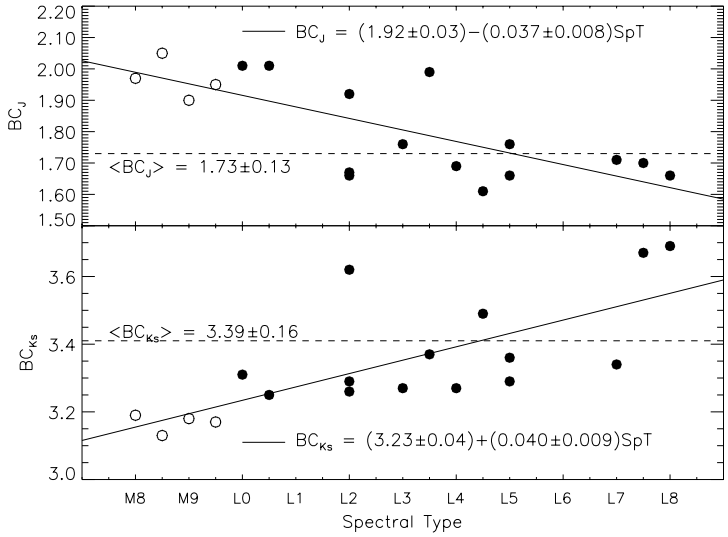

Figure 7.23: Bolometric corrections BC_J and BC_{Ks} versus spectral type as computed by Reid et al. (2001a). Both show roughly linear trends from M8 V to L8 V, with mean values for types L2 V through L8 V of $\langle BC_J \rangle = 1.73 \pm 0.13$ and $\langle BC_{Ks} \rangle = 3.39 \pm 0.16$.

bolometric correction will tend to overestimate T_{eff}.

Combining these bolometric corrections with the M_J values listed in Table 7.13 (correcting for known double objects using published flux ratios), we derive luminosity values as listed in Table 7.15. We have included two estimates for 2MASS 0559-1404 based on its possible duplicity. We also list luminosities derived for some of these objects from Leggett et al. (2001) and Reid et al. (2001a).

7.8.3 Brown Dwarf Radii

It is well established that substellar radii remain roughly constant for ages greater than 0.01 Gyr (Burrows & Liebert, 1993, see §1.2.2) with little variation due to metallicity (Chabrier & Baraffe, 2000). This feature is clearly demonstrated in Figure 1.6, which shows that the mean radii of brown dwarfs with temperatures below 2500 K vary by only 30–40% from 0.01–10 Gyr.

Using the Burrows et al. (1997) models, we determined the expected radius of an observed brown dwarf by performing a Monte Carlo simulation (see also §8.3.2) . Assuming a constant birth rate and mass function that goes as $\frac{dN}{dM} \propto M^{-\alpha}$, where $\alpha = 0$, 1, and 2 (Reid et al., 1999, favor $1 < \alpha < 2$), we determined the radii and effective temperatures of 10^5 simulated objects with masses between 1 and 100 M_{Jup} (the fully sample the L and T dwarf mass range) and ages 10^{-3} to 10 Gyr. We then selected only those objects with $400 \leq T_{eff} \leq 2500$ K. Results are shown in Figure 7.24. Note the paucity of objects in the $\alpha = 2$ subset, due to the dominance of low-mass and very cool (T_{eff} < 400 K) sources (only 0.6% of the input sources were recovered after the T_{eff} cut). The $\alpha = 0$ case, on the other hand, is comprised of more higher-mass objects, evolved high-mass brown dwarfs and stars, which typically have smaller radii due to gravitational contraction; this distribution has a broad peak at $R \sim 0.84$ R_{Jup}, with an extended tail toward larger radii.

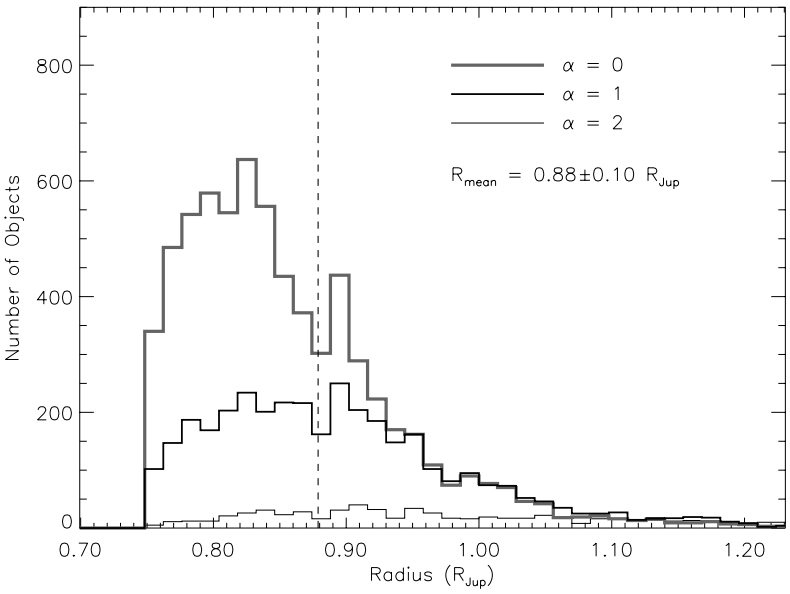

Figure 7.24: Simulation of observed brown dwarf radii based on the models of Burrows et al. (1997). Observed radii distributions of brown dwarfs with $400 \leq T_{eff} \leq 2500$ K, $1 \leq M \leq 100$ M_{Jup}, and $10^{-3} \leq \tau \leq 10$ Gyr, using three different power-law mass functions are shown. The number-weighted mean radius of all distributions is 0.88±0.10 R_{Jup}.

Table 7.14: Simulation of Observed Brown Dwarf Radii.

α (1)	$\sum N_i$ [a] (2)	$\bar{R}$ (R_{Jup}) (3)
0	6791	0.86±0.08
1	3650	0.90±0.10
2	647	0.98±0.15
all	11088	0.88±0.10

[a] Total number of simulated objects remaining out of 10^5 after $400 \leq T_{eff} \leq 2500$ K cut.

We computed the number-weighted mean radii for each distribution,

$$\bar{R} = \frac{\sum_i N_i R_i}{\sum_i N_i} \tag{7.22}$$

$$\sigma^2_{\bar{R}} = \frac{\sum_i N_i (R_i - \bar{R})^2}{\sum_i N_i}, \tag{7.23}$$

where N_i is the number objects in the bin $R_i\pm$ Mm. Values for $\bar{R}$, listed in Table 7.14, were within one standard deviation of the $\alpha = 1$ case, $\bar{R} = 0.90\pm0.10$ R_{Jup}, while the mean of all simulations was $\bar{R} = 0.88\pm0.10$ R_{Jup}. Hence, assuming a radius $R = \bar{R}_{\alpha=0} = (6.44\pm0.70)\times10^9$ cm = 0.90 R_{Jup} leads to typical errors of less than 11%, which we include in our uncertainty estimates of T_{eff}.

7.8.4 The Temperatures of L and T Dwarfs

Assuming a fixed radius, effective temperature can then be determined from Equation 7.17:

$$T_{eff}(K) = (\frac{L}{4\pi R^2 \sigma})^{0.25} \sim 600(\frac{L}{10^{-6} L_\odot})^{0.25}, \tag{7.24}$$

where the error from the assumption of a constant radius introduces an uncertainty of only $\sim 6\%$. Using this expression and luminosities from Table 7.15, we computed effective temperatures for late-M, L, and T dwarfs with known parallaxes. These values are listed in Table 7.15 and plotted versus spectral type in Figure 7.25. Uncertainties for the absolute magnitudes, bolometric corrections, and fixed radius have been propagated, yielding temperature uncertainties of typically 5–10%. Two points are shown for 2MASS 0559-1404, one assuming it is single (open symbol) and one assuming it is double (solid symbol). Also shown in Figure 7.25 are T_{eff} estimates from Leggett et al. (2001, triangles), based on K-band bolometric corrections and structure models from Chabrier et al. (2000a). The Leggett et al. (2001) temperatures are generally consistent with our estimates within the stated uncertainties, although we tend to derive slightly higher values for common objects. For comparison, we also plot the T_{eff} estimates for Gliese 229B (Marley et al., 1996) and Gliese 570D (Geballe et al., 2001a) as solid circles.

The data show a fairly monotonic decrease in T_{eff} with spectral type from L0 V to L8 V; a linear fit to both our data and that of Leggett et al. (2001) yields (dashed line):

$$T_{eff}(K) = (2380\pm40) - (138\pm8)\times SpT, \tag{7.25}$$

where SpT(L0) = 0, SpT(L5) = 5, etc. We compare this relation to the Kirkpatrick et al. (1999b, 2000), Basri et al. (2000), and Stephens et al. (2001) L dwarf temperature scales (solid lines) in Figure 7.25, where the Basri et al. (2000) scale has been adjusted to the Kirkpatrick et al. (1999b) L dwarf types using transformations given in Martín et al. (1999). These scales clearly bracket the effective temperatures calculated here for the mid- and late-L dwarfs, although all scales generally underestimate temperatures for the early L dwarfs by 200–400 K. Part of this deviation arises from the much shallower slopes in the literature temperature scales ($\sim$ 100 K per subtype) as compared to slope found in our data ($\sim$ 140 K per subtype). It is possible that we are biasing our T_{eff} estimates too high for the earliest L dwarfs if they are all stellar, and hence have larger radii than estimated; correcting our values would require a 30% increase in the radii in these objects, which we find difficult to reconcile with results of brown dwarf population simulations (see §8.3.2). Alternately, the BC_J corrections for the latest L dwarfs may be too low, as we expect these values to eventually turnover to match the higher values for the T dwarfs. Regardless, the L dwarf sequence does appear to form

Table 7.15: Luminosities and T_{eff} for L and T Dwarfs.

				This Work		Literature[a]	
Object	Type	M_J	BC_J	$\log \frac{L}{L_\odot}$	T_{eff}	$\log \frac{L}{L_\odot}$	T_{eff}
(1)	(2)	(3)	(4)	(5)	(6)	(7)	(8)
2MASS 0746+2000AB	L0 V	11.31±0.03	1.92±0.03	-3.59±0.02	2410±130		
HD 89744B	L0 V	11.97±0.09	1.92±0.03	-3.66±0.04	2310±130		
2MASS 0345+2540	L0 V	11.88±0.05	1.92±0.03	-3.62±0.02	2360±130	−3.59	2050–2350
2MASS 1439+1929	L1 V	11.96±0.04	1.88±0.03	-3.64±0.02	2340±130		
2MASS 1658+7027	L1 V	11.96±0.04	1.88±0.03	-3.64±0.02	2340±130		
GJ 1048B	L1 V	12.03±0.13	1.88±0.03	-3.67±0.05	2300±140		
Kelu 1	L2 V	12.04±0.09	1.85±0.03	-3.66±0.04	2310±130	−3.56	2100–2350
Gliese 618.1B	L2.5 V	12.90±0.18	1.83±0.04	-4.00±0.07	1910±130		
DENIS 1058-0548	L3 V	12.97±0.05	1.81±0.04	-4.02±0.03	1880±110	−3.98	1700–1950
2MASS 1146+2230AB	L3 V	12.05±0.06	1.81±0.04	-3.89±0.03	2020±110		
2MASS 0036+1821	L3.5 V	12.74±0.04	1.79±0.04	-3.92±0.02	1990±110		
2MASS 0326+2950	L3.5 V	12.77±0.11	1.79±0.04	-3.93±0.05	1980±120		
GD 165B	L4 V	13.06±0.18	1.77±0.04	-4.04±0.07	1860±120	−4.06	1650–1850
2MASS 2224-0158	L4.5 V	13.80±0.05	1.75±0.05	-4.33±0.03	1580±90		
Gliese 417B	L4.5 V	12.89±0.06	1.75±0.05	-3.96±0.03	1940±110		
2MASS 1507-0627	L5 V	13.49±0.03	1.73±0.05	-4.19±0.02	1700±100		
GJ 1001B	L5 V	13.20±0.04	1.73±0.05	-4.08±0.03	1820±100		
DENIS 1228-0558AB	L5 V	12.82±0.11	1.73±0.05	-4.19±0.05	1710±100	−4.00	1450–1650
2MASS 1328+2114	L5 V	13.43±0.30	1.73±0.05	-4.17±0.12	1720±140		
2MASS 0850+1057AB	L6 V	14.41±0.22	1.70±0.06	-4.66±0.09	1300±100		
2MASS 0825+2115	L7 V	14.97±0.05	1.66±0.06	-4.76±0.03	1230±70		
DENIS 0205-0159AB	L7 V	13.09±0.08	1.66±0.06	-4.31±0.04	1590±90	−4.06	1400–1600
2MASS 1632+1904	L8 V	14.81±0.11	1.62±0.07	-4.68±0.05	1290±80		
Gliese 584C	L8 V	14.97±0.12	1.62±0.07	-4.74±0.06	1240±80		
Gliese 337C	L8 V	14.14±0.09	1.62±0.07	-4.41±0.05	1500±90		
SDSS 1254-0122	T2 V	14.42±0.09	2.08±0.35	-4.70±0.14	1270±120		
2MASS 0559-0404	T5 V	13.80±0.04	2.43±0.07	-4.60±0.03	1350±80		
2MASS 0559-0404[b]	T5 V	14.55±0.04	2.43±0.07	-4.90±0.03	1130±70		
SDSS 1624+0029	T6 V	15.33±0.07	2.28±0.34	-5.15±0.14	980±100		
Gliese 229B	T6.5 V	15.51±0.05	2.19±0.10	-5.18±0.04	960±60	−5.18	890–1030
Gliese 570D	T8 V	16.47±0.05	2.09±0.10	-5.53±0.04	790±50	−5.53	784–824

[a] L dwarf values from Leggett et al. (2001); T dwarf values from Marley et al. (1996), Leggett et al. (1999), and Geballe et al. (2001a).
[b] Estimate assuming this object is an equal-magnitude double.

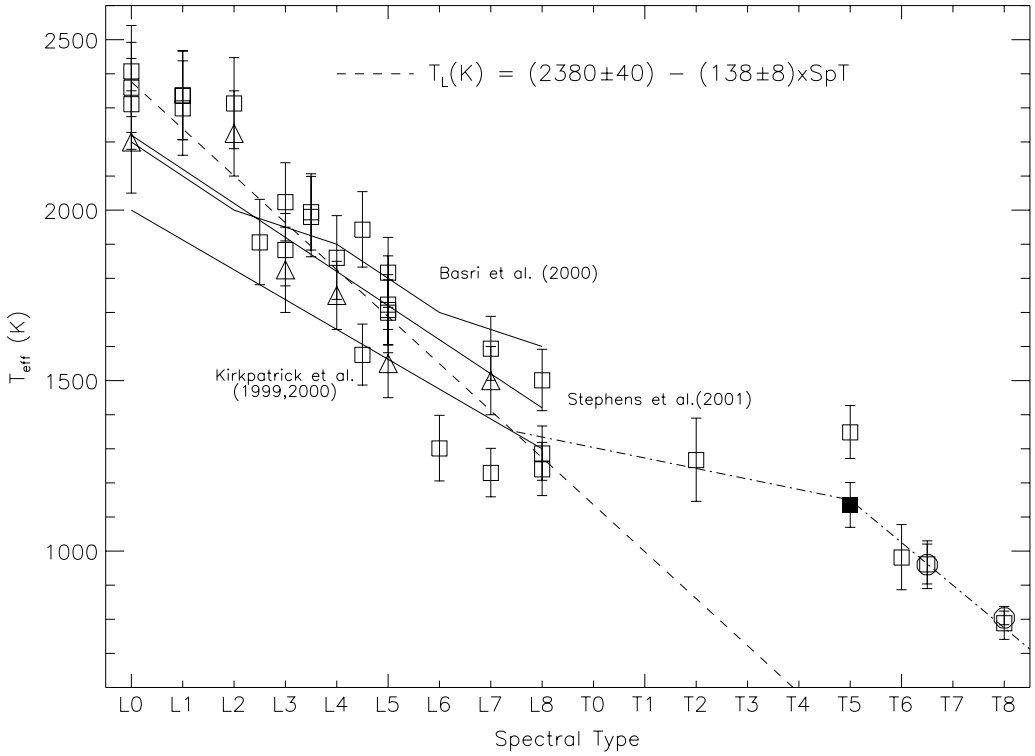

Figure 7.25: Effective temperatures for late-type dwarfs. Temperatures for L dwarfs were computed using bolometric corrections from Reid et al. (2001a), those for T dwarfs were computed using known are estimated bolometric corrections. Two estimates for 2MASS 0559-1404, assuming it is single (open symbol) or double (solid symbol), are shown. T_{eff} estimates from Leggett et al. (2001) are indicated by triangles. The two open circles plot previous T_{eff} estimates for Gliese 229B (Marley et al., 1996) and Gliese 570D (Geballe et al., 2001a). Spectral type temperature scales from Kirkpatrick et al. (1999b, 2000), Basri et al. (2000), and Stephens et al. (2001) are indicated, with Basri scale corrected to the Kirkpatrick et al. (1999b) spectral sequence. The dashed line shows a linear fit to T_{eff} for objects of type L0 V through L8 V, while the dot-dashed line traces a hypothetical T_{eff} scale from L8 V through T8 V.

a linear sequence in T_{eff}.

As we enter the T dwarf regime, there appears to be a significant shallowing in the spectral type temperature scale. The temperature of SDSS 1254-0122 is roughly equal to that of the latest L dwarfs, and 2MASS 0559-1404 is either hotter than most of the L8 dwarfs[3] or only $\sim$ 150 K cooler if we assume that it is a double. Indeed, within the uncertainties, *there is essentially no change in effective temperatures between types L8 V and T5 V*. Beyond T5 V, the effective temperatures once again decrease monotonically, with a slope similar to that of the L dwarfs.

7.8.5 Interpretation

Irrespective of the temperature offset of 2MASS 0559-1404, it is clear that the range of T_{eff} sampled by early T dwarfs is not large, as an extrapolation of Equation 7.25 into the T dwarf regime substantially underestimates the temperatures of these objects. Indeed, Kirkpatrick et al. (2000) points out that there appears to be a relatively small difference in T_{eff} between the coolest L dwarfs and Gliese 229B, only $\sim$ 350 K. How do we resolve this situation with the observed changes in spectromorphology and photometric colors, including the apparently continuous strengthening of H_2O indices across the L/T boundary? The solution to this problem may lie in the behavior of atmospheric dust. Recent "CLOUDY" models by Ackerman & Marley (2001) indicate that dust clouds, which significantly modify the emergent spectra of L dwarfs, reside at the 1500–1800 K temperature layer in brown dwarfs, and thus begin to settle below the photosphere around the L/T transition. Tsuji, Ohnaka, & Aoki (1999) find a similar critical temperature at T_{cr} = 1550 K. Loss of dust opacity likely causes substantial redistribution of emergent flux, increasing transparency in some spectral regions while also increasing H_2O and (ultimately) CH_4 band strengths as the photosphere cools. In addition, the cooling of the atmosphere above the dust layers will drive the formation of CH_4 and H_2O, increasing their column abundances and hence further increasing band strengths. These events should result in a significant strengthening of molecular bands over a narrow T_{eff} range. The dust loss scenario also explains the strengthening of the 1.25 μm K I doublet from L8 V to T5 V, inducing greater transparency at J-band and a corresponding increase in column abundance.

We gain another perspective of this evolution by examining the trends in absolute brightness across the L/T transition. Figures 7.26 and 7.27 plot M_J and M_{K_s} versus $J-K_s$ color, respectively, for the objects listed in Table 7.13, corrected for known duplicity. 2MASS 0559-1404 is plotted in these figures as both a single object (open symbol) and an equal-magnitude double (solid symbol). We compared these empirical values to predicted colors from the evolutionary and atmospheric models of Baraffe et al. (1998, 2001) and Allard et al. (2001). The atmosphere models of Allard et al. (2001) fall into two categories: the COND models, where dust is sequestered out of the atmosphere by gravitational settling (i.e., rain-out); and the DUSTY models, in which dust remains in the photosphere at its chemical equilibrium abundances. The former have been shown to match well with the spectrum of Gliese 229B (Allard et al., 1996), indicating significant dust depletion in this object. The latter models appear to match well with late-M and L dwarfs (Leggett et al., 2001). As shown in Figures 7.27 and 7.26, these models deviate sharply beyond $M_{K_s} \sim 10$ (spectral type M8–M9 V), resulting in a significant color gap between increasingly red, dusty atmospheres and clear atmospheres dominated by H_2O, CH_4 and CIA H_2 absorption.

We then examined the predicted magnitudes and colors for the Ackerman & Marley (2001) CLOUDY models, with data kindly provided by M. Marley. In general, this model adequately resolves the transition from the dusty atmosphere in the L dwarfs to the cleared atmospheres of the late T dwarfs. There are some discrepancies, however. The latest L dwarfs appear to occupy a niche between the DUSTY and CLOUDY models, as they are fainter (by nearly a full magnitude)

[3]Gliese 337C is the exception, but the temperature of this object may be too hot because of its possible duplicity.

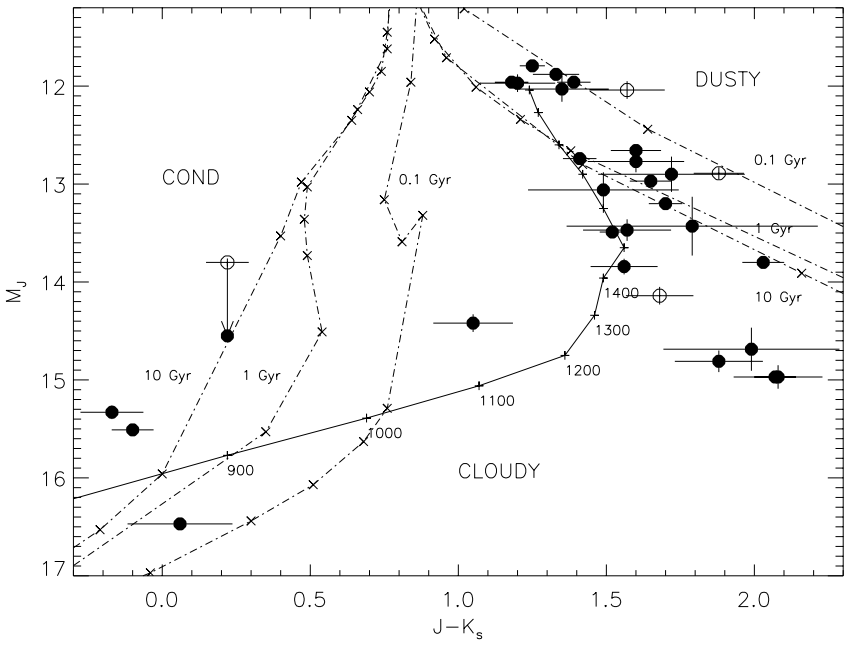

Figure 7.26: M_J versus J-K_s for objects in Table 7.13. Known doubles have been corrected using published flux ratios (Table 5.3), while suspected doubles are indicated by open circles. Also plotted are DUSTY and COND atmospheric models from Allard et al. (2001) for ages 0.1, 1.0, and 10 Gyr; and CLOUDY models from Ackerman & Marley (2001), for which temperatures are indicated. 2MASS 0559-1404 is plotted assuming it is single (solid circle) or an equal-magnitude double (open circle).

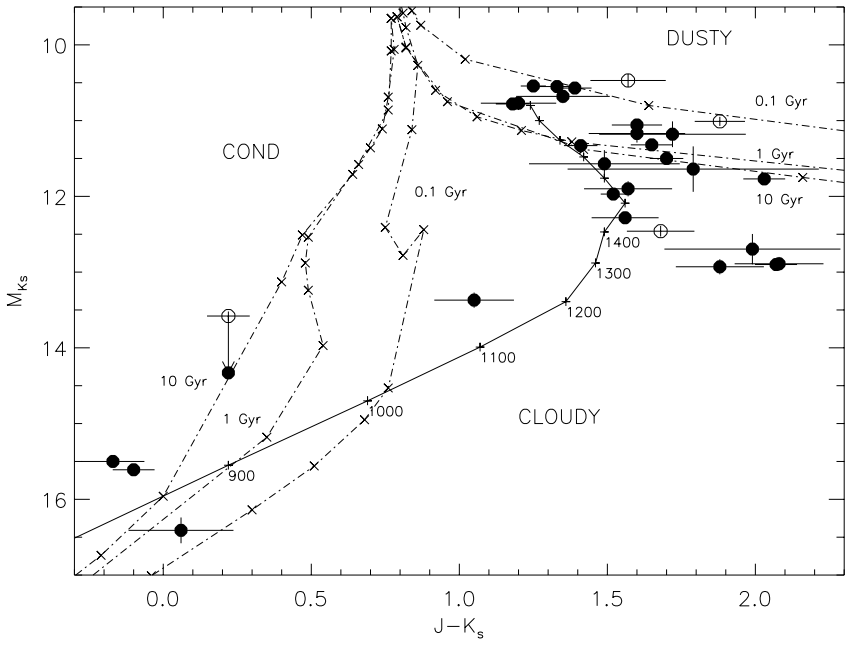

Figure 7.27: Same as Figure 7.27 for M_{K_s} versus J-K_s.

and redder than the predicted values for each model, respectively. 2MASS 0559-1404, on the other hand, is significantly more luminous than the predicted CLOUDY magnitudes at J and K_s, even with a correction to its potential duplicity. The first problem can be solved by reducing the rainout efficiency (i.e., allowing the dust clouds to remain in the upper atmosphere for cooler temperatures); however, this worsens the problem for the magnitudes of the T dwarfs, as the transition to cloud-free atmosphere happens at too cool of a temperature. As we have shown, the transition must in fact occur over a fairly narrow range of temperatures.

It is possible that the transition from dusty to dust-free atmospheres in brown dwarfs may not occur through the gradual settling of uniform dust clouds, but rather by a more rapid depletion. In this case, the temperature of the layers below the dust clouds remains roughly constant as dust rains out. The resulting increased transparency at the J-band window will allow light to be emitted from these hotter layers, and we would expect an *intrinsic* brightening at these wavelengths. At the K-band peak, which is still suppressed by H_2, H_2O, and CH_4 opacity, the dust rain out will not increase the emission from deeper layers, and the object may even become fainter at these wavelengths as thermal dust emission is lost. This is precisely the behavior observed from the latest L dwarfs to 2MASS 0559-1404, as M_J becomes brighter over this range while M_{K_s} is only slightly fainter.

We can also look for the presence of rapid dust depletion in spectral data. Figure 7.28 plots the near-infrared spectra of the L7 V DENIS 0205-1159AB (Leggett et al., 2001), SDSS 1254-0122 (Leggett et al., 2000b), 2MASS 0559-1404 (§3.1.1), and Gliese 229B (Geballe et al., 1996), each calibrated to absolute flux. Data for DENIS 0205-1159AB and 2MASS 0559-1404 have been divided by two to compensate for duplicity. The relative brightening at J-band from DENIS 0205-1159AB to 2MASS 0559-1404 is readily apparent in this figure, as the peak flux increases by roughly a factor of 1.5 in the opacity window on either side of the 1.1 μm H_2O band. Similar behavior is seen at

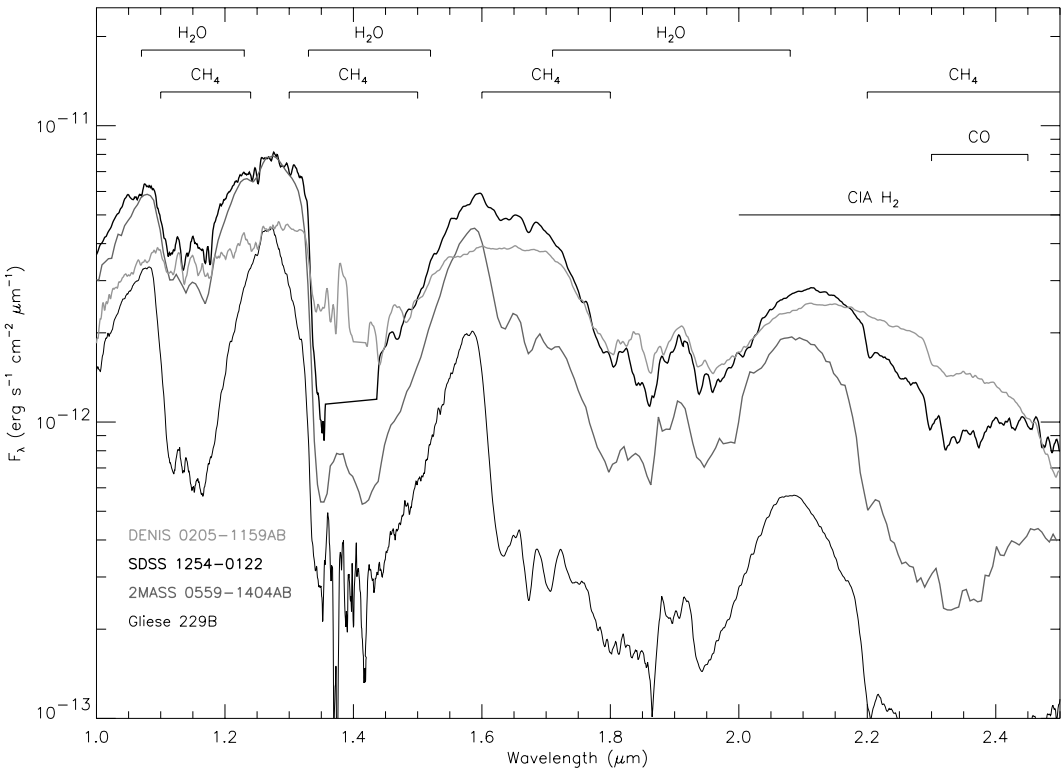

Figure 7.28: Near-infrared spectra of DENIS 0205-1159AB (Leggett et al., 2001, thick light grey line), SDSS 1254-0122 (Leggett et al., 2000b, thick black line), 2MASS 0559-1404 (§3.1.1, thick dark grey line), and Gliese 229B (Geballe et al., 1996, thin black line), calibrated to absolute flux using parallax data from Table 7.13. Data for DENIS 0205-1159AB and 2MASS 0559-1404 have been divided by two to compensate for duplicity. Spectra are smoothed to the resolution of the 2MASS 0559-1404 NIRC data. Major absorption bands of H_2O, CH_4, CO, and CIA H_2 are indicated.

H-band, particularly short-ward of the 1.6 μm CH_4 band. At K-band, there is a slight increase in the peak flux between DENIS 0205-1159AB and SDSS 1254-0122 (likely due to flux redistribution with the addition of CH_4 opacity in the latter object), while 2MASS 0559-1404 is fainter than both objects. As we go from 2MASS 0559-1404 to Gliese 229B, the overall flux levels generally drop uniformly, with slightly greater depression under CIA H_2 absorption, which is consistent with the similarity in colors between these two T dwarfs. This behavior suggests that dust depletion is near completion in 2MASS 0559-1404. The spectra are therefore consistent with the loss of photospheric dust over a narrow T_{eff} range.

Are the dust clouds really depleting rapidly? An alternative to a sudden and complete loss of dust opacity is non-uniform cloud coverage. Ackerman & Marley (2001) have proposed that holes in the dust clouds could result in discrete, transparent regions, which would be significantly brighter at J-band than cloud-covered regions. The holes can form from atmospheric turbulence, i.e., brown dwarf weather, and would be analogous to the 5 μm hotspots seen between NH_3 clouds on Jupiter (Westphal, Matthews, & Terrile, 1974). The "patchy cloud" scenario fits in with the non-periodic variability observed in late-L dwarfs (Bailer-Jones & Mundt, 1999; Bailer-Jones, 2001), which is consistent with meteorological phenomena rather than a magnetic source (Gelino et al., 2001; Martín, Zapatero Osorio, & Lehto, 2001). We should expect, therefore, significant variability at J-band in the latest L dwarfs and early T dwarfs as the gaps between the dust clouds evolve across the surface. Monitoring observations should be made to test this hypothesis.

Based on these considerations, we speculate that the evolution of brown dwarfs from spectral types L8 V to T5 V occurs over a narrow range in T_{eff}, perhaps only 200 K (dot-dashed line in Figure 7.25). This temperature difference is similar to that between Gliese 229B (T6.5 V) and Gliese 570D (T8 V). In these later objects, dust resides in a relatively narrow range of thermal layers, and its effect on the emergent spectrum below $T_{eff} \sim 1000$ K will no longer be important. Indeed, dust-free models by Tsuji et al. (1996) provided better fits to the spectrum of Gliese 229B than corresponding dusty models. The evolution of spectral features at this point will once again be tied to effective temperature, and spectral types later than roughly T6 V should sample a relatively broader range of T_{eff}. Parallax observations of more T dwarfs and measurement of bolometric luminosity are necessary to test these hypotheses, and variability observations of the latest L dwarfs and earliest T dwarfs could also provide clues to the behavior of atmospheric dust as it settles below the photosphere. Note that a narrow T_{eff} range for objects of type L8 V through T5 V would imply a paucity of these brown dwarfs relative to later-type T dwarfs; more accurate space densities are needed to test this prediction. Nonetheless, we believe that the rapid depletion of dust provides a natural explanation to the observed evolution of spectral features and estimated effective temperatures.

7.9 Summary

In this chapter, we have derived a classification scheme for T dwarfs based on the morphologies of near-infrared CH_4 and H_2O bands and J, H, and K flux peaks. This scheme segregates the currently known population into subtypes T1 V, T2 V, T3 V, T5 V, T6 V, T7 V, and T8 V. We have introduced a prescription for near-infrared classification using a suite of spectral indices that measure the strengths of CH_4 and H_2O bands, near-infrared colors, and the evolution of the K-band peak. The consistency of these separate indices and the agreement between data obtained on different instruments at different epochs suggests that the classification adequately represents the changes in spectral morphology amongst the current T dwarf sample. Atmospheric models, spectral indices, and the properties of the two known T dwarf companions Gliese 229B and Gliese 570D imply that at least on a fundamental level this scheme maps directly onto a decreasing temperature

sequence.

From the properties of spectral features, particularly H_2O bands, and the progression of near-infrared colors, it appears that the latest L dwarfs are not very different from the earliest T dwarfs. The possible role of CH_4 as a minor contributor in shaping the K-band peak of the latest L dwarfs, and the recent detection of CH_4 at 3.3 μm in objects as early as L5 V (Noll et al., 2000), lead us to believe that perhaps only one subclass exists between the latest L subtype (L8 V) and the earliest T subtype (T1 V). Thus, the gap between these two separately defined spectral classes appears to be effectively bridged.

Our classification scheme has also identified at least one peculiar object, 2MASS 0937+2931. This object is the bluest (in near-infrared colors) T dwarf so far identified, due to a highly suppressed K-band peak. The most likely source for increased opacity in this region is CIA H_2, the strength of which depends on the local gas pressure in the photosphere; hence, 2MASS 0937+2931 may be a high-gravity, hence high-mass and old, T dwarf. Alternately, this object may have significantly subsolar metallicity, resulting in an increase in the relative strength of CIA H_2. This is supported by the weakness of the 1.25 μm K I lines. Clearly, this object deserves further study, as its unique properties point out that factors other than temperature can shape the emergent spectra of T dwarfs.

We have also examined the feasibility of classification in the red optical, deriving indices based on key atomic, molecular, and morphological features. We find that the spectral slope from 8000–10000 Å, caused by the broadened K I line centered at 7665 and 7699 Å, and the 9250 Å H_2O bandhead, yield the best segregation into the near-infrared spectral types, to a typical accuracy of $\pm$1.0 subclasses. The complex evolution of features, the dominance of the heavily-broadened Na I and K I doublets, and the generally low signal-to-noise ratios attainable, make classification in this regime difficult. Nonetheless, these objects can be clearly separated from L dwarfs at these wavelengths.

The evolution of spectral features from late L to early T dwarfs is likely dominated by the behavior of atmospheric dust, which greatly influences the near-infrared spectra of L dwarfs but appears to be absent in T dwarfs such as Gliese 229B (Tsuji et al., 1996; Allard et al., 1996; Marley et al., 1996). The condensation and gravitational settling of dust clouds leads to a substantial evolution of spectral morphology, possibly over a narrow T_{eff} range. A rapid depletion of observed dust opacity, perhaps stimulated by the formation of holes in dust clouds extending to significantly hotter layers, could explain both the small effective temperature difference between the $\sim$ 1250 K L8 V Gliese 584C (Kirkpatrick et al., 2000) and the $\sim$ 1150 K T5 V 2MASS 0559-1404 (Table 7.15, assuming an equal magnitude double), and the intrinsic brightening of the latter object at J-band. One may argue that the morphological transition between the L and T classes is driven more by the physics of dust condensation than by the thermochemical formation of CH_4 bands (in addition, the latter process is likely driven by the former). Modeling the L/T transition clearly requires a more accurate treatment of the condensation, coagulation, and settling of dust species (Tsuji, Ohnaka, & Aoki, 1999; Ackerman & Marley, 2001). A similarly complex transition may occur with the condensation of H_2O at $T_{eff} \sim 400$ K (Burrows et al., 1997), a possible endpoint to the T spectral class.

Chapter 8 T Dwarfs and the Substellar Mass Function

Nothing is more certain than that worlds on worlds, and spheres on spheres, stretch behind and beyond the actually seen.
Edward Carpenter, *The Drama of Love and Death*

8.1 Motivation

One of the original motivations for identifying brown dwarfs was to determine their contribution to the Galactic mass budget. It was believed early on that these faint yet potentially prolific objects could comprise a significant fraction of the total Galactic mass, accounting for the so-called "dark matter" required to explain the dynamics of stars at the edge of our Galaxy and other galactic systems (Oort, 1932; Zwicky, 1933; Tarter, 1975; Bahcall, 1984). As an example, an extrapolation of the Salpeter mass function, $\Psi(\mathrm{M}) = \frac{dN}{dM} \propto \mathrm{M}^{-2.35}$ (Salpeter, 1955), which adequately represents stars with masses 0.3–10 $\mathrm{M}_\odot$ (Reid & Hawley, 2000), implies nearly 20,000 times more mass in brown dwarfs ($0.012 < \mathrm{M} < 0.08$ $\mathrm{M}_\odot$) than in stars ($0.08 < \mathrm{M} < 40$ $\mathrm{M}_\odot$)! As searches gained in sensitivity, however, it became clear that the mass function was much shallower for lower-mass stars. Successfully more constrictive upper limits and actual counts of brown dwarfs essentially eliminated the possibility that these objects are the major constituents of dark matter (Reid et al., 1999b).

Nevertheless, the number of brown dwarfs in the Solar Neighborhood could still be a significant fraction (or multiple) of the number of stars. Quantifying the mass function in the substellar regime enables us to explore the star formation process, its efficiency at small masses, and the limit at which small masses can be formed in isolation. In this chapter, we use the wdb0699 sample to derive the space density of T dwarfs, and use this value to constrain the form of the substellar mass function. We outline our derivation of the T dwarf space density in §8.2, where care has been taken in determining selection biases and the actual volume sampled. In §8.3, we construct brown dwarf populations through Monte Carlo simulations, assuming power-law mass functions and using the models of Burrows et al. (1997). We then discuss how our derived T dwarf space densities constrain the form of the substellar mass function, and compare our best-fit mass functions to results from Reid et al. (1999b) and various cluster surveys, the latter of which have recently begun to probe the substellar regime. We summarize our results in §8.4.

8.2 T Dwarf Space Density

8.2.1 Description of the Problem

The T dwarfs identified in our magnitude-limited, color-selected samples provide an empirical means of estimating the number of T dwarfs in the Solar Neighborhood, but only if we can fully characterize the volume searched and how well our sample represents the true T dwarf population. We therefore seek to derive the space density of T dwarfs, ν, from the number of objects identified, the search area explored, and the distance limit to which we can detect such objects, as a function of spectral

subclass S:

$$\nu(S) = \frac{3N(S)}{\Omega R^3(S)}, \tag{8.1}$$

where $N(S)$ is the number of detected objects in subclass S, Ω the angular area surveyed (in steradians), and $R(S)$ the limiting distance to which an object in subclass S can be detected in our survey. An implicit assumption in Equation 8.1 is that the true population is isotropically distributed across the sky. The maximum distance at which our brightest T dwarf, 2MASS 0559-1404, falls within our search criteria (assuming that it is single; see §6.4) is roughly 27 pc, much less than the estimated 300 pc scale height of the Galactic disk (Gilmore & Zeilik, 2000); hence, the assumption of isotropy is justified.

The quantity $\nu(S)$ measures our observed space density, which is biased by the criteria through which our T dwarf sample was selected. What we would really like to know is the *true* number of T dwarfs in our search volume with spectral type S, $N_o(S) = \chi(S)N(S)$, where χ is a correction factor that compensates for our selection biases. Furthermore, we must account for both a maximum (R_{max}) and minimum (R_{min}) distance over which we are sensitive to T dwarfs, since our selection criteria could conceivably cause us to omit nearby objects. The true space density of T dwarfs is then

$$\nu_o(S) = \frac{3\chi(S)N(S)}{\Omega(R^3_{max}(S) - R^3_{min}(S))} = \frac{\chi(S)N(S)}{V_{eff}(S)}, \tag{8.2}$$

where $V_{eff}(S)$ is the effective volume searched. In the following sections, we determine the values and uncertainties for each of these terms in order to derive a rigorous estimate of $\nu_o(S)$ for various subsets of spectral types T5 V, T6 V, T7 V, and T8 V.

8.2.2 Sample wdb0699 Revisited

To make the best possible determination of $N(S)$, we require as complete a search sample as possible. Because considerable follow-up remains for the rdb0400 and rdb0600 samples (see §§2.4.2.3 and 2.4.2.4), we have chosen to examine the statistics for the wdb0699 sample only, of which a large percentage has been characterized through follow-up imaging and spectroscopy.

The properties of the wdb0699 sample are summarized in §2.4.2.2. The search criteria include both color cuts (J−H < 0.3 and H−$K_s < 0.3$) and a magnitude limit (J < 16). Required detection at both J- and H-bands also impose an effective magnitude constraint which is sensitive to the completeness limits of 2MASS and the intrinsic colors of the objects. We will address how these constraints induce selection biases in §8.2.5. Additionally, the elimination of regions within $10''$ around USNO-A2.0 sources must be taken into consideration in the calculation of the search area (§8.2.3.2).

8.2.2.1 Sample Completeness

Tables A.3 and A.4 list confirmed candidates in the wdb0699 sample that have either had or not had spectroscopic and/or optical imaging follow-up. As discussed in §2.6, 70% of the confirmed wdb0699 candidates have been identified from these observations. The remaining 28 objects are generally comprised of sources close to bright optical stars and faint optical sources or proper motion stars based on examination of second-epoch DSS plates (many of which were not available at the time of the initial visual inspection, see §2.4.2.1). Since the majority of candidates close to bright optical sources with optical imaging follow-up have been identified as background stars ($\sim 90\%$), it is likely that those without follow-up imaging are also background stars. The few legitimate candidates (2MASS 0414-6916, 2MASS 1337+8636, and 2MASS 1356-0417) are both faint and red (J−$K_s >$

Table 8.1: T Dwarfs Identified in the wdb0699 Sample.

Object (1)	Type (2)	J (3)	J−H (4)	H−K_s (5)	m–M (6)
2MASSI J0243137−245329	T6 V	15.40±0.05	0.25±0.11	−0.06±0.20	
2MASSI J0415195−093506	T8 V	15.71±0.06	0.14±0.13	0.12±0.23	
2MASSI J0559191−140448	T5 V	13.82±0.03	0.14±0.05	0.07±0.06	0.03±0.03
2MASSI J0727182+171001	T7 V	15.55±0.07	−0.27±0.19	0.26±0.28	
2MASSI J0755480+221218	T5 V	15.72±0.07	0.06±0.16	−0.11±0.25	
2MASSI J0937347+293142	T6 Vp	14.65±0.04	−0.03±0.08	−0.86±0.25	
2MASSI J1047538+212423	T6.5 V	15.82±0.06	0.03±0.13	< -0.50	
2MASSI J1217110−031113	T7.5 V	15.85±0.07	0.06±0.14	< -0.12	
2MASSI J1225543−273946	T6 V	15.23±0.05	0.13±0.09	0.04±0.17	
Gliese 570D	T8 V	15.33±0.05	0.05±0.10	0.01±0.19	−1.14±0.02
2MASSI J1534498−295227	T5.5 V	14.90±0.04	0.01±0.10	0.03±0.14	
2MASSI J1546271−332511	T5.5 V	15.60±0.05	0.16±0.10	0.02±0.19	
2MASSI J2254188+312349	T5 V	15.28±0.05	0.24±0.10	0.21±0.17	
2MASSI J2356547−155310	T6 V	15.80±0.06	0.16±0.12	−0.19±0.21	

0.4), and are more likely to be background M dwarfs that have fallen below the detection limits of the DSS plates. We assume, therefore, that none of these candidates are bona-fide T dwarfs.

Similarly, the three unobserved candidates in Table A.5, 2MASS 0631-6652, 2MASS 1210+8950, and 2MASS 1302+8954, can be rejected as well. The first object lies 34.″2 from the V=7.33 M6 II/III star AY Doradus, and is likely a background star hidden in the glare of the brighter source. The latter two objects are at declinations too high to acquire with the Equatorial-mount telescopes used for follow-up observations, and these regions are eliminated from our search sample in §8.2.3.

Therefore, it is highly probable that we have followed up all of the actual T dwarfs in the wdb0699 sample, although we cannot explicitly rule out the presence of 1 or 2 *bona fide* redder T dwarfs that have not yet been identified.

8.2.2.2 Properties of T Dwarfs Identified in the wdb0699 Sample

Table 8.1 lists the T dwarfs identified in the wdb0699 sample, along with their observed J−H and H−K_s colors. Two objects in this sample, 2MASS 0559-1404 (Chapter 6) and Gliese 570D (Chapter 4), have parallax measurements and hence absolute brightness determinations. Binning these objects into integer subclasses, we find 5±2 T5–T5.5 objects, 5±2 T6–T6.5 objects, 2±1 T7–T7.5 objects, and 2±1 T8 objects, where uncertainties are assigned assuming Poisson statistics. The latter groups have much smaller detection numbers, and throughout the rest of this chapter we will also consider the groupings of 4±2 T7–T8 objects and 9±3 T6–T8 objects.

Mean colors for each of these groups are listed in Table 8.8, and Figure 8.1 plots the histograms of observed J−H and H−K_s colors for each of the subtype samples. Note the influence of small number statistics in the T7 and T8 subtype samples, particularly for T7 where only one measured H−K_s color is available. The blue H−K_s color of 2MASS 0937+2931 (§7.7) stands out in the T6 and the T6–T8 samples. Overall, observed J−H colors appear to peak around J−H = 0.0, with a slight tendency toward bluer colors for the later objects; while H−K_s colors appear to be redder in the later spectral types, with the caveat that small number statistics and large photometric errors must be kept into consideration.

We can use the identified T dwarfs in this sample to ascertain its completeness using the V/V_{max}

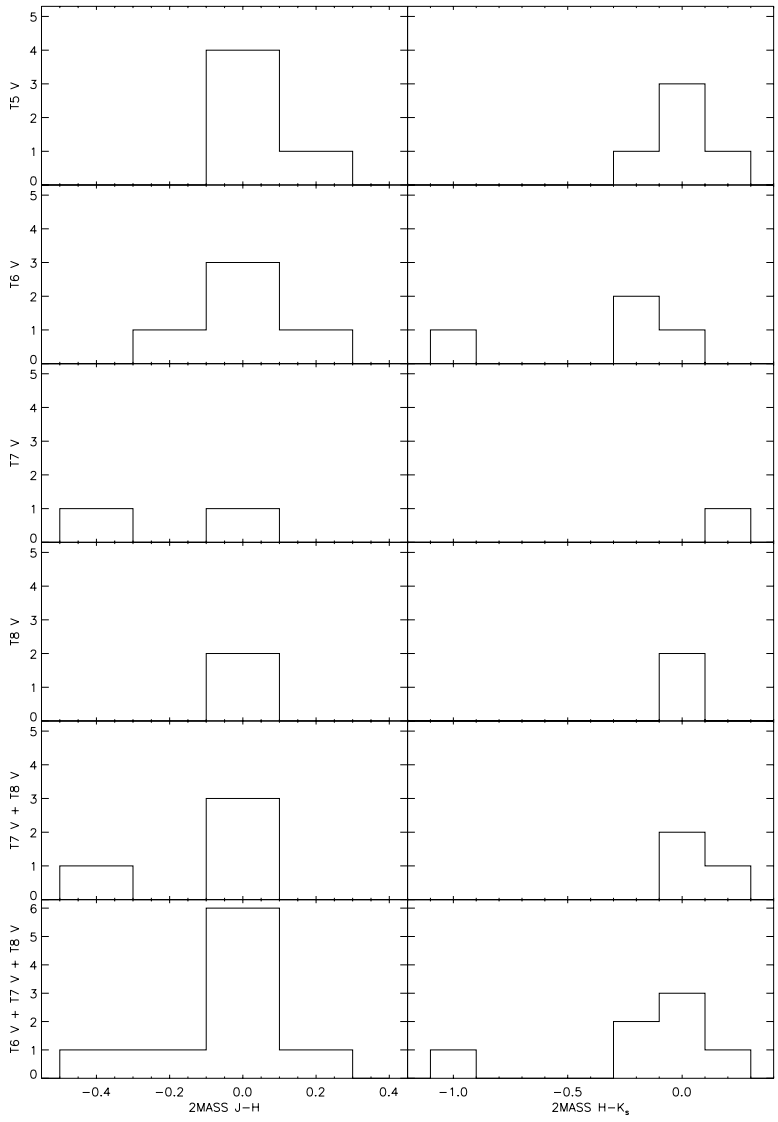

Figure 8.1: Histograms of $(J-H)_{obs}$ and $(H-K_s)_{obs}$ colors for various subtypes.

Table 8.2: V/V_{max} for T Dwarf Subtype Samples.

Subtypes (1)	$\langle V/Vmax \rangle$ (2)
T5–T5.5 V	0.38±0.13
T6–T6.5 V	0.49±0.13
T7–T7.5 V	0.67±0.20
T8 V	0.53±0.20
T7–T8 V	0.60±0.14
T6–T8 V	0.54±0.10
ALL	0.48±0.08

test, developed by Schmidt (1968) to examine the spatial distribution of quasars. For an isotropic distribution of N objects of constant brightness, the mean value is $\langle \mathrm{V/V}_{max} \rangle = 0.5$, where

$$\begin{aligned} V/V_{max} &= \frac{\frac{\Omega}{3} 10^{0.6(J-M_J)+3}}{\frac{\Omega}{3} 10^{0.6(J_{lim}-M_J)+3}} \\ &= 10^{0.6(J-16)}, \end{aligned} \tag{8.3}$$

with an uncertainty of $(12N)^{-0.5}$ (Gizis & Reid, 1999). Table 8.2 lists the mean values of $\mathrm{V/V}_{max}$ for the subtype samples under consideration. All but the T5 group appear to be isotropic within the uncertainties, consistent with the expected distribution and further evidence that the sample is complete. We are likely missing a few of the fainter T5 objects due to our color selection, although this distribution may be skewed by the very bright and possibly double 2MASS 0559-1404 (§6.4).

8.2.3 Calculating the Search Area

The total search area, Ω, has two basic contributions: first, the total area covered by the 2MASS scans at the time of selection from the 2MASS working database, minus any regions omitted due to their high star density (e.g., LMC, SMC, 47 Tuc) or inaccessibility for follow-up (i.e., large $|\delta|$); and second, any area eliminated by the selection criteria.

8.2.3.1 Total Area from Scans

At the time of sample selection, we also extracted information for scans present in the working database having a central $|b| > 15°$, a total of 23510 tiles. The total search area sampled by these scans was then computed as follows: first, for scans with $|\delta| < 70°$, the total number of tiles was multiplied by the conversion factor 0.716 deg^2, equal to the total area covered by the 2MASS IDR2 data release (19680.8 deg^2) divided by the total number of scans (27493). This compensates for tile overlap, which is approximately 10% for uniform sky coverage, and increases at higher declinations. The 22536 scans in the wdb0669 sample having $|\delta| < 70°$ yield an area of 16130 deg^2.

Because of increased tile overlap near the poles, each tile with $|\delta| > 70°$ was projected onto a Right Ascension/Declination grid, with points falling within the tile footprint flagged. The area, A_i, around each flagged point (in deg^2) was then calculated by

$$A_i = \epsilon_R \frac{180}{\pi} (\sin(\delta_i - \epsilon_D) - \sin \delta_i), \tag{8.4}$$

where ϵ_R and ϵ_D are the Right Ascension and Declination grid spacings, respectively (chosen to

be $0\overset{\circ}{.}05$ each to balance computational time and accuracy), and δ_i is the Declination of the grid point. Overlap with tiles centered at $|\delta| \sim 69°$ was computed and subtracted off the polar areas, as were regions with $|\delta| > 89\overset{d}{.}8$. These calculations gave polar areas of 432 deg^2 (North) and 133 deg^2 (South). Simulations of this technique on test regions of known area coverage indicated errors for $|\delta| > 70°$ at roughly 2–5%, implying uncertainties of 20 and 7 deg^2 for the North and South caps, respectively. We attempted to apply this projection technique to our entire scan area, but computational limits[1] limited our angular resolution, and we could not obtain accuracies over the entire region to better than 20%. Hence, we maintain our initial estimate for $|\delta| < 70°$.

We then excised areas around the LMC ($72° \leq$ R.A. $\leq 88°$, $-72.0° \leq \delta \leq -65.5°$), SMC ($10° \leq$ R.A. $\leq 20°$, $-71.5° \leq \delta \leq -74.0°$), and 47 Tuc ($5° \leq$ R.A. $\leq 7°$, $-71.9° \leq \delta \leq -72.3°$) from our search area (Figure 2.9), which accounted for only 45 deg^2 ($< 0.3\%$) of the total selected area, but over 27% of the originally selected (very likely background) sources (see §2.4.2).

Finally, we note that some objects selected from the database close to our Galactic latitude cutoff fell in scans with a center $|b| \leq 15°$, while other scans included in the above analysis were only partially within our nominal search area (see Figure 2.11). We counted 529 scans from which objects were extracted but were not included in the computation of the total scan area. Assuming equal numbers of selected partial scans, the areas from these two sets likely cancel each other out to within $\sqrt{529}\times 0.85$ deg^2 ~ 20 deg^2, which we adopt as the uncertainty in our scan area calculation. Including uncertainties from the polar regions, we therefore estimate the total area covered by the scans selected from the working database as 16650 ± 20 deg^2.

8.2.3.2 Correcting for Separation from Optical Counterparts

In our candidate selection, we excluded objects within $10''$ from any optical source in the USNO-A2.0 catalog (Monet et al., 1998). Hence, the $\sigma = 314$ arcsec^2 regions around these sources must be eliminated from our useable search area. The USNO-A2.0 is a massive catalog (5.3×10^8 sources), so counting all of the sources in our search area would be prohibitive; instead, we computed this correction statistically, by determining a mean optical source density as a function of Galactic latitude from variously sampled regions in the sky.

The relative area from which targets can be selected after compensating for the presence of optical sources, $\epsilon = \frac{A_{clear}}{A_{tot}}$, correcting for source overlap, can be derived by probability analysis. Given a total sample area, A_{tot}, the area excluded by a single source is σ, leaving $A^{(1)}_{clear} = A_{tot} - \sigma = A_{tot}(1 - \frac{\sigma}{A_{tot}})$ available from which to select T dwarf candidates. A second source randomly placed in this region also occupies area σ, but overlaps with the first source with probability $P^{(2)} = \frac{A_{tot} - A^{(1)}_{clear}}{A_{tot}} = \frac{\sigma}{A_{tot}}$, so that

$$\begin{aligned} A^{(2)}_{clear} &= A_{tot} - \sigma - (1 - P^{(2)})\sigma \\ &= A_{tot}(1 - \tfrac{\sigma}{A_{tot}})^2 \end{aligned} \tag{8.5}$$

is the free area remaining with two randomly placed sources. For N total optical sources in a particular area, this expression yields

$$\begin{aligned} A^{(N)}_{clear} &= A^{(N-1)}_{clear} - (1 - P^{(N)})\sigma \\ &= A^{(N-1)}_{clear} - \tfrac{A^{(N-1)}_{clear}}{A_{tot}}\sigma \\ &= A^{(N-1)}_{clear}(1 - \tfrac{\sigma}{A_{tot}}), \end{aligned} \tag{8.6}$$

[1] At the same resolution, the area for $|\delta| < 70°$, requires over 10^7 grid points.

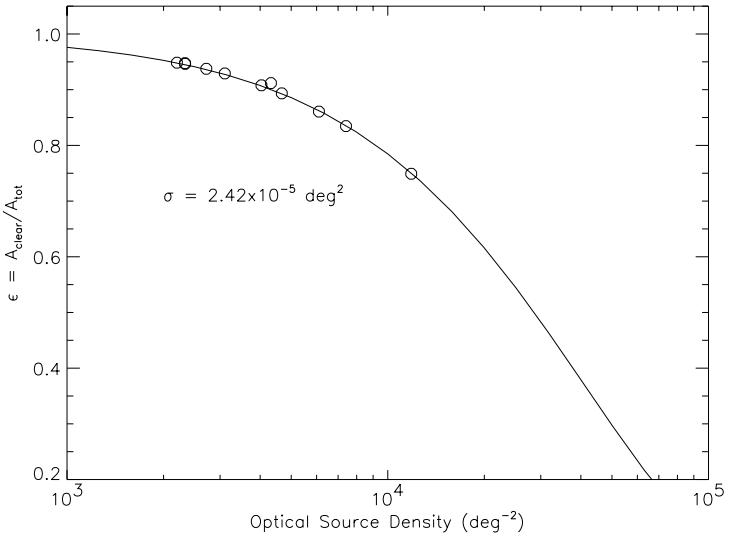

Figure 8.2: Predicted area corrections, $\epsilon = \frac{A_{clear}}{A_{tot}}$, for excluding regions around USNO optical sources as a function of source density. Measured values for ϵ in various selected fields are shown as open circles.

or, by recursion,

$$\epsilon = (1 - \frac{\sigma}{A_{tot}})^N. \tag{8.7}$$

Figure 8.2 plots this correction as a function of source density (essentially Equation 8.7 assuming $A_{tot} = 1$ deg^2) with $\sigma = \pi 10''^2 = 2.42\times10^{-5}$ deg^2. To check our analytical expression, we extracted USNO-A2.0 sources in various regions of the sky, explicitly removing objects within $10''$ of another source, and calculating the resulting free areal coverage. The agreement between these values and Equation 8.7 is excellent for mean number densities of 2200–12000 deg^{-2}. Note, however, that regions encompassing stellar clusters or other Galactic structure could result in an overcorrection (i.e., predicting too little free area) to the total area surveyed by this method.

We extracted source counts from the USNO-A2.0 catalog in 1° radius fields centered at $l = 0°$, 66°, 180°, and 310°, with b ranging from $-90°$ to 90°. From the resulting source densities, we can examine how ϵ varies as a function of b, as shown in Figure 8.3. As might be expected, the large source densities near the Galactic plane restricts the area that can be surveyed in these regions, although over-compensation due to source density structure may be an issue. Corrections are substantially smaller at higher Galactic latitudes. Figure 8.3 shows, however, that these corrections are not only dependent on latitude, but on Galactic longitude as well, depending on whether we are looking toward or away from the Galactic center ($l = 0°$ or 180°). When we convolve these distributions with our scan Galactic latitude distribution (Figure 2.12), we derive mean corrections ranging from 0.79 ($l = 180°$) to 0.91 ($l = 0°$). Since our scans are evenly distributed in Galactic longitude, we take as our correction the mean of the $l = 60°$ and $l = 310°$ values, $\epsilon = 0.85\pm0.03$, where the uncertainty is derived from the difference between these two distributions. Note that both the $l = 0°$ and $l = 180°$ values are within 2σ of this estimate.

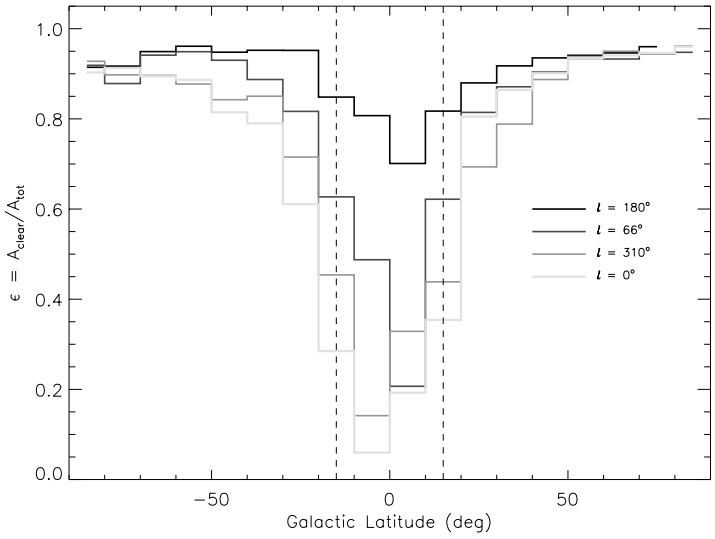

Figure 8.3: Area corrections as a function of Galactic latitude for four sampled longitudes.

8.2.3.3 Correcting for Source Confusion Around Bright Stars

A complementary correction to the area lost by excluding optical counterparts is the area occupied by the PSF wings of bright stars. These bright halos produce a "confusion" area, in which faint sources are either wiped out by the flux of the bright star or cannot be distinguished from the image artifacts this star creates (Figure 8.4). The confusion radii in arcseconds at J, H, and K_s bands is a function of apparent magnitude (T. Evans, priv. comm.):

$$\begin{aligned} r_J &= 12.28\times10^{0.197(6.2-J)} \\ r_H &= 9.44\times10^{0.216(6.2-H)} \\ r_{K_s} &= 7.10\times10^{0.265(6.2-K_s)} \end{aligned} \tag{8.8}$$

in the Northern Hemisphere, and

$$\begin{aligned} r_J &= 12.00\times10^{0.197(6.2-J)} \\ r_H &= 4.17\times10^{0.216(6.2-H)} \\ r_{K_s} &= 4.49\times10^{0.293(6.2-K_s)} \end{aligned} \tag{8.9}$$

in the South.

To estimate the search area eliminated by source confusion regions, we made source counts of bright stars in the 2MASS IDR2 with the same area constraints as our wdb0699 Sample; i.e., $|b| > 15°$, and eliminating the areas around the LMC, SMC, and 47 Tuc. The 2MASS IDR2 was used for this, as we were unable to reasonably extract the same scans observed in the wdb0699 sample from the current working database (due to sheer number of scans involved), and the release data has very similar spatial coverage (compare Figures 2.11 and 2.15). Stars counts were made in 0.5 mag bins at J-band, with confusions areas estimated by assuming the Northern Hemisphere relations (a conservative estimate, since the confusion radii for Southern Hemisphere data are typically smaller). These counts are accurate only for J > 5.5, as brighter stars are generally saturated in the 2MASS

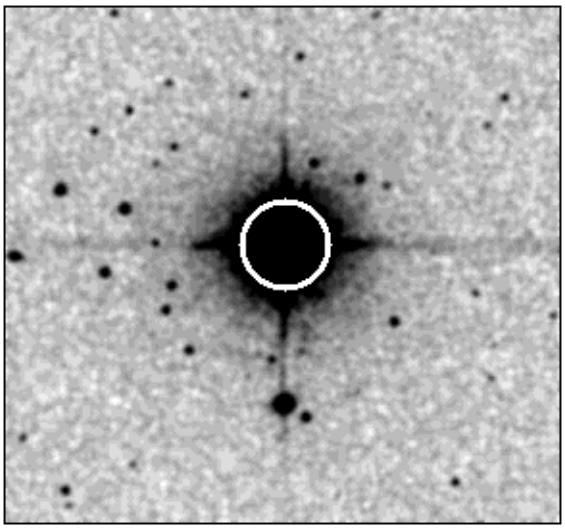

Figure 8.4: 2MASS J-band image of SAO 73156, a J=4.85 source in the 2MASS IDR2. Its confusion radius, within which faint sources cannot be reliably detected due the halo of the bright star, is indicated by a white circle.

Table 8.3: Confusion Area as a Function of J-band Magnitude.

Bin (mag) (1)	$\langle r_J \rangle$ ($''$) (2)	N (cnts) (3)	A (deg^2) (4)	N$_{corr}$ (cnts) (5)	A$_{corr}$ (deg^2) (6)
$J \leq 5^a$	22.64	1	0.00012	1	0.00012
$5 < J \leq 5.5^a$	18.90	271	0.023	268	0.021
$5.5 < J \leq 6$	15.06	3778	0.21	3772	0.20
$6 < J \leq 6.5$	12.00	7846	0.27	7835	0.27
$6.5 < J \leq 7$	9.57	11890	0.26	11869	0.26
$7 < J \leq 7.5$	7.63	17963	0.25		
$7.5 < J \leq 8$	6.08	27038	0.24		
$8 < J \leq 8.5$	4.85	40279	0.23		
$8.5 < J \leq 9$	3.86	58417	0.21		
$9 < J \leq 9.5$	3.08	84976	0.20		
$9.5 < J \leq 10$	2.45	129032	0.19		
$10 < J \leq 10.5$	1.96	187114	0.17		
$10.5 < J \leq 11$	1.56	271035	0.16		

[a]These bins are likely incomplete due to source saturation.

Table 8.4: Accounting of the wdb0699 Sample Search Area.

Contribution (1)	Area (deg^2) (2)
Scans with $\|\delta\| < 70$ deg^2	16132±20
Scans with $\|\delta\| > 70$ deg^2	563±22
Area of LMC	−38±0
Area of SMC	−7.0±0
Area of 47 Tuc	−0.3±0
Area around optical sources	−2500±500
TOTAL	14150±500

images and hence are not assigned a magnitude in the 2MASS IDR2. Counts and corresponding areas are listed in Table 8.3. For the brightest bins (5 < J < 8), we checked for source overlap and computed the individual areas per source to determine if our estimates for fainter (and more populous bins) were biased; these corrections were less than 10% of the original value, and hence we find the initial estimates to be reasonably accurate for our purposes.

The total confusion area per magnitude bin, $A(J)$, peaks at 6 < J ≤ 6.5 with $A = 0.27$ deg^2, then steadily drops off with fainter magnitudes. This decrease is due to the fact that the confusion area per star scales roughly as $r^2 \propto 10^{-0.39J}$, while the number of stars per bin appears to increase only as $10^{0.35J}$, and hence $A(J) \propto 10^{-0.04J}$. Extrapolating this relation down to J = 16 yields a confusion area of $\sim 1.8°$, while extrapolation to the brightest magnitude object likely to be observed by 2MASS[2], J ∼ -3, yields only $\sim 7°$; hence, the total search area lost to source confusion is relatively small. Furthermore, most of the brighter sources also have optical counterparts in the USNO-A2.0. Since areas of 10″ radii around these objects have already been excluded (§8.2.3.2), we are in some sense double counting these regions, and can in fact ignore the area lost by source confusion entirely.

8.2.3.4 Total Search Area

Table 8.4 summarizes the individual contributions to the total search area. By combining the corresponding uncertainties, we derive $\Omega = 14150 \pm 500$ deg^2. Note that the largest contribution to the total uncertainty is that associated with the area lost by rejecting optical counterparts, roughly 3.5%. This term is important, as without it we would underestimate the resulting space density by as much as 15%.

8.2.4 Calculating the Limiting Distances and V_{eff}

8.2.4.1 Absolute Brightness Scale

The total volume searched is a combination of the angular area surveyed, calculated above, and the limiting distances between which our objects are found. Distance estimates for any particular type of star can only be determined if the absolute brightness is known or can be estimated. Fortunately, four T dwarfs between T5 V and T8 V currently have known parallaxes (Table 7.13): the T5 V 2MASS 0559-1404, the T6 V SDSS 1624+0029, the T6.5 V Gliese 229B, and the T8 V Gliese 570D. The absolute J-band magnitudes of these objects are plotted in Figure 8.5. We have used the UKIRT

[2]This is an overly generous estimate, as an extrapolation of the total number of stars between −1.5 < J < 5 yields ∼ 4325 stars, while there are only 2353 saturated R1 sources in the 2MASS IDR2. The discrepancy is due to a combination of scale height effects and interstellar absorption.

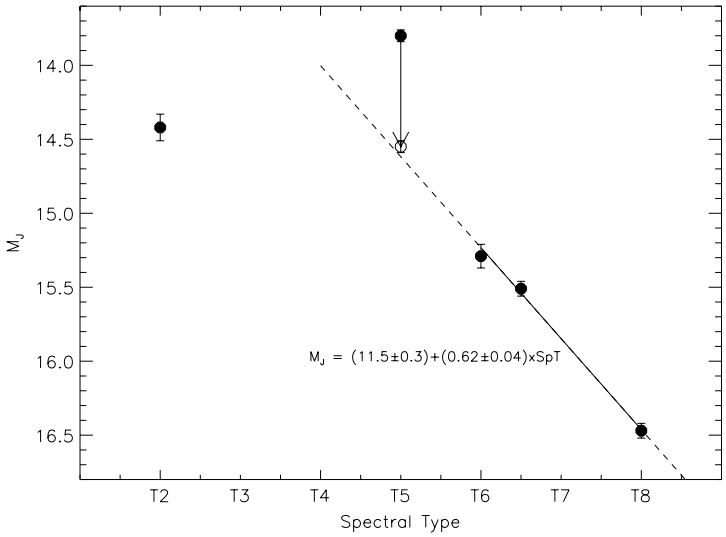

Figure 8.5: M_J versus spectral type for T dwarfs with known parallaxes. Data are from Table 7.13. 2MASS 0559-1404 is plotted as both a single object (solid circle) and half of an equal-magnitude binary (open circle). A linear fit to the three objects later than spectral type T5.5 V is shown as the solid and dashed (extrapolated) line.

J-band magnitude for Gliese 229B in this diagram (Leggett et al., 1999), as the differences between UKIRT and 2MASS J-band magnitudes for the T6 V SDSS 1624+0029 (Strauss et al., 1999) and the T6.5 V SDSS 1346-0031 (Tsvetanov et al., 2000) average out to zero.

As discussed in §7.8.5, there appears to be a distinct non-linearity in absolute J-band brightness from late-L to mid-T, culminating with the excessively bright 2MASS 0559-1404. Even assuming that 2MASS 0559-1404 is a double (open circle), there is little change in M_J between it and the T2 V SDSS 1254-0122. If we examine the T dwarfs of type T6 V and later, however, there appears to be a good linear relation between spectral type and M_J, which is not surprising since only three points currently exist. An uncertainty-weighted linear fit to these values (solid line in Figure 8.5) yields:

$$M_J = (11.5\pm0.3) + (0.62\pm0.04)\times SpT, \tag{8.10}$$

where SpT(T0) = 0, SpT(T5) = 5, etc. Interestingly, an extrapolation of this relation to T5 V matches the absolute brightness of 2MASS 0559-1404 assuming it is an equal-magnitude binary system. This match may be simply coincidence, however, and we will not read anything further into its reality.

We can use Equation 8.10 to estimate the absolute magnitude for each subtype sample later than T5 V, including the T7 V sample for which no measure currently exists. The scatter, σ_J, in M_J is assumed to be $\pm0.16\times\Delta$SpT mag for each subtype sample, i.e., one-quarter of the slope in Equation 8.10 times the range in spectral subtypes per sample, ΔSpT. We assigned $\sigma_J = 0.16$ mag for the T8 V subsample since a smaller value is not justifiable. Values are listed in Table 8.5. Note that we have considered two cases for the T5 V sample, 2MASS 0559-1404 as a single or double object. Admittedly, the estimates in Table 8.5 are based on fairly ad-hoc assumptions about the behavior of M_J as a function of spectral type, but lacking additional data, we adopt these as our

best guess.

8.2.4.2 Effective Radii and Volumes

The maximum distance to which an object of spectral type S with absolute brightness $\mathrm{M}_J(S)$ can be detected in our survey is

$$\begin{aligned} \log R_{max}(S) &= 0.2(J_{lim} - M_J(S)) + 1 \\ &= 4.2 - 0.2M_J(S), \end{aligned} \tag{8.11}$$

where $\mathrm{J}_{lim} = 16$. However, magnitude-limited surveys are affected by classical Malmquist bias (Malmquist, 1927; Reid & Hawley, 2000), which is caused by the intrinsic scatter in absolute brightness of the population under investigation. The observed sample is more sensitive to intrinsically brighter objects, particularly at greater distances. The result is the tendency to observe a greater volume than that defined by the mean absolute magnitude.

We therefore require an effective limiting distance, $\langle \mathrm{R}_{max} \rangle$, which can be derived by assuming that the distribution of absolute magnitudes M about some mean absolute magnitude M_o, with intrinsic scatter σ, is described by a Gaussian distribution,

$$\phi(M) = \frac{1}{\sqrt{2\pi}\sigma} e^{-(M-M_o)^2/2\sigma^2}. \tag{8.12}$$

For a given apparent magnitude m, the effective radius at which an object is likely to lie is

$$\langle R(m) \rangle = \frac{\int R(m,M) N(m,M) \phi(M) dM}{\int N(m,M) \phi(M) dM}, \tag{8.13}$$

where $R(m,M) = 10^{0.2(m-M)+1}$, and $N(m,M)$ is the differential number density of the population assuming an isotropic distribution:

$$\begin{aligned} N(m,M)dM &= n_o \left| \tfrac{dV}{dM} \right| dM \\ &= 4\pi n_o R^2(m,M) \left| \tfrac{dR}{dM} \right| dM \\ &= 4\pi n_o 10^{0.4(m-M)+2} (0.2 \ln 10) 10^{0.2(m-M)+1} dM \\ &= N_o 10^{0.6(m-M)+3} dM, \end{aligned} \tag{8.14}$$

with $N_o = 5.79 n_o$. Note that for fixed m, the number density increases for intrinsically brighter objects, which is precisely the effect predicted by Malmquist bias. The denominator in Equation 8.13 is

$$\begin{aligned} \int N(m,M)\phi(M)dM &= N_o 10^{0.6m+3} \int 10^{-0.6M} \tfrac{1}{\sqrt{2\pi}\sigma} e^{-(M-M_o)^2/2\sigma^2} dM \\ &= N_o 10^{0.6(m-M_o)+3} \tfrac{1}{\sqrt{\pi}} \int 10^{-0.6\sqrt{2}\sigma \overline{M}} e^{-\overline{M}^2} d\overline{M} \\ &= N_o R^3(m,M_o) e^{(0.6\sqrt{2}\ln 10\sigma)^2/4} \tfrac{1}{\sqrt{\pi}} \int e^{-\overline{M'}^2} d\overline{M'} \\ &= N_o R^3(m,M_o) 10^{2\ln 10 (0.3\sigma)^2}, \end{aligned} \tag{8.15}$$

while the numerator is

$$\begin{aligned} \int R(m,M)N(m,M)\phi(M)dM &= N_o 10^{0.8m+4} \int 10^{-0.8M} \tfrac{1}{\sqrt{2\pi}\sigma} e^{-(M-M_o)^2/2\sigma^2} dM \\ &= N_o 10^{0.8(m-M_o)+4} \tfrac{1}{\sqrt{\pi}} \int 10^{-0.8\sqrt{2}\sigma \overline{M}} e^{-\overline{M}^2} d\overline{M} \\ &= N_o R^4(m,M_o) e^{(0.8\sqrt{2}\ln 10\sigma)^2/4} \tfrac{1}{\sqrt{\pi}} \int e^{-\overline{M'}^2} d\overline{M'} \\ &= N_o R^4(m,M_o) 10^{2\ln 10 (0.4\sigma)^2}, \end{aligned} \tag{8.16}$$

Table 8.5: Effective Search Volumes.

Subtypes (1)	ΔSpT (2)	M_J (mag) (3)	R_{max} (pc) (4)	$\langle R_{max} \rangle$ (pc) (5)	R_{min} (pc) (6)	V_{eff} (pc^3) (7)
T5–T5.5 V	1.0	14.11±0.16	23.9	24.3±1.8	1.5	21000±4800
T5–T5.5 V[a]	1.0	14.86±0.16	16.9	17.2±1.3	1.1	7500±1700
T6–T6.5 V	1.0	15.53±0.16	12.4	12.7±0.9	0.8	3000±700
T7–T7.5 V	1.0	16.15±0.16	9.3	9.5±0.7	0.6	1250±300
T8 V	0.5	16.62±0.16	7.5	7.7±0.6	0.5	660±150
T7–T8 V	1.5	16.31±0.23	8.7	9.0±1.0	0.5	1100±350
T6–T8 V	2.5	16.00±0.39	10.0	11.2±2.0	0.6	2200±1300

[a] Assuming that the brightness standard, 2MASS 0559-1404, is an equal magnitude double.

so that

$$\begin{aligned} \langle R(m) \rangle &= R(m, M_o) 10^{2 \ln 10 (0.4^2 - 0.3^2) \sigma^2} \\ &= R(m, M_o) 10^{0.322 \sigma^2}. \end{aligned} \tag{8.17}$$

In general,

$$\langle R^j(m) \rangle = R^j(m, M_o) 10^{0.04605 j (j+6) \sigma^2}, \tag{8.18}$$

so we can calculate the uncertainty in the effective radius as

$$\begin{aligned} \sigma^2_{\langle R \rangle}(m) &= \langle R^2(m) \rangle - \langle R(m) \rangle^2 \\ &= R^2(m, M_o)(10^{0.737 \sigma^2} - 10^{0.645 \sigma^2}). \end{aligned} \tag{8.19}$$

The effective volume sampled for apparent magnitude m, $\langle V(m) \rangle$, actually depends on R^3, so that

$$\begin{aligned} 3 \langle V(m) \rangle / \Omega &= \langle R^3(m) \rangle \\ &= R^3(m, M_o) 10^{1.243 \sigma^2} \\ \sigma^2_{\langle R^3 \rangle}(m) &= R^6(m, M_o)(10^{3.316 \sigma^2} - 10^{2.486 \sigma^2}). \end{aligned} \tag{8.20}$$

Note that in each of these equations, the corrections applied depend only on σ, and tend to zero as the cosmic scatter becomes negligibly small.

Using the adopted absolute magnitudes and scatter values from Equation 8.10, and assuming $m = J_{lim} = 16$ mag, we derive the corrected maximum search radii, $\langle R_{max} \rangle$, as listed in Table 8.5. Note that due to the fairly large adopted values of σ_J (§8.2.4.1), the uncertainty in $\langle R_{max} \rangle$ ranges from 7–18%.

We must also consider the minimum search radius, effectively set by our search constraint of no optical counterpart in the USNO-A2.0 and no obvious counterpart in DSS images. The USNO-A2.0 catalog has a completeness limit of roughly 18–20 at R, which is a strong function of both plate quality and color, since USNO-A2.0 requires both blue and red plate detections. Reid et al. (1991) estimate the completeness of POSS-II at $R_E \sim 20.8$, similar to the SERC/ESO surveys, although there is a significant color term (> 1 mag) between the photographic red filter and the standard Cousins R_C, particularly for optically red objects (Tinney, Reid, & Mould, 1993). The shortest wavelength detection of a T dwarf is that of Gliese 229B by Golimowski et al. (1998) at 0.675 μm using the HST WF/PC2 instrument. This detection implies an effective R−J ~ 9, so our optical counterpart constraint imposes a maximum apparent J-band brightness of J $\gtrsim$ 10–11. Conservatively assuming the fainter limit, we calculated the minimum search radii, R_{min}, as listed in Table 8.5. Values for R_{min} range from 0.5–1.5 pc, and as such contribute no more than 0.03% to the total

search volume. We have therefore made no Malmquist corrections to these values.

Finally, the total effective search volumes,

$$V_{eff} = \frac{\Omega}{3}(\langle R^3_{max}\rangle - R^3_{min}), \tag{8.21}$$

were computed and are listed in Table 8.5. The uncertainty in V_{eff} is dominated by the uncertainty in $\langle R^3_{max}\rangle$, and we cannot constrain the search volumes to better than 25–60%. The two major contributions to this uncertainty are the largely unconstrained M_J relation for T dwarfs, and the significant binning of subtypes required by the small numbers of detections made, the latter increasing our adopted scatter and hence error in $\langle R^3_{max}\rangle$. Improved accuracy will require further search efforts as well as astrometric follow-up.

8.2.5 Correcting for Selection Biases

Correcting for selection biases in a magnitude-limited, color-selected sample is notoriously difficult, as objects can scatter into or out of our sample depending on both magnitude and color uncertainties. We are especially hampered in this case by working at the faint limits of 2MASS, where our sample may be complete at J-band (i.e., all sources detected down to J < 16) but woefully incomplete at H and K_s. Faint, viable objects drop out of the selected sample either by their non-detection at a particular band or, in the case of K_s, assignment of a band-filled magnitude, yielding only color limits. The color selection and loss of faint objects also leads to a bias in the mean observed colors of the population we are examining, making it difficult to derive an analytical expression for the number of objects inadvertently missed by our selection criteria.

8.2.5.1 Calculating Color Bias by Monte Carlo Simulation

To determine the completeness correction to our sample, we have done a Monte Carlo simulation of our search using the criteria listed in Table 2.8 and the photometric properties of 2MASS, as described in the 2MASS IDR2 Explanatory Supplement (Cutri et al., 2001). We modeled a control sample of T dwarfs, assuming that they are described by a single absolute magnitude, $M_{J_{init}}$, and initial colors $(J-H)_{init}$ and $(H-K_s)_{init}$. We again assume that the observed population is isotropic. The distribution of initial apparent J-band magnitudes, J_{init}, for the control sample then scales as

$$N(J_{init}) \propto 10^{0.6(J_{init}-M_{J_{init}})}, \tag{8.22}$$

as shown in Figure 8.6.

For the simulation, 10^6 objects were drawn from this distribution for each value of $(J-H)_{init}$ and $(H-K_s)_{init}$, chosen in the range −1.0 to 0.5 mag. The lower color limit encompasses all of the T dwarfs identified in the wdb0699 sample, while the upper limit is roughly 2σ above our color thresholds. We used the range $10 \leq J_{init} \leq 17$, where the minimum value is determined by our optical/near-infrared color cut, while the maximum is chosen to compensate for the scattering in of sources below our sample J-band magnitude limit. This implies that roughly 2.5×10^5 control objects have $J_{init} < 16$.

We then determined the measured ("biased") apparent magnitudes, J_{bias}, H_{bias}, and $K_{s_{bias}}$, by introducing a random scatter that scaled with the estimated magnitude uncertainty of the source. This quantity, σ_x (where x = J, H, or K_s), can be estimated as a function of apparent magnitude by examining the average scatter of 2MASS sources in various regions of the sky. This has been done by Cutri et al. (2001), and we reproduce the results in Figure 8.7. The top panel compares regions with Galactic latitudes below and above our $|b| = 15°$ constraint. As expected, there is a

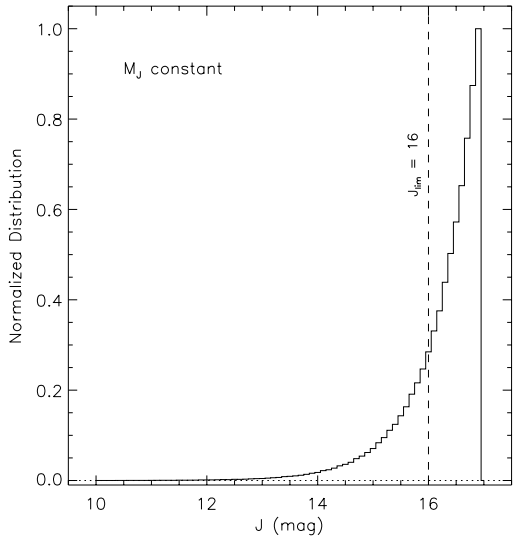

Figure 8.6: Number distribution of simulated T dwarfs population as a function of magnitude J_{init}. We have assumed that all objects are characterized by a single intrinsic magnitude $M_{J_{init}}$. Our search magnitude limit of J = 16 is indicated by the vertical dashed line.

slight increase in the photometric uncertainty at J-band as the source counts increase, largely due to increased confusion and background flux. H- and K_s-bands do not show the same increase however. The middle panel compares regions observed at Mt. Hopkins ($\delta > 0°$) to those observed at CTIO ($\delta < 0°$). J- and H-band uncertainties show little or no correlation with hemisphere, but there is some segregation in the uncertainties at K_s band. The differences are not significant as compared to the overall scatter in uncertainties as a function of magnitude, however, and we derive a mean σ relation by averaging the distributions with $|b| > 15°$, as shown in the bottom panel of Figure 8.7. Table 8.6 lists these values for reference. Note that data are not available for H > 16.5 and K_s > 16, as completeness drops off rapidly beyond these magnitudes.

Simulated measured magnitudes were then calculated by

$$\begin{aligned} J_{bias} &= J_{init} + R_N \times \sigma_J(J_{init}) \\ H_{bias} &= H_{init} + R_N \times \sigma_H(H_{init}) \\ K_{s_{bias}} &= K_{s_{init}} + R_N \times \sigma_{K_s}(K_{s_{init}}), \end{aligned} \tag{8.23}$$

where R_N is a random number selected from a normal distribution with unity width, and σ values (which were equated to the "measured" uncertainty in our simulation) were chosen by interpolating or extrapolating the data in Table 8.6.

We first rejected objects that had $J_{bias} \geq 16$. The volume effect on our initial distribution implies that there are roughly four times more objects in our control sample with $J_{init} > 16$ than with $J_{init} < 16$; hence, more objects will tend to be scattered into our sample (that would have originally not been selected) than scattered out. A measure of this preferential inclusion of faint sources is the

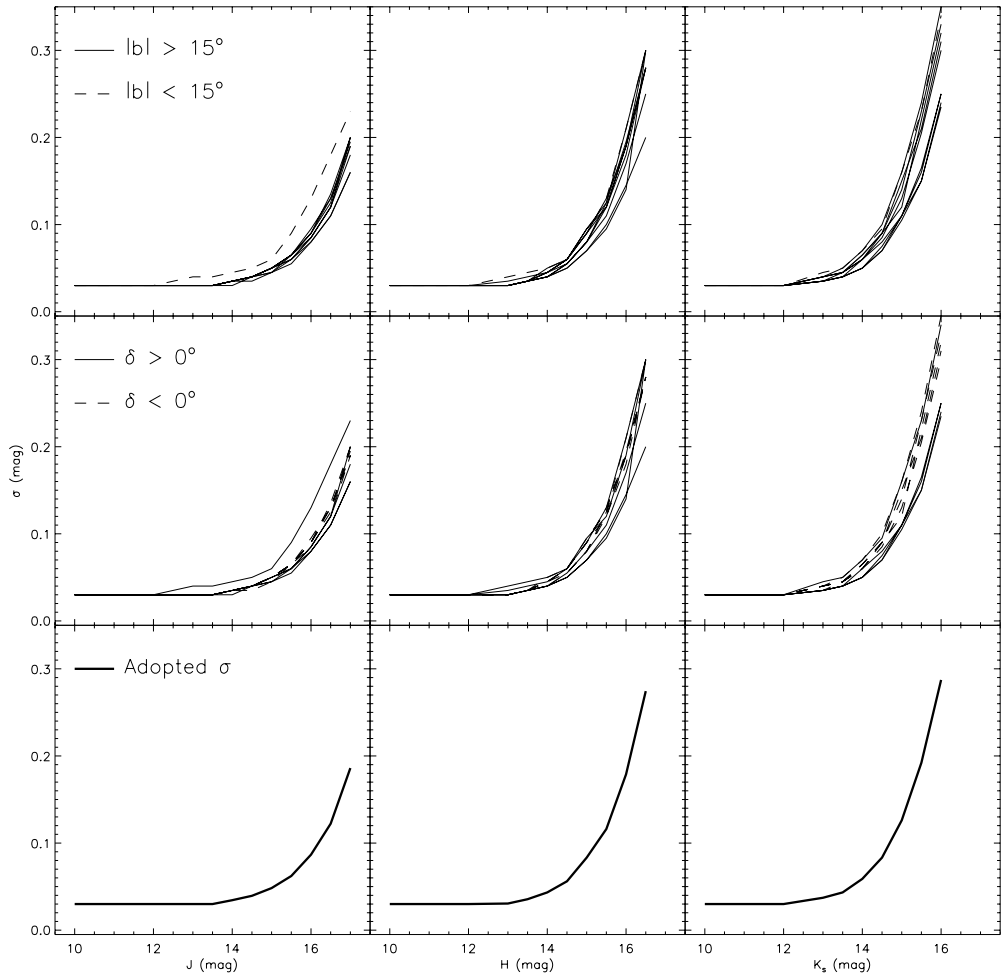

Figure 8.7: Photometric uncertainty versus 2MASS magnitude for various regions in the sky. J-, H-, and K_s-band uncertainties are plotted in the left, center, and right columns, respectively. The top row compares regions above (solid line) and below (dashed line) $|b| = 15°$. The middle row compares regions observed from the Northern (solid line) and Southern (dashed line) Hemispheres. The bottom row plots our adopted photometric uncertainties.

Table 8.6: 2MASS Photometric Error as a Function of Magnitude.

Mag. (1)	σ_J (2)	σ_H (3)	σ_{K_s} (4)
10.0	0.030	0.030	0.030
11.0	0.030	0.030	0.030
12.0	0.030	0.030	0.030
13.0	0.030	0.031	0.037
13.5	0.030	0.036	0.043
14.0	0.034	0.043	0.059
14.5	0.039	0.056	0.083
15.0	0.048	0.083	0.126
15.5	0.062	0.116	0.192
16.0	0.087	0.179	0.287
16.5	0.122	0.274	
17.0	0.186		

differential scatter of objects across the J = 16 threshold,

$$\Delta = \frac{\overline{N}_{in} - N_{out}}{\overline{N}_{in} + N_{in}}, \tag{8.24}$$

where $\overline{N}$ and N are the number of objects with $J_{init} \geq 16$ and $J_{init} < 16$, respectively ($\overline{N}/N \approx 4$) and the subscripts *in* and *out* refer to objects with $J_{bias} < 16$ and $J_{bias} \geq 16$. We obtain a mean value $\langle\Delta\rangle = 0.0153 \pm 0.0010$ from our simulations, which we can compare to the expected scatter from analytical expressions as a test of our simulation. The numbers $\overline{N}_{in}$, N_{in}, and N_{out} can be derived from

$$\begin{aligned} \overline{N}_{in} &= \int_{16}^{17} dJ_{init} N(J_{init}) P(J_{bias} < 16 | J_{init}) \\ N_{in} &= \int_{10}^{16} dJ_{init} N(J_{init}) P(J_{bias} < 16 | J_{init}) \\ N_{out} &= \int_{10}^{16} dJ_{init} N(J_{init}) P(J_{bias} \geq 16 | J_{init}), \end{aligned} \tag{8.25}$$

where

$$\begin{aligned} P(J_{bias} < 16 | J_{init}) &= \int_{10}^{16} dJ_{bias} \frac{1}{\sqrt{2\pi}\sigma_J} e^{-(J_{bias} - J_{init})^2 / 2\sigma_J^2} \\ P(J_{bias} \geq 16 | J_{init}) &= \int_{16}^{17} dJ_{bias} \frac{1}{\sqrt{2\pi}\sigma_J} e^{-(J_{bias} - J_{init})^2 / 2\sigma_J^2} \end{aligned} \tag{8.26}$$

are the probabilities for J_{bias} to be less than or greater than 16 mag given J_{init} and assuming a Gaussian distribution of uncertainties. $N(J_{init})$ scales as Equation 8.22. Choosing discrete values of σ_J ranging from 0.09 to 0.12 (corresponding to $16 \lesssim J_{init} \lesssim 16.5$; Table 8.6), these integrals yield values of $\Delta = 0.008$–0.014. This is consistent with the simulated Δ, if we assume that larger values of σ_J are more appropriate as they apply to the greater number of faint objects. The overall result is that more objects scatter in with $J_{init} \geq 16$ than scatter out with $J_{init} < 16$.

We then considered what sources would be undetected by 2MASS at each band, using 2MASS differential completeness values, C_x (where x is J, H, or K_s), determined from calibration scans (Cutri et al., 2001). Differential completeness measures the probability that a true source with apparent magnitude m will be detected by 2MASS[3]. As shown in Figure 8.8, listed values for C_J, C_H, and C_{K_s} (thick lines) are given over a narrow range of apparent magnitudes, so we have extrapolated

[3]A 2MASS source is considered "detected" if it is identified on more than 50% of the individual images (maximum six) taken in a particular region (Cutri et al., 2001).

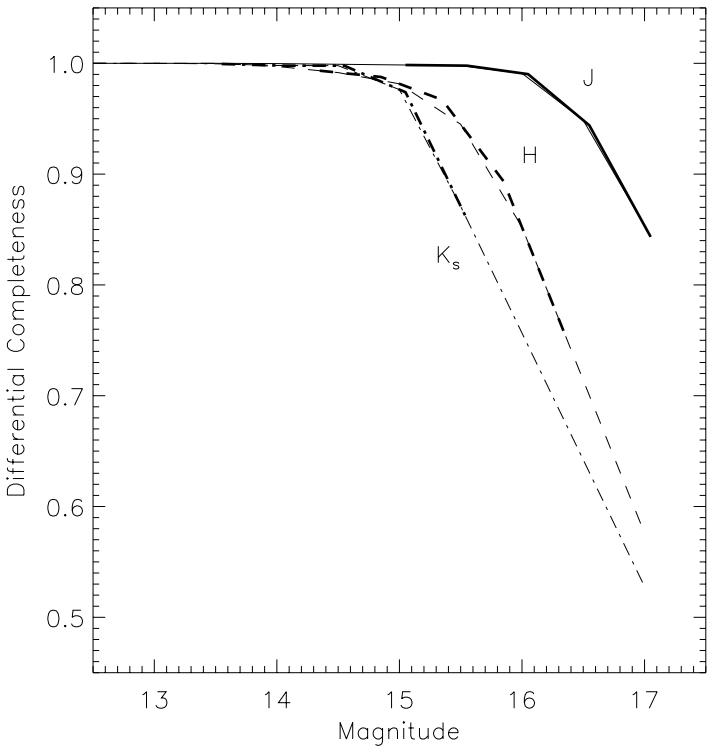

Figure 8.8: Differential completeness as a function of 2MASS magnitude. Values for C_J (solid line), C_H (dashed line), and C_{K_s} (dot-dashed line) are indicated. Heavier lines indicate data from Cutri et al. (2001), while extrapolations to $10 < J < 16$ are shown by the thinner lines.

Table 8.7: 2MASS Differential Completeness as a Function of Magnitude.

Mag. (1)	C_J (2)	C_H (3)	C_{K_s} (4)
10.0	1.000	1.000	1.000
11.0	1.000	1.000	1.000
12.0	1.000	1.000	1.000
13.0	1.000	1.000	1.000
13.5	1.000	1.000	1.000
14.0	1.000	0.997	0.998
14.5	0.999	0.992	0.998
15.0	0.999	0.981	0.976
15.5	0.998	0.945	0.871
16.0	0.991	0.852	0.757
16.5	0.949	0.714	0.642
17.0	0.853	0.576	0.528

to brighter magnitudes by adopting C = 1, and to fainter mags by extrapolating the last few data points. Our adopted completeness values are listed in Table 8.7. For each test source and at each band we computed the quantity:

$$\delta_x = C_x - R_U, \tag{8.27}$$

where x = J, H, or K_s, and R_U is a random number selected from a uniform distribution between 0 and 1. We rejected all sources for which $\delta_J < 0$ or $\delta_H < 0$, implying non-detection at either band.

Our original search criteria had no requirement for detection at K_s, so sources with $\delta_{K_s} < 0$ were not rejected. However, a source that is not detected by 2MASS at any one band is assigned a band-filled magnitude, in this case K_s^{fill}, which is essentially an upper brightness limit based on the background noise level. One would expect that this value varies considerably depending on the observing conditions, background features, and source density. Since these effects are difficult to model, we seek an average distribution for K_s^{fill}. Figure 8.9 plots the individual distributions for eight separate areas evenly distributed about the sky. Band-filled sources were selected from the working database in a 1° radius about the given coordinates, and constrained to be single sources at J- and H-bands (2MASS blend flags set to one), not extended, and having low probabilities of persistence; these are the same constraints made on the initial T dwarf sample. As expected, there are some minor variations in these distributions. Mean values of K_s^{fill} in the southern samples appear to be brighter than corresponding northern samples, differing by as much as 0.5 mag; the main Gaussian-like peak is more filled in as we increase the source density (i.e., lower $|b|$); and the faint-end "spike" in the distributions varies both in relative size and peak magnitude. Nonetheless, these distributions have fairly similar shapes, and we have obtained a mean K_s^{fill} distribution (center panel) by summing all of the normalized distributions together. Objects not detected at K_s in our simulation were then reassigned a random magnitude drawn from this distribution, so that $K_{s_{bias}} = K_s^{fill}$.

Finally, measured colors were computed from the bias magnitudes, and objects which had $(J-H)_{bias} \geq 0.3$ or $(H-K_s)_{bias} \geq 0.3$ were rejected. From our original input population, four distinct samples emerged: (1) N_1 objects with $J_{init} < 16$ that passed, (2) N_2 objects with $J_{init} < 16$ that were rejected, (3) N_3 objects with $J_{init} \geq 16$ that passed, and (4) N_4 objects with $J_{init} \geq 16$ that were rejected. The number of objects in the first three groups yield the proper correction factor to our observed population; that is, the ratio of the true number of sources to the number of

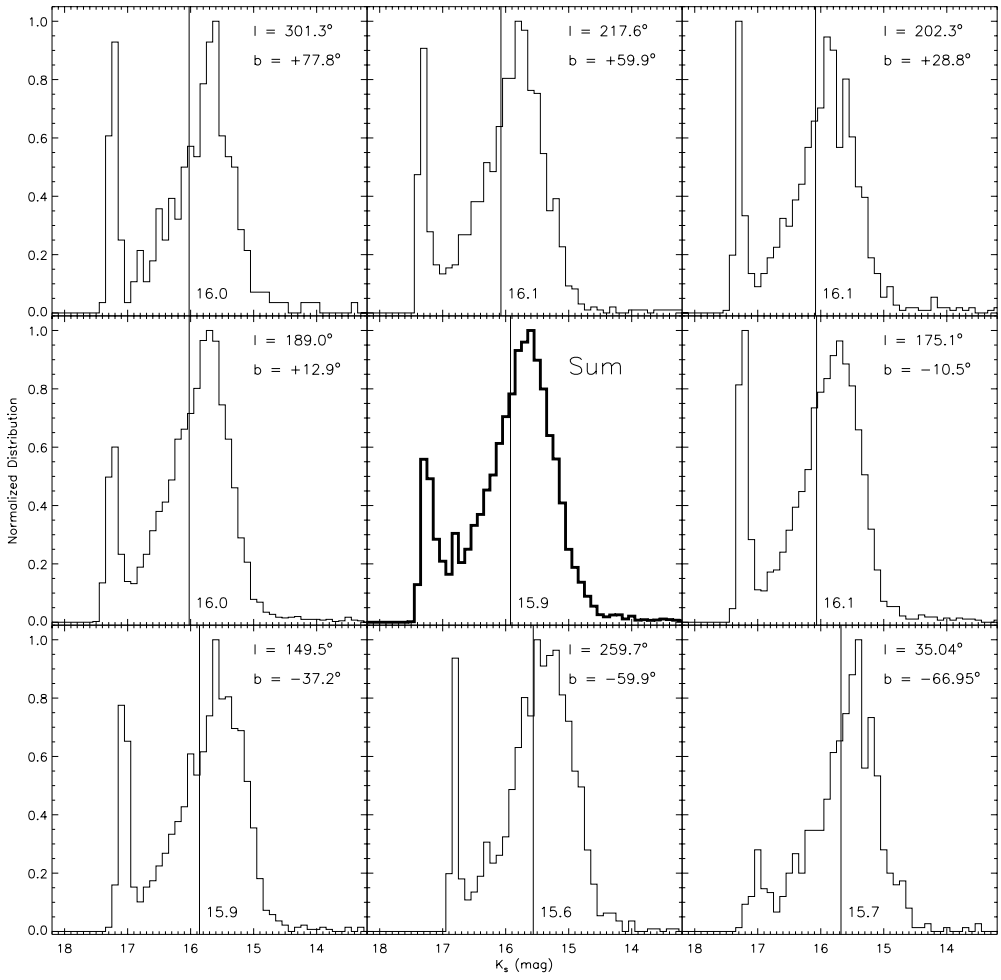

Figure 8.9: Normalized distributions of K_s^{fill} in various regions of the sky. Objects with J- and H-band detections but no K_s-band detection were selected in a 1° radius around the coordinates listed. The center panel plots our adopted mean distribution.

sources that were actually detected:

$$\chi = \frac{N_1 + N_2}{N_1 + N_3}. \tag{8.28}$$

Note that if $(J-H)_{init} \geq 0.3$ or $(H-K_s)_{init} \geq 0.3$, χ can become quite large, as we are sensitive only to the tail of the biased color distribution.

8.2.5.2 Results of the Simulation and Estimating a Correction

The search simulation outputs essentially three key quantities for each initial $(J-H)_{init}$ and $(H-K_s)_{init}$: the correction factor χ, and the uncertainty-weighted, mean bias colors $\langle (J-H)_{bias} \rangle$ and $\langle (H-K_s)_{bias} \rangle$. We can compare the latter two quantities to our observed T dwarf sample. Figure 8.10 plots the mean bias colors versus initial color for the parameter space explored. There is little deviation in J−H for $(J-H)_{init} < 0.1$ and $(H-K_s)_{init} < 0$; however, as $(J-H)_{init}$ increases above the 0.3 mag color limit, $\langle J-H \rangle_{bias}$ saturates at 0.2–0.3 mag, as we sample only those objects scattered into our selection bin. Redder values of $(H-K_s)_{init}$, on the other hand, bias resulting mean J−H colors toward the red. This is due to scatter in faint H_{bias} magnitudes, where the $(H-K_s) < 0.3$ color cut will generally select sources where H_{bias} has scattered to brighter magnitudes (e.g., $(H-K_s)_{init} \sim 0.5$ scatters to $\langle H-K_s \rangle_{bias} \sim 0.3$), with a corresponding shift in the $\langle J-H \rangle_{bias}$ color. Since the faintest H-band magnitudes will be present for the bluest J−H colors, this effect is most prominent for $(J-H)_{init} = -1.0$. The H−K_s colors show similar trends, although there is an additional bias toward slightly bluer output colors for $(H-K_s)_{init} > -0.1$. This bias is caused by the non-detection of faint K_s source and hence the preferential scatter of K_s magnitudes to brighter values; i.e., an over-luminosity effect. As $(H-K_s)_{init}$ tends to higher values, this effect becomes more pronounced, as we preferentially sample faint sources. These plots show that color biases of up to 0.2 mag are possible for intrinsic populations centered within the color-selection criteria, and can exceed 0.4 mag if the initial population is centered outside these criteria.

Figure 8.11 plots the correction value χ as a function of $(J-H)_{init}$ (abscissa) and $(H-K_s)_{init}$ (grey scale). As expected, values for χ are large for red $(J-H)_{init}$ and/or $(H-K_s)_{init}$ colors, as our search constraints only allow us to sample extremely scattered objects from the initial population. For blue $(J-H)_{init}$ colors, we begin to lose a significant number of objects to H- and K_s-band non-detection, and $\chi \gtrsim 2$ for $(J-H)_{init} = -1.0$. A minimum in the correction factor occurs for $-0.2 < (J-H)_{init} < 0.2$ and $(H-K_s)_{init} < 0.1$, where most of the initial objects will scatter within our selection criteria, and few objects have H and K_s magnitudes too faint to detect. Overall, χ ranges from 1.14 ($(J-H)_{init} = 0.05$, $(H-K_s)_{init} = -0.55$) to 690 ($(J-H)_{init} = (H-K_s)_{init} = 0.5$) in our simulation.

To determine the appropriate correction for each spectral type, we have made a statistical comparison between the weighted mean colors of our discovered objects and those of the simulation output. We used a variance test to examine the hypothesis $\mu_{obs} = \mu_{bias}$ by computing the statistic (Rinaman et al., 1996):

$$z = \left| \frac{\mu_{obs} - \mu_{bias}}{\sqrt{\frac{\sigma_{obs}^2}{N_{obs}} + \frac{\sigma_{bias}^2}{N_{bias}}}} \right|, \tag{8.29}$$

where $\mu = \langle J-H \rangle$ or $\langle H-K_s \rangle$ for the observed T dwarfs (*obs*) and objects detected in our simulation (*bias*), σ is the corresponding mean weighted color uncertainty, and N_{obs} and N_{bias} are the numbers of objects used to calculate these mean colors. Generally, $N_{bias} >> N_{obs}$, so the error term from the observed population dominates z. This statistic yields the probability that the mean colors are equal assuming a normal distribution, $\phi(z)$; i.e., we can choose a maximum z_{lim} such that if $z < z_{lim}$, the colors are equal within the uncertainties to a confidence level of $\phi(z_{lim})$. This test implicitly

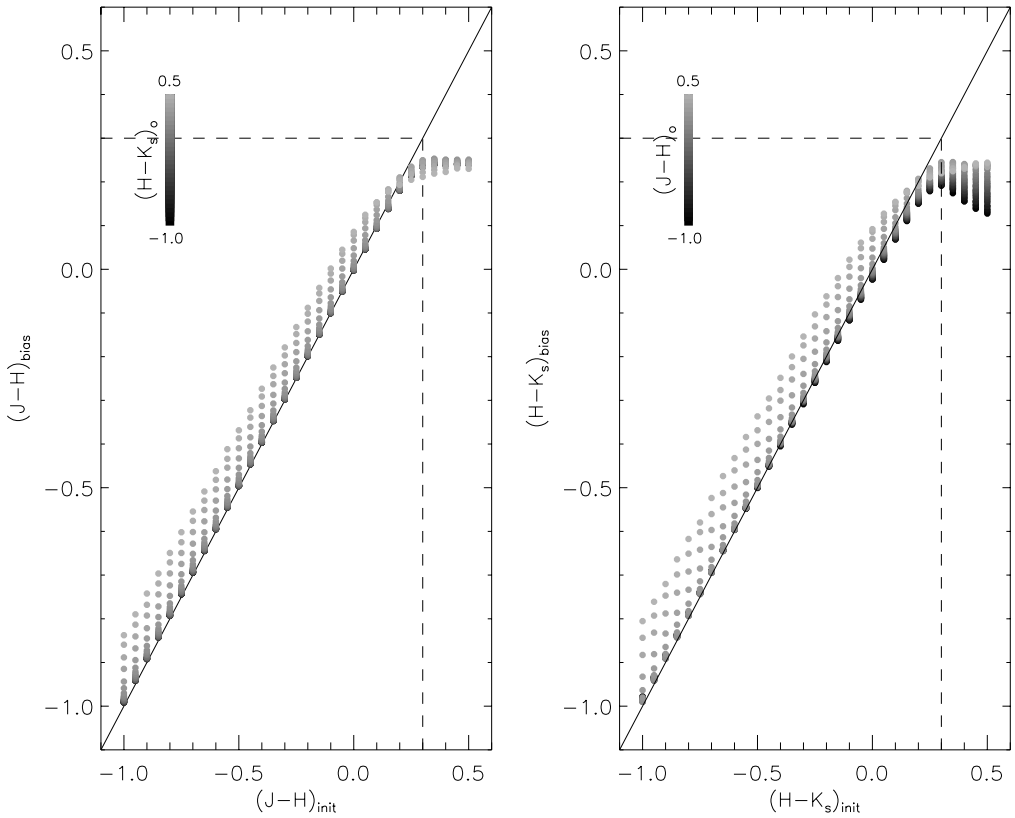

Figure 8.10: Uncertainty-weighted "bias" colors for objects selected in our search simulation. Comparison between $(J-H)_{bias}$ and $(J-H)_{init}$ is shown in the left panel, while comparison between $(H-K_s)_{bias}$ and $(H-K_s)_{init}$ is shown in the right panel. For each plot, the range in the opposite color is shown in greyscale. Solid lines trace out the expected values assuming no selection bias, while the dashed lines plot our search sample color constraints.

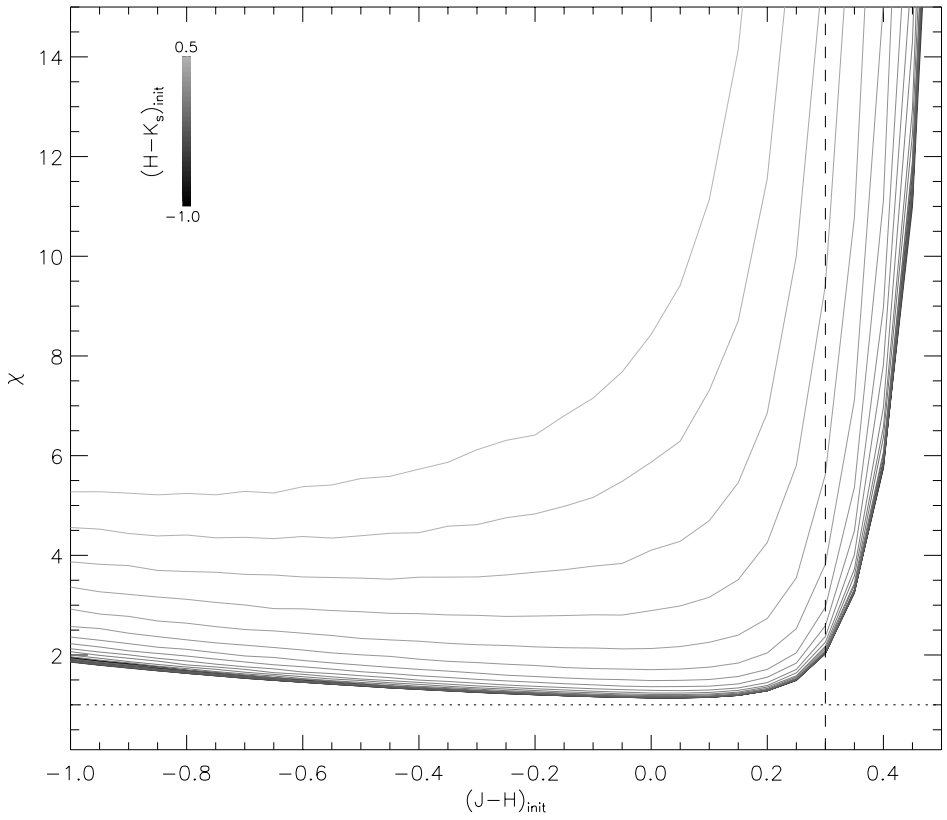

Figure 8.11: Values for the bias correction factor χ as a function of $(J-H)_{init}$ (abscissa) and $(H-K_s)_{init}$ (greyscale). $\chi = 1$ (no correction) is indicated by the dotted line, while our $J-H < 0.3$ search constraint is indicated by the dashed line.

Table 8.8: Color Bias Results.

		Observed[a]		Simulated[a]			
Subtypes (1)	N_{obs} (2)	$\langle$J−H$\rangle_{obs}$ (3)	$\langle$H−K$_s\rangle_{obs}$ (4)	$\langle$J−H$\rangle_{init}$ (5)	$\langle$H−K$_s\rangle_{init}$ (6)	χ (7)	N_{corr} (8)
T5–T5.5 V	5±2	0.13±0.04	0.07±0.05	0.13±0.03	0.08±0.03	$1.29^{+0.04}_{-0.01}$	$6.5^{+2.6}_{-2.6}$
T6–T6.5 V	5±2	0.09±0.05	−0.19±0.10	0.10±0.04	−0.20±0.07	$1.17^{+0.04}_{-0.02}$	$5.8^{+2.3}_{-2.3}$
T7–T7.5 V	2±1	−0.06±0.11	0.26±0.28	−0.07±0.13	0.02±0.29	$1.26^{+1.90}_{-0.09}$	$2.5^{+4.0}_{-1.3}$
T8 V	2±1	0.08±0.08	0.05±0.15	0.10±0.12	0.18±0.23	$1.57^{+5.58}_{-0.36}$	$3.1^{+11.3}_{-1.7}$
T7–T8 V	4±2	0.04±0.06	0.10±0.13	0.00±0.06	0.23±0.17	$1.71^{+3.77}_{-0.47}$	$6.8^{+15.5}_{-3.9}$
T6–T8 V	9±3	0.10±0.03	0.03±0.04	0.10±0.03	0.03±0.04	$1.25^{+0.00}_{-0.03}$	$11.3^{+3.8}_{-3.8}$

[a]Weighted mean colors.

assumes that the uncertainties σ_{obs} and σ_{bias} are non-correlated and Gaussian. We have chosen z_{lim} = 2.576, corresponding to a confidence level of 99.5%.

We compared this statistic for all values of (J−H)$_{init}$ and (H−K$_s$)$_{init}$ and for each of our observed subsamples. Figures 8.12, 8.14, 8.16, 8.18, 8.20, and 8.22 diagram these results, along with the distributions of colors for which $z < z_{lim}$. The mean of each distribution (solid circles) can be considered the "unbiased" color of that particular subsample, with an uncertainty (or intrinsic spread in values) estimated from the variance in the distribution. There is an implicit error of ±0.03 mag inherent to our initial color grid spacing of 0.05 mag. In general, the difference between the observed (open circles) and simulated colors is small, since the former quantity typically falls below the turnover points seen in Figure 8.10. Color distributions for the T5 and T6 subsamples are generally well constrained, due to their significant numbers of objects. The results for the T6 subsample may be skewed, however, by the anamolously blue 2MASS 0937+2931 (see §7.7). The T7 and T8 subsamples are much more poorly constrained, due primarily to their smaller numbers, tending to decrease the value of z for outlying comparison samples. For the T7 subsample, there is an additional problem caused by the red H−K$_s$ color of its sole K$_s$-detected member, 2MASS 0727+1710, which has H−K$_s$ = 0.26±0.28. This is well into the regime where simulated colors are significantly offset from their initial values, resulting in a color degeneracy. Combining the latter two subsets provides tighter constraints on the (J–H)$_{init}$ color, but still leads to an indeterminancy in the (H−K$_s$)$_{init}$ color. It should be noted that the redder values predicted for the latter subtypes do not imply that these objects *intrinsically* have red colors, but reflects the inability to differentiate between initial color sets due to the color selection bias. Finally, combining the T6, T7, and T8 subsamples yields the tightest constraint on initial colors, with $\langle$J–H$\rangle_{init}$ = 0.10±0.03 and $\langle$H–K$_s\rangle_{init}$ = 0.03±0.04.

Figures 8.13, 8.15, 8.17, 8.19, 8.21, and 8.23 plot the distribution of χ values satisfying $z < z_{lim}$ for each of the subsamples. Since all of the samples have $-0.1 \lesssim \langle$J-H$\rangle_{init} \lesssim 0.2$, we typically obtain the minimum values of χ in the trough of Figure 8.11, so there is a peak in all of the distributions at $\chi \sim 1.15$. However, subsamples with poor constraints on $\langle$H-K$_s\rangle_{init}$ colors allow substantially larger values. Because the resulting χ distributions are clearly non-Gaussian, we chose the median value as the most likely determination of χ, with upper and lower uncertainty bounds encompassing 50% of the distribution about the median. The T5, T6, and T6–T8 subsamples have fairly well constrained χ values with uncertainties of $\lesssim$ 5%, while the poorly represented T7 and T8 subsamples have much larger upper limits.

Table 8.8 summarizes the results of the color bias simulation, with derived values of χ and the resulting corrected detection numbers. Even for the well-represented T5 and T6 subsamples, corrections of up to 30% of the discovery numbers are required to compensate for our color selection biases. The error in the derived χ values are negligible, however, as compared to the Poisson

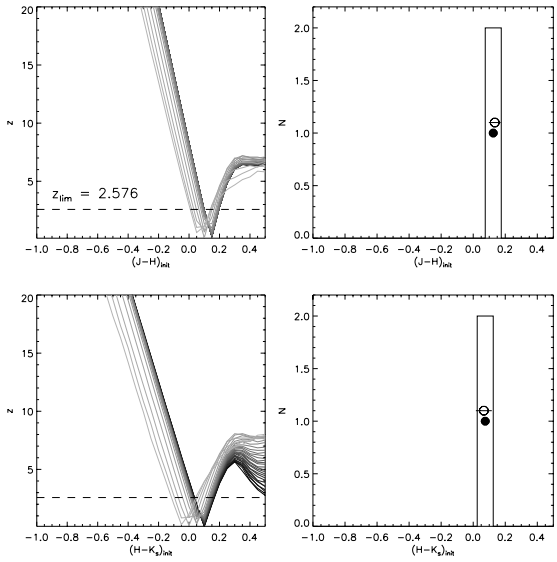

Figure 8.12: Statistical comparison of weighted mean bias colors to observed colors for objects with spectral types T5 V and T5.5 V. Left panels plot the statistic z versus $(\mathrm{J}-\mathrm{H})_{init}$ and $(\mathrm{H}-\mathrm{K}_s)_{init}$, with the maximum allowed $z_{lim} = 2.576$ indicated by the dashed line. Right panels plot the distribution of initial colors for cases matching both color constraints, along with the mean initial color (solid circle) and mean measured color (open circle).

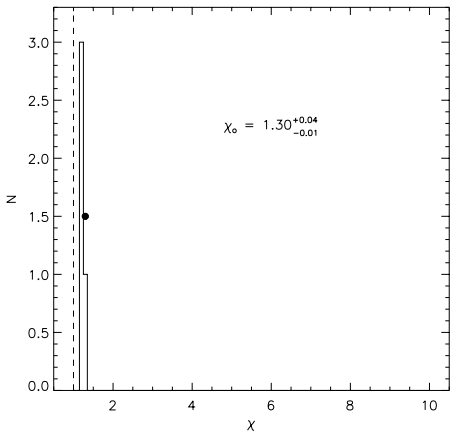

Figure 8.13: Distribution of χ values for simulated populations satisfying $z < z_{lim}$ in both J−H and H−$\mathrm{K_s}$ colors for T5–T5.5 V subtypes. The mean value is indicated by the solid point.

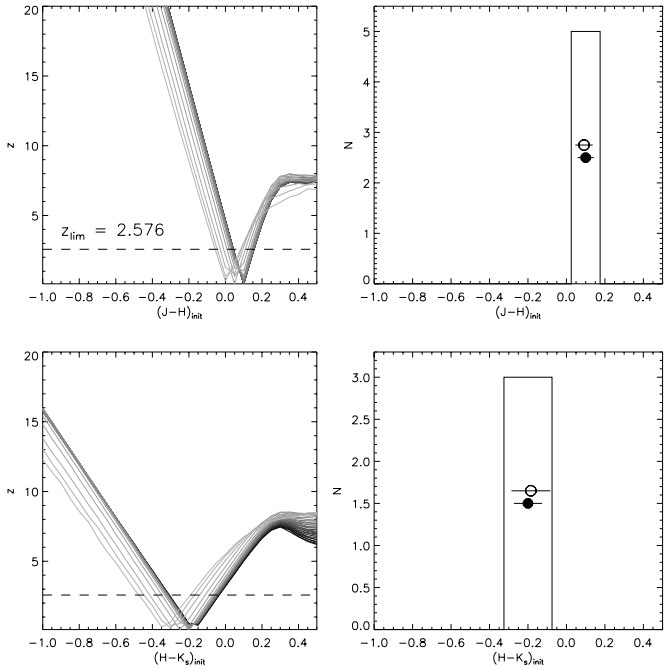

Figure 8.14: Same as Figure 8.12 for subtypes T6–T6.5 V.

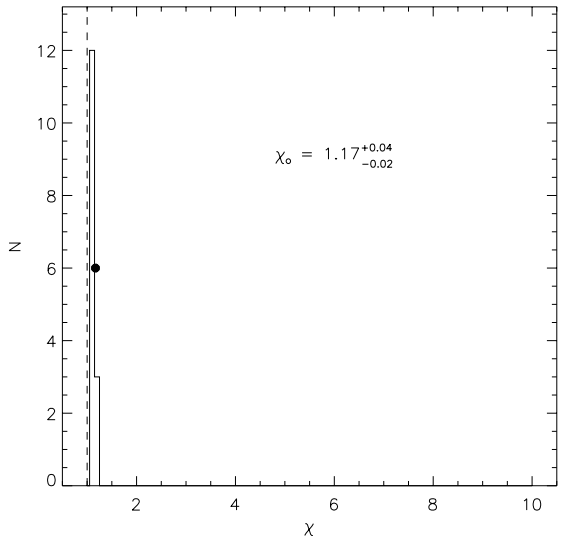

Figure 8.15: Same as Figure 8.13 for subtypes T6–T6.5 V.

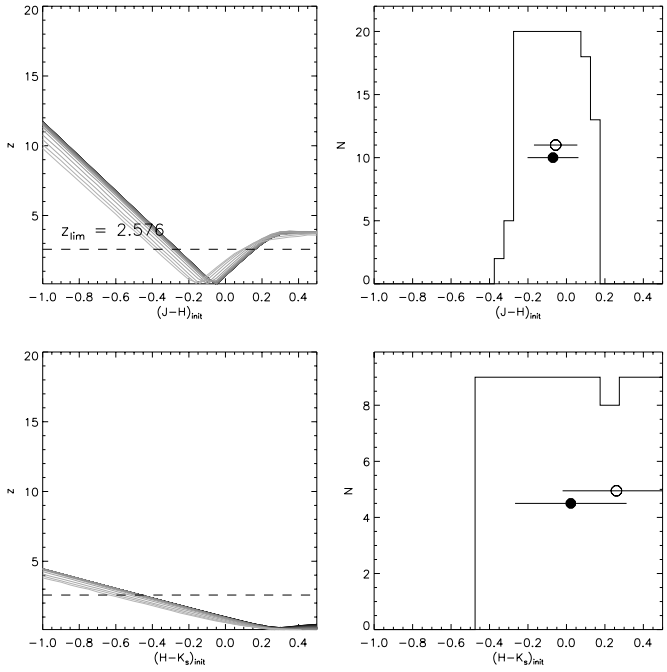

Figure 8.16: Same as Figure 8.12 for subtypes T7–T7.5 V.

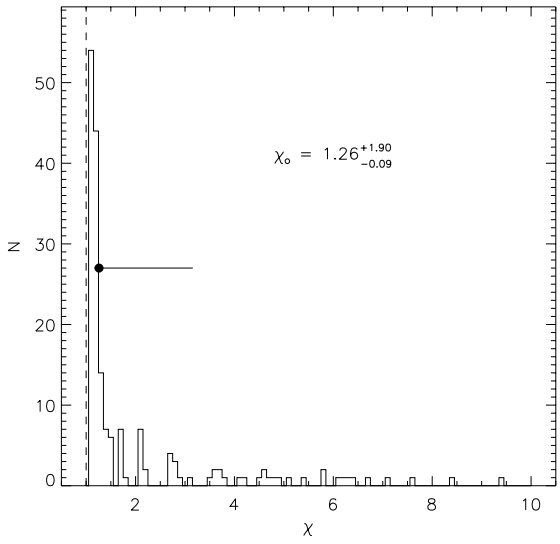

Figure 8.17: Same as Figure 8.13 for subtypes T7–T7.5 V.

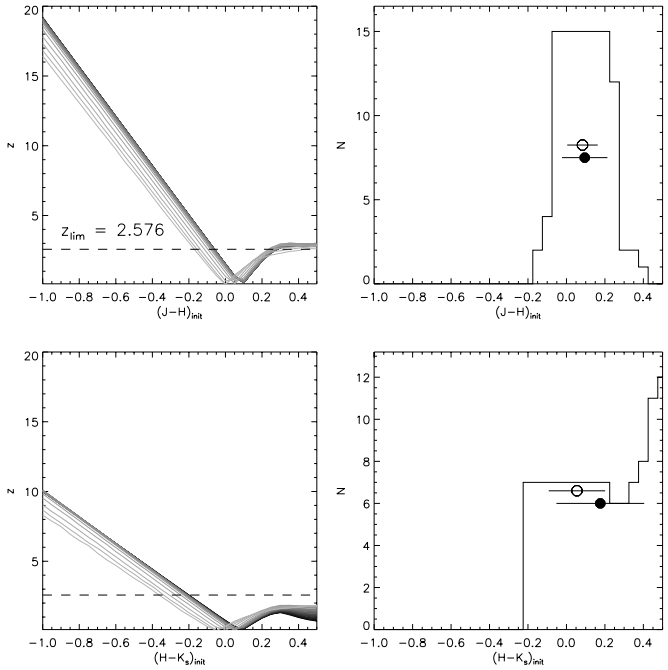

Figure 8.18: Same as Figure 8.12 for subtype T8 V.

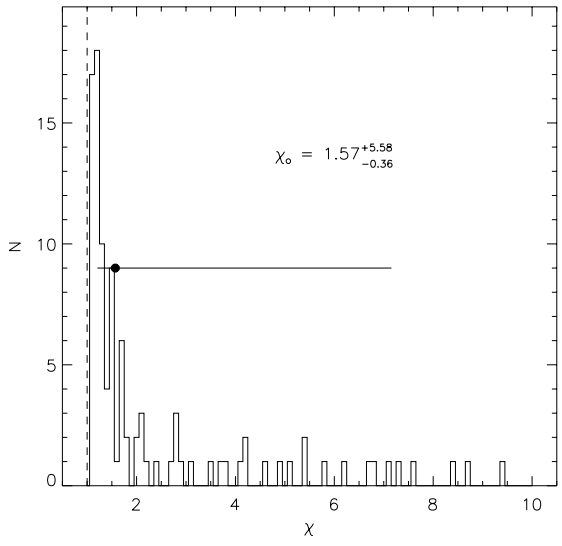

Figure 8.19: Same as Figure 8.13 for subtype T8 V.

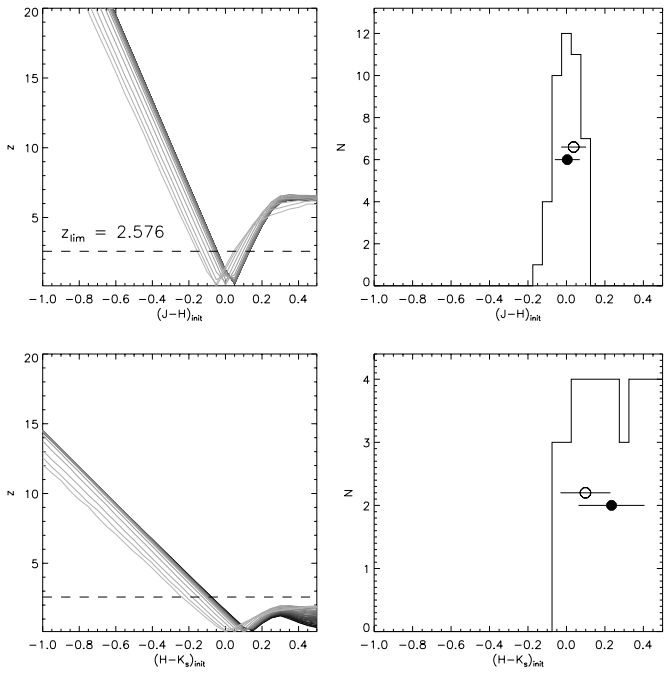

Figure 8.20: Same as Figure 8.12 for subtypes T7–T8 V.

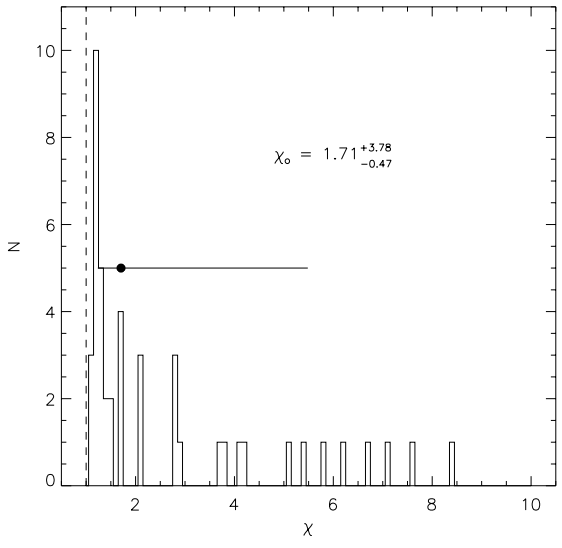

Figure 8.21: Same as Figure 8.13 for subtypes T7–T8 V.

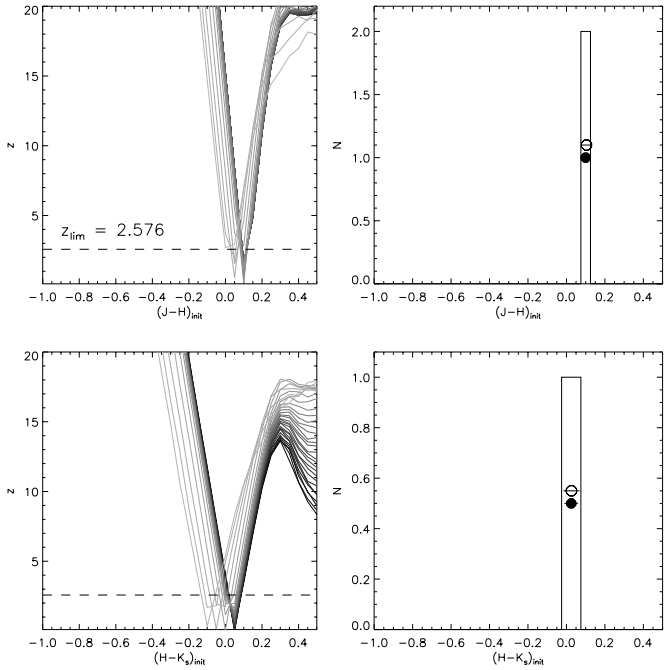

Figure 8.22: Same as Figure 8.12 for subtypes T6–T8 V.

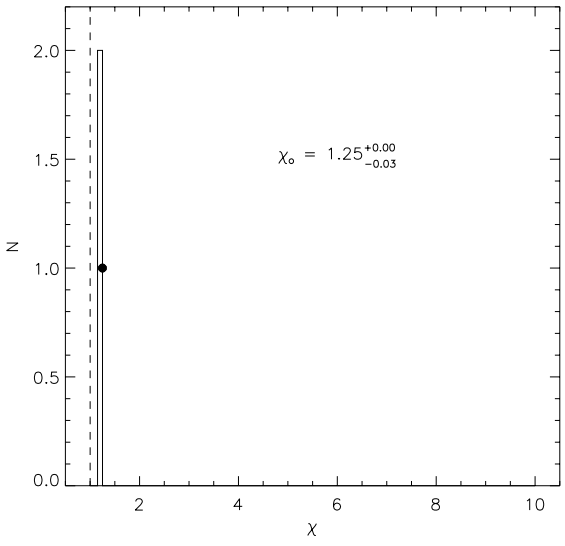

Figure 8.23: Same as Figure 8.13 for subtypes T6–T8 V.

uncertainties in these cases. Such is not the case for the T7 and T8 subsamples, where χ is poorly constrained and upper bounds are as much as 4.5 times greater than the corrected median values. These large errors are not unexpected, however, given the small numbers of objects present in these subsamples.

8.2.6 The Influence of Duplicity

One additional parameter that should be considered in our density estimates is that of duplicity. There is currently some controversy over the importance of binary systems in the determination of luminosity and/or mass functions. Dahn, Liebert, & Harrington (1986) initially proposed that discrepancies seen in luminosity functions derived from nearby star counts and deep photometric parallax surveys could be attributed to the influence of low-luminosity companions. Reid (1987), Reid et al. (1991), and Stobie, Ishida, & Peacock (1989) have found that duplicity cannot resolve the star count discrepancy, while Kroupa, Tout, & Gilmore (1993) and Kroupa (1995) claim that the contribution of unresolved systems is a critical bias in magnitude-limited samples. Multiple systems effect number counts in two ways: first, they generally increase the number of objects in a sample, preferentially adding members of fainter spectral types; and second, by allowing objects at greater distances to enter into the sample search volume. We can examine rough estimates of both effects to determine their influence on our sample. For this discussion, we compare to the results of L dwarf duplicity programs, as the T dwarf binary fraction is currently under investigation.

8.2.6.1 First Approach

One method by which we can estimate the effect of duplicity on T dwarf number counts is by adding the secondaries to our total population while compensating for the greater volume sampled for the combined system. This is essentially an "ignorance" approach; i.e., we assume we do not know ahead of time which objects in our sample our double, so we include all objects.

High resolution imaging observations of L dwarfs have shown that roughly 20% are found in double systems (Koerner et al., 1999; Reid et al., 2001b, Table 5.3). The majority of these are in nearly-equal-magnitude pairs, with the lowest secondary/primary flux ratio being that of 2MASS 0850+2057AB, $\Delta M = M_2 - M_1 = 1.3$ mag (Reid et al., 2001b); note, however, that small number statistics and selection effects must be considered. Based on the flux ratios of Table 5.3 and the absolute magnitude relation of Equation 8.10, we would expect (naively) that 60% of the T dwarf binaries would have a secondary of similar spectral type, while 40% would have a secondary one spectral type later (Figure 8.24). Therefore, the number added to each subtype group by binary secondaries is

$$\Delta N(S) = \alpha(0.6N(S) + 0.4N(S-1)), \tag{8.30}$$

where α is the binary frequency, taken to be 20%. Hence the T5 (assuming all contributions come from that class), T6, T7, and T8 number counts would increase by 1.3, 1.2, 0.8, and 0.6 objects, respectively, a relative increase of roughly 20%, 20%, 30%, and 20%.

The change in the effective volume sampled depends greatly on the typical relative flux of the secondary. Defining $\varrho = \frac{f_2}{f_1}$ as the secondary to primary flux ratio of a binary system, such a pair would be observed at a greater distance, d', than if it were single, d, with a ratio

$$\begin{aligned} (\tfrac{d'}{d})^2 &= \tfrac{f_1+f_2}{f_1} \\ &= 1+\varrho. \end{aligned} \tag{8.31}$$

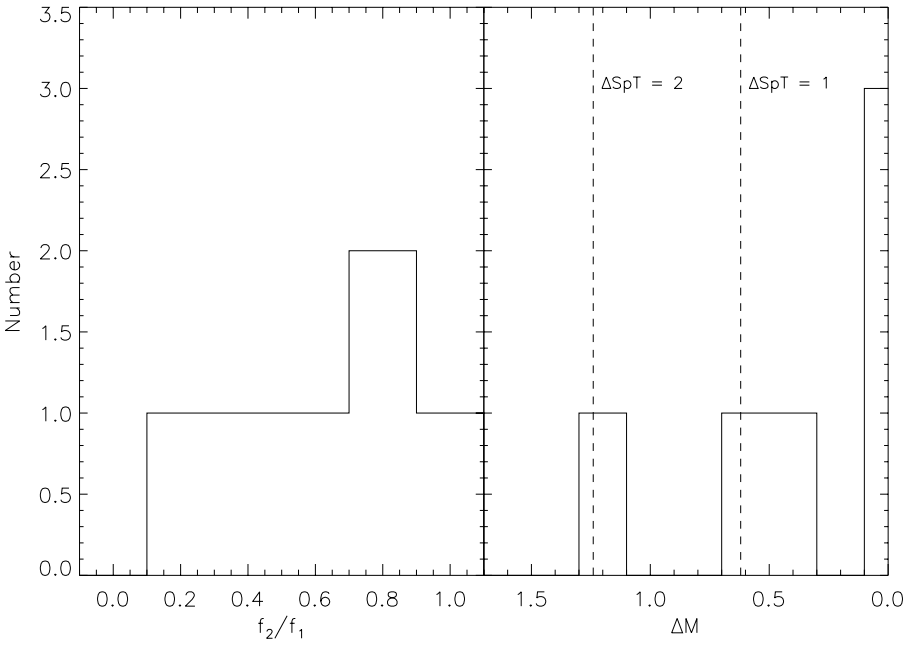

Figure 8.24: Distribution of binary L dwarf flux ratios. The left panel plots the ratio of secondary-to-primary flux, while the right panel plots the relative magnitude distribution. Approximate changes of one and two spectral types for the secondary are indicated.

The relative increase in the volume sampled by this binary is thus

$$\frac{V'}{V} = (1+\varrho)^{3/2}. \quad (8.32)$$

The relative increase in the volume sampled averaged over all members of a subtype is then

$$\langle\frac{V'}{V}\rangle = \alpha\langle(1+\varrho)^{3/2}\rangle + (1-\alpha), \quad (8.33)$$

where we can calculate $\langle(1+\varrho)^{3/2}\rangle$ from the flux ratio distribution function, $\epsilon(\varrho)$:

$$\langle(1+\varrho)^{3/2}\rangle = \int_0^1 (1+\varrho)^{3/2}\epsilon(\varrho)d\varrho. \quad (8.34)$$

Using the distribution of Figure 8.24 yields $\langle(1+\varrho)^{3/2}\rangle = 2.2$ (a flat distribution would give 1.9) Thus, $\langle\frac{V'}{V}\rangle = 1.24$; i.e., a roughly 20% increase in volume sampled. This approximately cancels the relative increase in detections, implying that duplicity has no real effect in our magnitude-limited sample. Note that increasing the binary fraction to 40% also results in a nearly equal increase in number counts and effective volume. Hence, the effect of duplicity on number counts, based on this analysis, is negligible.

8.2.6.2 Second Approach

We can also examine duplicity from another viewpoint, by assuming that we can in fact catalog which objects are double and eliminate those that fall out of our search criteria (i.e., an "omniscient" approach). In this case we explicitly calculate the individual magnitudes of double objects,

$$\begin{aligned} J_{primary} &= J_{tot} + 2.5\log(1+\varrho) \\ J_{secondary} &= J_{tot} + 2.5\log(1+\tfrac{1}{\varrho}), \end{aligned} \quad (8.35)$$

and check to see if either component (or both) are fainter than our limiting sample magnitude.

We performed a Monte Carlo simulation to calculate the fraction of objects retained in a magnitude-limited sample assuming isotropy and constant intrinsic magnitude (e.g., Figure 8.6). Hypothetically, this fraction can be greater than unity if a sufficient number of secondaries do not fall below the sample limits. We constructed 20 samples of 10^5 objects with $10 \leq J \leq 16$, and randomly selected a fraction α to be double. We then computed their component magnitudes assuming either the flux ratio distribution in Figure 8.24 or a flat distribution. Finally, we computed the number of individual objects with $J \leq 16$ and compared this to the initial sample. For $\alpha = 0.2$, the number of objects included in our sample decreases by 5.5% and 4.6% for L dwarf and flat flux ratio distributions, respectively. For $\alpha = 0.4$, the fractional change becomes 10.9% and 9.2%, respectively.

We would conclude from this analysis that T dwarf space densities must be scaled down by 5–10% to compensate for duplicity. However, these ratios are significantly less than the uncertainties in our volume estimates, and must be weighed against our lack of knowledge about the actual binary fraction of T dwarfs and corresponding flux ratio distribution. A more rigorous analysis requires high-resolution imaging and/or high-resolution spectroscopic monitoring of each target in our sample to identify those that are double systems. Based on the current uncertainties and lack of correction required from our first method, we do not correct our number counts to compensate for duplicity here. However, we warn the reader that our results could be overestimated by up to 10% based on this poorly constrained parameter.

Table 8.9: T Dwarf Space Densities.

Subtypes (1)	M_{bol} (mag) (2)	T_{eff} (K) (3)	χN (4)	V_{eff} (pc^3) (5)	ν_o (10^{-3} pc^{-3}) (6)
T5–T5.5 V	16.5	1400–1300	$6.5^{+2.6}_{-2.6}$	21000±4800	$0.31^{+0.14}_{-0.14}$
	17.2	1150–1050	$6.5^{+2.6}_{-2.6}$	7500±1700	$0.87^{+0.40}_{-0.40}$
T6–T6.5 V	17.8	1050–950	$5.8^{+2.3}_{-2.3}$	3000±700	$1.9^{+0.9}_{-0.9}$
T7–T7.5 V	18.3	950–850	$2.5^{+4.0}_{-1.3}$	1250±300	$2.0^{+3.2}_{-1.2}$
T8 V	18.7	850–750	$3.1^{+11.3}_{-1.7}$	660±150	4.7^{+17}_{-3}
T7–T8 V	18.4	950–750	$6.8^{+15.5}_{-3.9}$	1090±350	6.2^{+14}_{-4}
T6–T8 V	18.2	1050–750	$11.3^{+3.8}_{-3.8}$	2200±1300	$5.1^{+3.5}_{-3.5}$

8.2.7 The Space Density of T Dwarfs

Table 8.9 summarizes our final space density results. By propagating the uncertainties in our color bias corrections and volume estimates, we find that many of the samples cannot be constrained to better than a factor of 3–5, although results are more concise for the more heavily populated T5 and T6 groups.

When combined with our adopted M_J values, and assuming a bolometric correction BC_J that varies smoothly from spectral types T5 through T8: (Leggett et al., 1999; Burgasser et al., 2000b; Geballe et al., 2001a, Table 6.1):

$$BC_J = 2.96 - 0.11 \times SpT, , \tag{8.36}$$

we can calculate M_{bol} and thus derive the T dwarf luminosity function, $\Phi(M_{bol})$, as shown in Figure 8.25. We have plotted values for the individual subtype groups T5–T5.5, T6–T6.5, T7–T7.5, and T8; the first group has been plotted both assuming 2MASS 0559-1404 is single (open circle, dashed-line histogram) or double (filled circle, solid-line histogram). There appears to be a trend toward higher space densities for the fainter magnitudes, although the values are similar within the derived uncertainties. There does appear to be significantly fewer T5 objects than T8, however, regardless of the duplicity of 2MASS 0559-1404. This paucity is consistent with incompleteness in the T5 bin, particularly given the slightly low value derived for $\langle V/V_{max} \rangle$, and the slightly redder color of objects in this group (implying larger color bias corrections than derived). Therefore, we conclude that $\Phi(M_{bol})$ is flat within our uncertainties, with a possible indication of a rise toward fainter magnitudes.

8.3 T Dwarf Mass Function

While the derived space densities and luminosity function allow us to gauge how many T dwarfs are present in the Solar Neighborhood, or how many we are likely to detect with 2MASS or other surveys, the quantity that we ultimately seek is the substellar mass function, $\Psi(\mathrm{M}) = \frac{dN}{dM}$, as it is through mass, and not (present) brightness, that we can trace the process of star and brown dwarf formation. For stellar studies, the transformation from $\Phi(M_{bol})$ to $\Psi(\mathrm{M})$ is made through an appropriate mass-luminosity relation, essentially an inversion of the Hertzsprung-Russell diagram. This can be derived empirically (Henry & McCarthy, 1993) or from theoretical models. In the substellar regime, however, the transformation becomes ambiguous, as a brown dwarf with a fixed

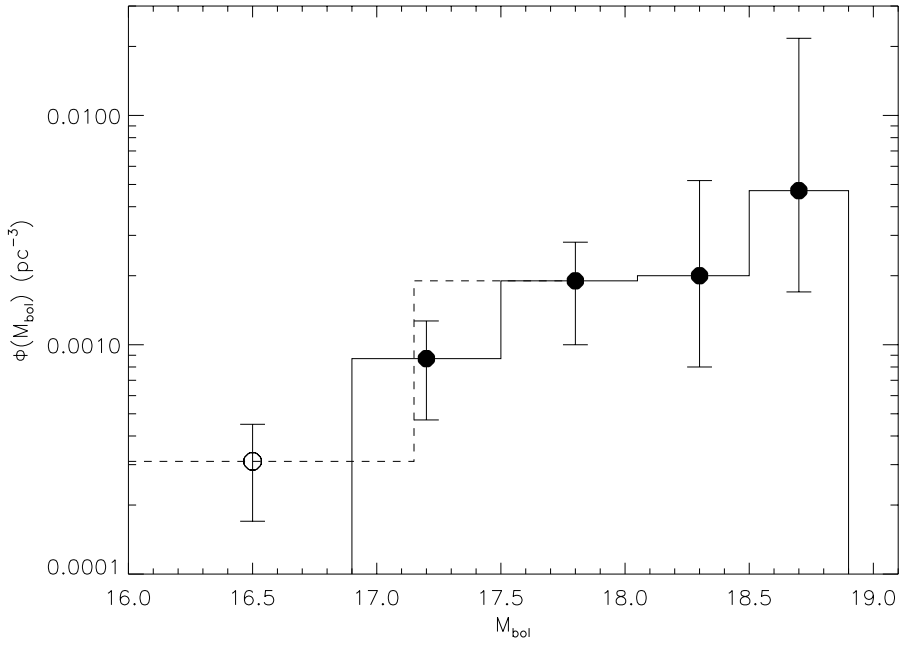

Figure 8.25: T dwarf luminosity function, $\Phi(M_{bol})$, and a function of bolometric magnitude. Space density and M_J values are those listed in Table 8.9, and we have corrected to M_{bol} using Equation 8.36. The dashed-lined histogram and open point at $M_{bol} = 16.5$ corresponds to the assumption that 2MASS 0559-1404 is single, while the neighboring point at $M_{bol} = 17.1$ assumes that it is double.

mass will have a range of luminosities as it evolves. In clusters, where one can assume a mean age for all members, this is not so critical; however, in the field, where a broad range of ages is represented, there is no direct means of converting substellar luminosities to masses, and hence no means of determining the mass function without explicit mass measurements of all objects in our sample.

We must therefore rely on the comparison of predicted observables from an assumed model to what is measured in our survey; in this case, the number density of objects as a function of spectral type, T_{eff}, or absolute brightness. Following the prescription of Reid et al. (1999b), we have constructed isotropic substellar populations through Monte Carlo simulations, using the evolutionary models of Burrows et al. (1997) and space density determinations from the 8-pc sample (Reid et al., 1999b). In §8.3.1 we describe the simulations and assumptions made, and present our results in §8.3.2. Finally, in §8.3.3, we compare our T dwarf space densities to predicted values as a function of T_{eff}, and compare our best-guess estimates to those of Reid et al. (1999b) and various cluster surveys.

8.3.1 Simulating the Solar Neighborhood

Because of limitations inherent to the available models and the derivation of the substellar mass function itself, some implicit assumptions had to be made before undertaking our simulation. The first of these is the form of the Galactic birth rate, $b(\tau)$, which can clearly influence the distribution of the time-dependent observables of brown dwarfs. Current evidence appears to be consistent with a constant birth rate over the age of the Galaxy (for a classical review see Miller & Scalo 1979). Soderblom, Duncan, & Johnson (1991) find no evidence of variation of the star formation rate over the past 10^9 years based on the activity distribution of G and K stars. Boissier & Prantzos (1999) also find little evidence for variation between recent and early times based on the metallicity distribution of G-dwarfs. Noh & Scalo (1990), however, examining the white dwarf luminosity function, find marginal support for a burst of star formation 300 Myr ago, in rough agreement with the claim of Barry (1988) that a recent increase in star formation began 400 Myr ago. The data indicative of variations in $b(\tau)$ are not definitive, however, so we follow the procedure of Reid et al. (1999b) and adopt a constant birthrate. It would be interesting in future simulations to examine the variation of observables with $b(\tau)$.

We are also constrained by the limitations of the evolutionary models of Burrows et al. (1997), which track brown dwarfs and low mass stars over ages 1 Myr $< \tau <$ 10 Gyr and masses 1 $<$ M $<$ 100 M_{Jup}. These models use grey atmospheres to determine the boundary conditions for the evolutionary calculations. The latest theoretical work from the Lyon group (Chabrier et al., 2000a) incorporates dusty photospheres self-consistently, but only span 900 $< T_{eff} <$ 2800 K and 100 Myr $< \tau <$ 10 Gyr, insufficient to cover the entire T dwarf regime. The Burrows et al. (1997) models are therefore superior in terms of parameter space explored. Chabrier et al. (2000a) find a 10% difference in T_{eff} between the adoption of DUSTY and COND atmospheres, which is an acceptable level of uncertainty for our calculations[4]. Figure 8.26 plots the evolutionary tracks of Burrows et al. (1997) in our defined parameter space. Note that stars with M $>$ 95 M_{Jup} do not evolve below T_{eff} = 2800 K.

We then constructed each test population by randomly selecting 105 test particles from the cumulative distribution

$$\begin{aligned} N(M) &= \int_M^{M+\delta M} \Psi(M')dM' \\ &\propto M^{1-\alpha}, \end{aligned} \tag{8.37}$$

where $\Psi(M) \propto M^{-\alpha}$. The choice of a power-law mass function was made in part to facilitate

[4]Note, however, the discrepancy between the Burrows et al. (1997) and Chabrier et al. (2000a) evolutionary models in Figure 1.5.

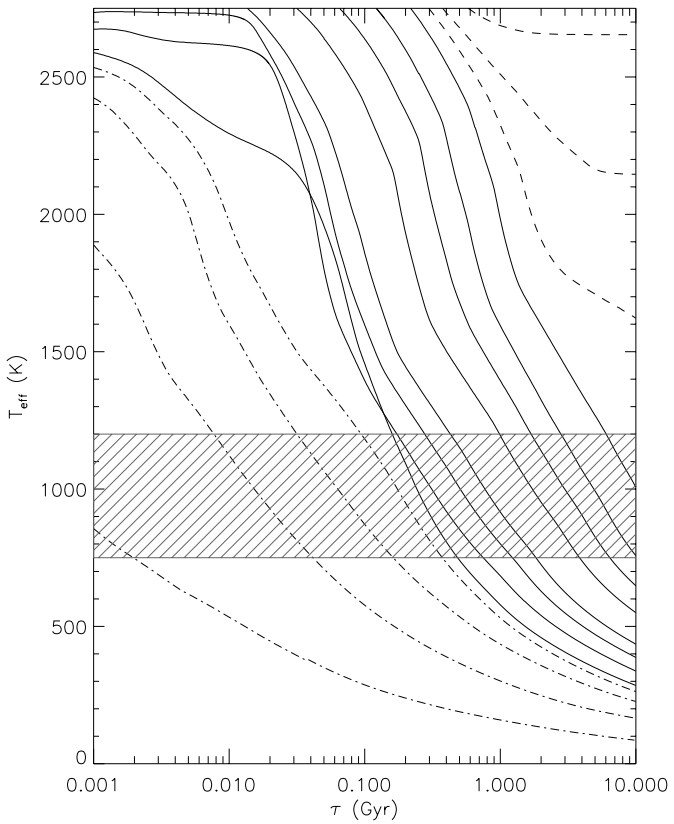

Figure 8.26: Evolutionary tracks from Burrows et al. (1997) in the $0.001 \leq \tau \leq 10$ Gyr, $T_{eff} < 2800$ K parameter space chosen for the mass function simulation. Tracks for 1, 5, 10, 13 (dot-dashed lines), 15, 20, 25, 30, 42, 52, 63, 74 (solid lines), 81, 85, and 90 M_{Jup} (dashed lines) are shown; tracks for masses greater than 95 M_{Jup} never reach temperatures below 2800 K. The hatched regions indicates the temperature range sampled by 2MASS T dwarfs.

comparison with published results, as well as for computational ease; future work may incorporate different function forms of Ψ(M) (i.e., log-normal distributions or piece-wise mass functions). We simulated various populations with $\alpha = -0.5$, 0.0, 0.5, 1.0, 1.5, 2.0, and 2.5. Objects were nominally constrained to the mass range $1 < M < 100$ M_{Jup}, although we experimented with different low-mass cutoffs, $M_{min} = 1$, 10, and 13 M_{Jup} (the latter consistent with the deuterium-burning limit). Each object was randomly assigned an age chosen from a uniform distribution between 1 Myr and 10 Gyr. We then used the Burrows et al. (1997) models to evolve these objects to their present day conditions, interpolating between different mass models when necessary. The resulting number densities were then normalized to the 8-parsec sample space density of Reid et al. (1999b), $\nu_{8pc} = 0.075$ pc^{-3} for $0.1 < M < 1.0$ $M_\odot$, by assuming a continuous mass function from 1 M_{Jup} to 1 $M_\odot$. Note that this may cause inconsistencies for populations with α significantly different than that derived by Reid et al. (1999b) for the 8pc sample[5], $\alpha_{8pc} = 1.13 \pm 0.14$ for $0.1 < M < 1.0$ $M_\odot$, or for a broken power-law. The value of ν_{8pc} corresponds to the number of stars per pc^3; using the systemic density $\nu^S_{8pc} = 0.057$ pc^{-3} results in distributions that are uniformly decreased by 24%.

8.3.2 Simulation Results

To make our comparison between empirical and simulated space densities, we chose as our medium effective temperature; i.e., $\nu(T_{eff})$. This choice avoids the need for atmospheric models to transform the model parameters (luminosity, T_{eff}, radius, mass) to band magnitudes (e.g., M_J), and we can instead rely on an empirical temperature scale based on our analysis in §7.8.4, which can be approximately expressed for T5 V through T8 V (assuming 2MASS 0559-1404 is a double) as

$$T_{eff} = 1600 - 100 \times SpT, \tag{8.38}$$

where SpT(T0) = 0, SpT(T5) = 5, etc. The temperature ranges appropriate to the various subtype samples are listed in Table 8.9. We could have just as easily made our comparison directly through the luminosity function in Figure 8.25; however, we find that effective temperature provides a more meaningful context for examining the observable evolution of brown dwarfs.

Figure 8.27 plots the simulated space densities for each of our α values, which are tabulated in Table 8.10. The approximate temperature range sampled by the 2MASS T dwarfs is indicated. The main difference between these populations is the vertical scaling, which increases by a factor of roughly 2.5 at 1500 K for each half-step increase in α. This is simply the result of the relative increase of low-mass brown dwarfs produced for higher values of α. At the low temperature end this relative increase is more pronounced as we convolve the effects of increased low-mass brown dwarf formation and the aggregate evolution of these objects. Indeed, there is a distinct turnover in space densities in the lowest values of α around 400 and 700 K. These temperatures are too low, however, for our space density measurements to sample.

We examine the contributions of different mass bins to the simulated temperature distributions in Figure 8.28, where we segregate "stars" ($75 < M < 100$ M_{Jup}; thick black line) from brown dwarfs ($13 < M < 75$ M_{Jup}; thick dark grey line) and low-mass brown dwarfs ($1 < M < 13$ M_{Jup}). Note that objects between 75 and 78 M_{Jup} are more aptly described as "transition objects" (or more precisely, high-mass brown dwarfs), as they have only evanescent hydrogen burning during their lifetimes which cannot completely compensate for radiative losses; hence, a number of these objects reach temperatures as low as 1100 K at 10 Gyr. The brown dwarf population makes up nearly all of the objects in this temperature regime, however. Very low mass objects below the deuterium-burning limit can be found in this region as well, but they do not make a significant contribution

[5]Based on the empirical mass/M_K relation of Henry & McCarthy (1993); using a theoretical calibration from Baraffe et al. (1998) yields $\alpha_{8pc} = 0.98 \pm 0.14$.

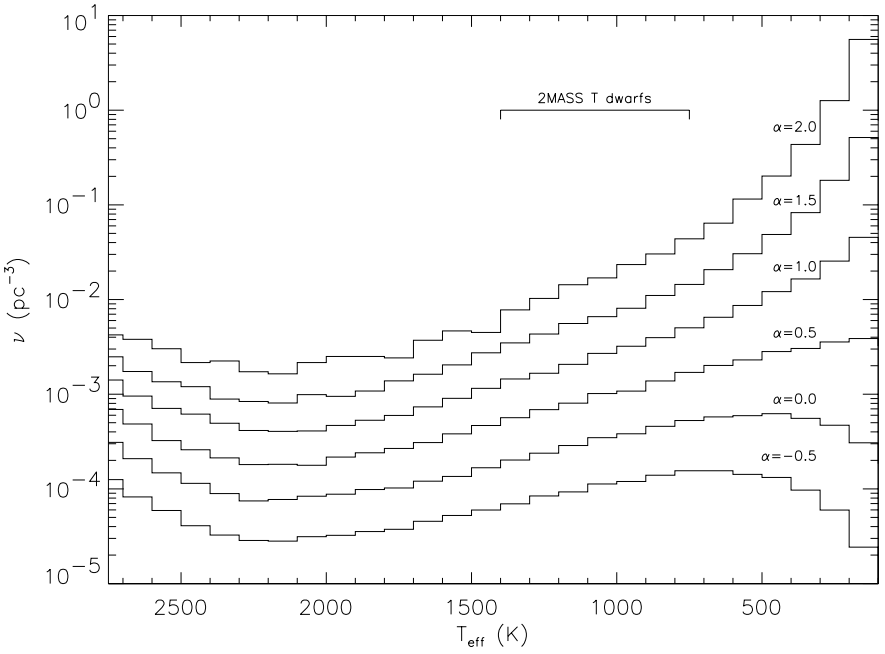

Figure 8.27: Simulated space densities as a function of T_{eff} for different power-law mass functions, $\Psi(M) \propto M^{-\alpha}$. The approximate temperature range sampled by the 2MASS T dwarfs is indicated.

Table 8.10: Space Densities from Mass Function Simulation.

	$\log \nu_\alpha$ (pc^{-3})					
T_{eff} (K)	-0.5	0.0	0.5	1.0	1.5	2.0
(1)	(2)	(3)	(4)	(5)	(6)	(7)
0–100	−6.28	−5.06	−3.73	−2.49	−1.27	−0.11
100–200	−4.62	−3.51	−2.41	−1.34	−0.29	0.75
200–300	−4.22	−3.33	−2.45	−1.59	−0.74	0.10
300–400	−4.01	−3.25	−2.52	−1.78	−1.08	−0.36
400–500	−3.88	−3.21	−2.55	−1.92	−1.31	−0.70
500–600	−3.85	−3.23	−2.64	−2.06	−1.52	−0.94
600–700	−3.81	−3.24	−2.70	−2.19	−1.68	−1.19
700–800	−3.81	−3.28	−2.77	−2.30	−1.84	−1.36
800–900	−3.86	−3.34	−2.86	−2.40	−1.96	−1.52
900–1000	−3.92	−3.42	−2.97	−2.49	−2.09	−1.63
1000–1100	−3.95	−3.46	−2.99	−2.57	−2.18	−1.77
1100–1200	−4.03	−3.54	−3.09	−2.68	−2.25	−1.84
1200–1300	−4.07	−3.62	−3.16	−2.78	−2.36	−1.99
1300–1400	−4.16	−3.69	−3.25	−2.84	−2.46	−2.11
1400–1500	−4.22	−3.78	−3.33	−2.94	−2.56	−2.35
1500–1600	−4.28	−3.87	−3.42	−3.04	−2.69	−2.33
1600–1700	−4.34	−3.92	−3.51	−3.13	−2.79	−2.43
1700–1800	−4.43	−3.99	−3.57	−3.22	−2.86	−2.62
1800–1900	−4.45	−4.01	−3.62	−3.27	−2.97	−2.60
1900–2000	−4.49	−4.06	−3.66	−3.33	−3.02	−2.60
2000–2100	−4.50	−4.08	−3.75	−3.39	−3.00	−2.67
2100–2200	−4.55	−4.11	−3.74	−3.39	−3.09	−2.78
2200–2300	−4.54	−4.13	−3.74	−3.38	−3.08	−2.76
2300–2400	−4.49	−4.05	−3.67	−3.31	−3.05	−2.65
2400–2500	−4.39	−3.94	−3.59	−3.21	−2.92	−2.67
2500–2600	−4.23	−3.83	−3.49	−3.15	−2.87	−2.52
2600–2700	−4.08	−3.68	−3.31	−3.02	−2.76	−2.42
2700–2800	−3.90	−3.51	−3.16	−2.85	−2.60	−2.37

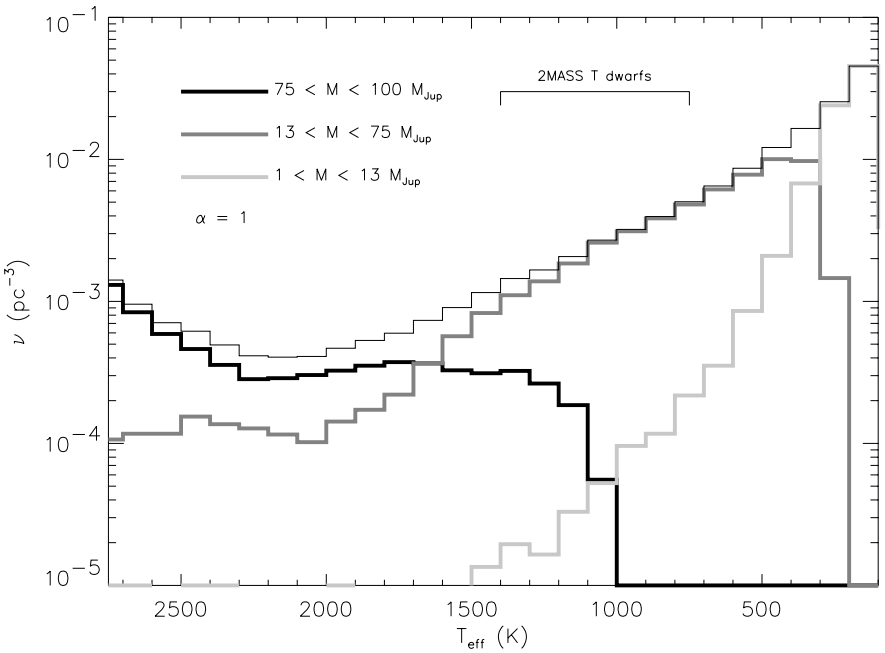

Figure 8.28: Individual contributions by stars ($75 < M < 100$ M_{Jup}; thick black line), brown dwarfs ($13 < M < 75$ M_{Jup}; thick dark grey line), and low-mass brown dwarfs ($1 < M < 13$ M_{Jup}; thick light grey line) for $\alpha = 1$. The total distribution is indicated by the thin black line. The approximate temperature range sampled by the 2MASS T dwarfs is indicated.

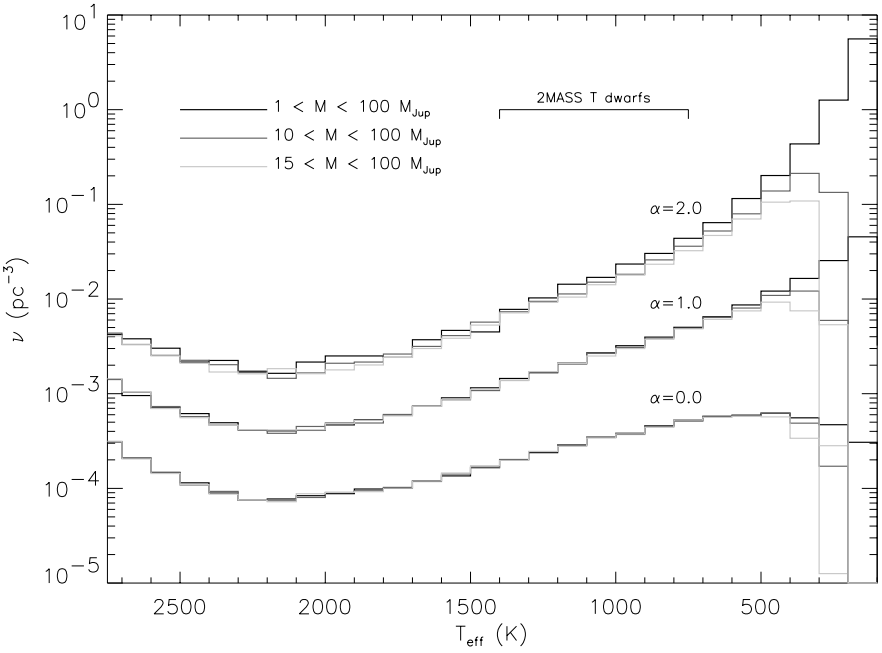

Figure 8.29: Simulated space densities for different cutoff masses: M_{min} = 1 (black), 10 (dark grey), and 13 M_{Jup} (light grey). The approximate temperature range sampled by the 2MASS T dwarfs is indicated.

above temperatures of 500 K. Only 1 out of every 33 objects with T_{eff} = 800 K will have M < 13 M_{Jup} according to these calculations.

Finally, Figure 8.29 shows the effects of adopting different values of M_{min}. The purpose of this experiment was to see if higher cut-off masses significantly influenced the resulting space densities in the T dwarf regime. While the loss of low-mass brown dwarfs dramatically reduces the number of objects for T_{eff} below 400 K, with greater effects seen for larger values of α, there is little change in the space densities at the temperatures we are sampling. Nevertheless, low-temperature brown dwarf counts in the field by SIRTF, SOFIA (e.g., pencil-beam searches), or NGSS could potentially constrain the minimum formation mass.

8.3.3 Constraints on the Substellar Mass Function and Comparison to Other Surveys

Figure 8.30 shows our space density estimates for the T dwarf subtype samples in Table 8.9 (circles) overlaid on the mass function simulations. The case for 2MASS 0559-1404 as a single object is segregated off as an open circle, and, in analogy to the luminosity function, lies at higher temperatures and lower space densities than the other subsamples. All of the values lie between $0.5 < \alpha < 1.0$, although the T5 subtype sample may be too low due to incompleteness. The rise seen in the luminosity function toward fainter subtypes can be explained by the inherent increase in the number of cool brown dwarfs in each of these mass functions, the result of aggregate thermal evolution of the population. Note, however, that our objects appear to rise more quickly than the constant α

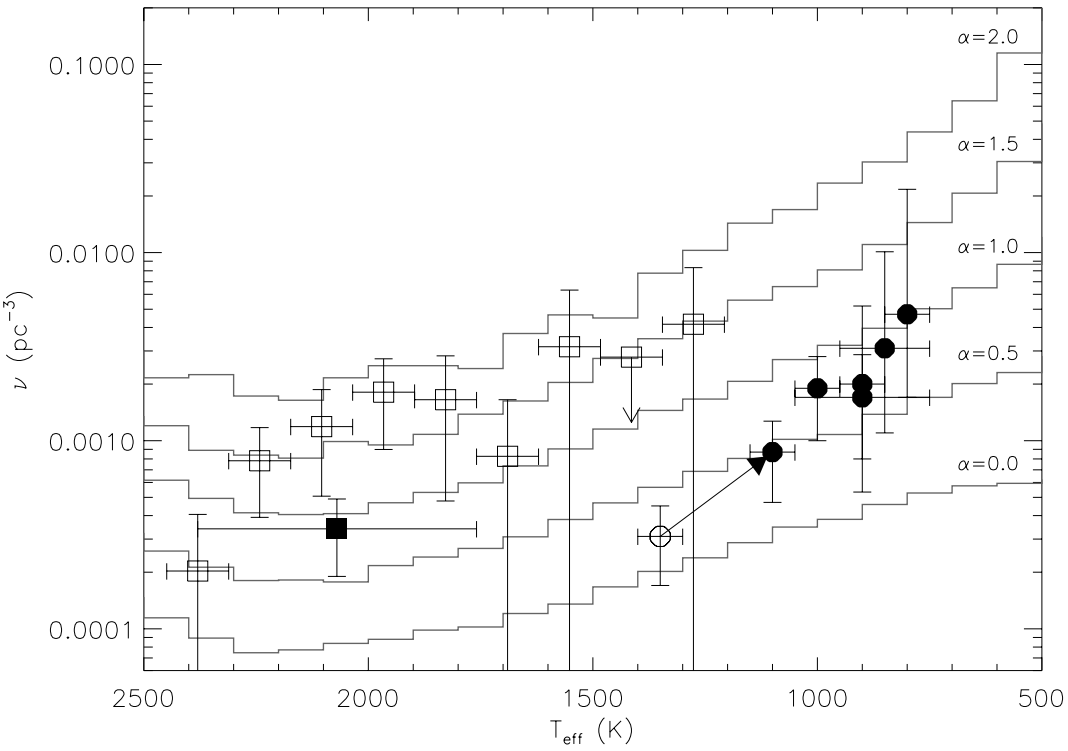

Figure 8.30: Comparison between the simulated and empirical space densities. Circles plot our T dwarf estimates, with the open circle indicating the value for the T5 V subtype sample assuming 2MASS 0559-1404 is a single object. Open squares plot estimates derived from Kirkpatrick et al. (1999b), while the solid square plots the space density estimate for L0–L4.5 V dwarfs from Gizis et al. (2000). Temperatures for the L dwarfs have been assigned using Equation 7.25.

slopes, although again the uncertainties are consistent with a flat distribution.

The value of α predicted by the T dwarf densities is significantly lower than that of Reid et al. (1999b). Based on L dwarf searches by Kirkpatrick et al. (1999b) and Delfosse et al. (1997), they predict a range of $1 < \alpha < 2$, favoring $\alpha = 1.3$. While consistent within the uncertainties for our sparse subsamples, these values are clearly too high to explain the space densities in our T6 and T7 subtype samples. We have therefore gone back and re-examined the Kirkpatrick et al. (1999b) sample to ascertain the source of this discrepancy. L dwarfs identified by these authors were selected in 371 deg^2 of 2MASS survey data. Candidates were required to have $K_s \leq 14$, $J-K_s \geq 1.3$, and no optical counterpart on POSS-I R-band plates. A total of 17 L dwarfs were identified in this sample, spanning the full range of L subtypes. By adopting mean absolute magnitudes for each subtype from values listed in Table 7.13 (corrected for known duplicity), we have used the detection numbers and magnitude limit from this search to derive rough estimates of L dwarf space densities, as listed in Table 8.11. We assume that counting errors dominate the uncertainty due to the small number of objects found in each bin. By assigning temperatures using Equation 7.25, we plotted these values in Figure 8.30. Note that the sparsity of detections in the L0 subtype sample is likely due to the

Table 8.11: L Dwarf Space Densities Derived from Kirkpatrick et al. (1999b).

Subtypes (1)	$\langle M_{bol} \rangle$ (mag) (2)	T_{eff}^a (K) (3)	N (4)	R_{max} (pc) (5)	ν (10^{-3} pc^{-3}) (6)
L0–L0.5 V[b]	10.7	2380	1±1	58	0.14±0.14
L1–L1.5 V	10.7	2240	4±2	58	0.54±0.27
L2–L2.5 V	11.2	2100	3±2	46	0.82±0.47
L3–L3.5 V	11.3	1970	4±2	44	1.3±0.6
L4–L4.5 V	11.7	1830	2±1	36	1.1±0.8
L5–L5.5 V	11.7	1690	1±1	36	0.57±0.57
L6–L6.5 V	12.7	1550	1±1	23	2.2±2.2
L7–L7.5 V	12.6	1410	0±1	24	< 1.9
L8 V	12.9	1280	1±1	21	2.9±2.9

[a]Derived from Equation 7.25.
[b]Sample believed to be incomplete due to color constraint (Reid et al., 1999b).

J−K$_s$ color cut (Reid et al., 1999b).

Clearly these values are consistent with a higher value of α, between 1 and 2, in support of the conclusions of Reid et al. (1999b). Indeed, most of the values lie above the $\alpha = 1.5$ line. However, these values have not been corrected for selection biases, and there may be systematic effects resulting in an overestimation of the true space density. Furthermore, the significant uncertainties for some of the L subtype bins make them consistent with a broad range of α values. Gizis et al. (2000) have derived the luminosity function for M8 V to L4.5 V from a magnitude-limited sample, using the V/V$_{max}$ technique (Schmidt, 1968) and corrections for Malmquist bias (Stobie, Ishida, & Peacock, 1989), deriving (2.11±0.92)×10^{-3} stars pc^{-3} for spectral types L0 V to L4.5 V. Plotting this value in Figure 8.30 (solid square), we see that these results are consistent with a lower value of $\alpha \sim 1.0$, similar to that derived for the T dwarfs. Hence, the larger values of α derived by Reid et al. (1999b) from the Kirkpatrick et al. (1999b) sample may be biased toward higher space densities or too uncertain to substantially constrain the mass function. Analysis of a larger, bias-corrected sample of L dwarfs is required to determine the origin of these discrepancies.

Finally, we can compare our results to those of recent cluster surveys which have begun to sample the full range of brown dwarf masses down to the Deuterium burning limit. Magnitude-limited surveys of the Pleiades generally favor power-law mass functions with $0 < \alpha < 1$ (Festin, 1998); Bouvier et al. (1998) find $\alpha = 0.6$, which Martín et al. (2000a) correct to 0.53 by accounting for duplicity; and Hambly et al. (1999) find $\alpha = 0.7$. In the Trapezium, Luhman et al. (2000) find $\alpha = 0.7$ in the mass range 0.035–0.56 M$_\odot$, while the Taurus cluster appears to have a much shallower relation due to the lack of brown dwarfs identified here (Luhman, 2000). The ρ Ophiuchus Cloud Core appears to follow $\alpha = 0.5$ from 0.08 to 0.4 M$_\odot$ (Luhman & Rieke, 1999). IC 348 has been studied by both Luhman et al. (1998) and Najita, Tiede, & Carr (2000), who find $\alpha = 0.6$ and 0.4–0.5, respectively, the latter measured over the entire brown dwarf range from 0.015 to 0.07 M$_\odot$. Finally, investigation of the Orion Nebula Cluster by Hillenbrand & Carpenter (2000) reveals a relatively shallow value of $\alpha = 0.43 \pm 0.05$ from 0.03–0.2 M$_\odot$. Clearly, cluster surveys are finding substellar mass functions that are quite shallow, consistent with what is seen for the field the T dwarfs. However, some of these clusters may have undergone limited mass segregation, resulting in a decrease in the number of low-mass members. Such would not be the case in the field. It is interesting to note that the higher value of α predicted by Reid et al. (1999b) is consistent with the

ρ Oph dust clump mass spectrum, scaling as $\alpha = 1.5$ for M < 0.5 M$_\odot$ (Motte, André, & Neri, 1998).

8.4 Summary

In this chapter, we have analyzed our wdb0699 search sample for the purpose of deriving a substellar mass function in the T dwarf regime. After first considering the completeness of this sample, we have rigorously derived the search volume, taking into consideration tile area and overlap, area around optical sources, confusion area around bright stars, distance scales, Malmquist bias, and duplicity. We have also examined selection biases inherent to this sample by way of Monte Carlo simulation. By matching the mean weighted colors of simulated samples to those of our candidates, we have derived appropriate corrections that take into account color selection, scattering about the cutoff magnitude, and detectability by 2MASS. We have used these results to derive a luminosity function for subtypes T5 V through T8 V, taking into account the possibility of 2MASS 0559-1404 (the luminosity standard for the T5 V subclass) being either a single or double object. The T dwarf luminosity function shows a marginal rise toward later spectral type, although the small number of detections generally restricts our ability to ascertain the reality of this rise.

We have then used the derived space densities to place constraints on the substellar mass function. Again, using Monte Carlo simulations we produced various populations of low-mass objects with 1 $<$ M $<$ 100 M$_{Jup}$ and 1 Myr $< \tau <$ 10 Gyr, assuming different power-law mass functions, a constant birth rate, and using the models of Burrows et al. (1997) to evolve the population to the current epoch. Results were normalized to the 8-parsec stellar density, 0.075 stars pc^{-3} with 0.1 $<$ M $<$ 1.0 M$_\odot$ (Reid et al., 1999b). We find that power-law mass functions with $0.5 < \alpha < 1.0$ provide the best match to our data, consistent with the low-mass stellar mass function, $\alpha \approx 1.0$. These results are at odds with the substellar mass function derived by Reid et al. (1999b) based on the L dwarf sample of Kirkpatrick et al. (1999b), where $1 < \alpha < 2$, with preference for $\alpha = 1.3$. We show that these parameters are indeed consistent with a rough estimate of the Kirkpatrick et al. (1999b) luminosity function, but without correction for selection biases. The luminosity function of Gizis et al. (2000) is more in line with what we find for the T dwarfs. Furthermore, cluster surveys universally find substellar mass functions that scale as $0 < \alpha < 1$. A more rigorous determination of the L dwarf luminosity function is required to reconcile this discrepancy.

Recieved aboard UA Flight 1215 on 4 August 2001:

```
.CHIVAUA 040233/DAV
AGM
AN N506UA/GL LAS
- /UA1215 DENLAX
- MESSAGE FROM CHIDO -

FI UA1773/AN N471UA
DT DDL DEN 040232 M13A
- /C4 DENLAX PLS SEND A MESSAGE TO
FLT 1215 AND INFORM THE
PILOTS THAT WE HAVE
PSNGR ADAM BURGASSERS
THESIS BLACK BOOK AND
WILL DELIVER TO LAX
.

CHIDO DAVE PIEKARSKI


UA 1215-03 DEN-LAX 02:33 08/04/01 .N506UA
----------------------------------------
```

Conclusions

The text is old, the orator too green.
William Shakespeare, *Venus and Adonis*

In 1995, the discovery of the uniquely cool brown dwarf Gliese 229B was announced, an object exhibiting CH_4 absorption features reminiscent of the reflectance spectrum of the giant planet Jupiter and the Saturnian moon Titan. This discovery, along with several others in concurrence, ushered in the era of observational substellar astronomy after literally decades of failed searches, false alarms, and upper limits. Yet despite the subsequent discovery of dozens of warmer brown dwarfs, including members of the newly defined L spectral class, none were found to be similar to Gliese 229B.

In this thesis, we have presented the discovery of 18 analogs to Gliese 229B, members of the spectral class T. We have identified these objects using the Two Micron All Sky Survey (2MASS), a three-band (J, H, and K_s) survey complete down J$\sim$15.8, H$\sim$15.4, and K_s $\sim$15.2, mapping the entire sky in the near-infrared. T dwarfs, which are cooler, fainter, and bluer than L dwarfs in the near-infrared, emit the majority of their flux in the 1–2.5 μm region; as such, 2MASS is perhaps the most sensitive tool currently available for identifying these very cool brown dwarfs.

We have described various early samples used to identify T dwarfs in 2MASS data. Due to limitations in selection efficiency, search area, and completeness, these early samples have been superseded by the three primary search samples described in §2.4. While each have slightly different magnitude and color constraints, they were essentially similar to our main wdb0699 sample, which includes objects with J- and H-band detections having J < 16, J$-$H < 0.3, H$-K_s < 0.3$, $|b| > 15°$, no USNO-A2.0 optical counterpart within $10''$, and no known minor planet association. The near-infrared color constraints were based on the observed colors of Gliese 229B and the high density of sources around the locus of the main sequence, while the effective optical/near-infrared color constraints were based on the known red colors of both L dwarfs and Gliese 229B. We made use of Digitized Sky Survey (DSS) scans of the POSS-I, POSS-II, SERC, and ESO surveys to eliminate faint optical sources and double stars, identified as contaminants in early search efforts. Follow-up near-infrared imaging campaigns to eliminate uncatalogued minor planets (which are prevalent in the near-infrared color space occupied by T dwarfs), and optical imaging to eliminate faint background stars (typically close to brighter optical sources) were also made. These efforts ultimately allowed us to whittle down an initial list of tens of thousands of candidates to a few dozen per sample.

We obtained spectroscopic observations of our candidate objects to determine if they were *bona fide* T dwarfs, as well as to investigate their spectral properties. Observations have confirmed the identification of 18 T dwarfs in our search samples, and have provided a means of interpreting their physical properties. Features important in the spectra of T dwarfs include the Na I and K I doublet lines centered at 5890/5896 and 7665/7699 Å, but broadened out over thousands of angstroms to produce a characteristic 7700–10000 Å red slope; additional alkali lines of Rb I at 7800 and 7948 Å, Cs I at 8521 and 8943 Å, K I at 1.169/1.177 and 1.243/1.252 μm; H_2O at 0.92, 1.15, 1.4, 1.8, and 2.4 μm; CO at 2.3 (for the early T dwarfs) and 4.7 μm; CH_4 at 0.89, 1.1, 1.35, 1.6, 2.2, and 3.3 μm; collision-induced H_2 absorption around 2.1 μm; and FeH at 0.99 μm. Not only have all of these features been detected in the spectra of T dwarfs, but they have differing strengths from object-to-object, implying that our search has uncovered not only Gliese 229B analogs, but a larger class of T dwarfs as well.

Three T dwarf discoveries were singled out for analysis: Gliese 570D, 2MASS 1237+6526, and

2MASS 0559-1404. The first is a common proper motion companion to the triple star system Gliese 570ABC. With an apparent separation of $258\farcs3 \pm 0\farcs4$, this object is the first widely-separated (a $> 1'$) brown dwarf companion found. More importantly, it is a full magnitude fainter than the only other known T dwarf companion Gliese 229B, and is roughly 200 K cooler. The temperature difference is reflected in the relatively deeper bands of H_2O and CH_4 in Gliese 570D, along with greater suppression of flux at K-band. We examined the properties of the K4 V primary in this system, and by using evolutionary models and adopting a luminosity of $(2.8 \pm 0.4)\times10^{-6}$ $L_\odot$, we have estimated the age of this object to be 6±4 Gyr, implying a mass of 52±16 M_{Jup} and temperature of 810±45 K, making Gliese 570D the coolest brown dwarf currently known.

2MASS 1237+6526 is a faint T dwarf (J = 16.03±0.09) selected in one of our early search samples. This object is distinguished by the presence of Hα emission in its optical spectrum with a relative luminosity of $\log(L_{H\alpha}/L_{bol}) = -4.3$, similar to that of late-type M dwarfs. Emission is quite unexpected in T dwarfs based on the observed decline in both emission frequency and strength beyond type M7 V. Indeed, 2MASS 1237+6526 is one of only two T dwarfs that has shown Hα in emission out of a sample of 16, and the other object, SDSS 1254-0122, is roughly 25 times less luminous in Hα flux. Furthermore, the emission appears to be steady over a 1.5 year period, as multiple epoch observations show no significant deviation in emission strength, and there appears to be no significant increase in continuum flux indicative of a flare event. After ruling out standard magnetic emission mechanisms and considering the possibility of acoustic heating and disk accretion (i.e., youth), we have proposed that 2MASS 1237+6526 may be an interacting brown dwarf binary system. In this case, an unseen, low-mass secondary overflows its Roche lobe and steadily loses mass onto the system primary. The emission line could then originate from shock heating or magnetic channelling. Given the small separations required for this scenario (a/R $\sim$ 2.5–5.5), we were able to test this hypothesis through photometric monitoring, searching for eclipsing events that are expected to occur with periods of 1–5 hours. Observations show no evidence for variability at the ±0.025 mag level for periods of 0.1–2.5 hours on two different nights. These limits rule out an interacting system with $i > 60^\circ$ and $M_2 > 22$ M_{Jup}, placing key constraints on the orientation and membership of an interacting pair. Finally, we drew analogies with another highly active dwarf, PC 0025+0446, which has shown steady emission at the $\log(L_{H\alpha}/L_{bol}) = -3.4$ level for 8 years. Observations of this object generally rule out the possibility of it being an interacting binary, and the most consistent explanation for its behavior would be youthful emission. Such may be the case for 2MASS 1237+6526, making it lowest mass brown dwarf so far identified, but further observations are required.

2MASS 0559-1404 is the brightest T dwarf so far identified, with J = 13.83±0.03, making it an excellent target for observations outside of the 1–2.5 μm spectral energy peak. Its discovery spectrum indicates that 2MASS 0559-1404 is a relatively warm T dwarf, based on its weak H_2O and CH_4 absorption, strong FeH, and greater emission at K-band. Further investigation in the red optical regime has shown the clear presence of the 7665/7699 Å K I doublet, as well as the red wing of the 5890/5896 Å Na I doublet. We find no 6708 Å Li line, which either indicates its depletion into LiCl and/or LiOH molecules, or implies that 2MASS 0559-1404 is an old, massive brown dwarf. The 3.0–4.7 μm spectrum of this object is dominated by the fundamental 3.3 μm CH_4 band, which is weaker than that seen in Gliese 229B. There are also indications of stronger CO absorption. Other molecular species such as NH_3 and H_2S are generally too weak to be detected at these wavelengths. Parallax measurements of this object made by the USNO Parallax Program show that 2MASS 0559-1404 is fairly overluminous with respect to other T dwarfs and the latest L dwarfs, suggesting that it may be a binary. HST images show no obvious companion. Based on the parallax observations, and a bolometric correction from the integrated 0.6–4.7 μm spectrum, we have estimated the temperature of this object at 1350±80 K if it is single, or 1130±70 K if it is an equal-magnitude double.

Based on the variations seen in the spectra of T dwarfs from this sample and those identified by the Sloan Digital Sky Survey, and led by the relative spectral differences in objects with well-constrained temperatures (i.e., 2MASS 0559-1404, Gliese 229B, and Gliese 570D), we have derived a classification scheme for T dwarfs. We chose to define this sequence in the near-infrared due to the greater accessibility for observation. Examination of the near-infrared spectra of the currently known population has identified seven distinct morphological groups, which we label T1 V, T2 V, T3 V, T5 V, T6 V, T7 V, and T8 V. The omissions are based on perceived incompleteness in the current sample, first (T0 V) between the latest L dwarfs and the earliest T dwarfs identified by SDSS, and second (T4 V) in the significant color differences between the latest SDSS transition object, SDSS 1021-0304, and our reddest T dwarfs (including 2MASS 0559-1404). After selecting standards in these groupings, we defined various spectral indices for the purpose of classification, based on variations in H_2O and CH_4 band strengths, near-infrared colors, and morphology of the K-band peak. We find that the H_2O bands at 1.1 and 1.4 (red wing) μm; CH_4 bands at 1.3, 1.6, and 2.2 μm; H/J and K/J colors; and the 2.11/2.07 flux ratio provide the most consistent trends among the standards. We have defined a recipe for classification using these indices by comparing them with our spectral standards. We also examined the behavior of other indices defined in the literature and find in particular that the Reid et al. (2001a) H_2O^B index is remarkably continuous from the latest M dwarfs to the latest T dwarfs. We readdressed the utility of classification in the red optical and have shown that, while data are difficult to obtain, a number of spectral indices can be defined to segregate the population into distinct subtypes, including the red wing of the broad K I line and the 9250 Å H_2O band depth. We then addressed the breadth of the L/T gap by examining the various near-infrared spectra of the L7 V DENIS 0205-1159AB found in the literature. We find evidence of a weak CH_4 feature intermittently appearing at 2.2 μm, although the variable nature of this feature requires more consistent follow-up. Nonetheless, the possible presence of CH_4 in DENIS 0205-1159 suggests that few subtypes remain between the L dwarfs (no near-infrared CH_4) and the T dwarfs. We also examined the spectra of the single "peculiar" object in our classification scheme, 2MASS 0937+2931, which has both weak K I lines and a highly suppressed K-band peak. We have speculated that this is the result of increased CIA H_2 opacity in a high-gravity or low-metallicity environment. Finally, using parallax measurements from the USNO Parallax Program, we examined brightness and effective temperature scales from early L to late T. Absolute brightness measures indicate a sharp discontinuity from late-L to mid-T. Comparison against the latest DUSTY, COND (Allard et al., 2001), and CLOUDY (Ackerman & Marley, 2001) models show that the evolution of objects across the L/T transition must occur rapidly, even under the assumption that 2MASS 0559-1404 is an equal-magnitude double. This may be due to heterogenous rainout of condensibles, as J-band flux would then be dominated by photospheric "holes" between clouds to hotter layers. The rapid evolution is reflected in our derived effective temperature scale (based on empirical bolometric corrections), which shows little change in T_{eff} between the latest L dwarfs and 2MASS 0559-1404 assuming it is double (this object is hotter than the latest L dwarfs if it is single). These calculations show that the early T dwarfs may have very dynamic atmospheres, and are excellent targets for monitoring observations to probe the effects of cloud formation.

Finally, using the wdb0699 search sample, we made constraints on the power-law index of the substellar mass function. The wdb0699 sample contains 14 T dwarf discoveries and is effectively complete, as remaining candidates appear to be close to bright optical sources, proper motion stars, or faint red background sources. Analysis of the V/V_{max} test for our T subtypes indicate that types T6 through T8 V are likely complete, while the T5 V sample is not due to our color constraints. We performed a rigorous analysis of this sample, including careful treatment of the search volume, taking into account Malmquist bias and search area lost to our selection constraints. We accounted for selection biases through a Monte Carlo simulation of our search criteria against hypothetical test

samples. The result is a luminosity function which appears to rise slightly toward fainter magnitudes. We then used Monte Carlo simulations to generate brown populations described by different power-law mass functions, $\Psi = dN/dM \propto M^{-\alpha}$. We assumed a constant birth rate from 1 Myr to 10 Gyr, using the evolutionary models of Burrows et al. (1997) and normalizing to the space density of objects $0.1 < \mathrm{M} < 1.0\ \mathrm{M}_{\odot}$ in the 8 pc sample (Reid et al., 1999b). Our results are consistent with $0.5 < \alpha < 1.0$, similar to values seen in young stellar clusters, but significantly shallower than the field mass function derived by Reid et al. (1999b) using the Kirkpatrick et al. (1999b) L dwarf sample. We believe that the discrepancy is due to selection biases in this early L dwarf sample, as our results are consistent with space density estimates by Gizis et al. (2000).

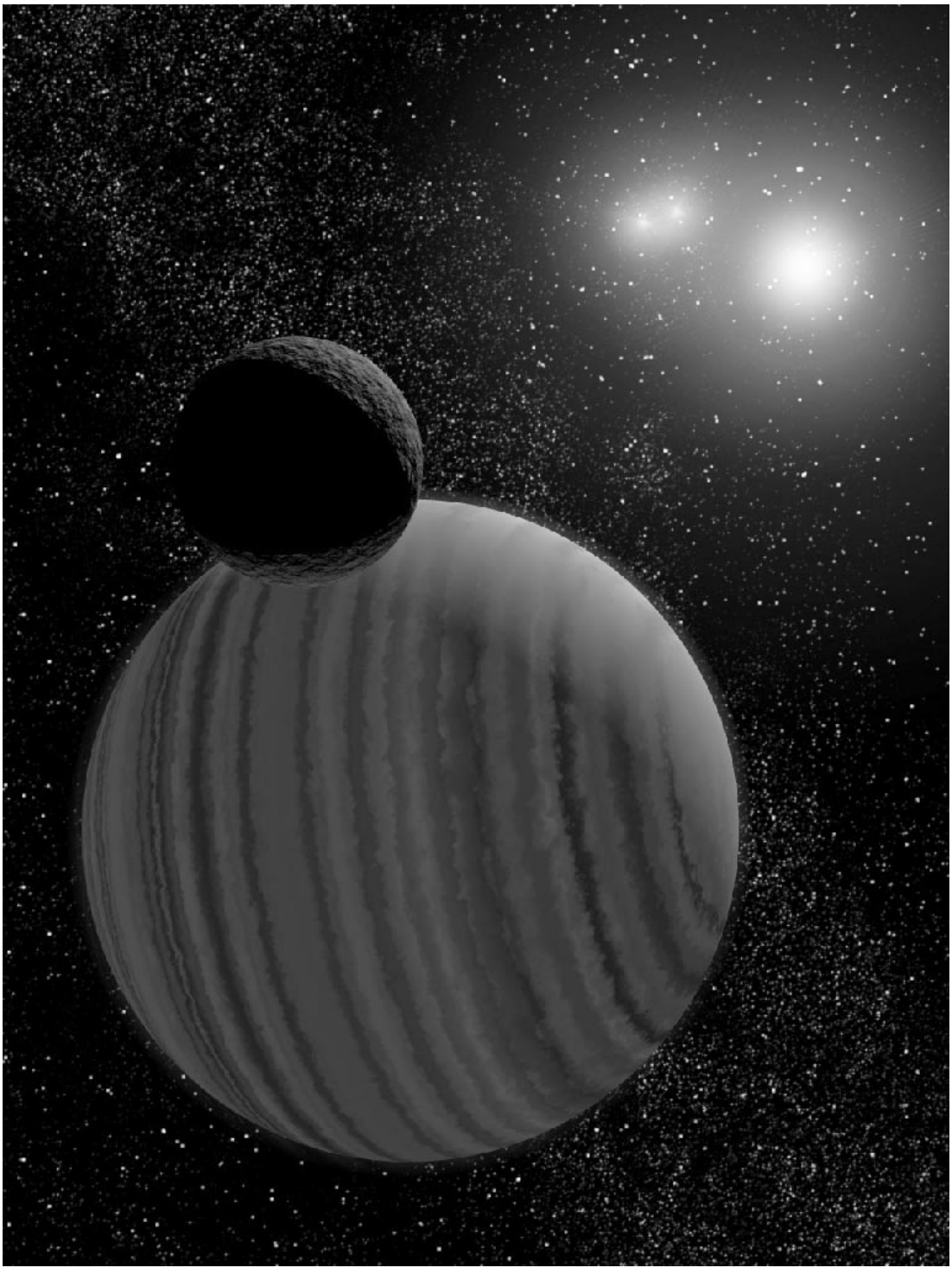

Gliese 570D plus companion. Artwork by Robert Hurt.

Appendix: T Dwarf Candidates

This Appendix contains tables and figures providing information for the wdb0699, rdb0400, and rdb0600 Samples, as described in §§2.4.2.2, 2.4.2.3, and 2.4.2.4. The tables include coordinates, 2MASS photometry, and current follow-up status for all candidates; positions, detection epochs, and possible asteroid associations for candidates unconfirmed in follow-up near-infrared imaging; observation dates and probable identifications for candidates with either optical and/or spectroscopic follow-up; and descriptions for objects either confirmed or not observed with no subsequent follow-up. Figures provide finder charts for all candidates in each Sample. This Appendix can be obtained from the following websites:

- http://www.gps.caltech.edu/~pa/adam/thesis/index.html
- http://www.astro.ucla.edu/~adam/thesis/index.html

or by contacting the author.

Bibliography

Ackerman, A. S., & Marley, M. S. 2001, ApJ, 556, in press

Alcock, C., et al. 1996, ApJ, 471, 774

Allard, F. 1990, Ph.D. Thesis, Ruprecht-Karls University, Heidelberg

Allard, F., & Hauschildt, P. H. 1995, ApJ, 445, 433

Allard, F., Hauschildt, P. H., Alexander, D. R., & Starrfield, S. 1997, ARA&A, 35, 137

Allard, F., Hauschildt, P. H., Alexander, D. R., Tamanai, A., & Schweitzer, A. 2001, ApJ, 556, 357

Allard, F., Hauschildt, P. H., Baraffe, I., & Chabrier, G. 1996, ApJ, 465, L123

Allen, D. A., & Cragg, T. A. 1983, MNRAS, 203, 777

Allende Prieto, C., & Lambert, D. L. 2000, AJ, 119, 2445

Anders, E., & Grevesse, N. 1989, Geo. Cosmo. Acta, 53, 197

Appenzeller, I., & Mundt, R. 1989, A&A Rev., 1, 291

Arias, E. F., Charlot, P., Feissel, M., & Lestrade, J.-F. 1995, A&A, 303, 604

Auman, J., Jr. 1967, ApJS, 14, 171

Baffa, C., et al. 2000, in The Scientific Dedication of the Telescopio Nazionale Galileo, in prep.

Bahcall, J. N. 1984, ApJ, 287, 926

Bailer-Jones, C. A. L. 2001, in Automated Data Analysis in Astronomy, ed. R. Gupta, H. P. Singh, & C. A. L. Bailer-Jones (New Delhi: Narosa Publishing House), in press

Bailer-Jones, C. A. L., & Mundt, R. 1999, A&A, 348, 800

—. 2001, A&A, 367, 218

Baliunas, S., Sokoloff, D., & Soon, W. 1996, ApJ, 457, L99

Baraffe, I., Chabrier, G., Allard, F., & Hauschildt, P. H. 1995, ApJ, 446, L35

—. 1998, A&A, 337, 403

—. 2001, in prep.

Barrado y Navascués, D., Stauffer, J. R., & Patten, B. M. 1999, ApJ, 522, L56

Barry, D. C. 1988, ApJ, 334, 436

Barry, D. C., Cromwell, R. H., & Hege, E. K. 1987, ApJ, 315, 264

Barsony, M., Schombert, J. M., & Kis-Halas, K. 1991, ApJ, 379, 221

Basri, G. 2000, ARA&A, 38, 485

Basri, G., & Marcy, G. W. 1995, AJ, 109, 762

Basri, G., Marcy, G. W., & Graham, J. R. 1996, ApJ, 458, 600

Basri, G., & Martín, E. L. 1999a, AJ, 118, 2460

—. 1999b, ApJ, 510, 266

Basri, G., Mohanty, S., Allard, F., Hauschildt, P. H., Delfosse, X., Martín, E. L., Forveille, T., & Goldman, B. 2000, ApJ, in press

Becklin, E. E., & Zuckerman, B. 1988, Nature, 336, 656

Beichman, C. 1987, ARA&A, 25, 521

Berger, E., et al. Nature, 410, 338

Bergeron, P., Wesemael, F., & Beauchamp, A. 1995, PASP, 107, 1047

Bessell, M. S. 1999, PASP, 111, 1426

Bessell, M. S., & Brett, J. M. 1988, PASP, 100, 1134

Bidelman, W. P. 1980, Publ. Warner & Swasey Obs., 2, 6

Biretta, J. A., et al. 2000, WFPC2 Instrument Handbook, Version 5.0 (Baltimore: STScI)

Boesgaard, A. M. 1970, ApJ, 161, 163 1990, ApJ, 351, 467

—. 1989, ApJ, 336, 798

—. 1991, ApJ, 370, L95

Boesgaard, A. M., & Friel, E. D.

Boeshaar, P. C., Tyson, J. A., & Seitzer, P. 1986, in Astrophysics of Brown Dwarfs, ed. M. Kafatos, R. S. Harrington, & S. P. Maran (Cambridge: Cambridge Univ. Press), p. 77

Bohn, H. U. 1984, A&A, 136, 338

Boissier, S., & Prantzos, N. 1999, MNRAS, 307, 857

Bookbinder, J. A. 1985, Ph.D. Thesis, Harvard University

Bopp, B. W. 1974, ApJ, 193, 389

Bouvier, J., Stauffer, J. R., Martín, E. L., Barrado y Navascués, D., Wallace, B., & Béjar, V. J. S. 1998, A&A, 336, 490

Brett, J. M. 1995, A&A, 295, 736

—. 1995, A&AS, 109, 263

Brett, J. M., & Plez, B. 1993, Proc. Astron. Soc. Australia, 10, 250

Bruzual, A. G., & Charlot, S. 1993, ApJ, 405, 538

Bryja, C., Humphreys, R. M., & Jones, T. J. 1994, AJ, 107, 246

Bryja, C., Jones, T. J., Humphreys, R. M., Lawrence, G., Pennington, R. L., & Zumach, W. 1992, ApJ, 388, L23

Buchholz, B., Ulmschneider, P., & Cuntz, M. 1998, ApJ, 494, 700

Burgasser, A. J. 2001, in The Fourth Tetons Summer Conference: Galactic Structure, Stars, and the Interstellar Medium, ed. C. W. Woodward, M. Bicay, & J. M. Schull (San Francisco: ASP), in press

Burgasser, A. J., Kirkpatrick, J. D., & Brown, M. E. 2001, in Ultracool Dwarf Stars: Proceedings of the Commissions 29 and 45, IAU General Meeting, 12 August 2000; to be published in Lecture Notes in Physics, ed. H. R. A. Jones & I. Steele (Heidelberg: Springer-Verlag), in press

Burgasser, A. J., Kirkpatrick, J. D., Reid, I. N., Liebert, J., Gizis, J. E., & Brown, M. E. 2000a, AJ, 120, 473

Burgasser, A. J., et al. 1998, BAAS, 193, 98.03

—. 1999, ApJ, 522, L65

—. 2000b, ApJ, 531, L57

—. 2000c, AJ, 120, 1100

—. 2000d, in From Giant Planets to Cool Stars, ASP Conf. Ser. 212, ed. C. A. Griffith & M. S. Marley (San Francisco: ASP), p. 65

—. 2001, ApJ, 563, in press

Burrows, A., Hubbard, W. B., & Lunine, J. I. 1989, ApJ, 345, 939

Burrows, A., Hubbard, W. B., Lunine, J. I., & Liebert, J. 2001, Rev. of Modern Physics, in press

Burrows, A., Hubbard, W. B., Saumon, D., & Lunine, J. I. 1993, ApJ, 406, 158

Burrows, A., & Liebert, J. 1993, Rev. Mod. Phys. 65, 301

Burrows, A., Marley, M. S., & Sharp, C. M. 2000, ApJ, 531, 438

Burrows, A., & Sharp, C. M. 1999, ApJ, 512, 843

Burrows, A., et al. 1997, ApJ, 491, 856

Buzasi, D. L. 1997, ApJ, 484, 855

Campbell, B., Walker, G. A. H., & Yang, S. 1988, ApJ, 331, 902

Cannon, A. J., & Pickering, E. C. 1901, Harvard College Observ. Ann., 28(II), 131

Cao, L. 1998, IAUC, 6994

Carpenter, J. M. 2001, AJ, 121, 2851

Carraro, G., Ng, Y. K., & Portinari, L. 1998, MNRAS, 296, 1045

Carter, B. S. 1990, MNRAS, 242, 1

Carter, B. S., & Meadows, V. S. 1995, MNRAS, 276, 734

Casali, M. M., & Hawarden, T. G. 1992, UKIRT Newsletter, 4, 33

Chabrier, G., & Baraffe, I. 1997, A&A, 327, 1039

—. 2000, ARA&A, 38, 337

Chabrier, G., Baraffe, I., Allard, F., & Hauschildt, P. 2000a, ApJ, 542, 464

Chabrier, G., Baraffe, I., & Plez, B. 1996, ApJ, 459, L91

Chabrier, G., Prassard, P., Fonatine, G., & Saumon, D. 2000b, ApJ, 543, 216

Chandrasekhar, S. 1939, An Introduction to the Study of Stellar Structure (New York: Dover)

Cuby, J. G., Saracco, P., Moorwood, A. F. M., D'Odorico, S., Lidman, C., Comerón, F., & Spyromilio, J. 1999, A&A, 349, L41

Cumming, A., Marcy, G. W., & Butler, R. P. 1999, ApJ, 526, 890

Cutri, R., et al. 1999, Explanatory Supplement to the 2MASS First Incremental Data Release, http://www.ipac.caltech.edu/2mass/releases/first/doc/explsup.html

—. 2001, Explanatory Supplement to the 2MASS Second Incremental Data Release, http://www.ipac.caltech.edu/2mass/releases/second/doc/explsup.html

D'Antona, F. 1987, ApJ, 320, 653

D'Antona, F., & Mazzitelli, I. 1985, ApJ, 296, 502

Dahn, C. C. 1997, in Fundamental Stellar Properties, The Interaction Between Observation and Theory, IAU Symposium 189, ed. T. R. Redding, A. J. Booth, & J. Davis (Dordrecht: Kluwer), p. 19

Dahn, C. C., Liebert, J., & Harrington, R. S. 1986, AJ, 91, 621

Danielson, R. E. 1966, ApJ, 143, 949

Dawson, P. C., & De Robertis, M. M. 2000, AJ, 120, 1532

Delfosse, X., et al. 1997, A&A, 327, L25

Depoy, D. L., Atwood, B., Byard, P. L., Frogel, J., & O'Brien, T. P. 1993, in Proceedings of SPIE, Vol. 1946, ed. A. M. Fowler (Bellingham: SPIE), 667

Dick, K. A., & Fink, U. 1977, J. Quant. Spec. Radiat. Transf., 18, 433

Donahue, R. A. 1993, Ph.D. Thesis, New Mexico State University

Dorman, B., Nelson, L., & Chau, W. 1989, ApJ, 342, 1003

Drilling, J. S., & Landolt, A. U. 2000, in Allen's Astrophysical Quantities, Fourth Edition, ed. A. N. Cox (New York: Springer-Verlag), p. 381

Duncan, D. K., Frazer, J., Lanning, H. H., Baliunas, S. L., Noyes, R. W., & Vaughan, A. H. 1984, PASP, 96, 707

Duquennoy, A., & Mayor, M. 1988, A&A, 200, 135

—. 1991, A&A, 248, 485

Durney, B. R., De Young, D. S., & Roxburgh, I. W. 1993, SoPh, 145, 207

Eggen, O. J. 1989, PASP, 101, 366

Eggleton, P. P. 1983, ApJ, 268, 368

Eggleton, P., & Kiseleva, L. 1995, ApJ, 455, 640

Elias, J. H., Frogel, J. A., Hyland, A. R., & Jones, T. J. 1983, AJ, 88, 1027

Elias, J. H., Frogel, J. A., Matthews, K. & Neugebauer, G. 1982, AJ, 87, 1029

Epchtein, N., et al. 1997, The Messenger, 87, 27

Fan, X., et al. 2000, AJ, 119, 928

Favata, F., Reale, F., Micela, G., Sciortino, S., Maggio, A., & Matsumoto, H. 2000, A&A, 353, 987

Fegley, B., & Lodders, K. 1996, ApJ, 472, L37

Fekel, F. C. 1997, PASP, 109, 514

Feltzing, S., & Gustafsson, B. 1998, A&AS, 129, 237

Festin, L. 1998, A&A, 333, 497

Fink, U., & Larson, H. P. 1979, ApJ, 233, 1021

Fischer, D. A., & Marcy, G. W. 1992, ApJ, 396, 178

Fleming, T. A., Giampapa, M. S., & Schmitt, J. H. M. M. 2000, ApJ, 533, 372

Fleming, T. A., Schmitt, J. H. M. M., & Giampapa, M. S. 1995, ApJ, 450, 401

Forrest, W. J., Barnett, J. D., Ninkov, Z., Skrutskie, M., & Shure, M. 1989, PASP, 101, 877

Forrest, W. J., Skrutskie, M. F., & Shure, M. 1988, ApJ, 330, L119

Forveille, T., et al. 1999, A&A, 351, 619

Fowler, A. 1904, MNRAS, 64, 16

Friel, E. D., & Boesgaard, A. M. 1992, ApJ, 387, 170

Fukugita, M., Ichikawa, T., Gunn, J. E., Doi, M., Shimasaku, K., & Schneider, D. P. 1997, AJ, 111, 1748

Gaidos, E. J., Henry, G. W., & Henry, S. M. 2000, AJ, 120, 1006

Geballe, T. R., Kulkarni, S. R., Woodward, C. E., & Sloan, G. C. 1996, ApJ, 467, 101

Geballe, T. R., Saumon, D., Leggett, S. K., Knapp, G. R., Marley, M. S., & Lodders, K. 2001a, ApJ, 556, 373

Geballe, T. R., et al. 2001b, ApJ, in prep.

Gelino, C. R., Marley, M. S., Holtzman, J. A., Ackerman, A. S., & Lodders K., ApJ, submitted

Gerardy, C. L., Fesen, R. A., Höflich, P., & Wheeler, J. G. 2000, AJ, 119, 2968

Gershberg, R. E. 1989, Mem. Soc. Astron. It., 60, 263

Gilmore, G. F., & Zeilik, M. 2000, in Allen's Astrophysical Quantities, Fourth Edition, ed. A. N. Cox (New York: Springer-Verlag), p. 471

Gizis, J. E., Kirkpatrick, J. D., Burgasser, A. J., Reid, I. N., Monet, D. G., Liebert, J., & Wilson, J. C. 2001a, ApJ, 551, L63

Gizis, J. E., Kirkpatrick, J. D., & Wilson, J. C. 2001, AJ, 121, 2185

Gizis, J. E., Monet, D. G., Reid, I. N., Kirkpatrick, J. D., Liebert, J., & Williams, R. 2000, AJ, 120, 1085

Gizis, J. E., & Reid, I. N. 1999, AJ, 117, 508

Gizis, J. E., et al. 2001b, AJ, submitted

Goldman, B., et al. 1999, A&A, 351, L5

Golimowski, D. A., Burrows, C. S., Kulkarni, S. R., Oppenheimer, B. R., & Brukardt, R. A. 1998, AJ, 115, 2579

Green, R. F., Schmidt, M., & Liebert, J. 1986, ApJS, 61, 305

Griffith, C. A., & Yelle, R. V. 1999, ApJ, 519, L85

Griffith, C. A., Yelle, R. V., & Marley, M. S. 1998, Science, 282, 2063

Grossman, A. S., Hays, D., & Graboske, H. C. 1974, A&A, 30, 95

Guenther, E. W., et al. 2000, A&A, 357, 206

Hahn, G., & Lagerkvist, C.-I. 1988, Icarus, 74, 454

Haisch, B., Strong, K. T., & Redonó, M. 1991, ARA&A, 29, 275

Halbwachs, J. L., Arenou, F., Mayor, M., Udry, S., & Queloz, D. 2000, ApJ, 355, 581

Hambly, N. C., Hawkins, M. R. S., & Jameson, R. F. 1993, A&AS, 100, 607

Hambly, N. C., Hodgkin, S. T., Cossburn, M. R., & Jameson, R. F. 1999, MNRAS, 303, 835

Hambly, N. C., Steele, I. A., Hawkins, M. R. S., & Jameson, R. F. 1995, MNRAS, 273, 505

Hamuy, M., Suntzeff, N. B., Heathcote, S. R., Walker, A. R., Gigoux, P., & Phillips, M. M. 1994, PASP, 106, 566

Hansen, C. J., & Kawaler, S. D. 1994, Stellar Interiors: Physical Principles, Structure, and Evolution (New York: Springer-Verlag)

Harris, D. E., & Johnson, H. M. 1985, ApJ, 294, 649

Harris, H. C., et al. 1999, AJ, 117, 339

Hartmann, L. 1990, in ASP Conf. Ser. 9, Cool Stars, Stellar Systems, and the Sun, ed. G. Wallerstein (San Francisco: ASP), 289

Hartmann, L., Kenyon, S., & Hartigan, P. 1993, in Planets & Protostars III, ed. E. H. Levy & J. I. Lunine (Tucson: Univ. Arizona Press), 497

Hauschildt, P. H., Lowenthal, D. K., & Baron, E. 2001, ApJS, 134, 323

Hawarden, T. G., et al. 2001, http://www.jach.hawaii.edu/JACpublic/UKIRT/astronomy/calib/faint_stds.html

Hawkins, M. R. S., & Bessell, M. S. 1988, MNRAS, 234, 177

Hawley, S. L., Gizis, J. E., & Reid, I. N. 1996, AJ, 112, 2799

Hawley, S. L., & Petterson, B. R. 1991, ApJ, 378, 725

Hayashi, C. 1961, PASJ, 13, 450

Hayashi, C., & Nakano, T. 1963, Prog. Theo. Physics, 30, 4

Hearnshaw, J. B. 1976, A&A, 51, 85

Hempelmann, A., Schmitt, J. H. M. M., Schultz, M., Ruediger, G., & Stepien, K. 1995, A&A, 295, 515

Henry, T. J., & Kirkpatrick, J. D. 1990, ApJ, 354, L29

Henry, T. J., & McCarthy, D. W.. Jr. 1990, ApJ, 350, 334

—. 1992, in Complementary Approaches to Double and Multiple Star Research, ed. H. A. McAlister & W. I. Hartkopf (San Francisco: ASP), p. 10

—. 1993, AJ, 106, 773

Henry, T. J., Soderblom, D. R., & Donahue, R. A. 1996, AJ, 111, 439

Henry, T. J., Soderblum, D. R., Donahue, R. A., & Baliunas, S. L. 1996, AJ, 111, 439

Henyey, L. G., LeLevier, R., & Levee, R. D. 1955, PASP, 67, 154

Hillenbrand, L. A., & Carpenter, J. M. 2000, ApJ, 540, 236

Howard, R. 2000, in Allen's Astrophysical Quantities, Fourth Edition, ed. A. N. Cox (New York: Springer-Verlag), p. 362

Hoxie, D. T. 1970, ApJ, 161, 1083

Hünsch, M., Schmitt, J. H. M. M., Sterzik, M. F., Voges, W. 1999, A&AS, 135, 319

Iben, I., Jr., & Renzini, A. 1983, ARA&A, 21, 271

Jameson, R. F., Sherrington, M. R., & Giles, A. B. 1983, MNRAS, 205, 39

Jameson, R. F., & Skillen, I. 1989, MNRAS, 239, 247

Jarrett, T. H., Chester, T., Cutri, R., Schneider, S., Skrutskie, M., & Huchra, J. P. 2000, AJ, 119, 2498

Johns-Krull, C. M., & Valenti, J. A. 1996, ApJ, 459, L95

Jones, H. R. A., Longmore, A. J., Allard, F., & Hauschildt, P. H. 1996, MNRAS, 280, 77

Jones, H. R. A., Longmore, A. J., Allard, F., Hauschildt, P. H., Miller, S., & Tennyson, J. 1995, MNRAS, 277, 767

Jones, H. R. A., Longmore, A. J., Jameson, R. F., & Mountain, C. M. 1994, MNRAS, 267, 413

Jones, H. R. A., & Tsuji, T. 1997, ApJ, 480, L39

Kafatos, M., Harrington, R. S., & Maran S. P. 1986, Astrophysics of Brown Dwarfs (Cambridge: Cambridge Univ. Press)

Keenan, P. C., & McNeil, R. C. 1989, ApJS, 71, 245

Kent, S. M. 1985, PASP, 97, 165

Kenworthy, M. H., et al. 2001, ApJ, 554, L67

Khare, B. N., & Sagan, C. 1984, Icarus, 60, 127

Kirkpatrick, J. D. 1998, in Brown Dwarfs and Extrasolar Planets, ASP Conf. Series 134, ed. R. Rebolo, E. L. Martín, & M. R. Zapatero-Osorio (San Francisco: ASP), p. 405

Kirkpatrick, J. D., Allard, F., Bida, T., Zuckerman, B., Becklin, E. E., Chabrier, G., & Baraffe, I. 1999a, ApJ, 519, 834

Kirkpatrick, J. D., Beichman, C. A., & Skrutskie, M. F. 1997, ApJ, 476, 311

Kirkpatrick, J. D., Dahn, C. C., Monet, D. G., Reid, I. N., Gizis, J. E., Liebert, J., & Burgasser, A. J. 2001a, AJ, 121, 3235

Kirkpatrick, J. D., Henry, T. J., & McCarthy, D. W., Jr. 1991, ApJS, 77, 417

Kirkpatrick, J. D., Kelly, D. M., Rieke, G. H., Liebert, J., Allard, F., & Wehrse, R. 1993, ApJ, 402, 643

Kirkpatrick, J. D., Liebert, J., Cruz, K. L., Gizis, J. E., & Reid, I. N. 2001b, PASP, in press

Kirkpatrick, J. D., Reid, I. N., Liebert, J., Gizis, J. E., Burgasser, A. J., Monet, D. G., Dahn, C. C., Nelson, B., & Williams, R. J. 2000, AJ, 120, 447

Kirkpatrick, J. D., et al. 1999b, ApJ, 519, 802

—. 2002, AJ, in prep.

Koerner, D. W., Kirkpatrick, J. D., McElwain, M. W., & Bonaventura, N. R. 1999, ApJ, 526, L25

Koester, D., Wegner, G., & Kilkenny, D. 1990, ApJ, 350, 329

Kraft, R. P. 1967, ApJ, 150, 551

Krishna Kumar, C. 1985, PASP, 97, 249

—. 1987, AJ, 94, 158

Krishnamurthi, A., et al. 1998, ApJ, 493, 914

Kroupa, P. 1995, ApJ, 453, 358

Kroupa, P., Tout, C. A., & Gilmore, G. 1993, MNRAS, 262, 545

Krotov, R., Wang, D., & Scoville, N. Z. 1980, ApJ, 240, 940

Kui, R. 1991, Ph.D. Thesis, National Univeristy of Australia

Kumar, S. S. 1963, ApJ, 137, 1121

Lachaume, R., Dominik, C., Lanz, T., & Habing, H. J. 1999, A&A, 348, 897

Lane, B. F., Zapatero Osorio, M. R., Britton, M. C., Martín, E. L., & Kulkarni, S. R. 2001, ApJ, in press

Latham, D. W., Stefanik, R. P., Mazeh, T., Mayor, M., & Burki, G. 1989, Nature, 339, 38

Leake, M., Gradie, J., & Morrison, D. 1978, Meteoritics, 13, 101

Leggett, S. K. 1992, ApJS, 82, 351

Leggett, S. K., Allard, F., Berriman, G., Dahn, C. C., & Hauschildt, P. H. 1996, ApJS, 104, 117

Leggett, S. K., Allard, F., Dahn, C., Hauschildt, P. H., Kerr, T. H., & Rayner, J. 2000a, ApJ, 535, 965

Leggett, S. K., Allard, F., Geballe, T., Hauschildt, P. H., & Schweitzer, A. 2001, ApJ, 548, 908

Leggett, S. K., Allard, F., & Hauschildt, P. H. 1998, ApJ, 509, 836

Leggett, S. K., & Hawkins, M. R. S. 1988, MNRAS, 234, 1065

—. 1989, MNRAS, 238, 145

Leggett, S. K., Toomey, D. W., Geballe, T. R., & Brown, R. H. 1999, ApJ, 517, L139

Leggett, S. K., et al. 2000b, ApJ, 536, L35

Leinert, C., Allard, F., Richichi, A., & Hauschildt, P. H. 2000, A&A, 353, 691

Leinert, C., Weitzel, N., Richichi, A., Eckart, A., & Tacconi-Garman, L. E. 1994, A&A, 291, L47

Lenzuni, P., Chernoff, D. F., & Salpeter, E. E. 1991, ApJS, 76, 759

Liebert, J., Cutri, R. M., Nelson, B., Kirkpatrick, J. D., Gizis, J. E., & Reid, I. N. 2000a, PASP, 112, 1315

Liebert, J., Dahn, C. C., & Monet, D. G. 1988, ApJ, 332, 891

Liebert, J., Kirkpatrick, J. D., Reid, I. N., & Fisher, M. D. 1999, ApJ, 519, L345

Liebert, J., Reid, I. N., Burrows, A., Burgasser, A. J., Kirkpatrick, J. D., & Gizis, J. E. 2000b, ApJ, 533, L155

Linsky, J. L., Wood, B. E., Brown, A., Giampapa, M. S., & Ambruster, C. 1995, ApJ, 455, 670

Liu, M. C., Graham, J. R., & Wright, G. S. 1996, ApJ, 470, 771

Livingston, W. C. 2000, in Allen's Astrophysical Quantities, Fourth Edition, ed. A. N. Cox (New York: Springer-Verlag), p. 151

Lodders, K. 1999, ApJ, 519, 793

Lodders, K., & Fegley, B., Jr. 1998, The Planetary Scientist's Companion (New York: Oxford Univ. Press)

Lomb, N. R. 1976, Ap&SS, 39, 447

Lowrance, P. J., et al. 1999, ApJ, 512, L69

—. 2000, ApJ, 541, 390

Lucas, P. W., & Roche, P. F. 2000, MNRAS, 314, 858

Luhman, K. L. 2000, ApJ, 544, 1044

Luhman, K. L., & Rieke, G. H. 1999, ApJ, 525, 440

Luhman, K. L., Rieke, G. H., Lada, C. J., & Lada, E. A. 1998, ApJ, 508, 347

Luhman, K. L., Rieke, G. H., Young, E. T., Cotera, A. S., Chen, H., Rieke, M. J., Schneider, G., Thompson, R. I. 2000, ApJ, 540, 1016

Lunine, J. I., Hubbard, W. B., Burrows, A., Wang, Y.-P., & Garlow, K. 1989, ApJ, 338, 314

Lunine, J. I., Hubbard, W. B., & Marley, M. S. 1986, ApJ, 310, 238

Luyten, W. J. 1976, LHS Catalogue (Minneapolis: Univ. Minn. Press)

—. 1979, A Catalogue of Stars with Proper Motions Exceeding 0.″5 Annually (Minneapolis: Univ. Minn. Press)

Maggio, A., Sciortino, S., Vaiana, G. S., Majer, P., Bookbinder, J., Golub, L., Harnden, F. R., Jr., & Rosner, R. 1987, ApJ, 315, 687

Malmquist, K. G. 1927, Lund. Medd. Series 11, 37

Marcy, G. W., Basri, G., & Graham, J. R. 1994, ApJ, 428, L57

Marcy, G. W., & Butler, R. P. 2000, PASP, 112, 137

Mariotti, J.-M., Perrier, C., Duquennoy, A., & Duhoux, P. 1990, A&A, 230, 77

Marley, M. S., & Ackerman, A. S. 2001, in Planetary Systems in the Universe: Observation, Formation and Evolution, IAU Symposium 202, in prep.

Marley, M. S., & Hubbard, W. B. 1988, Icarus, 73, 536

Marley, M. S., Saumon, D., Guillot, T., Freedman, R. S., Hubbard, W. B., Burrows, A., & Lunine, J. I. 1996, Science, 272, 1919

Martín, E. L. 1993, Ph.D. Thesis, Universidad de La Laguna

Martín, E. L. 1999, MNRAS, 302, 59

Martín, E. L., Basri, G., Delfosse, X., & Forveille, T. 1997, A&A, 327, L29

Martín, E. L., Basri, G., Gallegos, J. E., Rebolo, R., Zapatero Osorio, M. R., & Bejar, V. J. S. 1998a, ApJ, 499, L61

Martín, E. L., Basri, G., & Zapatero Osorio, M. R. 1999, AJ, 118, 1005

Martín, E. L., Basri, G., Zapatero Osorio, M. R., Rebolo, R., Lòpez, R. J. G. 1998b, ApJ, 507, L41

Martín, E. L., Brandner, W., & Basri, G. 1999, Science, 283, 1718

Martín, E. L., Brandner, W., Bouvier, J., Luhman, K. L., Stauffer, J., Basri, G., Zapatero Osorio, M. R., & Barrado y Navascués, D. 2000a, ApJ, 543, 299

Martín, E. L., Delfosee, X., Basri, G., Goldman, B., Forveille, T., & Zapatero Osorio, M. R. 1999, AJ, 118, 2466

Martín, E. L., Koresko, C. D., Kulkarni, S. R., Lane, B. F., & Wizinowich, P. L. 2000b, ApJ, 529, L37

Martín, E. L., Rebolo, R., Magazzú, A., & Pavlenko, Y. V. 1994, A&A, 282, 503

Martín, E. L., & Zapatero Osorio, M. R., & Lehto, H. J. 2001, ApJ, in press

Martín, E. L., et al. 1998c, ApJ, 509, L113

Mathiondakis, H., & Doyle, J. G. 1989, A&A, 224, 179

—. 1992, A&A, 262, 523

Matthews, K., Nakajima, T., Kulkarni, S. R., & Oppenheimer, B. R. 1996, AJ, 112, 1678

Matthews, K., & Soifer, B. T. 1994, in Infrared Astronomy with Arrays: The Next Generation, ed. I. McLean (Dordrecht: Kluwer), 239

Maury, A. C., & Pickering, E. C. 1897, Harvard College Observ. Ann., 28 (Part I), 1

Mayor, M., Duquennoy, A., Halbwachs, J.-L., & Mermilliod, J.-C. 1992, in Complementary Approaches to Double and Multiple Star Research, ASP Conference Series, Vol. 32, IAU Colloquium 135, ed. H. A. McAlister & W. I. Hartkopf (San Francisco: ASP), p. 73.

Mazeh, T., Goldberg, D., Duquennoy, A., & Mayor, M. 1992, ApJ, 401, 265

McCarthy, D. W., Jr., Probst, R. G., & Low, F. J. 1985, ApJ, 290, L9

McCaughrean, M., Reid, I. N., Tinney, C., Kirkpatrick, J. D., Hillenbrand, L., Burgasser, A. J., Gizis, J. E., & Hawley, S. L. 2001, Science, 291, 1487

McCook, G. P., & Sion, E. M. 1999, ApJS, 121, 1

McLean, I., et al. 2000, ApJ, 533, L45

McLean, I., et al. 2001, ApJ, submitted

Micela, G., Sciortino, S., Harnden, F. R., Jr., Kashyap, V., Rosner, R., Prosser, C. F., Damiani, F., Stauffer, J., & Caillault, J.-P. 1999, A&A, 341, 751

Monet, D. G., Dahn, C. C., Vrba, F. J., Harris, H. C., Pier, J. R., Luginbuhl, C. B., & Ables, H. D. 1992, AJ, 103, 638

Monet, D. G., et al. 1998, USNO-A2.0 Catalog (Flagstaff: USNO)

Morell, O. 1994, Ph. D. Thesis, Acta Universitas Upsaliensis

Morgan, D. H., Tritton, S. B., Savage, A., Hartley, M., & Cannon, R. D. 1992, in Digitised Optical Sky Surveys, ed. H. T. MacGillivray & E. B. Thomson (Dordrecht: Boston), p. 11

Morgan, W. 1950, Publ. Michigan Obs., 10, 33

Morgan, W. W., Keenan, P. C., & Kellman, E. 1943, An Atlas of Stellar Spectra, with an Outline of Spectral Classification (Chicago: Univ. Chicago Press)

Motte, F., André, P., & Neri, R. 1998, A&A, 336, 150

Mould, J. R. 1975, A&A, 38, 283

—. 1976, A&A, 48, 443

—. 1978, ApJ, 226, 923

Mould, J., Cohen, J., Oke, B., & Reid, N. 1994, AJ, 107, 2222

Muller, R. 2000, in Allen's Astrophysical Quantities, Fourth Edition, ed. A. N. Cox (New York: Springer-Verlag), p. 364

Murdoch, K. A., Hearnshaw, J. B., & Clark, M. 1993, ApJ, 413, 349

Murphy, D. C., Persson, S. E., Pahre, M. A., Sivaramakrishnan, A., & Djorgovski, S. G. 1995, PASP, 107, 1234

Najita, J. R., Tiede, G. P., & Carr, J. S. 2000, ApJ, 541, 977

Nakajima, T., Durrance, S. T., Golimowski, D. A., & Kulkarni, S. R. 1994, ApJ, 428, 797

Nakajima, T., Oppenheimer, B. R., Kulkarni, S. R., Golimowski, D. A., Matthews, K., & Durrance, S. T. 1995, Nature, 378, 463

Nakajima, T., Tsuji, T., Tamura, M., & Yamashita, T. 2000, PASJ, 52, 87

Nellis, W. J., Ross, M., & Holmes, N. C. 1995, Science, 269, 1249

Nelson, G. J., Robinson, R. D., Slee, O. B., Ashley, M. C. B., Hyland, A. R., Tuohy, I. R., Nikoloff, I., & Vaughan, A. E. 1986, MNRAS, 220, 91

Nelson, L. A., Rappaport, S. A., & Joss, P. C. 1986, in Astrophysics of Brown Dwarfs, ed. M. Kafatos, R. S. Harrington, & S. P. Maran (Cambridge: Cambridge Univ. Press), p. 177

Neugebauer, G., & Leighton, R. B. 1969, Two-Micron Sky Survey, A Preliminary Catalogue (Washington: NASA)

Neuhäuser, R., Guenther, E. W., Petr, M. G., Brandner, W., Huélamo, N., & Alves, J. 2000, A&A, 360, L39

Noh, H. R., & Scalo, J. 1990, ApJ, 352, 605

Noll, K. S., Geballe, T. R., Leggett, S. K., & Marley, M. S. 2000, ApJ, 541, L75

Noll, K. S., Geballe, T. R., & Marley, M. S. 1997, ApJ, 489, L87

Noyes, R. W., Hartmann, L. W., Baliunas, S. L., Duncan, D. K., & Vaughan, A. H. 1984, ApJ, 279, 763

Oke, J. B., & Gunn, J. E. 1992, PASP, 94, 586

—. 1983, ApJ, 266, 713

Oke, J. B., et al. 1995, PASP, 107, 375

Olivia, E., & Origlia, L. 1992, A&A, 254, 466

Oort, J. 1932, Bull. Astron. Inst. Netherlands, 6, 249

Oppenheimer, B. R., Basri, G., Nakajima, T., & Kulkarni, S. 1997, AJ, 113, 296

Oppenheimer, B. R., Golimowski, D. A., Kulkarni, S. R., Matthews, K., Nakajima, T., Creech-Eakman, M., & Durrance, S. T. 2001, AJ, 121, 2189

Oppenheimer, B. R., Kulkarni, S. R., Matthews, K., & Nakajima, T. 1995, Science, 270, 1478

Oppenheimer, B. R., Kulkarni, S. R., Matthews, K., van Kerkwijk, M. H. 1998, ApJ, 502, 932

Oppenheimer, B. R., Kulkarni, S. R., & Stauffer, J. R. 2000, in Protostars and Planets IV, ed. V. Mannings, A. P. Boss, & S. S. Russell (Tucson: Univ. Arizona Press), 1313

Osterbock, D. E. 1989, Astrophysics of Gaseous Nebulae and Active Galactic Nuclei (Mill Valley: University Science Books)

Pallavicini, R., Golub, L., Rosner, R., Vaiana, G. S., Ayres, T., & Linsky, J. L. 1981, ApJ, 248, 279

Parker, E. N. 1955, ApJ, 122, 293

Pavlenko, Ya., Zapatero Osorio, M. R., & Rebolo, R. 2000, A&A, 355, 245

Perrier, C., & Mariotti, J.-M. 1987, ApJ, 312, L27

Perryman, M. A. C., et al. 1997, A&A, 323, L49

—. 1998, A&A, 331, 81

Persson, S. E., Murphy, D. C., Krzeminski, W., Roth, M., & Rieke, M. J. 1998, AJ, 116, 2475

Phillips, J. G., Davis, S. P., Lindgren, B., & Balfour, W. J. 1987, ApJS, 65, 721

Pickering, E. C. 1890, Harvard College Observ. Ann., 27, 1

Piskunov, N., Wood, B. E., Linsky, J. L., Dempsey, R. C., & Ayres, T. R. 1997, ApJ, 474, 315

Powell, A. L. T. 1972, MNRAS, 155, 483

Prato, L., Ghez, A. M., Piña, R. K., Telesco, C. M., Fisher, R. S., Wizinowich, P., Lai, O., Acton, D. S., & Stomski, P. 2001, ApJ, 549, 590

Press, W. H., Teukolsky, S. A., Vetterling, W. T., Flannery, B. P. 1992, Numerical Recipes, Second Edition (New York: Cambridge University Press)

Prinn, R. G., & Barshay, S. S. 1977, Science, 198, 103

Probst, R. 1983, ApJS, 53, 335

—. 1983, ApJ, 274, 237

Probst, R. G., & O'Connell, R. W. 1982, ApJ, 252, L69

Rebolo, R., Martín, E. L., Basri, G., Marcy, G. W., & Zapatero Osorio, M. R. 1996, ApJ, 469, L53

Rebolo, R., Martín, E. L., & Magazzu, A. 1992, ApJ, 389, L83

Rebolo, R., Martín, E. L., & Zapatero Osorio, M. R. 1998, Brown Dwarfs and Extrasolar Planets, ASP Conf. Series 134 (San Francisco: ASP)

Rebolo, R., Zapatero Osorio, M. R., Madruga, S., Béjar, V. J. S., Arribas, S., & Licandro, J. 1998, Science, 282, 1309

Rebolo, R., Zapatero Osorio, M. R., & Martín, E. L. 1995, Nature, 377, 129

Reid, I. N. 1987, MNRAS, 225, 873

—. 1991, AJ, 102, 1428

Reid, I. N., Burgasser, A. J., Cruz, K., Kirkpatrick, J. D., & Gizis, J. E. 2001a, AJ, 121, 1710

Reid, I. N., & Gizis, J. E. 1997, AJ, 113, 2246

Reid, I. N., Gizis, J. E., Kirkpatrick, J. D., & Koerner, D. 2001b, AJ, 121, 489

Reid, I. N., & Hawley, S. L. 2000, New Light on Dark Stars (Chichester: Praxis)

Reid, I. N., Hawley, S. L., & Gizis, J. E. 1995, AJ, 110, 1838

Reid, I. N., Kirkpatrick, J. D., Gizis, J. E., Dahn, C. C., Monet, D. G., Williams, R. J., Liebert, J., & Burgasser, A. J. 2000, AJ, 119, 369

Reid, I. N., Kirkpatrick, J. D., Gizis, J. E., & Liebert, J. 1999a, ApJ, 527, L105

Reid, N., Tinney, C. G., & Mould, J. 1994, AJ, 108, 1456

Reid, I. N., et al. 1991, PASP, 103, 661

—. 1999b, ApJ, 521, 613

Rieke, G. H., & Lebofsky, M. J. 1985, ApJ, 288, 618

Rieke, G. H., & Rieke, M. J. 1990, ApJ, 362, L21

Rinaman, W. C., Heil, C., Strauss, M. T., Mascagni, M., & Sousa, M. 1996 in CRC Standard Mathematical Tables and Formulae, Thirtieth Edition, ed. D. Zwillinger (Boca Raton: CRC), p. 569

Rocha-Pinto, H. J., & Maciel, W. 1998, MNRAS, 298, 332

Rosenthal, E. D., Gurwell, M. A., & Ho, P. T. P. 1996, Nature, 384, 243

Rudy, R. J., Erwin, P., Rossano, G. S., & Puetter, R. C. 1992, ApJ, 384, 536

Ruiz, M. T., Leggett, S. K., & Allard, F. 1997, ApJ, 491, L107

Rutledge, R. E., Basri, G., Martín, E. L., & Bildsten, L. 2000, ApJ, 538, L141

Saar, S. H., & Osten, R. A. 1997, MNRAS, 284, 803

Salpeter, E. E. 1955, ApJ, 121, 161

Saumon, D., Bergeron, P., Lunine, J. I., Hubbard, W. B., & Burrows, A. 1994, ApJ, 424, 333

Saumon, D., Chabrier, G., & Van Horn, H. M. 1995, ApJS, 99, 713

Saumon, D., Geballe, T. R., Leggett, S. K., Marley, M. S., Freedman, R. S., Lodders, K., Fegley, B., Jr., & Sengupta, S. K. 2000, ApJ, 541, 374

Scargle, J. D. 1982, ApJ, 263, 835

Schiavon, R. P., Barbuy, B., & Singh, P. D. 1997, ApJ, 484, 499

Schmidt, M. 1968, ApJ, 151, 393

Schneider, D. P., Greenstein, J. L., Schmidt, M., & Gunn, J. E. 1991, AJ, 102, 1180

Schneider, D. P., Gunn, J. E., & Hoessel, J. G. 1983, ApJ, 264, 337

Schrijver, C. J. 1987, A&A, 172, 111

Schweitzer, A., Gizis, J. E., Hauschildt, P. H., Allard, F., & Reid, I. N. 2001, ApJ, 555, 368

Secchi, A., Father 1867, MNRAS, 28, 196

Shipman, H. L. 1986, in Astrophysics of Brown Dwarfs, ed. M. Kafatos, R. S. Harrington, & S. P. Maran (Cambridge: Cambridge Univ. Press), p. 71

Shu, F. H., Adams, F. C., & Lizano, S. 1987, ARA&A, 25, 23

Simons, D. A., & Becklin, E. E. 1992, ApJ, 390, 431

Skrutskie, M. F. 1990, in Astrophysics with Infrared Arrays, ASP Conf. Series 14, ed. R. Elston (San Francisco: ASP), p. 304

Skrutskie, M. F., Forrest, W. J., & Shure, M. 1989, ApJ, 312, L55

—. 1989, AJ, 98, 1409

Skrutskie, M. F., et al. 1997, in The Impact of Large-Scale Near-IR Sky Surveys, ed. F. Garzon (Dordrecht: Kluwer), p. 25

Skumanich, A. 1972, ApJ, 171, 565

Smith, D. W., Johnson, P. E., Buckingham, W. L., & Shorthill, R. W. 1992, Icarus, 99, 485

Soderblom, D. R., Duncan, D. K., Johnson, D. R. H. 1991, ApJ, 375, 722

Soderblom, D. R., Fedele, S. B., Jones, B. F., Stauffer, J. R., & Prosser, C. F. 1993a, AJ, 106, 1080 (erratum 1995, AJ, 109, 1402)

Soderblom, D. R., Jones, B. F., Balachandran, S., Stauffer, J. R., Duncan, D. K., Fedele, S. B., & Hudon, J. D. 1993b, AJ, 106, 1059

Soderblom, D. R., Pilachowski, C., Fedele, S. B., & Jones, B. F. 1993c, AJ, 105, 2299

Spiegel, E. A., & Weiss, N. O. 1980, Nature, 287, 616

Stahler, S. W. 198, PASP, 100, 1474

Stahler, S. W., & Walter, F. M 1993, in Planets & Protostars III, ed. E. H. Levy & J. I. Lunine (Tucson: Univ. Arizona Press), 405

Stauffer, J. R., Hamilton, D., & Probst, R. G. 1994, AJ, 108, 155

Stauffer, J. B., & Hartmann, L. W. 1986, PASP, 98, 1233

Stauffer, J. R., Hartmann, L. W., Jones, B. J., & McNamara, B. R. 1989, ApJ, 342, 285

Stauffer, J., Herter, T., Hamilton, D., Rieke, G. H., Rieke, M. J., Probst, R., & Forrest, W. 1991, ApJ, 367, L23

Stauffer, J. R., Schild, R., Barrado y Navascués, D., Backman, D. E., Angelova, A. M., Kirkpatrick, J. D., Hambly, N., & Vanzi, L. 1998, ApJ, 504, 805

Stauffer, J. R., Schultz, G., & Kirkpatrick, J. D. 1998, ApJ, 499, 199

Stauffer, J. R., et al. 1999, ApJ, 527, 219

Steele, I. A., Jameson, R. F., Hodgkin, S. T., & Hambly, N. C. 1995, MNRAS, 275, 841

Stephens, D. C., Marley, M. S., Noll, K. S., & Chanover, N. 2001, ApJ, in press

Stern, R. A., Schmitt, J. H. M. M., & Kahabka, P. T. 1995, ApJ, 448, 683

Stevenson, D. J. 1991, ARA&A, 29, 163

—. 1999, Nature, 400, 32

Stobie, R. S., Ishida, K., & Peacock, J. A. 1989, MNRAS, 238, 709

Strassmeier, K., Washuettl, A., Granzer, Th., Scheck, M., & Weber, M. 2000, A&AS, 142, 275

Strauss, M. A., et al. 1999, ApJ, 522, L61

Stringfellow, G. S. 1986, in Astrophysics of Brown Dwarfs, ed. M. Kafatos, R. S. Harrington, & S. P. Maran (Cambridge: Cambridge Univ. Press), p. 190

Stringfellow, G., Black, D. C., & Bodenheimer, P. 1990, ApJ, 349, L59

Sykes, M. V., Cutri, R. M., Fowler, J. W., Tholen, D. J., Skrutskie, M. F., Price, S., & Tedesco, E. F. 2000, Icarus, 146, 161

Tarter, J. 1975, Ph.D. Thesis, University of California, Berkeley

Terebey, S., van Buren, D., Padgett, D. L., Hancock, T., & Brundage, M. 1998, ApJ, 507, L71

Testi, L., et al. 2001, ApJ, submitted

Thackreh, A., Jones, H., & Hawkins, M. 1997, MNRAS, 284, 507

Tholen, D. J., Tejfel, V. G., & Cox, A. N. 2000, in Allen's Astrophysical Quantities, Fourth Edition, ed. A. N. Cox (New York: Springer-Verlag), p. 293

Thoren, P., & Feltzing, S. 2000, A&A, 363, 692

Tinney, C. G. 1995, The Bottom of the Main Sequence — and Beyond (Berlin: Springer-Verlag)

—. 1996, MNRAS, 281, 644

Tinney, C. G., Delfosse, X., & Forveille, T. 1997, ApJ, 490, L95

Tinney, C. G., Delfosse, X., Forveille, T., & Allard, F. 1998, A&A, 338, 1066

Tinney, C. G., Mould, J. R., & Reid, I. N. 1993, AJ, 105, 1045

Tinney, C. G., & Reid, I. N. 1998, MNRAS, 301, 1031

Tinney, C. G., Reid, I. N., & Mould, J. R. 1993, ApJ, 414, 254

Tokunaga, A. T. 2000, in Allen's Astrophysical Quantities, Fourth Edition, ed. A. N. Cox (New York: Springer-Verlag), p. 151

Tokunaga, A. T., & Kobayashi, N. 1999, AJ, 117, 1010

Trimble, V. 1990, MNRAS, 242, 79

Tsuji, T., Ohnaka, K., & Aoki, W. 1996, A&A, 305, L1

—. 1999, ApJ, 520, L119

Tsuji, T., Ohnaka, K., Aoki, W., & Nakajima, T. 1996, A&A, 308, L29

Tsvetanov, Z. I., et al. 2000, ApJ, 531, L61

Ulmschneider, P., Theurer, J., & Musielak, Z. E. 1996, A&A, 315, 212

Ulrich, R. K. 1976, ApJ, 210, 377

Urban, S. E., Corbin, T. E., & Wycoff, G. L. 1998, AJ, 115, 2161

Ushomirsky, G., Matzner, C., Brown, E., Bildsten, L., Hilliard, V., & Schroeder, P. 1998, ApJ, 497, 253

van Altena, W. F., Lee, J. T., & Hoffleit, E. D. 1995, The General Catalog of Trignometric Stellar Parallaxes, 4^{th} Edition (New Haven: Yale Univ. Obs.)

VandenBerg, D. A., Hartwick, F. D. A., & Dawson, P. 1983, ApJ, 266, 747

Veeder, G. J., Matson, D. L., Owensby, P. D., Gradie, J. C., Bell, J. F., & Tedesco, E. F. 1995, Icarus, 114, 186

Vogt, S. S., et al. 1994, SPIE, 2198, 362

Wade, R. A., Hoessel, J. G., Elias, J. H., & Huchra, J. P. 1979, PASP, 91, 35

Wallerstein, G., & Knapp, G. R. 1998, ARA&A, 36, 369

Walter, F. M., & Barry, D. C. 1991, in The Sun in Time, ed. C. P. Sonett, M. S. Giampapa, & M. S. Matthews (Tucson: Univ. Arizona Press), 633

Walter, F. M., Bowyers, S., Linsky, J. L., & Garmice, G. 1980, ApJ, 236, L137

Westphal, J. A., Matthews, K., & Terrile, R. J. 1974, ApJ, 188, L111

White, R. D., Ghez, A. M., Reid, I. N., & Schultz, G. 1999, ApJ, 520, 811

Wielen, R. 1977, A&A, 60, 263

Wiese, W. L., Smith, M. W., & Glennon, B. M. 1966, Atomic Transition Probabilities, Vol. 1. (Washington, D. C.: GPO)

Wilson, A. G. 1952, Trans. I. A. U., 8, 335

Wilson, J. C., Skrutskie, M. F., Colonno, M. R., Enos, A. T., Smith, J. D., Henderson, C. P., Gizis, J. E., Monet, D. G., & Houck, J. R. 2001a, PASP, 113, 227

Wilson, J. C., et al. 2001b, AJ, in press

—. 2001c, ApJ, in preparation

Wilson, O. C. 1963, ApJ, 138, 832

Wing, R. F. 1991, in The Infrared Spectral Region of Stars, ed. C. Jaschek & Y. Andrillet (Cambridge: Cambridge Univ. Press), p. 301

Winglee, R. M., Dulk, G. A., & Bastian, T. S. 1986, ApJ, 309, L59

Wolf, C., et al. 1998, A&A, 338, 127

York, D. G., et al. 2000, AJ, 120, 1579

Zacharias, N., et al. 2000, AJ, 120, 2131

Zapatero Osorio, M. R., Béjar, V. J. S., Martín, E. L., Rebolo, R., Barrado y Navascuès, D., Bailer-Jones, C. A. L., & Mundt R. 2000, Science, 290, 103

Zapatero Osorio, M. R., Béjar, V. J. S., Rebolo, R., Martín, E. L., & Basri, G. 1999, ApJ, 524, L115

Zapolsky, H. S., & Salpeter, E. E. 1969, ApJ, 158, 809

Zuckerman, B., & Becklin, E. E. 1992, ApJ, 386, 260

Zwicky, F. 1933, Helvetica Phys. Acta, 6, 110